Keele
UNIVERSITY

This work is protected by copyright and other intellectual property rights and duplication or sale of all or part is not permitted, except that material may be duplicated by you for research, private study, criticism/review or educational purposes. Electronic or print copies are for your own personal, non-commercial use and shall not be passed to any other individual. No quotation may be published without proper acknowledgement. For any other use, or to quote extensively from the work, permission must be obtained from the copyright holder/s.

Understanding chromotropic materials with combined in-situ Neutron Diffraction and Raman Spectroscopy

Sarah Kathryn Dugmore
Doctorate of Philosophy in Chemistry
December 2024
Keele University

Acknowledgements

In conjunction with my supervisors Dr Richard Jones and Dr Silvia Capelli, we collaborated with groups at ISIS, Harwell and CNR, Italy. The team of HRPD: Dr Dominic Fortes, Dr Johannes Meusburger, Dr Sacha Fop and Dr Christopher Howard, with further support from Dr Chris Ridley and Dr Craig Bull as well as Dr Gavin Stenning, Dr James Taylor and, Dr Daniel Nye from the Materials Characterisation Laboratory. Dr Stewart Parker for the DFT work using CASTEP and Dr Svemir Rudiç for the TOSCA data. The team at IFAC, CNR: Dr Leonardo del Rosso and Professor Lorenzo Ulivi.

Abstract

In recent years, in many fields of scientific research, the multi-technique approach has grown into a robust method for the experimental characterisation of complex materials. The combination of diffraction, spectroscopy and other non-destructive techniques is nowadays seen as fundamental in order to understand in full the structure-properties relationship of functional materials for technological applications, especially when different techniques can be applied *in situ* to the same sample.

This thesis covers the technical development and testing of a new sample-environment equipment devoted at performing simultaneous *in situ* Raman scattering and Neutron diffraction measurements on the single crystal neutron diffractometer SXD at ISIS Neutron and Muon Facility in Harwell. This work reports the improvements to the equipment design, as well as examples of applications of the combined techniques to the study of two classes of chromotropic compounds: i) organic photo- and thermo-chromic materials, and ii) spin crossover complexes.

The organic chromic materials are Salicylaldehyde Aniline (SA) derivatives, a class of compounds that demonstrate photochromism and/or thermochromism *via* an enol to keto tautomerisation. Along with an investigation into SA derivates already known, two new SA derivates, one thermochromic and one photochromic, were structurally investigated for the first time. We identified a relationship between the dihedral angle between the two benzyl rings and the time and ease of conversion between the enol and keto states for the photochromic compounds. For the thermochromic compounds it was identified that there is a significant contribution to the chromotropism from the fluorescence displayed at low temperatures.

The Spin Crossover (SCO) complexes are metal-organic compounds that demonstrate chromotropism by effect of a change in the spin distribution of unpaired electrons in the transition metal atom, that can be induced by temperature change, light irradiation, or pressure. The investigation into SCO complexes lead

to an expansion on the structural study of Ni(cyclam)I_2, a thermochromic SCO, as well as the structural identification of a phase transition in the SCO precursor material $Co(PF_6) \cdot 6H_2O$ that was not identified before.

For the complete characterisation of the materials in this thesis, along with Raman scattering and Neutron diffraction other experimental techniques were also used: Single Crystal X-ray Diffraction (SCXRD), Infra-Red (IR) spectroscopy, NMR (^1H and ^{13}C), DSC and Inelastic Neutron Scattering (INS), as well as DFT calculations.

Contents

ACKNOWLEDGEMENTS ..... **I**

ABSTRACT ..... **II**

CONTENTS ..... **IV**

FIGURE LIST ..... **V**

CONSTANTS ..... **XIV**

1 INTRODUCTION **1**

2 TECHNIQUE FUNDAMENTALS **5**

2.1 Diffraction 5
2.2 Raman Spectroscopy 34
2.3 CASTEP 45
2.4 Neutron Spectroscopy 47

3 DEVELOPMENT OF *IN SITU* RAMAN SCATTERING AND NEUTRON DIFFRACTION **52**

4 PHOTOCHROMISM AND THERMOCHROMISM IN SALICYLALDEHYDE ANILINE DERIVATIVES **66**

4.1 Introduction and Literature Review 66
4.2 Experimental 100
4.3 Results and Discussion 164
4.3.1 Type 1: Hydroxy with single atom substitutions on either ring. *164*
4.3.2 Type 2: 3-Methoxy substituted on the aldehyde ring side. *174*
4.3.3 Type 3: 3,5-ditertbutyl substituted on the aldehyde ring side. *182*
4.4 Conclusions 254

5 SPIN CROSSOVER PHENOMENA **257**

5.1 Introduction and Literature review 257
5.2 Experimental 274
5.3 Results and Discussion 277
5.3.1 M(tetrazole)$_6$BF$_4$ *277*
5.3.2 Co(tetrazole)$_6$(PF$_6$)$_2$ *280*
5.3.3 Ni(Cyclam) *286*
5.4 Conclusion 294

6 CONCLUSIONS **298**

7 FUTURE WORK **300**

8 APPENDIX **302**

8.1 Salicylaldehyde aniline derivatives 302
8.2 Spin Crossover complexes 440

Figure List

Figure 1: Table of possible Bravais lattice types for each crystal system. Image from Research Gate[7] 6
Figure 2: Table of crystal systems and associated point groups 7
Figure 3: a) a schematic representation of different screw axis, b) a schematic representation of a glide plane[8] 7
Figure 4: Schematic representation of the diffraction phenomenon in 2-dimensional crystals. 8
Figure 5: Construction of an Ewald sphere. When the reciprocal-lattice point crosses the surface of the sphere, the trigonometric condition $1/d = (2/\lambda)\sin\theta$ is fulfilled. This is the three-dimensional illustration of Bragg's law $\lambda = 2d\sin\theta$.[9] 10
Figure 6: Example of the relationship between scattering factor and scattering angle of Carbon and Iron. 12
Figure 7: Lab X-ray machine setup including dual x-ray tubes (green arrow), sample position (red arrow), cryo temperature stream (orange) and position sensitive detector (blue arrow). 14
Figure 8: layout of ISIS neutron and muon source [Ref] 21
Figure 9: Graph showing the wavelength range for different moderator types [Ref] 23
Figure 10:Schematic of the separation by TOF of Bragg reflections occurring at parallel planes in a lattice, which would have the exact Bragg diffraction angle 25
Figure 11: image of the position of SXD relative to the Target on TS1 26
Figure 12:layout of the detectors on SXD a) real view of detector layout with Bragg peaks during an experiment, b) schematic of SXD instrument design, c) image of SXD instrument in the pit showing PMTs at the back of the detectors. 27
Figure 13: Sample environment set ups: a) Paris-Edinburgh press. b) compact stress/strain rig. c) CCR. d) furnace 28
Figure 14: : Relative scattering cross sections of atoms in both X-ray (top) and Neutron (bottom) diffraction 28
Figure 15: Spectral representation of Raman and Rayleigh scattering[Ref] 37
Figure 16: Dispersive Raman System[1] figure representation 42
Figure 17: General schematic of an indirect-geometry crystal analyser spectrometer at a spallation source.[Ref] 50
Figure 18: instrument set up on TOSCA[1] 50
Figure 19: Raman central stick schematic for TOSCA[1] 52
Figure 20: Raman central stick design for VISION[2] 53
Figure 21: slice view of the initial central stick design with labelled sections 54
Figure 22: Extended focus lens and Raman spectrometer with attached probe 54
Figure 23: Design drawings of a) first stage single chamber sample environment compared to b) the initial dual chamber 55
Figure 24: Stages of sample environment design a) initial vanadium can, b) Dual camber quartz capilliary, c) single chamber quartz capillary. 55
Figure 25: Raman Scattering Central stick a) inside the SXD sample pit and b) on the crane for moving into put 56
Figure 26: Redesign of the top of the focusing lens a) design sketch, b) 3D representation drawing, c) final redesigned product. 57
Figure 27: design schematic and final product of end stage sample environment design a) design sketch, b) final product of top flange, c) final redesigned product of capillary with screw thread top. 58
Figure 28: spectra comparing the a) dual and b) single sample chamber intensities of 3,5-di-tertbutylsalicylidene-2-iodoaniline 59
Figure 29: enclosed attachment for focusing camera at correct distance for sample 59
Figure 30: stages of design for top of central stick. a) initial design, b) drawing of upgraded top, c) photograph of upgraded top final product. 60
Figure 31: full image of final central stick design 61
Figure 32: Space position of sample environment on SXD 61
Figure 33: internal schematic of B&W Tek i-Raman Plus probe head 65
Figure 34: schematic of the transition between enol, cis-keto and trans-keto tautomers 67
Figure 35: Structures of the selected N-salicylideneanilines used in this study. 1) N-(4-hydroxy-phenyl)-2-hydroxybenzaldehyde-imine, 2) N-(5-chloro-2-hydroxybenzylidene)-4-hydroxyaniline, 3) N-(5-chloro-2-

hydroxysalicylidene)-aniline , 4) 3,5-ditertbutylsalicylidene-3-nitroaniline, 5) N-(2-hydroxy-3-methoxybenzilidene)-3-nitroaniline.....70
Figure 36: Second set of salicylaldehyde derivative compounds 6-19. 6) N-(2-hydroxy-3-methoxybenzilidene)-aniline, 7) N-(2-hydroxy-3-methoxybenzilidene)-4-hydroxyaniline, 8) N-(2-hydroxy-3-methoxybenzilidene)-4-bromoaniline, 9) N-(2-hydroxy-3-methoxybenzilidene)-4-iodoaniline, 10) 3,5-di-tertbutylsalicylideneaniline, 11) 3,5-di-tertbutylsalicylidene-4-iodoaniline, 12) 3,5-di-tertbutylsalicylidene-4-bromoaniline, 13) N-5-chlorosalicylidene-4-bromoaniline, 14) N-5-chlorosalicylidene-4-iodoaniline, 15) N-salicylidene-4-iodoaniline, 16) N-salicylidene-4-bromoaniline, 17) N-benzilidene-4-hydroxyaniline, 18) 3,5-ditertbutylsalicylidene-2-iodoaniline, 19) 3,5-di-tertbutylsalicylidene-3-iodoaniline. 71
Figure 37: structure of compound 1 **: a)** N-(4-hydroxy-phenyl)-2-hydroxybenzaldehyde-imine ,b) N-(4-hydroxy-phenyl)-2-hydroxybenzaldehyde-imine atom labelled 72
Figure 38: Polymorph (I) (left) and Polymorph (II) (right) reproduced from data[17,18].....73
Figure 39: Structure of compound 2 N-(5-chloro-2-hydroxybenzylidene)-4-hydroxyaniline (right), and labelled structure (left) 74
Figure 40: Structure of compound 3 N-(5-chloro-2-hydroxybenzylidene)-aniline 76
Figure 41: structure of compound 4 N-(2-hydroxy-3,5-di-tertbutylsalicylidene)-3-nitroaniline 77
Figure 42: Structure of compound 5 N-(2-hydroxy-3-methoxybenzilidene)-3-nitroaniline 79
Figure 43: Structure of compound 6 (6-Methoxy-2-[(E)-phenyliminomethyl]-phenol).....81
Figure 44: Structure of compound 7 2-(((4-hydroxyphenyl)imino)methyl)6-methoxyphenol 83
Figure 45: Structure of compound 8 N-(2-hydroxy-3-methoxybenzilidene)-4-bromoaniline 84
Figure 46: Structure of compound 9 N-(2-hydroxy-3-methoxysalicylidene)-4-Iodoaniline 86
Figure 47: Structure of compound 10 N-(3,5-di-tert-butylsalicylidene)aniline 88
Figure 48: Structure of compound 11 N-(3,5-di-tert-butylsalycilidene)-4-iodoaniline 90
Figure 49: Structure of compound 12 N-(3,5-di-tert-butylsalycilidene)-4-bromoaniline.....91
Figure 50: Structure of compound 13 N-5-chlorosalicylidene-4-bromoaniline(left) and 14 N-5-chlorosalicylidene-4-iodoaniline (right) 93
Figure 51: Structure of compound 15 N-salicylidene-4-iodoaniline 94
Figure 52:Structure of compound 16 N-salicylidene-4-bromoaniline 95
Figure 53: Structure of compound 17 N-benzilidene-4-hydroxyaniline.....96
Figure 54: Structures of compounds 18 3,5-ditertbutylsalicylidene-2-iodoaniline (left) and compound 19 3,5-ditertbutylsalicylidene-3-iodoaniline (right) 97
Figure 55: Reaction scheme for compound 1.....100
Figure 56: Hydrogen labelled diagram of compound 1.....101
Figure 57: ^{1}H NMR spectrum of compound 1.....102
Figure 58: Carbon numbered diagram of compound 1.....102
Figure 59: ^{13}C NMR spectrum of compound 1 103
Figure 60: Solution UV-Vis absorption spectrum of compound 1 in ethanol 103
Figure 61: IR spectrum of compound 1 crude product.....104
Figure 62: Reaction scheme for compound 2.....105
Figure 64: ^{1}H NMR spectrum of compound 2 106
Figure 63: Labelled hydrogen diagram of compound 2.....106
Figure 65: Labelled-carbon diagram of compound 2 107
Figure 66: ^{13}C NMR spectrum of compound 2 107
Figure 67: Solution UV-Vis absorption spectroscopy absorption spectrum of compound 2 in ethanol.....108
Figure 68:IR spectrum of compound 2.....108
Figure 69: Raman Spectrum of compound 2 (785 nm) 109
Figure 70: Reaction scheme for compound 3.....110
Figure 71: Labelled hydrogen diagram of compound 3.....110
Figure 72: ^{1}H NMR spectrum of compound 3 111
Figure 73: Labelled carbon diagram of compound 3 111
Figure 74: ^{13}C NMR spectrum of compound 3.....112

Figure 75: UV-Vis absorption spectrum for compound 3 in ethanol 112
Figure 76: IR spectrum of compound 3 113
Figure 77: Raman Spectrum of compound 3 (785 nm) 113
Figure 78: synthesis schematic of compound 4 114
Figure 80: ^{1}H NMR spectrum of compound 4 115
Figure 79: Labelled Hydrogen diagram of compound 4 115
Figure 81: Labelled carbon diagram of compound 4 116
Figure 82: 13C NMR spectrum of compound 4 116
Figure 83: UV-Vis absorption spectrum of compound 4 in ethanol 117
Figure 84: IR spectrum of compound 4 117
Figure 85: Reaction scheme for compound 5 119
Figure 86: labelled hydrogen diagram of compound 5 120
Figure 87: ^{1}H NMR spectrum of compound 5 120
Figure 88: labelled carbon diagram of compound 5 120
Figure 89: ^{13}C NMR spectrum of compound 5 121
Figure 90: UV-Vis absorption spectrum of compound 5 in ethanol 121
Figure 91: IR spectrum of compound 5 122
Figure 92: Raman spectrum of compound 5 at 295 K 122
Figure 93: Reaction scheme of compound 6 123
Figure 94: Labelled hydrogen diagram of compound 6 123
Figure 95: 1H NMR spectrum of compound 6 124
Figure 96: Labelled carbon diagram of compound 6 124
Figure 97: 13C NMR spectrum of compound 6 125
Figure 98: IR spectrum of compound 6 125
Figure 99: UV-Vis absorption spectrum of compound 6 in ethanol 126
Figure 100: Reaction synthesis of compound 7 127
Figure 101: Labelled hydrogen diagram of compound 7 127
Figure 102: ^{1}H NMR spectrum of compound 7 128
Figure 103: labelled carbon diagram of compound 7 128
Figure 104:13C NMR spectrum of compound 7 128
Figure 105: UV-Vis absorption spectrum of compound 7 in ethanol 129
Figure 106: IR spectrum of compound 7 129
Figure 107: Reaction scheme for compound 8 130
Figure 108: Labelled hydrogen diagram of compound 8 130
Figure 109: 1H NMR spectrum of compound 8 131
Figure 110: Labelled carbon diagram of compound 8 131
Figure 111: 13C NMR spectrum of compound 8 131
Figure 112: UV-Vis absorption spectrum of compound 8 in ethanol 132
Figure 113: IR spectrum of compound 8 132
Figure 114: Reaction scheme for compound 9 synthesis 133
Figure 115: labelled hydrogen diagram of compound 9 133
Figure 116: 1H NMR spectrum of compound 9 134
Figure 117: Labelled carbon diagram of compound 9 134
Figure 118: 13C NMR spectrum of compound 9 134
Figure 119: UV-Vis absorption spectrum of compound 9 in ethanol 135
Figure 120: Reaction scheme for compound 10 136
Figure 121: Labelled hydrogen diagram of compound 10 136
Figure 122: 1H NMR spectrum of compound 10 137
Figure 123: labelled carbon diagram of compound 10 137
Figure 124: 13C NMR spectrum of compound 10 138
Figure 125: UV-Vis absorption spectrum of compound 10 in ethanol 138

Figure 126: IR spectrum of compound 10 139
Figure 127: Reaction scheme for compound 11 140
Figure 128: labelled hydrogen diagram of compound 11 140
Figure 129: 1H NMR spectrum of compound 11 141
Figure 130: Labelled carbon diagram of compound 11 141
Figure 131: 13C NMR spectrum of compound 11 142
Figure 132: UV-Vis absorption spectrum of compound 11 in ethanol 142
Figure 133: IR spectrum of compound 11 143
Figure 134: Reaction scheme for compound 12 144
Figure 135: labelled hydrogen diagram of compound 12 144
Figure 136: 1H NMR spectrum of compound 12 145
Figure 137: labelled carbon diagram of compound 12 145
Figure 138: ^{13}C NMR spectrum of compound 12 145
Figure 139: UV-Vis absorption spectrum of compound 12 in ethanol 146
Figure 140: IR spectrum of compound 12 146
Figure 141: reaction scheme for compound 13 147
Figure 142: Photograph of stacked plates of compound 13 147
Figure 143: labelled hydrogen diagram of compound 13 148
Figure 144: 1H NMR spectrum of compound 13 148
Figure 145: labelled carbon diagram of compound 13 148
Figure 146:13C NMR spectrum of compound 13 149
Figure 147:UV-VIs absorption spectrum of compound 13 149
Figure 148: IR spectrum of compound 13 150
Figure 149: Raman Spectrum of compound 13 150
Figure 150: reaction scheme for compound 14 151
Figure 151: labelled hydrogen diagram of compound 14 151
Figure 152:1H NMR spectrum of compound 14 152
Figure 153: labelled carbon diagram of compound 14 152
Figure 154:13C NMR of compound 14 152
Figure 155: UV-Vis absorption spectrum of compound 14 153
Figure 156: IR spectrum of compound 14 153
Figure 157: reaction scheme for compound 15 154
Figure 158: Labelled hydrogen diagram of compound 15 154
Figure 159:1H NMR spectrum of compound 15 154
Figure 160: Labelled carbon diagram of compound 15 155
Figure 161:^{13}C NMR spectrum of compound 15 155
Figure 162:UV-VIs absorption spectrum of compound 15 155
Figure 163: IR spectrum of compound 15 156
Figure 164: Raman Spectrum of compound 15 156
Figure 165: reaction scheme for compound 16 157
Figure 166: labelled hydrogen diagram of compound 16 157
Figure 167:1H NMR spectrum of compound 16 157
Figure 168: Labelled carbon diagram of compound 16 158
Figure 169:13C NMR spectrum of compound 16 158
Figure 170: IR spectrum of compound 16 158
Figure 171: reaction scheme for compound 17 159
Figure 172: labelled hydrogen diagram of compound 17 159
Figure 173:1H NMR spectrum of compound 17 160
Figure 174: Labelled carbon diagram of compound 17 160
Figure 175:13C NMR spectrum of compound 17 160

Figure 176: UV-Vis absorption spectrum of compound 17 161
Figure 177: IR spectrum of compound 17 161
Figure 178: Labelled hydrogen diagram of compound 18 162
Figure 179:1H NMR spectrum of compound 18 162
Figure 180: Labelled carbon diagram of compound 18 163
Figure 181:13C NMR spectrum of compound 18 163
Figure 182: 50 % ellipsoids of N-(5-chloro-2-hydroxybenzylidene)-4-hydroxyaniline at 295 K 165
Figure 183: Images demonstrating thermochromic colour change in the material at a) 295 K and b) 120 K. 165
Figure 184: Neutron diffraction ellipsoid model of the asymmetric unit cell 166
Figure 185: General zwitterionic structure of SA compounds 166
Figure 186: packing of the unit cell from neutron diffraction at 10 K of compound 1 167
Figure 187: Raman spectra at 295 K (Top) and 100 K (Bottom) of compound 1 showing the increase of fluorescence at low temperatures 169
Figure 188: INS (orange) and combined keto and enol (blue) calculated data of 4-(2- Salicylidene)-hydroxyaniline ... 170
Figure 189: comparison of INS plots of the calculated spectrum of the pure enol tautomer (blue) against the experimental INS spectrum (orange) of compound 1 171
Figure 190: comparison of INS plots of the calculated spectrum of the pure keto tautomer (blue) against the experimental INS spectrum (orange) of compound 1 171
Figure 191: Packing of P 21/ n polymorph 172
Figure 192: Structures of compound 3 at 298 K, 140 K, 120 K - Left to Right 172
Figure 193: Compound 3 at a) 120 K from SCXRD, b) 10 K from single crystal neutron diffraction 173
Figure 194: a) Packing of $Pca2_1$ compound 3 (II) and, b) image of a crystal of compound 3 (II) used for SCXRD 174
Figure 195:Images of the crystal of compound 5 used for SCXRD at 293 K showing an orange needle and b) 130 K showing a yellow needle 175
Figure 196: Structure of triclinic polymorph N-(3-methoxysalicylidene)-4-iodoaniline at 295 K (left) and 100 K (right) 176
Figure 197: Crystal of triclinic polymorph N-(3-methoxysalicylidene)-4-iodoaniline at various temperatures left to right:- 295, 200 and 100K 176
Figure 198: distance between molecules showing halogen bonding at 295 K (left) and 100 K (right) in the triclinic polymorph of N-(3-methoxysalicylidene)-4-iodoaniline 177
Figure 199: Top packing at 295 K, Bottom packing at 100 K of the triclinic polymorph of N-(3-methoxysalicylidene)-4-iodoaniline 178
Figure 200: Packing of orthorhombic polymorph of N-(3-methoxysalicylidene)-4-iodoaniline 178
Figure 201: intermolecular distances for orthorhombic polymorph of N-(3-methoxysalicylidene)-4-iodoaniline at a) 120 K and b) 220 K 179
Figure 202: Raman Spectrum of N-(3-methoxysalicylidene)-4-iodoaniline at 295 K 180
Figure 203: crystal of 3-methoxysalycilideneaniline at 293, 200 and 100 K left to right 180
Figure 204: labelled close contacts at 50 K , 100 K, 200 K and 293 K. 181
Figure 205: a) 290 K and b) 55 K structures from X-ray diffraction of compound 10 183
Figure 206: Images of a crystal of compound 10 at 290, 120 and 55 K left to right 184
Figure 207: 250 K neutron diffraction structure of compound 10 185
Figure 208: reconstruction in reciprocal space at a) 250 K and b) 60 K of compound 10 from neutron diffraction data 185
Figure 209: reciprocal space reconstruction from X-ray diffraction at 55 K of compound 10 186
Figure 210: Raw data comparisons on detectors forward scattering (detector 6) and backscattering (detector 3) of compound 10 187
Figure 211: images of a crystal of compound 10 pre and post neutron experiment for comparison 187
Figure 212: Raman spectra collected at room temperature of compound 10 188
Figure 213: Variable temperature insitu Raman Spectra of compound 10. Orange – 60K, blue- 90 K, purple – 120 K, green – 250 K and red – 250 K <K>300 K 189

Figure 214: Keto formation monitoring region of the Insitu Raman spectra for compound 10. Orange – 60K, blue- 90 K, red – 120 K, green – 250 K. 189
Figure 215: Comparison of INS (pink) and Raman (blue) Spectra for compound 10 190
Figure 216: experimental INS for compound 10 191
Figure 217: Comparison of INS (blue) and CASTEP calculated data (orange) for compound 10 192
Figure 218: overly of the calculated Keto tautomer INS spectrum (Blue) and the experimental INS spectrum (orange) of compound 10 193
Figure 219: overly of the calculated Enol tautomer INS spectrum (Blue) and the experimental INS spectrum (orange) of compound 10 193
Figure 220: Non-irradiated (left) and irradiated (right) crystals of compound 11 195
Figure 221: a) Non-irradiated and b) Irradiated (right) states of 3,5-ditertbutylsalicylidene-3-Iodoaniline 195
Figure 222: SCXRD structures a) non-irradiated (left) and b) irradiated (right) of compound 11 201
Figure 223: Molecular structure of the non-irradiated 3,5-ditertbutylsalicylidene-3-Iodoaniline at 293 K. (Ellipsoids represented at 50% level) 202
Figure 224: ellipsoidal irradiated structure of 3,5-ditertbutylsalicylidene-3-Iodoaniline at 293 K 202
Figure 225: packing of a) Non-irradiated and b) irradiated (right) structures of compound 19 showing variations intermolecular distances. 203
Figure 226: Dihedral angles of the a) irradiated and b) non-irradiated states of compound 19. 204
Figure 227: torsion angles across C-N bridge in the a) irradiated and b) non-irradiated structures of compound 19. 205
Figure 228: SCXRD structure of compound 18: a) Enol tautomer , b) Keto tautomer. 205
Figure 229: Raman spectra of compound 11 at 298 K 206
Figure 230: 1640 - 800 cm^{-1} region of offline low temperature collection for compound 18 207
Figure 231: Comparison between insitu (Green) and High resolution (red) Raman spectra at 110 K for compound 18 207
Figure 232: Spectra of tautomer monitoring region. 11 K (Green), 50 K (Blue), 170 K(Purple), 280 K (Red) of compound 18 showing development of new peaks associated with the keto tautomer upon decreasing temperature.. 209
Figure 233: Graph showing the trend of intensities in the peaks assigned to the keto tautomer for compound 18. 209
Figure 234: Graph showing the trend of intensities in the peaks assigned to the enol tautomer for compound 18. 210
Figure 235: Graph showing the trend of intensities in the peak assigned to both tautomers for compound 18. 210
Figure 236: Raman spectra expansions demonstrating peak changes between 290 and 170 K in compound 18. 211
Figure 237: Raman spectra expansion of the lattice vibration region between 170 and 100 K of compound 18 212
Figure 238: Raman spectra expansions demonstrating peak changes between 100 and 50 K in compound 18 213
Figure 239: Raman spectra expansions demonstrating peak changes between 50 and 11 K for compound 18. 214
Figure 240: Neutron diffraction structure of compound 11 at 250 K (left) and 110 K (right) 216
Figure 241: Raman spectra of compound 11 collected in-situ when the neutron beam was on(purple) and off (red) . 217
Figure 242: Neutron diffraction structure of irradiated state of compound 11. 218
Figure 243: Raman spectra collected in-situ at 110 K (purple), 250 K (red) and RT (pink) 218
Figure 244: Comparisons of variable temperature non-irradiated and 280 K irradiated Raman spectra of compound 11. Orange- irradiated, purple – irradiated extended collection, blue- 250 K on beam line, green – 110 K on beam line and red - 295 K. 220
Figure 245: Structure for neutron diffraction experiment at 110 K of compound 18 220
Figure 246: reciprocal space reconstructions at a) 110 K and b) 10 K of compound 18 from neutron diffraction data on SXD 221
Figure 247: 50 K X-ray diffraction reciprocal space reconstruction of compound 18 222
Figure 248: comparisons of a) pre- and b) post- neutron experiment crystals, c) close up image of post neutron experiment crystal damage in 3,5-ditertbutylsalicylidene-2-iodonailine. 222
Figure 249: Variable temperature Raman spectra collected insitu of compound 18. Blue - < 30 K, red – second check at 10 K, green, 295 K, turquoise – 10 K. 223

Figure 250: expansions of insitu Raman spectra expansions. 1000- 650 cm^{-1} region (top), 650-350 cm^{-1} region (middle), 450 -40 cm^{-1} region (bottom). Blue- below 30 K, Red- 10 K, Green – 295 K. 224
Figure 251: 1350 - 1000 cm^{-1} expansion of the insitu Raman spectra for compound 18: 300 K green, <30 K blue, 10 K red. 225
Figure 252: 480-30 cm^{-1} expansion of High resolution (blue) and insitu (red) Raman spectra of compound 18 226
Figure 253: 1650-1090 cm^{-1} expansion of High resolution (blue) and in situ (red) Raman spectra of compound 18.... 226
Figure 254: 1640-1090 cm^{-1} expansion of High resolution (red) and insitu (blue) Raman spectra of compound 18 (top), 1090-60 cm^{-1} expansion of High resolution (red) and insitu (blue) Raman spectra of compound 18 (bottom).... 227
Figure 255: 1640-1090 cm^{-1} expansion of High resolution (red) and insitu (purple) Raman spectra of compound 18 (top), 1090 - 60 cm^{-1} expansion of High resolution (red) and insitu (purple) Raman spectra of compound 18 (bottom) 228
Figure 256: a) intermolecular interactions of Iodine in compound 18. b) intermolecular interactions of Iodine in compound 19. c) intermolecular interactions of Iodine in compound 11..... 230
Figure 257: Pre (a) and Post (b) irradiated crystals of N-(3,5-ditertbutylsalicylidene)-4-Bromoaniline 231
Figure 258: Crystal of compound 5 at a) 200 K and b) 120 K 231
Figure 259: images of compound 5 in three states under in situ UV-irradiation during SCXRD a) non irradiated, b) 11.5 hours irradiation, c) 16.5 hours irradiation..... 232
Figure 260: Raman spectra expansions of compound 12 showing the development of new peaks accompanying the enol to keto tautomerisation. Front-to back decreasing in temperature..... 233
Figure 262: 1680 to 1500 cm^{-1} wavenumber region of irradiated Raman spectra of compound 12 234
Figure 261: Key area Raman spectra expansion of compound 12..... 234
Figure 263: 680 to 400 cm^{-1} wavenumber region irradiated Raman spectra of compound 12..... 235
Figure 264: Raman Spectra of third set-up for compound 12. Increasing in temperature back to front. 236
Figure 265: Structure of N-(-3,5-ditertbutylsalicylidene)-3-nitroaniline at a) 295.6 K and b) 100 K 238
Figure 266: photo of the a) Non-Irradiated crystal and b) Irradiated crystal of compound 4..... 239
Figure 267: Irradiated structure of compound 4 240
Figure 268: pseudo 3 molecule asymmetric unit of 3,5-ditertbutylsalicylidene-3-nitroaniline 241
Figure 269: Raman spectra of compound 4 at 293 K..... 242
Figure 270: Irradiated and non-irradiated Raman Spectra of compound 4. Purple -post irradiation at 30 % power, Red- post irradiation at 65 % power and blue – non irradiated..... 243
Figure 271: a) Notch filters and entrance to monochromator, b) initial flight path of laser with mirror and pinholes to move the laser to the correct height, c) sample position, d) schematic of monochromator 244
Figure 272: view of irradiated sample in the sample position in the high resolution Raman scattering set up. 245
Figure 273 : Variable temperature Raman spectra of compound 4 in the non-irradiated state. Orange – 20 K, pink – 270 K, green – 70 K, red – 140 K, blue – 298 K. 245
Figure 275: 1100 to 550 cm^{-1} window of Raman spectra for compound 4. Orange – 20 K, pink – 270 K, red – 70 K, turquoise – 140 K, blue – 298 K. 246
Figure 274: 1650 to 1090 cm^{-1} window of Raman spectra for compound 4. Orange – 20 K, pink – 270 K, red – 70 K, turquoise – 140 K, blue – 298 K. 246
Figure 276: : 650 to 60 cm^{-1} window of Raman spectra for compound 4. Orange – 20 K, pink – 270 K, red – 70 K, turquoise – 140 K, blue – 298 K. 247
Figure 277: Raman spectra of the irradiated state of compound 4. Purple – 20 K irradiated, blue – 70 K irradiated, orange – 140 K irradiated, red 270 K irradiated. 248
Figure 278: expansions of Raman spectra for compound 4 irradiated state. Purple – 20 K irradiated, blue – 70 K irradiated, orange – 140 K irradiated, red 270 K irradiated. 248
Figure 279: comparison of irradiated and non-irradiated Raman spectra at 140 K (top; orange-140 K irradiated, red-140 K non-irradiated) and 295 K (bottom; blue – irradiated 30 % power, purple – irradiated 65 % power, red-non-irradiated) of compound 4 249
Figure 280: comparisons of the insitu irradiated (red) Raman spectra of compound 4 against the offline irradiated (purple) and offline non-irradiated (green) spectra. 250
Figure 281: Neutron diffraction structure of compound 4 251

Figure 282: Electronic configuration for the effect of temperature on spin transition[7] 260
Figure 283: Electronic system for the effects of pressure on spin state transitions[7] 261
Figure 284: Electronic system for iron(II) complexes[16] 263
Figure 285:Magnetic Susceptibility of Co(tetrazole)$_6$(BF_4)$_2$ between 300 and 2 K 277
Figure 286: Magnetic Susceptibility of Ni(tetrazole)$_6$(BF_4)$_2$ between 300 and 2 K with Curie-Weiss Law 278
Figure 287: Magnetic Susceptibility of Co(tetrazole)$_6$(BF_4)$_2$ between 300 and 2 K with Curie-Weiss Law 279
Figure 288: Scatter on X-ray detector from glass phase Co(tetrazole)(PF_6) 280
Figure 289: Crystal of Co(PF)$_6$ 6 H_2O 281
Figure 290: a) 295 K Rhombohedral structure of Co(PF_6) · 6 H_2O, b) 150 K Monoclinic structure of Co(PF_6) · 6 H_2O 281
Figure 291: views along the a) c-axis and b) b-axis of the 295 K Rhombohedral structure of Co(PF_6) · 6 H_2O 282
Figure 292: views along the a) a-axis and b) b-axis of the 150 K Monoclinic structure of Co(PF_6) · 6 H_2O 283
Figure 293: DSC graph of Co(H_2O)$_6$(PF_6) showing the hysteresis in the phase change between the rhombohedral high temp phase and the monoclinic low temp phase. 283
Figure 294: Hydrogen bonding in monoclinic phase of Co(H_2O)$_6$(PF_6) 284
Figure 295: Hydrogen bonding in the Rhombohedral phase of Co(H_2O)$_6$(PF_6) 285
Figure 296: Left to Right – 295, 250, 180, 120 and 90 K 286
Figure 297: Expected bond lengths and structure of the LS structure 286
Figure 298: Angles between I-Ni-N at a) 295 K and b) 90 K for Ni(cyclam)I_2 287
Figure 299: Intermolecular distances and angles at a) 90 K and b) 295 K of Ni(cyclam)I_2 288
Figure 300: Close contacts for Ni(cyclam)I_2 at 180 K 288
Figure 301: Mounted crystal of Ni(cyclam)I_2 at 300 K, 320 K, 340 K, 360 K, 370 K, 380 K, 390 K, 400 K, 410 K, 390 K, 380 K,360 K, 340 K from left to right. 289
Figure 302: Close contacts for Ni(cyclam)I_2 between 300 K and 410 K 290
Figure 303: Angles between I-Ni-N a) 400 K and b) 410 K of Ni(cyclam)I_2 290
Figure 304: I-Ni-N angle difference with respect to temperature for Ni(cyclam)I_2. 291
Figure 305: Graph of Ni-I bond length variations with respect to temperature experimental vs published for Ni(cyclam)I_2. Exp line is red upon cooling 291
Figure 306: Graph of Ni-N1 bond length variations with respect to temperature experimental vs published for Ni(cyclam)I_2. Exp line is red upon cooling 293
Figure 307: Graph of Ni-N2 bond length variations with respect to temperature experimental vs published for Ni(cyclam)I_2. Exp line is red upon cooling 293
Figure 308: Structure of the second polymorph of Ni(cyclam)I_2 294
Figure 309: Expansion 1 of ^{1}H NMR for compound 1 302
Figure 310: Expansion 2 of ^{1}H NMR for compound 1 302
Figure 311: Expansions of ^{13}C NMR spectrum for compound 1 304
Figure 312: Expansions of ^{1}H NMR spectrum for compound 2 311
Figure 313: Expansions of ^{13}C NMR spectrum for compound 2 312
Figure 314: ^{1}H NMR expansions for compound 3 315
Figure 315: Expansion of ^{13}C NMR spectrum of compound 3 316
Figure 316: ^{1}H NMR spectrum expansions for compound 4 322
Figure 317: 13C NMR spectrum expansions for compound 4 323
Figure 318: ^{1}H NMR spectrum expansions of compound 5 337
Figure 319: 13C NMR spectrum expansion of compound 5 338
Figure 320: 1H NMR spectrum expansions of compound 6 340
Figure 321: 13C NMR expansions for compound 6 341
Figure 322:1H NMR spectrum expansions for compound 7 344
Figure 323: 1H NMR spectrum expansions for compound 8 347
Figure 324: 13C NMR spectrum expansion for compound 8 348
Figure 325: 1H NMR spectrum expansion for compound 9 351
Figure 326: 13C NMR expansion for compound 9 352
Figure 327:1H NMR expansions for compound 10 356

FIGURE 328: 1H NMR SPECTRUM EXPANSIONS FOR COMPOUND 11 373
FIGURE 329: 1H NMR EXPANSIONS FOR COMPOUND 12 387
FIGURE 330: 13C NMR EXPANSIONS FOR COMPOUND 12 388
FIGURE 331: 1H NMR EXPANSIONS FOR COMPOUND 13 410
FIGURE 332: 1H NMR EXPANSIONS FOR COMPOUND 14 412
FIGURE 319: ^{13}C NMR SPECTRUM EXPANSION OF COMPOUND 15 415
FIGURE 334:1H NMR SPECTRUM EXPANSION OF COMPOUND 16 416
FIGURE 335:1H NMR SPECTRUM EXPANSIONS OF COMPOUND 18 420
FIGURE 336: 13C NMR SPECTRUM EXPANSION OF COMPOUND 18 421

Constants

Symbol	Name	Value	SI unit
e	Elementary charge	$1.602176634\times10^{-19}$	C
ħ	Reduced Planck constant	$1.05456\text{x}10^{-3}$	J s
m_p	Proton rest mass	$1.6726219237(5)\times10^{-27}$	kg
k_B	Boltzmann constant	$1.381\text{ x }10^{-23}$	$J\ K^{-1}$
h	Plank's constant	$6.626\text{x}10^{-34}$	$J\ Hz^{-1}$
M	Mass of Ion		
ω_0	angular frequency	2π/t(time in sec)	s^{-1}
$\boldsymbol{\beta}$	Inverse Boltzmann Constant by temperature	$1/k_BT$(in Kelvin)	J^{-1}
c	speed of light	299,792,458	m/s
K	Force constant		dynes/cm
ϕ	Weiss constant		

1 Introduction

The changes in the structure of molecular compounds by the application of external stimuli, in particular light and temperature, have drawn increasing attention as they offer the prospect of developing new memory storage and switching devices. Two of the most widely investigated areas are chromotropism and spin crossover materials. Chromotropism is the process for which a change in colour of a material in its crystalline state occurs by the action of external stimuli, which could be either electromagnetic radiation (photochromic materials) or heat (thermochromic materials). Photochromic materials in particular have long been used in ophthalmic lenses, with increasing interest for their use in electronic applications. Typically, photochromism is visibly seen by a deeping colour upon irradiation, while thermochromism is visibly seen as a loss of colour with a decrease in temperature, although reverse thermochromism has also been reported.

Spin crossover materials are compounds in which an external stimulus produces a change in the electronic structure of the material. Specifically this covers a change in the spin state involving the d-orbitals of a transition metal atom in a metal-organic complex, often producing a concomitant change in colour and a modification of the physical properties.

In order to understand the mechanism of reaction to the stimuli and the inter/intra-molecular interactions involved in the process, it is important to enable the “interrogation” of the structure of these functional materials while “in-action”, i.e. during the changing process.

The crystal structure of these chromic and spin-crossover materials can be studied by diffraction techniques before and after the transformations, but the result will always be a time and space averaged picture of the material. On the other hand, spectroscopic techniques can detect quite quickly any change that is occurring in a material, but without being able to precisely explain the change in term of atomic rearrangement of the atoms in the material.

The idea behind this thesis work is to combine diffraction and spectroscopy, more precisely Neutron diffraction and Raman spectroscopy, to be able to study *in situ* the evolution of these materials while subjected to external stimuli.

This work reports the process of developing the capability to measure simultaneously Neutron Diffraction and Raman scattering *in situ* on the single crystal neutron diffractometer SXD at the ISIS Neutron and Muon Facility. The development of the instrumentation and procedure for the simultaneous use of these techniques, was completed in stages as additional requirements became apparent during the testing stages and initial experiments. Issues that were addressed included ease of alignment and sample transfer, as well as orienting the crystal sample in the neutron beam. This new type of sample environment will allow, for example, for *in situ* neutron photocrystallography to be offered to users at a neutron pulsed source, which had previously been prohibitively difficult due to the enclosed nature of these type of diffraction instruments.

The combination of Neutron diffraction and Raman scattering is useful due to the differing time scales and sensitivities of the two techniques. The shorter time scale of Raman Scattering as compared to Neutron Diffraction, allows for an earlier identification of phase changes, allowing, for example, the neutron diffraction experiment to be designed in a much more effective way. Furthermore, Raman Scattering has a greater sensitivity to heavier atoms, complementing the sensitivity to lighter atoms of Neutron Diffraction.

Two classes of materials were investigated in this study: i) a series of salicylaldehyde aniline (SA) derivatives which display both types of chromotropism: photochromism, upon irradiation with UV light (365 nm) and thermochromism upon change in temperature; and ii) spin-crossover compounds, metal organic complexes that change colour due to a change in their electronic structure.

With respect to the SA derivative compounds the process by which chromotropism occurs is considered to be by a tautomerisation between enol and keto states via intramolecular transfer of a single proton, which can be precisely located only with neutron diffraction data. Due to the presence of two benzene rings in the molecule, the majority of SA derivative compounds show fluorescence under both the green (532 nm) and near IR (780/5 nm) lasers. This is particularly important in the case of thermochromic materials for which the fluorescence increases as the temperature is reduced into the temperature range where the tautomerisation is expected to occur. Hence, some considerations regarding fluorescence will have to be made during both experimental planning and the analysis of the chromotropic properties.

The phenomenon of Spin Crossover (SCO) is classified as a shift between high spin and low spin states that occur at the metal centre of the complex. SCO compounds have multiple and different ways of showing chromotropism: Thermal irradiation, Light-Induced Excited Spin State Trapping (LIESST), i.e. the change of the electronic spin state by use of light, Reverse-LIESST and Pressure. In the compounds considered herein the bi-valence metals at the centre of the complexes are Iron, Cobalt, and Nickel, while the organic ligands are 2-picolylamine (2-pic), isoxazole, tetrazole and cyclam (1,4,8,11-tetraazacyclotetradecane). SCO complexes tend to be air sensitive in nature, making the process of crystal growth and the subsequent handling for experiments particularly difficult, therefore requiring careful planning.

The compounds and complexes studied within this project, were synthesised at Keele University and ISIS by myself with two additional compounds synthesised by a student at Keele University working with Dr Richard Jones. These materials were then characterised using a variety of techniques at both Keele University and in the Materials Characterisation Laboratory at ISIS, along with the ISIS neutron experiments. These included, NMR, IR spectroscopy, Solution UV-Vis, magnetic susceptibility, as well as X-ray and Neutron diffraction, and Raman Spectroscopy. In order to complete the assignment of the Raman peaks, DFT calculations were also performed with the software package CASTEP.

In chapter 2 the major techniques used over the course of this thesis will be introduced along with the fundamentals of crystallography. In Chapter 3 the design and development of the Raman scattering central stick for use on SXD in discussed. Chapter 4 the results will be presented for the work on the salicylaldehyde aniline derivatives and the use of the central Raman scattering stick. Chapter 5 covers the production and analysis of SCO materials and their precursors. In Chapter 6 there will be overall conclusions of the thesis and possibilities for future work. Finally the appendix where extended structural data for the compounds can be found.

2 Technique Fundamentals

2.1 Diffraction

2.1.1 Fundamentals of Crystallography and Diffraction

Crystallography is the branch of science concerned with determining the mutual arrangement of atoms in crystalline solids and relating their structure to their macroscopic physical properties. Unless otherwise referenced the information in this chapter has been obtained from Principles of Neutron Scattering from condensed matter (Boothroyd, A.)[1], Crystal structure analysis (Clegg, w. *et al*)[2] and Pulsed Neutron scattering (Windsor C. G.)[3].

2.1.2 Crystals and symmetry

A crystal, or a crystalline solid, is a homogenous material in which its constituents (atoms, molecules, or motifs) are arranged in a three dimensional ordered pattern. Independently of the complexity of the motif, if this is repeated periodically along three non-planar directions at regular intervals *a, b* and *c*, such translational geometry can be described by a periodic sequence of points, called a *lattice*.

Any lattice point can be chosen to be the origin of the lattice, meaning that any other point in the lattice is defined by the vector $u\boldsymbol{a}+v\boldsymbol{b}+w\boldsymbol{c}$, where ***a, b*** and ***c*** are the basis vectors of the lattice and they define a parallelepiped, called the *unit cell*. The directions specified by these vectors are the *crystallographic axes* of the unit cell and form a right-handed, local coordinate system. The angles between the axes are indicated by α (angle between **b** and **c**), β (between **a** and **c**) and γ (between **a** and **b**) and the volume of the Unit cell is calculated as:

$$V = a \cdot b \times c = b \cdot c \times a = a \cdot c \times b. \qquad \textit{Eq. 1}$$

When a, b and c are mutually perpendicular with lattice points at the corner of the unit cell, the lattice is described as a Primitive (P) cubic lattice. If additional lattice points are located at the centre of the unit cell, or on the faces of the unit cell, different lattice types can be identified: Body-Centred (I), Face-Centred (F) and, Side-Centred (C). These are called the Bravais lattice types.

Varying the lengths of a, b, and c and/or the angles between them, one can generate seven different crystal systems: triclinic, monoclinic, orthorhombic, tetragonal, rhombohedral, hexagonal, and cubic, as can be seen in Fig 1 , though not all lattice types are possible in each system.

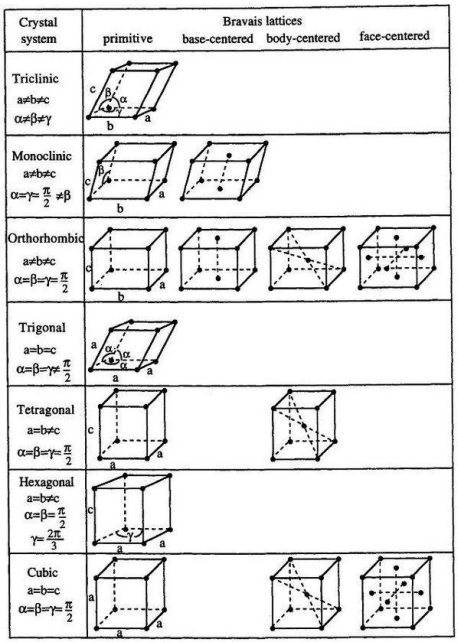


Figure 1: Table of possible Bravais lattice types for each crystal system. Image from Research Gate[4].

There are two types of symmetry in the crystal system classification: point symmetry and translational symmetry. Point symmetry is defined as a geometrical operation that transform the object but leaving at least one point of it fixed. The application of any point symmetry operation leaves the object in a state that is undistinguishable from the original one and a series of point symmetry operations returns the object to its original position (point group). Within a point group the symmetry operations can include rotations, reflections, inversions, or a combination of each.

Specifically in crystals the point group and translational symmetry must be compatible. 1, 2, 3, 4 and 6-fold rotational axes are compatible with the 14 bravais lattices, which restricts the number of possible point groups to 32 (Fig 2). Point symmetry is used to classify crystal systems.

Crystal System	32 Crystallographic Point Groups						
Triclinic	**1**	-1					
Monoclinic	**2**	***m***	2/*m*				
Orthorhombic	222	***mm2***	*mmm*				
Tetragonal	**4**	-4	4/*m*	422	***4mm***	-42*m*	4/*mmm*
Trigonal	**3**	-3	32	***3m***	-3*m*		
Hexagonal	**6**	-6	6/*m*	622	***6mm***	-62*m*	6/*mmm*
Cubic	23	*m-3*	432	-43*m*	*m*-3*m*		

Figure 2: Table of crystal systems and associated point groups

The overall symmetry of a crystal includes both lattice translations and point group symmetries, but there are also two types of symmetry operators that combine point group operations and translation, they are screw axis and glide planes. A screw axis is a rotational axis associated with a fractional translation within the lattice, while a glide plane has the same fractional translation associated with a mirror plane (Fig 3).

The combination of all the symmetry operations in the different Bravais lattice give rise to a total of 230 space groups (these can be found in the International Tables for Crystallography, https://it.iucr.org/).

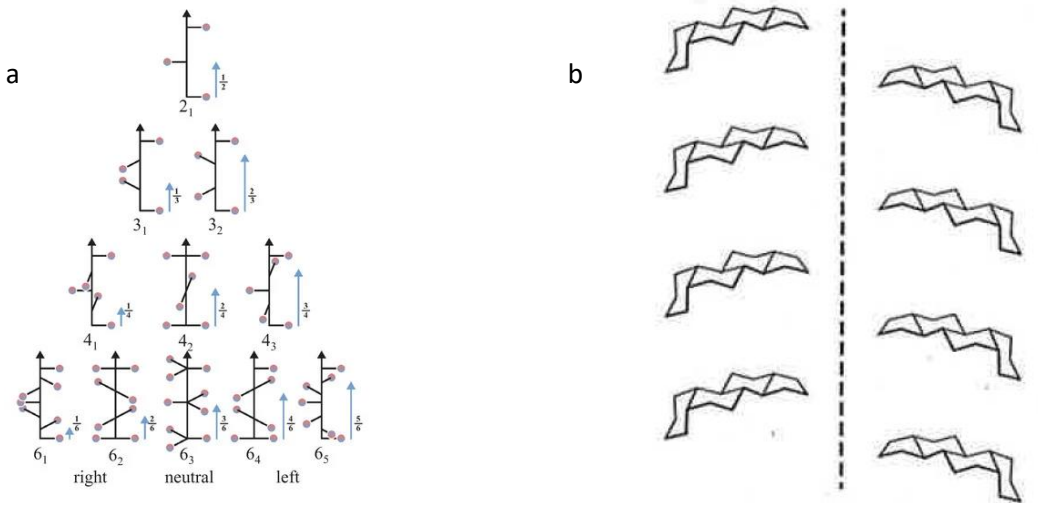


Figure 3: a) a schematic representation of different screw axis, b) a schematic representation of a glide plane[5]

2.1.3 Diffraction as a phenomenon

Diffraction is the physical phenomenon for which waves (sound waves or electromagnetic waves such as light and x-rays) or objects with wavelike properties (like electrons or neutrons) spread when hitting an obstacle, producing interference. The phenomenon is most pronounced when the wavelength of the radiation is of the same order of magnitude of the linear dimensions of the obstacle (for example the diffraction of light through a grating).

The underlying understanding of diffraction is that the lattice points within a crystal lie on planes. The average distance between lattice planes in a crystal is usually of the order of tens of Amstrong (Å), i.e. 10^{-10} m, which is also the typical wavelength of x-rays, and can also be achieved by selecting electrons and neutrons travelling at the corresponding energy.

When the incoming probe (for example x-ray radiation or a neutron beam) hits the crystal, part of it is reflected by the crystal planes (with a reflection angle equal to the incident one) and part keeps travelling through the crystal to be reflected from a deeper parallel plane.

A set of parallel planes in a crystal is defined by its Miller Indices (hkl): if one plane passes through the origin, the next parallel one intersects the crystallographic vectors a , b and c at a/h, b/k, and c/l respectively. The distance between consecutive planes is called d-spacing and is indicated by d_{hkl}.

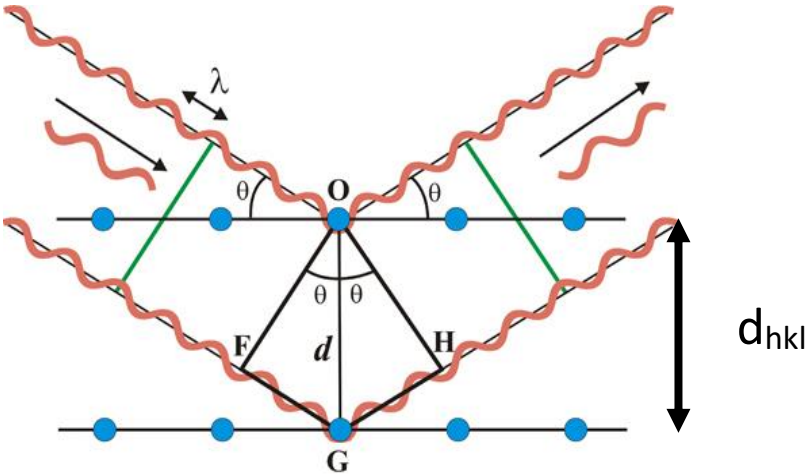


Figure 4: Schematic representation of the diffraction phenomenon in 2-dimensional crystals.

In figure 4 a schematic representation of the diffraction phenomenon in 2-dimensional crystals is shown. The blue dots denote the lattice points in the crystal, θ is the angle of incidence of the incoming radiation on the (hkl) plane, d_{hkl} is the spacing between two parallel planes and λ is the wavelength of the incoming radiation. In 1912, William Laurence Bragg[6] discovered the mathematical relation between wavelength, d-spacing and incident angle for each order of consecutive parallel planes (defined by the integer "n") :

$$n\lambda = 2d_{hkl}sin\theta_B \qquad \textit{Eq. 2}$$

This relation is universally known as the "Bragg law" and the angle θ is called the Bragg angle. Because of its capability of "seeing" the atoms in materials, diffraction is the "gold standard" technique to gain detailed information on the arrangements of atoms and molecules in a crystalline material, i.e. on the atomic/molecular interactions that give rise to its macroscopic properties. For example, diffraction is often used to detect changes in materials (phase transitions) or to identify specific crystalline forms (polymorphism).

2.1.4 Reciprocal lattice

Introduced by Paul Ewald in 1921[7] the concept of reciprocal lattice is basically a mathematical tool that relates the lattice points in a crystal with the corresponding spots on the diffraction pattern.

The reciprocal lattice can be defined in terms of the **a**, **b**, and **c** axes of the crystallographic unit cell, when they satisfy the following conditions:

$$a^* \cdot a = b^* \cdot b = c^* \cdot c = 1 \qquad \textit{Eq. 3}$$

$$a^* \cdot b = a^* \cdot c = b^* \cdot a = b^* \cdot c = c^* \cdot a = c^* \cdot b = 0 \qquad \textit{Eq. 4}$$

Consequently the axes of the reciprocal lattice can be written as:

$$a^* = \frac{1}{V}(b \times c) \qquad b^* = \frac{1}{V}(c \times a) \qquad c^* = \frac{1}{V}(a \times b) \qquad \textit{Eq. 5}$$

where × represent the vector product. This definition states that each reciprocal axis is always perpendicular to the plane containing the other two direct axes.

Because of this relation between direct and reciprocal lattice axes, each set of diffracting planes in the crystal can be associated with a specific node in the reciprocal lattice. This relation can be explained intuitively with the use of a geometrical construct called the Ewald sphere, as given in Fig 5.

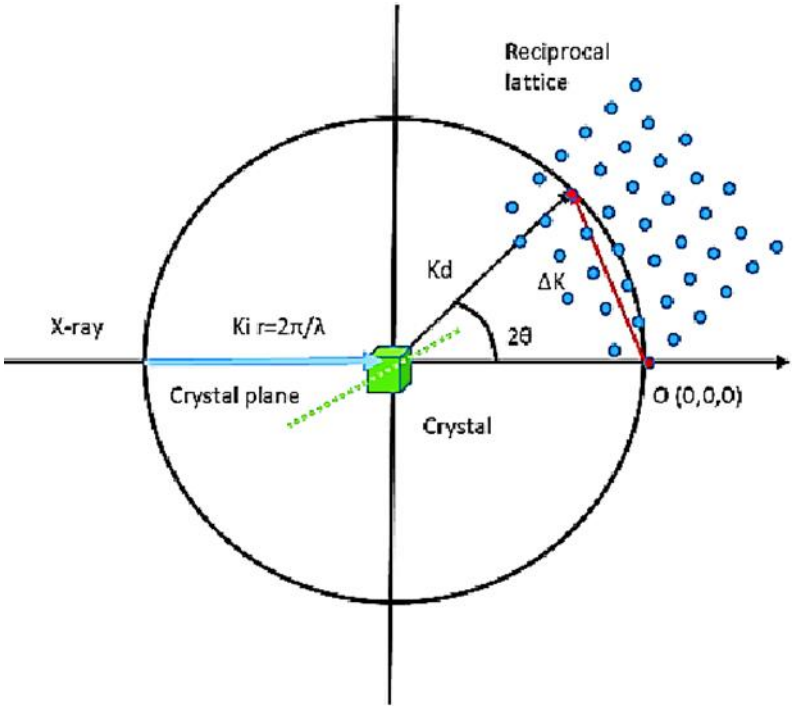


Figure 5: Construction of an Ewald sphere. When the reciprocal-lattice point crosses the surface of the sphere, the trigonometric condition 1/d = (2/λ)sinϑ is fulfilled. This is the three-dimensional illustration of Bragg's law λ = 2dsinϑ. [8]

For each wavelength λ used in a diffraction experiment, the Ewald sphere has a radius of 1/λ. When rotating a crystal, each reciprocal lattice node will intersect the Ewald sphere. At that point the crystallographic planes corresponding to the specific lattice node will satisfy the Bragg Law and consequently a diffraction spot will be produced.

2.1.5 X-ray diffraction

X-rays are a form of electromagnetic radiation with short wavelength and high frequency. Discovered in 1895 by Wilhelm Konrad Röntgen while investigating the effect of electrical charges passing through a vacuum tube[9], the new rays were named "X" because previously unknown, and immediately recognised for their possible medical applications. It was only after the experiment by Friedrich, Knipping and Laue in 1912[10] that x-rays started shaping the development of modern solid-state physics and materials science, including mineralogy, chemistry, and molecular biology, i.e. all the physical sciences for which it is of fundamental importance to understand the relation between structure and physical properties of materials.

Thompson scattering is the name given to the process by which x-rays are scattered from electrons. The scattering occurs due to the electrons moving in the electric field of the incident x-rays beam, which is, in fact, an electromagnetic wave. In an atom, the interaction between the incident x-ray beam and the electromagnetic field generated by the motion of the charged particle itself, gives rise to various phenomena: absorption, emission, and fluorescence, (which give rise to a number of spectroscopic techniques); and scattering, which could be elastic or inelastic. In the following we will focus on elastic scattering, i.e. diffraction.

When x-rays hit a crystal, each lattice point within the crystal acts as a source of a new electromagnetic wave. The interference between the waves emerging from nearby lattice point can be constructive or destructive and will also depend on the path length covered by the scattered beam.

The diffraction pattern from a crystal is the result of the convolution of the content of the single unit cell and the crystal lattice. Every atom in the unit cell contributes a certain number of electrons, therefore, according to the content of the unit cell, in terms both of number and types of atoms, the single unit cell will have a total number of electrons and a specific value of electron density when expressed in relation to the volume of the unit cell (number of electrons per cubic Ångstrom, $e/Å^3$).

To determine how each point in the unit cell will diffract the incident beam, we need to know the position of every atom and which planes are in diffraction condition. The resulting diffraction amplitude is given by the Structure Factor *F(hkl)*:

$$F(hkl) = \frac{1}{V}\sum_{j=1}^{N} f_j \, exp\,[-2\pi i(hx_j + ky_j + lz_j)] \quad \textit{Eq. 6}$$

where V is the volume of the unit cell, *N* is the total number of atoms in the unit cell, (x_j, y_j, z_j) the coordinates of the *j*-th atom and f_j the atomic scattering factor, which represent the scattering amplitude of the neutral, isolated atom and depends on the atomic number Z (i.e. the total number of electrons for the given atoms). The atomic scattering factor is equal to Z at zero scattering angle and decays with increasing scattering angle because of the destructive interference of the wave scattered by every single electron (Fig 6).

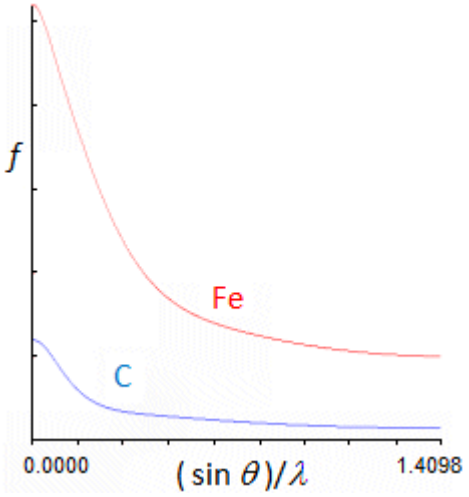


Figure 6: Example of the relationship between scattering factor and scattering angle of Carbon and Iron.

Since the diffracting power of a material depends on the electrons it contains, the expression for the structure factor can be rewritten in terms of electron density:

$$F(hkl) = \frac{1}{V}\sum_{j=1}^{N} \rho_j \, exp\,[-iQ \cdot r_j] = \frac{1}{V}\sum_{j=1}^{N} \rho_j \, exp\,[-2\pi i(hx_j + ky_j + lz_j)] \quad \textit{Eq. 7}$$

The mathematical relation between structure factor and electron density is a Fourier Transform:

$$\rho(xyz) = \frac{1}{V}\sum_{hkl} F(hkl) exp\,[-2\pi i(hx + ky + lz)] \quad \textit{Eq. 8}$$

In a diffraction experiment we measure the intensity of the diffracted beam in order to reconstruct the content of the unit cell. The intensity of each spot in the diffraction pattern is proportional to the square of the structure factor. If the content of the unit cell is known (i.e. number and types of atoms in the unit cell), a model can be constructed assigning arbitrary coordinates to the atoms, then, with a least square procedure that changes the coordinates of the atoms, the model is changed until it reproduces the observed diffraction intensities.

2.1.5.1 Practical aspects of X-ray diffraction

X-ray diffraction can be carried out on both powder and single crystal samples using slightly different methods and experimental set ups. Powder samples can be analysed using Debye-Scherrer rings which are typically integrated to give the one-dimensional diffraction pattern, whereas single crystal samples are usually analysed by integrating the individual Bragg peaks in three-dimensional reciprocal space.

A standard single crystal instrument in a laboratory set up has the sample position where the crystal is mounted, the mobile detector opposite the X-ray production tubes and a cryo-system for temperature control (Fig 7).

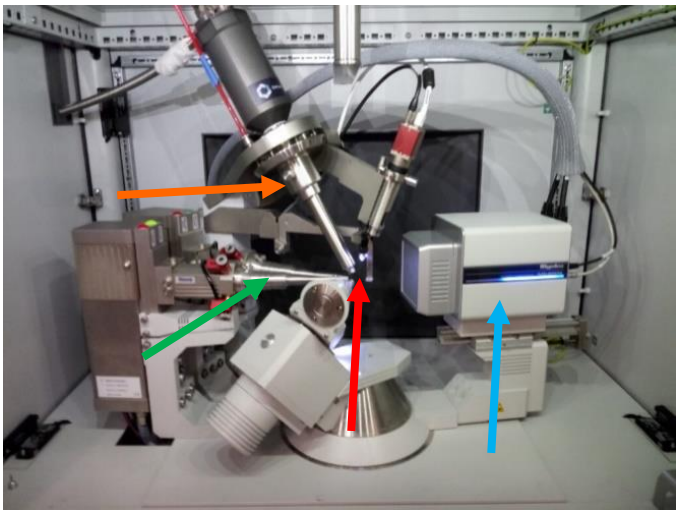


Figure 7: Lab X-ray machine setup including dual x-ray tubes (green arrow), sample position (red arrow), cryo temperature stream (orange) and position sensitive detector (blue arrow).

In a typical laboratory setting, X-rays are produced within an x-ray tube, in which high energy electrons emitted from an anode interacts with a metal cathode under vacuum. The kinetic energy produced in the interaction is emitted as electromagnetic radiation with very short wavelength (x-rays). According to the material of the cathode, x-ray tubes can produce a characteristic x-rays radiation, for example, a copper cathode will produce radiation of wavelength 1.54184 Å, while a molybdenum one will give x-rays of 0.71073 Å wavelength. Copper is a preferred choice for weakly diffracting or small crystals as the longer wavelength means the X-rays produced are lower in energy and therefore, it lowers the risk of radiation damage. The longer wavelength of the copper source is also useful for large unit cells as it has better separation of the reflections in the diffraction pattern. Molybdenum on the other hand, has lower absorption effects which is important for heavy atom structures as well as having a better measurement resolution. The shorter wavelength of a molybdenum source, means that the X-rays are higher in energy than seen with the cooper and hence, penetrate further into the sample.

The choice of X-ray source in a laboratory setting is often either copper or molybdenum depending on the sample composition and expected unit cell size. Screening crystals allows for the identification of weakly scattering or poor quality crystals so they can be quickly discarded. When a suitable crystal is found, which diffracts well, a selection of frames covering a small region of reciprocal space are then collected. The diffraction pattern is usually recorded with position sensitive, area detectors. From the coordinates of the Bragg spot on the detector and the angles of the goniometer when it was recorded, the d-spacing of each single Bragg reflection can be calculated. With this information, an indexing software can determine the length of the unit cell axes and their relative orientation in respect to the incident beam and, can assign hkl indexing to every recorded Bragg spot. This information allows to determine the Bravais lattice and predict where every other Bragg peak will lay, giving the possibility to plan a full data collection in terms of total number of frames, detector positions, and crystal orientation in the incident beam.

The important parameters for total data collection are the crystal symmetry, diffraction intensity on the images and the mosaic spread. It is important to choose the proper exposure time for each frame in the data collection, and this can be determined using the intensities of the Bragg peaks obtained in the initial assessment measurements. When a crystal is strongly diffracting extended exposure can lead to detector overload, i.e. errors in the determination of the intensities for some of the strongly diffracting Bragg peaks. On the other hand, if exposure time is too short, the weakly diffracting peaks, especially at high Bragg angle, might be ill defined, resulting in a final structural determination that is not very accurate.

Hydrogen atoms are almost impossible to locate with good precision using X-ray diffraction on account of their unique electron count. This means that, very often, hydrogen atoms have a larger positional s.u.s than other atoms when freely refined. Furthermore, their atomic positions are shifted significantly towards the bonding atom because the electron is involved in the bonding.

2.1.6 Neutron Diffraction

2.1.6.1 Neutron properties

Neutrons are subatomic particles with a mass of 1.675 x 10^{-27} kg, no charge, a spin state of ½ and a magnetic moment m_n= −0.966 x 10^{-26} J/T =−1.042 × 10^{-3} μ_B = -1.913 μ_N, where μ_B is the Bohr magneton (= e$\hbar$/2m_e = 9.274 x 10^{-24} J/T) and μ_n is the nuclear magneton (= e$\hbar$/2m_p= 5.058 x 10^{-27} J/T). These fundamental physical properties make the neutron a highly effective probe to investigate condensed matter. The neutron-matter interaction is usually described within the concept of wave-particle duality, in which the momentum, p=m_nv, and energy, E, of the particle are linked to the wavelength λ via the de Broglie equation:

$$p = \frac{h}{\lambda} \quad \textit{Eq. 9}$$

Using the Planck-equation :

$$E = h\nu \quad \textit{Eq. 10}$$

where *h* is Planck's constant and ν=c/λ is the frequency of oscillation of the wave, the energy of the neutrons E=1/2 $m_n$$v^2$ can be expressed as:

$$E = \frac{p^2}{2m_n} = \frac{h^2}{2m_n\lambda^2} = k_B T \quad \textit{Eq. 11}$$

Assuming thermal equilibrium (E=k_BT), at room temperature (~300 K) the average wavelength of neutrons is 1.8 x 10^{-10} m, i.e. 1.8 Å, and the energy is about 25 meV. In condensed matter, this wavelength is comparable with the separation between atoms and the energy is about that of collective vibrational modes, making "thermal" neutrons ideally suited to probe both the atomic-scale structures and dynamics of materials in the solid state. Furthermore, the charge neutrality of neutrons allow them to penetrate deeply into samples (~ cm) as they only very weakly interact with condensed matter. In comparison, a beam of x-rays of 1 Å wavelength has an energy of 12.5 keV, i.e. about 6 orders of

magnitude bigger, making x-ray diffraction a much more destructive technique as compared to neutron diffraction.

Although neutral in charge, the intrinsic magnetic moment of the neutrons allows them to interact with magnetic flux variations in materials and hence, probe magnetism. The magnetic flux variations can be caused by a lack of uniformity in the sample's magnetism, intrinsic spin of any unpaired electrons or the spin orbital motion. Any interaction depends on the orientation of the magnetic moment relative to the scattering vector, this means analysing the scattering process with relation to the polarisation of the incident and scattered beam can give extra information on the magnetism.

The most important interaction neutrons have with matter is with atomic nuclei (strong nuclear force – short range, order 10^{-15} m). The short range of this type of nuclear force implies that there is only a small probability for the incoming neutrons to be scattered as they pass close to an atom. This is because in a solid or liquid the separation between atomic nuclei is of the order of 10^{-10} m, while the size of a nucleus is about 5 order of magnitude smaller (~10^{-15} m).

The nature of the neutron-nucleus interaction and the fact that neutrons are not electrically charged, allows neutrons to penetrate quite deeply in any material. This high degree of penetration results in a neutron scattering measurement that practically neglects any surface effect, giving information on the bulk of the material. Furthermore, the small amount of energy transported by the incident neutron beam, will not ionize or damage the sample.

The main advantages of using neutrons to study materials are:

- Complementary information from x-rays
- Unparalleled capacity of locating light atoms in the presence of heavy atoms
- Distinguish isotopes and increased accuracy in bond length determination
- Unique probe for magnetic materials

Furthermore:

- Neutrons can be used as a non-destructive technique (delicate samples will not be damaged ➔ applications in Cultural heritage and biology)
- The high penetration means that the bulk of the material can be studied avoiding bias from localised surface effects
- Complex sample environments can be used, such as cryostats, pressure cells or magnets, as well as perform various types of *in situ*/in-operando experiments.

2.1.6.2 Coherent scattering

The condition for coherent scatter is determined by Bragg's Law, $\lambda = 2d \sin\theta_B$. Due to $\sin\theta_B < 1$ only a given set of crystal planes can be found where wavelength , $\lambda < 2d$ (interplanar spacing times by two). The maximum wavelength is known as the Bragg cut-off and given by $\lambda_c = 2d_{max}$,if $\lambda < \lambda_c$ then no Bragg scattering occurs. For a single crystal sample the occurrence of Bragg scattering is not only reliant on having energies above the Bragg scattering cut-off, but also the crystal orientation. The energy dependence of the nuclear absorption can be given as:

$$\sigma_a(E) = \sigma_a\,(25.3\ meV) \times \left(\frac{25.3}{E}\right)^{1/2} \qquad \textit{Eq. 12}$$

E must be in meV and 25.3 meV is the reference energy at which σ_a is usually tabulated.

Most atomic scattering lengths for neutron scattering have been comprehensively calculated and tabulated it is rare to have to calculate them for an individual material. An example of what can be found in these tables include:

1) $\bar{b}$, coherent bound scattering length
2) σ_s, bound – atom total scattering cross section defined as $\sigma_s = 4\pi\overline{|b|^2}$
3) σ_a, absorption cross section

Some elements can be split by isotope as well as giving values for the averaged natural isotopic mix.

Hydrogen has a large incoherent scattering component. The cross section of ^{2}H is smaller than that of ^{1}H, so can be used as a substitute to reduce incoherent scatter. Applying this effect to enhance the coherent scatter of parts of the molecule by replacing ^{1}H with ^{2}H is known as isotopic labelling.

Coherent scattering (Neutron Diffraction) is used to gather information at the atomic scale of a materials structure. In the simplest form the assumption is made that the structures are rigid hence, the energy before and after the neutron scatters remains constant. The approximation for this is the static state approximation. Starting from the coherent differential cross section:

$$\left(\frac{d\sigma}{d\Omega}\right)_{coh} = \sum_{jk} \overline{b_j^*} \ \overline{b_k} \ exp\left[iQ \cdot \left(r_k - r_j\right)\right] \qquad \textit{Eq. 13}$$

As the aim is to identify the principle diffraction features from different structure types it is acceptable to neglect the atomic motion, even though at absolute zero temperature the atoms are not truly stationary.

2.1.6.3 Practical aspects of neutron diffraction

Neutrons can be produced in different ways:

i) Radioactive decay

ii) Fusion of light nuclei

iii) Fission of heavy nuclei

iv) Spallation

Radioactive decay occurs when a heavy nucleus (Z > 83) naturally releases alpha particles, i.e. Helium nuclei that, when passing through lighter atoms like beryllium or graphite, further emit neutrons. Other atoms, like californium (^{252}Cf) decays into two lighter nuclei spontaneously emitting neutrons.

Fusion of light nuclei such as deuterium and tritium produces a helium nucleus and a high energy neutron:

$^{2}H + {}^{3}H \rightarrow {}^{4}He + n$

Nuclear fission of heavy nuclei produce neutrons via a self-sustaining chain reaction, with fission materials such as ^{235}U or ^{239}Pu. An example of reaction is:

$^{235}U + n \rightarrow {}^{236}U^{*} \rightarrow {}^{94}Kr + {}^{139}Ba + 3\,n$

The initial heavy nuclei is excited by an outside source , then it dissipate the excess energy by breaking down into lighter nuclei and producing neutrons that will restart the reaction on another heavy nucleus.

At a spallation source, neutrons are produced by the bombardment of a heavy metal target with high energy particles. ISIS is an example of a Spallation Neutron Source (fig 8). The target is composed of tungsten and the high energy particles are protons travelling at ~84% of the speed of light(~ 1 GeV).

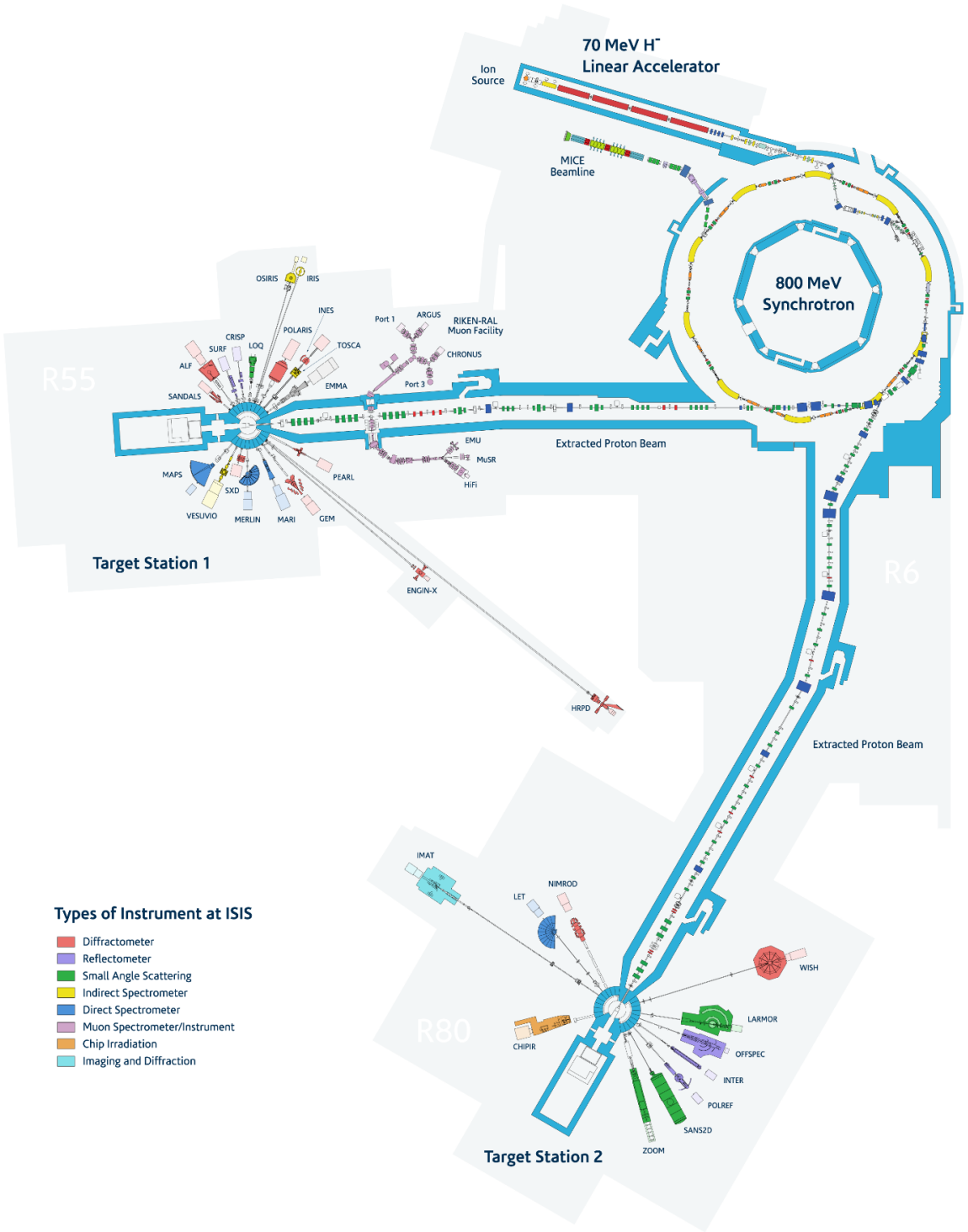


Figure 8: layout of ISIS neutron and muon source[11]

To achieve very high speed, particles are accelerated with the aid of specifically designed magnets, that work better when the charge on the particle is negative. To this aim, instead of using protons directly, an ion source produces H- ions that are then accelerated in a linear accelerator via radio-frequency quadrupoles (RFQ) to about 70 MeV. This produces bunches of protons that are subsequently injected into a synchrotron that will accelerated them to 800 MeV by a series of dipoles and quadrupoles, called also “lattice magnets”. When the bunches of protons arrive at the peak energy, they are extracted down one of two kicker magnets to be sent to the two target stations: 4 bunches go to TS1, 1 bunch goes to TS2. The atomic nuclei of the metal target hit by the protons get excited and de-excite emitting pulses of neutrons with frequencies of 50 and 10 Hz respectively for TS1 and TS2. With an average energy of 20-30 MeV there are around 30 neutrons produced per incident proton.

ISIS runs on tantalum-clad tungsten targets. The core of the target in TS1 is ~100 mm wide and ~100 mm high whilst being around 300 mm long. This is divided into 10 plates of the tantalum-clad tungsten which are water cooled on both sides. The cooling water dissipates the majority of the ~140kW power of the incident beam. The proton beam profile is roughly Gaussian in shape with 1/e radius of 2.53 cm.

When the neutrons are emitted from the target, they carry too much energy, and they need to be slowed down before passing down the beamtubes to the instruments. This is the job of the moderators surrounding the target. A moderator is a medium in which the neutron can lose energy by collisions. There are 4 moderators around TS1, two contain water at 300 K, one has liquid methane at 100 K, while the fourth moderator is liquid hydrogen at 20 K. According to the material and the temperature of the moderator, the emerging neutrons will have distributions of energies, and therefore wavelengths, that will match the requirements of specific techniques and/or instruments (see Fig 9). For example the water and the methane moderators on TS1 are used by diffraction instruments because their wavelength

distributions are peaked at about 1 and 2 Å respectively, i.e. ideally suited to match the interplanar distances in crystalline materials.

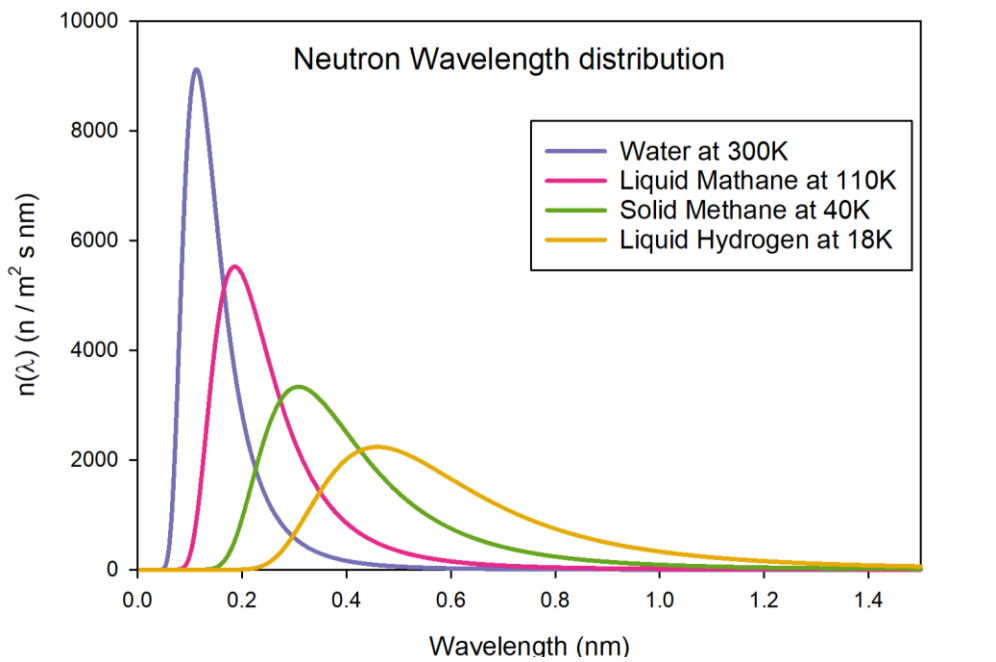


Figure 9: Graph showing the wavelength range for different moderator types[12]

In order to maximise the number of neutrons passing through moderators, the space between different moderators is filled with reflectors. The reflectors consist of beryllium rods encased in stainless steel and their function is to reflect into the moderator the neutrons that otherwise would be lost.

In order to take advantage of the spherical emission of neutron and in an effort to maximise their use, moderators and reflectors are in very close proximity to the target, but this area is very much radioactive and adequate shielding has to be put in place. The shielding consists of several meters of steel and a further meter of concrete called the 'monolith'. The steel is used to attenuate the energy of the neutrons escaping from the target and not captured by reflectors/moderators, and the concrete absorbs what emerge from the steel.

2.1.6.4 Practical aspects of neutron diffraction at a spallation source

At a pulsed source, the neutrons emitted have a distribution of energies and therefore of wavelengths. This means that the available radiation is polychromatic. The moderators help selecting a specific range of energies that will fit a particular scattering technique. For example, the distribution of energies peaked around 1 or 2 Å are better fitted for diffraction instruments, while distributions peaked at longer wavelengths (~ 5 Å) are better suited for reflectometers or small angle scattering instruments. In diffraction, the Laue method uses polychromatic radiation to measure many Bragg reflections simultaneously but the real advantage of using the Laue method at a pulsed source is the possibility of discriminating in time-of-flight. Every diffraction instrument at a pulsed source is equipped with detectors that, on top of recording the position of the Bragg reflections (single-crystal instrument), or the Debye-Sherrer lines (powder instrument), can also record the time at which each neutron has arrived at that position.

Employing the de Broglie equation as well as the non-relativistic momentum of the neutron ($p = m_n v$), the time-of-flight (t) for a neutron with a given wavelength (λ) is:

$$t = \frac{m_n}{h} L\lambda \qquad \textit{Eq. 13}$$

Where $L = L_1 + L_2$ = the total flight path from the source to the detector.

There are two distinct advantages to using a TOF diffraction instrument. The first one is that the superposition of different orders of a set of Bragg planes, that have the exact same diffraction angle and would overlap in the positional diffraction pattern, can be separated by their TOF (Fig 10).

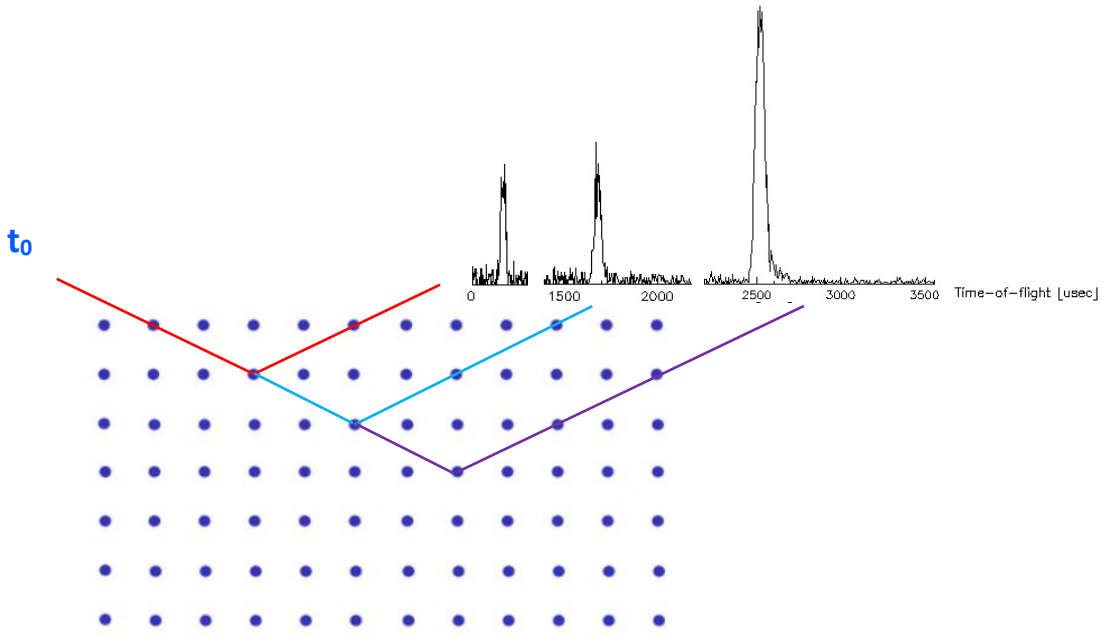


Figure 10:Schematic of the separation by TOF of Bragg reflections occurring at parallel planes in a lattice, which would have the exact Bragg diffraction angle.

The second advantage is that the background surrounding a Bragg peak is solely the result of the incident wavelength producing that peak, this makes them more easily identifiable. With TOF the scattering vector Q has a radial path at a fixed angle, 2θ, in reciprocal space. Consequently when $2\theta = 2\theta_B$the TOF scan at the detector at 2θ equates to a radial scan in reciprocal space at the lattice vector where the reflection can be observed. This means that Q with TOF can be described by:

$$Q = \frac{2m_n}{\hbar}\frac{L\sin\theta}{t} \quad \textit{Eq. 14}$$

2.1.6.5 SXD

SXD is the only single-crystal diffractometer at ISIS and uses the time-of-flight Laue technique to determine crystal structures (Fig 11). The instrument faces the room temperature water moderator and is positioned on the 50 Hz TS1 on port S3. The sample position is at 8.3 m from the moderator face and the maximum beam aperture is 14 x 14 mm^2. The resolution $\left(\frac{\Delta d}{d}\right)$ of the instrument is around 0.5 % in the backscattering direction and up to 1% at 90°.[13]



Figure 11: image of the position of SXD relative to the Target on TS1

There are 11 position sensitive detectors in different arrangements around the sample position (Fig 12):

1) Six detectors are placed in the equatorial plane at longitudes $\pm 37.5°$, $\pm 90°$ and $\pm 142.5°$ and at a distance from the sample L_2 = 0.225 m

2) Four detectors are inclined at $-45°$ in respect to the incident beam and at longitudes of $0°$, $\pm 90°$ and $\pm 180°$ at a distance from the sample of L_2 = 0.27 m

3) A final detector closes the pseudo-half-sphere coverage around the sample from the bottom, at a latitude of -90° and longitudes of $0°$ at a distance from the sample of L_2 = 0.28 m

10 of the detectors are 2D position sensitive ZnS/^{6}LiF scintillators with an active area of 192 x 192 mm^2, optically encoded, via 32 PMTs per detector, to give 64 x 64 pixels and a resulting spatial resolution of 3 x 3 mm^2. These detectors have an efficiency of 20% at 1 Å, with a light decay time of 80 µs.

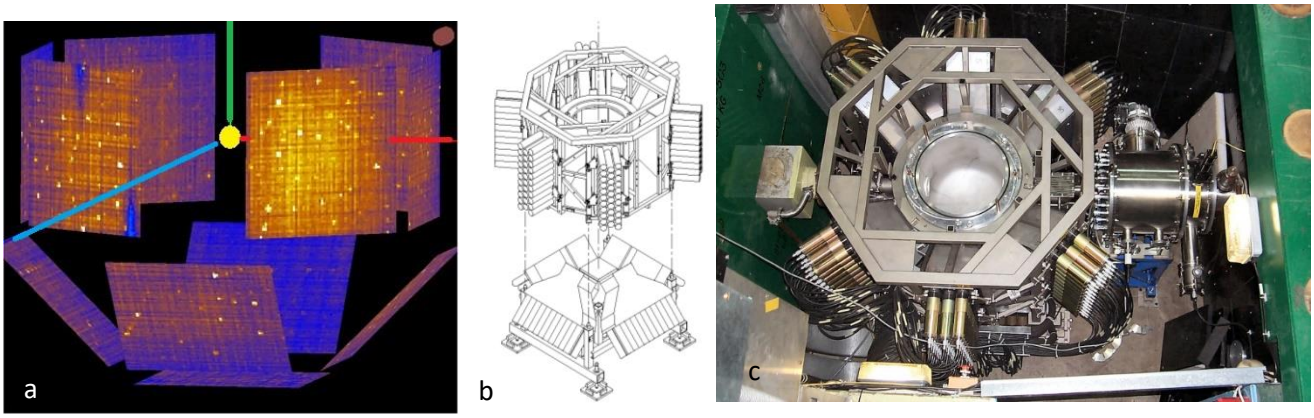


Figure 12:layout of the detectors on SXD a) real view of detector layout with Bragg peaks during an experiment, b) schematic of SXD instrument design, c) image of SXD instrument in the pit showing PMTs at the back of the detectors.

The 11th detector is currently a prototype detector of the new wavelength shifting fibre (WSF) technology developed at ISIS[14]. The detector consists of a double layer of orthogonal fibres planes placed between two ZnS:Ag/^{6}LiF scintillator screens for an increase in efficiency of ~4 compared to the older scintillator detectors. The two layers are separated by thin reflective foils (50 µm thick) on both the front and back of each layer to remove light cross talk, a 5 mm B4C plate is placed at the back of the two layers to reduce neutron background. ^{6}Li absorbs the neutrons producing charged particles, α and ${}^{3}_{1}H$, which ionize the ZnS:Ag emitting broad band blue light (450 nm centre) to be absorbed by the WLS fibres.

The sample sits at the centre of the detectors arrangement and is usually stationary during a measurement on SXD. To obtain a good coverage of reciprocal space and to correct for the fact that there are gaps between the detectors, discrete rotations of the sample are used during a full data collection, according to the crystal symmetry.

Different sample environments (Fig 13) are available on SXD in order to study samples in different conditions of temperature, pressure, humidity, electric field, or other type of stimuli.

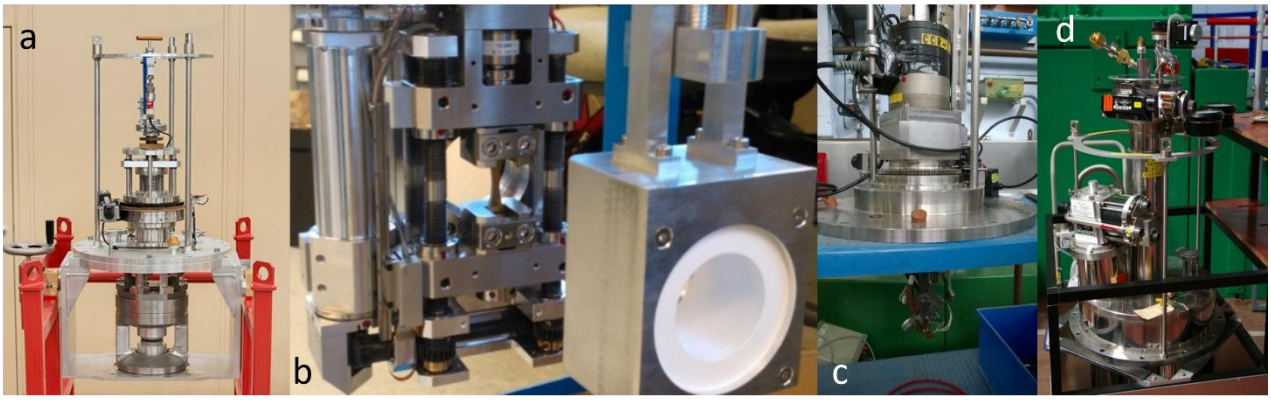


Figure 13: Sample environment set ups: a) Paris-edinburgh press. b) compact stress/strain rig. c) CCR. d) furnace

2.1.7 Comparing and contrasting Neutron and X-ray diffraction

As discussed above both Neutrons and X-rays can be used in diffraction to study the structure of crystalline materials. There are different benefits to the use of each of them as irradiation probe. X-rays and Neutron interact with different parts of the atom: whilst X-rays interact with the electron cloud, Neutrons interact with the nucleus. This means that the X-rays scattering power of an atom depends on its Z , therefore X-ray diffraction is very sensitive to heavy atoms. In contrast, the neutron scattering power of an atom is completely independent of Z, meaning that neutron diffraction is much more sensitive to light atoms and can distinguish isotopes of the same atom (Fig 14).

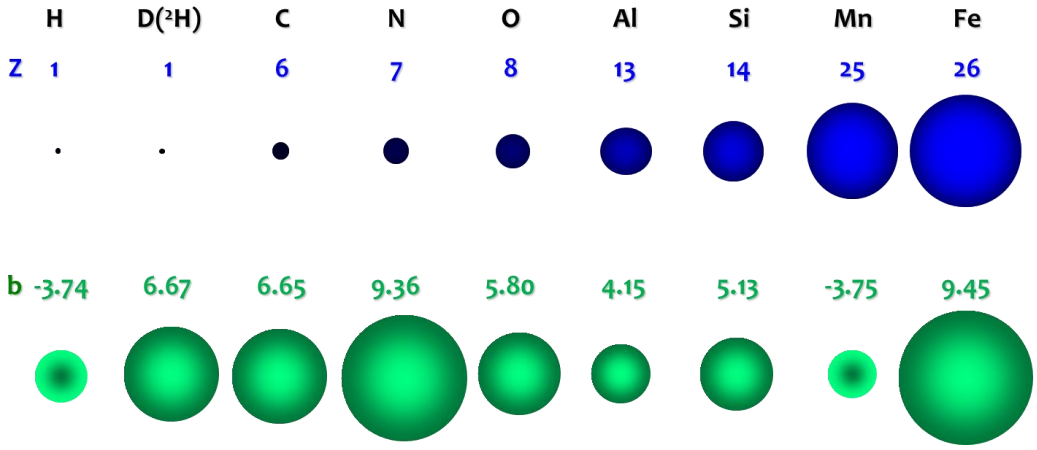


Figure 14: : Relative scattering cross sections of atoms in both X-ray (top) and Neutron (bottom) diffraction

Neutron diffraction is a better technique for studying processes involving the movement of light atoms such as hydrogens, because it can locate them more precisely especially in the presence of heavier atoms, which would otherwise dominate an X-ray diffraction pattern. An additional advantage of Neutron diffraction is that, in comparison to the use of X-rays, it is a non-destructive technique and so can be used for Heritage or biological samples which would be irreparably damaged if studied using X-ray diffraction.

A down side to Neutron diffraction, however is, that to complete an experiment a larger sample size (> 1 mm^3) is required to that for an X-ray diffraction experiment (<1 mm^3). This is particularly an issue for biological or small molecule samples where large sample sizes are difficult to obtain. This is similarly seen with samples requiring expensive isotopic substitution, or rare earth metals. Neutrons are also more difficult to access as applications for time at neutron facilities around the world is often difficult to gain.

It is also difficult to study materials containing specific elements using Neutron diffraction. Elements such as ^{10}B, ^{113}Cd, ^{157}Gd are strongly neutron absorbing. This means they do not diffract the neutrons strongly and when present in significant abundance investigating them can require either extended experimental times relative to other lower absorbing elements or alterations and preparations which can be costly as well as time consuming.

Neutron sources are usually “less powerful” than x-rays sources in terms of emitted radiation (i.e. incident flux arriving at the sample, especially when comparing any neutron source with a synchrotron). Furthermore as the neutrons interact with the nuclei there is more material for them to interact with as there is more in the nuclei (neutrons and protons) than with the electrons. This can cause difficulties in studying meta-stable samples which decay over time, or irradiated samples which revert to the non-radiated state on a shorter time scale than which the experiment can be completed. This is particularly seen in single crystal neutron diffraction experiments where collection time for a single orientation is on the scale of hours compared to in some cases minutes for a complete single crystal X-ray diffraction experiment.

2.1.8 General process for a diffraction experiment and data processing

There are a number of different factors that need to be taken into account during a diffraction experiment and when processing the resulting data. As discussed above, crystal quality and coverage of the reciprocal space have an effect on the data collection time and quality. When processing the data there are further factors such as absorption corrections along with thermal diffuse scattering. These are discussed in more detail below.

2.1.9 Debye-Waller factor and ADPs

For diffraction refinements there are a set of parameters which describe the Debye-Waller factor, taking into account random thermal motion of the atoms and has the form:

$$exp(-W) = exp\{-\frac{1}{2}\langle(Q \cdot \hat{u})^2\rangle\} \quad \textit{Eq. 15}$$

This equation (eq. 15) has a value of between 0 and 1. W can be given by:

$$W = \frac{\hbar Q^2}{4M\omega_0} coth\,(^1/_2\,\beta\hbar\omega_0) \quad \textit{Eq. 16}$$

The factor is not dependant on the neutron energy transfer but rather, the scattering vector (Q) and temperature, and is a result of the motion of the nucleus. The inherent motion in a nucleus means that the scatter of the neutron occurs as if from a diffuse object. The overall effect is to reduce the amplitude if the scattered beam in relation to what is expected from a point like object.

$\hat{u}$ is the atomic equilibrium displacement operator. Written in matrix form the factor in exponent becomes:

$$Q^T U Q \quad \textit{Eq. 17}$$

For this equation U is a 3x3 symmetric matrix made up of $U_{11} = \langle\hat{u}_x^2\rangle$, $U_{12} = U_{21} = \langle\hat{u}_x\hat{u}_y\rangle$... . There can be at most six independent components of U, known as the anisotropic displacement parameters

(ADPs). Typically, in crystal refinement packages ADPs are defined with regards to crystallographic axes and denoted by $\beta_{ij}, U_{ij}\ or\ B_{ij}$.

β_{ij} is a dimensionless ADP, U_{ij} has dimensions of (length)^2 related to the mean squared displacement amplitude $\langle \hat{u}_x^2 \rangle$. B_{ij} is a scaling of U_{ij} by a factor of $8\pi^2$. The amplitude of the scattered beam, is consequently calculated taking into account not just the instantaneous position of the of the nth-atom (r_n) (like in eq. 7, where $(iQ \cdot r_n)=2\pi i(hx_n+ky_n+lz_n)$)but its time-averaged position plus its instantaneous displacement (r_n+u_n):

$$F(hkl) = \frac{1}{V}\sum_{j=1}^{N} \rho_j exp[-iQ \cdot (r_n + u_n)] \quad \textit{Eq. 18}$$

2.1.10 Attenuation: absorption/ self-shielding

Where μ is the linear attenuation coefficient, assuming it is independent of positions of atoms and hence, homogeneous, the attenuation is caused by scattering both incoherent and coherent as well as nuclear absorption.

$$\mu = n(\sigma_s + \sigma_a) \quad \textit{Eq. 19}$$

With n being the number density of the formula unit of a crystallographic unit cell, σ_s and σ_a being the total scattering and total absorption for that unit cell respectively. As σ_s is a complicated function of neutron energy the self-shielding can be difficult to calculate. The energy dependence can be separated into three parts:

1) If the kinetic energy of the neutrons is greater than the binding energy of the atoms, they recoil under impact with the neutrons. The effect of this is to reduce the scattering cross-section to that of free atoms.

2) There is an inelastic contribution to σ_s from the motion of the atoms. This is proportional to $1/k_i^2$ at energies below K_BT.

3) The maximum scattering angle is 180° which imposes a cut-off on Q and limits the removal of neutrons from the beam *via* coherent scatter.

The condition for coherent scatter is determined by Bragg's Law, $\lambda = 2d \sin\theta_B$. Due to $\sin\theta_B < 1$ only a given set of crystal planes can be found where wavelength , $\lambda < 2d$ (interplanar spacing times by two). The maximum wavelength is known as the Bragg cut-off and given by $\lambda_c = 2d_{max}$,if $\lambda < \lambda_c$ then no Bragg scattering occurs. For a single crystal sample the occurrence of Bragg scattering is not only reliant on having energies above the Bragg scattering cut-off, but also the crystal orientation.

The energy dependence of the nuclear absorption can be given as:

$$\sigma_a(E) = \sigma_a\,(25.3\ meV) \times \left(\frac{25.3}{E}\right)^{1/2} \quad \textit{Eq.20}$$

E must be in meV and 25.3 meV is the reference energy at which σ_a is usually tabulated.

Due to the sample size there is a possibility of a neutron scattering twice. The phenomenon of multiple scattering increases the intensity of a single scatter signal. Multiple scattering in Bragg scatter is a special case, in this situation the intensity of the desired Bragg reflection is reduced (extinction) or the peak appears at a forbidden position.

2.1.11 Short Range Order

The lower limit of diffractometer resolution is typically in the range of 10^1-10^3 unit cells per direction. Below this limit in even one direction the Bragg peaks are not resolution limited and hence, the scatter contains features relating to the shape and size of the system. The lack of localisation of coherent scattering in reciprocal space is known as diffuse scattering.

2.1.12 Correlation length

A model for describing the disorder in condensed matter is where the average coherence of the order decays exponentially with distance for a crystalline material. This type of disorder is found where random dislocations or twin boundaries occur dividing the system into multiple odd sized domains. Within each

domain there is complete order, however, at the boundary between domains the periodicity is interrupted. The assumption made in this model is that the chance of encountering a phase boundary is the same at any point within the crystal.

2.1.13 Thermal Diffuse Scattering (TDS)

TDS is a process by which the features resulting from crystal diffraction can be broadened. Inelastic scattering from phonons is recorded because of the diffractometer's imperfect energy resolution, and a consequence of crystal dynamics. The recorded intensity is an integral of all the scattering inelastic/elastic weighted by the probability function describing the energy resolution of the instrument. Instruments that do not have an energy analyser (removal of neutrons with energy change after scatter on diffractometers with a monochromatic beam) are more effected than others.

Strong TDS can be a result of Low-Energy acoustic phonons where the wavevectors are close to the vectors of the reciprocal lattice. The TDS causes either a diffuse peak under the Bragg peak or enhanced scattering surrounding the peaks in this situation. The ratio between the speed of sound within the crystal, and the speed of the neutron, can determine which possibility will be observed. TDS can be used to develop corrections that enable more accurate Bragg intensities to be observed. However, the neglect of them only causes errors in atomic displacement parameters not the refined atomic coordinates.

2.2 Raman Spectroscopy

Unless otherwise referenced the information and images in this section were obtained from IR and Raman Spectroscopy: principles and spectral interpretation (Larkin, P. J.)[15]

Raman Spectroscopy is an analysis technique that allows for the measurement of a molecule's vibrational modes and is generally best used to characterise the symmetric vibrations of non-polar groups. Raman spectroscopy is a 2-photon inelastic light scattering event. The incident photon has vastly larger energy than that between the vibrational quantum energy levels, and hence loses part of that energy to the molecular vibrations while the remaining energy is scattered as a photon with reduced frequency. The interaction between the light and matter is an off-resonance condition which can change the Raman polarisability of the molecule.

The vibrational peaks can be characterised by 3 different factors: frequency (energy), intensity (polarisability) and band shape (bond environment). The frequencies are dependent on the masses of the atoms, the geometric arrangement, and the strength of the chemical bonds. The resulting spectra gives information on molecular structure, dynamics, and chemical environment.

There are two main ways in which Raman spectra can be interpreted:

1) Mathematical – using group theory to predict the form and frequencies of the molecular vibrations.
2) Empirical – using characteristic frequencies (from published tables) for different chemical functional groups.

Often mixing the two methods gives the most easily interpretable results, particularly when using the mathematical approach to perfect the functional group assignments from the empirical approach.

The most relevant parameters are:

1) wavelength λ, the length of a single wave.

2) frequency υ, number of cycles per unit of time.

3) wavenumbers $\bar{\nu}$, number of waves per unit of length.

$$\bar{\nu} = \frac{\nu}{(c/n)} = \frac{1}{\lambda} \qquad \textit{Eq. 21}$$

Where *c* is speed of light and *n* is the refractive index of the medium.

According to quantum theory radiation is emitted from a source as discreet units (photons) the frequency of which (υ) and energy (E_p) are linked by $E_p = h\,\upsilon$.

Where h is Planck's constant which equals 6.6256×10^{-27} joule sec.

Where a photon has a specific energy, it can be absorbed/emitted by a molecule. In absorption spectroscopy, the increase in energy takes the molecule from its ground state to an excited state. If the rotational (E_{rot})/ Electronic (E_{el}) / Vibrational (E_{vib}) energy of a molecule is changed by ΔE this can be described by: $\Delta E = E_p = h\upsilon = hc\bar{\nu}$

When a photon is absorbed, the energy of a molecule increases, hence ΔE is positive, implying that, in first-approximation, the total energy is given by the sum of its different components:

$E_T = E_{el} + E_{vib} + E_{rot.}$

The molecular motion resulting from the characteristic vibrations within molecules, can be described by the internal degrees of freedom using the 3n-5 and 3n-6 rule of thumb for linear and non-linear molecules, respectively. n is the number of atoms in a molecule with 3 being the directions of the freedom of motion described by x, y, and z. Three of the degrees of freedom are rotational while a further three are translational. The change in the angles between bonds, or the distances between atoms are explained by the remaining 3n-6 degrees for non-linear molecules.

2.2.1 Raman Scattering process

The classical description of the light scattering by a molecule involves the production of electromagnetic radiation of oscillating dipoles which are induced in a molecule by the electromagnetic field of the incident radiation. An induced dipole moment caused by the deformation of the electron cloud surrounding a molecule by the application of an external field, is proportional to the molecular polarisability (α) of a molecule. For the photons of scattered light Rayleigh scattering is the predominant process over Raman scattering.

A traditional Raman set up uses a monochromatic radiation source produced by a laser. Different wavelength regions are available for the excitation laser source, UV, visible and near IR(785 or 1064 nm). There is no energy loss during the elastic Rayleigh scattering, however the photons do lose some energy relative to the excitation laser based on the vibrational displacement (atomic coordinates) of the sample. A change in the polarisability of a molecular vibration is necessary for Raman bands to be observed.

Both Rayleigh and Raman scattering are 2 photon processes involving the scattering of an incident light source ($hc\bar{\nu}_L$), from a 'virtual' state. An incident photon is absorbed by a transition from a ground to a 'virtual' state, a 'new' photon is then scattered as a transition away from the 'virtual' state back to the ground.

Rayleigh scattering has an intensity that is 3 orders of magnitude less than the incident radiation, it is however the most probable scattering event to occur. As the scattering event is elastic in nature there is no change in the energy.

In comparison, for the strongest scatters, the intensity of the Raman scattered signal is 6 orders of magnitude smaller than the incident radiation. There is also a lower probability of Raman scattering occurring than Rayleigh scattering. The transition from the 'virtual' state to the first excited state of a molecular vibration causes the photons to scatter. The scattered photon has a different frequency and

energy as the molecule changes its vibrational energy ($\bar{\nu}_m$) during the inelastic collision between the molecule and photon.

Raman scattering can be split into two different types: Stokes and anti-Stokes (Fig 15). Stokes scattering results from molecules moving from the ground state to the excited state ($hc(\bar{\nu}_L - \bar{\nu}_m)$), while anti-Stokes scattering is caused by molecules moving from the excited state to the ground state ($hc(\bar{\nu}_L + \bar{\nu}_m)$). The absolute temperature of a sample as well as the energy difference between the excited and ground states determine the intensity of the Stokes bands. The ratio between Stokes and anti-Stokes bands can be defined by the Boltzmann distribution as thermal equilibrium. As most molecules are found in the ground state at ambient temperature Stokes bands have a greater intensity than anti-Stokes.

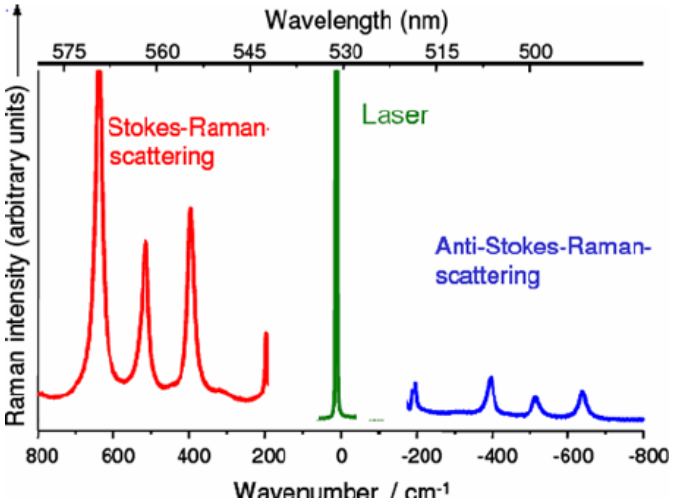


Figure 15: Spectral representation of Raman and Rayleigh scattering[16]

The intensity of Raman scattered radiation (I_R) can be illustrated d by:

$$I_R \propto \nu^4 I_O N \left(\frac{\delta\alpha}{\delta Q}\right)^2 \quad \text{Eq. 22}$$

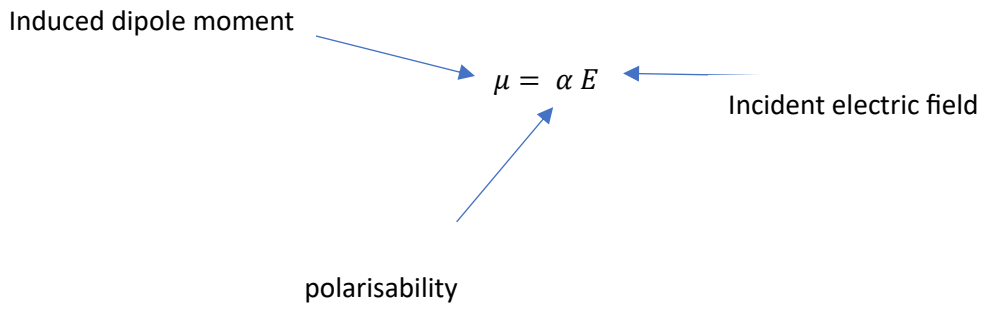
Where, I_O is the intensity of the incident laser, N is the number of scattering molecules in a given state, ν is the exciting laser frequency, α is the polarisability of the molecules and Q is the vibrational amplitude of the bond.

Raman signal strength is dependent on multiple parameters:

1) Concentration of the sample (useful for quantitative analysis).
2) Energy and flux of the incident laser radiation.
3) The number of Raman active molecular vibrations have inducible polarisation.
4) The change in polarisability with respect to changes in the vibrational amplitude must be greater than 0.

2.2.2 Classical description of the Raman effect.

Descriptions of Raman spectroscopy using classical arguments describe the nature of the interactions of an oscillating electric field. The electromagnetic field perturbs the charged particles of the molecule inducing a dipole moment:



Both polarisability and incident electric field are variable with time. The electric field of the radiation oscillates as a function of time at frequency v_0, this causes oscillation of the dipole moment at the same frequency. The magnitude of polarisability can vary slightly with time at a slower molecular vibrational frequency v_m. Both of these effects together modulate the dipole moment, this can be resolved mathematically into 3 steady amplitude components with frequencies v_0, $v_0 + v_m$, $v_0 - v_m$. The oscillations of the dipole moment causes the emission of radiation described previously as Rayleigh, Stokes, and anti-Stokes. Where no polarizability is possible, no Raman scattering occurs.

2.2.3 Symmetry: Raman active vibrations.

Raman active vibrations are defined by the symmetry or lack of symmetry found in a molecule. Symmetric (in-phase) vibrations and non-polar groups are easily studied by Raman. By classifying a molecule by its symmetry, it is possible to understand the relationship between the vibrational spectrum and the structure of the molecule. Symmetry elements include one or multiple of the following:

1) Planes of symmetry
2) Axes of symmetry
3) Centres of symmetry

Group theory is the mathematical way of applying symmetry elements to vibrational spectroscopy, this helps to predict which vibrations will be Raman active. The collection of symmetry elements leads to a point group classification for a molecule. If a molecule has a centre of symmetry the rule of mutual exclusion means that any vibrations that are IR active will not be Raman active, this does not apply for molecules without a centre of symmetry where some vibrations can be both Raman and IR active.

Cartesian displacement vectors of vibrational modes can be modified via symmetry elements. For non-degenerate vibrational modes, the Identity (I) in group theory is either (+1) if the original form does not change or (-1) if change to the original form occurs. Doubly degenerate vibrational modes have the same vibrational frequency due to the symmetry.

2.2.4 Calculating vibrational Spectra.

The group frequencies currently used within Raman spectroscopy are based on the theory that they are the results of localised group vibrations, and on our understanding of molecular vibrations as a whole.

As a polyatomic molecule oscillates about an equilibrium position with a small amplitude, the potential energy can be expressed as a Taylor series:

$$V = V_0 + \sum_{i=1}^{3N} \left(\frac{\delta V}{\delta q_i}\right)_e dq_i + \frac{1}{2}\sum_{i=1}^{3N}\sum_{j=1}^{3N} \left(\frac{\delta^2 V}{\delta q_i \cdot q_j}\right)_e dq_i dq_j + \cdots \quad \textit{Eq. 23}$$

With q_i the internal coordinates.

This equation can be simplified because:

1) $V_0 = 0$ as the vibrational energy is chosen as vibrating atoms about the equilibrium position.

2) The first derivative is 0 in the minimum energy configuration.

3) Within the harmonic approximation, all terms in the Taylor series larger than second order can be omitted.

As a result, using Newton's second law of motion equation 26 can be reduced to :

$$\frac{d^2 q_i}{d^2 t^2} = -\left(\frac{\delta V}{\delta q_i}\right) = -\sum_{j=1}^{3N} \left(\frac{\delta^2 V}{\delta q_i \cdot \delta q_j}\right)_e q_j \quad \textit{Eq.24}$$

When solved, this equation gives a determinant whose eigenvalues ($m\omega^2$) provides the frequencies (ω) of the vibrational modes. The atomic displacements for each vibrational mode are given by the corresponding eigenvectors. For each normal mode a corresponding force constant can be calculated:

$$\frac{\delta^2 V}{\delta q_i \cdot \delta q_j} \qquad \textit{Eq.25}$$

A number of computational options are available which make use of the force constant to obtain molecular force fields. Both quantum mechanical and empirical force field methods can be used to calculate vibrational frequencies.

Due to the computational demands necessary for quantum mechanical methods, even though they are more robust, are generally only used on small molecules. Slight differences between calculated and experimental values are usually encountered, mainly due to the approximations used in the calculations: molecules have both harmonic and anharmonic components; the size of the basis set might not be ideal, or electron correlation could be omitted in the calculations. As a result, scaling factors must be introduced to bring the calculated values closer to the experimental ones.

Both *ab initio* and semi-empirical methods require force constants calculated by either density functional theory (DFT), or Hartree-Fock (HF) methods. Both methods involve molecular orbital calculations of isolated molecules in vacuum. Intensities as well as vibrational frequencies must be taken into account for full vibrational analysis to be accurate in assigning vibrational modes.

HF calculations using a moderate basis set can differ up to 10 – 15 % from experimental values, requiring the use of a multiplying scaling factor of about 0.85 - 0.90. The use of post-HF methods, like configuration interaction (CI), Møller Plessant perturbation (MP2) or Multi-configuration self-consistent field (MCSF), can resolve the issue to an extent. The use of a large basis set might reduce the importance of the scaling factor, bringing its value to 0.92 – 0.96.

DFT based methods are able to account for a significant amount of electron correlation, with a variety of gradient-corrected exchange functions to aid in calculating the derived force constants. The use of the appropriate functional (as for example BLYP/B3LYP) can bring the scaling factor close to 1 (0.96 - 1.05). For each method, the appropriate choice of basis set is paramount to define the ground energy state of the molecule and therefore produce accurate calculations. A basis set is the combination of Gaussian functions which represent the electronic configuration of each atom in a molecule; the linear combination of atomic orbitals produce molecular orbitals, which describe the overall electronic configuration of the molecule. In order to get the best description of the ground energy state of the molecule, a geometrical optimisation of the molecular structure is also performed.

2.2.5 Raman instrumentation.

In Raman spectroscopy, a focused laser beam is imaged on the sample. The emitted light is collected and focused into a wavelength-sorting device. There are two basic experimental systems, dispersive and Fourier transform. Dispersive instruments make use of monochromators, whilst Fourier transform instruments make use of interferometers.

2.2.5.1 Dispersive systems

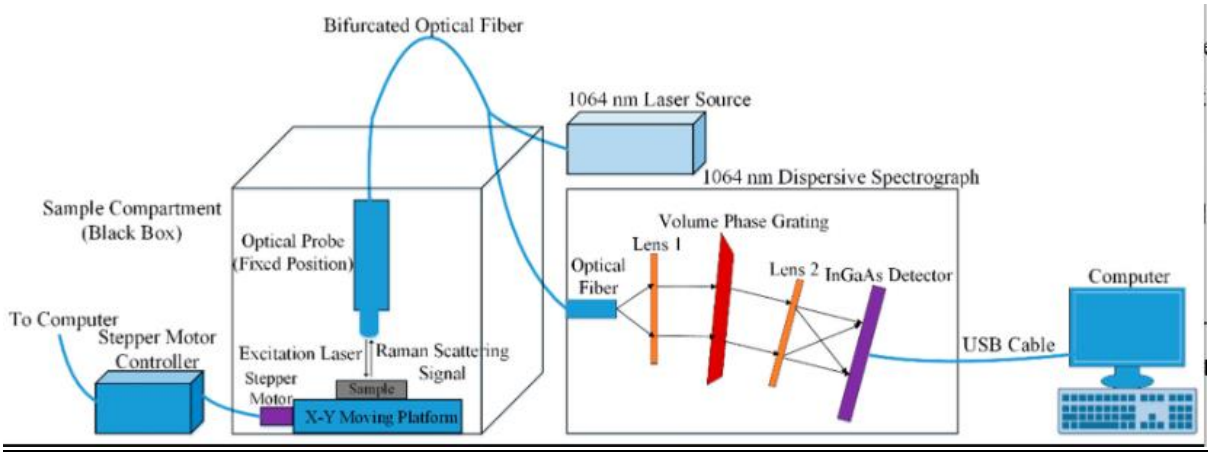


Figure 16: Dispersive Raman System[17] figure representation

A monochromator scans the wavelength of the emitted radiation and consists of an entrance slit, followed by a mirror which ensures the light rays are parallel, a diffraction grating, a focusing mirror to direct the dispersed radiation to the exit slit and hence the detector. If the monochromator type is scanning, a scanning mechanism will pass the dispersed radiation over the slit which isolates the frequency range falling on the detector (Fig 16).

Polychromatic radiation needs to be split into its monochromatic components using a diffraction grating, which bends the radiation by an angle that causes dispersion of the different wavelengths. The diffraction grating has to consist of multiple parallel lines (grooves) on a reflective planar/concave support spaced at distances similar to that of the wavelength analysed.

As the incident radiation beam approaches the adjacent grooves in-phase it is reflected with a path length difference. The path length is determined by the groove-spacing, angle of incidence (α), and the angle of reflectance of the radiation (β).

2.2.5.2 Dispersive Raman Instruments

Raman instrumentation should have the capability of removing extremely strong Rayleigh scattered radiation whilst still retaining the ability to analyse the weak Raman scattered radiation. Choosing optical material and detector type is dependent on the excitation wavelength of the laser used. Both optical throughput and spectral resolution need to be optimised which is difficult due to their often-conflicting nature.

The collection optics are designed to collect as much Raman scattered light as possible which are then transferred to the monochromator/inferometer. The use of a highly sensitive array of detectors with a high throughput single monochromator coupled with Rayleigh rejection filters, dramatically improve the performance of dispersive Raman. The Rayleigh filters allow for the use of a single grating improving the optical throughput. Array detectors also improve the signal-to-noise ratio, a result of the 'multi-channel advantage'. Multi-channel advantage means that the images are simultaneously obtained using different filters and the area array, hence, the Raman spectrum for each pixel can be reconstructed quickly based on the measurements of different narrow bands[18]. An array detector is typically either a photodiode array (AD) or a Charge-coupled device (CCD) where each element/pixel records a different spectral band.

As there is a limit to the possible elements in the detector (256, 512, 1064 pixels) compared to the resolvable spectral elements, compromises must be made. Hence, the coverage of the complete spectral range (4000 –40 cm^{-1}) requires low resolution, while high resolution can be obtained only on a smaller spectral range. The best way to cover the entire frequency range at high resolution is to scan in segments and assemble the resulting spectra from a multi-channel instrument. Even though Raman light scatters

in all directions, most instrument configurations have the detectors placed at 90° or in backscattering geometry (180°). The backscattering geometry is preferably used in FT-Raman spectrometers.

Most commercial grade FT-Raman spectrometers use Nd:YAG 1064 nm lasers with notch filters at the laser wavelength (to reduce Rayleigh scattering), high quality inferometers and sensitive detectors. The advantage of using a near-IR wavelength excitation is that it greatly reduces any effect of fluorescence on a vast majority of compounds which have excitations in the visible wavelength band, allowing more compounds to be studied. There are, however, limitations due to sensitivity and absorption. V^4 dependence is an intrinsic limitation of sensitivity using near-IR excitation on the Raman intensity, this can be mitigated by an increase in the sensitivity of the detector.

FT-Raman uses an inferometer to combine individual components (light sources) to form an interference pattern which can be recorded and then analysed. Use of an inferometer, along with computation using the fast Fourier transform, enables the generation of Raman spectra from a time dependant inferogram.

2.2.6 Effect of Hydrogen bonding on Raman spectra

Raman Spectroscopy is very sensitive to hydrogen bonding. A hydrogen bond can be termed as X-H---Y where X-H is from one group while Y is from another. If the X is a highly electronegative atom the X-H bond can be partially ionic, while the H---Y is electrostatic with slight weak covalent characteristics. In most cases, a hydrogen bonded X-H group has a decreased stretching frequency, the band also broadens and increases in intensity. X-H bending bands tend to increase in wavenumber upon hydrogen bonding to a lesser extent than that of the stretching bands. Intramolecular hydrogen bonding can have a significant effect on Raman spectra favouring pseudo-five/six membered ring formation. Conjugated intramolecular hydrogen bonded systems (keto/enol) result in very strong hydrogen bonds.

2.2.7 Fermi Resonance

Fermi resonance is a phenomenon that occurs when two vibrations that possess suitable symmetry and have similar energy, mix with each other. The two vibrations are usually a fundamental vibration and an overtone or a combination band and should appear in the spectrum as two peaks, one strong and one weak. For the effect of mixing the resulting spectrum shows 2 bands that are relatively strong with one of them nearly coincident to the fundamental band. The intensity of the resonance band is greater than that expected for an overtone band, and changes in the crystalline state can also affect those intensities.

2.3 CASTEP

To complete the peak assignments for the Raman spectra, DFT calculations were performed using CASTEP. CASTEP is a periodic DFT calculation programme, that can be used to calculate multiple different material properties. The importance of choosing a periodic DFT code is that it takes into account both the inter and intra molecular effects of the vibrational frequencies (in contrast to other single molecule DFT software, like for example DMOL3 which only takes into account the intra molecular effects). Due to the computational power required for these calculations, a high-performance computing cluster known as SCARF was used to run the code. The first calculation step for the vibrational frequencies is a geometry optimisation until convergence is reached (convergence criterium is a set minimum variation in total energy), using the GGA (Generalised Gradient Approximation)-BLYP functional and norm conserving pseudopotentials. Sampling the Brillouin zone, the K-point sets were customised individually to have 16 points for each material. Once the geometry optimisation is done, the vibrational frequencies of the periodic structure can be calculated. The programme is set to automatically calculate the IR frequencies and corresponding intensities and, if any frequencies are Raman active or inactive. Raman intensities are not calculated due to the computationally intensive nature of the process. The calculated frequencies could then be transferred to materials studio, in which the vibrations can be analysed to produce the assignments with regards to the structure of the compound under study. The resulting

assignments can then be matched to the peaks in the experimental data, and any changes within the spectra for each material is also observed and tracked.

2.4 Neutron Spectroscopy

Unless otherwise referenced the information in this section has been gathered from Principles of Neutron Scatter from condensed matter (Boothroyd, A.)[1].

As said earlier, a beam of neutrons of 1 Å wavelength, not only has a wavelength that fits the interatomic distances in crystalline materials but also has an energy that matches that of excitations typical of atomic and molecular oscillation (in the range of meV). When a neutron interacts with a nucleus the scattering can be elastic or inelastic. In the former, the neutron emerging from the scattering has the same energy as the incoming one, while in the latter there is a change in the energy carried by the neutron. Diffraction falls by definition in the elastic scattering category, while spectroscopy deals with inelastic scattering.

Neutron Spectroscopy is, therefore, the technique that allows us to extract details on the motion of atoms in materials by measuring the change in energy during the neutron-nucleus interaction.

Inelastic neutron scattering can be used to probe multiple different excitations in condensed matter, for example (in order of increasing energy): rotational tunnelling of molecular groups, diffusion and spin fluctuations, acoustic and optical phonons, magnons, molecular vibrations and crystal field excitations.

There are multiple advantages to utilising Neutron Spectroscopy over the more standard Photon spectroscopy (like IR and Raman, see Chapter 2.2), the major advantages are:

1) all vibrational modes are measurable in neutron spectroscopy because selection rules do not apply. Selection rules dictate which change of electronic state is visible with a given photon spectroscopy. For example: when the polarisability of a molecule changes due to a specific molecular deformation, the corresponding vibrational mode is Raman active. Instead, when it is the dipole moment to change due to a molecular deformation, the corresponding mode is IR active.

2) Isotopic labelling is possible for multiple elements and often necessary due to the strong incoherent scatter of hydrogen containing compounds.

3) Ability to probe materials that are non-transparent to light.

4) Using the Born approximation, the peak intensities are proportional to the amount of sample in the beam and the square of the mode amplitudes. Hence, they are relatively easy to model.

There are, however, some disadvantages to Neutron vibrational spectroscopy in comparison to Photon spectroscopy:

1) Neutron spectroscopy requires a relatively large sample size (> 1 g)

2) The energy resolution is poorer than photon spectroscopy in general.

3) Neutrons are not as easy to produce as a beam of light, and hence, cannot be easily used in a standard laboratory setting unlike IR and Raman Spectroscopy.

2.4.1 Time-Of-Flight Neutron Spectroscopy

The essence of Neutron Spectroscopy rely in the capability of detecting the changes in energy that neutrons experience when interacting with the nuclei. As seen in eq. 10-14, the change in energy is directly related to the change in wavelength, which is related to the speed of the neutron via the de Broglie relation and hence to the time a neutron take to travel from the sample to the detector:

$$\lambda = ht / mL$$

(where h is the Planck constant, t is time, m the mass of the neutron and L the sample-detector distance). Measuring the time-of-flight of neutrons is therefore the best way to detect their change in energy. At a pulse source, this technique takes full advantage of the nature of the source, while at reactors sources choppers are used to shape the incoming neutron beam in pulses, making it much easier to define a t_0 time for the start of the neutron's travel.

ToF spectrometers are particularly useful for studying a broad range of wavevectors or energies simultaneously. When surveying large regions of (Q, ω) space, ToF provides an understanding of excitation spectra and the respective backgrounds in a great level of detail.

There are additional benefits in the applications of a pulsed source:

1) There is a high flux of epithermal neutrons (i.e. VESUVIO) which can be used to measure high-energy excitations/momentum distributions.

2) There is an inherently low background, by the time the spectrum is recorded the fast neutron background has generally decayed to zero.

2.4.2 Atomic vibrations in crystals

Atoms vibrate about an equilibrium position and the vibrations across sites are coupled by interatomic forces. Harmonic approximation can be used when the interatomic separation is large in comparison to the amplitude of vibration. For this to be the case, the equilibrium position of the atoms needs to be the minimum of a quadratic potential. When all the atoms vibrate at the same frequency the coupled oscillation in harmonic crystals are described as a set of normal modes. The exchange between these normal modes and the energy quanta is the cause of inelastic neutron scattering from the atomic vibrations.

2.4.3 TOSCA

TOSCA is a vibrational spectroscopy instrument measuring ToF spectrum using an indirect geometry set up (Fig 17). Indirect or inverted geometry fixes k_f (final wavevector) and then use ToF to define k_i (initial wavevector). The ToF at a spallation source such as ISIS is measured from the initial burst of high energy neutrons at the target. These are then passing through the 300 K water moderator where they are slowed down. As in the case of SXD, the Maxwellian energy distribution emerging from the moderator is peaked around 1Å. The very fast neutrons are then further suppressed by a t_0 chopper. E_f or final energy is then selected by an analyser crystal Bragg reflection typically this is the 002 reflection of a pyrolytic graphite crystal with a filter repressing higher order reflections .

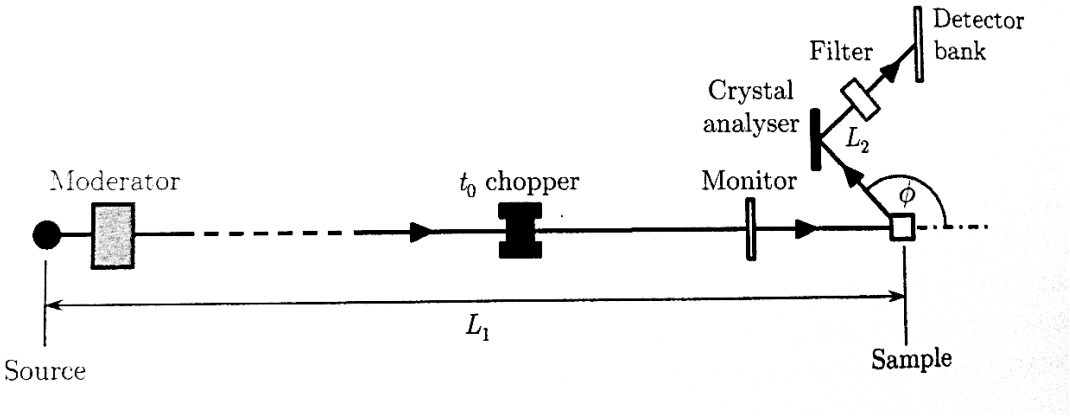


Figure 17: General schematic of an indirect-geometry crystal analyser spectrometer at a spallation source.[1]

Importantly in indirect-geometry spectrometers a wide range of energy transfer in neutron energy loss ($\hbar\omega > 0$) can be accessed from a single E_f.

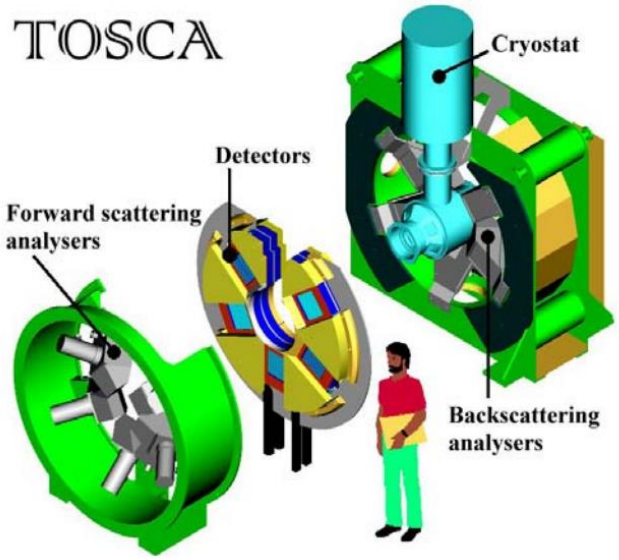


Figure 18: instrument set up on TOSCA[19]

Experiments on TOSCA (Fig 18) are typically run at 10 K, this means that the majority of the vibrations seen are fundamental vibrations as the molecules are in the lowest energy ground state.

2.5 References

1 A. T. Boothroyd, *Principles of Neutron Scattering from Condensed Matter*, Oxford University Press, 2020.

2 C. William, ed., *Crystal structure analysis: Principles and practice*, International Union of Crystallography, [Chester, England], 2001.

3 *Pulsed neutron scattering*, Taylor & Francis, London, 1981.

4 B. Previdello, Orientation effect on Pd/Pt(hkl) nanofilms : electro-deposition, characterization and electrochemical Pd-H isotherms, Doctoral dissertation, Grenoble., 2013.

5 X-ray Crystallography - William Clegg - Google Books, https://books.google.co.uk/books?hl=en&lr=&id=x8b9CAAAQBAJ&oi=fnd&pg=PP1&dq=william+clegg+crystallography&ots=idKtzv5OUW&sig=upaXPPEJesvopV3Bb3rbU18QuN8#v=onepage&q=william%20clegg%20crystallography&f=false, (accessed 29 November 2023).

6 W. L. BRAGG, Proc. Cambridge Phil. Soc., 1913, 17, 43–57.

7 P. P. Ewald, Zeitschrift für Kristallographie - Crystalline Materials, 1921, 56, 129–156.

8 P. Edlund, , Structural Features of Bacteriophytochromes. Photoactivated Proteins studied by Serial Femtosecond Crystallography,Doctoral disseration Gothenburg, 2018.9 W. C. Roentgen, Session Physical Medicine Society, 1895, 137, 132–141.

9 W. C. Roentgen, Session Physical Medicine Society, 1895, 137, 132–141.

10 F. W. , P. and L. M. Knipping, Bayer. Akad. Wiss. München, 1912, 303–322.

11 J. W. G. Thomason, *Nucl. Instrum. Methods Phys. Res. Sect. A*, 2019, **917**, 61–67.

12 Produced by Dr Siliva Capelli

13 D. A. Keen, M. J. Gutmann and C. C. Wilson, J. Appl. Cryst. 2006, 39, 714–722.

14 G. Mauri, G. J. Sykora, E. M. Schooneveld, S. Capelli, M. Gutmann, S. Howarth, S. E. Mann, F. Zuddas and N. J. Rhodes, Novel high efficiency 2D position sensitive ZnS:Ag/ 6 LiF scintillator detector for neutron diffraction . (2023) submitted for publication to *J. App. Cryst.*

15 *Infrared and Raman Spectroscopy: Principles and Spectral Interpretation*, Elsevier Science & Technology Books, 2017.

16 N. Tarcea, T. Frosch, P. Rösch, M. Hilchenbach, T. Stuffler, S. Hofer, H. Thiele, R. Hochleitner and J. Popp, *Space Sci. Rev.*, 2007, **135**, 281–292.

17 K. Chao, S. Dhakal, J. Qin, M. Kim and Y. Peng, *Applied Sciences 2018, Vol. 8, Page 431*, 2018, **8**, 431.

18 X. Fan, L. Liu, Z. Kang, Y. Zeng, … Y. Z.- and undefined 2020, *spectroscopyonline.comXG Fan, L Liu, ZM Kang, YJ Zeng, YL Zhi, X WangSpectroscopy, 2020•spectroscopyonline.com*.

19 S. F. Parker, C. J. Carlile, T. Pike, J. Tomkinson, R. J. Newport, C. Andreani, F. P. Ricci, F. Sacchetti and M. Zoppi, Physica B Condens Matter, 1997, 241–243, 154–156.

3 Development of *in situ* Raman Scattering and Neutron Diffraction

The development of simultaneous Raman Scattering and Neutron Scattering, began around 2009 with the development of a Raman stick to be used in conjunction with TOSCA, the inelastic scattering instrument at ISIS[1].

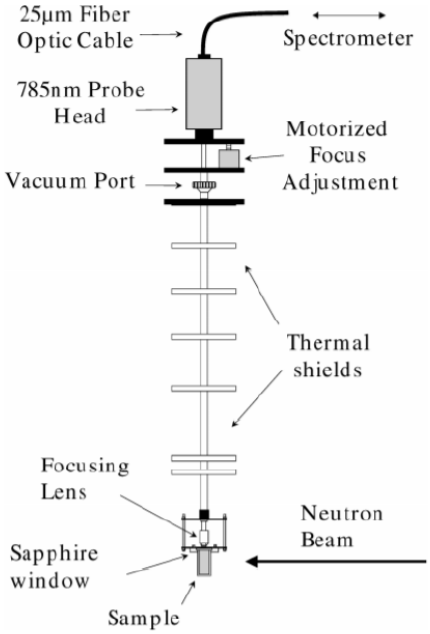


Figure 19: Raman central stick schematic for TOSCA[1]

The stick design included multiple thermal shields, a motorised focus adjustment, focusing lens, sapphire optical window, vacuum port, probe head for the laser and a fibre optic cable to the spectrometer. The centre stick itself is made of two concentric steel tubes with thin walls, which are 1.65 m in length (Fig 19).

A second Raman centre stick was developed for use on VISION[2], a neutron spectroscopy instrument at OakRidge National Laboratory (USA) in 2018 (Fig 20). This stick also included a gas handling system and a different Raman laser set up in that the fibre optic cabling went through the cryogenic chamber of the stick to finish ~25 cm above the sample position.

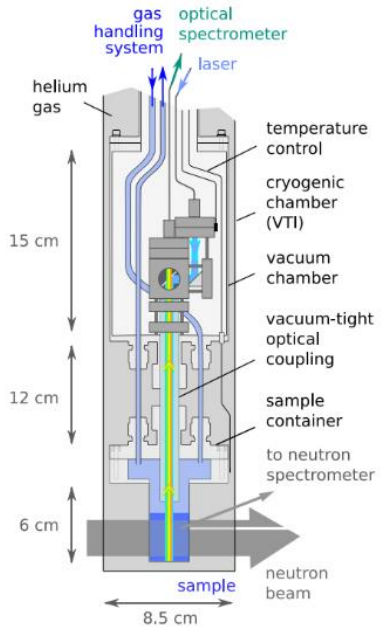


Figure 20: Raman central stick design for VISION[2]

Our design for the Raman stick (see Fig 21) has been adapted from the idea of the TOSCA stick. The main body of the stick was designed so that the length of the stick could be adjusted to fit multiple instruments. At the same time as a long range focusing lens was used to fit the Raman laser probe head at the top of the stick (Fig 22). The initial design and build of the stick was completed by the design team at ISIS, with the scientific advice of Dr Dominic Fortes. The sample position was initially split into two separate chambers, one for the neutron diffraction sample and an optical chamber enclosed by a quartz window for the Raman sample (Fig. 23a/24b). The neutron sample chamber initially was a Vanadium can as is traditionally used in most neutron diffraction experiments. The use of an opaque Vanadium Can meant that for use on SXD the effective position of the crystal could not be assessed, but only a rough estimate of it could be used to centre the stick on the instrument, having the sample at the correct beam position. This also required the use of a large

incoming beam cross section increasing the background noise which could compromise the intensity of the weak peaks at high diffraction angles.

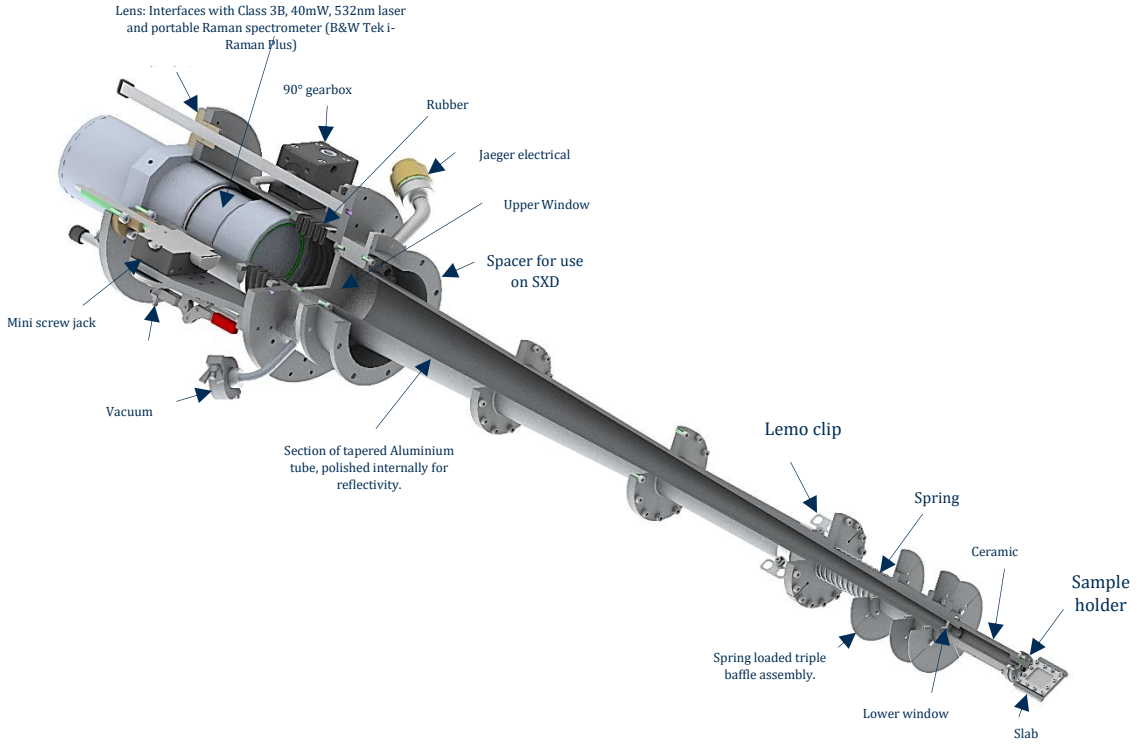


Figure 21: slice view of the initial central stick design with labelled sections



Figure 22: Extended focus lens and Raman spectrometer with attached probe

In order to visualise the crystal in the neutron diffraction chamber, the material for the chamber itself was changed from Vanadium to quartz (Fig. 23b). This had the advantage of positioning the crystal at the correct height for being at the exact beam position once the stick was placed in the instrument. The quartz capillary does give rise to some background noise, but not of the same nature as the Vanadium. In the latter case the background noise is given by the incoherent diffraction of the Vanadium, i.e. it is the same in all directions, at all angles; instead the quartz diffracts as an amorphous material, i.e. with few broad amorphous lines at low diffracting angles and almost zero contribution at higher angles.

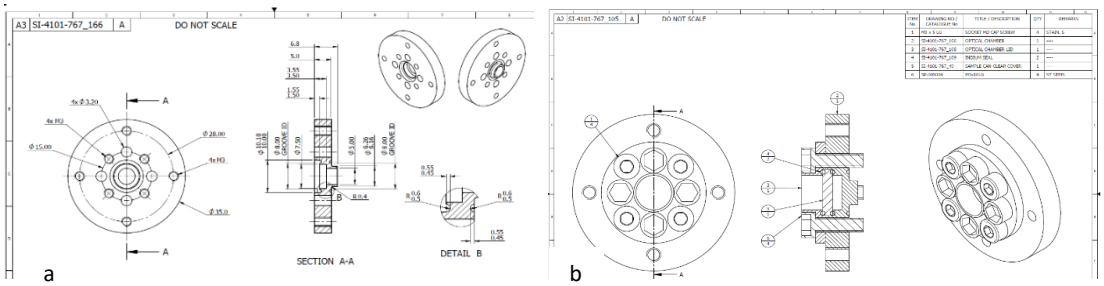


Figure 23: Design drawings of a) first stage single chamber sample environment compared to b) the initial dual chamber

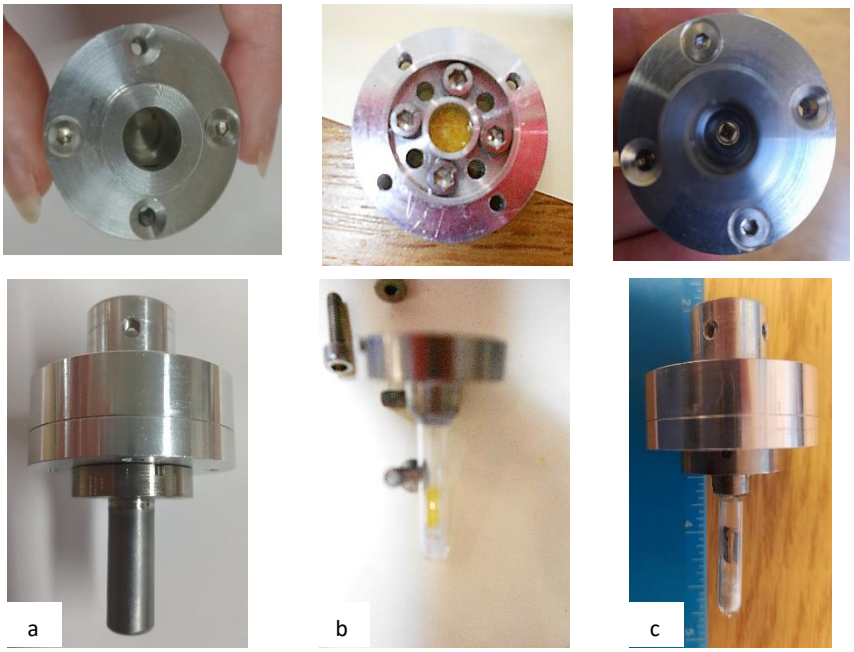
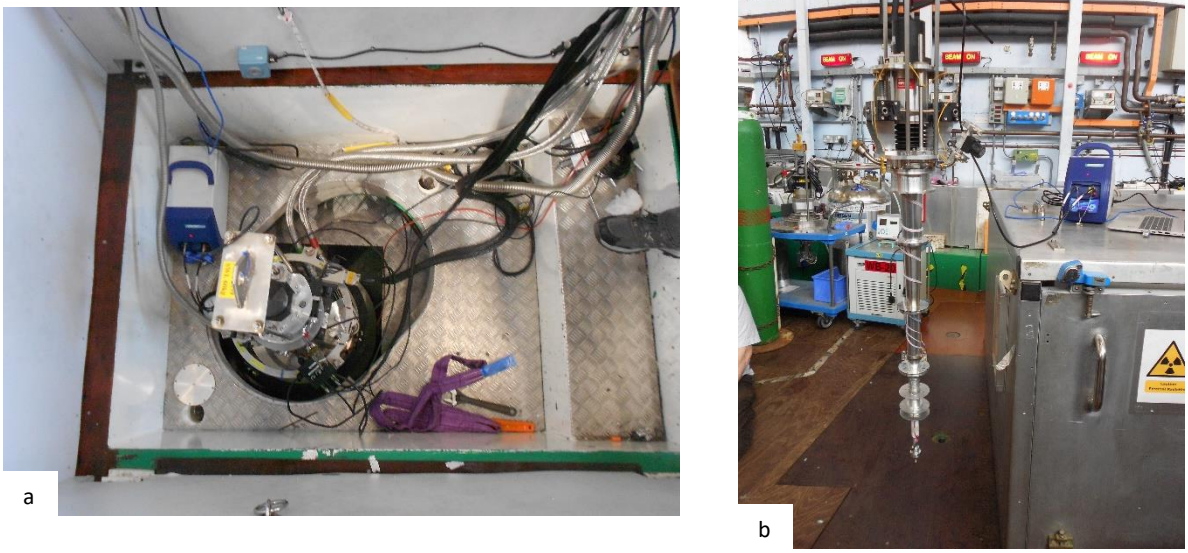


Figure 24: Stages of sample environment design a) initial vanadium can, b) Dual camber quartz capilliary, c) single chamber quartz capillary.

A further development of the stick was the use one of a unique chamber for both the diffraction and the Raman experiments. The new piece basically got rid of the optical chamber: a hole allowed the laser beam from the Raman spectrometer to reach the position of the crystal in the diffraction chamber, that was sealed with an optical window (Fig 23c/24a). The Raman beam was focussed on the sample via a long focusing lens, the centring of the sample and the focussing of the laser could be completed off-line, before positioning the stick on the SXD instrument.



a b

Figure 25: Raman Scattering Central stick a) inside the SXD sample pit and b) on the crane for moving into put

When first using the two-chamber design of the stick on SXD to collect data, it was found that the weight of the stick as a whole caused some issues to the motor driving the rotation of the stick itself on the instrument, preventing access to the full rotation range of 350^{o} (fig 25). The problem was solved by replacing the motor with a more powerful one. In moving the stick from the stand where the alignment of the laser was completed to the instrument, we noticed that the slightest pull on the cables connecting the spectrometer could knock the laser out of alignment. Investigating the matter, we found a lack of stability at the point where the laser was attached to the long focusing lens. Whilst some movement was necessary to enable the different lasers to be interchanged without damage, too much

movement could cause alignment losses during the experiments. In order to understand the problem, the telescopic lens was imaged to verify its internal structure. This then allowed for changes to be made: to increase the stability of the lens and reduce the movement of the laser tip, a cylinder was inserted into the top section of the lens. The modified stick was then once again tested offline, and it was found that although the problems with the laser alignment were solved, there was still not a strong enough signal going back to the spectrometer to collect data (fig 26). The free rotation of the laser probe head within the lens increased the overall range of motion of the stick during the neutron diffraction experiment without affecting the alignment of the sample in respect to the laser and avoiding the possibility of the cables getting entangled.

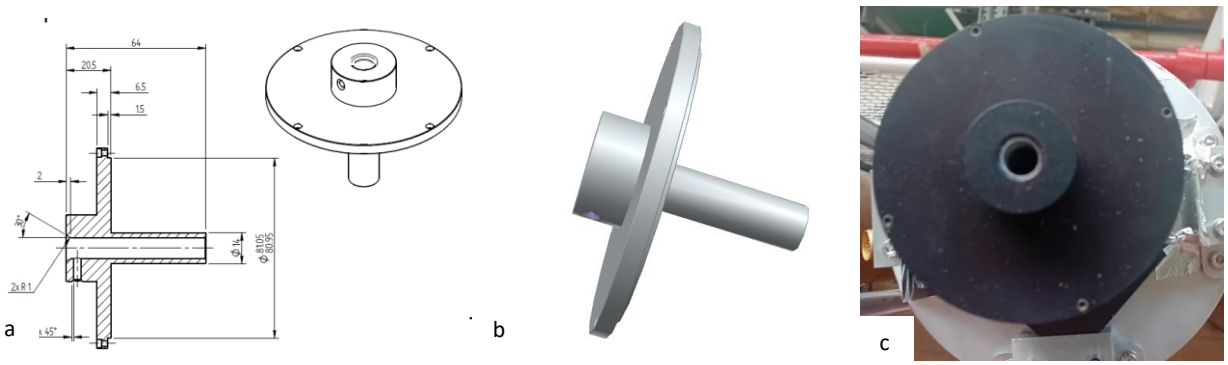


Figure 26: Redesign of the top of the focusing lens a) design sketch, b) 3D representation drawing, c) final redesigned product.

After a period of inactivity of the setup due to the long shutdown at ISIS, in which the sample holder was stored separately from the stick, we found that the quartz capillary had bent at an angle from the inline position that allows the laser to hit the sample. This might have been caused by the irradiation from the red 780 nm laser heating the glue holding the quartz to the aluminium support and causing it to become malleable. This observation led to additional conversations on ways to modify the sample holder that would also allow for an easier change of the quartz capillaries. The decision was made to alter the design in such a way that the capillary would no longer be solidly attached to the main aluminium plate but,

could be attached to it via a thread extruding for the main plate. This implied it was no longer necessary to take completely apart the whole sample chamber in order to change sample. The new design resulted in a much easier and faster switch between samples as well as the possibility of having assorted diameters for the capillaries (Fig 27). A further benefit of the new sample chamber was an easier handling of any air-sensitive or light-sensitive materials (in our case the transport of the irradiated state of the photochromic compounds).

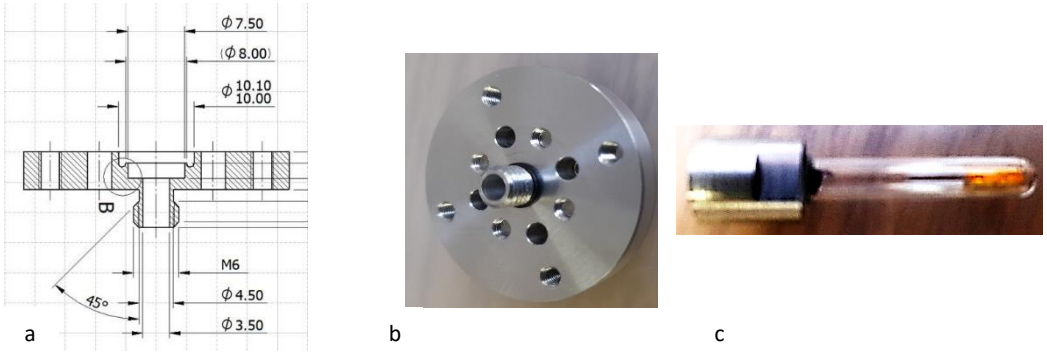


Figure 27: design schematic and final product of end stage sample environment design a) design sketch, b) final product of top flange, c) final redesigned product of capillary with screw thread top.

The new sample chamber was tested offline using a ruby crystal, the 532 nm laser, and an alternative Ocean optics HR spectrometer (provided by Dr Chris Ridley) that had a wavelength range suitable for use with the ruby crystals whilst still using a laser that could eventually be used during an experiment. The use of the ruby crystals allowed for millisecond collection times which meant seeing in "real time" the effect of minor changes to the laser position on the centring. Once the laser was focused and aligned to give the strongest signal from the ruby, the spectrometer was switched back to the near IR (785 nm) laser and the ruby crystal was switched for the 2-Iodo-(3,5-di*tert*butylsalicylidene)-aniline sample in order to test whether the new setup would match the conditions of the experiment previously completed using the dual chamber sample holder. After adjusting laser power output and exposure time, the results of the experiment were deemed equivalent to those obtained with the dual sample chamber, proving that the new sample chamber setup did work (Fig 28).

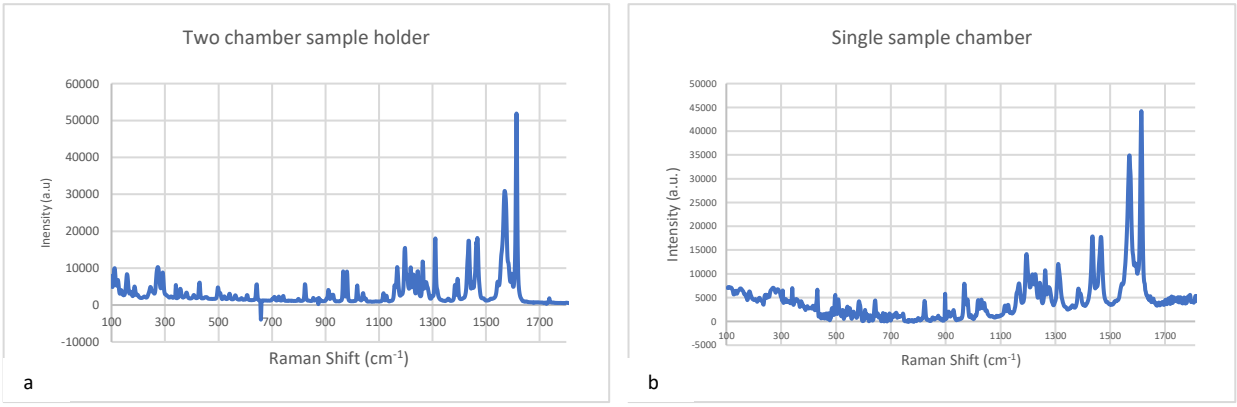


Figure 28: spectra comparing the a) dual and b) single sample chamber intensities of 3,5-di-tertbutylsalicylidene-2-iodoaniline

When we repeated the experiment *in situ* with the Raman Stick inserted in the CCR on SXD, the laser was focused at the position determined offline, such that the sample would be at the correct height in respect to the incoming beam for the neutron experiment. The lens was fixed in place once aligned using the camera which can be placed into the sample position (fig 29). Test data sets were collected to allow for optimisation of the experimental set up to get the strongest peak intensities with the lowest signal to noise ratio. Overall, the peak intensities were weaker than previously seen with a higher signal to noise ratio, this could be due to a difference in the capillary material as well as the overall CCR environment. Another reason for the weak signal could be the quality and positioning of the sample within the capillary not being completely optimised for the Raman data collection over the Neutron experiment.



Figure 29: enclosed attachment for focusing camera at correct distance for sample

To reduce the overall weight of the central stick the top portion in which the lens rests was redesigned to remove superfluous parts as compared to the original design (Fig 30).

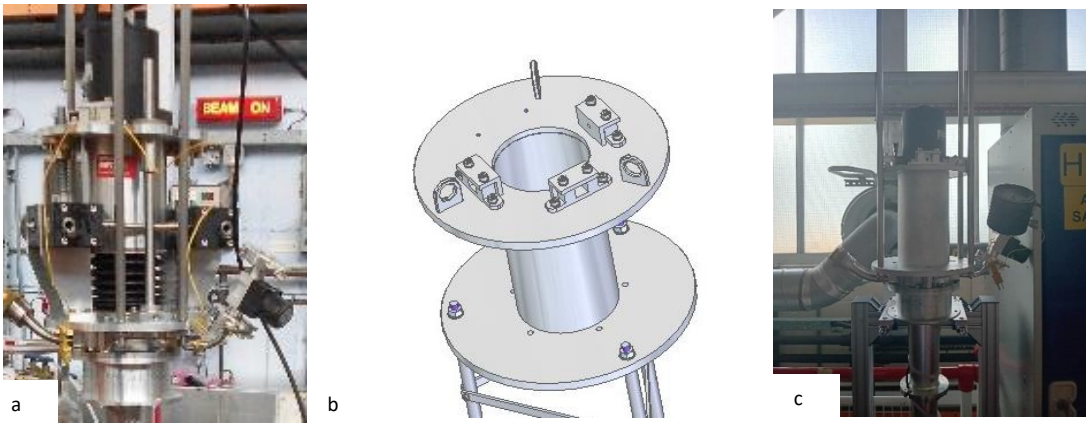


Figure 30: stages of design for top of central stick. a) initial design, b) drawing of upgraded top, c) photograph of upgraded top final product.

In order to avoid shadows on the diffraction pattern from the bulky aluminium part of the sample holder, the crystal should sit at the bottom of the quartz capillary, but the changes made to the sample holder resulted also in a different position of the crystal with respect to the neutron beam on SXD. To fix this problem, the spacer connecting the sample chamber to the end of the central stick had to be modified to account for the change in height and allow the crystal to sit again in the correct position in the neutron beam (Fig. 31/32).



Figure 31: full image of final central stick design



Figure 32: Space position of sample environment on SXD

To keep the sample in a fixed position in the capillary, i.e. both in the Neutron beam and in the focus of the Raman laser, small amounts of vacuum grease were added to each end of the crystal keeping it attached to the capillary's wall.

Procedure for alignment and set up for the *in situ* Raman collection stick on SXD.

1) Make sure sample position is at the correct height for the SXD instrument (using the correct spacer).
2) Find the focus of the laser through the lens for the given sample distance.
3) Attach the camera to the stick at the sample position and check the laser position and alignment within the stick (<10 % power output).
4) Once laser is aligned and fixed into position replace the camera with the sample chamber.
5) Run a short dark and initial data collection (75000 ms, 2 iterations, 80 % power) to check that data can be collected from the sample (making sure that the laser cannot be seen by the naked eye).
6) Using the initial data collection, optimise the time per run, number of iterations and power level to give the best statistics in the shortest time frame. Remembering that the relationship between data intensity and the collection set up is non-linear, particularly for power and collection time per iteration.
7) If necessary, collect multiple complete data sets. These can then be averaged out to improve the overall statistics of the data (especially when the sample gives a weak or noisy signal)

3.1 Conclusion

In this section the design and improvement of the Raman scattering central stick for use on SXD was discussed. This includes changes to the sample position to allow for direct irradiation of the sample in the neutron beam by the Raman laser, improvements to the top section to prevent movement of the laser probe head and, reduce the weight iof the stick by removal of superfluous sections.

3.2 Further developments to the stick could include:

1) an automated centring/focusing of the laser onto the sample. This would require further changes to the lens as the focus is currently manual with a thin thread. The thin thread of the lens means that there is a large focusing range and that a very large number of rotations are required to make any significant changes to the focussing length. Changes to the top of the lens could allow for sideways controls, to position the laser correctly with respect to the central stick whilst keeping the lens in place and consequently reducing the time spent on sample alignment prior to each experiment.
2) an extra attachment for a UV 365 nm lamp (or for other sources of light that could trigger changes in the sample) that could be inserted in place of the Raman laser. This could allow for continuous *in situ* irradiation of the sample during the neutron diffraction experiment.
3) a movable mirror and a long distance camera, to align the laser on the sample *in situ* once the central stick is in the CCR on SXD. The camera can then also be used to monitor any changes to the sample state or position throughout the experiment. The mirror could also be used to swich from Raman laser to another source of irradiation for the sample.
4) The Raman signal emerging from the sample is quite weak, so to improve that, one could think of coating the inside of the quartz capillary with a very thin layer of a

'neutron transparent' but reflective material, to help increasing the strength of the signal travelling back to the spectrometer. To retain the visibility of the crystal within the chamber the coating would have to be very thin, or similar in design to a mirror which can be seen through in one direction.

3.3 Specifics of B&W Tek i-Raman Plus lasers and spectrometer.

The central stick design fits the laser head probe (Fig 33) of two B&W Tek i-Raman Plus spectrometers, 532 nm and 780 nm which have green and near IR lasers respectively. The use of two different wavelengths result in a wide range of sample that can be studied, especially those (usually organic materials) affected by fluorescence at 532 nm that give a nice signal with the 780 nm laser. The flexible fibre optic cables which attach the laser probe head to the spectrometer allow for a range of motion and the placement of the spectrometer in the sample pit but away from the edge of the cryostat. As discussed in chapter 2.3 (pg. 43) the resolution of Raman Spectrometers is played off against the range over which data can be collected. For this spectrometer the resolution is also played off against the portability of the spectrometer as well. As a result to have the near 3000 cm^{-1} and near 4000 cm^{-1} data collection range for the 785 nm and 532 nm lasers respectively the resolution of the two spectrometers is 4.5 cm^{-1} . Such a resolution does mean that subtle changes to the Raman Spectra can be more difficult to evaluate, and in some cases additional measurements on a higher resolution instrument offline could be required.



Figure 33: internal schematic of B&W Tek i-Raman Plus probe head.

3.4 References

1 M. A. Adams, S. F. Parker, F. Fernandez-Alonso, D. J. Cutler, C. Hodges and A. King, *Appl Spectrosc*, 2009 , **63**, 727–732.

2 Gillis, R. C., Cheng, Y. Q., Gallmeier, F. X., Hartl, M. A., Huegle, T., & Iverson, E. B. (2018). A sample holder for simultaneous Raman and neutron vibrational spectroscopy. *Rev. Sci. Instr.*, 89(1); https://doi.org/10.1063/1.4997933

4 Photochromism and Thermochromism in Salicylaldehyde Aniline Derivatives

4.1 Introduction and Literature Review

Photochromism can be defined as the reversible photocolourisation of a single chemical species, between two states which have distinguishably different absorption spectra. This is brought about by an action of absorbing electromagnetic radiation in at least one direction[1]. The process of photochromism is similar enough to other photochemical reactions in that it presents the same problem of the photoproduct not forming in a separate phase. The salicylaldehyde aniline (SA) derivative system often represents a photoequilibrium, the reversible nature of photochromism is what separates it from general photochemical reactions[6]. A photochromic system consists of two tautomers each with different colours that mutually interchange in their excited states[7]. For example, photochromic SA compounds are pale yellow at room temperature and become red upon irradiation. In comparison, thermochromism is the reversible change of colour based on a variation in temperature[8]. The resulting absorption spectra is similar to that of the photoproduct produced in photochromism. Thermochromic SAs are orange/red at room temperature and become yellow at lower temperatures[9].

Many salicylaldehyde aniline derived Schiff bases are either photo- or thermo-chromic in the crystalline state. For these compounds it is suggested in the literature that the cause of this phenomena is intra-molecular tautomerisation from the enol form, to either the cis or trans keto form (figure 34), with all N-salicylideneaniline being photochromic in rigid glasses[10].

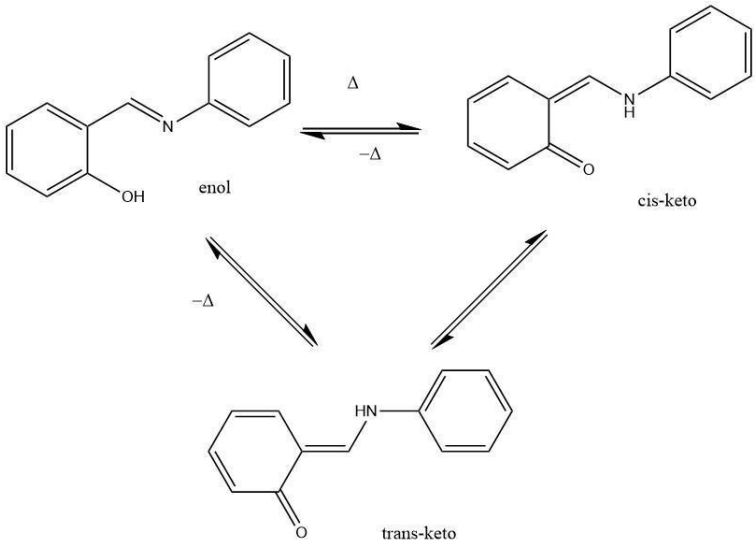


Figure 34: schematic of the transition between enol, cis-keto and trans-keto tautomers

The majority of literature agrees that thermo and photochromism are mutually exclusive. In the case of SA compounds it is believed that the cis-keto form is linked with thermochromism, while the trans-keto form is linked to photochromism. However, some reports suggest there are possibilities for a compound to display both properties as the process shifts from one tautomer to another in equilibria, and hence with tuning could be forced to fully transform into the desired trait[11,12]. There can also be some temperature dependency to photochromic compounds which display a paler colour at lower temperatures, even though the colour of the photo product is maintained over that of the enol form. More recent studies have again suggested that the enol form is colourless in photochromic materials, as was originally put forward by Cohen *et al*[1,2].

As the trans isomer requires the framework to be sufficiently "open", the non-planar (dihedral angle between sub-units $\phi > 30$) N-salicylideneaniline are traditionally photochromic.

Three mutually dependant factors can cause the chromism in SA compounds:

1) the transfer of a proton caused by the intramolecular O···N hydrogen bonds

2) a change in the tautomeric form

3) a contribution from fluorescence (particularly in those where the change is thermochromic) and not only the absorption of visible light as a consequence of the change in molecular geometry and tautomeric shift.

Within the molecule the N-aryl bond is substantially twisted, with the salicylaldimine group planar and exhibiting intramolecular H-bonding, the aniline ring is rotated by ~50° with respect to the plane, precluding the formation of any close contacts. The basicity of the N-atom is lower in non-planar molecules as the lone pair does not interact with the aniline ring, this allows for stronger OH···N. The photoproduct is formed from excitation to the cis-keto state when irradiated with UV light, then proceeding to the trans-keto state via geometric changes caused by proton transfer. Before the irradiation takes place for the majority of photochromic compounds are known in their enol form, with the exception of 4-iodo-3,5-di-*tert*-butylsalicylidenaniline. The decay rate (reversion to enol tautomer) of the photoproduct (keto tautomer) remains unaffected by deuteration of the -OH group. This while supporting that the structure is stabilised by cis to trans isomerism, also indicates that this conversion is the rate determining step of the reaction rather than the keto-to-enol conversion[8,13].

Additional classifications have been suggested for photochromic compounds:

a) Photo reversible: the initial form (A) absorbs at a shorter wavelength than the photoproduct (B), there is a reversion to A *via* exposure to white light as well as thermal reversion. Some materials can be reversed by both thermal and photo stimulation.

b) Reversible photochromic systems: A absorbs at a longer wavelength than B ($\lambda_B < \lambda_A$)

c) Multireversible photochromic systems: more than one chromophore is present, but it is not always clear if more than one is active.[3]

There has been a lot of interest in recent decades in N-salicylideneaniline Schiff bases due to their applications in technology[1] (optical switches). As such, there is also research around compounds with similar structures (e.g. N-salicylidenealkylarylamines), some of which are simultaneously photo- and

thermo-chromic, suggesting that the planarity of the molecule is not the sole factor facilitating the proton transfer, but the electron density of the imine nitrogen also plays an important role stabilising the keto form over the enol one. Earlier work suggests there is no correlation between the substituents on the rings and photochromicity[4], but it seems overall agreed that the ortho-hydroxy group is essential to the process.

A further difference between the photo and thermochromic behaviours of N-salicylideneanilines reported in the literature, is that the thermochromic compounds display fluorescence, which increases in strength as with lowering temperature[6]. The thermochromic compounds also show an increase in the population of the keto form over the less stable enol form.[5] Such a shift in population, however, can be affected by the solvent used for fluorescence spectroscopy. The use of hydrocarbon solvents shifts the equilibrium of N-salicylideneanilines so that the population of the cis-keto form instead increases at lower temperatures[6]. The keto form displays an absorption band in the visible region whereas none is present for the enol form. The absorption band appears at 4800 $\dot{A}$, and its intensity decreases with the temperature[2].

Large substituent groups on the rings such as tert-butyl groups hinder the formation of the cis-keto form, so that a compound containing one or more large groups is more likely to be photochromic than thermochromic. The thermochromic compounds are further restricted in their structural conformation by the locking of the intramolecular hydrogen bonding salicylaldimine group. The reaction proceeds through the formation of H-bonded cyclic dimers. The electron density of the imine-N is a crucial part in thermochromism, this means any substituents on the ring weakening the O-H bond or, that enhance the imine-N ability to accept H^+ (forming a string NH bond) would favour thermochromic traits over photochromic ones[16].

Five N-salicylideneanilines that displayed either photo- or thermo- chromic properties were chose for this study (Figure 35). For all compounds the characterisation was found to be incomplete, because there are no published neutron diffraction data, and for 4 out of 5 compounds no Raman spectroscopy data have been reported, as well as limited IR data were published.

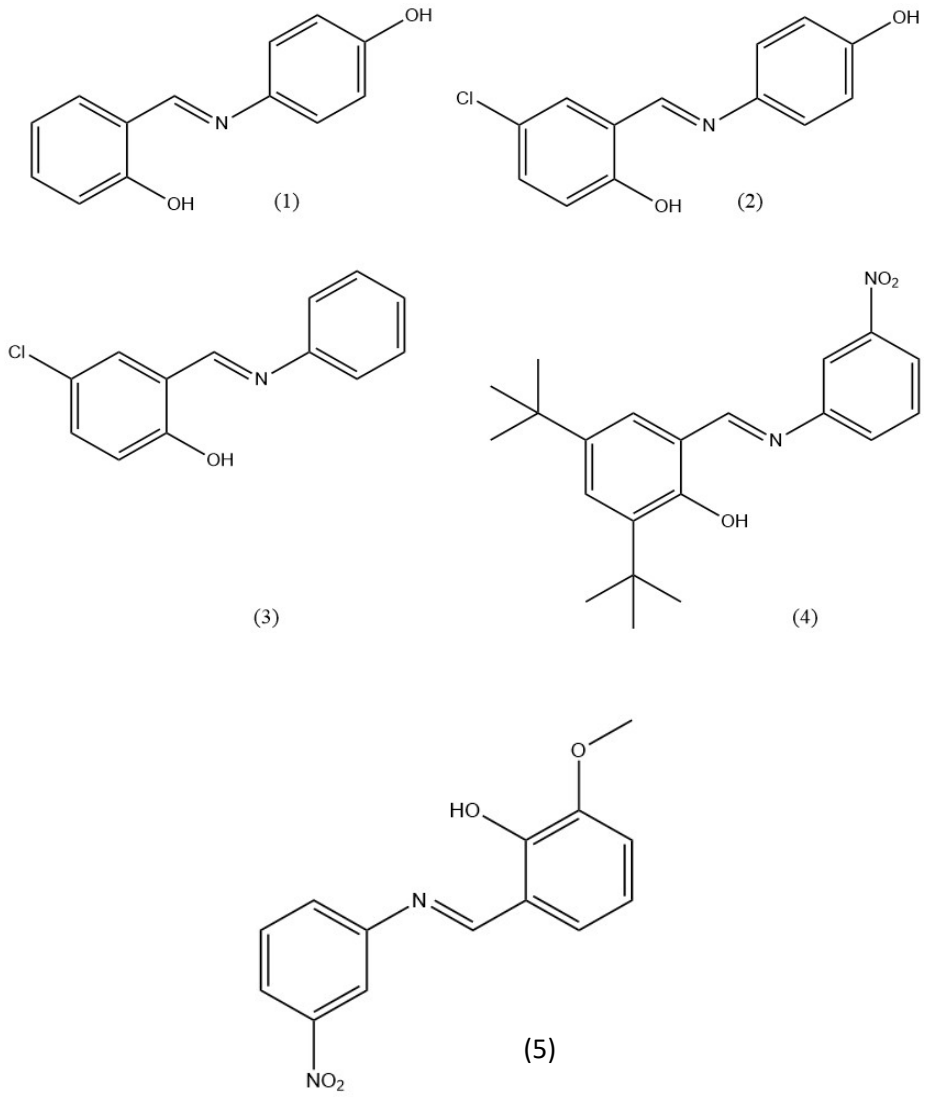


Figure 35: Structures of the selected N-salicylideneanilines used in this study. 1) N-(4-hydroxy-phenyl)-2-hydroxybenzaldehyde-imine, 2) N-(5-chloro-2-hydroxybenzylidene)-4-hydroxyaniline, 3) N-(5-chloro-2-hydroxysalicylidene)-aniline, 4) 3,5-ditertbutylsalicylidene-3-nitroaniline, 5) N-(2-hydroxy-3-methoxybenzilidene)-3-nitroaniline

A further series of 14 compounds were synthetised (Fig 36), each of them presenting variations on the ring substituents as compared to the original five compounds. For some of these previous x-ray structures were published. These were chosen to from different series to track the effect of changing the substituents on one or the other of the two rings whist keeping the other ring consistent.

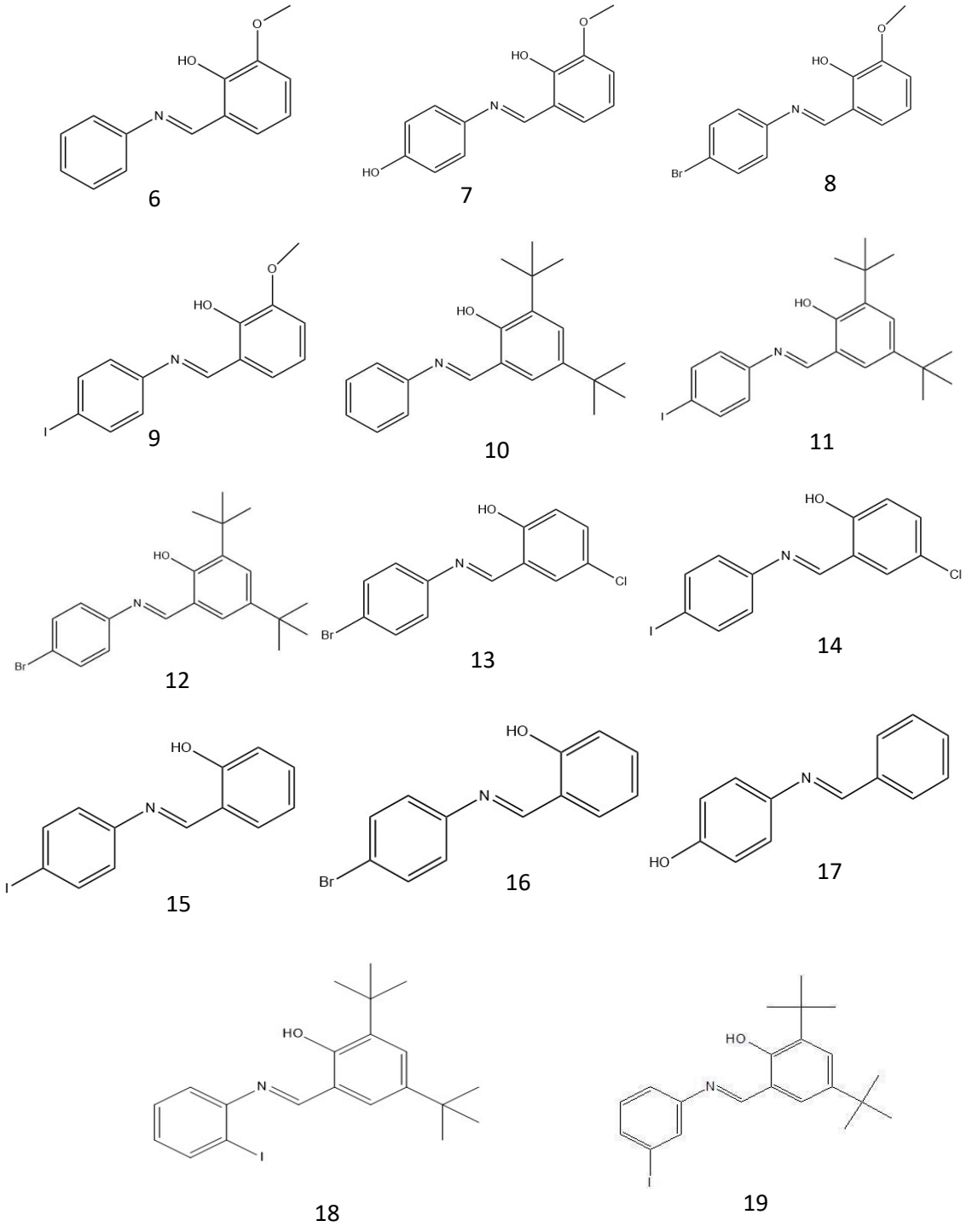


Figure 36: Second set of salicylaldehyde derivative compounds 6-19. 6) N-(2-hydroxy-3-methoxybenzilidene)-aniline, 7) N-(2-hydroxy-3-methoxybenzilidene)-4-hydroxyaniline, 8) N-(2-hydroxy-3-methoxybenzilidene)-4-bromoaniline, 9) N-(2-hydroxy-3-methoxybenzilidene)-4-iodoaniline, 10) 3,5-di-tertbutylsalicylideneaniline, 11) 3,5-di-tertbutylsalicylidene-4-iodoaniline, 12) 3,5-di-tertbutylsalicylidene-4-bromoaniline, 13) N-5-chlorosalicylidene-4-bromoaniline, 14) N-5-chlorosalicylidene-4-iodoaniline, 15) N-salicylidene-4-iodoaniline, 16) N-salicylidene-4-bromoaniline, 17) N-benzilidene-4-hydroxyaniline, 18) 3,5-ditertbutylsalicylidene-2-iodoaniline, 19) 3,5-di-tertbutylsalicylidene-3-iodoaniline.

*4.1.1 Compound **1:** N-(4-hydroxy-phenyl)-2-hydroxybenzaldehyde-imine*

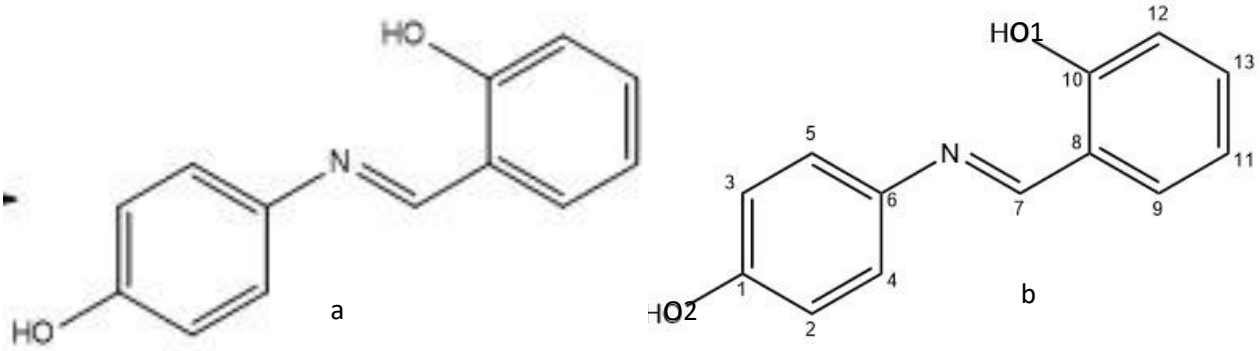
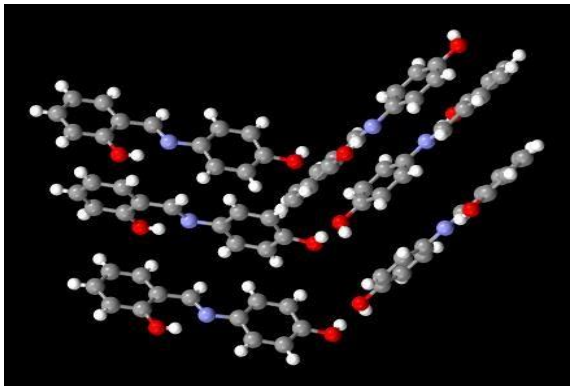


*Figure 37: structure of compound 1 **: a)** N-(4-hydroxy-phenyl)-2-hydroxybenzaldehyde-imine ,b) N-(4-hydroxy-phenyl)-2-hydroxybenzaldehyde-imine atom labelled*

There are two published polymorphs for compound 1 (fig 37), both crystallising in the monoclinic system. The first polymorph produces brown prismatic shaped crystals and the crystal structure can be refined in the space group P 2_1/C, with a very long a axis and a monoclinic angle close to 90 (a=22.041(5)Å, b=10.820 (5)Å, c=8.924(5)Å, β=91.550°)[7]. The second polymorph gives orange block crystals and its structure can be refined in the space group C 2/C[8]. Both studies on compound 1 were completed at room temperature.

The content of the unit cell of polymorph (i) consists of two crystallographically independent molecules linked via intermolecular hydrogen bonding, while that of polymorph (i) has only one molecule. There are slight variations in the geometric data for the two structures as shown below (Fig 38). The structural analysis for polymorph (i) is superior to that for polymorph (ii) in that it reaches a better R value, but there is reasonable consistency for the bond lengths and angles for both polymorphs. To note the short O-H bonds of the hydroxyl group in both structures of around 0.8 Å is likely due to theatre of positioning hydrogens from Xray diffraction data as discussed in chapter 2.1.



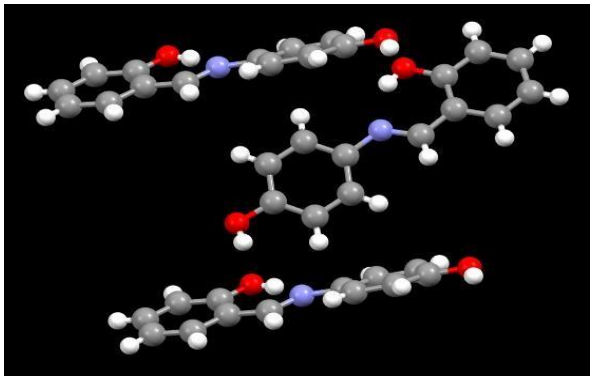


Figure 38: Polymorph (i) (left) and Polymorph (ii) (right) reproduced from data[17,18]

Experimental Raman and IR data were collected for this compound[8] on the $P2_1/c$ polymorph. Computational studies using the software program Gaussian (G03). Structure **1** adopts the enol conformation at room temperature in both polymorphs, with strong intramolecular hydrogen bonding between the imine nitrogen and the 2-hydoxy group stabilising the structure, as well as inter molecular H-bonding developing the packing arrangement.

In polymorph (i) , both the two independent molecules are nearly planar with a dihedral angle of the ring-C-N-ring bridge of 12.3° and 9.7°. In the packing the molecules are arranged in a herringbone motive with an angle of 73.07° between the average molecular planes. For polymorph (ii) the dihedral angle of the C-N bridge is 14.94° (fig 38).

Though there are no published variable temperature x-ray data for this compound, based on the structural description and the responses of similar compounds to variations in temperature this material is likely to be thermochromic. A study of **1** confined in a zeolite show that the structure behaves as expected of a photochromic material.[9] This was thought to be due to the zeolite structure stabilising the zwitterionic form of the molecule, which is the form exited to the photoproduct (keto tautomer); this occurs via an E/Z isomerisation involving partial C=C bonds. The resultant coloured photoproduct has a lifetime of over a week[9].

*4.1.2 Compound **2: N-(5-chloro-2-hydroxybenzylidene)-4-hydroxyaniline***

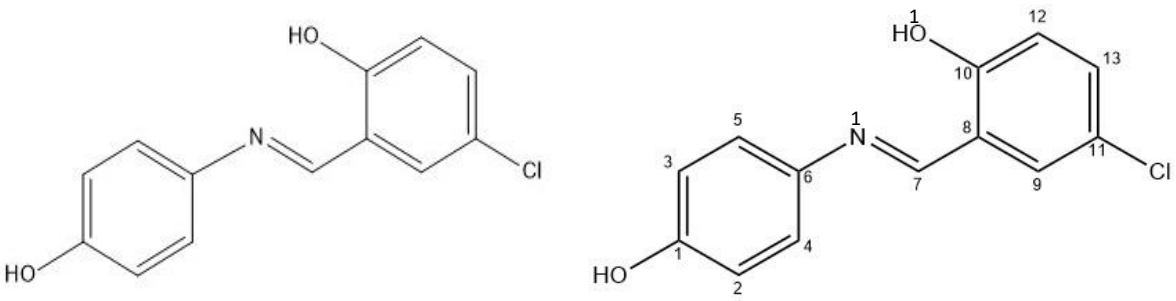


Figure 39: Structure of compound 2 N-(5-chloro-2-hydroxybenzylidene)-4-hydroxyaniline (right), and labelled structure (left)

A variable temperature SCXRD study of compound 2 (Fig 39) found it crystallise in the monoclinic system with space group P 21/a.[10] It was shown that the lattice parameters contracted with decreasing temperature with corresponding decreases in volume and in the monoclinic β angle[10]. There is also an increase in the C-N bond lengths as the temperature is decreased with a corresponding decrease in the C-O bond length which are indications of tautomerisation.

The fluorescence behaviour of single crystals of compound has been studied in-depth: in the fluoresence spectra it is shown that there is an increase in fluorescence at 520 nm with decreasing temperature and a new band being formed at 470 nm, which is close to that of the absorption band of the NH form at 485/480 nm[10]. The sample becomes paler as the temperature is lowered, and at 298 K has λ_{max} at 560 nm. J. Harada *et al.* concluded on the basis of the variation in bond lengths with temperature that there is an equilibrium between the OH and NH form of 2 . A study in solution of the thermochromism and piezochromism of unsaturated compounds using similar methods to those of Theilacker *et al*[11], showed that the energy difference calculated between the two forms, keto and enol, is small. The paler colour is caused by the increase in intensity of the fluorescence band, in contrast to the colour deepening that would have been expected by the increase in intensity of the 485 nm NH band which occurs as the temperature is lowered. There have been very few in-depth studies to explain the effect of fluorescence on the thermochromism of salicylideneanilines in the solid state. Thus these results whilst indicating that this effect cannot be ignored, have not been conclusively proved, and cannot be firmly stated as fact.

It has been suggested that the para-hydroxyl group on the aniline ring stabilises the keto-form, but the structural refinements suggest a co-existence of both the keto and enol form in the crystal structure at all temperautures.[10]

*4.1.3 Compound **3: N-(5-chloro-2-hydroxysalicylidene)-aniline***

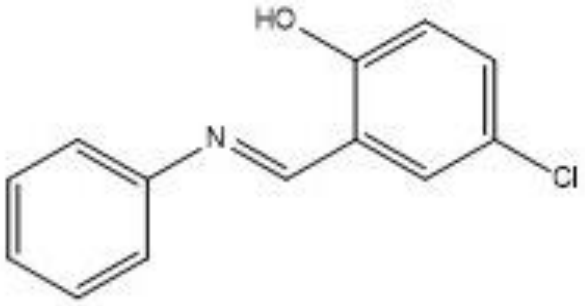


Figure 40: Structure of compound 3 N-(5-chloro-2-hydroxybenzylidene)-aniline

3 (Fig 40) is a thermochromic material. Its structure has been determined in 2 studies, respectively at 90 K and room temperature, both reporting orthorhombic symmetry in the P c a 2_1 space group[23/4]. The changes in the unit cell parameters with temperature are consistent with the expansion of a solid, and there appear to be minimal changes in the molecular orientation and shape There is no time lag in the change of colour of the material on cooling and displays no hysteresis.

As with other thermochromic materials the intensity of the absorption peak measured using UV spectroscopy at 476 nm decreases with temperature. By measuring the area under the absorption curve the energy difference between the two species of thermochromic crystals, red (high temp, enol), yellow (low temp, keto) was calculated at 7.36 kJ mol^{-1} for **3.** However, because of overlap of the absorption bands at high frequencies it was necessary to use the lower frequency region.

As seen in other thermochromic materials, **3** displays fluorescence (λ_{max} = 530 nm) that increase in intensity as the temperature in lowered. The light emitted at room temperature is yellow while at low temperatures the light emitted is to green. The lifetime of the emitting species is less than a few microseconds.

In addition to studies in the crystalline state **3** has also been examined in solution and as a rigid glass[16] in which it did not demonstrate the expected chromtropic properties.

4.1.4 Compound 4: N-(2-hydroxy-3,5-di-tert-butylsalicylidene)-3-nitroaniline

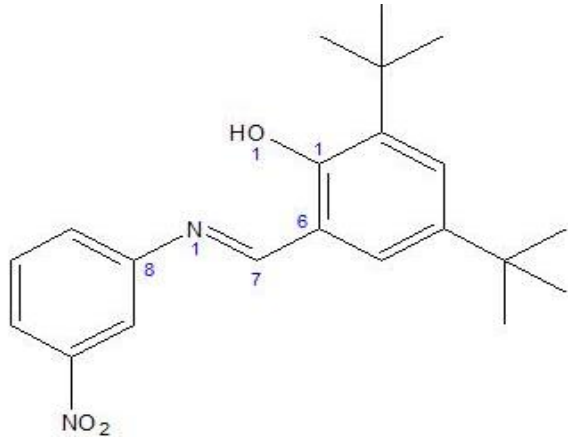


Figure 41: structure of compound 4 N-(2-hydroxy-3,5-di-tertbutylsalicylidene)-3-nitroaniline

Full SCXRD analysis was undertaken on compound 4 (Fig 41) at 295 K finding a centro-symmetric triclinic system (space group P $\bar{1}$) pre and post irradiation with 365 nm lamp[4]. This demonstrated changes in the bond lengths between atoms involved in the enol to keto tautomerisation, such as extensions of the C-N bond and contraction of the C-O bond as the switch between the two states.

Pulsed irradiation with an optical parametric oscillator with a wavelength of 730 nm at room temperature showed that compound **4** is phtotochromic[27]. The photoproduct (keto tautomer) can also be formed using a 365 nm high-pressure mercury lamp or a UV-LED lamp of the same frequency. The colour change in the crystal (from yellow to orange) is also accompanied by a bending of the crystal, the extent of which is seemingly dependent on the UV and visible light intensity. [25] [12]

The lifetime of the trans-keto photoproduct is 42 days via thermal fading in the dark at 25 °C. The long reversion time is due to the stabilisation of the trans-keto form exploiting the intermolecular hydrogen bonding, and the dimer formation between the N-H group of the imine and the oxygen atom of the nitro group. This time however can be dramatically reduced by illumination with a 530 nm light (63 seconds) or increasing the intensity of the visible light up to 10 mW cm^{-3} (1400 seconds).[25,12] The motion of the phototransformation is that of a bicycle pedal motion similar to that of the motion found in stilbenes and azobenzenes without demonstrating any major changes to the structure.

To form enough of the photoproduct that it is detectable via x-ray diffraction there are conditions that need to be met.[13]

1) The absorbance of the crystal at the wavelength must be very small.

2) Light should not be strongly absorbed only by the coloured species.

It is difficult to meet both of these conditions at the same time in photoreversible systems.

The irradiation of **4** with UV light (365 nm) yields the coloured species with an absorbance at 480 nm, because the irradiation is carried out with a strongly absorbing material the intensity of the light drops off in the bulk of the crystal, hence the excitation only occurs close to the surface of the crystal. The use of longer wavelengths allow the light to penetrate further into the crystal allowing the reaction to occur all the way through and so meets the first of the conditions. The longer wavelength however matches with the absorption band of the photoproduct and hence erases the colouration.[13]

The problem of erasing the colour due to the adsorption of the longer wavelength can be solved by using 730 nm radiation to induce a two-photon excitation. This gives the molecules the same energy as a single photon excitation with 365 nm. The lower probability of two-photon excitation in comparison to one-photon excitation, allows for the irradiation of the bulk of the crystal as the intensity of the light does not decrease much as it moves into the bulk.

4.1.5 Compound 5: N-(2-hydroxy-3-methoxybenzilidene)-3-nitroaniline

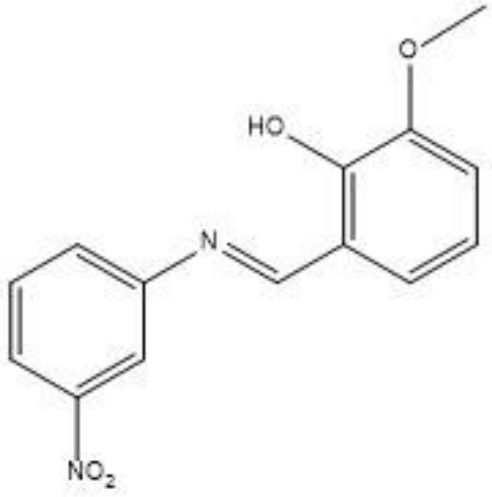


Figure 42: Structure of compound 5 N-(2-hydroxy-3-methoxybenzilidene)-3-nitroaniline

Compound 5 (Fig 42) has two recorded polymorphs reported in literature.[14] Polymorph (i) was studied at 295 K and 120 K, showing an orthorhombic symmetry with the space group Pcba. Polymorph (ii) was only studied at 295 K and was found to be triclinic with the space group P $\bar{1}$.

In the structure the molecule assumes a planar conformation with torsion angles of 1.4 and -0.9 between the atoms linking the aromatic rings and the rings themselves. The packing is characterised by a herringbone-type motif with a 53.7° angle. Such an arrangement in the crystal gives rise to two different O···H short contacts. One involving one oxygen from the Nitro (NO_2) group and the hydrogen atom on the methyl group, the second is between the other oxygen on the nitro group but with the iminic carbon hydrogen.

The crystal structure of polymorph (ii) is characterised by stacked layers of dimers. There is an intramolecular hydrogen bond between the -OH hydroxy group and the iminic group, as well as between the nitro group and the iminic carbon hydrogen.

Due to the slightly higher melting point, it has been suggested that polymorph (ii) is the more stable form but as the melting point experimental values are within 1°C they are both relatively close in stability.

Both polymorphs when immersed in liquid nitrogen change in colour from red/orange to pale yellow, hence both are thermochromic. When removed from the nitrogen the polymorphs quickly revert to

their original colour. When the low temperature diffraction data was collected on polymorph (i) the expected keto tautomer was not observed, instead the structure still showed with the enol form as found at room temperature. However, the C=N bond was elongated compared to that of the pure enol tautomer, suggesting that there is some keto character to the compound which was not present in a large enough concentration in the solid to be unambiguously confirmed by the x-ray diffraction analysis.

4.1.6 Compound 6: (6-Methoxy-2-[(E)-phenyliminomethyl]-phenol)

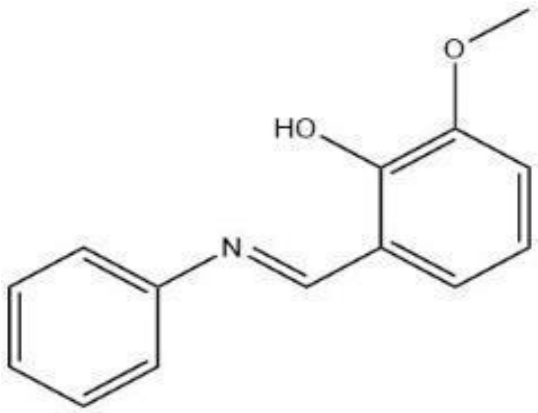


Figure 43: Structure of compound 6 (6-Methoxy-2-[(E)-phenyliminomethyl]-phenol)

There is one identified polymorph[15,16] of compound 6 (6-Methoxy-2-[(E)-phenyliminomethyl]-phenol) (Fig 43). Both measurements of this polymorph, at 293 K and 296 K, found an orthorhombic system in space group P $2_12_12_1$. The unit cell in both cases has Z=4, showing intermolecular bonding between the methoxy oxygen and a hydrogen from the aniline ring. In both reports structure, the molecule is[15] not co-planar with angles between the planes of the rings of 38.86° and 30.57°.[15,16] Although it is accepted that the planarity of the molecule is an indication of thermochromic behaviour, the dihedral angle reported for this compound is not as large as would be expected for a photochromic material.

Three intramolecular transitions have been revealed in a UV-Vis solution measurement[17] in DMF. These transition with λ_{max} at 302, 332, 269 nm are assigned as the π→π*, n→π* of the azomethine moiety and π→π* of the benzene ring respectively. The fluorescence spectra was also collected in a DMF solution using an excitation wavelength of 398 nm and resulting in an emission peak at 467 nm[17].

For compound 6 there are both ^{13}C[18] and ^{1}H NMR[17] data as well as IR data[17] reported (Appendix A). The IR data determines the presence of the C=N vibration band at 1612 cm^{-1} with a band for the C_{Ph}-O vibration at 1195 cm^{-1}. The ^{1}H NMR[17] shows a peak indicative of the CH=N hydrogen at 8.93 ppm. The ^{13}C data[18] in full shows 12 distinct carbon environments with 2 pairs of equivalent hydrogens.

There was no solid-state UV-Vis data for this compound, nor was there any temperature dependent data collected to determine the likely thermochromic properties of the material. However, data has

been collected for the metal complexed version of compound 6 which could determine the possible photophysical properties.[17]

4.1.7 Compound 7: 2-(((4-hydroxyphenyl)imino)methyl)6-methoxyphenol

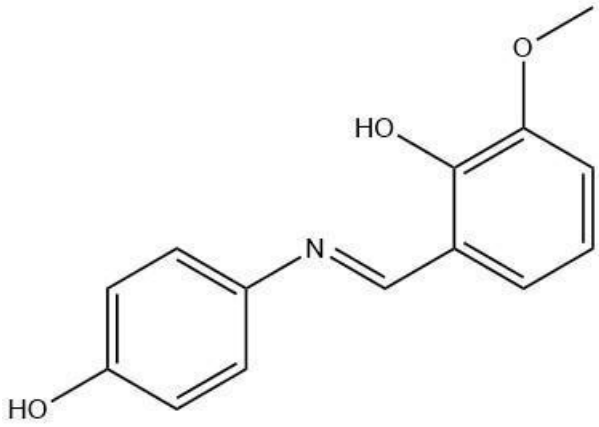


Figure 44: Structure of compound 7 2-(((4-hydroxyphenyl)imino)methyl)6-methoxyphenol

2-(((4-hydroxyphenyl)imino)methyl)6-methoxyphenol (Fig 44) has been used as a ligand in La(III)[19] complexes and as a potential TLR2 inhibitor[20]. The study into La(III) complexes was in relation to applications for *in-vitro* antimicrobial activities. These studies included ^{1}H and ^{13}C NMR, IR, and melting point analysis (72°C), the crystal structure of the compound in and of itself was not investigated. No UV-Vis absorption data nor any investigation into probable photo or thermochromic properties have been found in literature.

4.1.8 Compound 8: N-(2-hydroxy-3-methoxybenzilidene)-4-bromoaniline

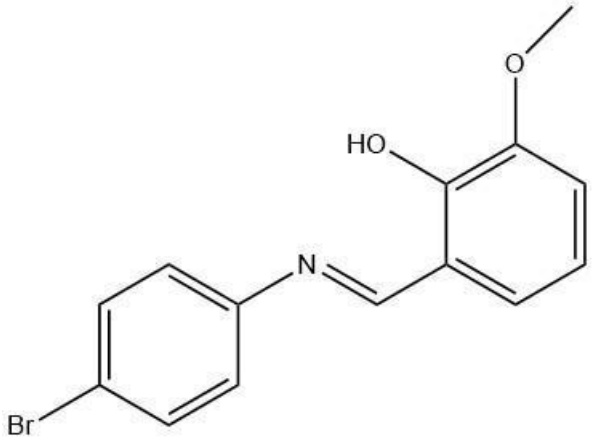


Figure 45: Structure of compound 8 N-(2-hydroxy-3-methoxybenzilidene)-4-bromoaniline

There are two published[21] structures for compound 8 (Fig 45), one at 293 K and another at 147 K. These were determined on two different crystals as part of a study into the halogen bond effect on thermo- and photo-chromic behaviour. After the initial studies the compound they were used as moiety in the preparation of molecular co-crystals with 1,2,4,5-tetrafluoro-3,6-diiodobenzene.

Compound 8 was used to investigate the effect that packing has on the photo- and thermo-chromic properties of the material. It was suggested that the more densely packed a crystal the more likely the material would demonstrate thermochromic attributes. However, it was found that with some N-salicylideneanilines and N-salicylideneaminopyridines in both single component systems and co-crystal systems, dense packing could lead to photochromism[22,23]. This leads to the conclusion that the environment in which the compound is found plays a key part in the appearance of its thermo- and/or photochromic traits, as suggested earlier for another compound being placed inside Zeolites[9], co-crystallisation or being included in other porous materials like MOFs, can lead to a complete change in the macroscopic properties.

Although earlier papers had suggested that photo and thermochromic attributes are mutually exclusive, particularly for pyridine based Schiff bases or co-crystal systems, compound 8 was found to exhibit both thermo and photochromic properties.[21] Photochromic capabilities of 8 were assessed by irradiation with a 365 nm lamp resulting in significant variation of the features in the absorption spectra recorded after irradiation. Thermal fading of the photochromic material was observed at 604

minutes but, compound 8 could be photochemically reverted by exposure to 546 nm wavelength light. Furthermore, 8 also demonstrated some thermochromic behaviour (colour change at low temperature), but the keto form could not be isolated in the structure determination at the temperatures studied.

4.1.9 Compound 9: N-(2-hydroxy-3-methoxysalicylidene)-4-Iodoaniline

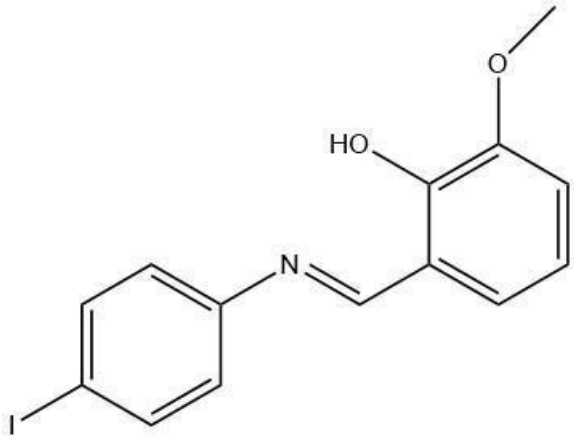


Figure 46: Structure of compound 9 N-(2-hydroxy-3-methoxysalicylidene)-4-Iodoaniline

Studied alongside compound 8 above[21], compound 9 (Fig 46) forms multiple solvent-dependent polymorphic crystals.

1) Triclinic system with a P-1 space group forms from ethylacetate into red prisms at 293 K and 108 K.
2) Monoclinic system with a $P2_1/c$ space group forms from ethanol as red blacks at 293 K.
3) Orthorhombic system with a $P2_12_12_1$ space group forms from toluene as orange prisms.

The crystal structure of the triclinic polymorph shows two molecules in the asymmetric unit, disposed almost orthogonally to each other with the terminal C-I bond pointing in the direction of the salicylic ring and formin a C-I…π interaction. Such molecular arrangement leads to the presence of large cavities in the structure, allowing enough space for the rotation around the N=C bond between cis and trans forms . The absorption spectra of this polymorph has two distinct bands: one extending below 430 nm λmax, the other in the region of 430-550 nm. These absorption bands are assigned to the π---π* interaction of the enol form and to the cis-keto form respectively. Similarly, two peaks are found in the emission spectra after excitation at λmax = 480nm at 606 nm, with a shoulder at 570 nm at 298 K. At 77 K the band split into 3 peaks 570, 604 nm with a shoulder at 652nm.

The monoclinic polymorph, show positional disorder along a pseudo-mirror plane perpendicular to the plane of the molecule. The individual molecule within the unit cell are nearly planar, and arranged along the c-axis in such a way that they create a zig-zag pattern that forms by a series of I·····I type 2

halogen bonds, as well as C····H····π interaction. The orthorhombic polymorph is isomorphic to compound **8** but showing also positional disorder

The photochromic capabilities of all polymorphs were assessed by irradiation with a 365 nm lamp to identify changes in the absorption spectra, but after irradiation no appreciable changes were observed.

4.1.10 Compound 10: N-(3,5-di-tert-butylsalicylidene)aniline

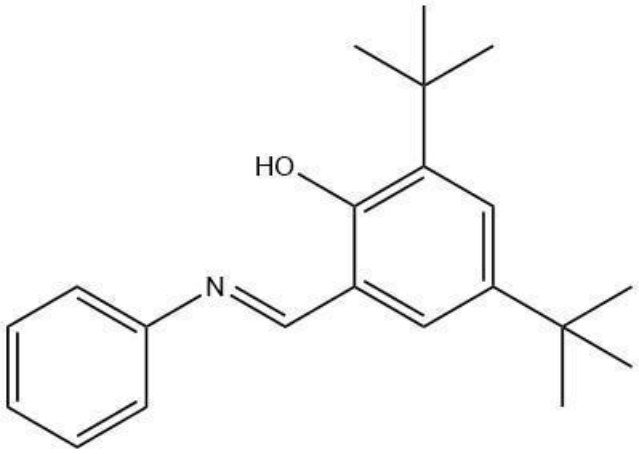


Figure 47: Structure of compound 10 N-(3,5-di-tert-butylsalicylidene)aniline

Compound 10 (Fig 47) was studied under the hypothesis that it could demonstrate both thermo- and photo-chromic capabilities simultaneously. Having been previously classed as a purely thermochromic material[23]. A study evaluating the expectations of photo and thermochromic behaviour based on the presence of *tert*-butyl groups[24] in 2019, found three polymorphs which displayed varying properties dependant on temperature ranges, and how the unit cells were packed. Two of the three described polymorphs are not thermodynamically stable and transform into the third at differing rates and temperatures. Another study into the photochromic capabilities and links to the molecular structure was completed in 2012.[25]

The most thermodynamically stable polymorph (I) was obtained from crystallisation in acetonitrile, to give an orthorhombic structure with space group $Pna2_1$. At room temperature the crystals appeared yellow but showed orange luminescence upon UV irradiation, which deepened the overall colour of the crystal. When cooled to 77 K using liquid nitrogen the general colour of the crystal paled but the UV-induced luminescence colour change became more noticeable.

The second polymorph (II) crystallises in the monoclinic system ($P\ 2_1/c$ space group) and demonstrates both photo and thermochromic behaviour. However, when heated above 60 °C it transforms into the third polymorph with P n a 2_1 symmetry. During the phase transition (monoclinic to orthorhombic), a demonstratable colour change can be noticed, from the orange emission to a

green-yellow, as such this polymorph is thermochromic from -75 °C to 45 °C and photochromic ≤ 0 °C.

The third polymorph (III), which crystallises in the orthorhombic system with space group Pccn, is even less thermodynamically stable than the (II) and transforms into the stable polymorph (I) after 10 minutes at room temperature, from orthorhombic Pccn to monoclinic $Pna2_1$. However, $Pna2_1$ is not a monoclinic space group therefore could be a typographical error, or an error in the data processing. Further investigation and attempts at replication of the method and results would be required to aid in the confirmation of the theory presented that there are operating windows for the demonstration of thermo-/photochromicity.

A third study[25] found the orthorhombic $Pna2_1$ structure with an internal dihedral angle of 21.6°. As with other experiments no reaction to the photoirradiation was seen.

A spectroscopic and electrochemical study was performed in 2004[26] which included IR and electronic spectra. The study reported the C=N bond to be at 1614 cm^{-1} in the IR spectra, while, in the electronic absorption spectra, bands below 290 nm and between 329-365 nm were assigned as π- π * and n – π * transitions which involve the C=N and benzene molecular orbitals respectively. The intensity of the bands in the 440-460 nm region were found to depend on the solvent polarity (the less polar the solvent the weaker the bands) and were assigned to n(O) – π* transitions in the keto-amine/ zwitterionic structure.

4.1.11 Compound 11: N-(3,5-di-tert-butylsalycilidene)-4-iodoaniline

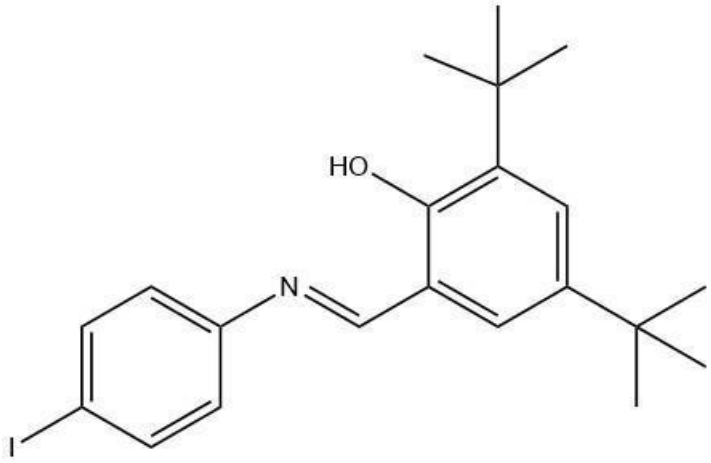


Figure 48: Structure of compound 11 N-(3,5-di-tert-butylsalycilidene)-4-iodoaniline

Compound 11 (Fig 48) has been identified as a photochromic material in the solid state, with a monoclinic crystal system and a P $2_1/c$ space group [27]. The structure demonstrates partial disorder around the bridging atoms and the hydroxyl group, this has an 0.64/0.36 occupancy factor (enol/keto). As predicted for the dominant structure of photochromic anils, there is a dihedral angle between the two rings of 64.4°.

Upon irradiation in the solid state with a 365 nm wavelength laser, the usually yellow crystal becomes a deep orange/red in colour evolving an adsorption band around 480 nm. The irradiated compound was reverted either by being left to thermally fade or by re-irradiation with a 490 nm wavelength. The thermal fading had a reaction rate constant of 4.2×10^{-5} for k_1 and 4.8×10^{-6} for k_2. When examined for Non-linear optical (NLO) activity using second harmonic generation (SHG), there was no detectable signal from either powder or crystal form. Only a signal reaching a maximum of 2 (vs urea) could be detected, indicating that the fundamental and harmonic wavelengths were outside the keto and enol adsorption bands, and could be attributing the signal to either NLO property changes and/or structural changes in the material.

No assessment of full conversion between the enol and keto states has been attempted on compound 11. Furthermore, no Raman data was collected although, IR data has been collected along with ^{1}H and ^{13}C NMR.[27]

4.1.12 Compound 12: N-(3,5-di-tert-butylsalycilidene)-4-bromoaniline

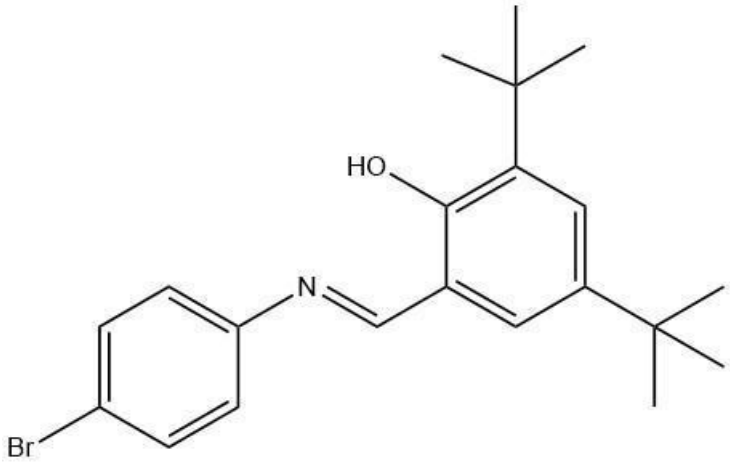


Figure 49: Structure of compound 12 N-(3,5-di-tert-butylsalycilidene)-4-bromoaniline

For compound 12 (Fig 49) spectroscopic and electrochemical characterisation are available, together with NMR, IR, ESR and cyclic voltametry.[25]

There are two published crystal structures for this compound. The first was published[25] as part of a study into the photochromicity of salicylideneaniline derivative crystals, with a monoclinic P 2_1/c space group and unit cell parameters similar to the 4-iodo compound structure. The dihedral angle between the two rings in the molecule is 27.5° and, shows significant changes in the UV spectrum between 450–550 nm after irradiation with a 365 nm source. Together with the crystal structure, the study suggests that the steric hindrance of large tert-butyl (or similar) groups, can prevent any display of photochromicity.

The second structure was published[28] as an investigation into phase transitions and chromic behaviour. Finding the same unit cell and space group as the previously reported structure, the paper also reported not only the demonstration of photochromicity visually, but also the existence of reverse thermochromicity (Fig 50) i.e. the phenomenon for which rather than losing colour, the crystal becomes darker with decreasing temperature. Having also collected Raman spectra before and after UV irradiation, there was a development of new peaks on the post irradiation spectrum not previously reported (Fig 51).

The compound was included in a study of the kinetics and reaction rate of the thermal back reaction (keto to enol transition at 295 K) of a series of di-*tert*-butyl compounds. The study concluded that the thermal back reaction had a first order or pseudo first order reaction rate for the thermal back reaction. The maximum charge density change for the photo-isomerism was observed upon irradiation using 365 nm wavelength. This demonstrated a consecutive two-step decay, both of which are first order for the photochrome and corresponds to the suggested two-step isomerisation to the stable form (enol), k_1 = 1.0 x 10^{-3} with k_2 = 1.8 x 10^{-4}. The paper investigated the effects of both substituent as well as its position upon a series of mono substituted anilines. It was found that for the fluoro-, chloro- and methoxy groups the reaction rate for the isomers decreased in the order of para> ortho> meta. The lower rate constants found in the meta isomer, compared to the para and ortho isomer, suggest that a mesomeric effect , or a participation in the resonance of the substituents in the kinetics on top of the size effect of the amine residue.[28]

The decrease in the electronegativity of the substituent groups F > Cl > Br > OCH_3 > H > CH_3 > $C(CH_3)_3$, as well as their size $C(CH_3)_3$ > CH_3 > H, has a discernible effect on the decrease in the rate constants the study obtained: F > Cl > OCH_3 > $C(CH_3)_3$ > Br > CH_3 > H. The change in molecular shape, however, is also constrained by the photoirradiation.

The spectroscopic and electrochemical study[26] of the compound showed in IR spectrometry the C=N is assigned to the band at 1616 cm^{-1}, in the electronic absorption spectra bands below 290 nm and between 329-365 nm were assigned as π- π * and n – π * transitions, which involve the C=N and benzene molecular orbitals respectively. The bands in the 440-460 nm region were found to be very solvent dependant according to the solvent polarity (the less polar the solvent the weaker the bands) and were linked to n(O) – π* transitions in the keto-amine/ zwitterionic structure.[26]

4.1.13 Compound 13 N-5-chlorosalicylidene-4-bromoaniline and compound 14 N-5-chlorosalicylidene-4-iodoaniline

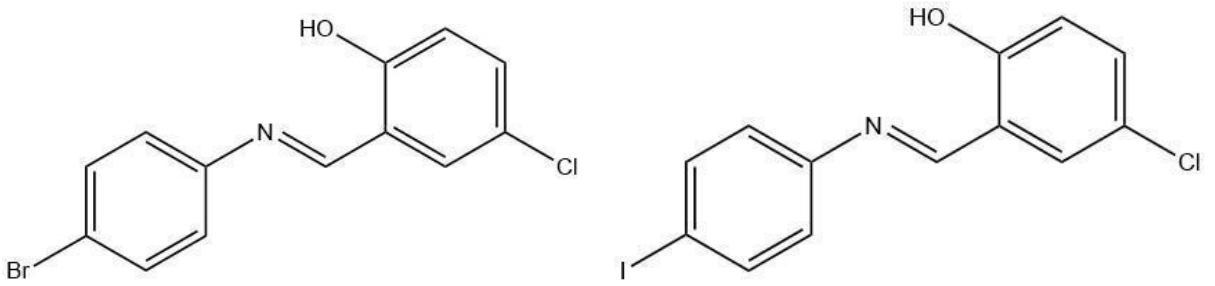


Figure 50: Structure of compound 13 N-5-chlorosalicylidene-4-bromoaniline(left) and 14 N-5-chlorosalicylidene-4-iodoaniline (right)

No published data could be found on either of these two compounds (Fig 50). However, there is published information about the chloro-compound[29]. The data suggests that the chloro-derivative forms two polymorphs with different colours and unit cells even though the space group remains the same (Appendix A). The two polymorphs formation seems to be solvent dependent with methanol and ethanol giving rise to the yellow crystals of polymorph (I), while dichloromethane (DCM), acetone and acetonitrile from the orange crystals of polymorph (II). The two polymorphs can be switched between each other upon heating above 150 °C, whilst the recrystalised product upon cooling is only of the yellow polymorph. The yellow crystals have a dihedral angle between the two rings of 44.6(1)° with stacked layers of molecules along the b-axis, within each layer there are a series of H·····Cl intermolecular interaction distances in the range of 3.00(1) to 3.11(1) Å. There are also halogen bond interactions (type 1; with interatomic distances of 3.39(2) Å) between the chlorines where the molecules are packed in a head-to-tail arrangement. In the orange crystals the molecules have a more planar conformation with a dihedral angle of 2.85(1)° between the rings, and form ribbons arranged in an orthogonal cross pattern. The molecules themselves are packed in a head-to-head arrangement, with inter-ribbon distance of 3.41 Å, each ribbon formed of slipped stacking along the b-axis. Where the ribbons cross, there are type-2 halogen bonds between the chlorine atoms with interatomic distances of 3.46(1) and 3.51(2) Å.

It is possible that either 13 or 14 or both, could be isostructural with the chloro isomer, that could be used for further comparisons.

4.1.14 Compound 15 N-salicylidene-4-iodoaniline

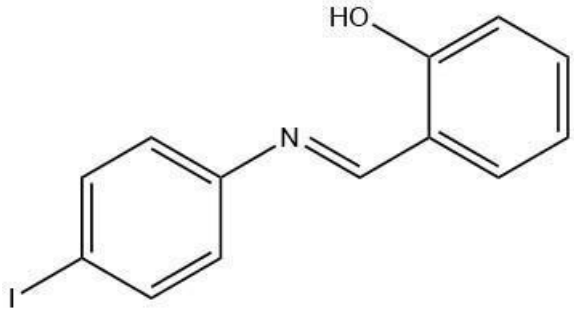


Figure 51: Structure of compound 15 N-salicylidene-4-iodoaniline

There is a single published structure of compound 15[30](Fig 51), this was an orthorhombic system with a P b m a or P b 2_1 a space group and designated the compound as a thermochromic material. Also mentioned in the same paper are both the 2-iodo and 3-iodo isomer each being photo and thermochromic respectively. There has previously been published IR and NMR data[31]. The key peaks identified at 1564 cm^{-1} (C=N) and 1280 cm^{-1}(C-O) in the IR spectrum. In The ^{1}H NMR spectrum the key identified peaks were at 12.36 ppm (OH) and 8.49 ppm (CH=N)

4.1.15 Compound 16 N-salicylidene-4-bromoaniline

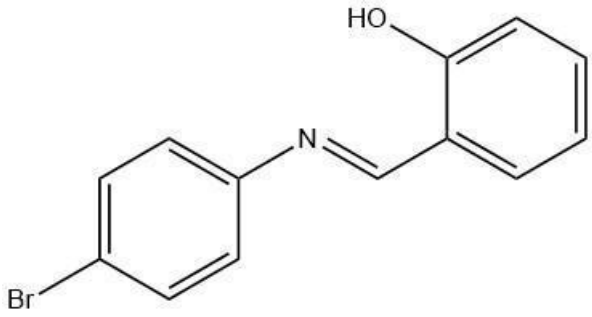


Figure 52:Structure of compound 16 N-salicylidene-4-bromoaniline

Previous structural work on compound 16 (Fig 52) found an orthorhombic system with the space group $Pbc2_1$ (a:7.17 Å, b:6.23 Å, c:26.7 Å, Z=4)[32]. Compound 16 was identified as a photochromic material demonstrating no thermochromic behaviour.[32] There is also published NMR, IR, and UV-vis data[33,34] as well as some fluorescence data[34]. The solution UV-vis spectrum was completed in multiple different solvents along with the fluorescence data collection. Within the UV-vis the change in solvent caused differences to the intensities of the absorption bands but did not shift the peaks noticeably in either direction. In comparison, in the fluorescence data there were wider variations in the intensities of the peaks as well as a disappearance and merging of some peaks, meaning that fluorescence presentation is solvent dependant.

4.1.16 Compound 17 N-benzilidene-4-hydroxyaniline

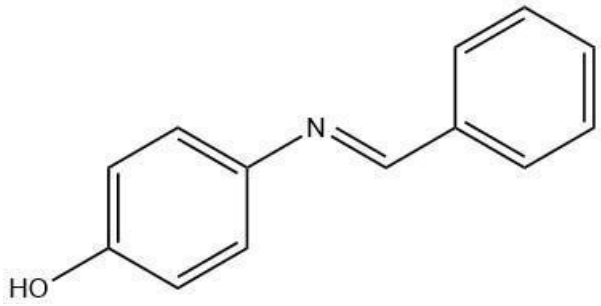


Figure 53: Structure of compound 17 N-benzilidene-4-hydroxyaniline

There is one published structure for compound 17[34] (Fig 53), as part of a study into the role hydrogen bonds play in altering the packing of crystals. There is also NMR data, collected as part of a study on the selective alkylation of aminophenols[35], as well as a study of the effect of hydroxyl groups on UV-Vis absorption spectra λ_{max}[36]. On top of this IR data and melting point were collected as part of a study into antifungal treatments[37]. A huge discrepancy between melting points determined in different studies 184-186 °C[37] vs 97-98 °C[35], could be caused by differences in purity levels or polymorphs. The first used a method which included sodium borohydride and drying using $NaSO_4$ while the second was a simple one pot condensation reaction with recrystallisation for purification. Further NMR data[38], this time including ^{13}C, were collected during a study of the effect the hydroxyl group had on the reduction potential of the compound.

4.1.17 Compound 18 3,5-ditertbutylsalicylidene-2-iodoaniline and compound 19 3,5-ditertbutylsalicylidene-3-iodoaniline

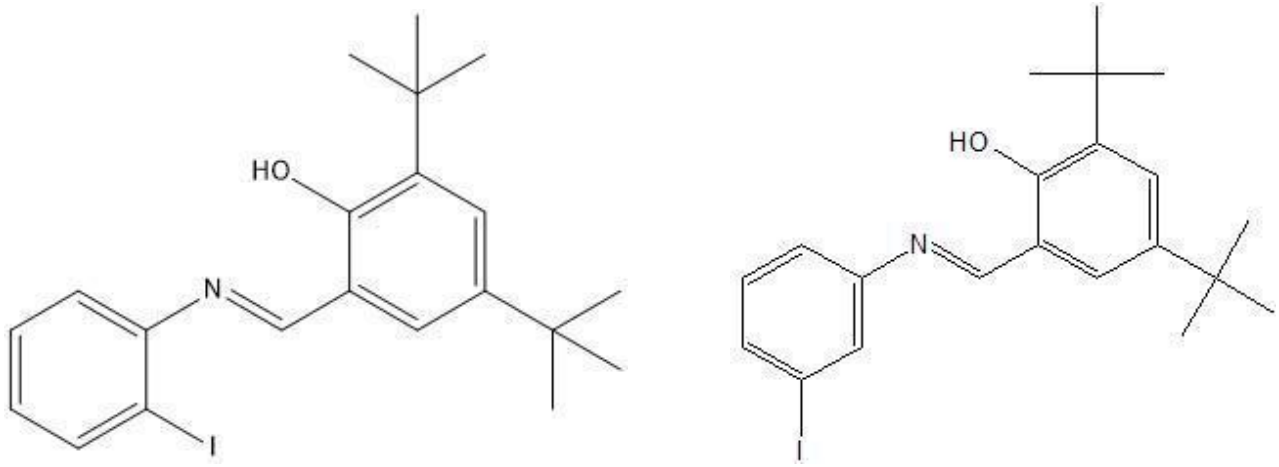


Figure 54: Structures of compounds 18 3,5-ditertbutylsalicylidene-2-iodoaniline (left) and compound 19 3,5-ditertbutylsalicylidene-3-iodoaniline (right)

Compounds 18 and 19 (Fig 54) have no published data currently available, though they are analogues to compound 11 therefore we could expect these materials to display similar properties.

The incomplete nature of characterisation of these compounds discussed above is likely due to the difficulty and complexity of the experiments involved. The importance of using techniques such as Raman and IR spectroscopy, which allow for the analysis of the vibrational frequency of the bonds and can take place *in situ* to monitor the progression of the reaction, is to be emphasised in the case of these compounds that can switch between the two states (enol to keto) with a corresponding change in single to double bond character of the C-N bond.

Neutron data allows for the accurate positioning of hydrogen atoms in a system and can therefore be used to gain a view of the positioning of the NH, OH split at any given point. This is a better description than the secondary analysis employed with other forms of structural data collection, which require estimating the percentage found in one form or another based on the relative intensities of peaks sensitive to the shift, usually those of the nitrogen or the oxygen. Neutron diffraction also allows for a higher resolution than x-ray analysis so can better separate the two superimposed molecules, and hence define which tautomer is present in the higher amount. Rather than splitting the occupancies of the oxygen atoms to find hydrogen positions as with x-ray diffraction, the hydrogen occupancies can be ascertained directly from the data. This does, however, lead to complications with the size of crystal necessary for such analysis, and the impact that has on the demonstration of the properties of the materials as an average of the entire crystal.

The distinct lack of variable temperature studies for the majority of these compounds, is likely due not only to the difficulty and time taken to do such analysis, but also the difficulty obtaining crystals of a high enough quality for the data to be refined within acceptable limits.

There is some CPMAS NMR data published on a few of these compounds and other similar derivatives, though again none of these have been done at variable temperatures meaning there is no isolated spectrum of either of the tautomers. For these only key peaks have been published rather than complete data sets and there are no complete spectra.

On some compounds there are more in depth variable temperature diffuse reflectance experiments, as well as variable temperature solution UV-Vis experiments. The solid state diffuse reflectance is

more practical for these compounds as they interact differently depending on the state they are in. Variable temperature gives an indication of the prevalence of each form at a given temperature, but it is done through secondary manipulation rather than direction information, also, the temperatures reached do not give the isolation of each tautomer so there will be characteristics present for each of them.

Over the course of this chapter I will discuss the characterisation of a series of thermochromic and photochromic SA derivatives, as described above. This will included SCXRD and Raman Spectroscopy along with initial characterisation using NMR (^{1}H and ^{13}C), Infra Read Spectroscopy (IR) and Solution UV-Vis Spectroscopy. For the Thermochromic compounds the discussion will include the effect of fluorescence on the chromotropism displayed, as well as the relative planarity of the compounds. For the photochromic compounds along with the continued discussion of the fluorescence displayed there is also an investigation into the ease of conversion to the UV (365 nm) irradiated state and the stability of the state over time in different conditions. Across both forms of chromotropism a study was completed of the influence of position of substituent as well as substituent type on both the aldehyde and aniline ring side. The thermochromic compounds covered are Salicylidene-4-hydroxyaniline, N-(5-chloro-2-hydroxybenzylidene)-4-hydroxyaniline, N-(2-hydroxy-3-methoxybenzilidene)-4-bromoaniline, N-(2-hydroxy-3-methoxybenzilidene)-3-nitroaniline, (6-Methoxy-2-[(E)-phenyliminomethyl]-phenol, N-(3,5-di-tert-butylsalicylidene)-2-iodoaniline and N-(3,5-di-tert-butylsalicylidene)aniline. The photochromic compounds are N-(3,5-di-tert-butylsalicylidene)-4-iodoaniline, N-(3,5-di-tert-butylsalicylidene)-3-iodoaniline, N-(3,5-di-tert-butylsalicylidene)-3-nitroaniline and, N-(3,5-di-tert-butylsalicylidene)-4-bromoaniline.

4.2 Experimental

For each compound a small mass of the relevant Salicylaldehyde was dissolved in a solvent (ethanol or methanol compound depending), along with corresponding aniline. The resulting mixture was then heated under reflux condition for 3-4 hours. Where the compound had precipitated out the solid was removed *via* Büchner filtration before being recrystalised from different solvents to form the highest quality crystal. Where no precipitate formed, the solution was left to evaporate in air before the crude product was recrystallised. Salicylidene-4-hydroxyaniline was an isolated case where, post evaporation, a thick oil was left in the vessel which had to be placed on a rotary evaporator to remove the last of the solvent.

^{1}H and ^{13}C NMR were used for confirmation of a successful synthesis whilst further characterisation was completed using IR and solution UV-Vis spectroscopy as well as Raman scattering. Beyond this the crystal structure was determined using single crystal X-ray diffraction (Keele, Bruker instrument and ISIS, Rigaku instrument) and single crystal neutron diffraction (ISIS, SXD), full experimental details beyond those discussed in the results and discussion can be found in the appendix.

4.2.1 Compound 1 Salicylidene-4-hydroxyaniline

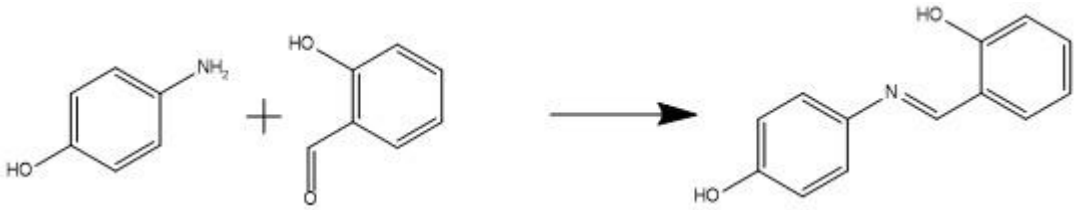


Figure 55: Reaction scheme for compound 1

4-Hydroxyaniline (1.0416 g, 9.5 mmol) was dissolved in ethanol (25 mL) heat at reflux until completely dissolved. Salicylaldehyde (1 mL) was added, forming a light brown solution, and left at reflux for 4 hours (Fig 55). The solution was taken off the heat and allowed to cool to room temperature overnight. With no indication of crystal/precipitate formation the solution was placed in an ice bath for 30 minutes, again there was no indication of precipitate/crystal growth. The solution was then placed in a freezer overnight.

When checked the following forming no crystal growth had occurred, after being left to evaporate leaving behind a viscous orange oil, the solution was hence place on a rotary evaporator taking down gradually to 27 mbar to drive off the solvent. This left a brick orange/red solid. Any solid that could not be removed was redissolved in 10 mL methanol and the solvent left to evaporate leaving red crystals after 2 days.

The crude red product was dissolved in ethanol and left to slowly evaporate in a cool environment for 4 weeks forming large red hexagonal plate crystals.

The Crude product was characterised using ^{1}H NMR (^{1}H NMR (400 MHz, DMSO) δ 13.41 (s, 1H), 9.66 (s, 1H), 8.89 (s, 1H), 7.58 (dd, *J* = 7.7, 1.6 Hz, 1H), 7.39 – 7.28 (m, 3H), 6.94 (dd, *J* = 13.5, 7.5 Hz, 2H), 6.86 – 6.80 (m, 2H)). and ^{13} C NMR (^{13}C NMR (101 MHz, DMSO) δ 160.63, 160.54, 157.31, 139.61, 133.09, 132.67, 123.11, 119.82, 119.53, 116.92, 116.46.) to confirm production of the correct material (Fig 56 to 59) expansions for the NMR spectra can be found in the appendix.

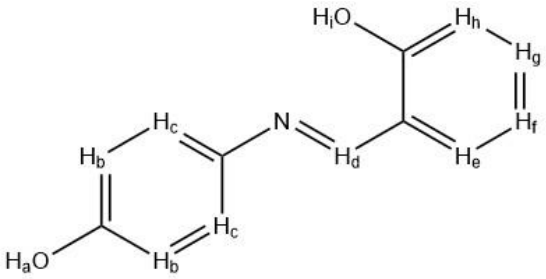


Figure 56: Hydrogen labelled diagram of compound 1

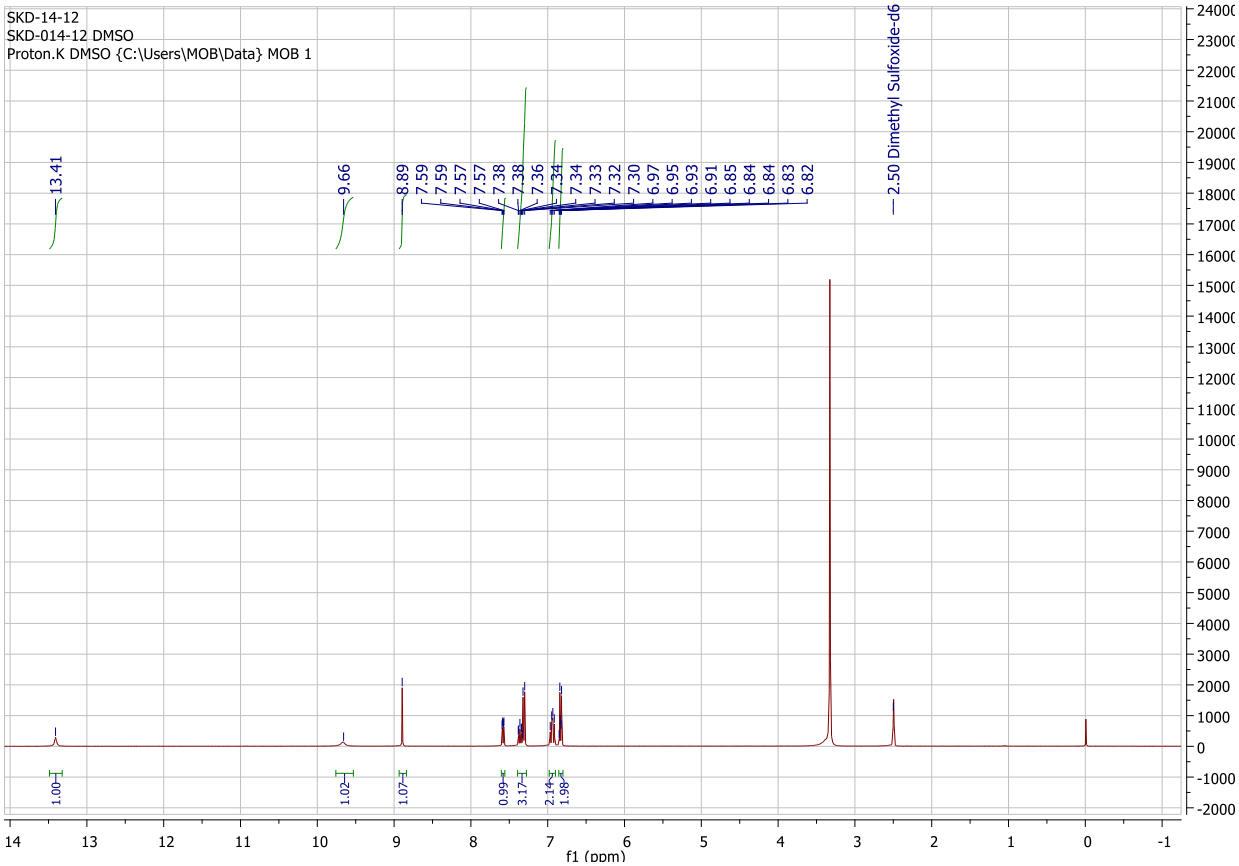


Figure 57: ^{1}H NMR spectrum of compound 1

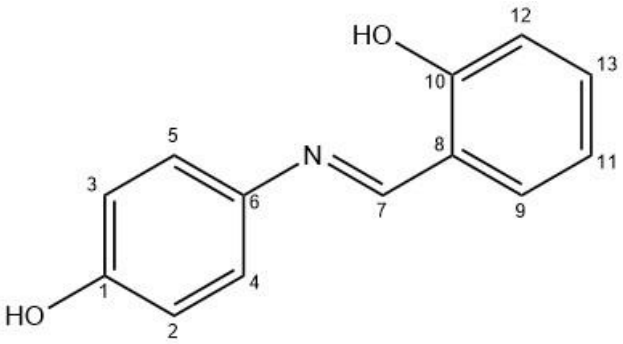


Figure 58: Carbon numbered diagram of compound 1

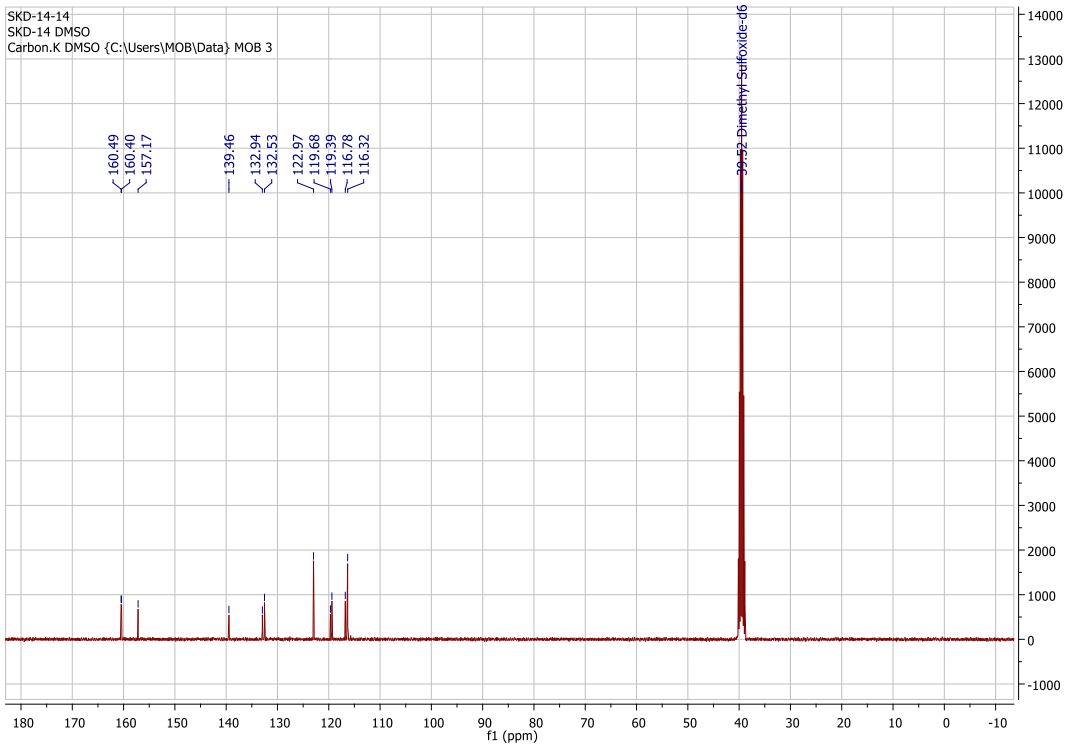


Figure 59: ^{13}C NMR spectrum of compound 1

The recrystallised product was then further characterised using solution UV-Vis spectroscopy (Fig 60) and IR spectroscopy (Fig 61).

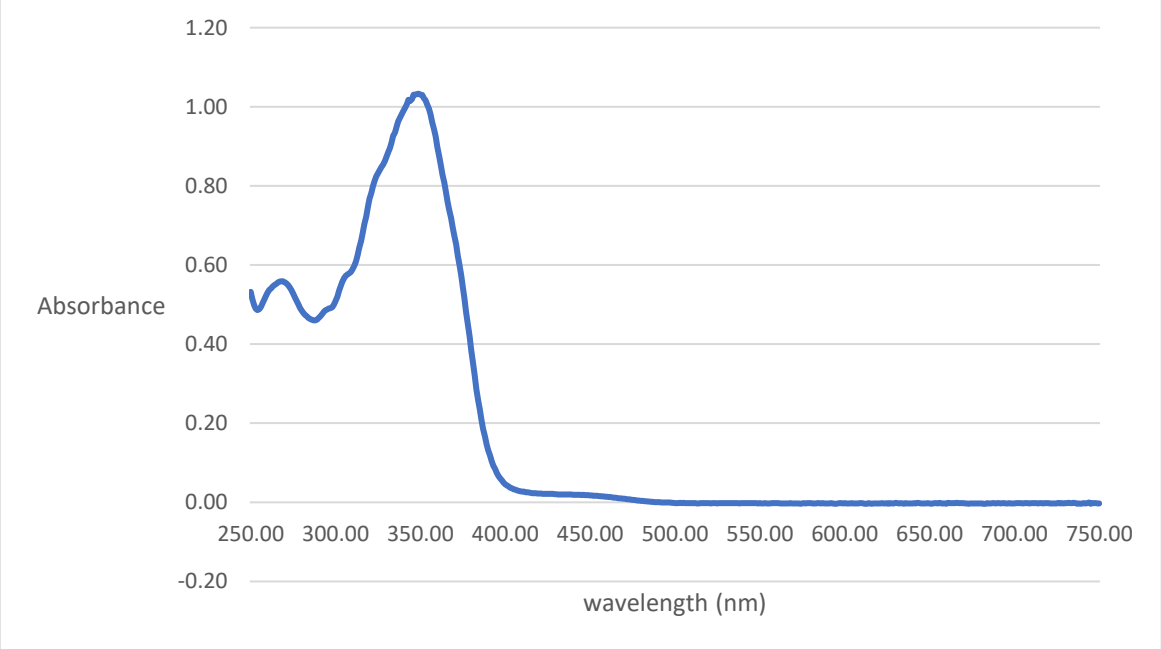


Figure 60: Solution UV-Vis absorption spectrum of compound 1 in ethanol

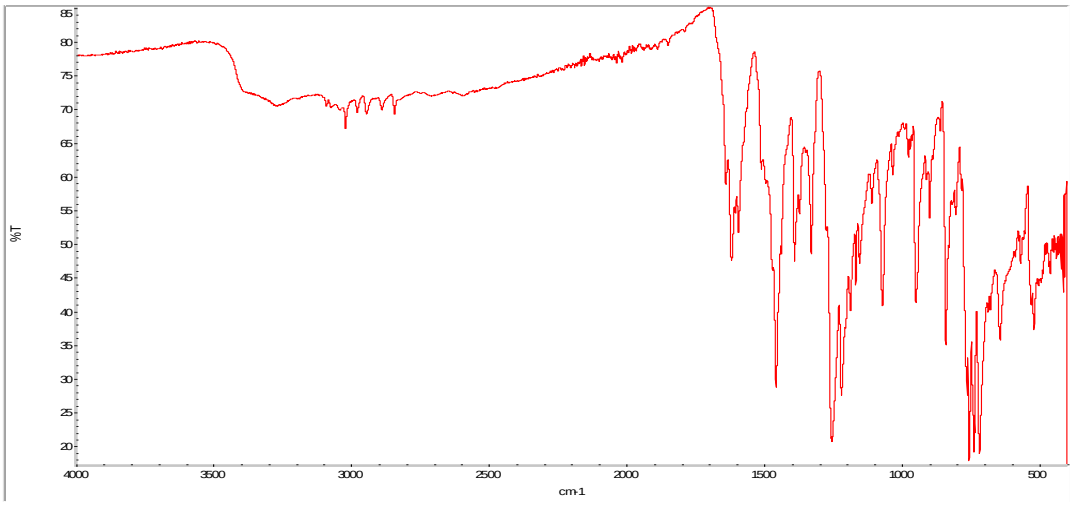


Figure 61: IR spectrum of compound 1 crude product

SCXRD data was collected at Keele on the Molybdenum source at 130, 160 and 293 K, as well as at 50 K at ISIS using the Rigaku instrument using the Helix cooling temperature system. ToF neutron single crystal data was collected on SXD at ISIS at 300, 210, 120, 70 and 10 K. The results of the crystallography will be discussed in detail in a later chapter.

4.2.2 Compound 2: 5-Chlorosalicylidine-4-hydroxyaniline

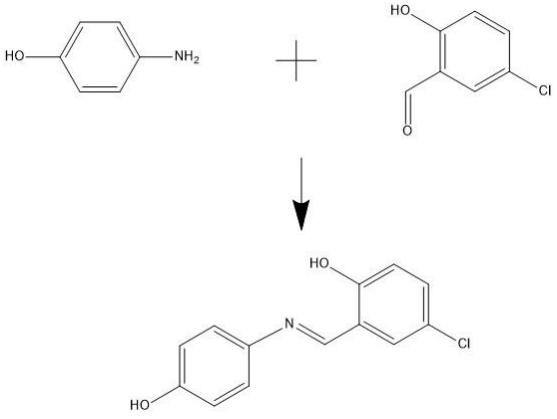


Figure 62: Reaction scheme for compound 2

5-Chlorosalicylaldehyde (7 g, 0.045 mol) dissolved initially in ethanol (60 mL) at 50 °C for 20 minutes in a 200 mL round bottomed flask (RBF)). As the aldehyde did not dissolve further ethanol was added (60 mL), and continued heating until completely dissolved. In a separate 200 mL RBF 4-Hydroxxyaniline (10 g, 0.092 mol) was dissolved in ethanol (80 mL) at 50 °C for 20 minutes to create a dark brown solution (Fig 62).

The aldehyde solution was poured into the flask containing the aniline solution when forming first a dark brown solution then a bright orange precipitate formed. The flask was then placed into an ice bath for 20 minutes before being filtered and washed with ice cold ethanol (10.11 g).

After 2 weeks a further black solid was collected from the filtrate and washed in ice cold ethanol. Leaving behind dark brown crystals.

^{1}H (Fig 63/4) and ^{13}C (Fig 65/6) NMR were completed to confirm synthesis of the correct product. ^{1}H NMR (400 MHz, DMSO) δ 13.40 (s, 1H), 9.73 (s, 1H), 8.88 (s, 1H), 7.67 (d, *J* = 2.7 Hz, 1H), 7.38 (dd, *J* = 8.8, 2.7 Hz, 1H), 7.34 – 7.28 (m, 2H), 6.96 (d, *J* = 8.8 Hz, 1H), 6.87 – 6.81 (m, 2H).

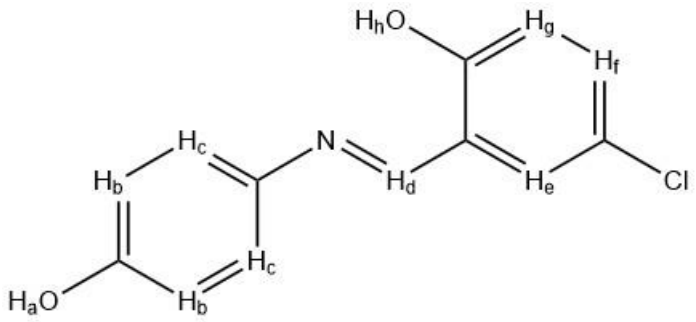


Figure 64: Labelled hydrogen diagram of compound 2

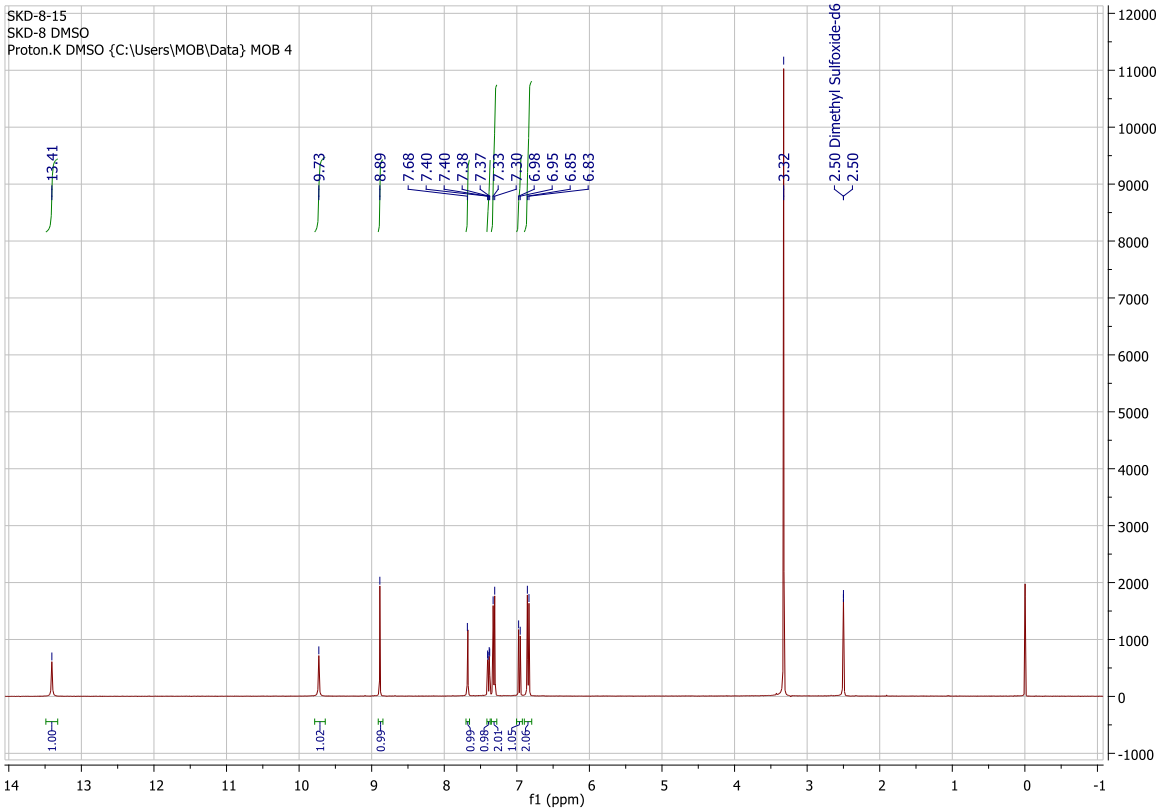


Figure 63: ^{1}H NMR spectrum of compound 2

^{13}C NMR (101 MHz, DMSO) δ 158.82, 158.70, 157.28, 138.87, 131.97, 130.79, 122.81, 122.34, 120.69, 118.46, 116.00.

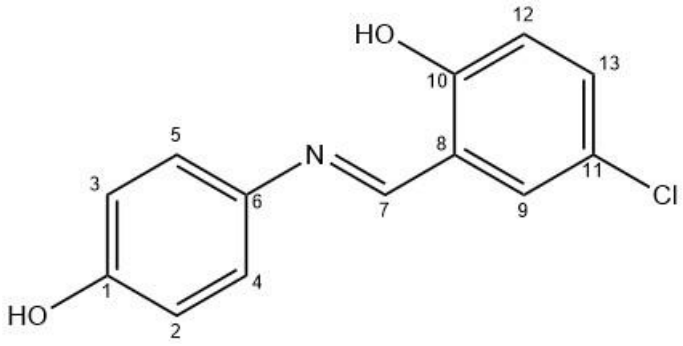


Figure 65: Labelled-carbon diagram of compound 2

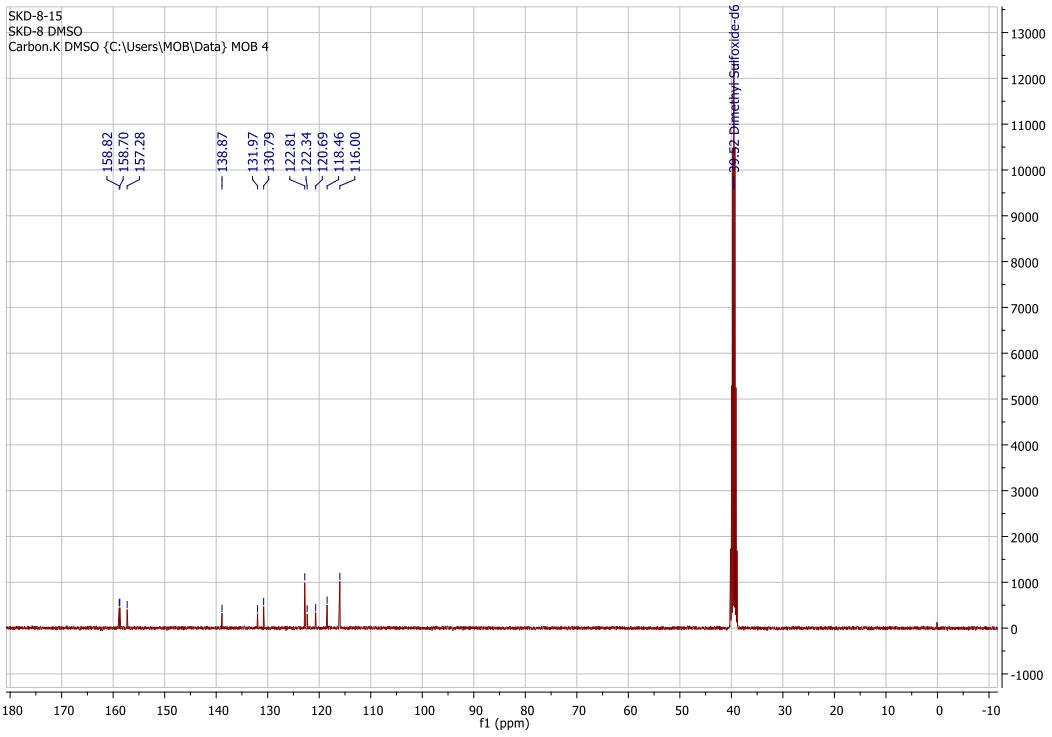


Figure 66: ^{13}C NMR spectrum of compound 2

As with compound 1 both solution UV-Vis spectroscopy (Fig 67)and IR (Fig 68) were completed on the sample along with Raman scattering (Fig 69).

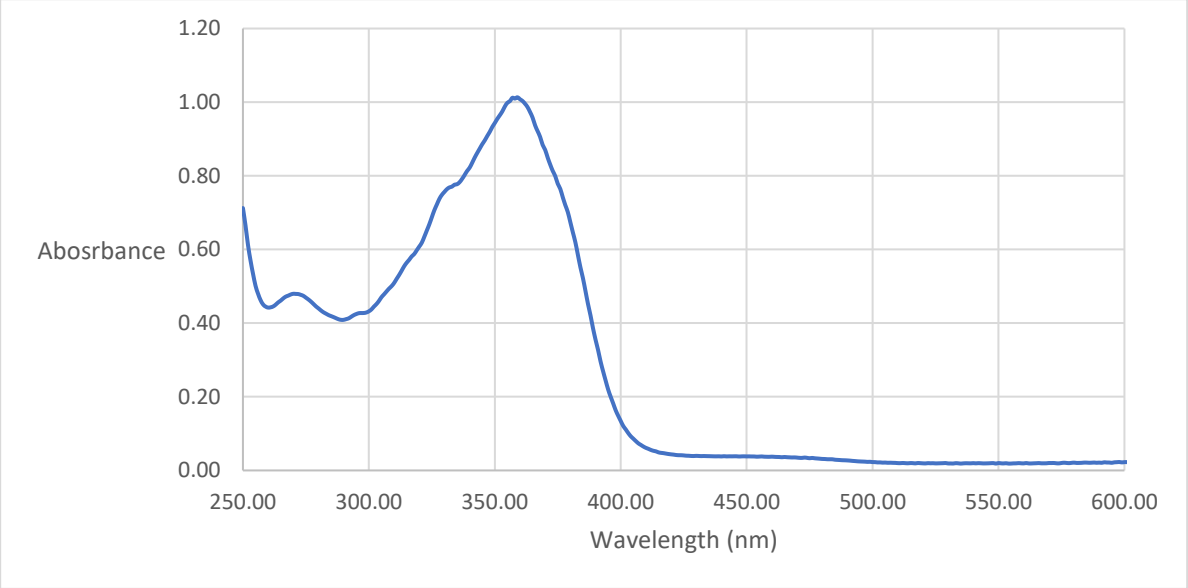


Figure 67: Solution UV-Vis absorption spectroscopy absorption spectrum of compound 2 in ethanol

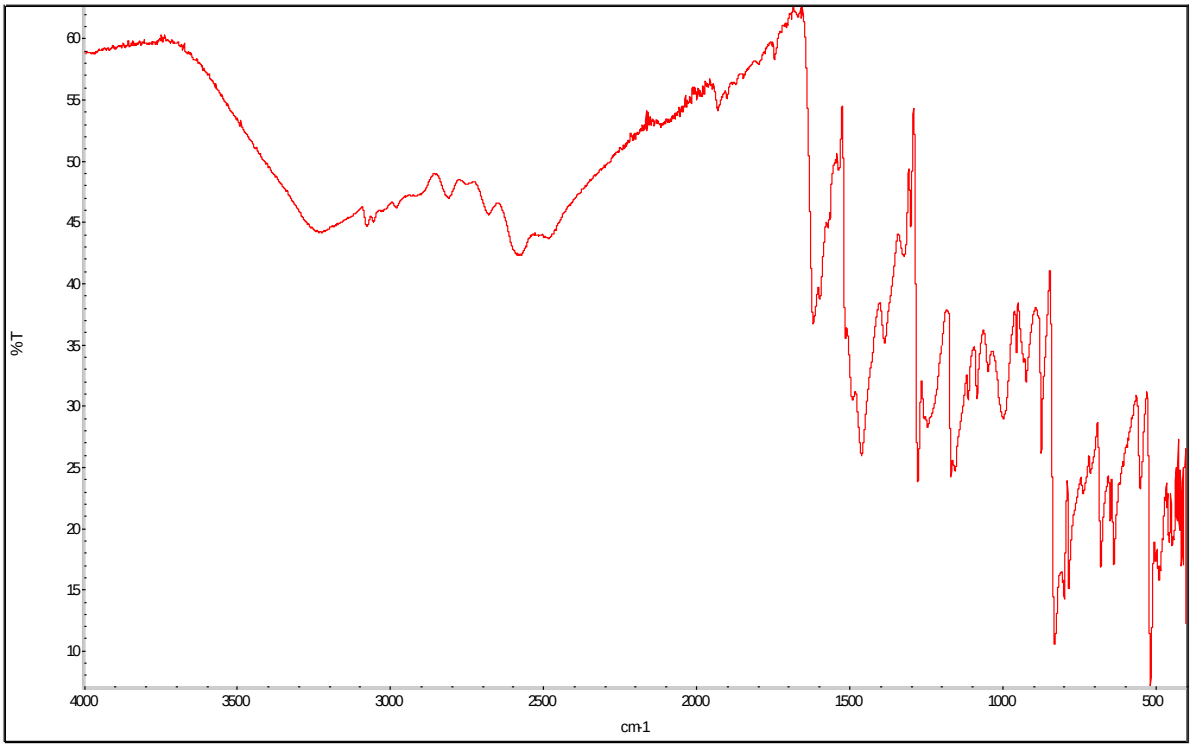


Figure 68:IR spectrum of compound 2

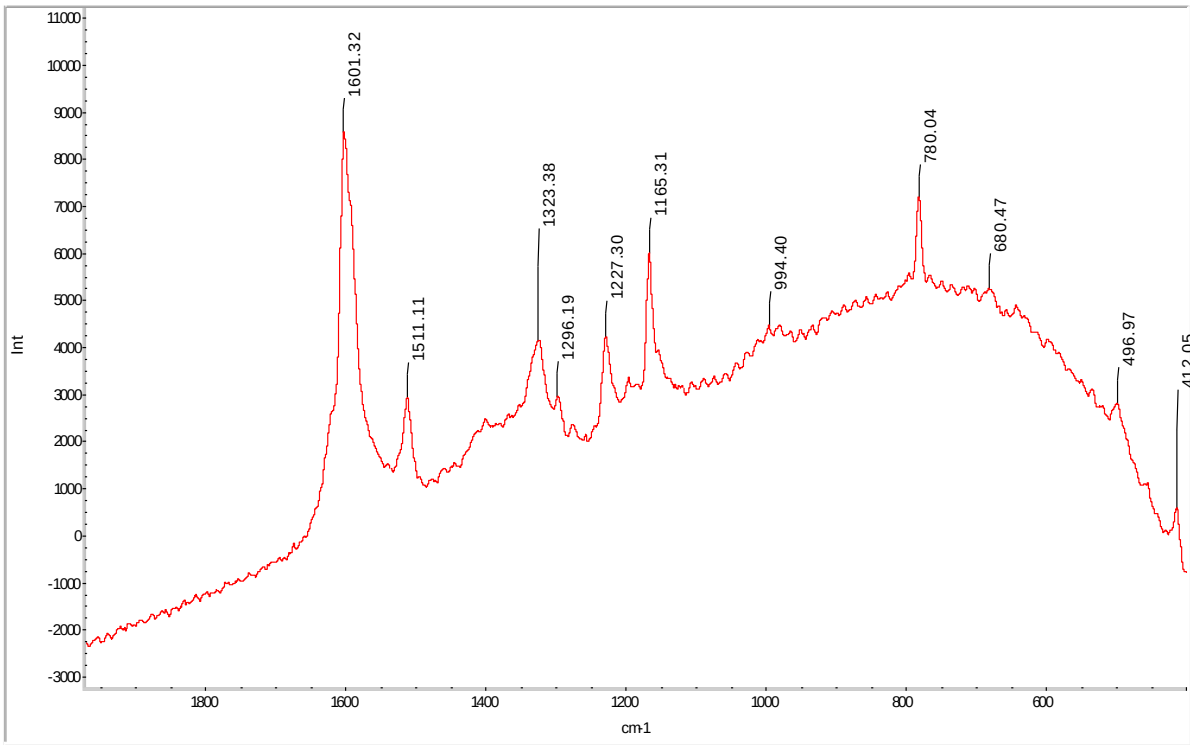


Figure 69: Raman Spectrum of compound 2 (785 nm)

The SCXRD data was again collected at Keele at 230, 200, 170, 140 and 110 K using a molybdenum source on a Bruker model SCXRD, full details found in the appendix.

4.2.3 Compound 3: 5-Chlorosalicylideneaniline

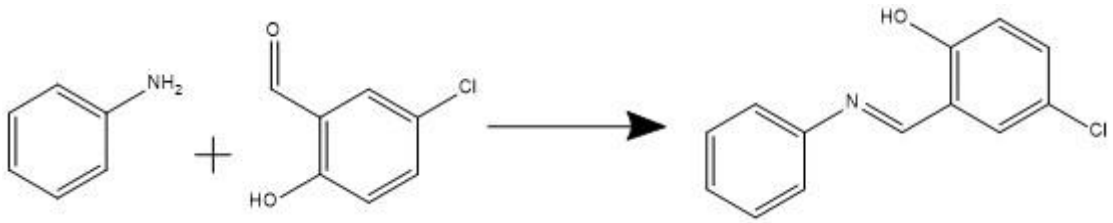


Figure 70: Reaction scheme for compound 3

5-Chlorosalicyladeyhde (1.7024 g, 0.01) was dissolved in ethanol (60 mL) at 45 °C, in a 100 mL RBF, this formed a slightly purple solution. 1 mL aniline was dissolved in ethanol (10 mL) this was then added to the aldehyde forming a dark red/brown solution heat at 45C and stirred for 10 minutes before being taken of the heat and left to cool to room temperature before being placed in an ice bath where, orange crystals were formed (0.4204 g) (Fig 70).

Having left the filtrate for 6 days; dark orange needles were formed(1.6999 g). the resulting filtrate was again left for a week producing dark brown crystals (0.0567 g).

Recrystallisations in ethanol produced orange needle like crystals similar to that of compound 2. However recrystallisation in diethyl ether formed yellow plates identified as a second polymorph *via* SCXRD.

The crude product was characterised with ^{1}H (Fig 71/72) and ^{13}C NMR (Fig 73/74), NMR (400 MHz, DMSO) δ 13.02 (s, 1H), 8.93 (s, 1H), 7.75 (d, *J* = 2.7 Hz, 1H), 7.50 – 7.37 (m, 5H), 7.35 – 7.30 (m, 1H), 7.00 (d, *J* = 8.8 Hz, 1H), ^{13}C NMR (101 MHz, DMSO) δ 162.02, 158.92, 147.90, 132.74, 131.03, 129.51, 127.26, 122.55, 121.41, 120.59, 118.64, to confirm the completion of the reaction.

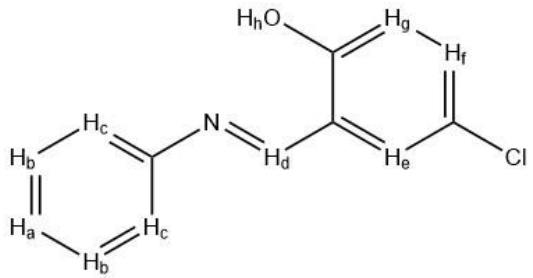


Figure 71: Labelled hydrogen diagram of compound 3

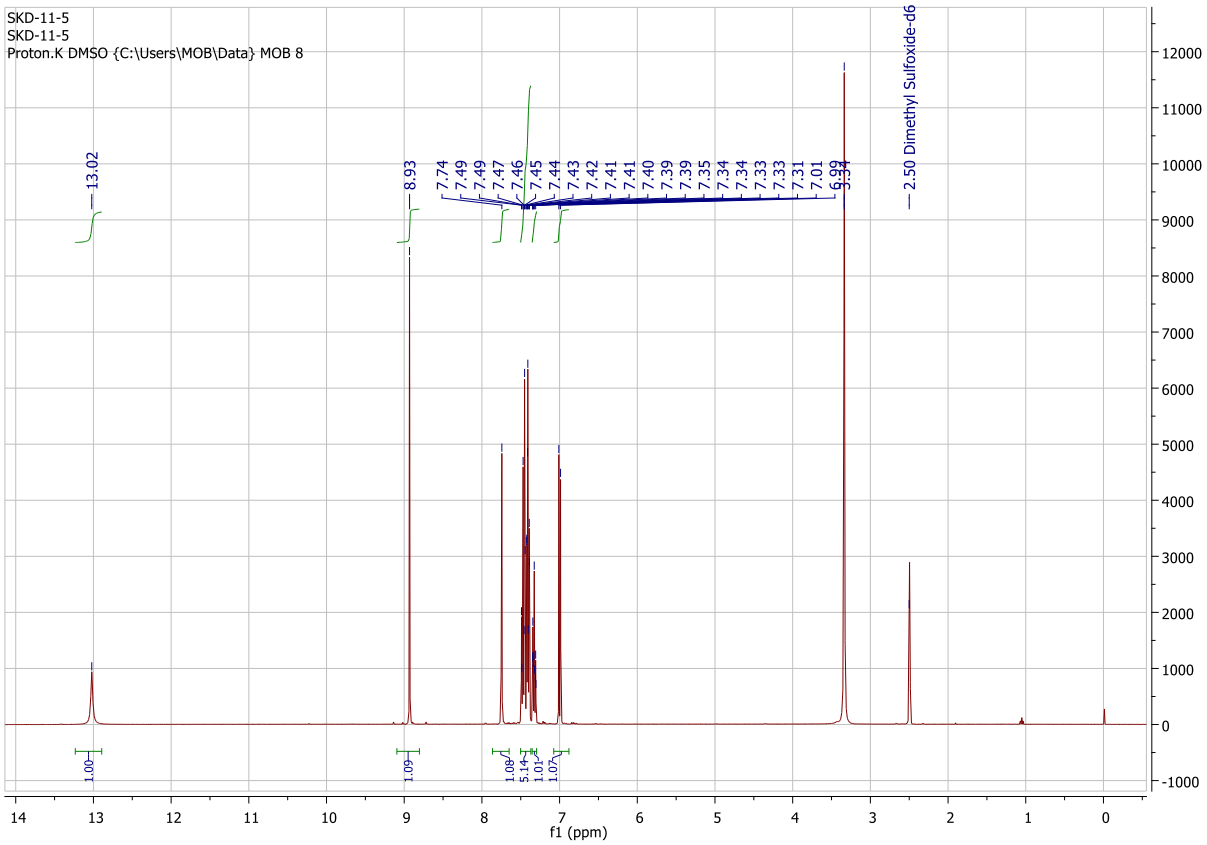


Figure 72: ^{1}H NMR spectrum of compound 3

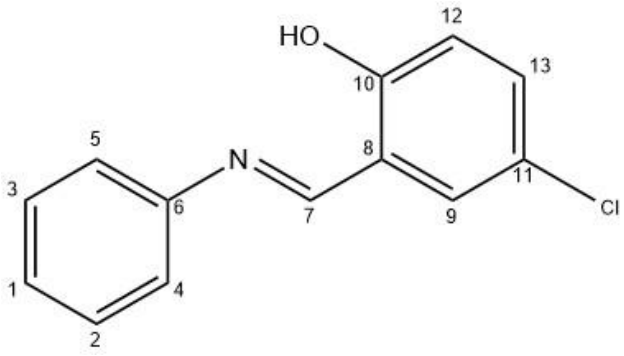


Figure 73: Labelled carbon diagram of compound 3

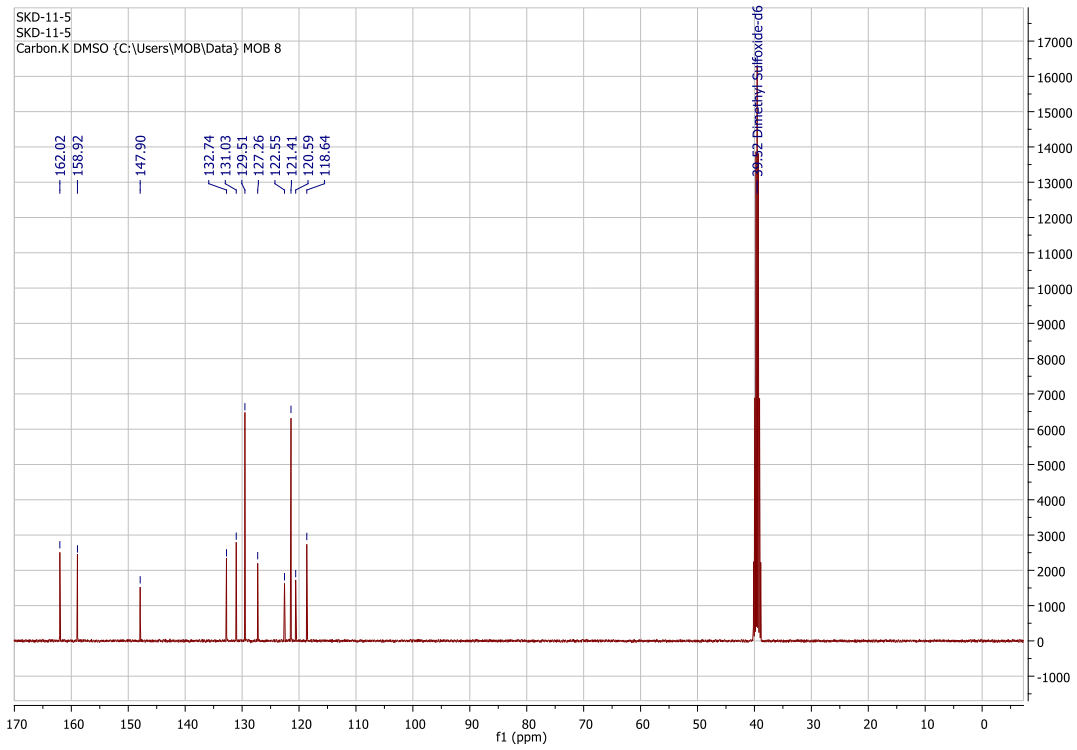


Figure 74: ^{13}C NMR spectrum of compound 3

Solution UV-Vis (Fig 75) and IR spectroscopy (Fig 76) were used as further methods of characterisation along with Raman Spectroscopy (Fig 77) all collected at 295 K.

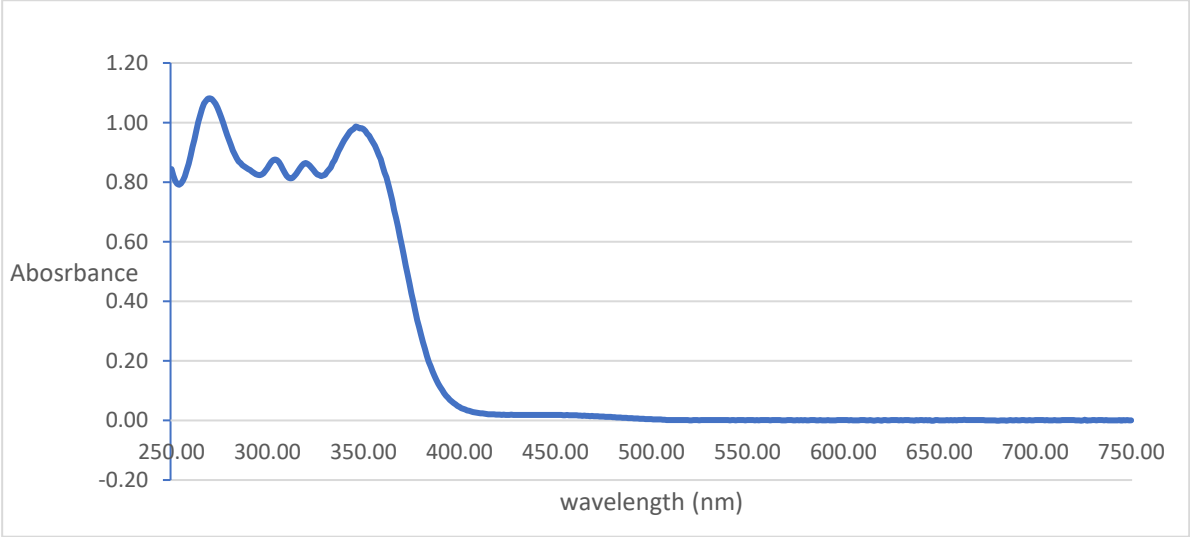


Figure 75: UV-VIs absorption spectrum for compound 3 in ethanol

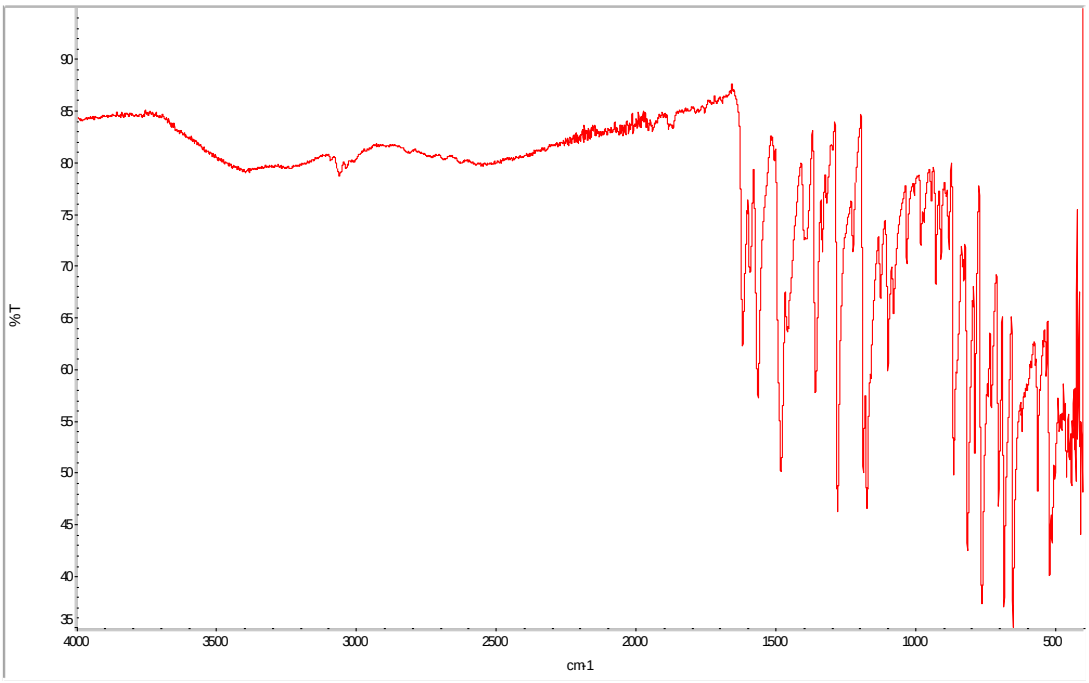


Figure 76: IR spectrum of compound 3

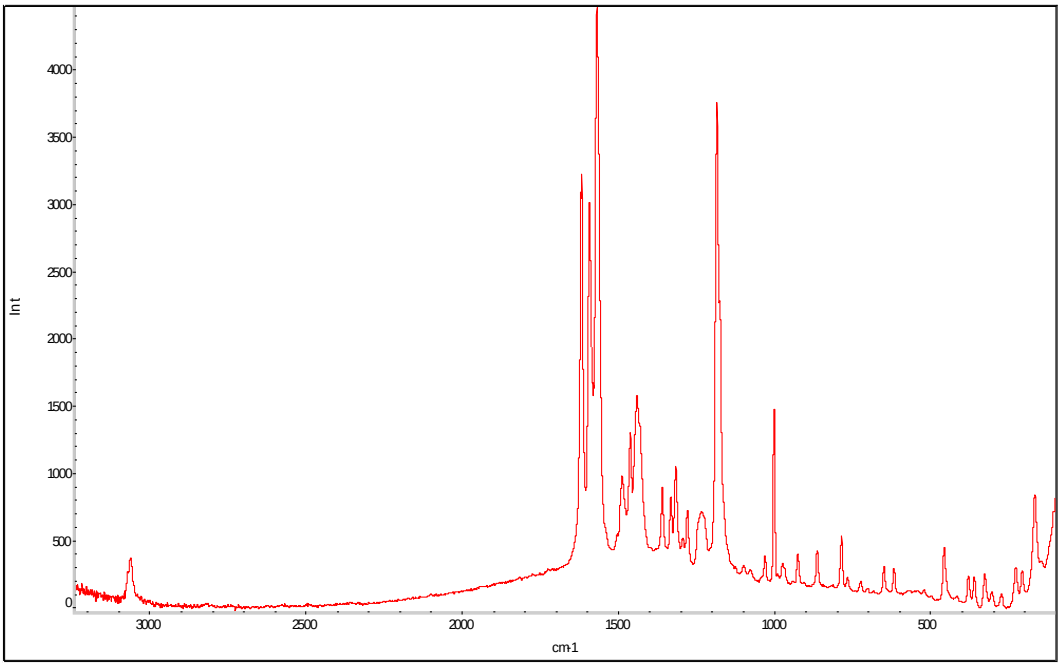


Figure 77: Raman Spectrum of compound 3 (785 nm)

SCXRD data was collected at Keele at 120, 140 and 298 K using the system as described for compound 1 and 2 for the first polymorph whilst for the second polymorph the data was collected at 120 and 290 K, this will be discussed in greater detail later on. As with compound 1 the neutron data was collected at ISIS this time at only 120 and 10 K.

4.2.4 Compound 4: 3,5-ditertbutylsalicylidene-3-nitroaniline

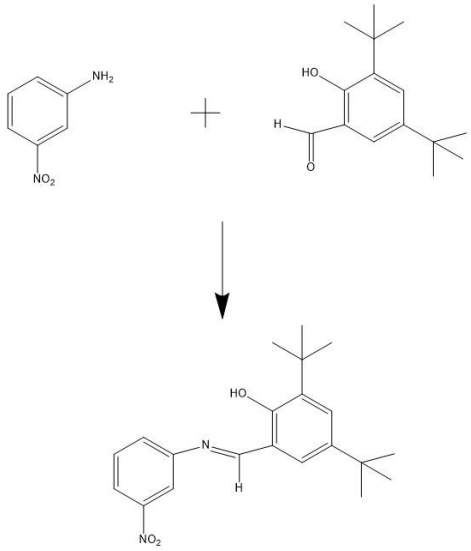


Figure 78: synthesis schematic of compound 4

3,5-Di-tert-Butylsalicylaldehyde (10.01g, 0.043 mol) added to 60 mL ethanol and heated at 55 °C for 10 minutes until dissolved into a pale yellow solution this was kept warm and stirring while the 3-nitroaniline was dissolved.

3-Nitroaniline (5.89 g, 0.043 mol) was added to 30 mL ethanol in a 100 mL RBF and heated at 55 °C for 10 minutes, the initial solution was orange in colour. About half of the solid dissolved so a further 30 mL ethanol was added and continually heat and stirred until the remaining solid was dissolved.

The two solutions were then mixed forming an orange solution heated and stirred at 40 °C for 20 minutes before being placed under reflux for a further 4.5 hours (Fig 78). The solution was taken off the hat and left to stand overnight cooling at room temperature. The precipitate formed overnight was filtered off (10.02 g), the filtrate was left to stand and formed a further powder like precipitate (0.1624 g). Hence, the filtrate was returned to the RBF which was then placed in the fridge once stoppered for six days resulting in further crystal formation (2.5106 g).

The crude product was characterised by NMR both ^{1}H (Fig 79/80) and ^{13}C (Fig 81/82), ^{1}H NMR (400 MHz, $CDCl_3$) δ 13.18 (s, 1H), 8.73 (s, 1H), 8.15 (t, *J* = 1.8 Hz, 1H), 8.14 – 8.09 (m, 1H), 7.66 – 7.52 (m, 3H), 7.30 (d, *J* = 2.4 Hz, 1H), 1.50 (s, 9H), 1.36 (s, 9H), ^{13}C NMR (101 MHz, $CDCl_3$) δ

181.66, 166.02, 158.42, 149.95, 141.08, 137.23, 130.17, 129.17, 127.89, 127.36, 120.98, 117.90, 115.63, 35.12, 34.21, 31.41, 29.39.

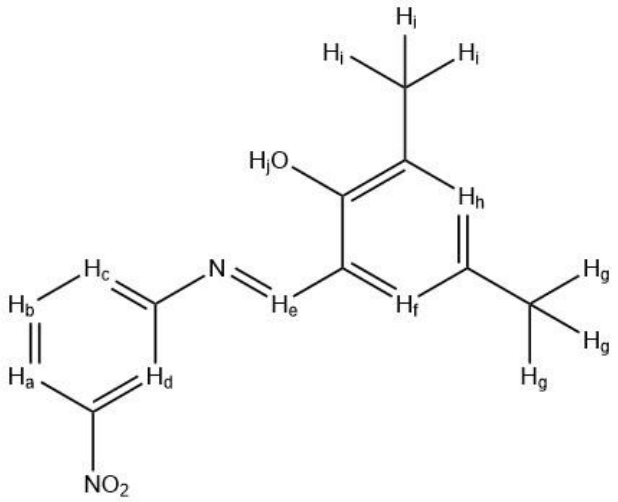


Figure 80: Labelled Hydrogen diagram of compound 4

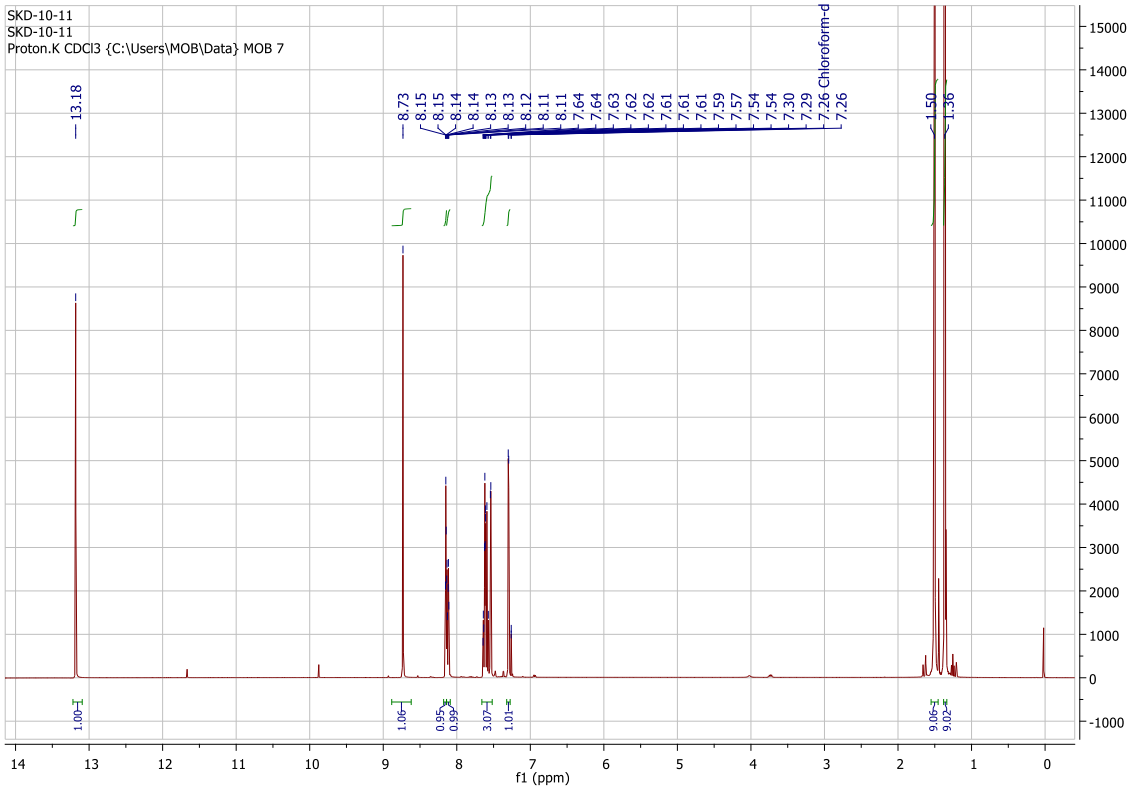


Figure 79: ^{1}H NMR spectrum of compound 4

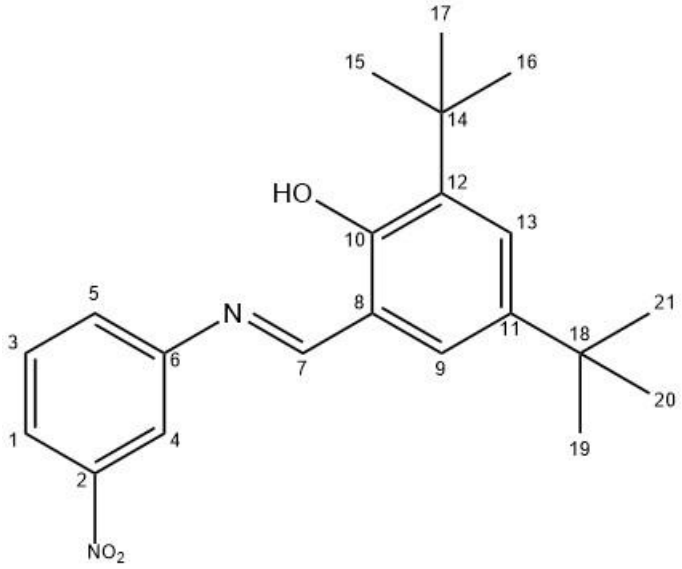


Figure 81: Labelled carbon diagram of compound 4

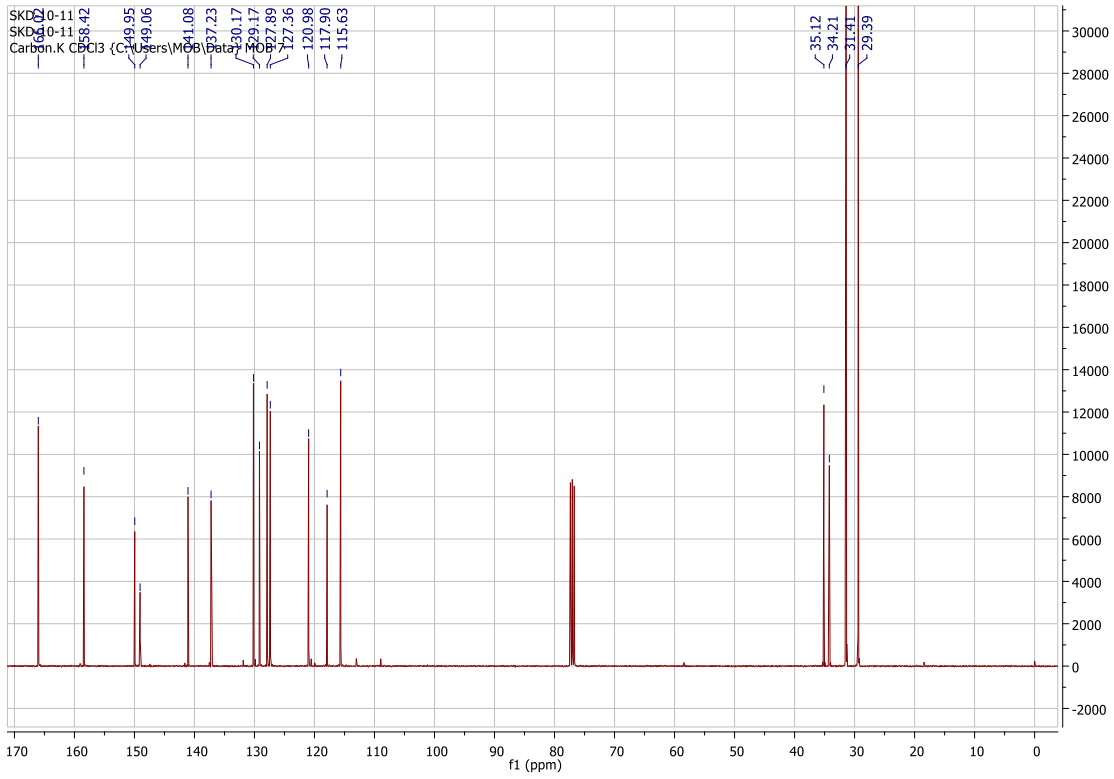


Figure 82: 13C NMR spectrum of compound 4

Further characterisation was completed using Solution UV-Vis (Fig 83) and IR (Fig 84) spectroscopy at 295 K. Raman scattering was completed at multiple temperatures using both a

bench top Raman spectrometer and the *insitu* Raman scattering setup for neutron diffraction (discussed in more detail later).

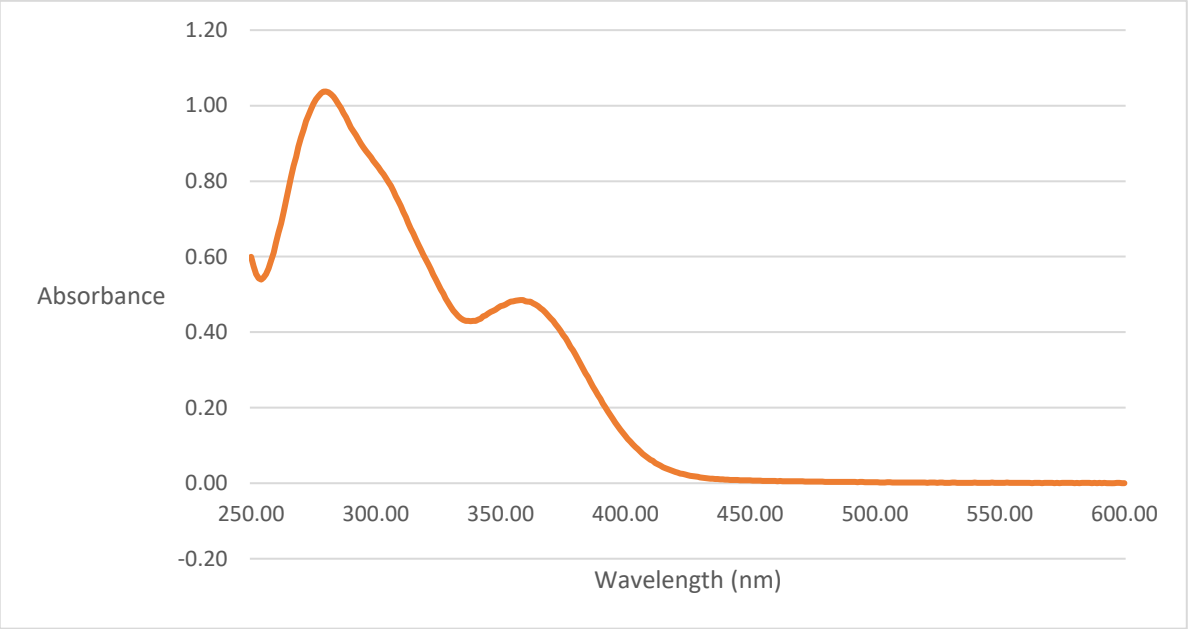


Figure 83: UV-Vis absorption spectrum of compound 4 in ethanol

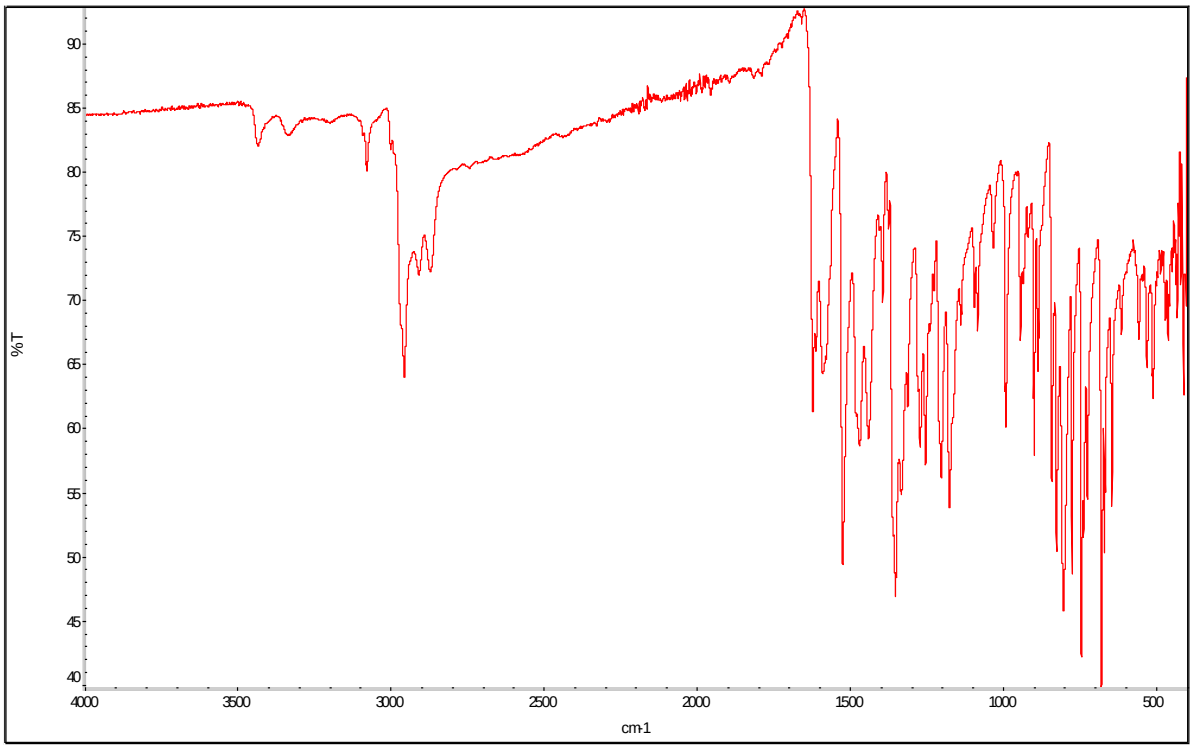


Figure 84: IR spectrum of compound 4

SCXRD data (discussed in more detail later) was collected at ISIS using both the Molybdenum and Copper sources under UV irradiated and non-irradiated conditions. With neutron diffraction single crystal data also collected at ISIS using the *insitu* Raman scattering probe.

4.2.5 Compound 5: 3-methoxysalicylidene-3-nitroaniline

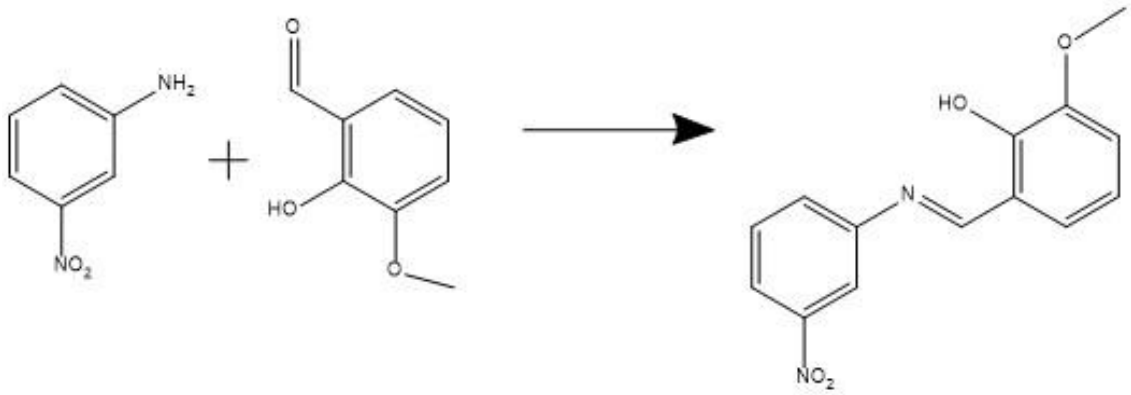


Figure 85: Reaction scheme for compound 5

3-Nitroaniline (0.59 g, 4.27 mmol) was dissolved in ethanol (20 mL) at 50 °C for 20 minutes forming an orange solution. 2-Hydroxy-3-methoxybenzlaldehyde (1.0040 g, 6.60 mmol) was dissolved in ethanol (20 mL) also at 50 °C for 20 minutes forming a pale yellow solution. The two solutions were mixed and left to stir at 50 °C for a further 40 minutes the solution retaining its orange colour. Having been left to cool to room temperature an orange fibrous precipitate formed and was filtered off (0.74 5g), more precipitate formed in the filtrate overnight (0.0525 g). Once the remaining solvent had evaporated the resulting solid was a mixture of small red block and colourless needles (Fig 85).

0.006 g was dissolved in ethanol (10 mL), a further 0.0068 g was dissolved in a one-to-one mixture of ethanol and methanol. After 4 days the one-to-one mixture and produced yellow needles that broke down on attempted removal. Further recrystallisations attempts were made using toluene and acetone both producing orange needle morphology crystals.

Characterisation of the crude product was completed using ^{1}H (Fig 86/87) and ^{13}C (Fig 88/89) NMR; ^{1}H NMR (400 MHz, DMSO) δ 12.51 (s, 1H), 9.07 (s, 1H), 8.24 (t, *J* = 2.1 Hz, 1H), 8.15 (ddd, *J* = 8.2, 2.2, 1.0 Hz, 1H), 7.86 (ddd, *J* = 8.0, 2.0, 1.0 Hz, 1H), 7.74 (t, *J* = 8.1 Hz, 1H), 7.31 (dd, *J* = 7.9, 1.4 Hz, 1H), 7.17 (dd, *J* = 8.0, 1.4 Hz, 1H), 6.94 (t, *J* = 7.9 Hz, 1H), 3.83 (s, 3H), ^{13}C NMR (101 MHz, DMSO) δ 166.02, 150.72, 149.84, 148.91, 148.23, 131.01, 128.74, 124.16, 121.40, 119.50, 119.10, 116.29, 116.02, 56.13.

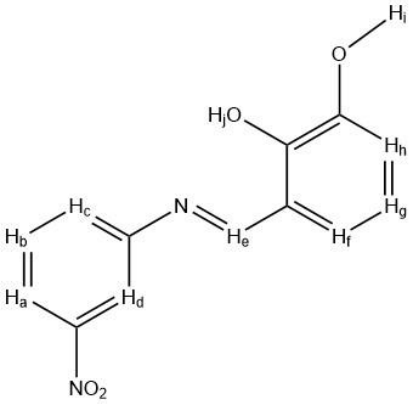


Figure 86: labelled hydrogen diagram of compound 5

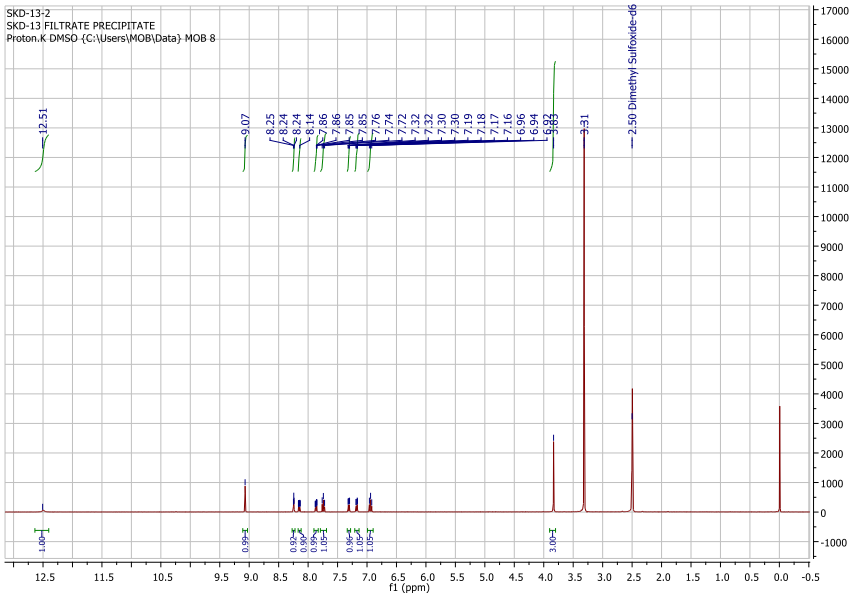


Figure 87: ^{1}H NMR spectrum of compound 5

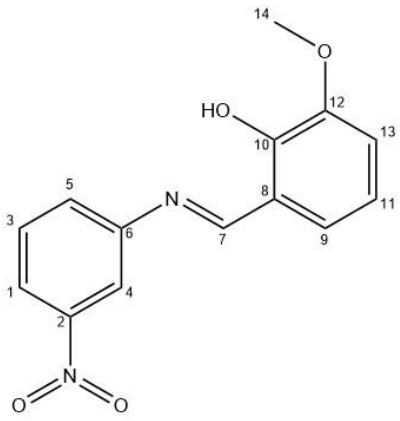


Figure 88: labelled carbon diagram of compound 5

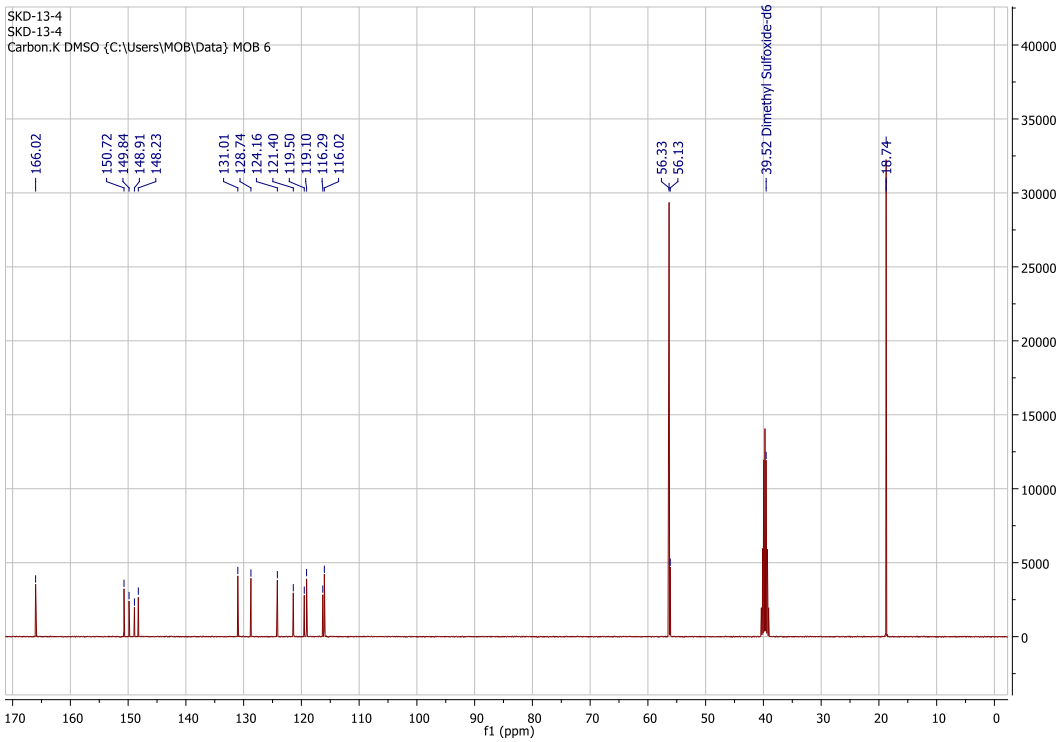


Figure 89: ^{13}C NMR spectrum of compound 5

As with previous compounds solution UV-Vis (fig 90) and IR (fig 91) spectroscopy along with Raman scattering (fig 92) were completed at 295 K to round out the characterisation as SXCRD was not possible due to the non-crystalline nature of the purified product.

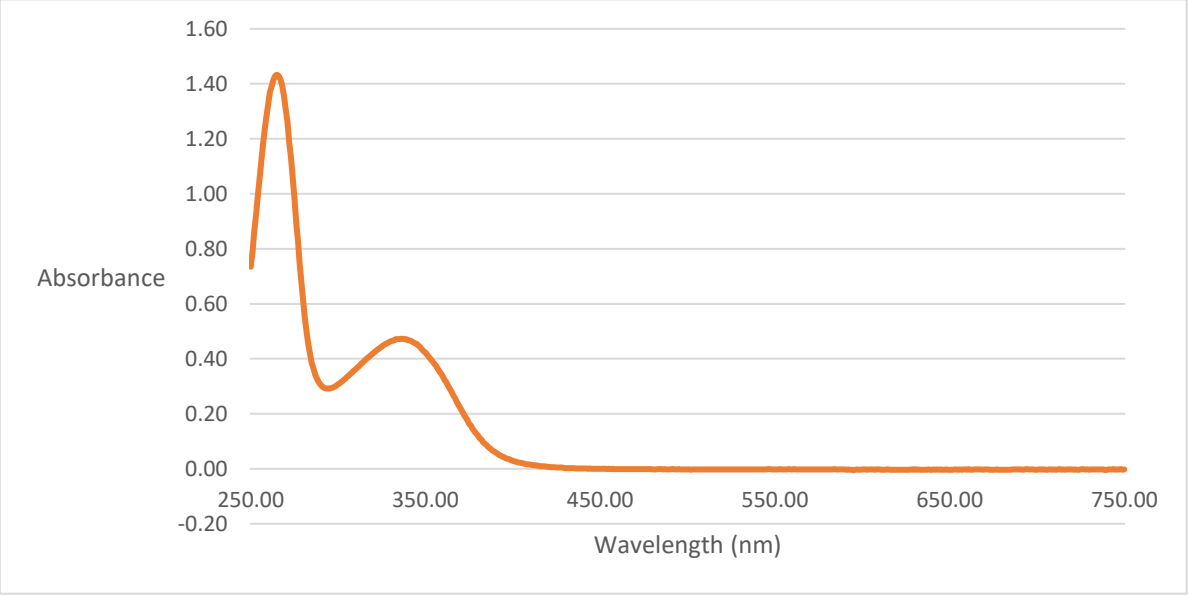


Figure 90: UV-Vis absorption spectrum of compound 5 in ethanol

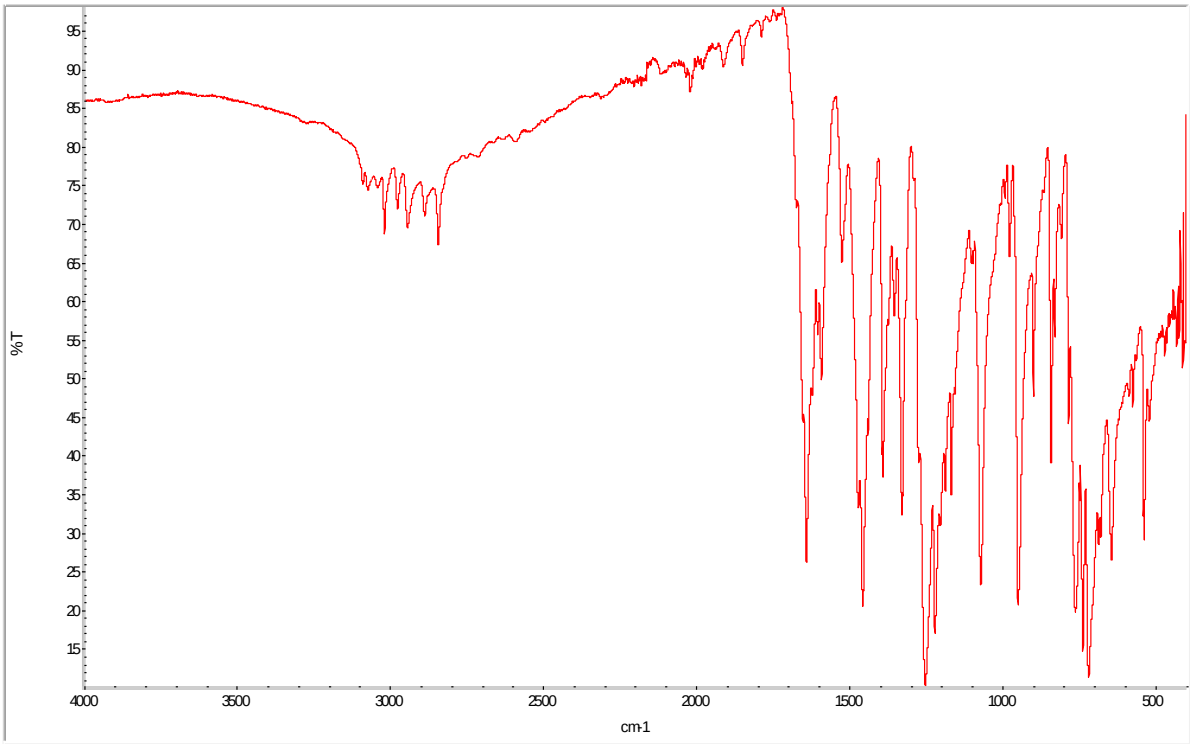


Figure 91: IR spectrum of compound 5

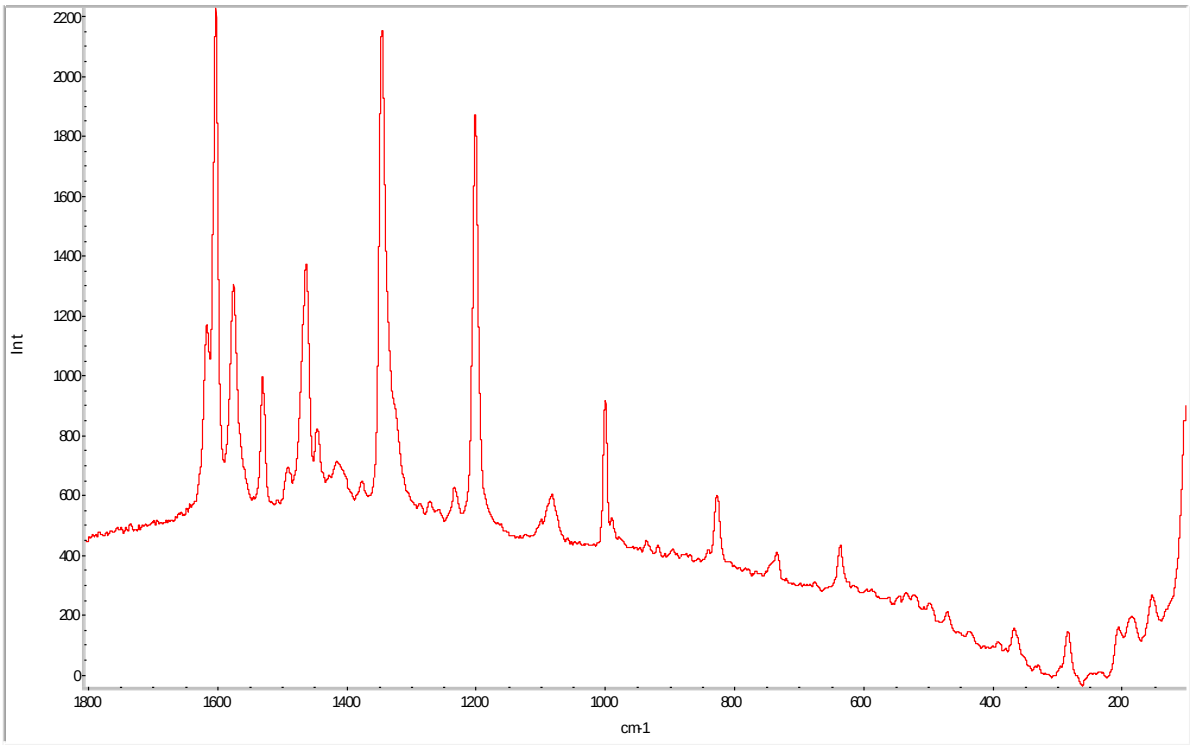


Figure 92: Raman spectrum of compound 5 at 295 K

4.2.6 Compound 6: 3-methoxysalicylideneaniline

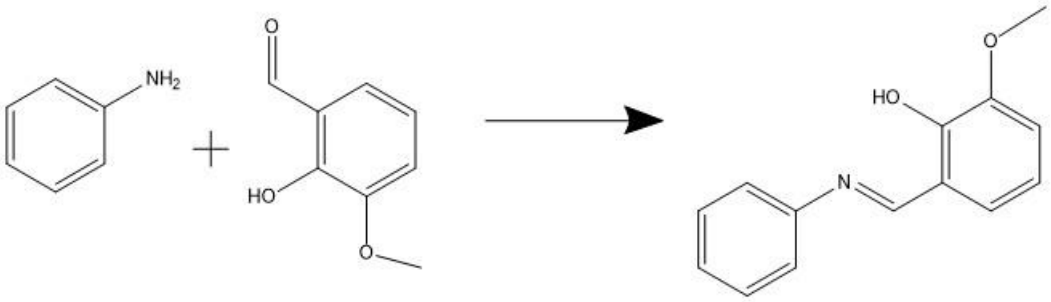


Figure 93: Reaction scheme of compound 6

To a solution of 2-hydroxy-3-methoxybenzaldehyde (1.6789 g, 0.011 mol) in methanol (40 mL), aniline (1 mL, 1.0217 g mol^{-1}, 0.011 mol) was added. This turned the solution for yellow to orange which upon refluxing for 3 hours turned almost red in colour. The solution was then left to evaporate producing red crystalline solid. The crude product was recrystallised from ethyl acetate via slow evaporation to produce deep red crystals (Fig 93).

Synthesis completion was confirmed using ^{1}H (fig 94/95) and ^{13}C (Fig 96/97) NMR; ^{1}H NMR (400 MHz, DMSO) δ 13.23 (s, 1H), 8.95 (s, 1H), 7.49 – 7.44 (m, 2H), 7.41 (d, *J* = 7.1 Hz, 2H), 7.31 (t, *J* = 7.2 Hz, 1H), 7.24 (dd, *J* = 7.9, 1.4 Hz, 1H), 7.13 (dd, *J* = 8.0, 1.3 Hz, 1H), 6.91 (t, *J* = 7.9 Hz, 1H), 3.82 (s, 3H), ^{13}C NMR (101 MHz, DMSO) δ 163.68, 150.58, 147.91, 147.89, 129.48, 126.98, 123.91, 121.34, 119.19, 118.58, 115.60, 55.89.

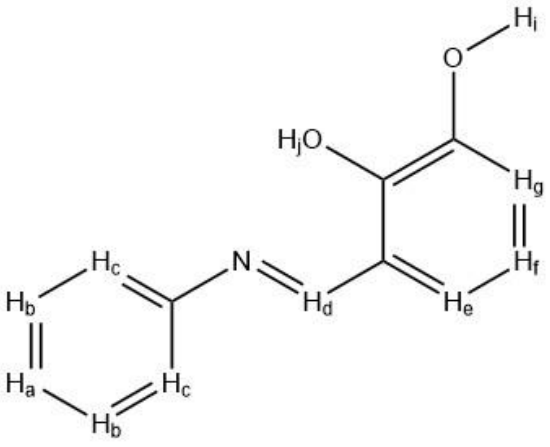


Figure 94: Labelled hydrogen diagram of compound 6

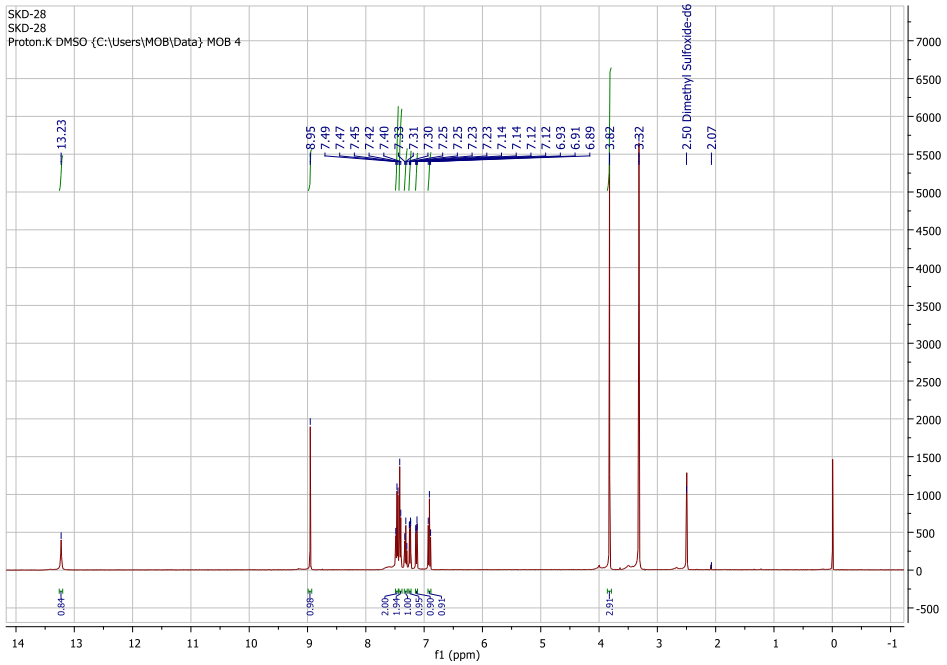


Figure 95: 1H NMR spectrum of compound 6

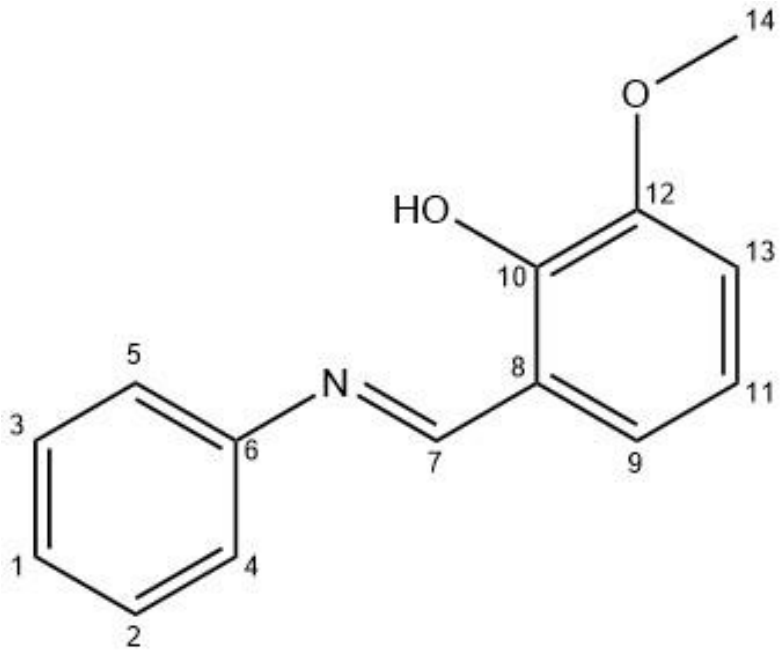


Figure 96: Labelled carbon diagram of compound 6

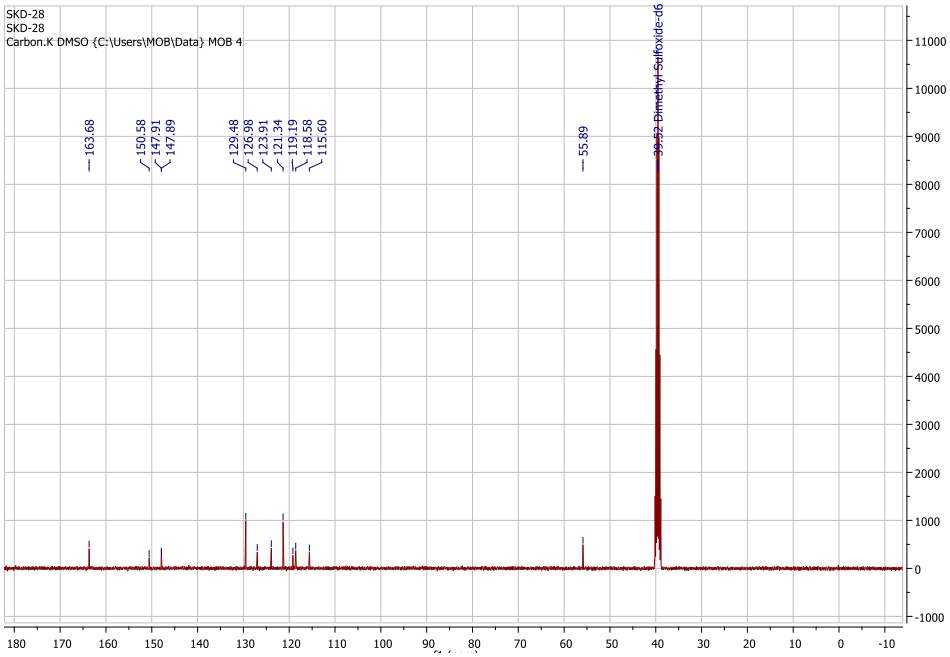


Figure 97: 13C NMR spectrum of compound 6

IR (Fig 98) and UV-Vis (Fig 99) spectroscopy were used to continue the characterisation of the material. SCXRD data was collected at 50, 100, 200 and 293 K using the Molybdenum source at ISIS and will be discussed in more detail in the next chapter.

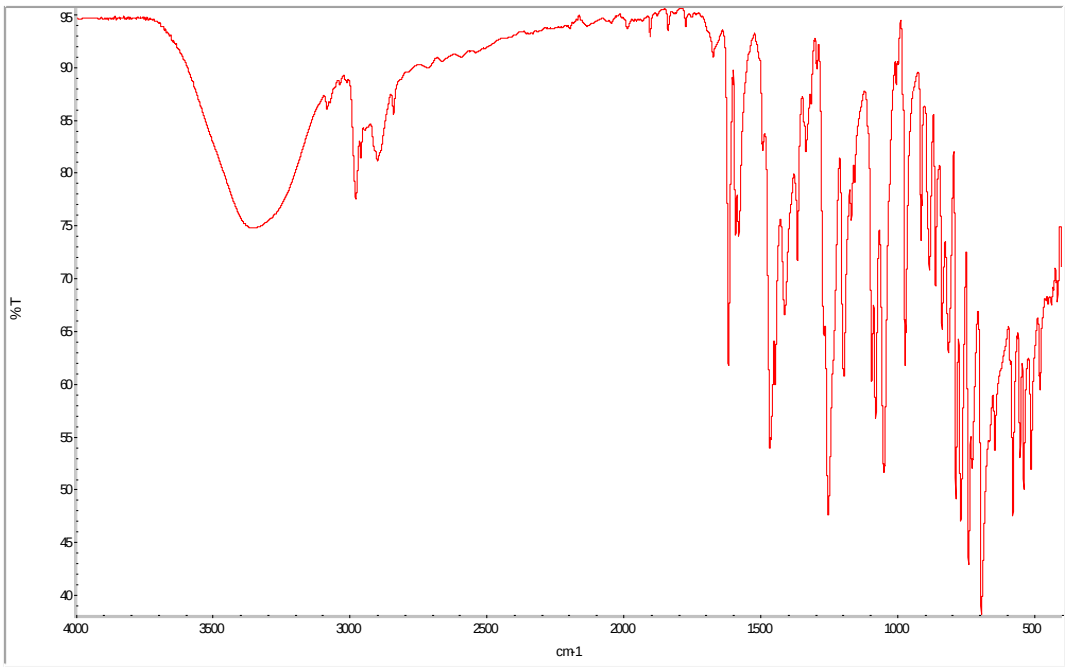


Figure 98: IR spectrum of compound 6

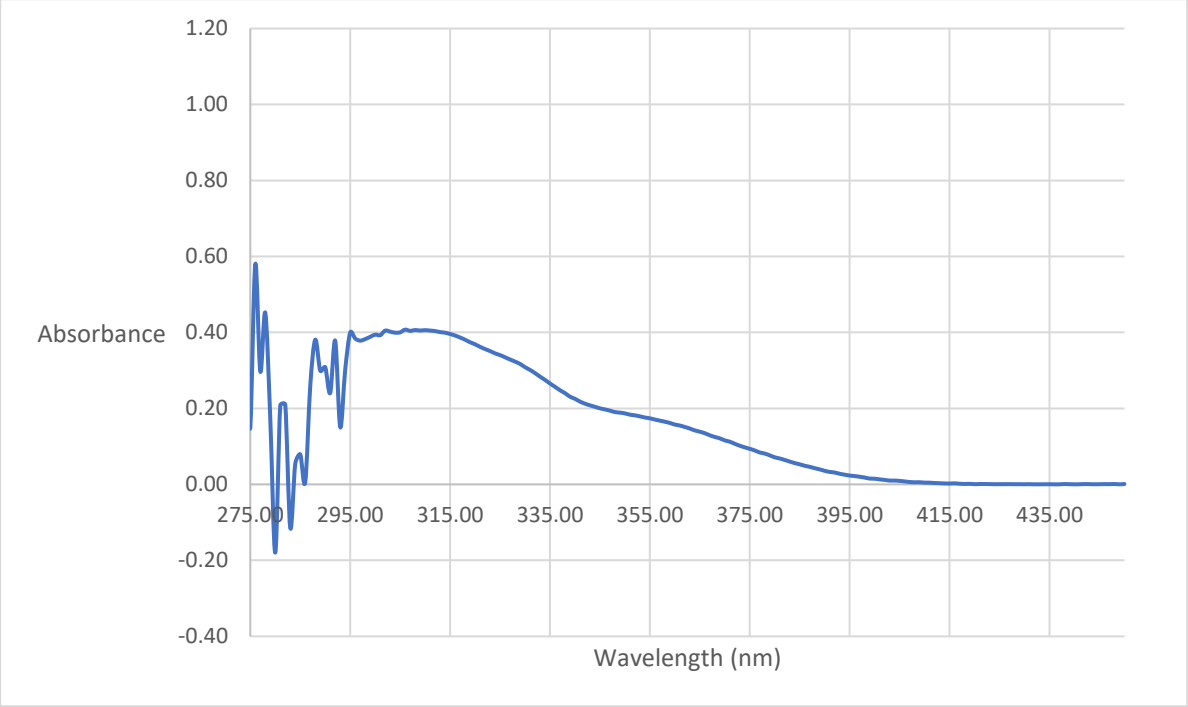


Figure 99: UV-Vis absorption spectrum of compound 6 in ethanol

4.2.7 Compound 7: 3-methoxysalicylidene-4-hydroxyaniline

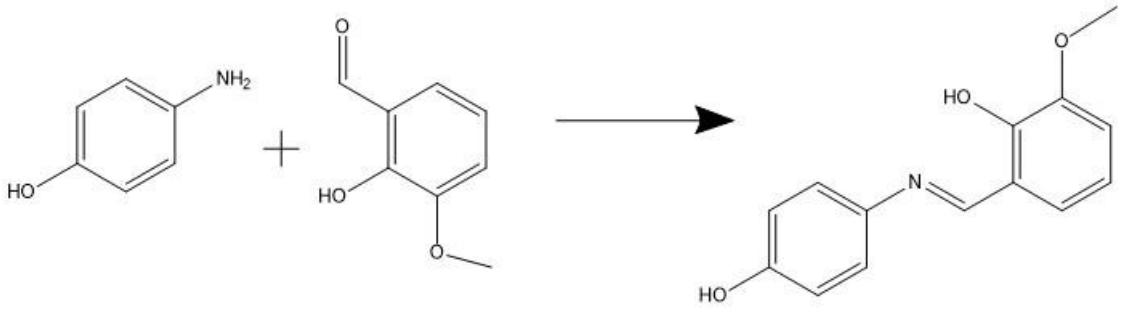


Figure 100: Reaction synthesis of compound 7

To a solution of 4-hydroxyaniline (5.38 mmol, 0.5871 g) in methanol (30 mL), 2-hydroxy-3-methoxybenzaldehyde (5.44 mmol, 0.8274 g) in methanol (20 mL) was added and left to stir at room temperature for 4 hours (Fig 100).

The resulting deep orange solution was then placed on the rotary evaporator however was most of the solvent was removed the viscous oil remaining began to bubble as if boiling so the product was removed and a further 20 mL methanol was added and the resulting solution left for the solvent to evaporate off, resulting in a semi-crystalline solid product.

Characterised by ^{1}H and ^{13}C NMR (Fig 101 to 104) to confirm production of the correct product; ^{1}H NMR (400 MHz, DMSO) δ 13.59 (s, 1H), 9.64 (s, 1H), 8.88 (s, 1H), 7.31 (d, *J* = 8.8 Hz, 2H), 7.17 (dd, *J* = 7.8, 1.3 Hz, 1H), 7.07 (dd, *J* = 8.0, 1.3 Hz, 1H), 6.87 (t, *J* = 7.9 Hz, 1H), 6.84 (d, *J* = 8.7 Hz, 2H), 3.80 (s, 3H), ^{13}C NMR (101 MHz, DMSO) δ 160.35, 156.99, 150.40, 147.85, 139.00, 123.71, 122.63, 119.33, 118.41, 115.97, 115.03, 55.84, 48.61. Final characterisation was competed using IR and UV-Vis spectroscopy (Fig 106 and 105 respectively).

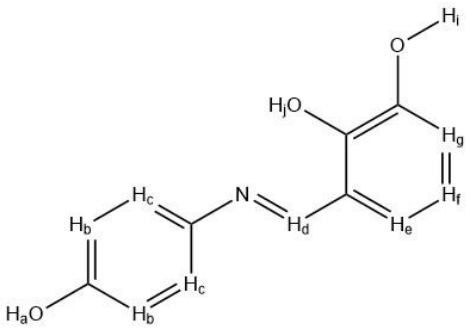


Figure 101: Labelled hydrogen diagram of compound 7

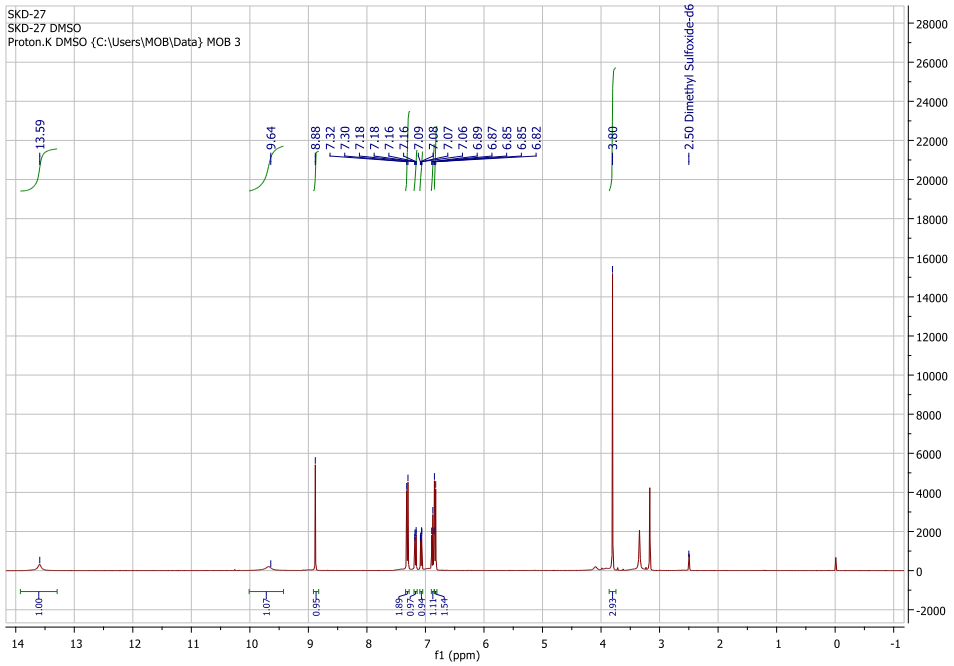


Figure 102: ^{1}H NMR spectrum of compound 7

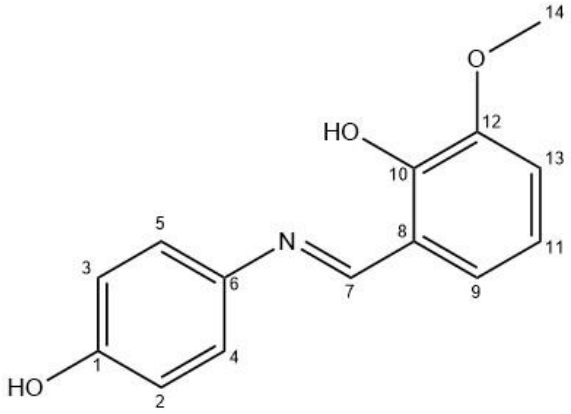


Figure 103: labelled carbon diagram of compound 7

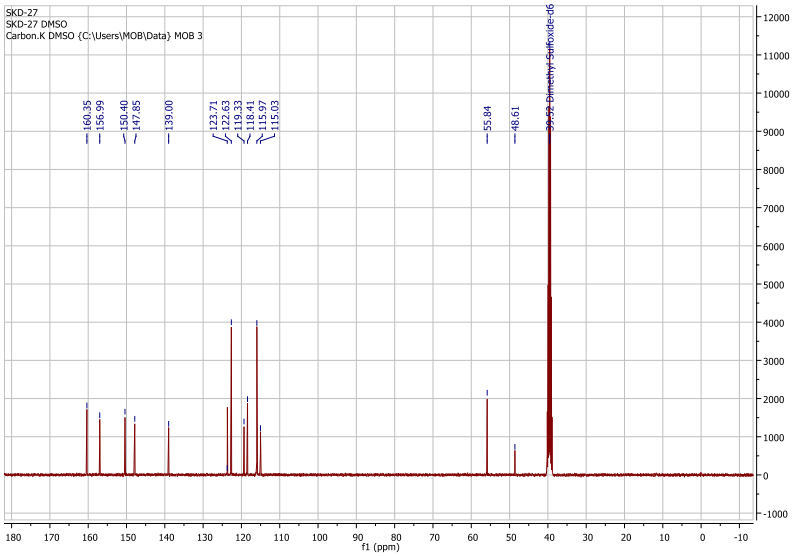


Figure 104:13C NMR spectrum of compound 7

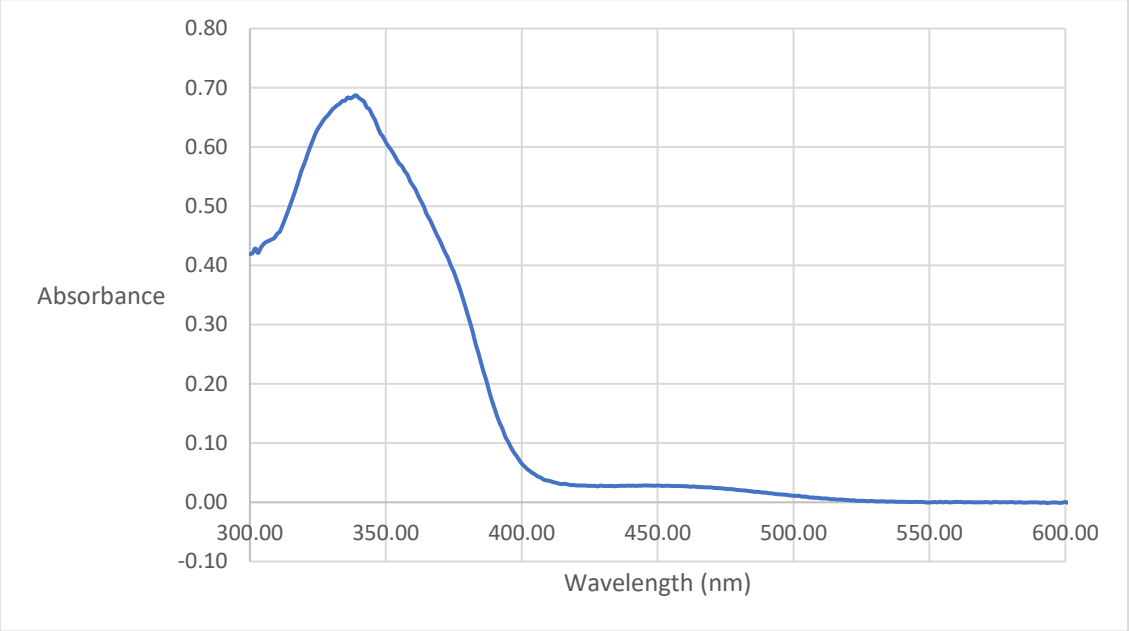


Figure 105: UV-Vis absorption spectrum of compound 7 in ethanol

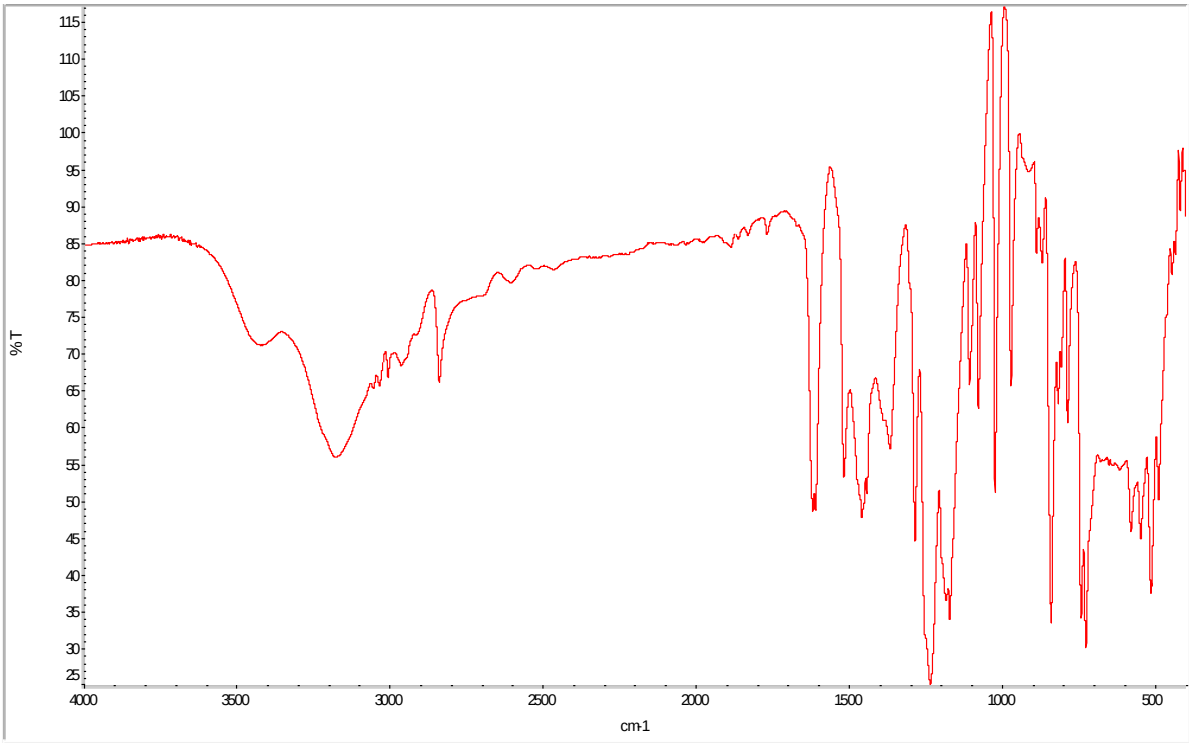


Figure 106: IR spectrum of compound 7

4.2.8 Compound 8: 3-methoxysalicylidene-4-bromoaniline

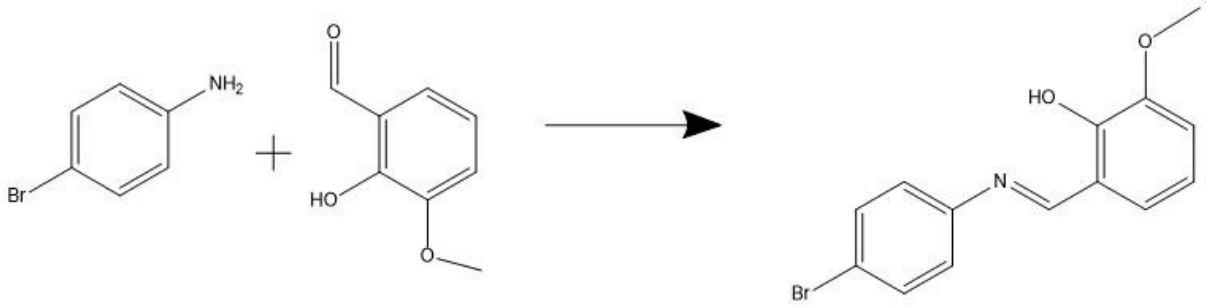


Figure 107: Reaction scheme for compound 8

To a solution of 4-bromoaniline (1.1655 g, 0.007 mol) in ethanol (50 mL), 2-hydroxy-3-methoxybenzaldehyde (1.0881g, 0.007 mol) in ethanol (10 mL) was added and refluxed for 3 hours forming an orange solution. This was then allowed to cool to room temperature forming an orange precipitate (Fig 107, Table 39(appendix))

A small mass of the precipitate was recrystallised from acetone, further recrystallisations were completed in ethyl acetate producing red needles.

As stated previously compound production was confirmed using ^{1}H and ^{13}C NMR (Fig 108 to 111);^{1}H NMR (400 MHz, $CDCl_3$) δ 13.36 (s, 1H), 8.61 (s, 1H), 7.57 – 7.50 (m, 2H), 7.20 – 7.13 (m, 2H), 7.05 – 6.98 (m, 2H), 6.90 (t, *J* = 7.9 Hz, 1H), 3.94 (s, 3H), ^{13}C NMR (101 MHz, $CDCl_3$) δ 163.19, 151.50, 148.66, 147.42, 132.67, 124.02, 122.98, 120.63, 119.11, 118.89, 115.21, 56.38.

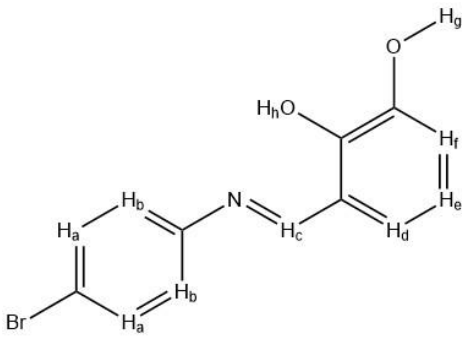


Figure 108: Labelled hydrogen diagram of compound 8

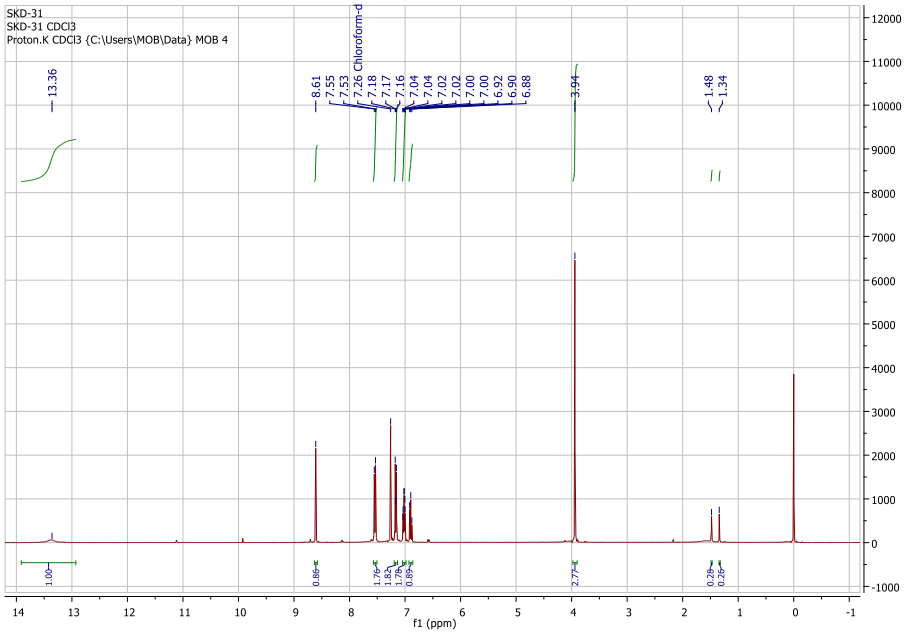


Figure 109: 1H NMR spectrum of compound 8

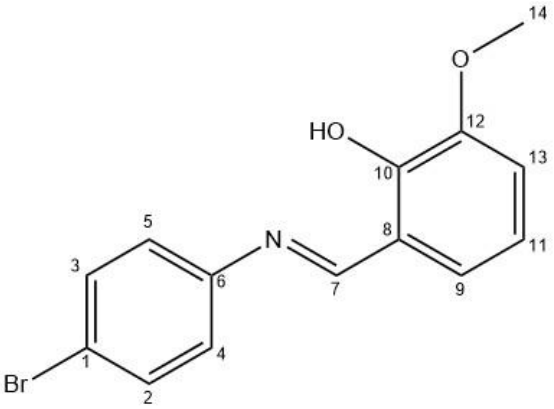


Figure 110: Labelled carbon diagram of compound 8

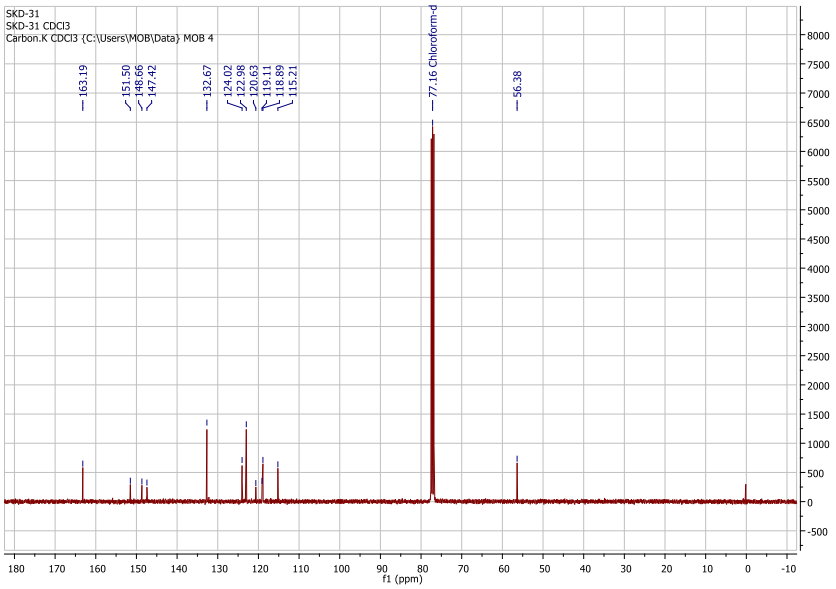


Figure 111: 13C NMR spectrum of compound 8

Further characterisation was completed using solution UV-Vis and IR spectroscopy (Fig 112 and 113).

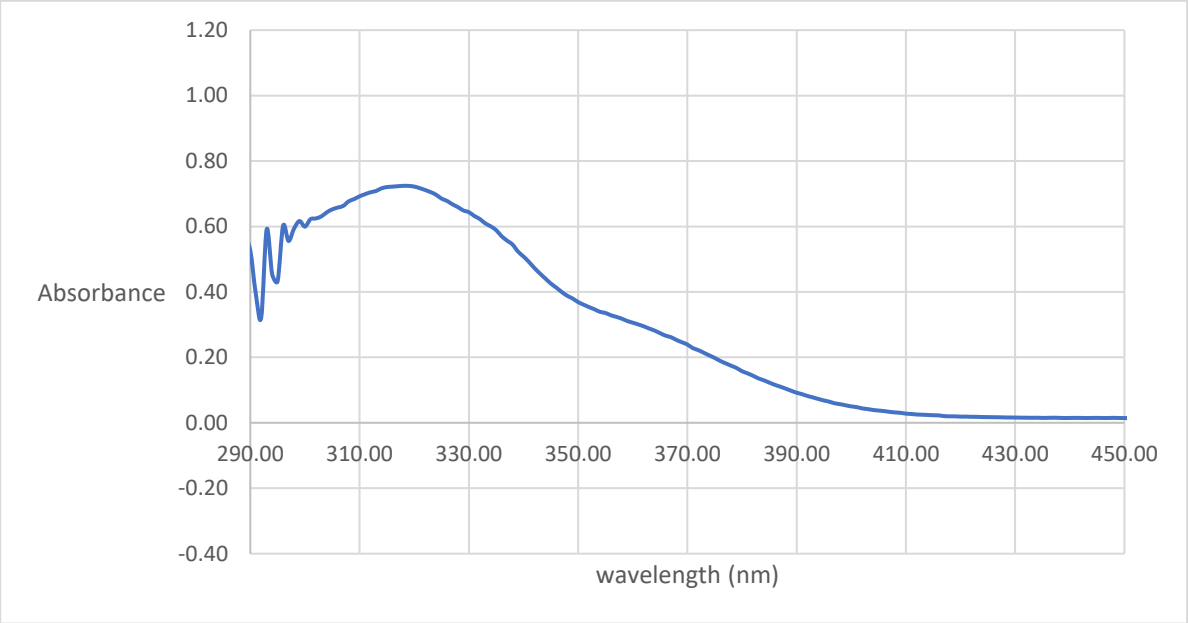


Figure 112: UV-Vis absorption spectrum of compound 8 in ethanol

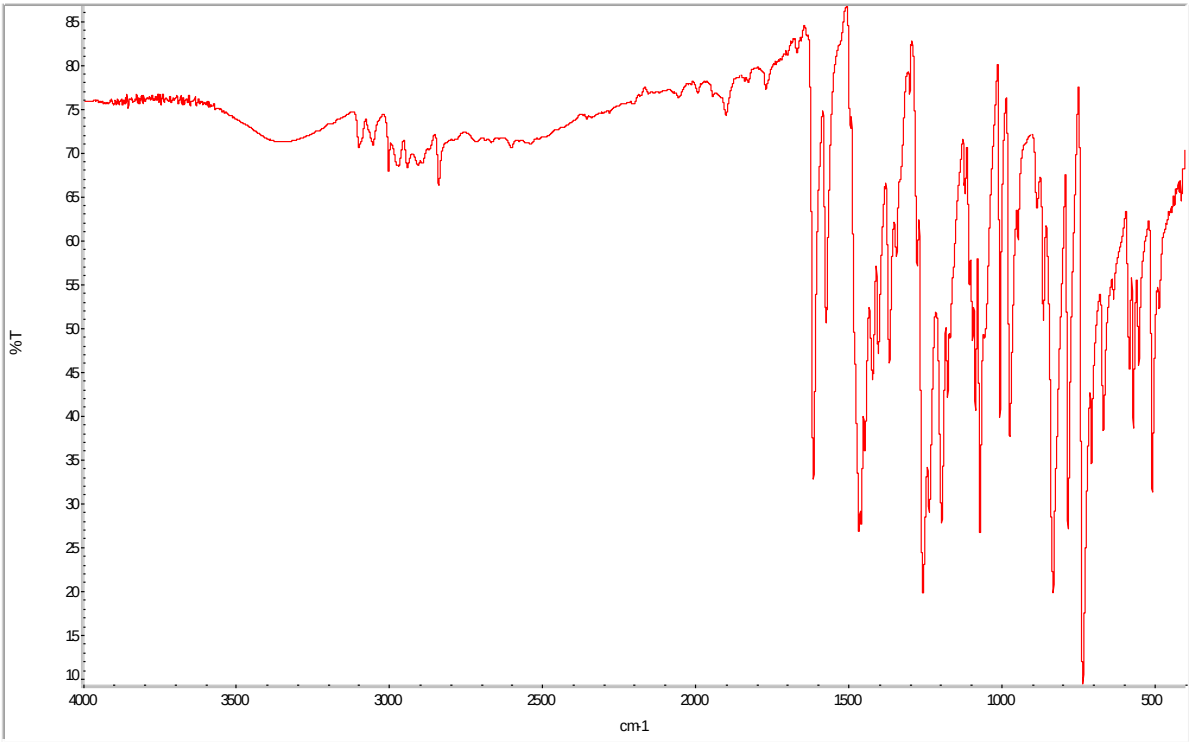


Figure 113: IR spectrum of compound 8

SCXRD data was collected on the SCXRD at ISIS, Harwell at 120, 250 and 293 K using a molybdenum source and will be discussed in greater detail later on.

4.2.9 Compound 9: 3-methoxysalicylidene-4-iodoaniline

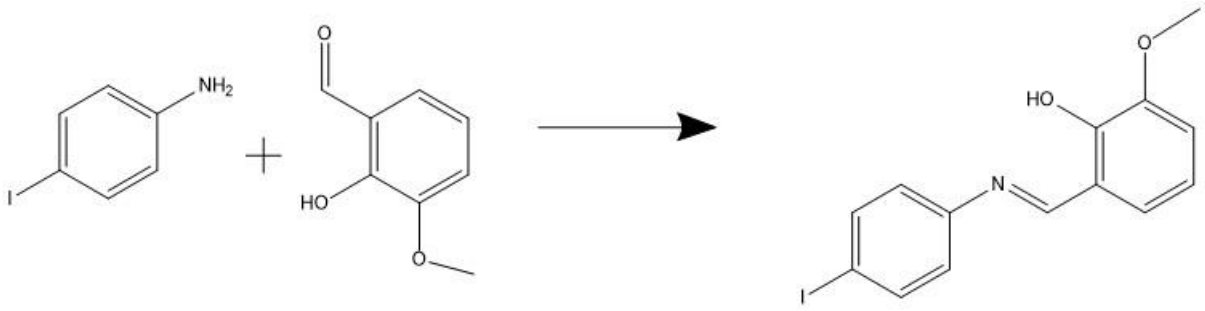


Figure 114: Reaction scheme for compound 9 synthesis

To a solution of 4-iodoaniline (1.4383 g, 0.007 mol) in ethanol (30 mL), 2-hydroxy-3-methoxybenzaldehyde (1.0408 g, 0.007 mol) in ethanol (10 mL) was added and refluxed for 3 hours forming an orange solution. After around 20 minutes an orange precipitate crashed out the solution was allowed to continue refluxing to encourage the reaction to go to completion (Fig 114). This was then allowed to cool to room temperature.

The precipitate was filtered off and dried under büchner filtration resulting in an orange powder. A small mass of the product was recrystallised in 15 mL acetone. Further recrystallisations were completed in ethanol, ethyl acetate and toluene.

Preliminary Characterisation was completed using ^{1}H and ^{13}C NMR (Fig 115 to 118); ^{1}H NMR (400 MHz, $CDCl_3$) δ 13.36 (s, 1H), 8.61 (s, 1H), 7.74 (d, *J* = 8.0 Hz, 2H), 7.07 – 6.98 (m, 4H), 6.90 (t, *J* = 7.6 Hz, 1H), 3.94 (s, 3H), ^{13}C NMR (101 MHz, $CDCl_3$) δ 163.02, 151.34, 148.46, 138.46, 123.83, 123.11, 118.68, 115.04, 77.28, 77.16, 76.96, 76.64, 56.18. Along with the NMR solution UV-Vis spectroscopy (Fig 119) was also used.

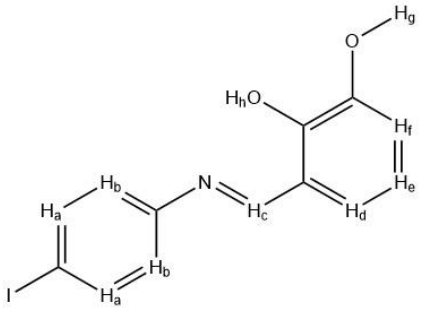


Figure 115: labelled hydrogen diagram of compound 9

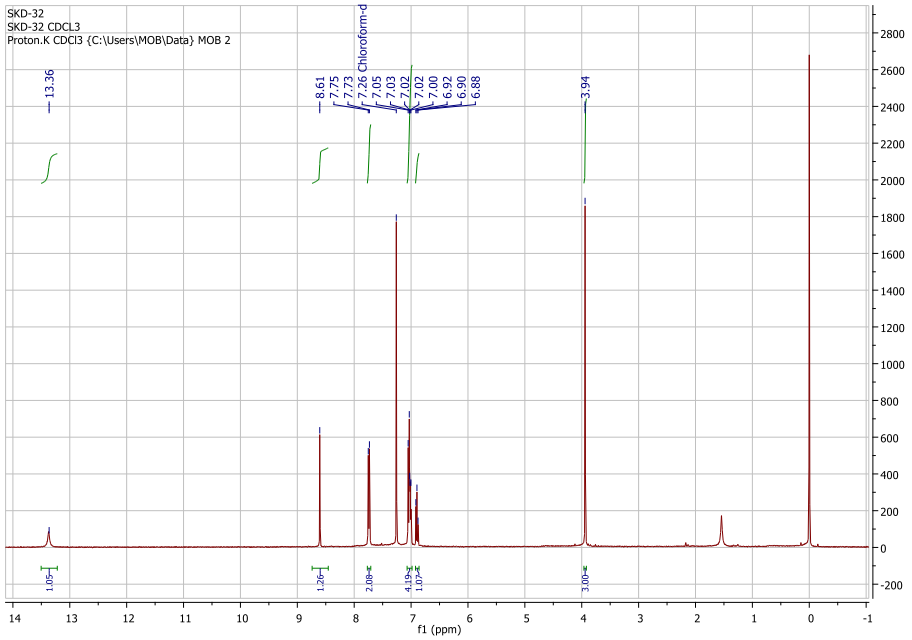


Figure 116: 1H NMR spectrum of compound 9

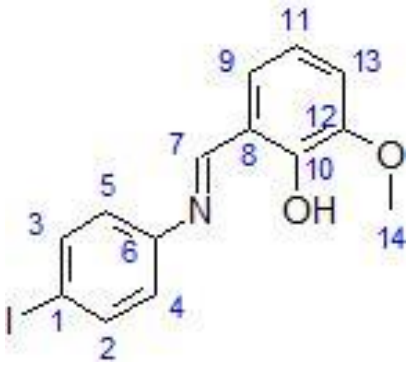


Figure 117: Labelled carbon diagram of compound 9

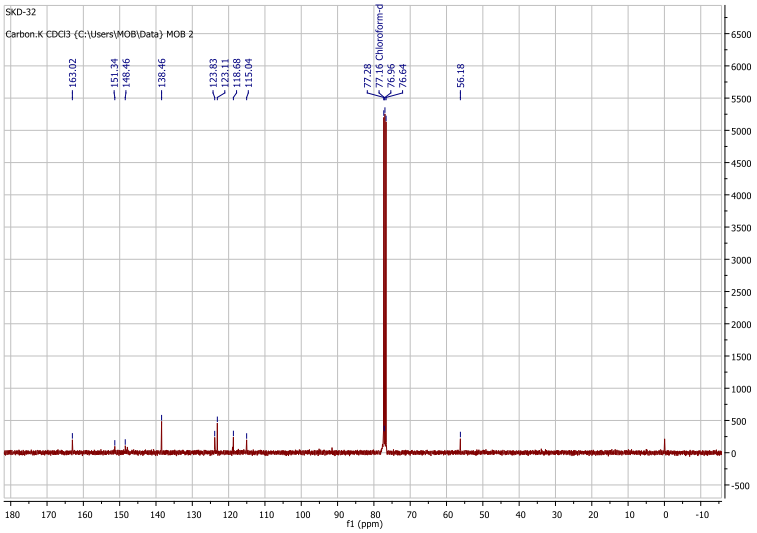


Figure 118: 13C NMR spectrum of compound 9

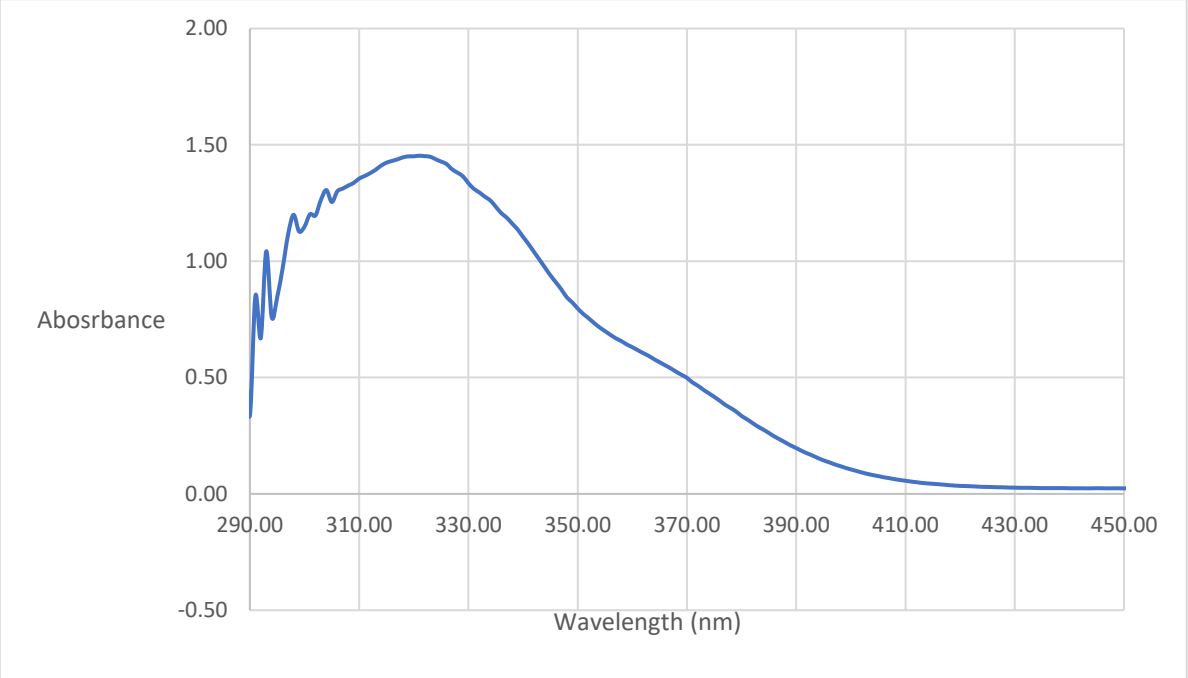


Figure 119: UV-Vis absorption spectrum of compound 9 in ethanol

SCXRD was completed on both polymorphs of the compound at ISIS, at 100, 200 and 295 K for the triclinic polymorph and 120 and 220 K for the orthorhombic polymorph.

4.2.10 Compound 10: 3,5-ditertbutylsalicylideneaniline

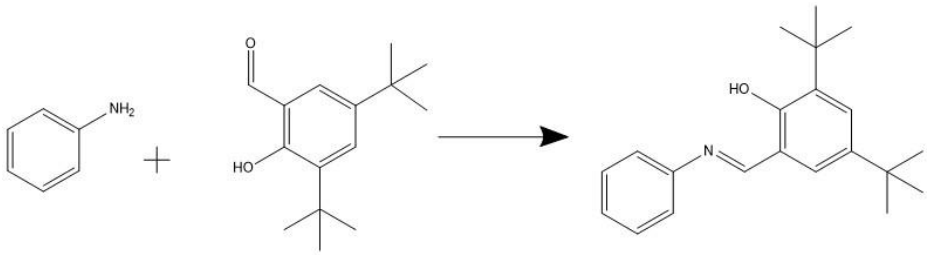


Figure 120: Reaction scheme for compound 10

To a solution of 3,5-di-tert-butylsalicaldehyde (2.46 g, 0.01 mol) in ethanol (50 mL) aniline was added (1 mL), this turned the solution from its original pale yellow to a deep golden yellow. The resulting solution was left to reflux for 4 hours, the colour becoming closer to orange after around 20 minutes (Fig 120).

This was then left to cool to room temperature overnight, a yellow precipitate forming which was the filtered (2.4171 g, 0.007 mol, 74.40 % yield). 0.1 g of which was recrystallised in a 2:1 ratio ethanol: methanol mixture totalling 30 mL, after 1 week yellow needle crystals had formed.

Further recrystallisations in ethanol *via* slow evaporation produced yellow plate crystals.

^{1}H NMR and ^{13}C NMR (Fig 121 to 124) confirmed the progress of the reaction to form the anticipated product; ^{1}H NMR (400 MHz, $CDCl_3$) δ 13.70 (s, 1H), 8.64 (s, 1H), 7.46 (d, *J* = 2.3 Hz, 1H), 7.41 (t, *J* = 7.7 Hz, 2H), 7.30 – 7.24 (m, 3H), 7.22 (d, *J* = 2.3 Hz, 1H), 1.48 (s, 9H), 1.33 (s, 9H), ^{13}C NMR (101 MHz, $CDCl_3$) δ 163.65, 158.09, 148.57, 140.39, 136.82, 129.16, 127.84, 126.64, 126.35, 121.01, 118.13, 34.94, 34.02, 31.31, 29.27.

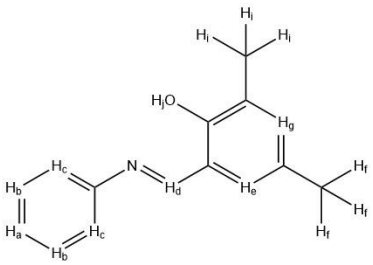


Figure 121: Labelled hydrogen diagram of compound 10

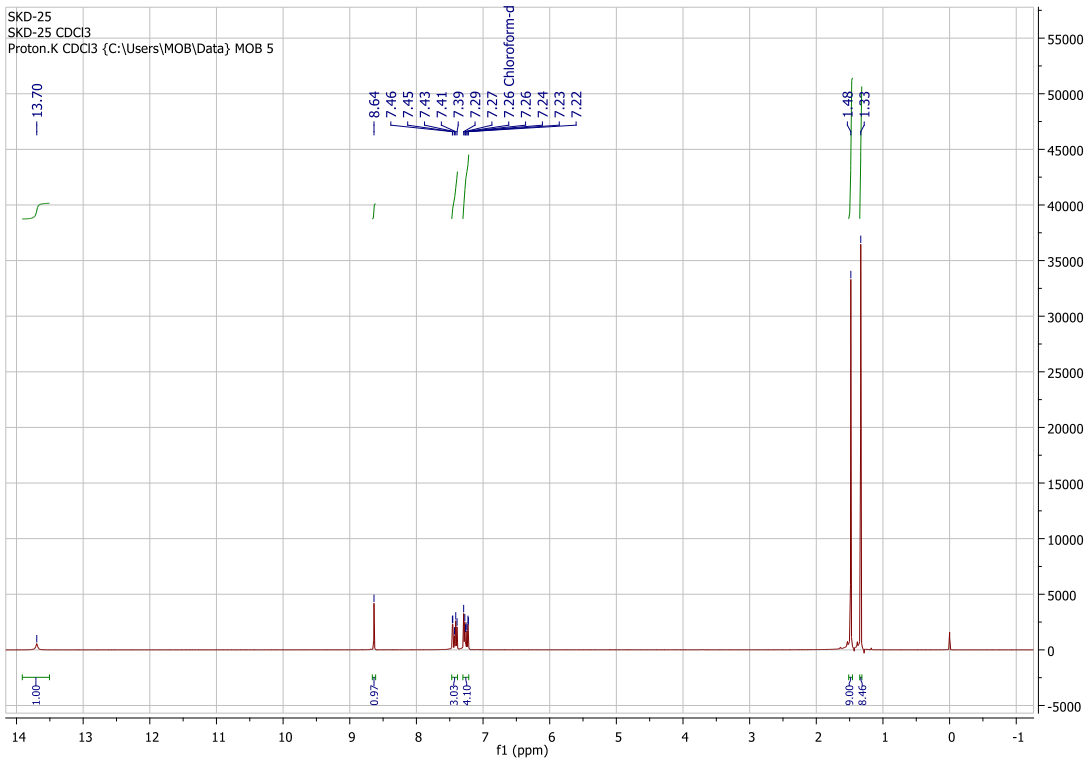


Figure 122: 1H NMR spectrum of compound 10

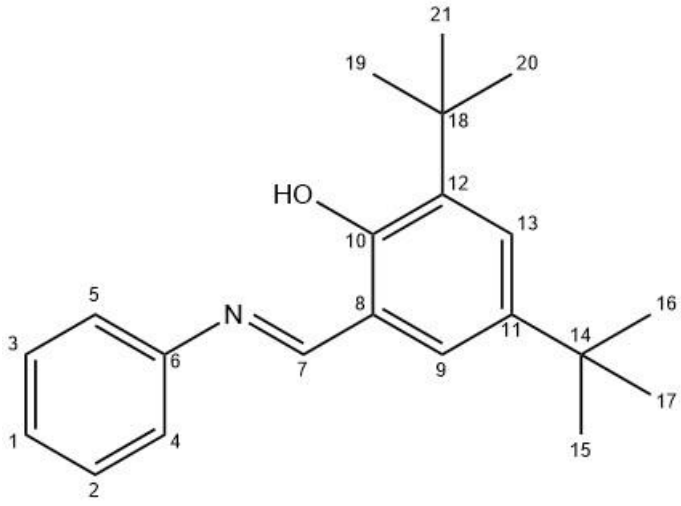


Figure 123: labelled carbon diagram of compound 10

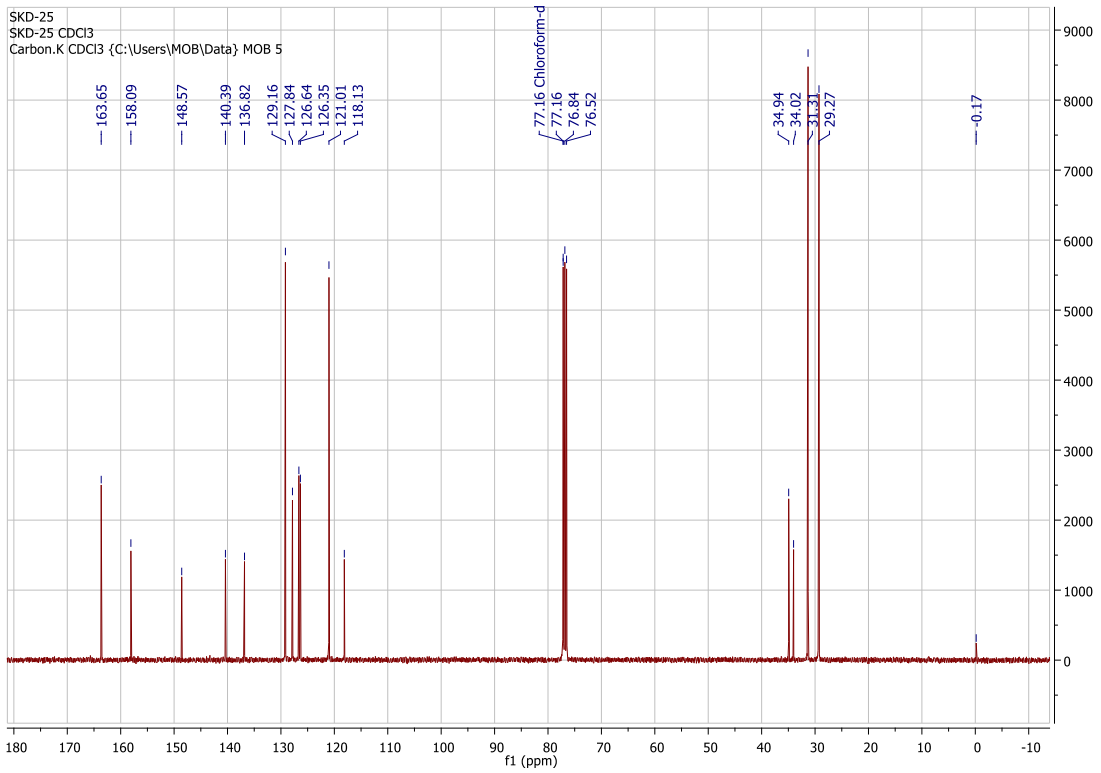


Figure 124: 13C NMR spectrum of compound 10

Solution UV-Vis and IR spectroscopy (Fig 125 and 126) were used to complete the preliminary characterisation, with Raman Scattering, Neutron spectroscopy along with SCXRD and single crystal Neutron diffraction also completed to be discussed in more detail in the next chapter.

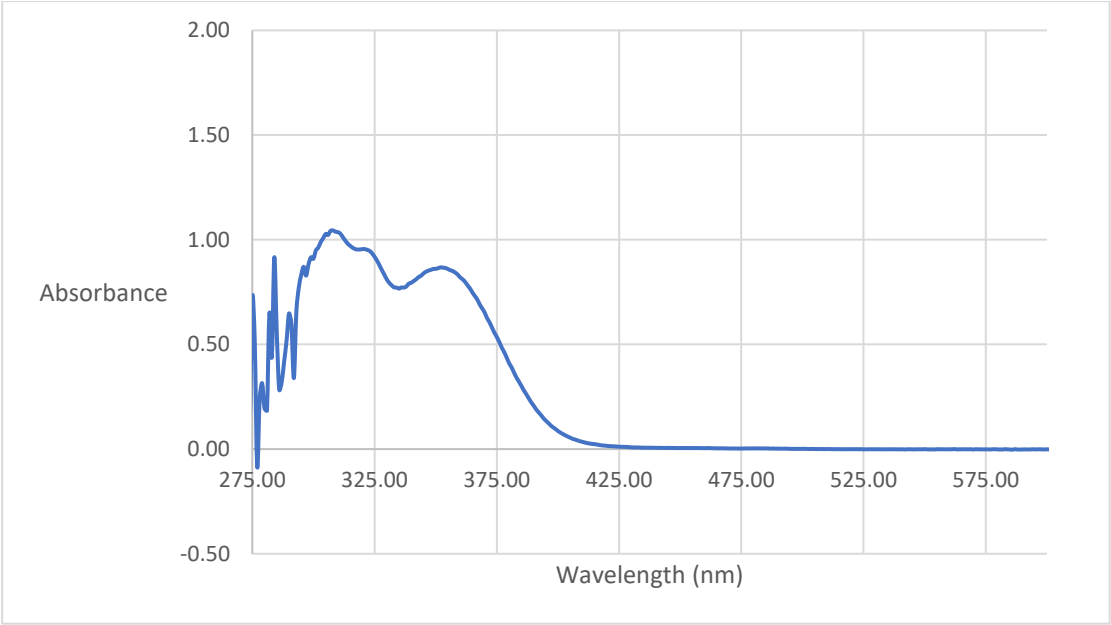


Figure 125: UV-Vis absorption spectrum of compound 10 in ethanol

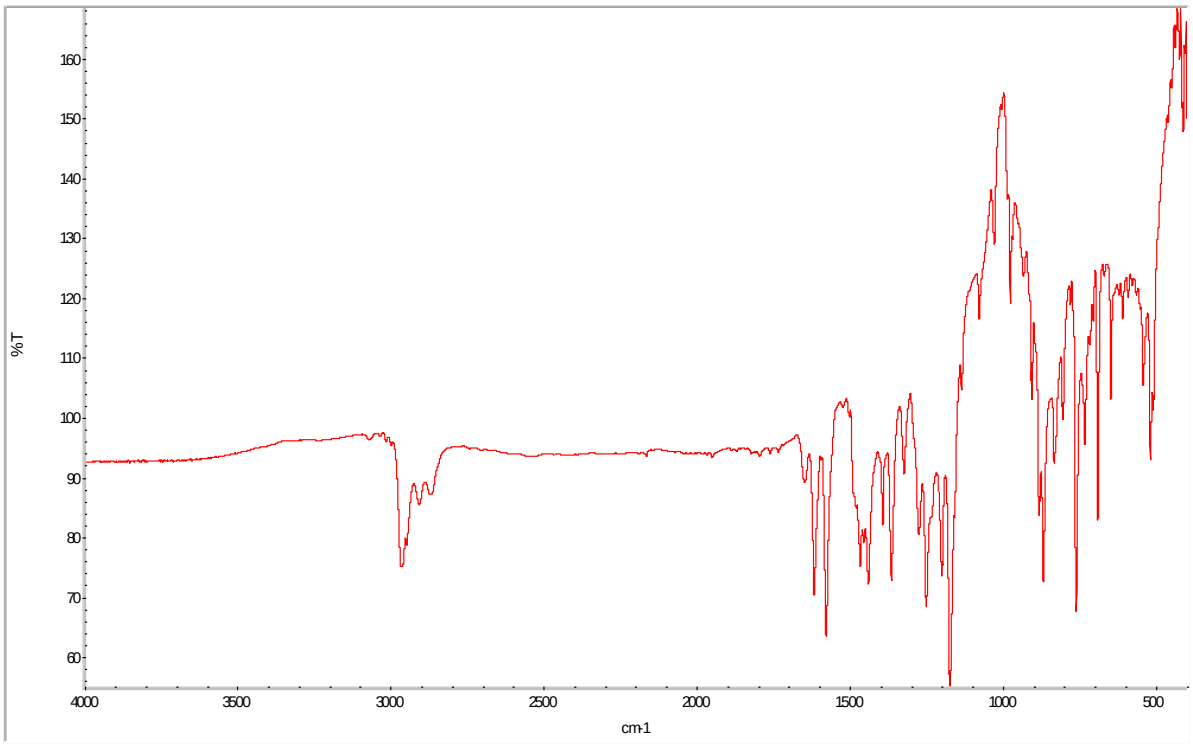


Figure 126: IR spectrum of compound 10

4.2.11 Compound 11: 3,5-ditertbutylsalicylidene-4-iodoaniline

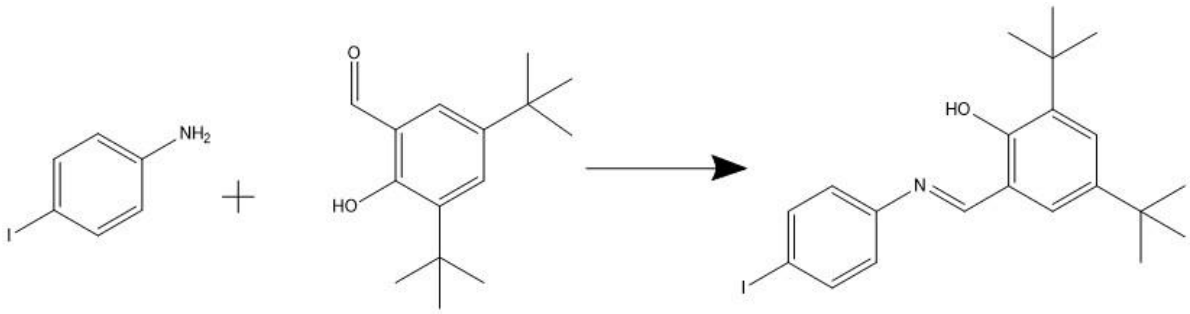


Figure 127: Reaction scheme for compound 11

To a solution of 4-iodoaniline (0.9495 g, 0.004 mol) in ethanol (40 mL), 3,5-di-*tert*-butylsalicaldehyde (1.0701 g, 0.005 mol) in was added whilst stirring. This turned the solution from pale purple to a pale yellow, after refluxing for 3 hours this darkened to a golden yellow (fig 127).

Left to evaporate yellow block crystals were formed, these were then recrystallised *via* slow evaporation of ethanol.

Preliminary characterisation using NMR (^{1}H and ^{13}C) confirmed the production of the target product (Fig 128 to 131); ^{1}H NMR (400 MHz, $CDCl_3$) δ 13.46 (s, 1H), 8.61 (s, 1H), 7.73 (d, *J* = 8.6 Hz, 2H), 7.47 (d, *J* = 2.3 Hz, 1H), 7.22 (d, *J* = 2.3 Hz, 1H), 7.04 (d, *J* = 8.6 Hz, 2H), 1.48 (s, 9H), 1.33 (s, 9H), ^{13}C NMR (101 MHz, $CDCl_3$) δ 164.32, 158.43, 148.55, 140.91, 138.55, 137.24, 128.57, 127.09, 123.32, 118.29, 91.17, 35.25, 34.34, 31.60, 29.56.

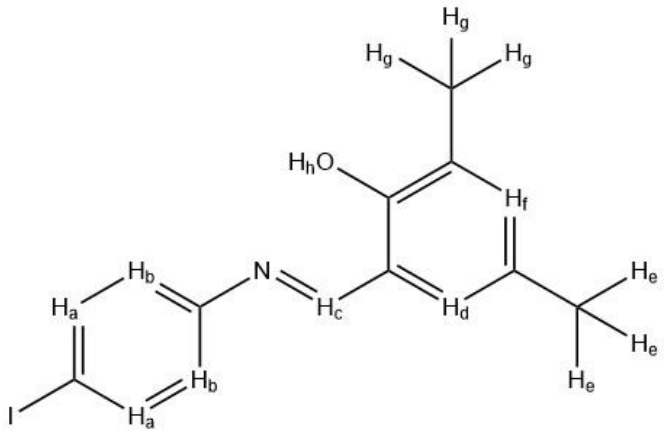


Figure 128: labelled hydrogen diagram of compound 11

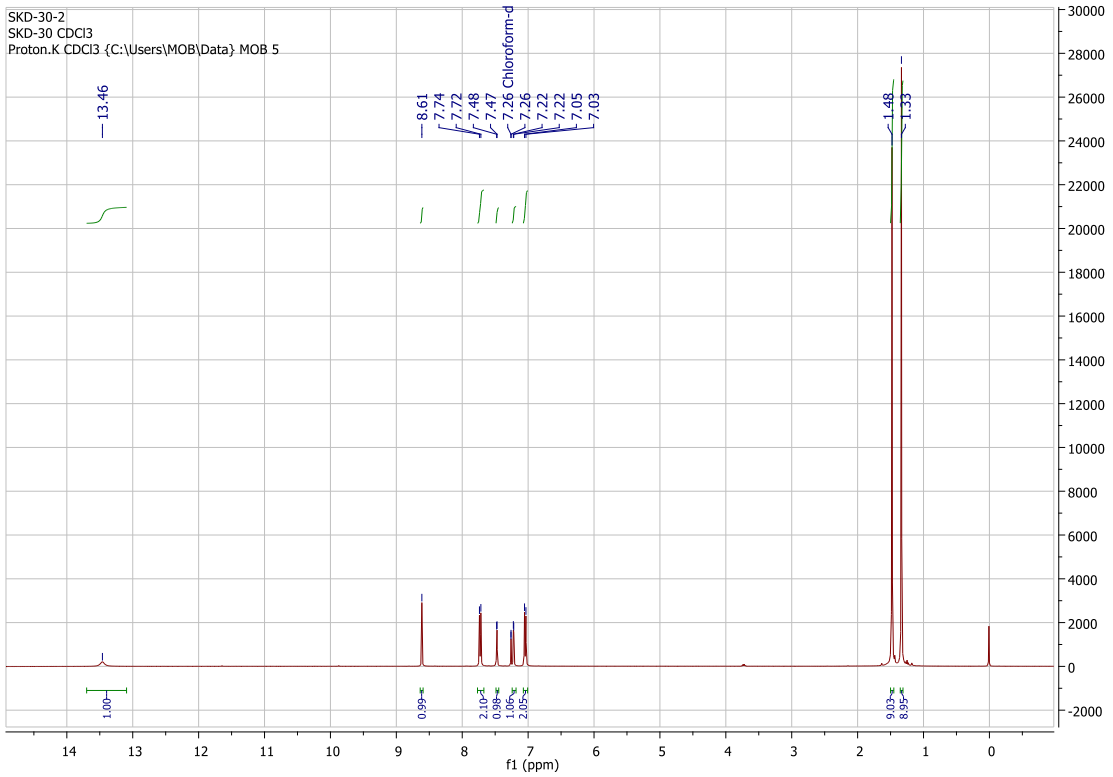


Figure 129: 1H NMR spectrum of compound 11

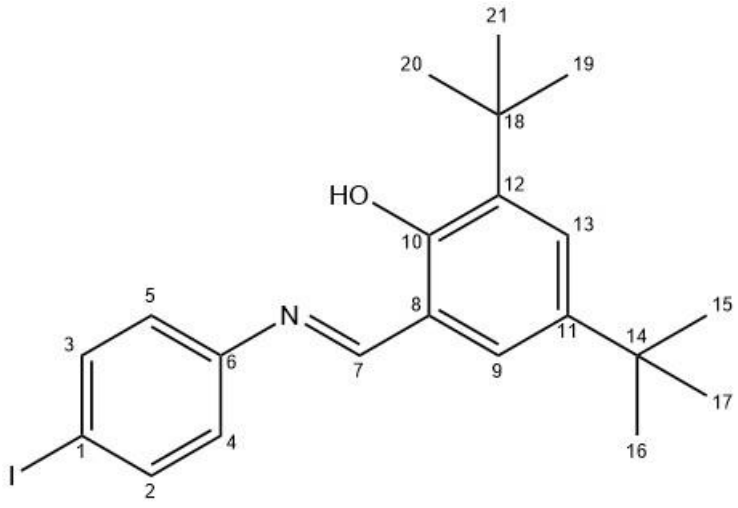


Figure 130: Labelled carbon diagram of compound 11

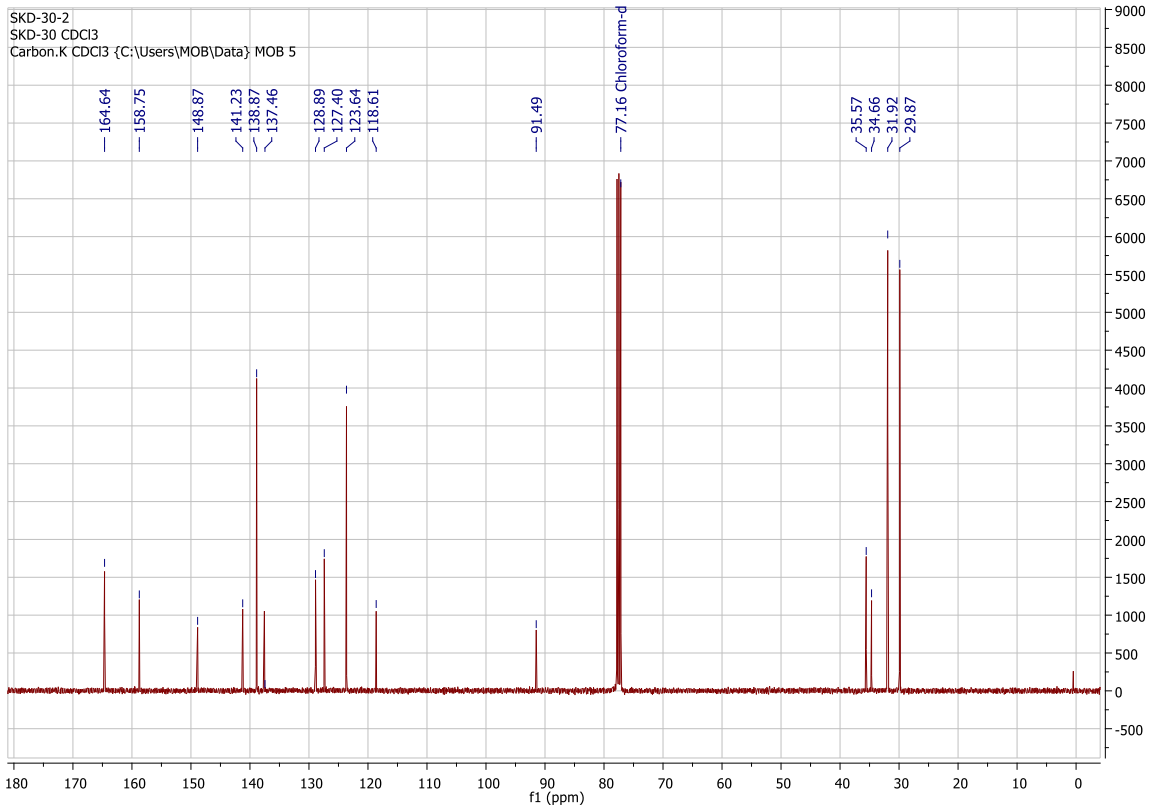


Figure 131: 13C NMR spectrum of compound 11

UV-Vis and IR spectroscopy (Fig 132 and 133) completed the initial characterisation with Raman scattering, SCXRD and Neutron diffraction used for a more detail investigation of both the UV irradiated and non-irradiated samples (expanded upon in the next chapter).

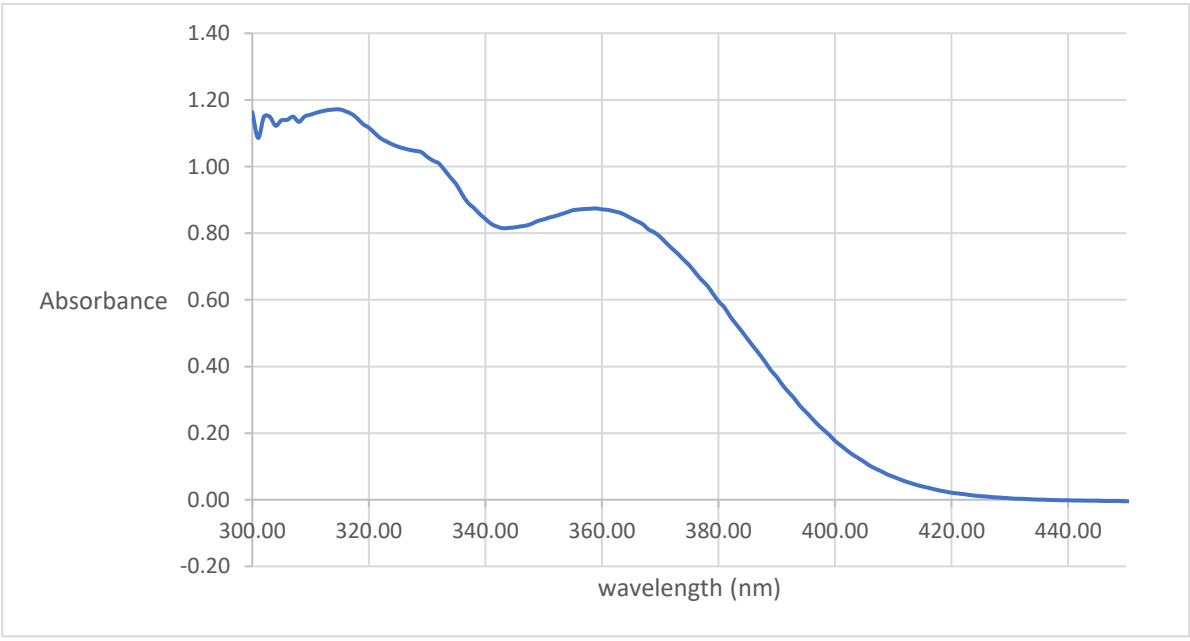


Figure 132: UV-Vis absorption spectrum of compound 11 in ethanol

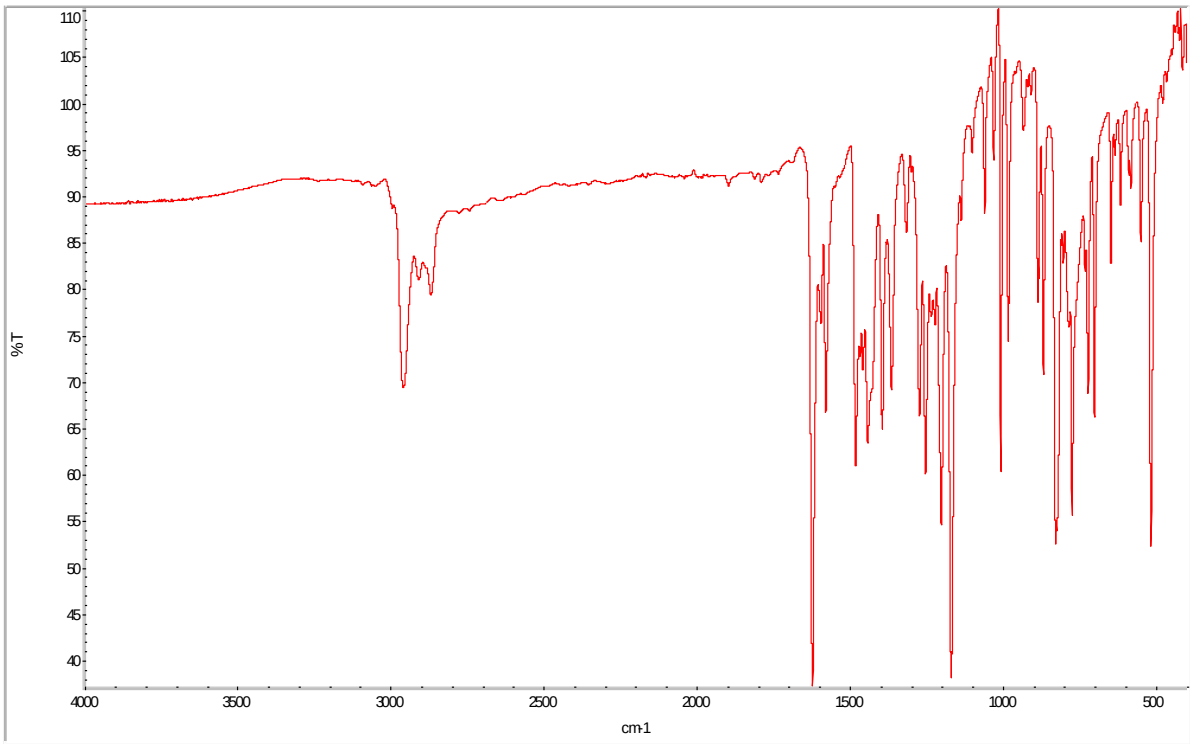


Figure 133: IR spectrum of compound 11

4.2.12 Compound 12: 3,5-ditertbutylsalicylidene-4-bromoaniline

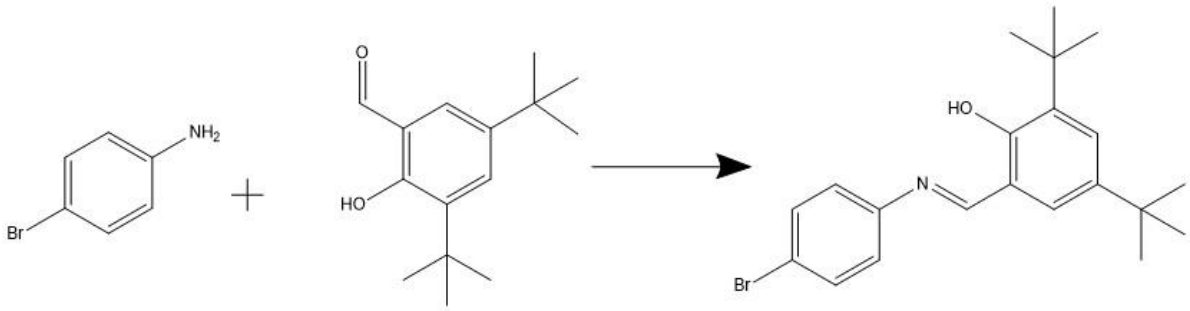


Figure 134: Reaction scheme for compound 12

To a solution of 3,5-di-tert-butylsalicaldehyde (1.0142 g, 0.004 mol) in ethanol (40 mL), 4-bromoaniline (0.7330 g, 0.004 mol) was added whilst stirring. This turned the solution from near colourless to a pale yellow, after refluxing for 3 hours this darkened to a straw yellow (Fig 134).

Having been left for 16 hours a yellow precipitate formed which was then filtered off and the filtrate retained a small mass of which was recrystalised from acetone. Further samples suitable for X-ray and neutron diffraction were then grown via recrystallisation of slow evaporation of ethanol and ethyl acetate respectively.

Preliminary characterisation using NMR (^{1}H and ^{13}C) confirmed production of the target compound (Fig 135 to 138); ^{1}H NMR (400 MHz, DMSO) δ 13.72 (s, 1H), 8.99 (s, 1H), 7.65 (d, *J* = 8.7 Hz, 2H), 7.50 (d, *J* = 2.4 Hz, 1H), 7.45 – 7.42 (m, 1H), 7.41 (t, *J* = 3.3 Hz, 2H), 1.42 (s, 9H), 1.30 (s, 9H), ^{13}C NMR (101 MHz, DMSO) δ 166.27, 157.99, 147.48, 140.75, 136.34, 132.79, 128.28, 128.11, 124.06, 119.91, 118.67, 35.10, 34.41, 31.72, 29.72.

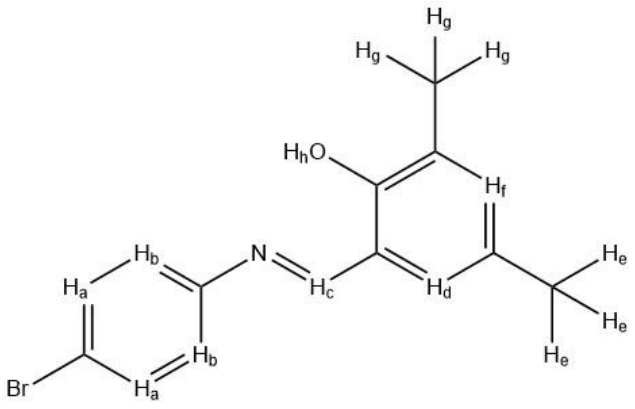


Figure 135: labelled hydrogen diagram of compound 12

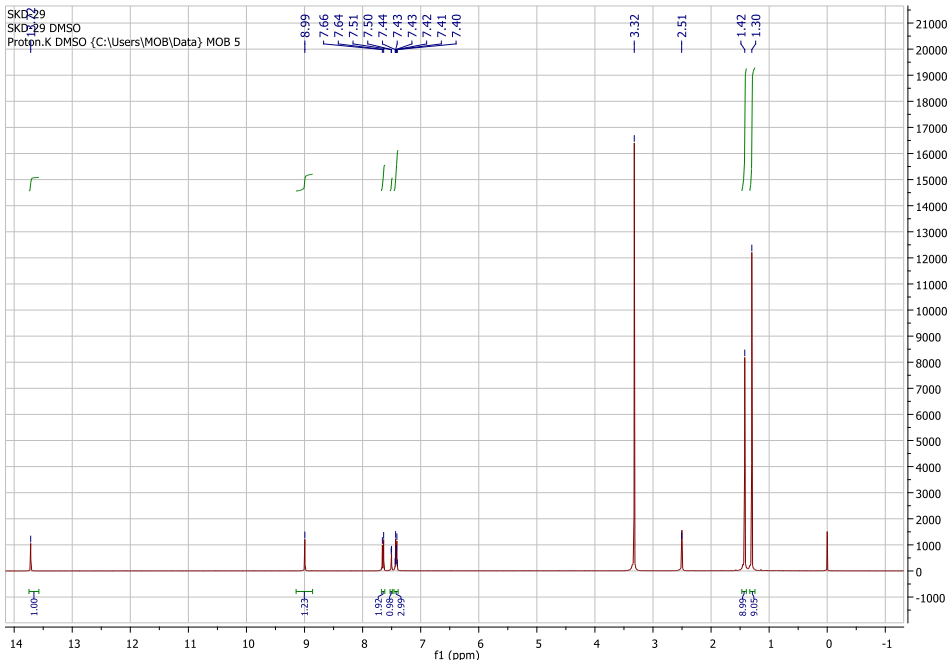


Figure 136: 1H NMR spectrum of compound 12

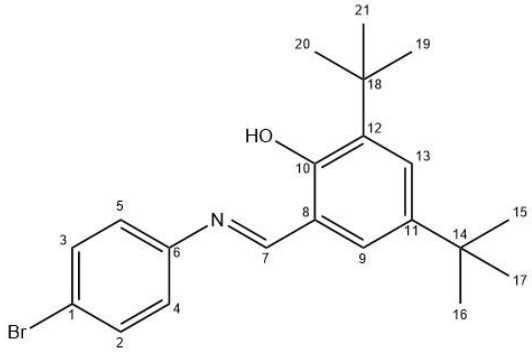


Figure 138: labelled carbon diagram of compound 12

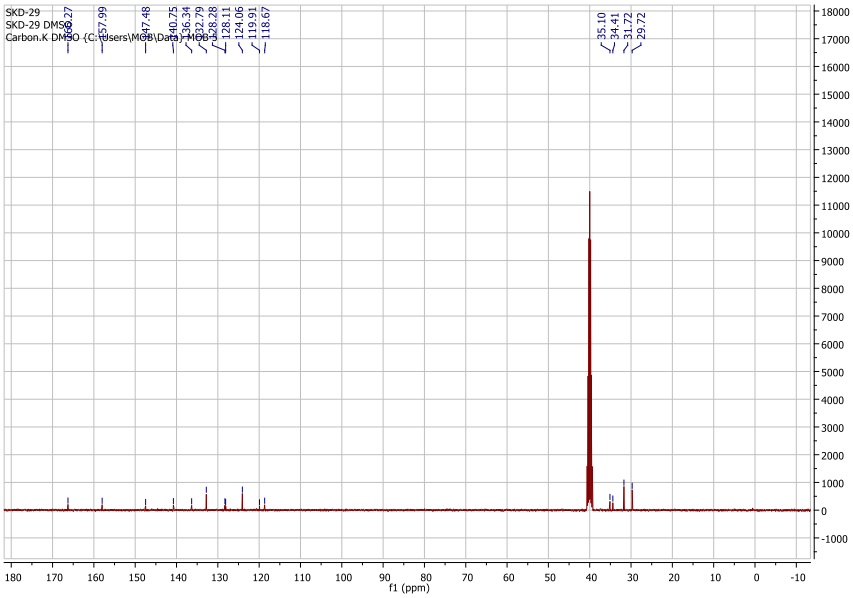


Figure 137: ^{13}C NMR spectrum of compound 12

UV-Vis and IR spectroscopy (Fig 139 and 140) completed the initial characterisation with Raman scattering, SCXRD and Neutron diffraction used for a more detail investigation of both the UV irradiated and non-irradiated samples (expanded upon in the next chapter).

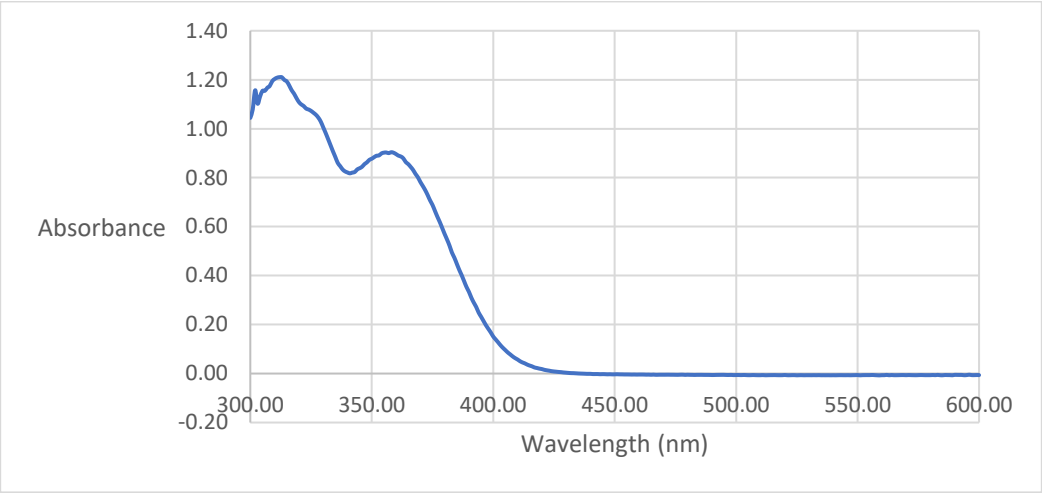


Figure 139: UV-Vis absorption spectrum of compound 12 in ethanol

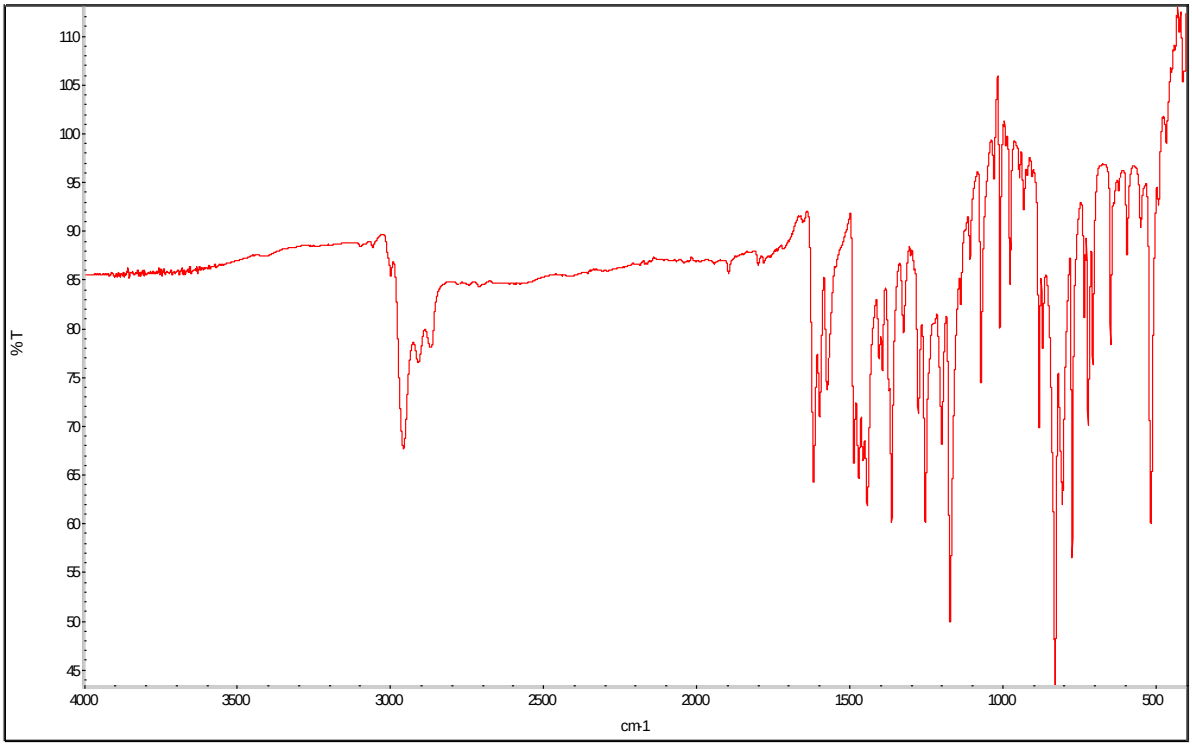


Figure 140: IR spectrum of compound 12

4.2.13 Compound 13: 5-Chlorosalicylidene-4-bromoaniline

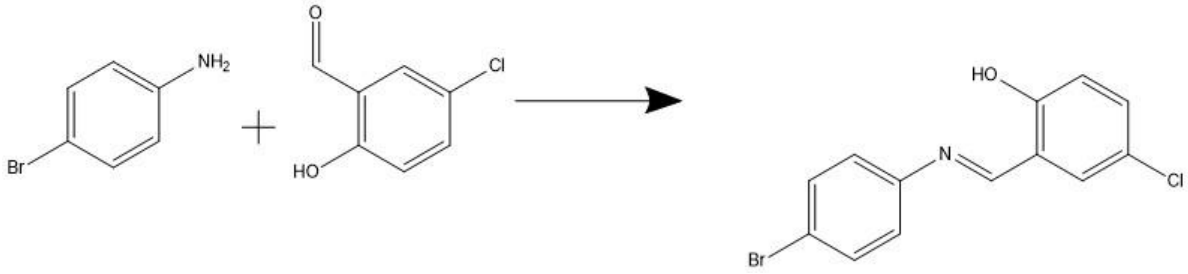


Figure 141: reaction scheme for compound 13

To a solution of 5-chlorosalicylaldeyhde (1.0061 g, 0.006 mol) in ethanol (40 mL), 4-bromoaniline (1.1248 g, 0.007mol) was added turning the solution from a pale purple to a burnt orange before a precipitate began to form. This solution was then left to reflux for 3 hours, before the yellow precipitate was filtered off and the filtrate retained (Fig 414). Recrystalised from ethyl acetate large clear block crystals formed, upon examination these were revealed to be a series of stacked thin plate crystals unusable for single crystal diffraction (Fig 142).

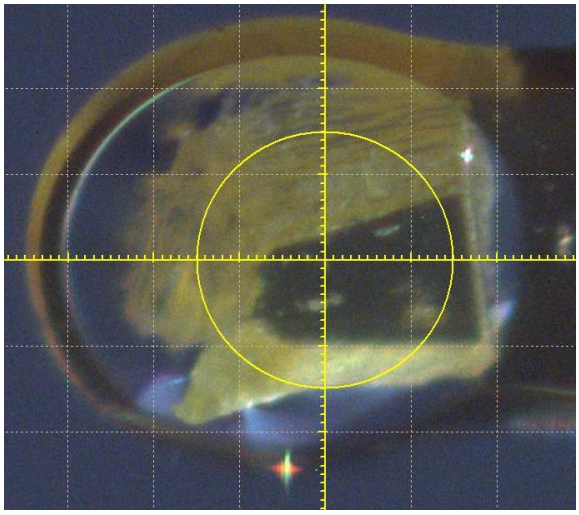


Figure 142: Photograph of stacked plates of compound 13

Formation of the target compound was verified using ^{1}H and ^{13}C NMR (Fig 143 to 146); ^{1}H NMR (400 MHz, $CDCl_3$) δ 12.97 (s, 1H), 8.53 (s, 1H), 7.56 (d, *J* = 8.2 Hz, 2H), 7.37 (d, *J* = 2.5 Hz, 1H), 7.33 (dd, *J* = 9.1, 2.9 Hz, 1H), 7.16 (d, *J* = 8.1 Hz, 2H), 6.98 (d, *J* = 8.8 Hz, 1H), ^{13}C NMR (101 MHz, $CDCl_3$) δ 162.15, 160.04, 147.44, 133.73, 133.07, 131.78, 123.29, 119.40.

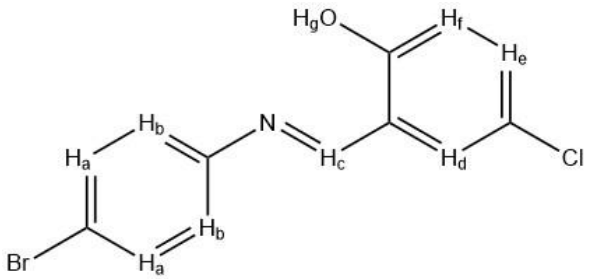


Figure 143: labelled hydrogen diagram of compound 13

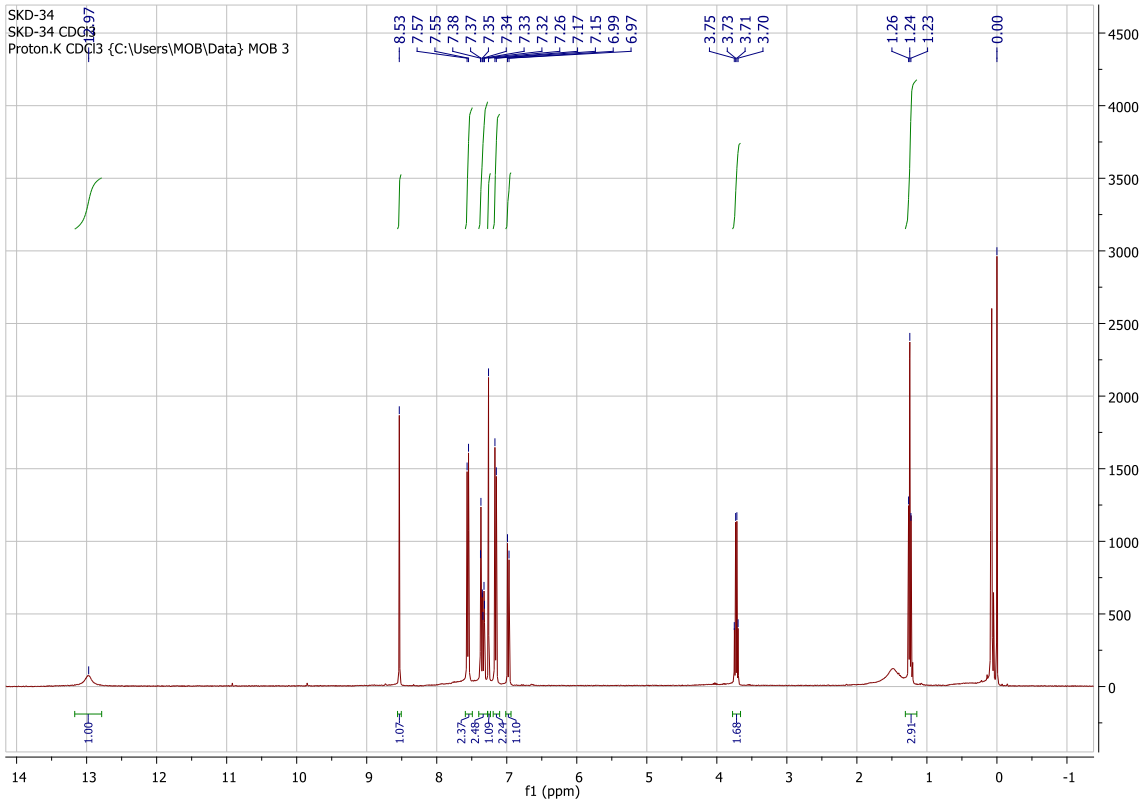


Figure 144: 1H NMR spectrum of compound 13

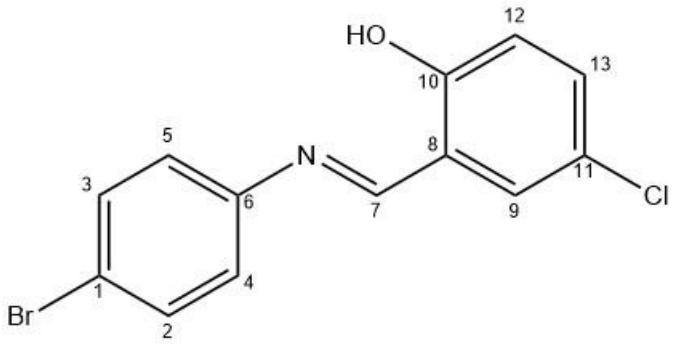


Figure 145: labelled carbon diagram of compound 13

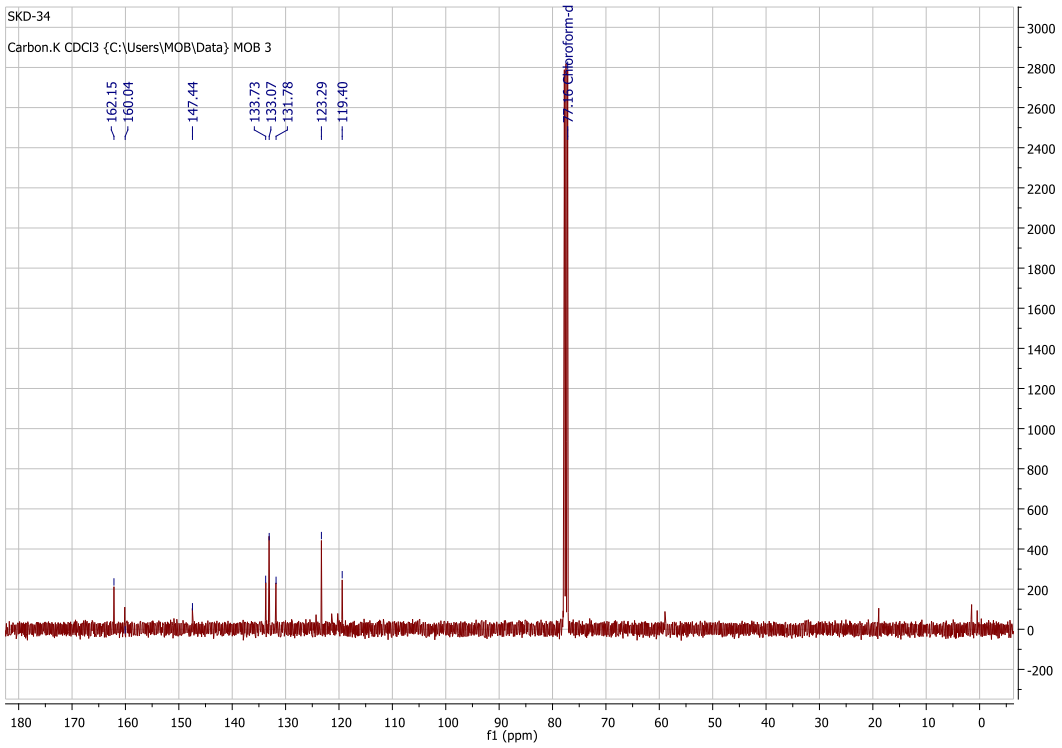


Figure 146:13C NMR spectrum of compound 13

Solution UV-Vis and IR spectroscopy along with Raman scattering were completed at 295 K (Fig 147,148 and 149 respectively), to compile the preliminary characterisation.

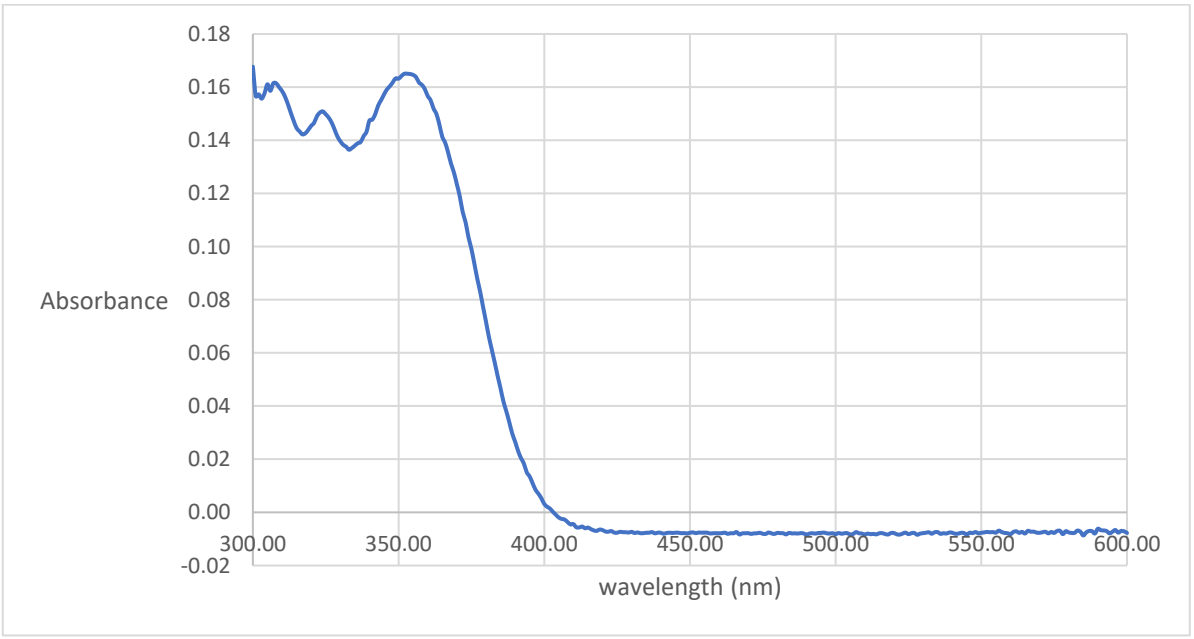


Figure 147:UV-VIs absorption spectrum of compound 13

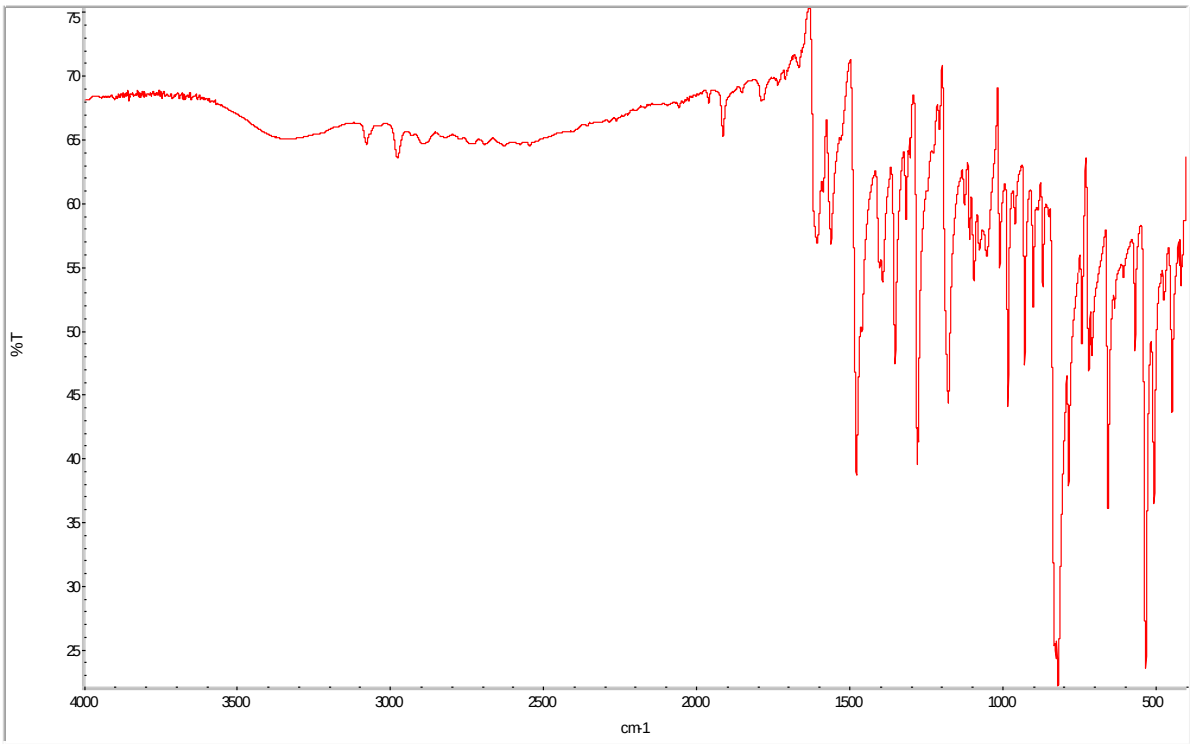


Figure 148: IR spectrum of compound 13

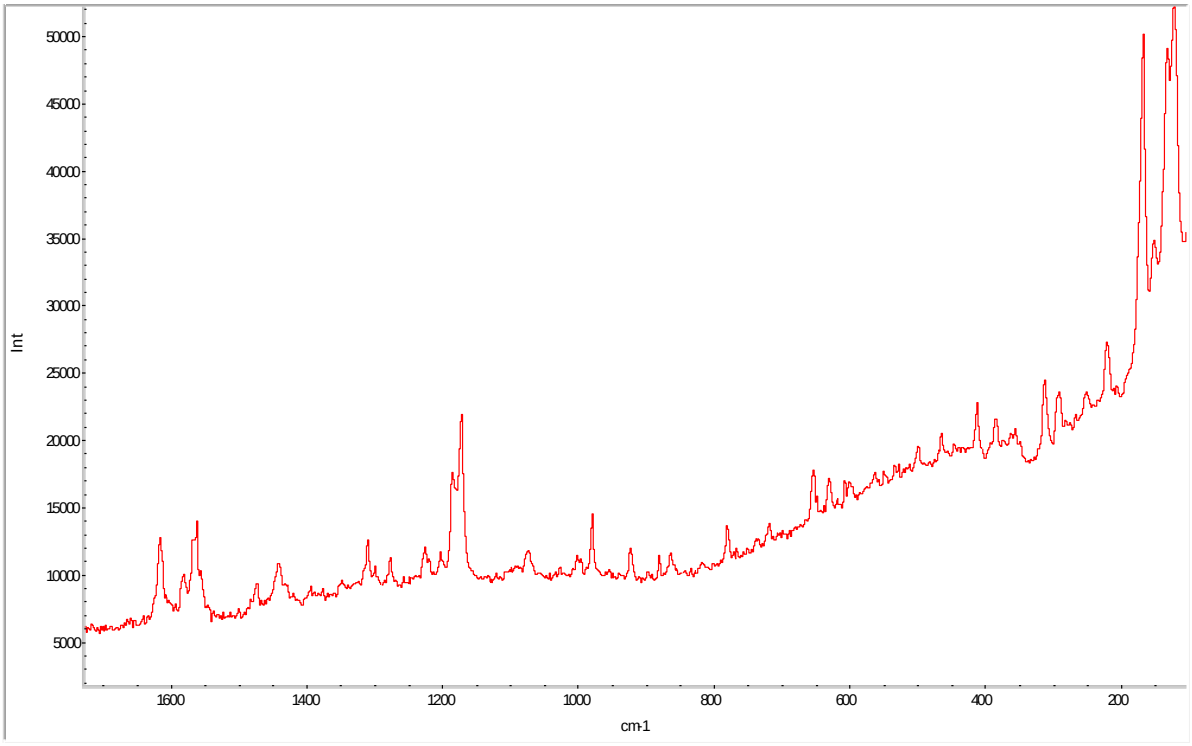


Figure 149: Raman Spectrum of compound 13

4.2.14 Compound 14: 5-Chlorosalicylidene-4-iodoaniline

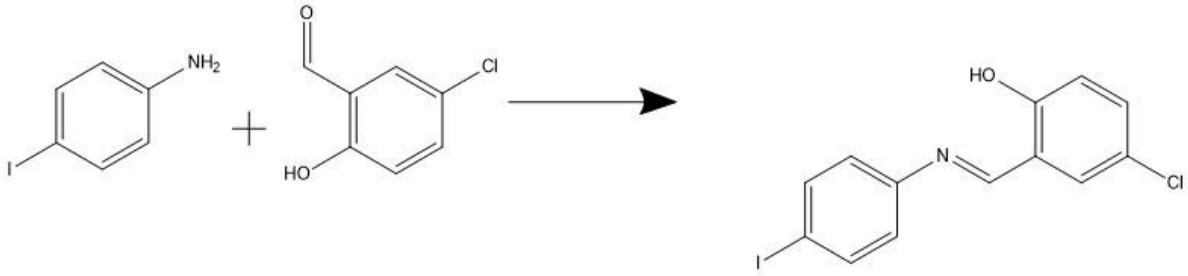


Figure 150: reaction scheme for compound 14

To a solution of 5-chlorosalicylaldeyhde (1.0718 g, 0.007 mol) in ethanol (40 mL), 4-iodoaniline (1.4981 g, 0.007mol) was added turning the solution from a pale purple to a golden yellow with a precipitate appearing near instantaneously. This solution was then left to reflux for 2.5 hours, before the yellow precipitate was filtered off and the filtrate retained (Fig 150). The precipitate was recrystallised in ethanol to form paper thin plate like crystals. To verify that the precipitate was the target product ^{1}H and ^{13}C NMR were conducted (Fig 151 to 154); ^{1}H NMR (400 MHz, DMSO) δ 12.73 (s, 1H), 8.93 (s, 1H), 7.85 – 7.79 (m, 2H), 7.75 (d, *J* = 2.7 Hz, 1H), 7.45 (dd, *J* = 8.8, 2.7 Hz, 1H), 7.25 – 7.19 (m, 2H), 7.00 (d, *J* = 8.8 Hz, 1H), ^{13}C NMR (101 MHz, DMSO) δ 162.81, 159.47, 148.42, 138.85, 133.59, 131.49, 124.38, 123.28, 121.29, 119.31, 93.21, 56.75, 39.52, 19.18.

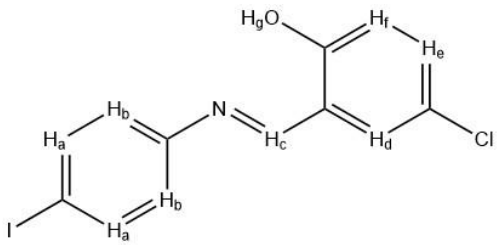


Figure 151: labelled hydrogen diagram of compound 14

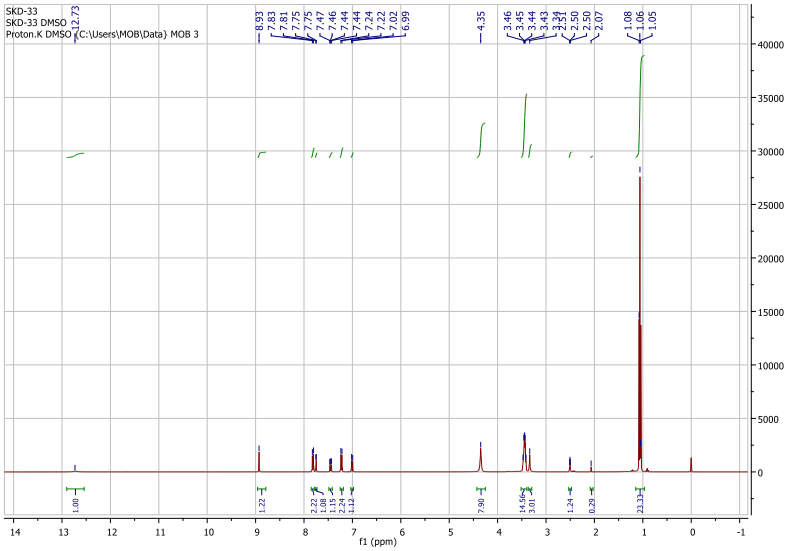


Figure 152:1H NMR spectrum of compound 14

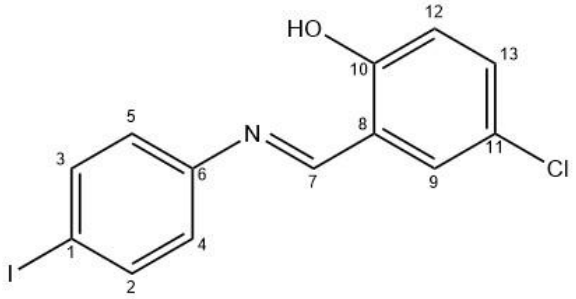


Figure 154: labelled carbon diagram of compound 14

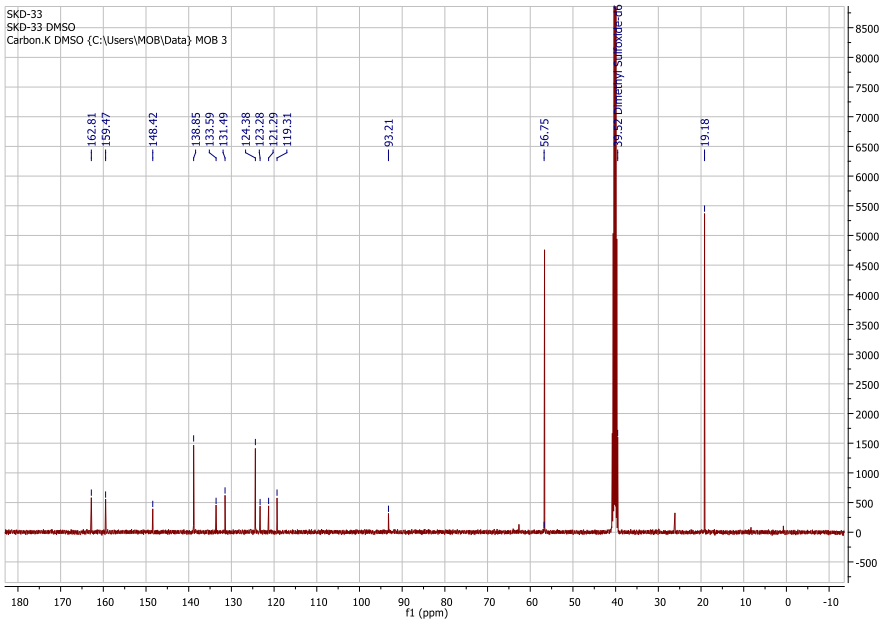


Figure 153:13C NMR of compound 14

Final characterisation was completed using UV-Vis and IR spectroscopy (Fig 155 and 156).

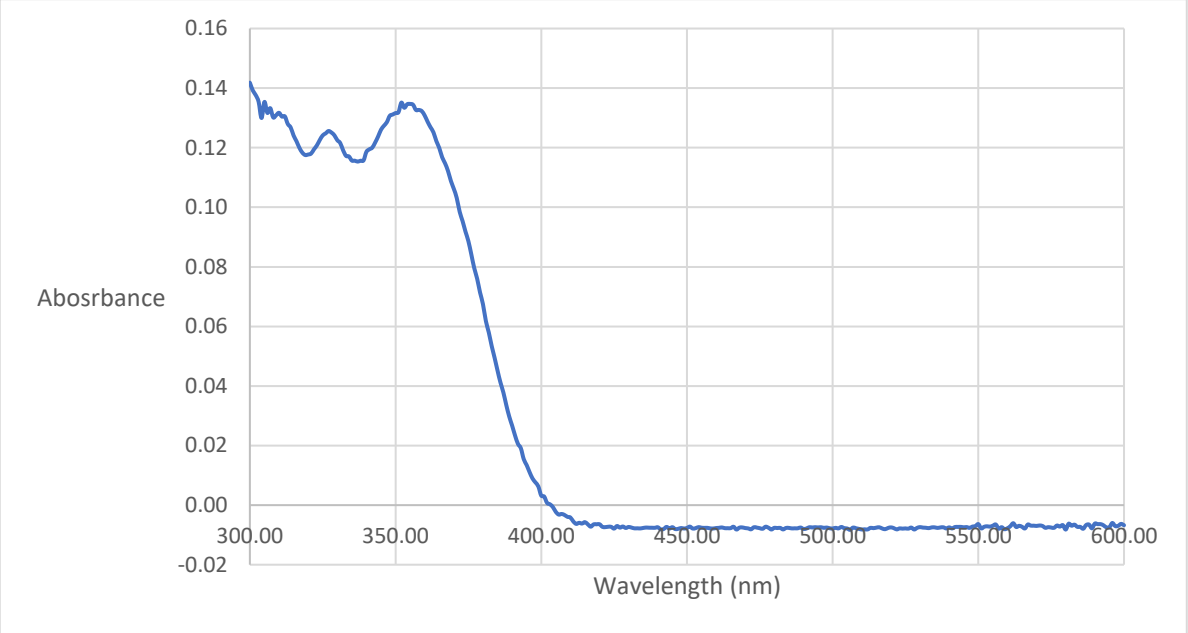


Figure 155: UV-Vis absorption spectrum of compound 14

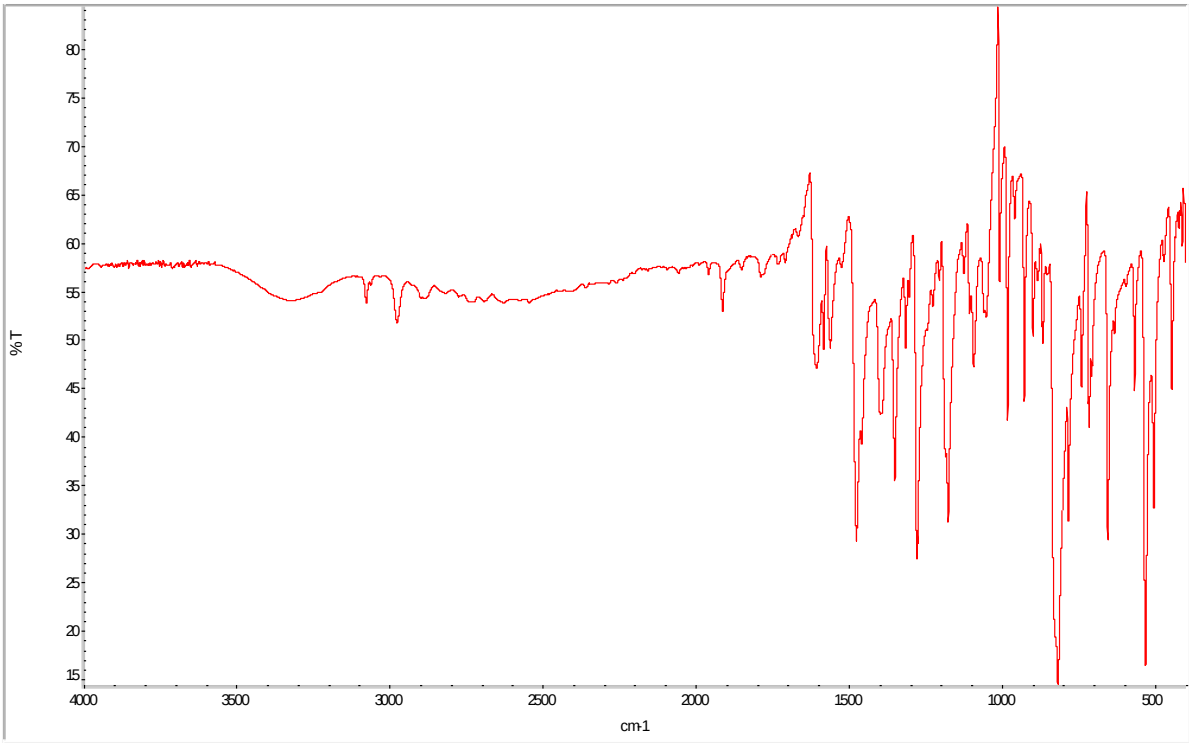


Figure 156: IR spectrum of compound 14

4.2.15 Compound 15: salicylidene-4-iodoaniline

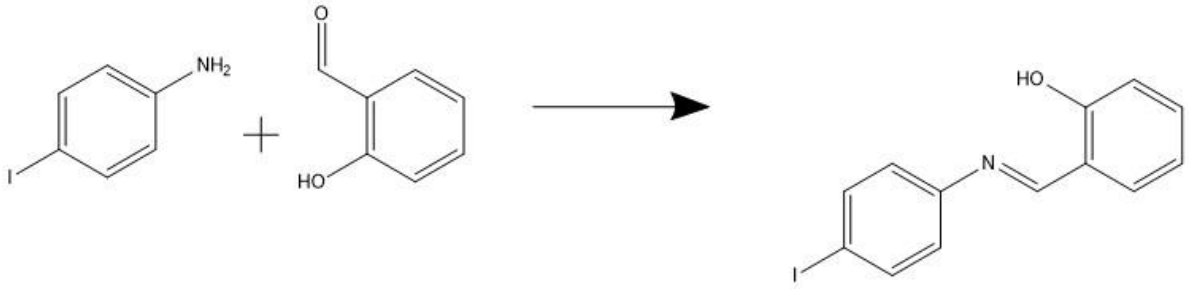


Figure 157: reaction scheme for compound 15

To a solution of 4-iodoaniline (2.0847 g, 0.01mol) in ethanol (40 mL), salicylaldehyde (1.3 mL, 1.1674 g mol^{-1}, 0.009 mol) was added turning the solution from a pale purple to yellow which deepened upon being left to reflux for 3 hours, before the yellow precipitate was filtered off and the filtrate retained (Fig 157). The precipitate was characterised using ^{1}H and ^{13}C NMR (Fig 158 to 161); ^{1}H NMR (400 MHz, $CDCl_3$) δ 12.89 (s, 1H), 8.50 (d, *J* = 11.4 Hz, 1H), 7.65 (t, *J* = 9.9 Hz, 2H), 7.34 – 7.23 (m, 2H), 7.00 – 6.81 (m, 4H), ^{13}C NMR (101 MHz, $CDCl_3$) δ 163.54, 161.60, 148.66, 138.95, 133.98, 132.89, 123.61, 119.68, 117.82, 91.96. Further characterisation was conducted using UV-Vis, IR spectroscopy and Raman scattering (Fig 162 to 164).

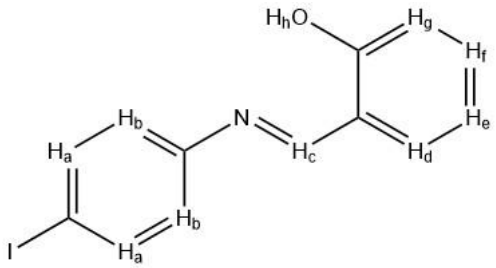


Figure 158: Labelled hydrogen diagram of compound 15

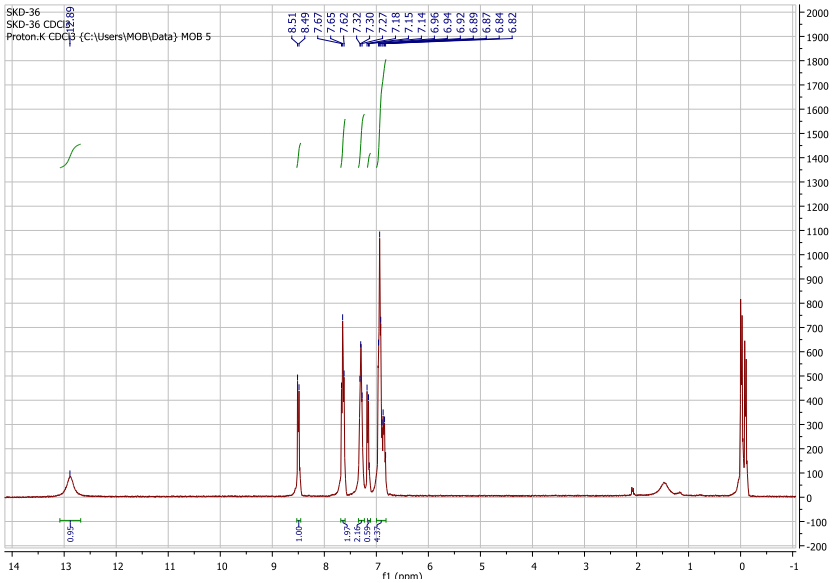


Figure 159:1H NMR spectrum of compound 15

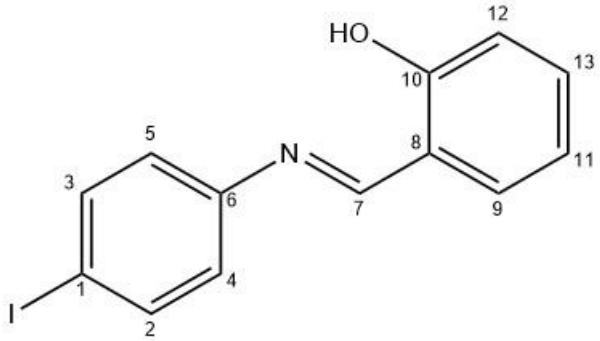


Figure 160: Labelled carbon diagram of compound 15

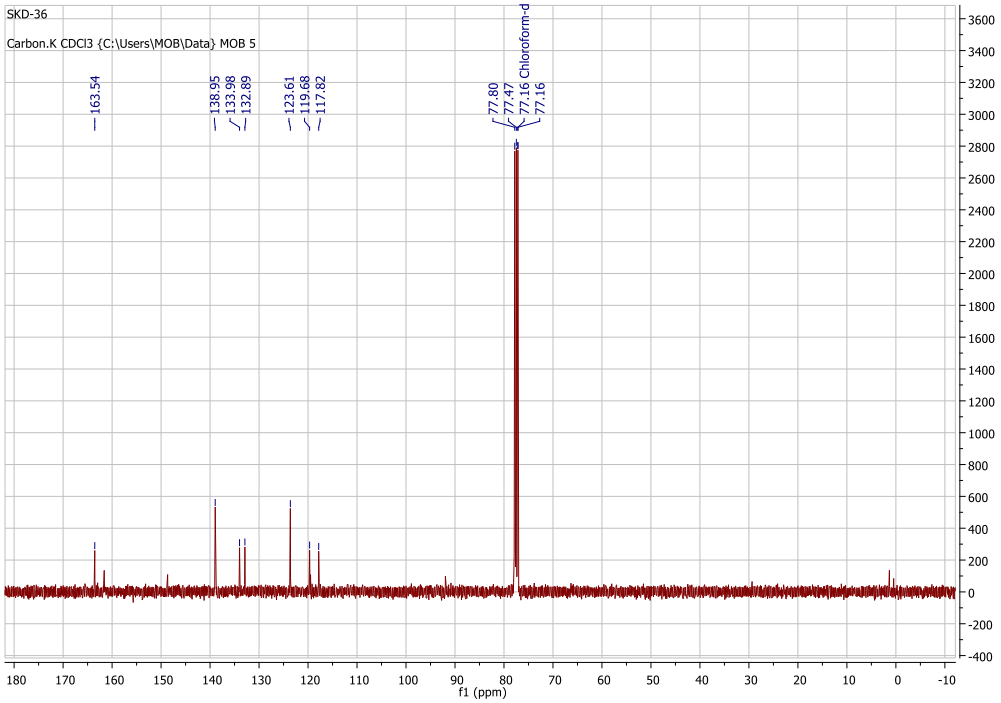


Figure 161:[13]C NMR spectrum of compound 15

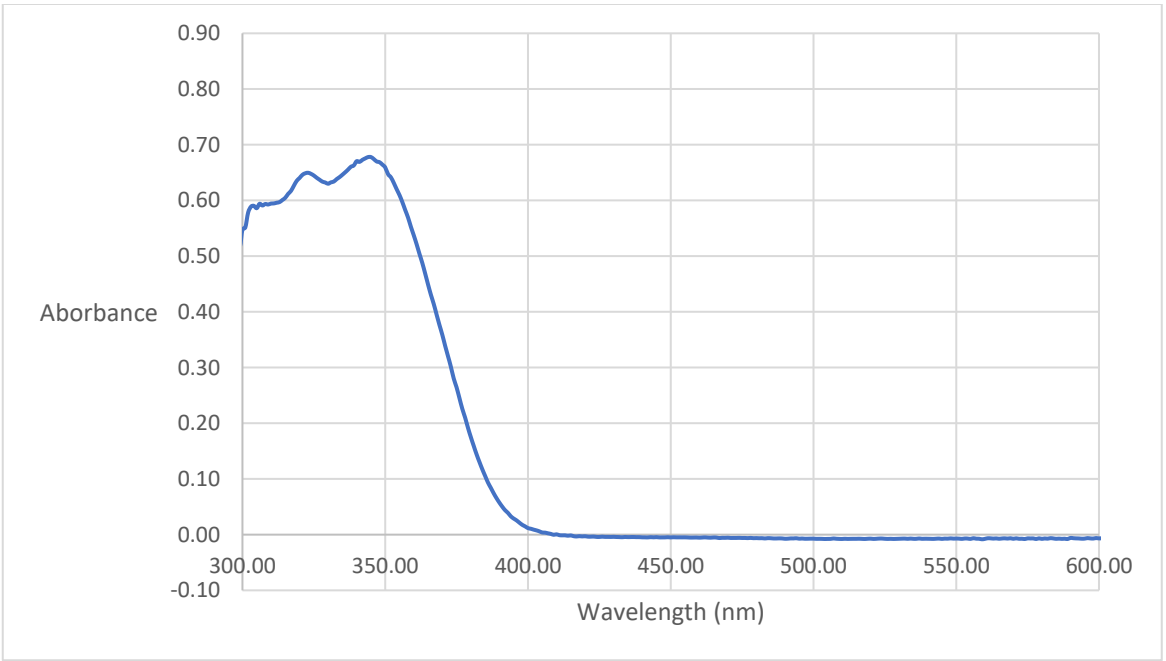


Figure 162:UV-VIs absorption spectrum of compound 15

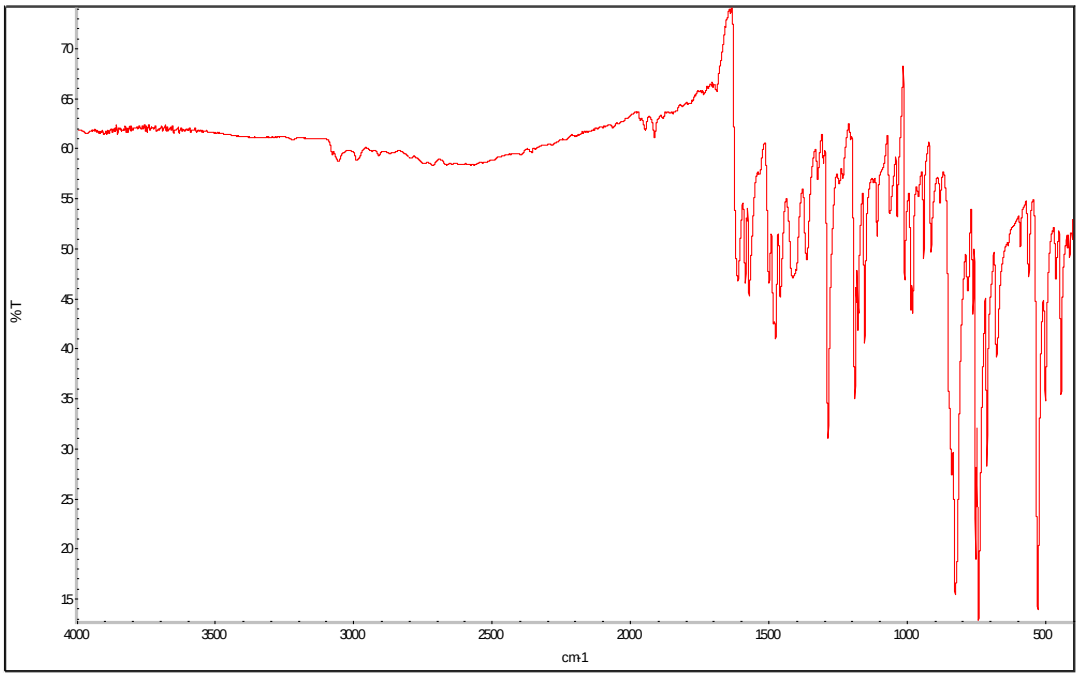


Figure 163: IR spectrum of compound 15

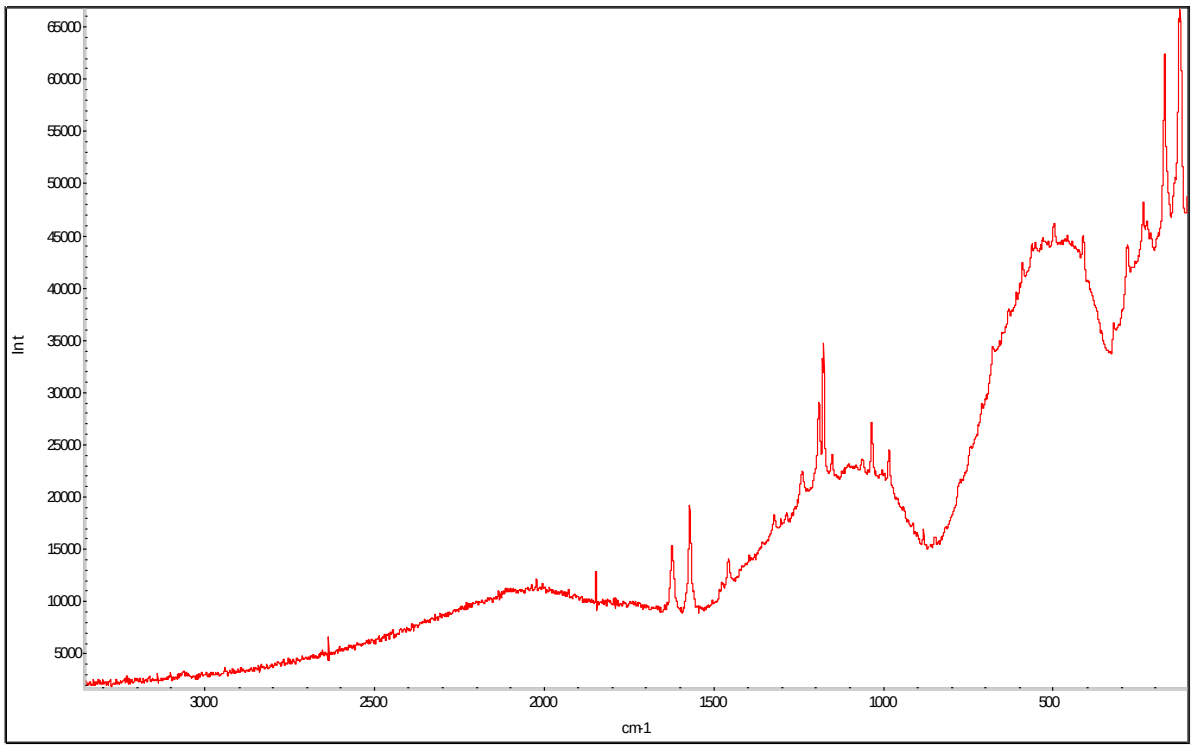


Figure 164: Raman Spectrum of compound 15

4.2.16 Compound 16: Salicylidene-4-bromoaniline

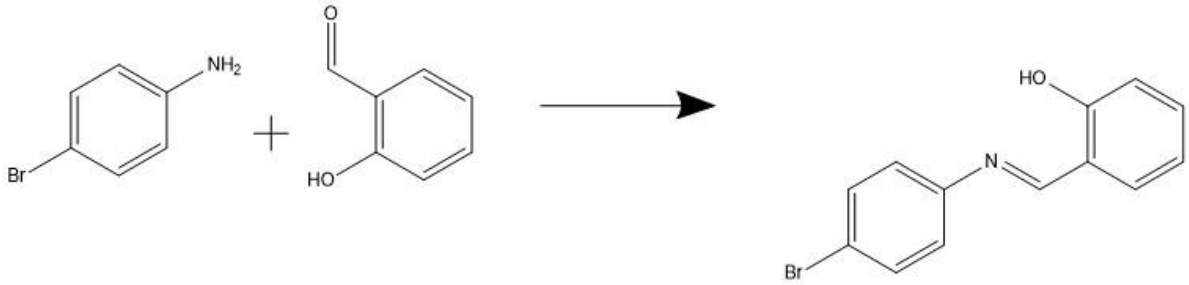


Figure 165: reaction scheme for compound 16

To a solution of 4-bromoaniline (1.6483 g, 0.01mol) in ethanol (40 mL), salicylaldehyde (1.3 mL, 1.1674 g mol^{-1}, 0.009 mol) was added turning the solution from a pale purple to yellow which deepened upon being left to reflux for 3 hours, before the yellow precipitate was filtered off and the filtrate retained (Fig 165). ^{1}H and ^{13}C NMR (Fig 166 to 169) verified that the target compound was produced; ^{1}H NMR (400 MHz, $CDCl_3$) δ 12.97 (s, 1H), 8.60 (s, 1H), 7.55 (d, *J* = 8.1 Hz, 2H), 7.42 – 7.37 (m, 2H), 7.16 (d, *J* = 8.1 Hz, 2H), 7.03 (d, *J* = 8.6 Hz, 1H), 6.96 (t, *J* = 7.5 Hz, 1H), ^{13}C NMR (101 MHz, $CDCl_3$) δ 163.20, 161.28, 147.68, 133.66, 132.66, 132.57, 122.97, 120.54, 119.38, 119.18, 117.49. Further characterisation was conducted using IR spectroscopy (Fig 170).

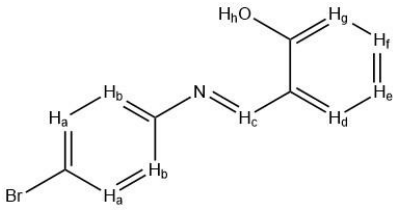


Figure 166: labelled hydrogen diagram of compound 16

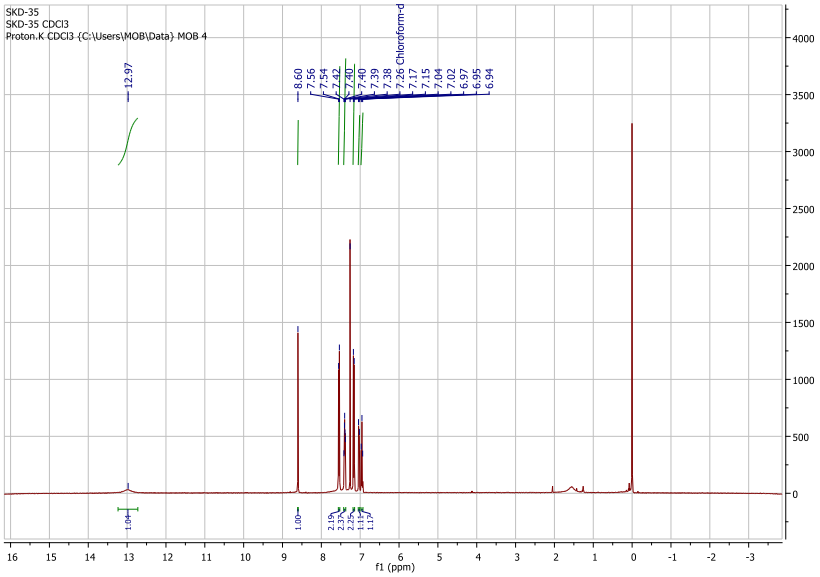


Figure 167:1H NMR spectrum of compound 16

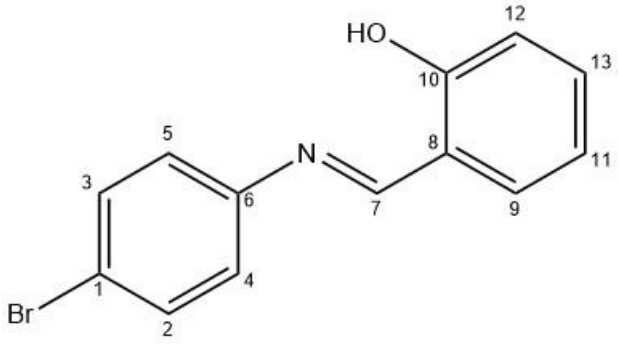


Figure 168: Labelled carbon diagram of compound 16

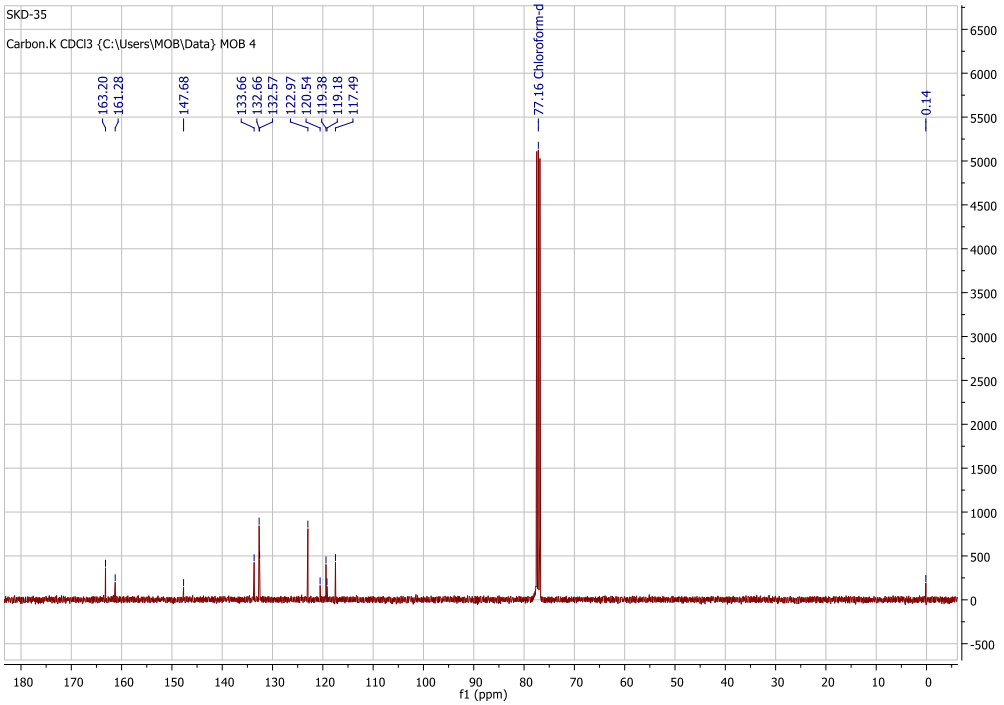


Figure 169:13C NMR spectrum of compound 16

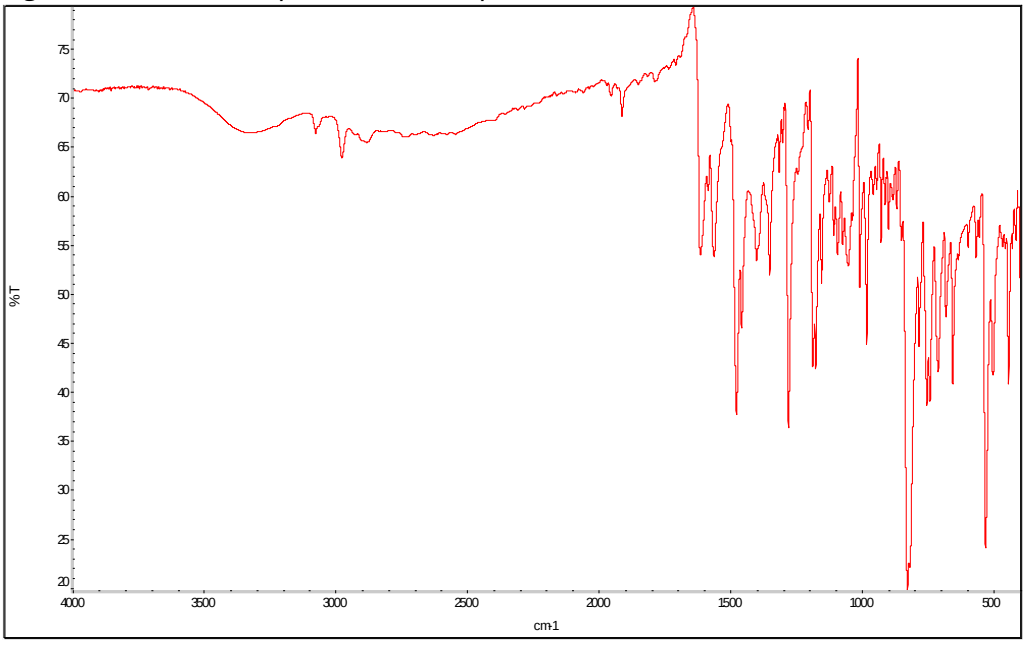


Figure 170: IR spectrum of compound 16

4.2.17 Compound 17: benzylidene-4-hydroxyaniline

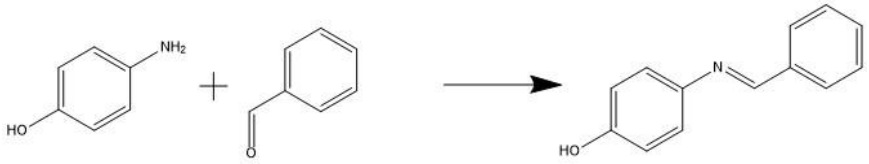


Figure 171: reaction scheme for compound 17

To a solution of 4-hydroxyaniline (1.187 g, 0.01 mol) in ethanol (30 mL) benzaldehyde (1.1 mL, 0.01 mol) was added. The resulting solution was refluxed for 3 hours, this was then allowed to cool to room temperature before being placed in an ice-bath (Fig 171).

A fine powder precipitate formed that could not be filtered off, so the solution was placed in an evaporation dish and left for 3 days. This resulted in the formation of a fine beige powder. Small masses < 0.1 g were recrystallised in methanol and acetone. The acetone recrystallisation lead to thin film like crystalline product, the methanol recrystallisation in contrast lead to small suitably x-ray sized needles.

Preliminary characterisation on the precipitate confirmed the production of the end product *via* ^{1}H and ^{13}C NMR (Fig 172 to 175); ^{1}H NMR (400 MHz, DMSO) δ 9.52 (s, 1H), 8.60 (s, 1H), 8.01 – 7.80 (m, 2H), 7.48 (t, 3H), 7.20 (d, *J* = 11.8 Hz, 2H), 6.80 (d, *J* = 11.8 Hz, 2H), ^{13}C NMR (101 MHz, DMSO) δ 156.93, 156.11, 142.36, 136.25, 130.63, 128.53, 128.04, 122.28, 115.49.

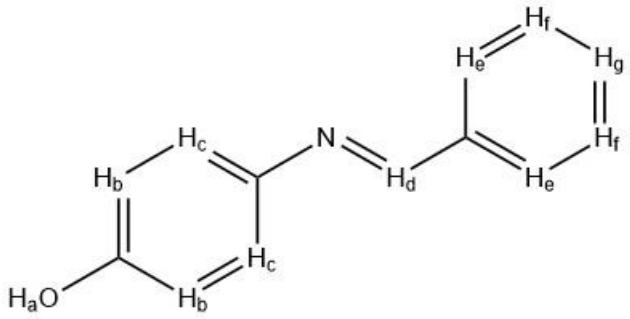


Figure 172: labelled hydrogen diagram of compound 17

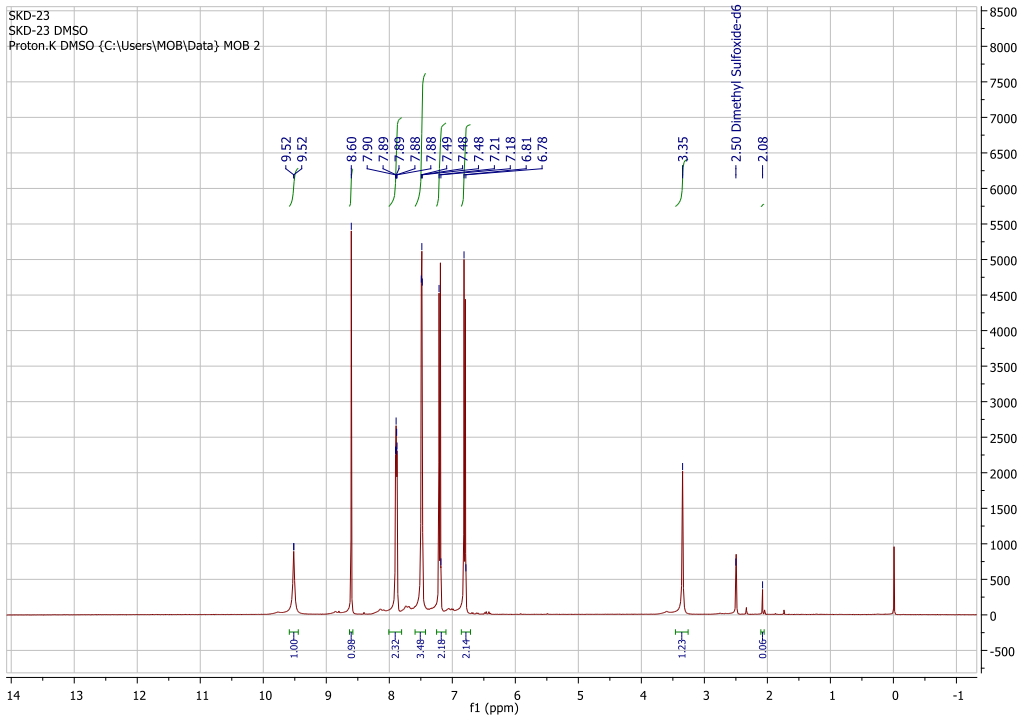


Figure 173:1H NMR spectrum of compound 17

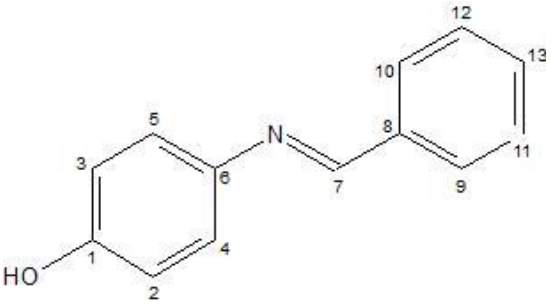


Figure 174: Labelled carbon diagram of compound 17

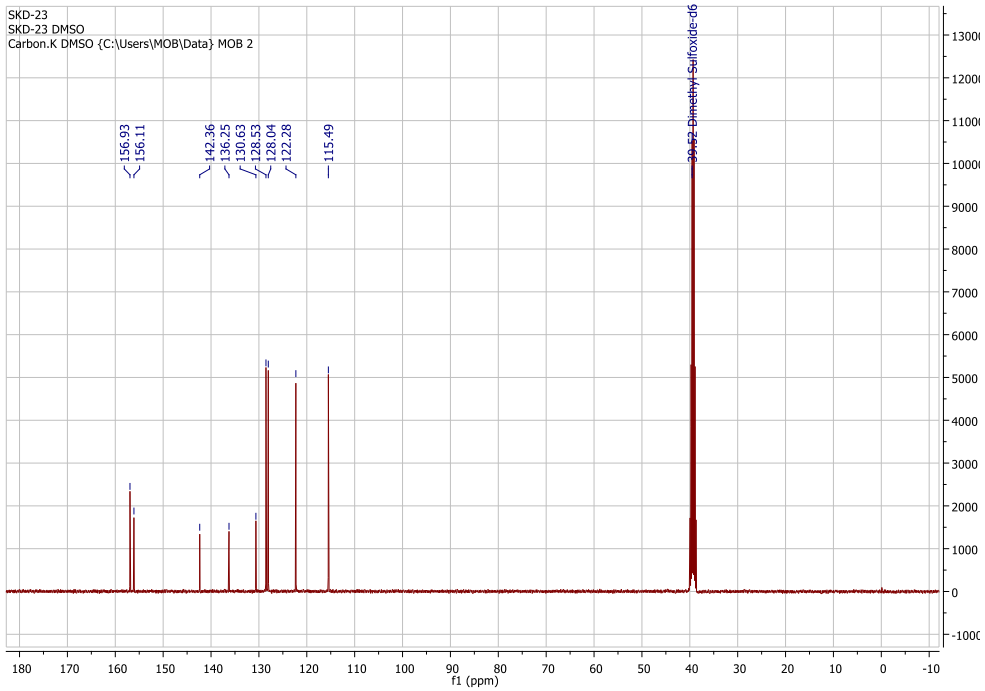


Figure 175:13C NMR spectrum of compound 17

Solution UV-Vis and IR spectroscopy were utilised to round out the preliminary characterisation (Fig 176 and 177). SCXRD data was collected at 120 and 220 K using the Molybdenum source at Keele.

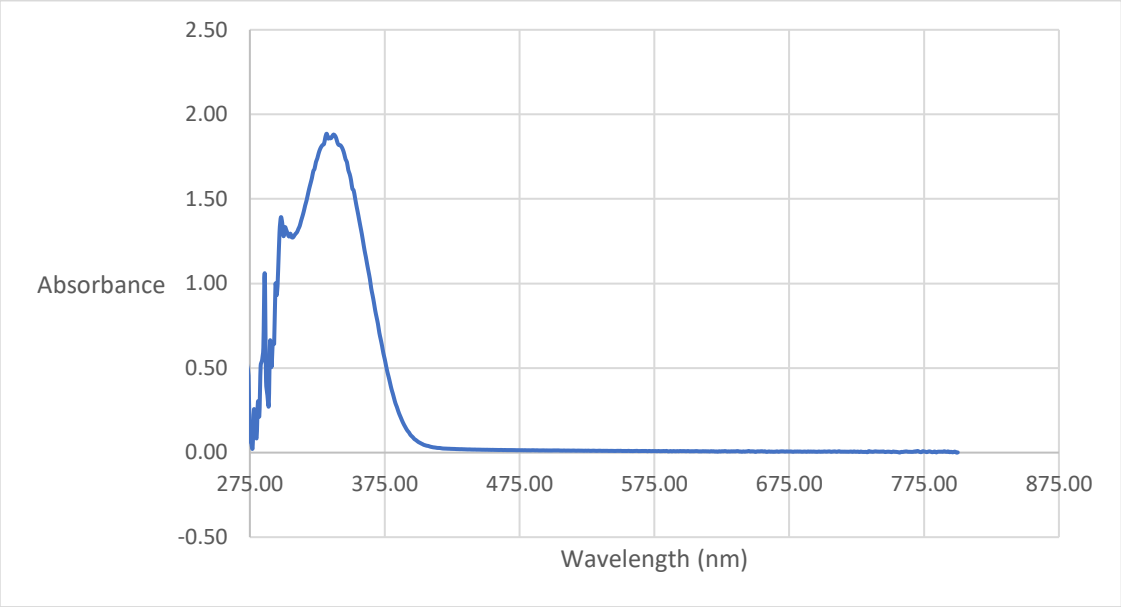


Figure 176: UV-Vis absorption spectrum of compound 17

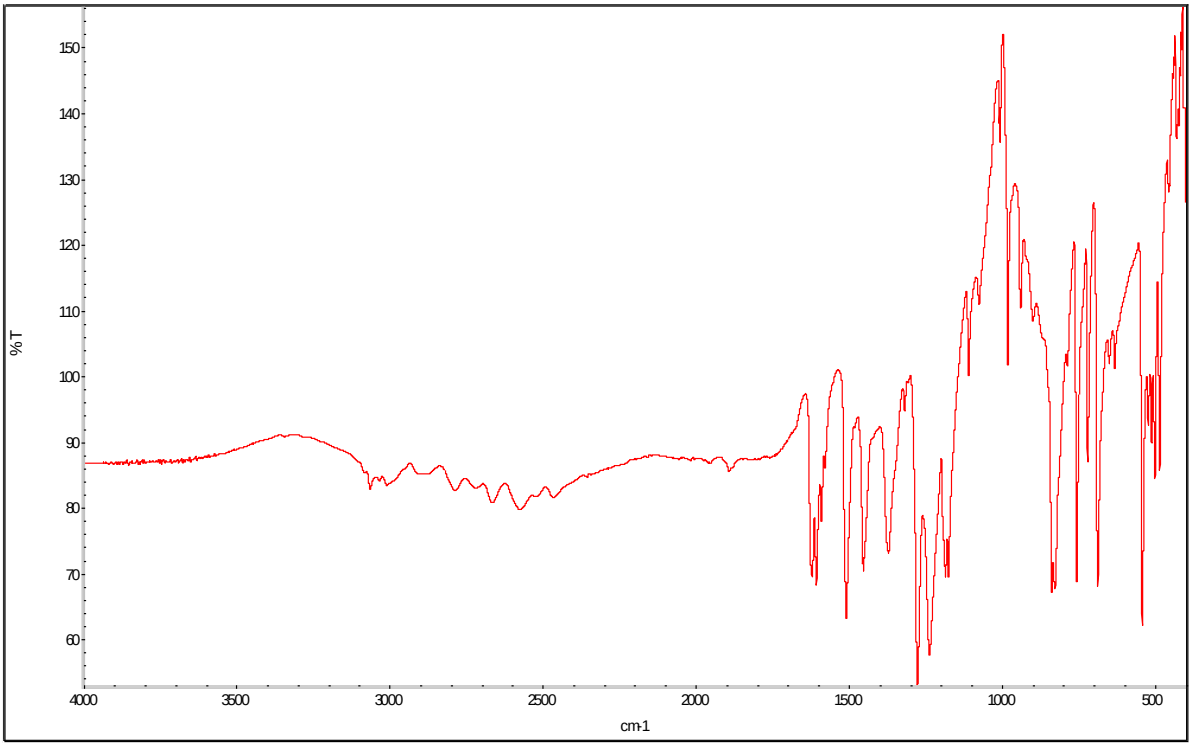


Figure 177: IR spectrum of compound 17

4.2.18 Compound 18: 3,5-ditertbutylsalicylidene-2-iodoaniline

Synthesis of compound 18 was completed by MChem student Caitlin Doyle as a part of her project using the same synthesis set up as those described above for compound 10. Preliminary Characterisation on the sample using ^{1}H and ^{13}C NMR (Fig 178 to 181)) showed production of the target product; ^{1}H NMR (400 MHz, $CDCl_3$) δ 13.21, 8.51, 7.93, 7.93, 7.91, 7.91, 7.49, 7.49, 7.42, 7.42, 7.40, 7.40, 7.40, 7.40, 7.38, 7.38, 7.23, 7.23, 7.16, 7.15, 7.14, 7.13, 6.99, 6.99, 6.97, 6.97, 6.97, 6.97, 6.95, 6.95, 1.49, 1.33, ^{13}C NMR (101 MHz, $CDCl_3$) δ 164.52, 158.39, 150.42, 140.68, 139.34, 137.24, 129.42, 128.64, 127.75, 127.12, 118.62, 118.07, 96.00, 35.18, 34.19, 31.45, 29.41.

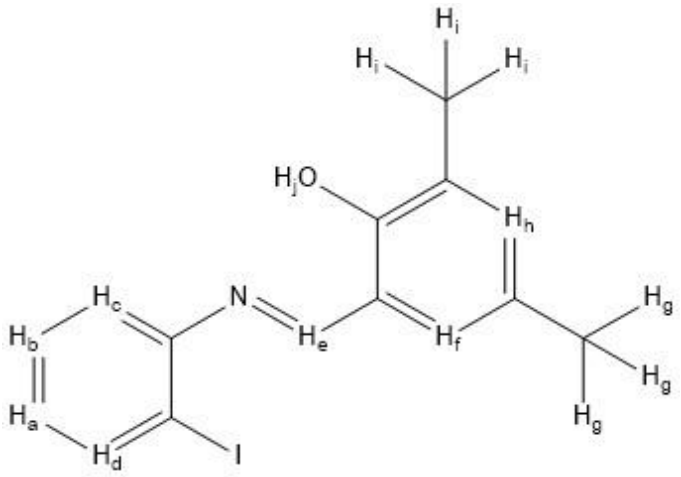


Figure 178: Labelled hydrogen diagram of compound 18

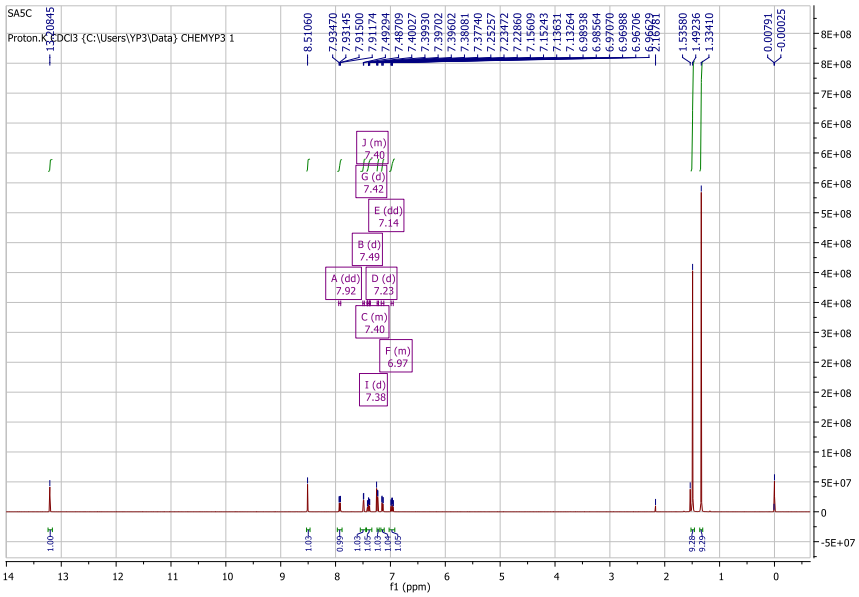


Figure 179:1H NMR spectrum of compound 18

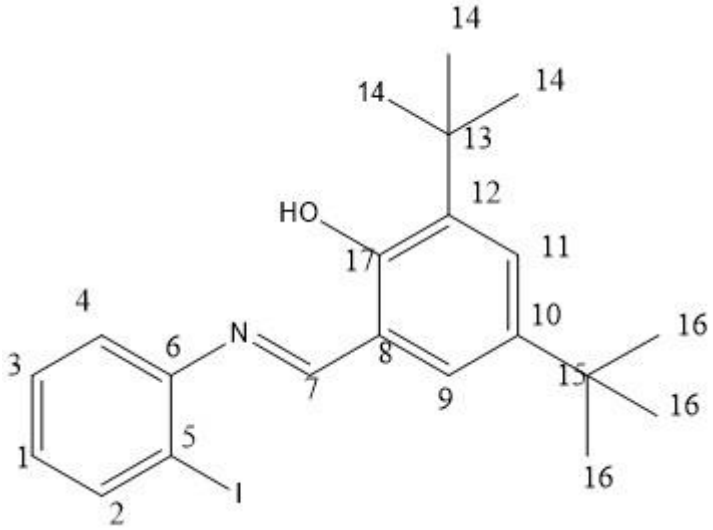


Figure 181: Labelled carbon diagram of compound 18

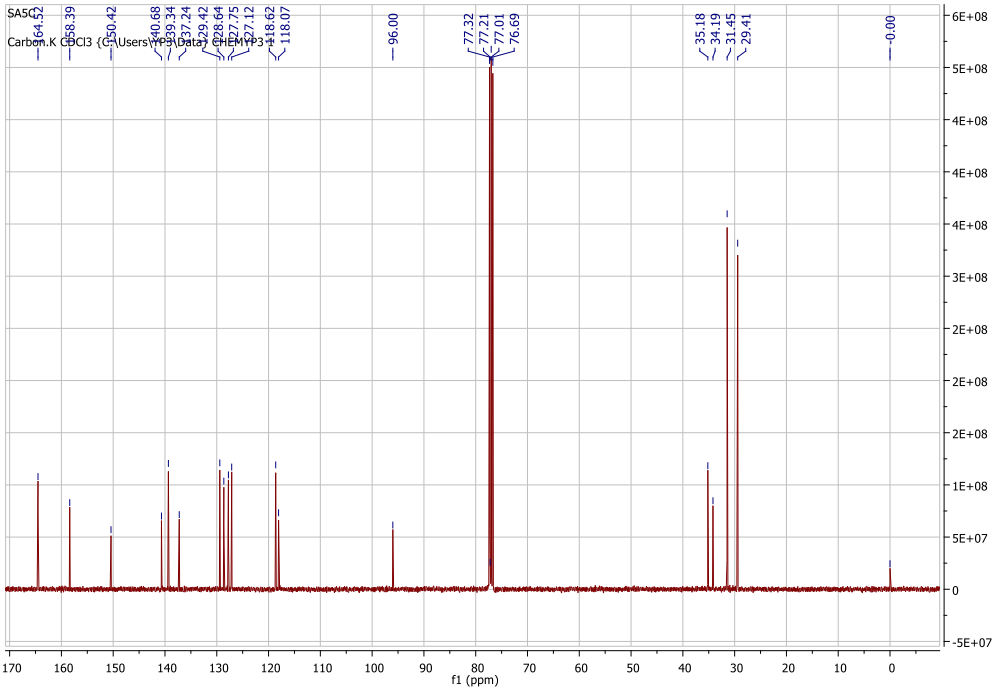


Figure 180:13C NMR spectrum of compound 18

Raman scattering, SCXRD and neutron diffraction were completed at variable temperatures to be discussed in more detail in the next chapter.

4.2.19 Compound 19: 3,5-ditertbutylsalicylidene-3-iodoaniline

Compound 19 was synthesised by Dr Richard Jones using the methodology described at the beginning of this chapter. The resulting crude product was recrystalised in methanol and SCXRD at 295 K was completed on both the UV irradiated and non-irradiated crystal, confirming the structure of the target product. This will be expanded upon in the next chapter.

4.3 Results and Discussion

When discussing the results of the data collected for the salicylaldehyde aniline derivatives, the compounds can be split into four types:

1) Hydroxy with single atom substitutions on either ring.
2) 3-Methoxy substituted on the aldehyde ring side.
3) 3,5-di*ert*butyl substituted on the aldehyde ring side.
4) No hydroxy substituent on the aldehyde ring in the second position.

4.3.1 Type 1: Hydroxy with single atom substitutions on either ring.

There were seven compounds under this type of substitution, of those seven; four (compounds 13-16) did not produce single crystals and as such only preliminary characterisation was conducted as described in the experimental chapter. Of the remaining three compounds, only two (compounds 1 and 3) produced crystals large enough for neutron diffraction. All of the compounds were assessed for photochromism by irradiation under a 365 nm UV source, none of which demonstrated the property.

N-(5-chloro-2-hydroxybenzylidene)-4-hydroxyaniline (compound 2) was found to visibly demonstrate thermochromism. A monoclinic P $2_1/c$ space group was identified, the colour of the crystal changed from orange to yellow, as the temperature is decreased from 260 K through 200 K to 110 K. The internal dihedral angle of the molecule shifts from 30.48° at 230 K to 30.57° at 110 K. This is unusually large for a thermochromic material where the dihedral angle is expected to be below 20°. The dihedral angle is however, within the 40° - 30° region where the material can be identified as either thermo- or photochromic. At 230 K the keto/enol hydrogen can be found at a ratio of 63.6: 36.4 whereas at 110 K the hydrogen can be found in the keto position on the nitrogen with an 100% occupancy. The change in the position of the hydrogen from being on the oxygen at 295 K (Fig 182) to on the nitrogen at 110 K is as expected for the SA

class of thermochromic compounds. The full details of the unit cells and agreements for the SCXRD can be found in the appendix.

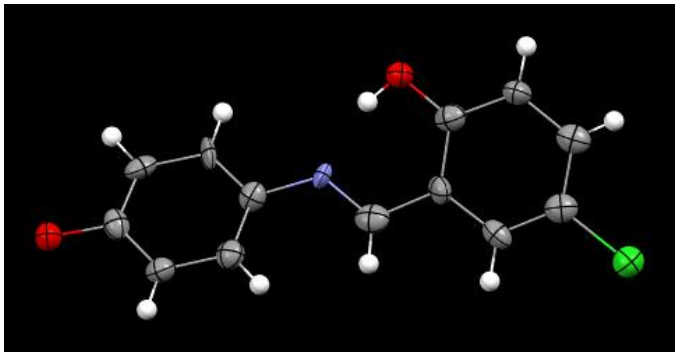


Figure 182: 50 % ellipsoids of N-(5-chloro-2-hydroxybenzylidene)-4-hydroxyaniline at 295 K

The Raman spectrum at 295 K as shown in Fig 69 shows a reasonable level of fluorescence which would only be expected to increase with a decrease in temperature.

Salicylidene-4-hydroxyaniline (compound 1) demonstrated an enol to keto tautomerisation accompanied by a colour change from a deep red to a pale yellow with decreasing temperature (Fig 183).[3]

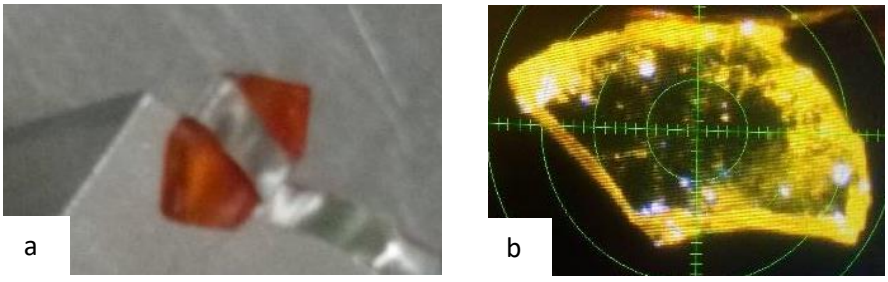


Figure 183: images demonstrating thermochromic colour change in the material at a) 295 K and b) 120 K.

We collected a series of temperature-dependent single crystal X-ray data sets at 293, 160, 130, 120 and 50 K. The space group of $P2_1/c$ was confirmed at all temperatures, and the changes in the unit cell parameters are as expected for normal thermal contraction. The asymmetric unit consists of two independent molecules with dihedral angles between the rings of ~10° and ~15° respectively. There was a demonstratable decrease in the enol hydrogen occupancy, but no major variation in the C-N and C-O bond lengths, as it would be expected to accompany this change (Table 1).

Table 1: X-ray Hydrogen occupancies and key bond lengths for compound 1.

Temperature (K)	NH occupancy (mol 1)	OH Occupancy (mol 1)	NH occupancy (mol 2)	OH occupancy (mol 2)	C-O bond length (mol 1)	C-N bond length (mol 1)	C-O bond length (mol 2)	C-N bond length (mol 2)
293	8.2(2)	91.8(1)	0	100 (1)	1.35(1)	1.29(2)	1.35(1)	1.28(1)
160	20.7(3)	79.3 (4)	0	100 (1)	1.33(1)	1.31(1)	1.37(3)	1.3(1)
130	29.5(12)	70.5 (4)	41.8 (12)	58.2 (12)	1.35(3)	1.29(2)	1.36(1)	1.29(2)
50	26.1 (23)	73.9 (3)	27 ()	73 (32)	1.36(3)	1.29(3)	1.35(2)	1.29(1)

To fully investigate the tautomerisation, i.e. have a clear understanding of the transfer of a single hydrogen atom between the oxygen and imine-nitrogen, a neutron diffraction study was performed on the single crystal diffractometer SXD at the ISIS neutron and muon source, Harwell (Fig 184). Neutrons have a much higher sensitivity to hydrogens than X-rays and so was the most informative technique to use. The data was collected at 300, 210, 120, 70 and 10 K. We found that there was no intra molecular hydrogen transfer in either of the molecules in the unit cell, and the bond lengths for the C-O and C-N, bonds that would be significantly affected by the tautomerism, remained almost constant between the values typically expected for double and single bond lengths (Table 2). This suggests that there may be some zwitterionic characteristics to the material (Figure 185).

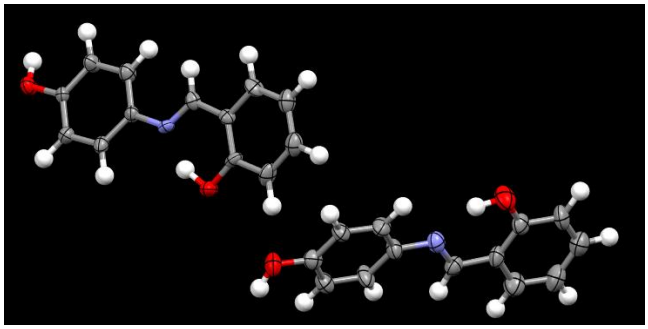


Figure 184: Neutron diffraction ellipsoid model of the asymmetric unit cell

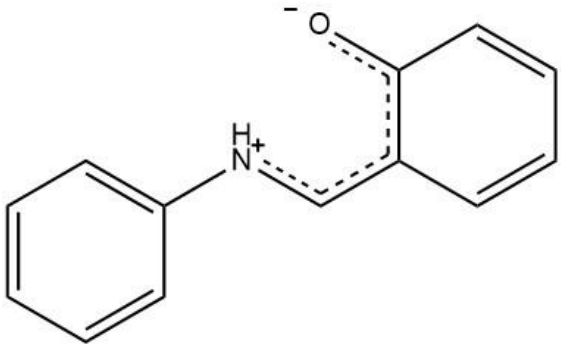


Figure 185: General zwitterionic structure of SA compounds

Table 2: Neutron key bond lengths for compound 1.

Temperature (K)	C-N (Å)	C-O (Å)	C-N (Å)	C-O (Å)
10	1.30(1)	1.36(1)	1.30(1)	1.36(2)
70	1.30(1)	1.36(2)	1.31(3)	1.37(1)
120	1.30(2)	1.35(1)	1.30(1)	1.36(2)
210	1.30(1)	1.35(1)	1.30(3)	1.36(1)
300	1.29(3)	1.35(3)	1.32(2)	1.36(1)

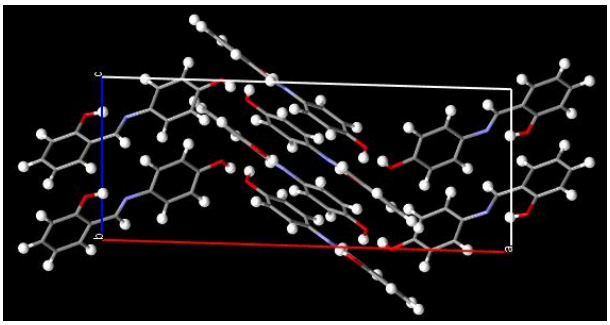


Figure 186: packing of the unit cell from neutron diffraction at 10 K of compound 1

As there were still visible changes to the colour of the crystal whilst lowering the temperature, other causes for thermochromism needed to be investigated. The first idea proposed was that variations in the packing density were the root cause of chromotropism. We found that the packing density increased as the temperature decreased. The starting packing fraction was 68.35 % at 300 K up to 71 % at 10 K (Fig 186). There are also changes in the dihedral angles between the rings from 300 K to 10 K as seen in Table 3, for the individual molecules.

Table 3: Neutron dihedral angles for compound 1

Temperature (K)	**dihedral angle 1 (°)**	**dihedral angle 2 (°)**
300	11.39(3)	15.95(3)
210	11.00(2)	15.45(2)
120	10.70(3)	15.25(3)
70	10.68(3)	14.93(3)
10	10.12(1)	15.09(1)

During an x-ray diffraction experiment on the irradiated state of the photochromic 3,5-di*tert*butyl-(salicylidene)-4-iodoaniline, we noticed that the Mo source (λ=0.71073 Å) was producing radiation damage to the sample (expanded in chapter 4.3.2), but it did not influence the tautomerisation. In the context of compound 1, we wanted to check whether the use of a slightly longer x-ray wavelength (Cu-k_{α}, λ=1.54056 Å), i.e. a radiation with lower energy, would also produce radiation damage or could influence the tautomerism. If found that the wavelength change did not have an influence on the tautomerisation, then the lack of change in the neutron experiment could have been due to other reasons such as the difference in sample size, or differences in mosaicity or penetration of the sample by the neutron beam.

When comparing the crystals grown for neutron diffraction to those used for X-ray diffraction under a microscope, the major difference was the presence of growth lines in the large crystals suitable for neutron diffraction, this affects the mosaic spread of the crystals by introducing defects. These growth lines were not found in the smaller crystals used for X-ray studies. An increased mosaic spread introduces more opportunities for self-absorption to occur. With X-ray diffraction you see more of the surface effects over the bulk effects compared with neutron diffraction, this is important for the SA samples as it could not be assessed as to how far the conversion penetrates into the bulk of larger crystals at low temperatures. As such it is feasible

that the bulk of the crystal used for the neutron experiment has not converted from the enol to keto tautomer.

A Raman spectroscopy experiment was conducted to further investigate any structural changes to the molecule caused by temperature variations. At room temperature (295 K) a spectrum was collected between 100 and 3400 cm^{-1}, using a 780 nm laser and a 50 µm slit which showed little background fluorescence. When the temperature was lowered to 100 K, all but the tips of the strong peaks at around 1580-1640 cm^{-1} were masked by fluorescence (Figure 187). This suggested that some of the colour change in the crystal could be attributed to the display of

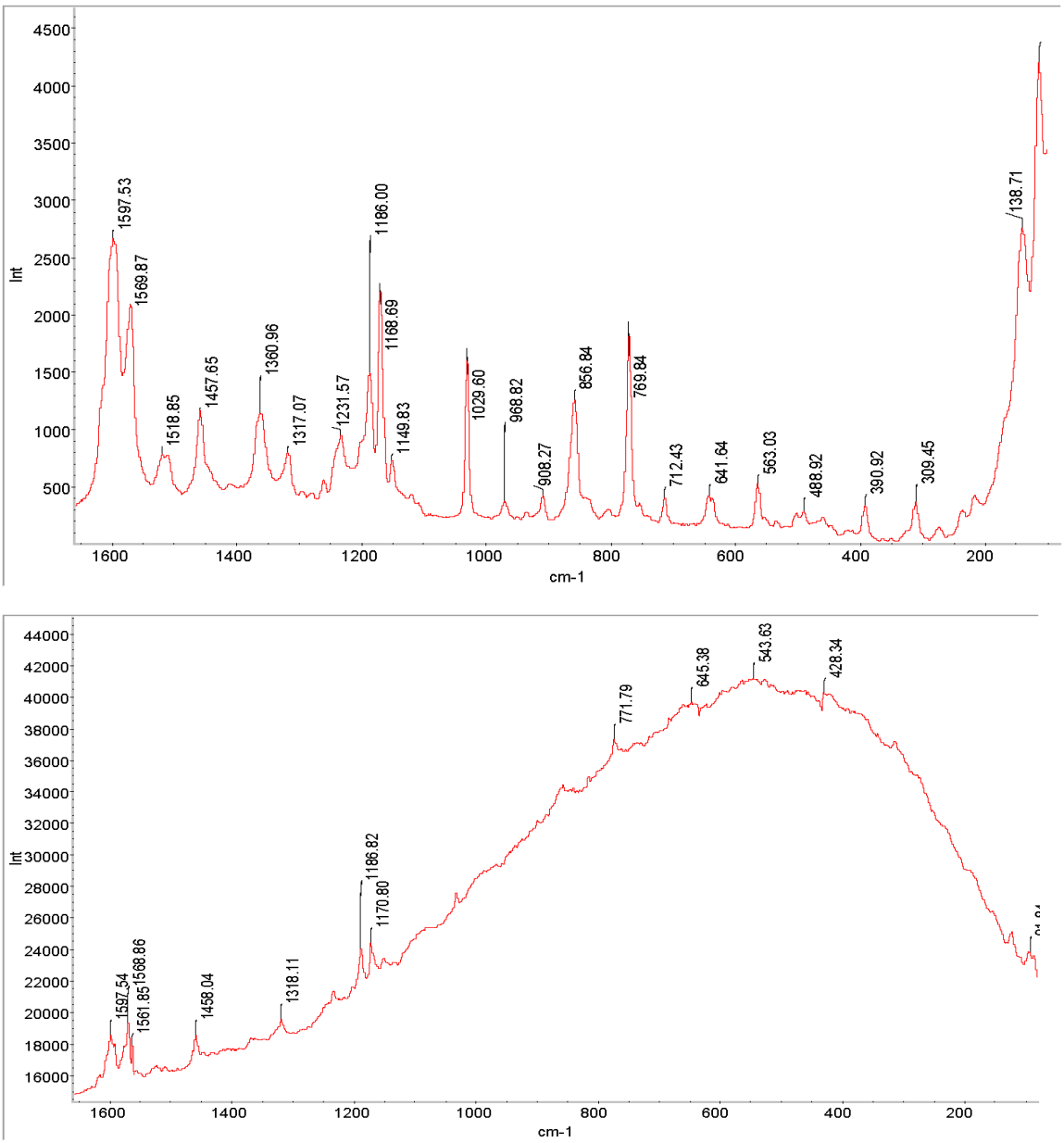


Figure 187: Raman spectra at 295 K (Top) and 100 K (Bottom) of compound 1 showing the increase of fluorescence at low temperatures

fluoresence by the molecule. Studies on other thermochromic materials have shown that there is an increase in fluorescence as the temperature is decreased[5,6].

Because of the high level of fluorescence at low temperatures, the use of Raman spectroscopy at these temperatures will not give any meaningful information on the structural changes of these molecules. Consequently, an inelastic neutron scattering (INS) experiment was conducted on the neutron spectrometer TOSCA at ISIS. A merged spectra of the calculated vibrational frequencies of the two tautomers (enol to keto, ratio 1:1) was overlaid on the experimental data (Fig 188). The two spectra show some agreement and, confirms that the true ratio between tautomers is likely to be closer to 1:1 than 70:30. It was only possible to attempt single tautomer plots which showed a worse agreement than a 1:1 ratio (Fig 189 and 190) confirming a mixture was present. Full peak assignments for the Raman and INS data can be found in the Appendix.

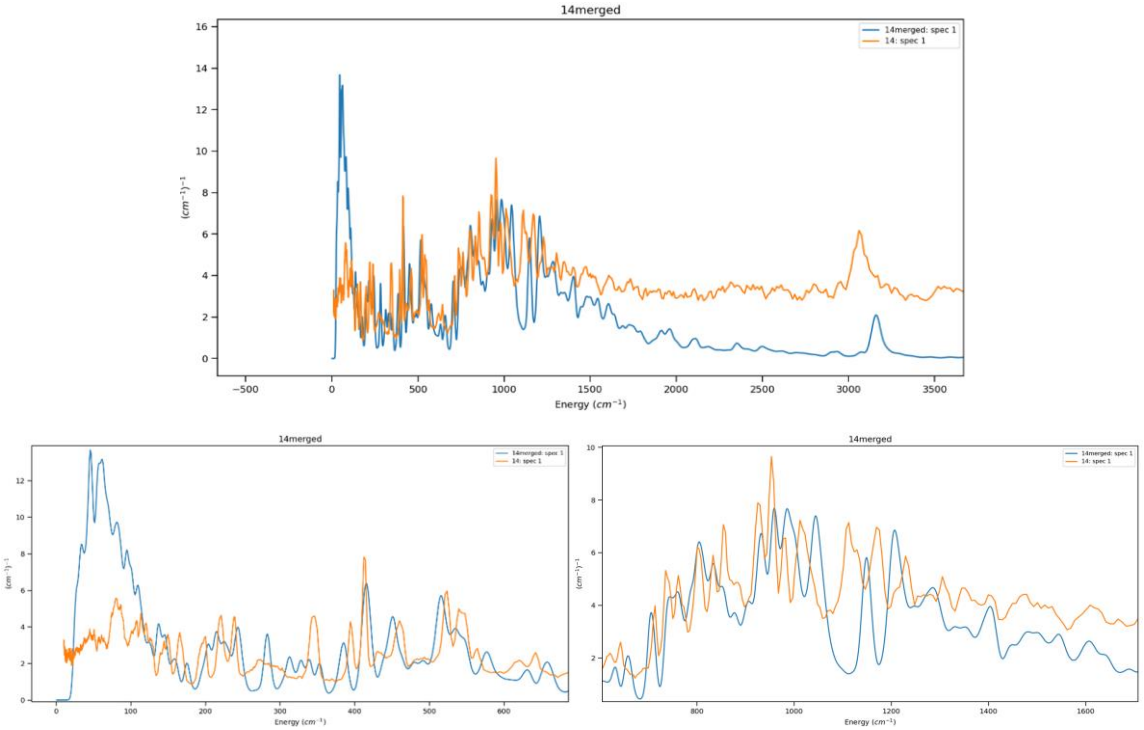


Figure 188: INS (orange) and combined keto and enol (blue) calculated data of 4-(2- Salicylidene)-hydroxyaniline

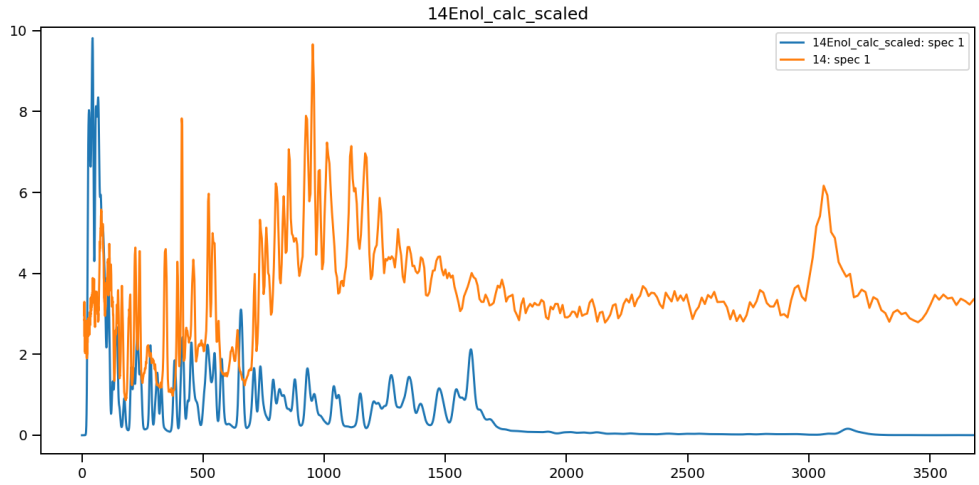


Figure 189: comparison of INS plots of the calculated spectrum of the pure enol tautomer (blue) against the experimental INS spectrum (orange) of compound 1

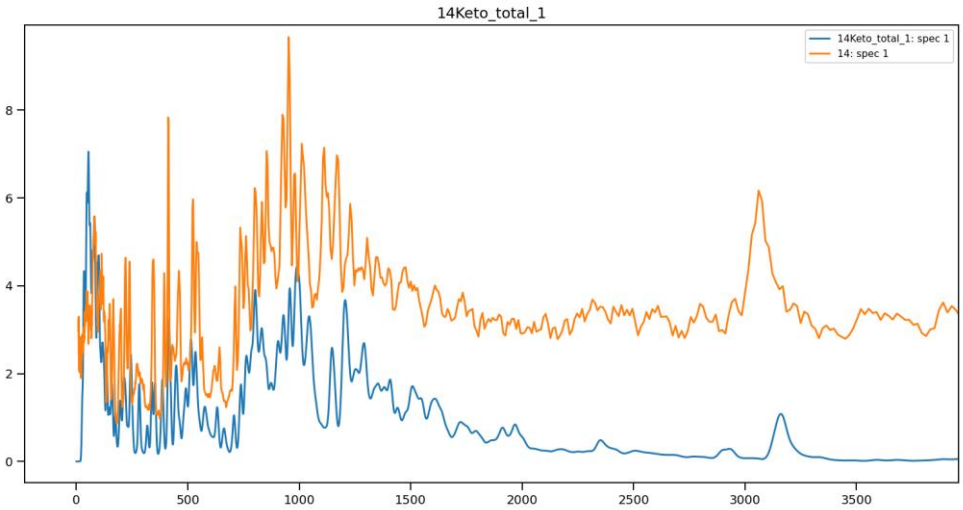


Figure 190: comparison of INS plots of the calculated spectrum of the pure keto tautomer (blue) against the experimental INS spectrum (orange) of compound 1

The final compound of this type is N-(5-chloro-2-hydroxysalicylidene)-aniline. Two polymorphs of this compound were identified, the two were initially separated by the physical morphology. The first polymorph was orange at room temperature and when taken to 140 K or below the crystals become yellow with a needle like morphology. The second polymorph was yellow to

start becoming paler upon cooling below 295 K, here the physical morphology was hexagonal plate like crystals similar to those seen for Salicylidene-4-hydroxyaniline.

X-ray diffraction experiments were performed at 298 K, 140 K and 120 K on polymorph I. This polymorph was found to have a monoclinic unit cell with space group P 2_1/ n (Fig 191).

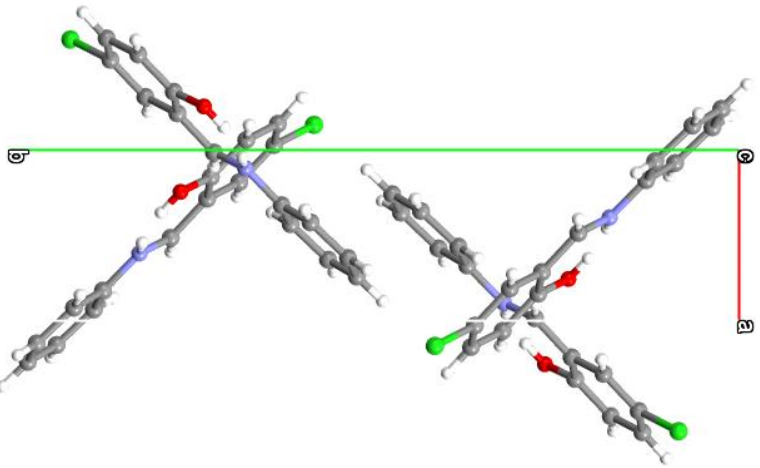


Figure 191: Packing of P 21/ n polymorph

At both 140 and 120 K there is increased occupancy of the suggested Keto hydrogen position on the Nitrogen, of 22.0 (2) and 49.0 (13) % respectively whilst at 298 K the enol tautomer has 100 % occupancy (Fig 192). The dihedral angle between the two rings was calculated to be around 6°.

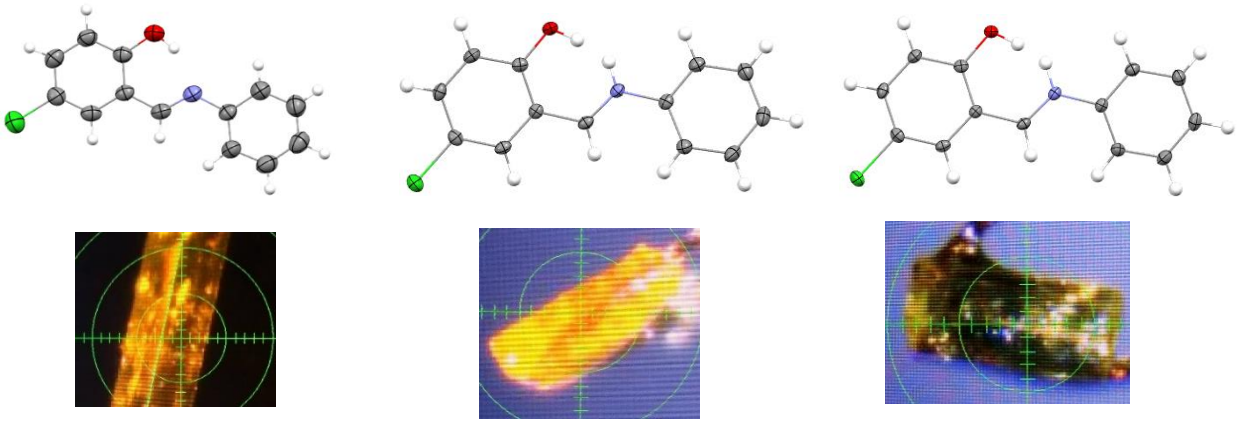


Figure 192: Structures of compound 3 at 298 K, 140 K, 120 K - Left to Right

However, no significant changes of the C-O and C-N bond lengths that would be expected from the tautomerisation were observed at 120 K. This could be due to the molecules being zwitterionic (as shown in figure 60), and in an equilibrium between the keto and enol states. Another reason could be that the change in bond length is not linear and even in the case of a 1:1 ratio the observed bond lengths would not be the simple average of the keto and enol lengths.

Neutron diffraction experiments were then conducted at 120 and 10 K. As the tautomerisation is seen by the intramolecular proton transfer between the oxygen of the OH (enol) to the nitrogen on the imine group (transforming the OH into a keto oxygen), Neutron diffraction is the best technique to probe the molecular structure. At 120 K the keto position of the hydrogen participating in the intramolecular transfer is found at an occupancy of 6.0(15) %, this is not maintained at 10 K where the keto occupancy reduces to 2.0(21) % (Fig 193). As seen during the X-ray experiment, there are no significant changes in the bond lengths for those bonds involved in the tautomerisation between the Enol and Keto tautomers. Due to the small size of the crystal comparatively for neutron diffraction experiments, the data could only be refined isotropically due to it being weak.

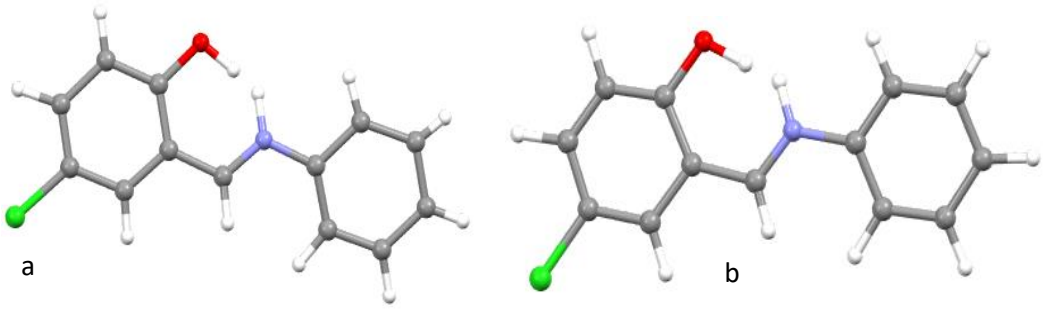


Figure 193: Compound 3 at a) 120 K from SCXRD, b) 10 K from single crystal neutron diffraction

The second polymorph (compound 3 (II)) was grown from diethyl ether, forming orange/yellow plate like crystals with an orthorhombic symmetry ($Pca2_1$ space group) (Fig 194). As with the first polymorph these crystals were thermochromic. Upon performing X-ray diffraction experiments a keto occupancy of 32.0 (12) % was found at 120 K (identified by the occupancy of the hydrogen on the imine-Nitrogen), with only the enol tautomer found at 290 K.

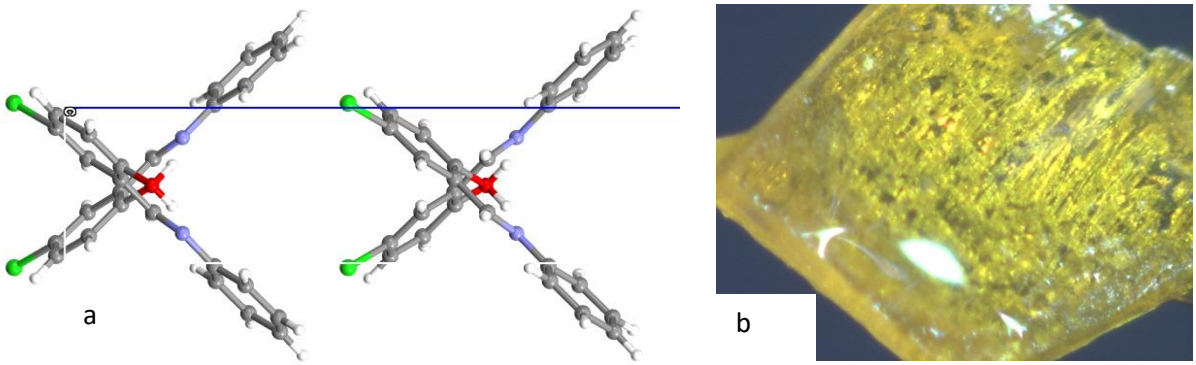


Figure 194: a) Packing of $Pca2_1$ compound 3 (II) and, b) image of a crystal of compound 3 (II) used for SCXRD

Whilst the polymorph formed is solvent dependent, for 4-Chloro-(salicylidene)-aniline the thermochromic nature of the compounds is not. The orthorhombic polymorph is also quite planar with a dihedral angle of only 1°, the smallest of any of the compounds measured here.

For Type 1 compounds in this series all were shown to be thermochromic in nature and had dihedral angles of less than 40° (where identified). Also consistent across all compounds was a high level of fluorescence displayed in the Raman scattering spectra. For the majority of the compounds the high fluorescence was displayed even at 295 K, the anomaly in this is salicylidene-4-hydroxyaniline where little to no fluorescence is shown at 295 K but, the increase in fluorescence demonstrated is significant has the temperature was lowered to 100 K where it masks all of the identifying peaks in the Raman spectrum.

4.3.2 Type 2: 3-Methoxy substituted on the aldehyde ring side.

Five compounds substituted at the three position with a methoxy group were investigated. Based on previous research (see 4.1) all compounds were expected thermochromic in nature. Only one of the compounds 2-(((4-hydroxyphenyl)imino)methyl)6-methoxyphenol (compound 7) did not produce usable single crystals allowing for only preliminary characterisation to occur. For the remaining compounds SCXRD confirmed them to be thermochromic in nature.

N-(2-hydroxy-3-methoxybenzilidene)-4-bromoaniline SCXRD was collected at 120, 250 and 293 K finding an orthorhombic P $2_12_12_1$ space group, the colour change from red through orange to yellow, as the temperature is decreased from 293 K through 250 K to 120 K. The internal dihedral angle of the molecule shifts from 12.99° at 293 K to 10.84° at 120 K. At 120 K the keto/enol

hydrogen can be found 100 % in the enol position on the oxygen whereas at 293 and 250 K the hydrogen can be found in the keto position on the nitrogen.

For N-(2-hydroxy-3-methoxybenzilidene)-3-nitroaniline SCXRD data was collected at Keele at 293 and 130 K. Anomalously for the SA series a disorder between the expected enol tautomer and the keto tautomer is seen at 293 K at a ratio of 84.0(5):16.0(5) with only the enol tautomer present at 130 K. This is unusual as there is still a visible colour change to the crystal upon cooling from orange to yellow (Fig 195). Suggesting that other causes such as fluorescence need to be considered.

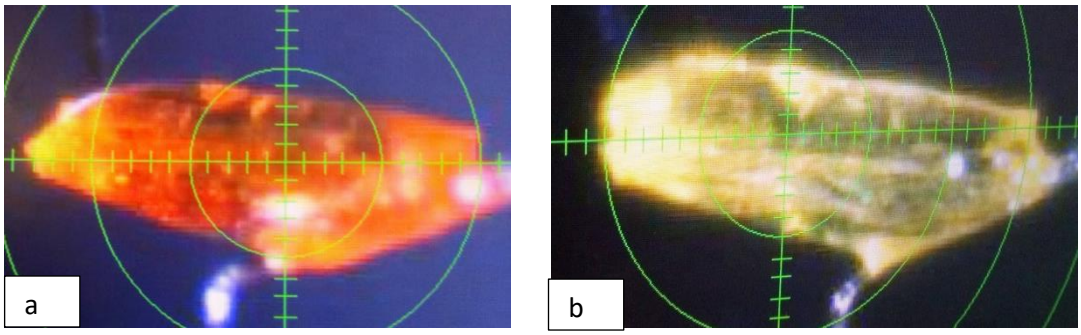


Figure 195:Images of the crystal of compound 5 used for SCXRD at 293 K showing an orange needle and b) 130 K showing a yellow needle

We collected data on two of the three known polymorphs of N-(3-methoxysalicylidene)-4-iodoaniline, the triclinic solvate and the orthorhombic system. Both crystals were red in colour one possessed a needle morphology, whilst the other a plate like morphology.

As already reported in the literature the triclinic $P\bar{1}$ structure has two independent molecules and was found to contain disordered solvate molecules that could not be located in the refinement. The terminal iodine atom in one molecule is aligned directly with the aniline ring of the second, forming a halogen – π interaction. Halogen bonding is a term used to describe the electrophilic interaction of a halogen atom with a nucleophilic region of atom on the same or a different moiety[43]. The basis for this is found in sigma hole theory, an explanation of which suggests that the area of positive charge that is designated as the sigma hole is caused by a belt of negative electrostatic potential resulting from the three pairs of unpaired electrons on the atom, this leaves the outermost part of the atom positively charged[44]. The sigma hole is found

on the opposite side of the halogen atom to where it is covalently bonded to the rest of the molecule. The strength of such bonds can be increased by attaching the halogen to a moiety that is particularly electronegative in itself[44]. The strength of the halogen bond formed can be influenced to an extent by the hybridisation of the adjacent carbon to the halogen bonded atom[45]. Analogously to the notation HB indicating Hydrogen Bonds, a Halogen bond can be denoted using the term "XB" where the X represents the halogen atom[43].

The dihedral angles between the rings on each of the molecules were found to be 20.73(1)° and 6.33(1)° at 295 K, making one molecule significantly more planar than the other. As the temperature is decreased the larger of the two angles decreases slightly (19.82(2)° at 200 K and 19.59(1)° at 100 K) whilst, the smaller of the two angles increases (6.88(3)° at 200 K and 7.63(2)° at 100 K). At both 295 K and 200 K N-(3-methoxysalicylidene)-4-iodoaniline is found completely in the enol tautomer, at 100 K there is an increase in the keto tautomer hydrogen occupancy (NH) to 47 (1) % on only one of the two molecules (the more planar of the two), the second molecule remains in the enol tautomer (Fig 196). This further demonstrates the link between the planarity of the molecule and thermochromism resulting from enol to keto tautomerisation.

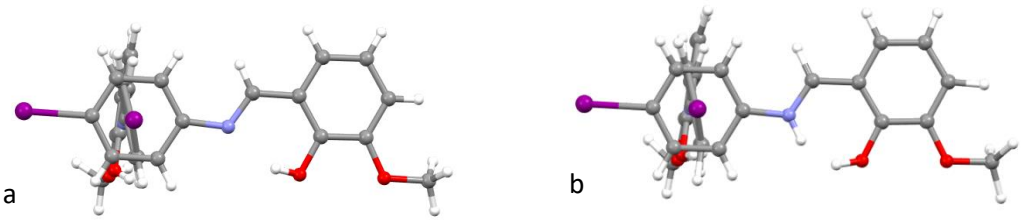


Figure 196: Structure of triclinic polymorph N-(3-methoxysalicylidene)-4-iodoaniline at 295 K (left) and 100 K (right)

As the temperature is decreased the colour of the crystal changes from a deep red to a pale yellow (Fig 197).

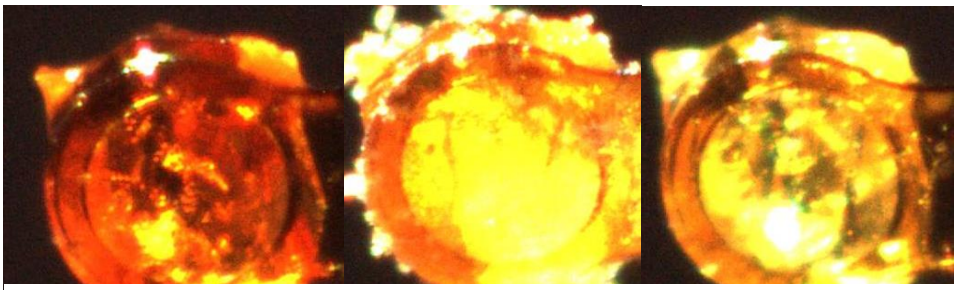


Figure 197: Crystal of triclinic polymorph N-(3-methoxysalicylidene)-4-iodoaniline at various temperatures left to right:- 295, 200 and 100K

Another observation made as the temperature decreased, was that the distance between the Iodine atom of the first molecule and the aniline ring of the second molecule decreases. From 3.563(23) Å at 295 K to 3.465(11) Å at 100 K (Fig 198).

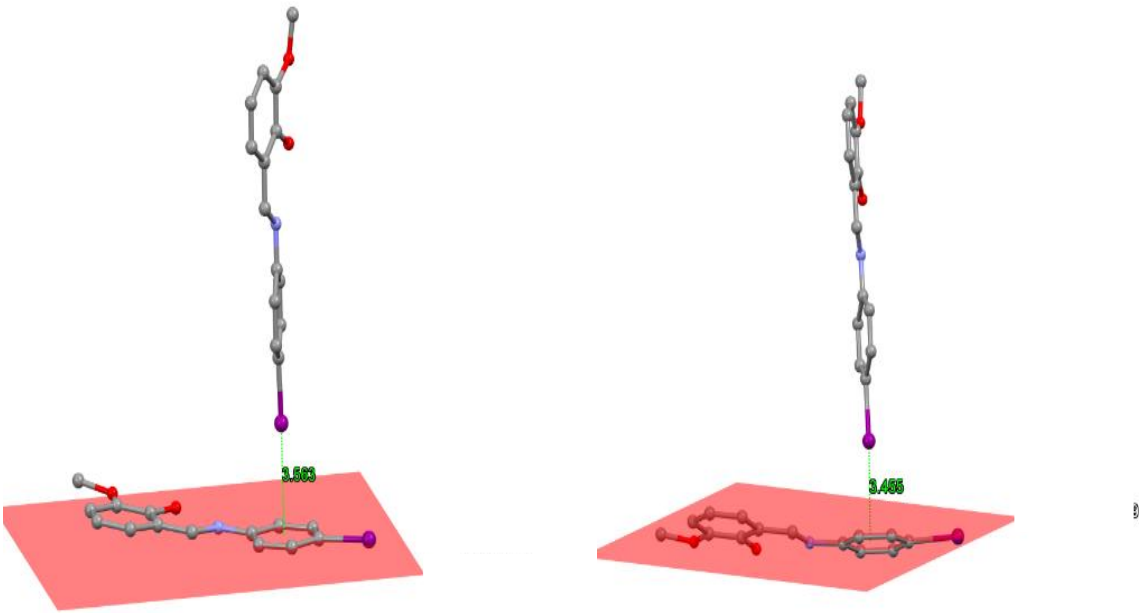


Figure 198: distance between molecules showing halogen bonding at 295 K (left) and 100 K (right) in the triclinic polymorph of N-(3-methoxysalicylidene)-4-iodoaniline

A decrease can also be calculated in the distance between molecular planes from 6.144(2) Å at 295 K to 5.763(1) Å at 100 K. Between the matching planes of the second molecule the distance decreases from 11.240(1) to 11.014(1) Å at 295 and 100 K respectively (Fig 199). This increases the strength of interaction and reduces the possibility of the molecules rotating.

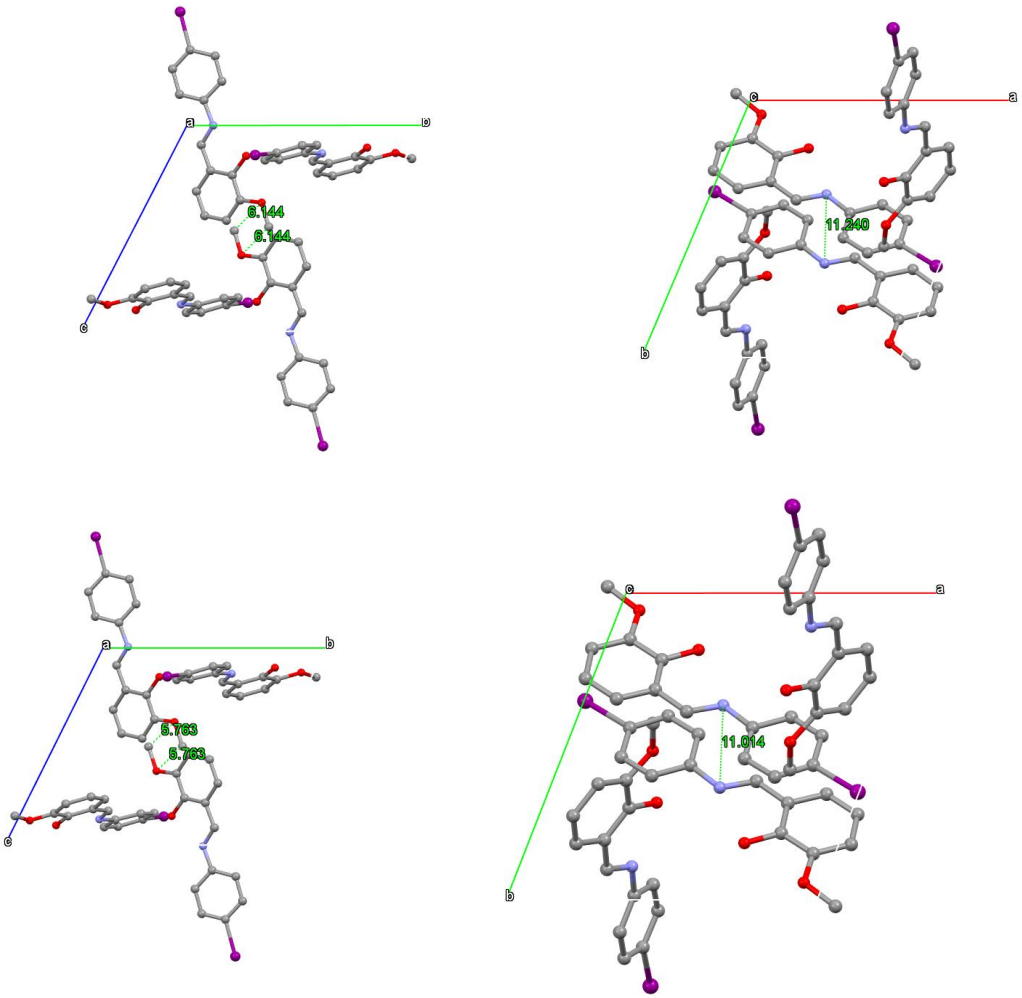


Figure 199: Top packing at 295 K, Bottom packing at 100 K of the triclinic polymorph of N-(3-methoxysalicylidene)-4-iodoaniline

The second polymorph crystalises in the orthorhombic system, with space group $P\,2_1\,2_1\,2_1$ (Fig 200). X-ray data collected at 220 K showed the enol tautomer to be present, whilst at 120 K, the compound was found in both the enol and keto tautomers in the proportion 93(1) to 7(1) %.

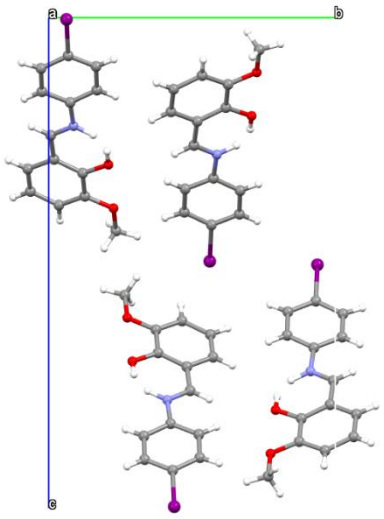


Figure 200: Packing of orthorhombic polymorph of N-(3-methoxysalicylidene)-4-iodoaniline

Investigating the close contacts at 120 K and 220 K (Fig 201) the close contact distances increase with respect to the change in temperature between the zig-zag molecular planes from 2.712(2) Å at 220 K to 2.844(3) Å at 120 K. Within the head to tail stacked zig-zag the distance between the iodine atoms and the aniline ring increased as the temperature was decreased from 2.951(3) Å at 220 K to 3.050(1) Å at 120 K.

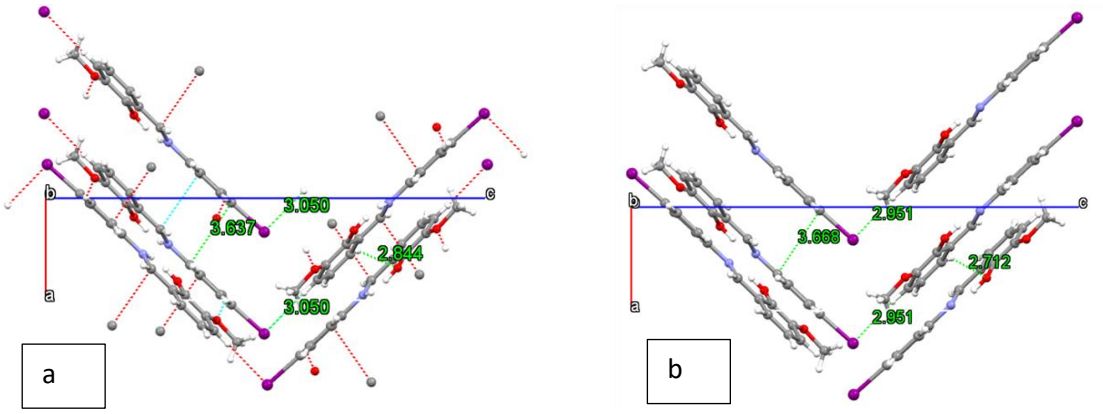


Figure 201: intermolecular distances for orthorhombic polymorph of N-(3-methoxysalicylidene)-4-iodoaniline at a) 120 K and b) 220 K

Raman Scattering data was collected as part of attempts to collect Neutron diffraction data on SXD (Fig 202) for compound N-(3-methoxysalicylidene)-4-iodoaniline using the *in situ* Raman scattering central stick. Unfortunately because the larger crystals for the sample were not single, attempts at collecting the neutron diffraction data were not successful as it was impossible to index the Bragg peaks with any of the known unit cells. As seen with a number of other materials within this compound class, the level of fluorescence present in the material made the Raman spectra unusable for structural interpretation. The strongest peaks in the region of 1600 cm^{-1} usually associated with vibrations from the enol/keto OH and NH bonds are the only ones identifiable.

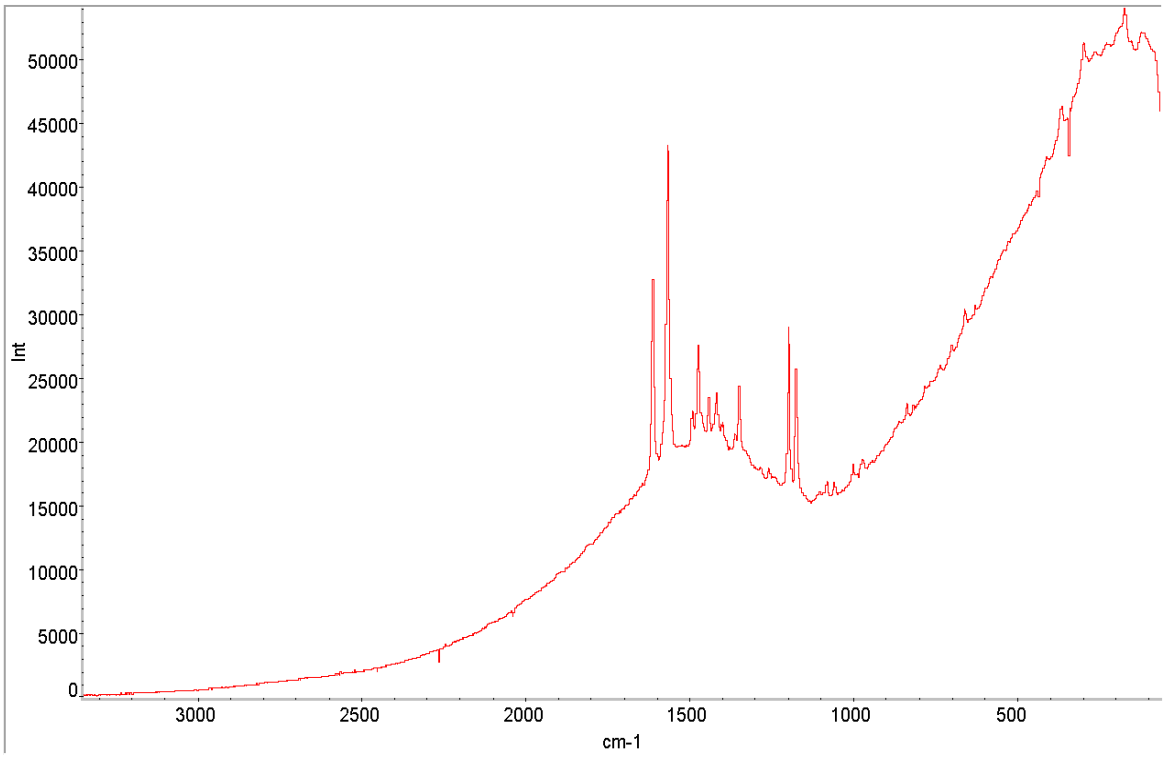


Figure 202: Raman Spectrum of N-(3-methoxysalicylidene)-4-iodoaniline at 295 K

During the SCXRD experiment for 3-methoxysalicylideneaniline (compound 8) we observed that the crystals undergo a series of colour changes upon cooling being red at room temperature orange at 200 K and finally yellow at 100 K (Fig 203) a further partial collection was completed at 50 K (see appendix). The system identified was orthorhombic with a $P\,2_12_12_1$ space group (full details can be found in the appendix).

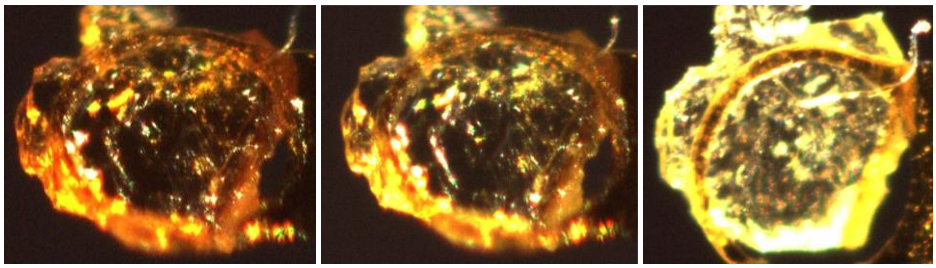


Figure 203: crystal of 3-methoxysalycilideneaniline at 293, 200 and 100 K left to right

The internal dihedral angle of the molecule shifts from 30.03° at 293 K to 30.38° at 100 K. The molecules are stacked head to tail along the c- axis in zig-zag chains of alternating directions. Unlike with other compounds in this class there was no observable enol to keto tautomerisation between 293 K and 50 K in the X-ray diffraction results. However, there were noticeable changes in the hydrogen bonding distances. Across different distances there were a mixture of reductions and extensions (Fig 204). Between 293 K and 200 K there were decreases in all hydrogen bonding distances, whilst between 200 K and 100 K there were decreases in three hydrogen bonding distances (red arrow) with increases in those remaining. Between 100 K and 50 K, there were decreases in only two of the hydrogen bonding distances (red arrow) with the rest showing increases.

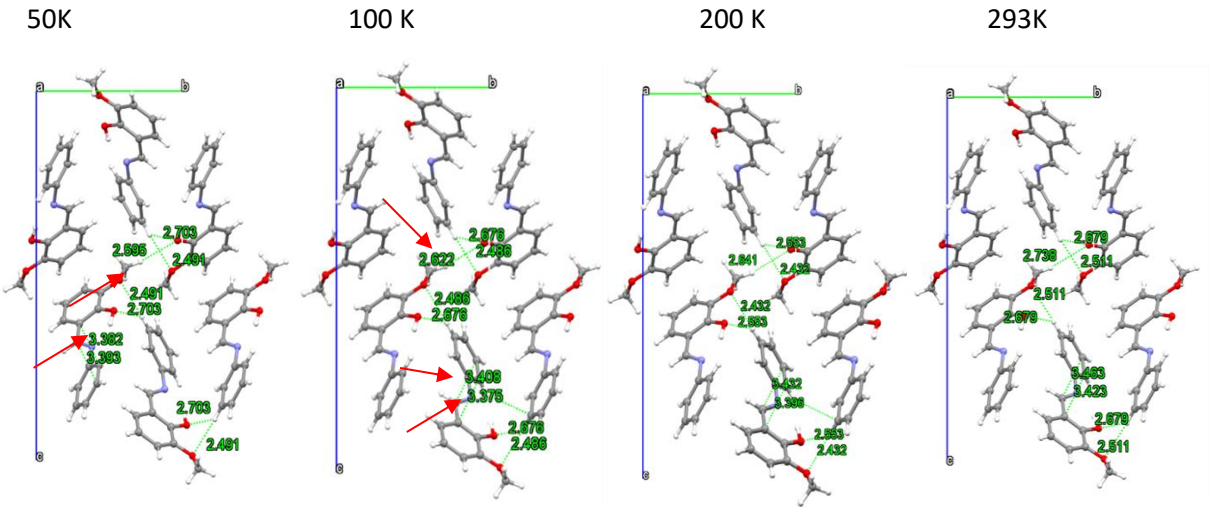


Figure 204: labelled close contacts at 50 K , 100 K, 200 K and 293 K.

Though attempts were made to collect Raman Scattering data on this material (table top spectrometer), the level of fluorescence present rendered the resulting spectra unusable for recognition of molecular configuration. As previously posited[1] fluorescence also has an effect on the colour change seen in thermochromic salicylaldehyde aniline derivatives. For 3-methoxysalicylideneaniline the slight variations in packing and the increased fluorescence at low temperatures have a large effect on the colour observed. It must also be noted however, that as little as 5 % tautomerisation between enol and keto states can cause the colour change, and a bulk average analysis technique such as diffraction cannot always identify the change[3].

Within the 3-methoxy substituted series there was two compounds that did not display the expected tautomerisation, 3-methoxysalicylideneaniline which showed no tautomerisation and N-(2-hydroxy-3-methoxybenzilidene)-3-nitroaniline which showed a reverse transition from the keto tautomer being present at 293 K to only the enol tautomer being present at 130 K. Both polymorphs of N-(3-methoxysalicylidene)-4-iodoaniline along with its bromo analogue demonstrated the expected enol to keto tautomerisation with respect to a decrease in temperature. The lack of tautomerisation observed between the enol and keto tautomers for half of this series whilst still observing a visible colour change suggests the increased importance of the fluorescence effect for these compounds, demonstrated by the level of fluorescence in the Raman spectra for each compound.

4.3.3 Type 3: 3,5-di*tert*butyl substituted on the aldehyde ring side.

The six compounds in type 3 (N-(3,5-di-*tert*-butylsalycilidene)-4-iodoaniline, N-(3,5-di-*tert*-butylsalicylidene)-3-nitroaniline, N-(3,5-di-*tert*-butylsalycilidene)-4-bromoaniline, 3,5-di*tert*butylsalicylidene-3-iodoaniline, N-(3,5-di-*tert*-butylsalicylidene)aniline and 3,5-di*tert*butylsalicylidene-2-iodoaniline) all have the same configuration of the salicylaldehyde moiety, while they differ in the substituent on the aniline ring. The systematic study of these compounds offered the possibility to analyse the effect on the material properties of the electronegativity of the substituent and of its position. With in the type there were a mix of thermochromic, and photochromic properties displayed, this is in opposition to the other two types of SA's already discussed. Within this the compounds can be discussed as 3 series based on the substitution on the aniline ring side with a separate parent compound (N-(3,5-di-*tert*-butylsalicylidene)aniline) as a baseline for what is to be expected. These groups are:

1) The 4- ,3- and 2-iodoaniline analogues
2) 4-bromo and 4-iodoaniline analogues
3) 3-iodoaniline and 3-nitroaniline

4.3.3.1 Parent compound - N-(3,5-di-tert-butylsalicylidene)aniline

N-(3,5-di-*tert*-butylsalicylidene)aniline is a thermochromic material and can be used as a based compound for type 3 materials. The thermochromic properties of N-(3,5-di-tert-butylsalicylidene)aniline were investigated first using SCXRD. SCXRD data was collected at various temperatures between 290 and 55 K. The molecule was found to have an internal dihedral angle of around 21.0(1)° (290 K), as the temperature decreased the keto hydrogen occupancy increased (Fig 205). The increase in keto occupancy does not occur uniformly with decreasing temperature. The small electron cloud of hydrogen atoms makes them difficult to locate using X-rays, this is increased by the hydrogen atoms in consideration being in close position and only partially occupied sites, proving the requirement for neutron to confirm the hydrogen atom positions.

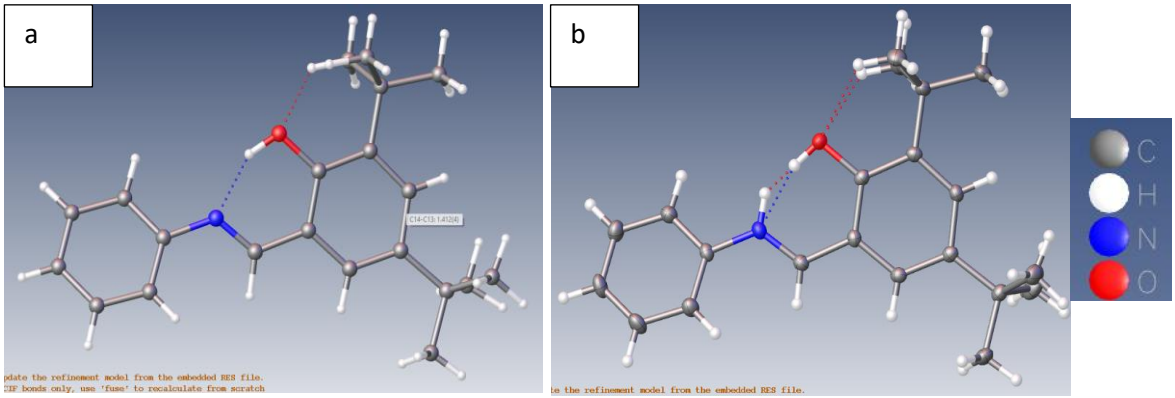


Figure 205: a) 290 K and b) 55 K structures from X-ray diffraction of compound 10

The hydrogen atom positions next to the oxygen and nitrogen atoms were identified in the Fourier difference density map, these positions were then refined restraining the maximum occupancy to 1 where hydrogen positions were found on both (Table 4).

Table 4: Keto Hydrogen occupancies from X-ray diffraction for compound 10.

Temperature (K)	**Keto Hydrogen Occupancy (%)**
290	0
120	11.6(4)
90	0
85	0
80	0
75	19.7(3)
70	26.6(8)
65	0
55	37.2(2)

At 55 K using the oxford helix system the crystal is usually housed in a beryllium cap that is the end of the helium nozzle, preventing ice build-up. To be able to get an image of the crystal at this temperature the nozzle had to be lifted once the experiment was completed allowing some ice to build up on the sample (Fig 206).

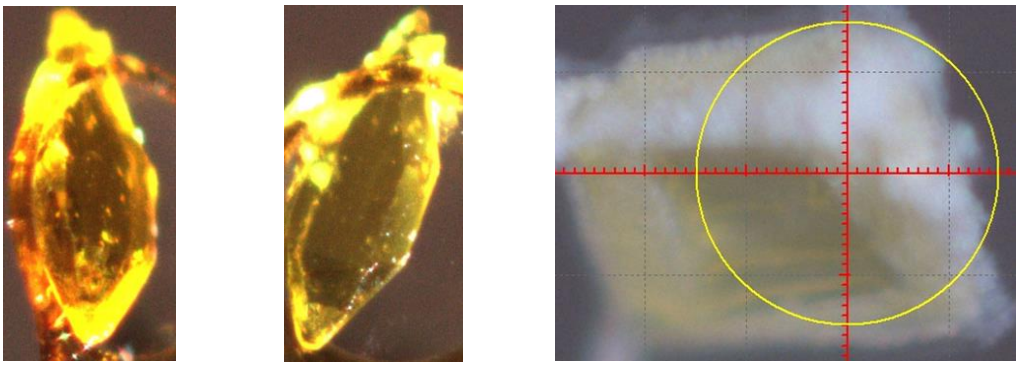


Figure 206: Images of a crystal of compound 10 at 290, 120 and 55 K left to right

The second step of the investigation into the intramolecular proton transfer in this compound, neutron diffraction experiments were completed at 250 K (Fig 207) and 60 K. As with the neutron experiments of the other 3,5-di*tert*butylsalicylidene based compounds, the *in situ* Raman Scattering central stick was used.

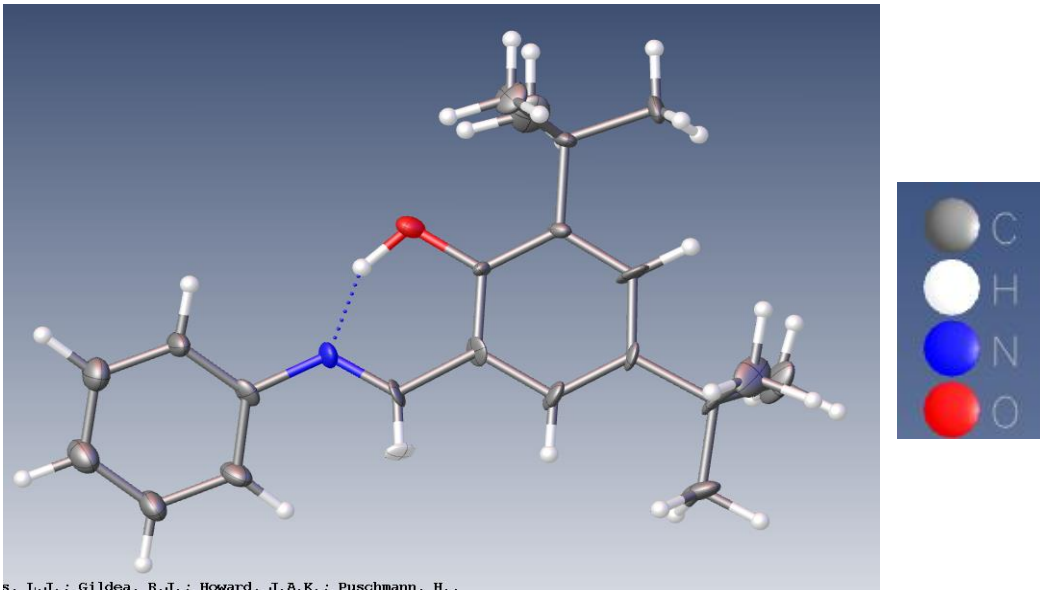


Figure 207: 250 K neutron diffraction structure of compound 10

At 250 K, a well refined structure of the enol tautomer was obtained as expected. When lowering temperature to 60 K a loss in intensity of the Bragg peaks could be observed. A reconstruction in reciprocal space at both 250 K and 60 K showed a complete degradation of the diffraction pattern at the lower temperature , presenting only dotted rings (Fig 208).

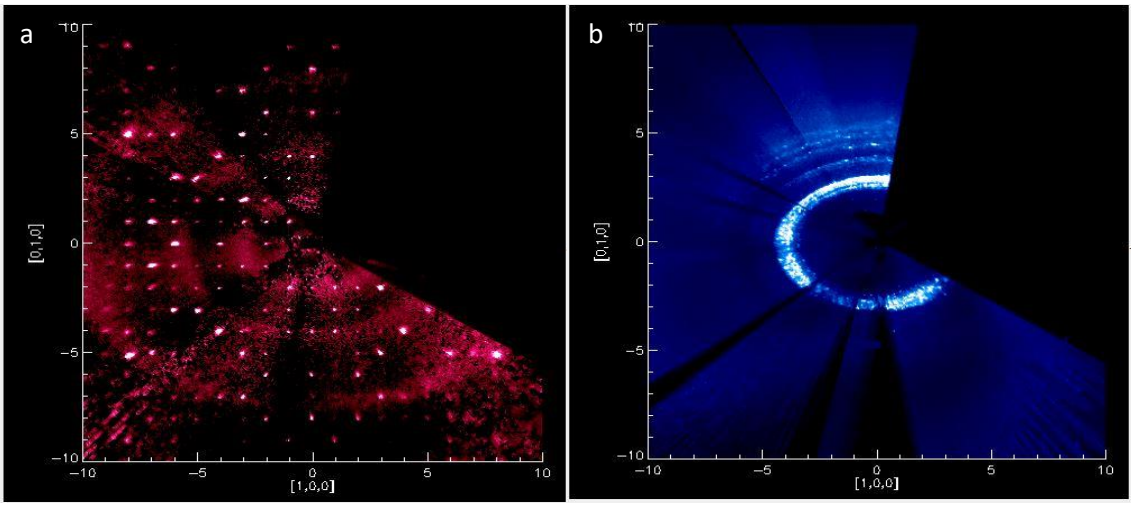


Figure 208: reconstruction in reciprocal space at a) 250 K and b) 60 K of compound 10 from neutron diffraction data

The 60 K neutron reciprocal space reconstruction was then compared to the equivalent plot for the X-ray diffraction data collected at 55 K. In the X-ray diffraction case, multiple Bragg peaks can be seen for each Bragg reflection (Fig 209). It is probable that this splitting is due to shifting and misaligning of microdomains within the crystal. In the larger crystal necessary for neutron diffraction, misaligning is further exaggerated, along with the presence of growth faults already present at room temperature, similarly to what was observed for compound 18 (discussed in detail later).

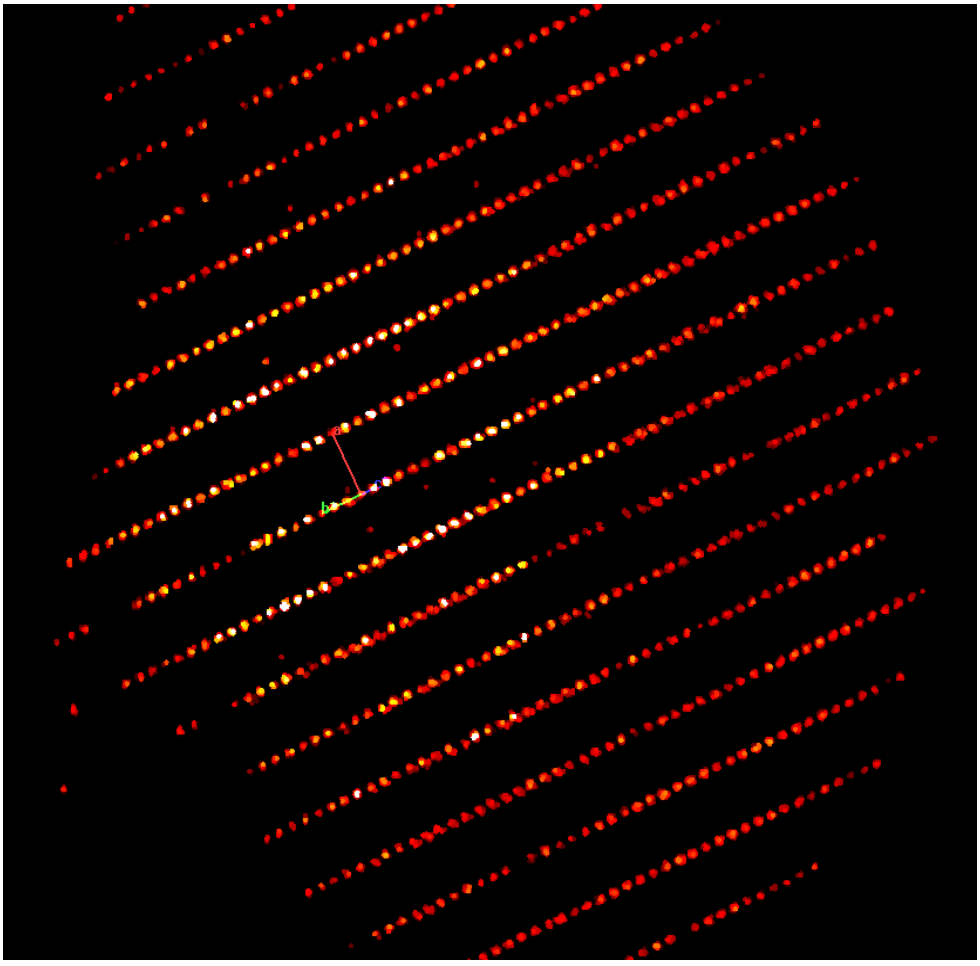


Figure 209: reciprocal space reconstruction from X-ray diffraction at 55 K of compound 10

Examination of the raw data from the neutron diffraction experiment, the strongest peaks are visible for the forward scattering detectors. In contrast, in the back scattering detectors the peaks were very weak or indistinguishable from the background (Fig 210).

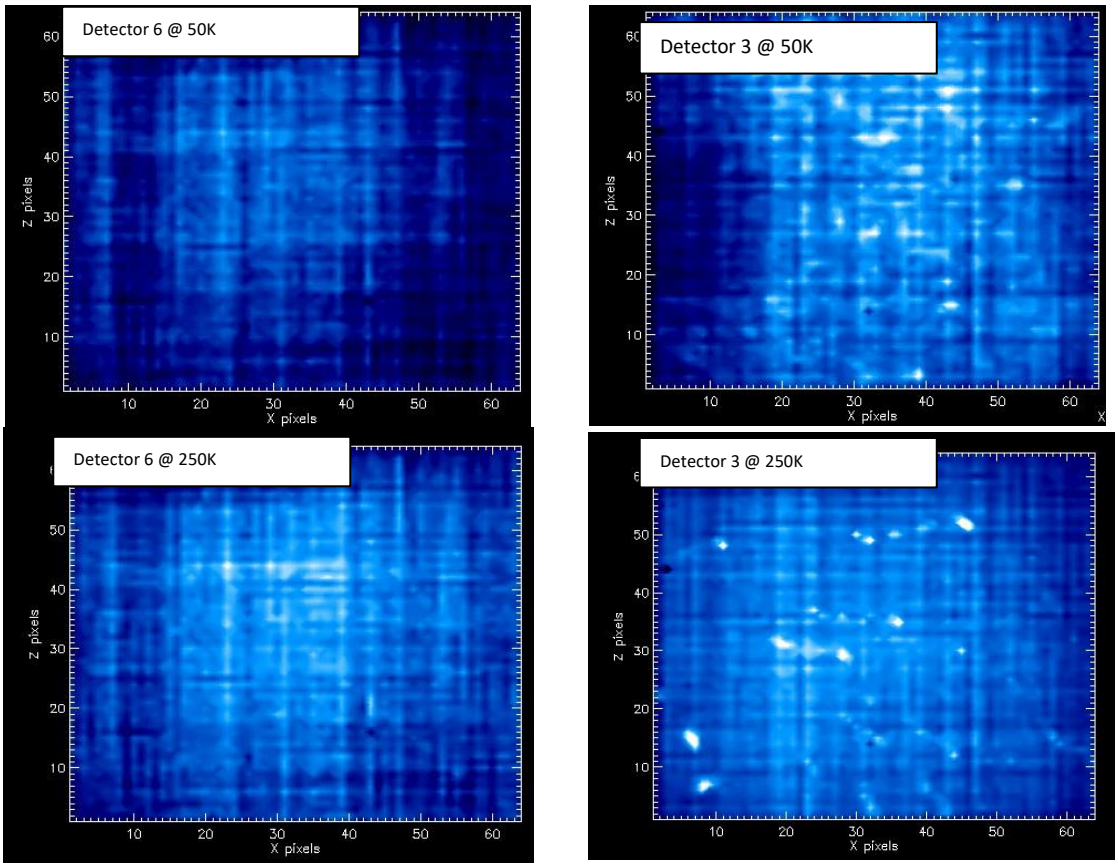


Figure 210: Raw data comparisons on detectors forward scattering (detector 6) and backscattering (detector 3) of compound 10

Images were taken of the crystal both before and after the neutron diffraction experiment. There were no major changes to the overall integrity of the crystal visible such as fractures, any new striations, or internal defects (Fig 211).

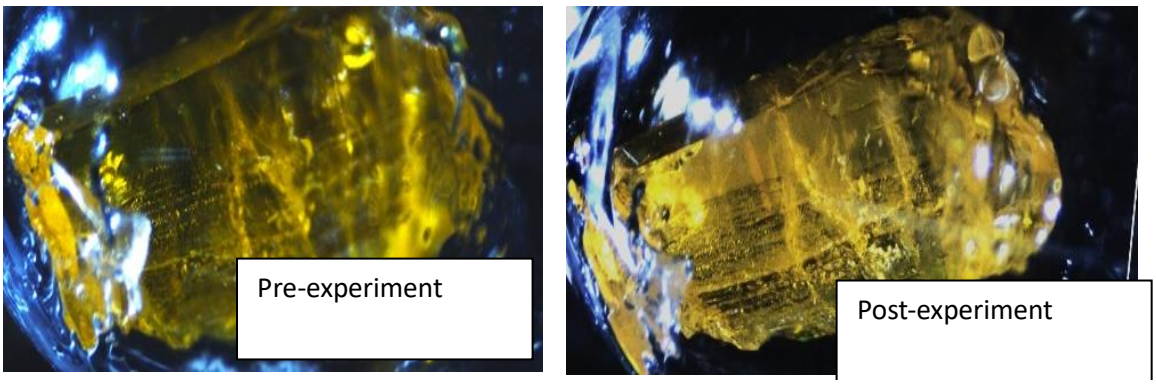


Figure 211: images of a crystal of compound 10 pre and post neutron experiment for comparison

A Raman scattering spectrum was initially collected at room temperature but found to be unusable due to the high level of fluorescence displayed by the sample, masking all but the strongest peaks (Fig 212).

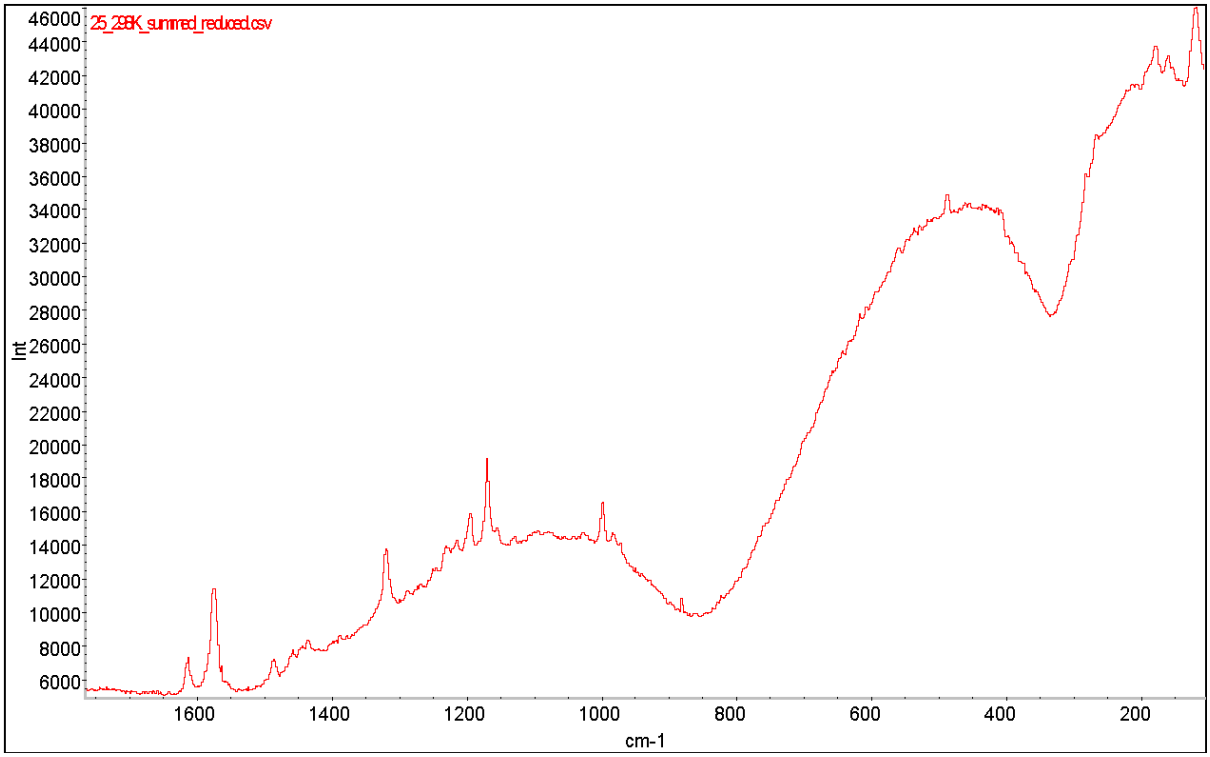


Figure 212: Raman spectra collected at room temperature of compound 10

During the neutron experiment Raman Spectra were collected at 250 K, 120 K, 90 K and 60 K upon cooling and between 250 K and 300 K upon warming. A higher fluorescence background was present in the warming spectrum compared to the others; this is a contradiction to what is normally expected for a typical thermochromic material where the level of fluorescence observed is predicted to increase as the temperature is decreased (Fig 213).

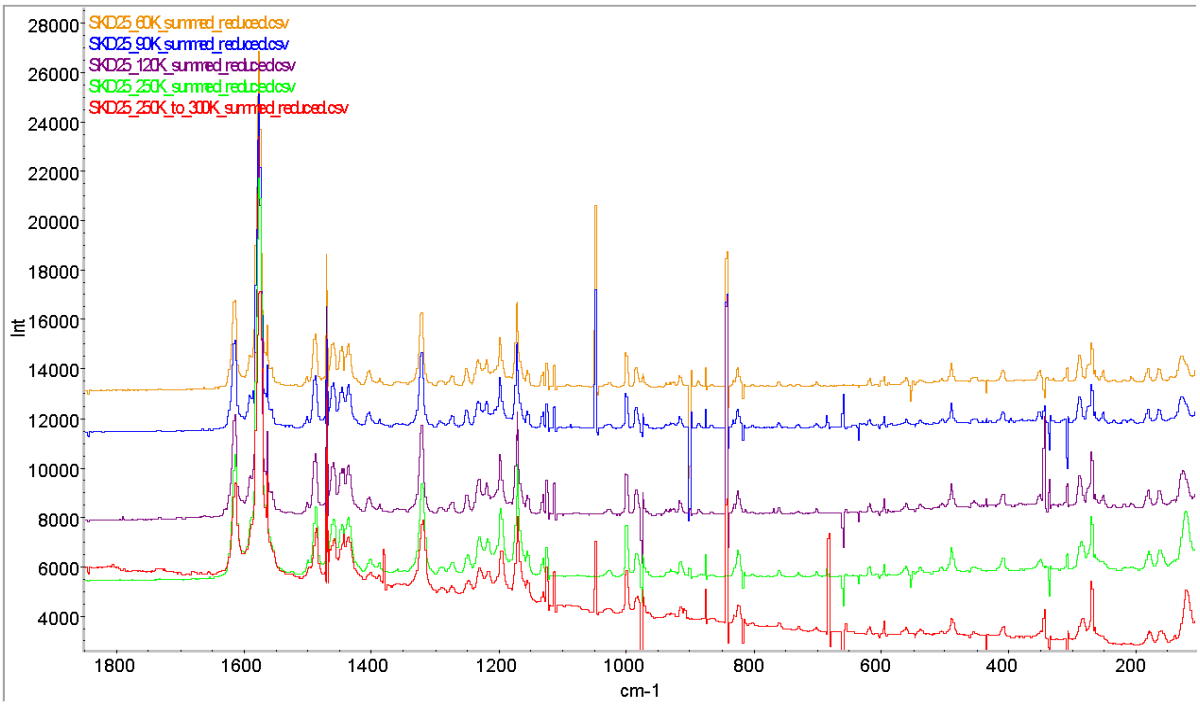


Figure 213: Variable temperature insitu Raman Spectra of compound 10. Orange – 60K, blue- 90 K, purple – 120 K, green – 250 K and red – 250 K <K>300 K

The presence of a peak at 1110 cm^{-1} (black arrow), which is solely due to the keto tautomer can be used to monitor the change in the molecular configuration, with the keto tautomer forming noticeably at 120 K and not increasing significantly below this temperature (Fig 214).

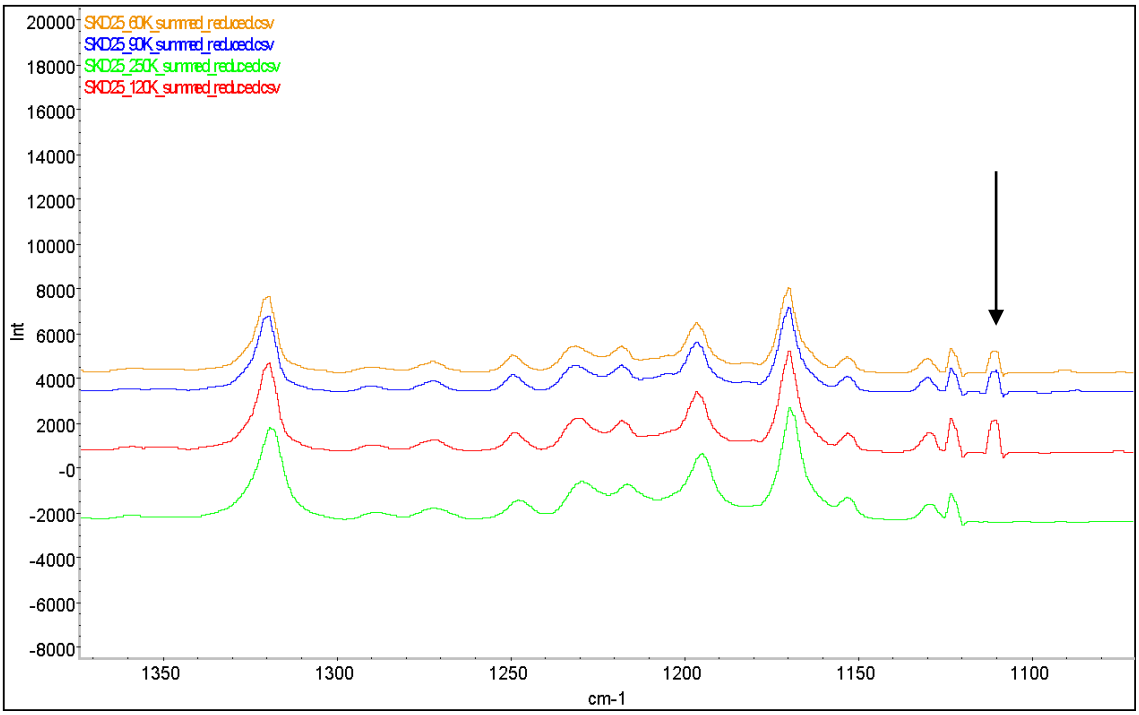


Figure 214: Keto formation monitoring region of the Insitu Raman spectra for compound 10. Orange – 60K, blue- 90 K, red – 120 K, green – 250 K

The observable consistency within the Raman Spectra demonstrates that the changes noticeable during the Neutron experiment, whilst effecting the macrostructure of the sample, does not affect the structure of the individual molecules and hence the tautomerisation between the enol and keto structures.

Due to the high level of fluorescence present at room temperature, an inelastic neutron scattering (INS) experiment at 10 K was conducted. This technique is complementary to the Raman scattering experiment, as the vibrations seen are the same as what is expected from IR and Raman spectra combined, due to the lack of selection rules. The difference between how INS and Raman scattering experiments work is described in chapter 2.2 and chapter 2.4. For INS, fluorescence is not an issue, because the sample is not irradiated with light, and hence, vibrational information could be gained that would not otherwise be possible (Fig 215).

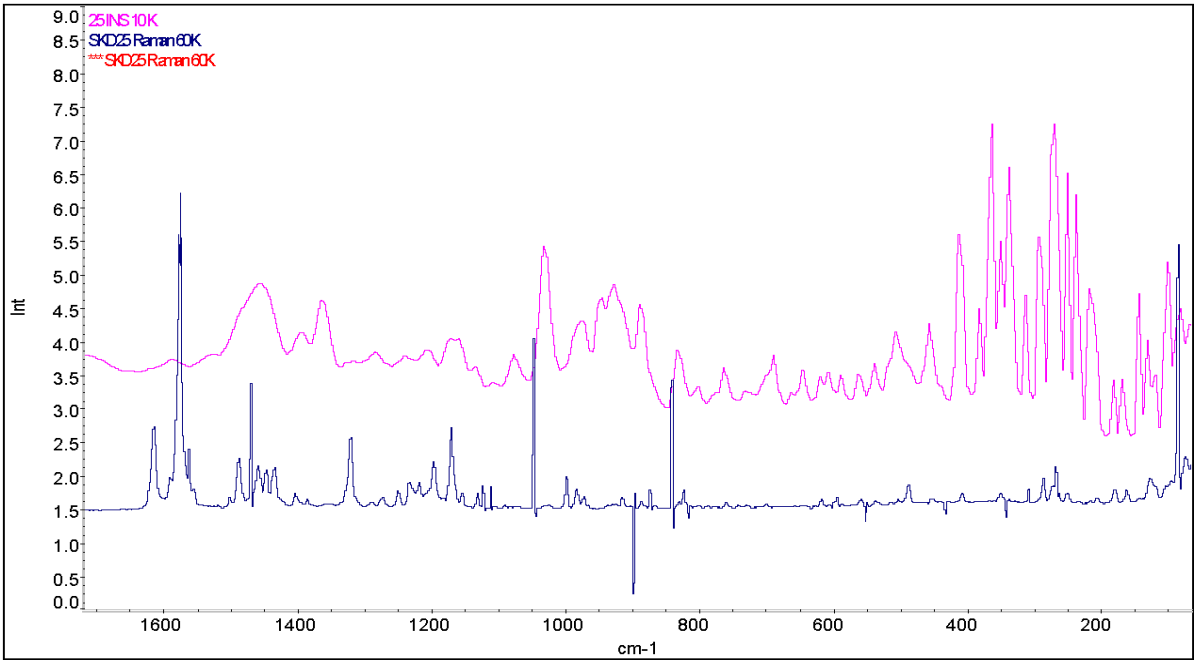


Figure 215: Comparison of INS (pink) and Raman (blue) Spectra for compound 10

The theoretical vibrational spectra of both tautomers were calculated using CASTEP, and the results were then inputted into MANTID for visualisation (Fig 216). The spectra of the two tautomers were then combined in a 50:50 ratio, and compared to the experimental INS data (Fig 217).

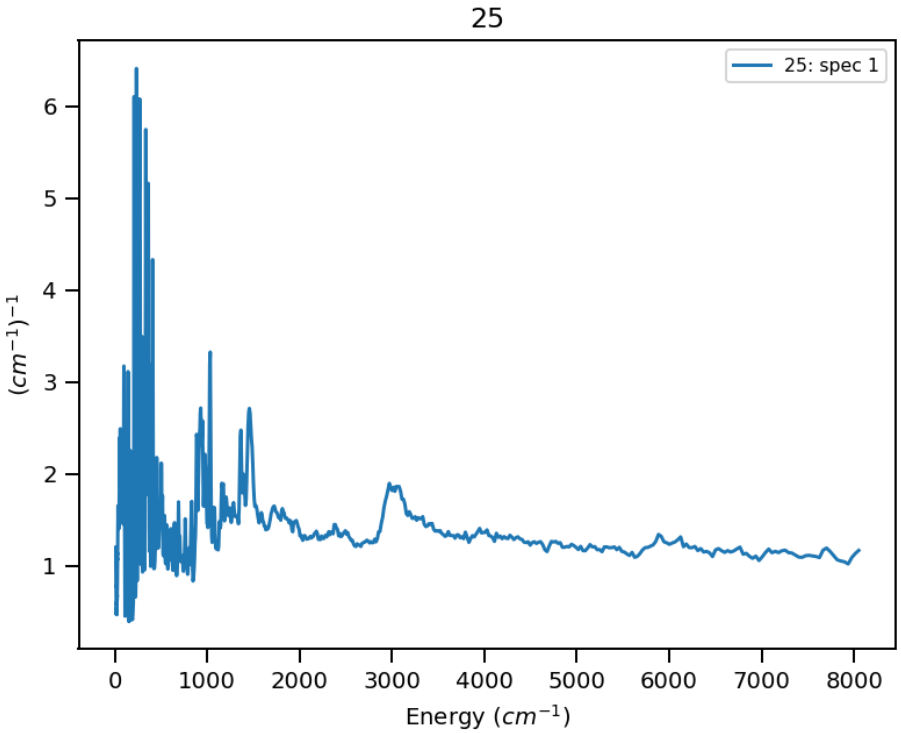


Figure 216: experimental INS for compound 10

The overall match between calculated and experimental data is sufficient to suggest that the true percentage of each tautomer is closer to the 50:50 ratio hypothesised (Fig 217) than purely one of the tautomers. This is shown by comparisons of the calculated spectra of the pure tautomers against the experimental spectrum (Fig 218 and 219).

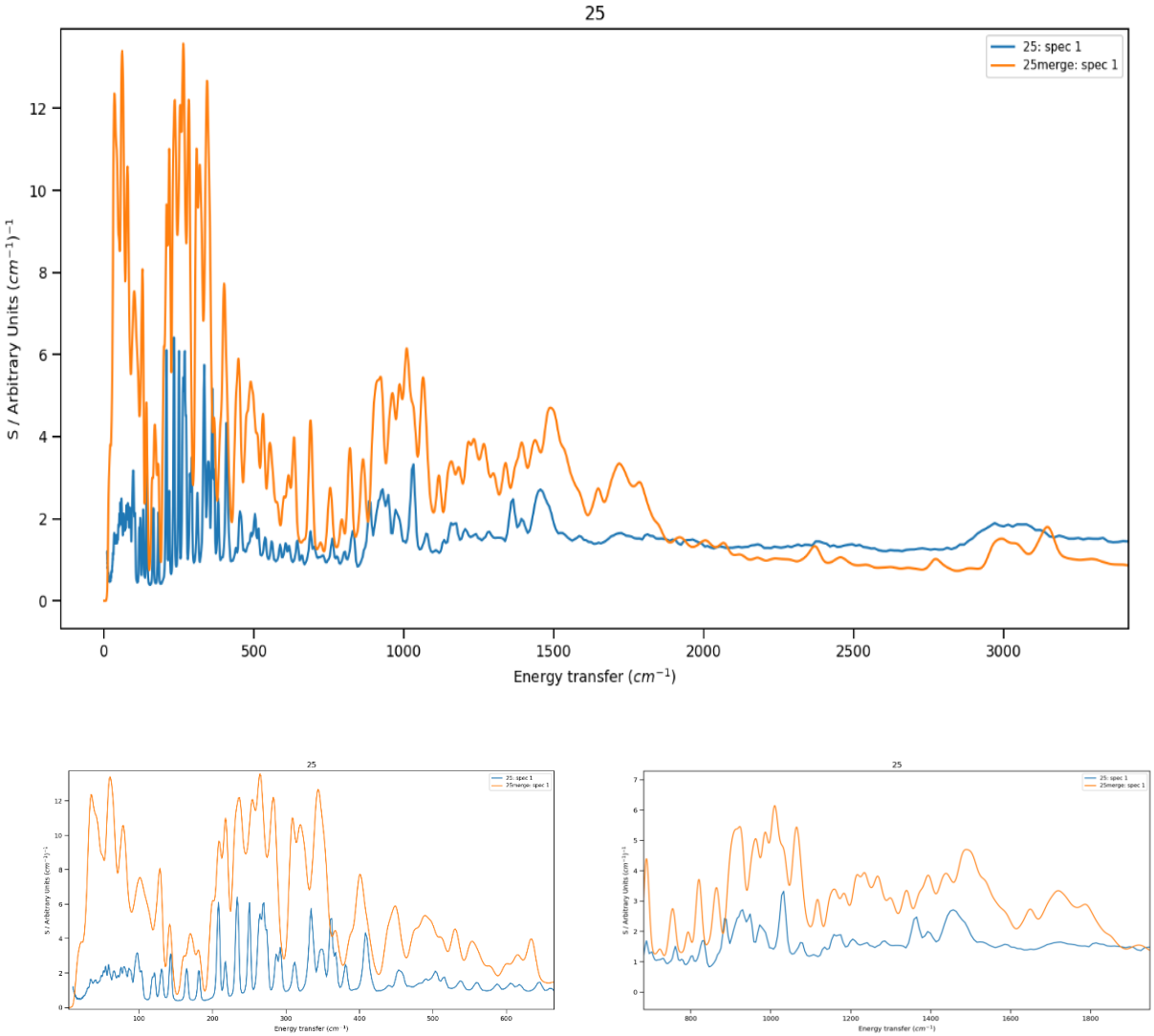


Figure 217: Comparison of INS (blue) and CASTEP calculated data (orange) for compound 10

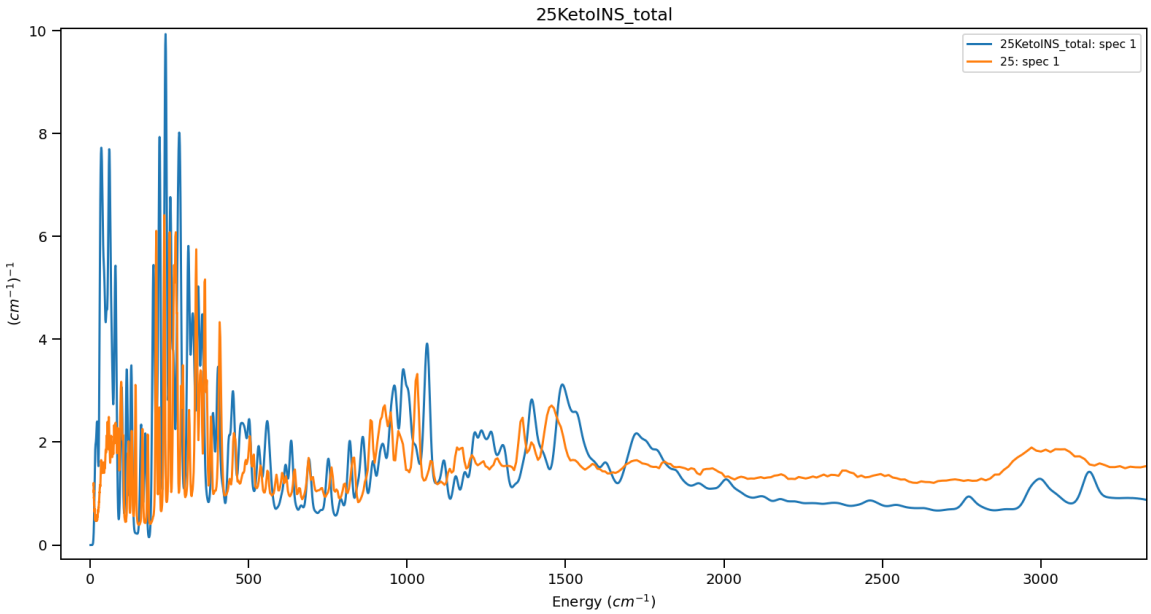


Figure 218: overlay of the calculated Keto tautomer INS spectrum (Blue) and the experimental INS spectrum (orange) of compound 10

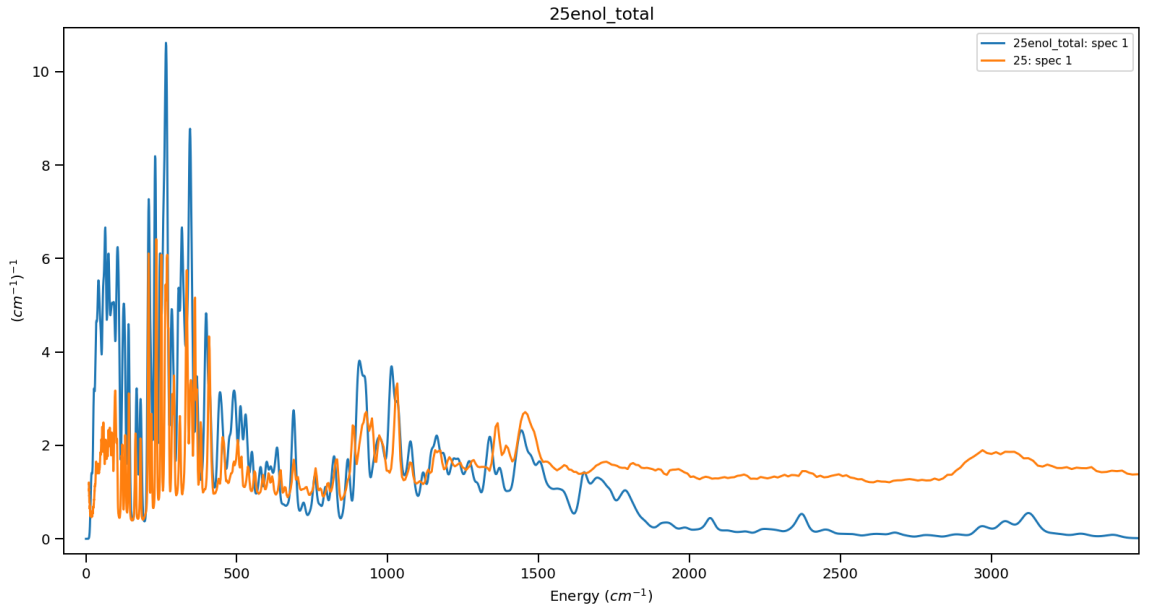


Figure 219: overlay of the calculated Enol tautomer INS spectrum (Blue) and the experimental INS spectrum (orange) of compound 10

The parent compound (10) with no substituents on the aniline ring, showed thermochromism also demonstrating the smallest dihedral angle (21°) and a high basicity of the Imine-nitrogen, making it a better hydrogen acceptor in type 3. Compound 10 is also the most fluorescent of the group, to the point where a usable Raman spectrum at room temperature (295 K) could not be

recorded. Unusually for a thermochromic material the level of fluorescence displayed decreased with temperature and usable Raman spectra were obtained when the sample was taken below 250 K. This could be due to the decreased number of resonance structures for compound 10 making it easier to excite and more likely to release the energy when it does.

From organic chemistry it can be suggested there is a relationship between the fluorescence and the number of overall resonance structures a compound has[45,23]: the more resonance structures, the lower the level of fluorescence. There is also a correlation between temperature and fluorescence in that as the temperature is decreased there is an increase in the level of fluorescence demonstrated, there are some anomalies to this, as seen for compound 10 where as the temperature is decreased so is the level of fluorescence demonstrated.

4.3.3.2 Group 1 Iodoaniline

Both the 4-iodo and 3-iodo aniline based compounds (11 and 19) were identified as photochromic materials whilst the 2-iodoaniline based compound (18) was identified as thermochromic. This group can be used to demonstrate the effect the movement of a single atom position can have on chromotropism in this compound class.

When first tested to confirm the photochromic nature of N-(3,5-di-*tert*-butylsalycilidene)-4-iodoaniline a crystal was placed under UV (365 nm) irradiation for 30 minutes in a lamp box usually used for TLC plate staining visualisation, a slight colouration was noticeable on the crystal from yellow to deep orange/red colour, this became more clearly visible after around 3 hours of irradiation (Fig 220). Exposure to natural white light for as little as 5-10 minutes caused the sample to revert to its non-irradiated colour state, when left in the dark at 298 K (Average Room Temperature) the reversion time extends to 3 weeks. After irradiating the sample overnight the crystal was cut through to confirm that the colour change penetrated throughout the sample and was not just a surface effect.

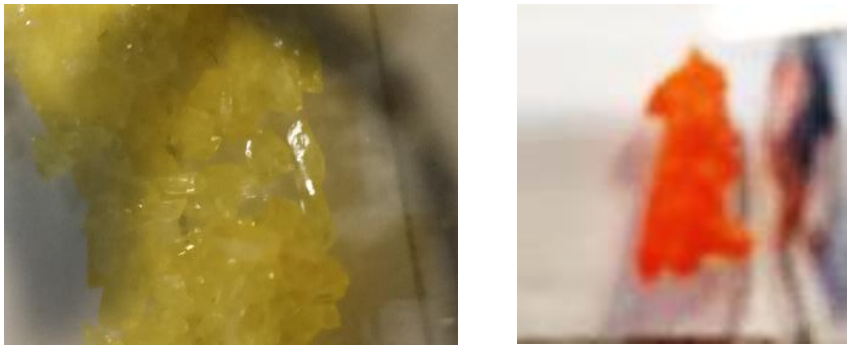


Figure 220: Non-irradiated (left) and irradiated (right) crystals of compound 11

A small mass (1 g) of N-(3,5-di-*tert*-butylsalycilidene)-3-iodoaniline was placed into a dark box and illuminated with a 365 nm UV lamp to assess its photochromic properties. After 24 hours exposure to UV light, the sample had transitioned from near colourless to orange red (Fig 221).

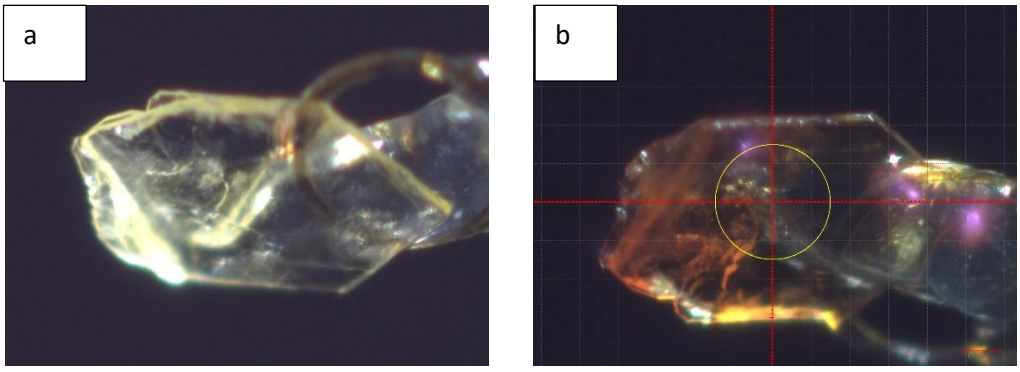


Figure 221: a) Non-irradiated and b) Irradiated (right) states of 3,5-ditertbutylsalicylidene-3-Iodoaniline

To assess for any photochromic properties in the 2-iodo analogue similar to those seen in the 4-iodo, a small mass of the sample was placed in a clear vial in a dark box with a 365 nm LED UV lamp and left for over 24 hours. The sample showed no change in the colour indicating that the material was likely to be thermochromic.

The next stage of the investigation was to complete SCXRD experiments on each of the three iodo compounds. The first series of SCXRD experiments was completed on the 4-Iodo analogue, data were collected on the sample at 120 and 290 K to investigate the effects of temperature changes on the photochromic material. The material was found to have both the cis-keto and enol state at both temperatures, at a consistent ratio of 60(2):40(2), enol: keto. The dihedral

angle of the compound was calculated to be 65°. As discussed in chapter 4.1 an internal dihedral angle larger than 40° results in the expectation that a compound is photochromic.

In order to study the structural changes associated with the colour change in the sample under a 365 nm lamp, an x-ray diffraction experiment with *in situ* UV irradiation, was performed. The initial attempt at *in situ* irradiation of compound 3,5-di*tert*butyl-(salicylidene)-4-iodoaniline was attempted on the SCXRD instrument using an LED 365 nm UV-lamp. The sample area was initially prepared by, covering the front view window with aluminium foil kept in place using tape and turning off the internal light sources. The UV lamp was attached over the incoming x-ray beam and kept in-place using tape. A single crystal of the non-irradiated sample was placed on a pin using a viscous oil and centred.

After an initial data collection of the non-irradiated sample, the UV lamp was switched on additional data collections were set up to occur for 2 hours waiting 3 hours in between over 4 collections under continuous irradiation. The first data set evidenced an enol to keto ratio of 67 to 33 %, this was the standard expected starting point based on previous SCXRD experiments (VT SCXRD data tables in appendix). After two cycles of UV-irradiation the diffraction data did not show the expected changes in the keto to enol ratio that have been suggested by offline irradiation and collection attempts. It was then noted that at the back of the SCXRD instrument had a whole in the containment for the wiring that allowed natural light onto the sample area, possibly counteracting the irradiation effects. An attempt was made to cover up using the same type of aluminium foil that covered the front window but was noted after a data collection cycle that it had slipped so was re-attached using a stronger tape. The experiment was continued for the remaining 3 cycles as well as additional cycles the first after a three hour wait then again, every hour for 4 hours before the UV-lamp was switched off then the data was collected after a three hour delay then every hour for a further four hours. All the data was then processed and showed no change in the keto to enol ratio, this was rationalised as being caused by too much natural light getting into the sample data collection area causing reversion of the irradiated

state. Another hypothesis was that the reversion to the non-irradiated state could have been caused by the x-ray beam itself, meaning that the energy of the Mo radiation is high enough to block the tautomeric effect of the UV-irradiation, causing the molecule to remain in the enol state.

To check this hypothesis, another experiment with a different x-ray source was done to check whether a visible reversion of the irradiated crystal from red/orange to yellow could be observed. This test was done on the Laue diffractometer in R53 which is equipped with a Tungsten source, also this instrument could be operated such that all external light could be eliminated. A crystal of compound 11 was irradiated in a dark box (polystyrene box sealed in a black PVC bag), for 40 hours. The viewing window of the laue diffractometer was covered using aluminium foil and tape to block out all natural light, and the internal lamp was switched off. The irradiated sample was then removed from the dark box to be mounted and centred on the diffractometer in dimmed light, trying to minimise all exposure to natural white light to less than 5 minutes.

Due to the Laue diffractometer having a different source than the single crystal diffractometer (tungsten compared to molybdenum) the voltage and current needed to be altered, as well as the time scale, to match as close as possible the power of 50 W that we calculated would hit the crystal during the SCXRD collection using the Molybdenum source. Starting from a reduced power, we progressively incremented it and checked whether reversion had occurred after each x-ray exposure.

The initial exposure was for 10 minutes at 20 kV and 5 μA resulting in a power of 0.01 Watt. The compound retained its orange colour indicative of the irradiated state. After another 10 minutes exposure at 20 kV and 50 μA (i.e. power of 1 Watt), the compound still maintained its orange colour. After another two sets of exposures at 50 kV and 50 μA (power of 2.5 Watt), for 20 minutes, the second at the same power for 1 hour 20 minutes, there were still no indicators of reversion having taken place.

Though accumulatively only matching just over half of the exposure of one cycle on the SCXRD, there were no indications that the irradiated compound was reverting to its non-irradiated state. Hence the conclusion that the previous issues encountered with the irradiation process of the first attempt at *in situ* irradiation on the SCXRD machine, were more likely to have been caused by exposure to natural light than by exposure to the x-ray beam. The next step was to better block out all the natural light from the SXCRD machine using blackout material to block both the wire outlets and the viewing window, making sure that no other sources of light could contaminate the environment.

A second attempt at *in situ* irradiation was made using a copper source rather than the usual molybdenum, as both sources are available on the SCXRD instrument. Analogously to the first experiment the data collection started on the non-irradiated crystal, then a 3 hour irradiation was timed before a new data collection was started. A further 6 hours of irradiation was completed before the third set of diffraction data was collected. The results showed a progression of the cis-keto element of the molecule to a trans-keto state, while maintaining the overall ratio between the keto and enol states with relative consistency.

While seeing this change using the copper source was encouraging it was important to collect the data again using the molybdenum source for consistency over the sample collection. Hence, a third *in situ* irradiation was completed on a new sample using the same set up as the second attempt only this time using the molybdenum source instead of the copper.

From the molybdenum source data collection, it was found that even after 18 hours of irradiation the same transition from a cis-keto state to a trans-keto state did not occur. This could not have been due to a lack of irradiation as with the first attempt, as the crystal was a deep orange/red when removed from the sample cabinet. A possibility for the differing results between the two sources is radiation damage occurring, another is that the wavelength of the molybdenum is such that it pushes the sample back into the irradiated excited state rather than the irradiated ground state.

Due to the different results obtained with Copper and Molybdenum as sources in SCXRD when using the same set up, further experiments were devised to investigate the extent of the possible radiation damage and to gain knowledge regarding the behaviour of photochromic materials in general, for future reference when studying these types of compounds.

A crystal of 3,5-di*tert*butyl-(salicylidene)-4-iodoaniline was selected and mounted on a loop pin using grease before being placed in a dark box and irradiated using the 365 nm lamp (5 W) for 6 hours. Upon removal of the pin from the dark box, the pin was covered with a case and wrapped in aluminium foil to prevent exposure to natural white light.

The SCXRD had been prepared using aluminium foil and tape along with blackout curtain material, to block any light from entering the data collection cabinet. The internal lights were switched off where possible, leaving one light source pointed away from the goniometer head to be used for centring the crystal and was turned off immediately after.

A pre-experiment was collected using the copper source to calculate the best strategy for complete data collection. This was to an aimed resolution of 0.78 Å with an I/sigma of 19 for a total time of 58 minutes. The resulting structure of the irradiated crystal showed the expected irradiated trans-keto along with the cis-enol form.

A second pre-experiment was run using the molybdenum source of the same irradiated sample. The aimed resolution was maintained at 0.78 Å with an I/sigma of 19 for a total time of 1 hour 28 minutes. The resulting structure showed the cis-keto form along with the enol form matching that expected of a non-irradiated sample. However, when the crystal was removed from the cabinet it was still orange in colour indicative of the retainment of the irradiated state.

The next step was to re-collect the same data with molybdenum on the irradiated sample with a reduced power setting cutting the amperage by half. The knowledge obtained from this series of experiments was used in subsequent data collections for the two other photochromic materials produced.

A third set of data was collected with the copper source on the irradiated sample previously used. This showed the same results as seen with the Mo radiation, a cis-cis keto-enol mix, suggesting that there is some radiation damage from the molybdenum source present.

In view of the possible radiation damage for the Mo source, a second crystal was irradiated in a dark box and irradiated using the 365 nm lamp (5 W) for 16 hours, and used to collect data with a reduced current (0.5 amp half of what is normally used). The data was then collected in a full experiment with an extended strategy to improve the statistics at lower power.

The resulting structure showed the same cis-cis keto-enol that was observed with the full power and the non-irradiated sample. This suggests that the problem is related to the wavelength of the molybdenum, i.e. the intrinsic energy of the radiation, rather than the power at which the source operates. Molybdenum also has a K_{α} energy over twice that of copper, 17.45 keV compared to 8.1478 keV

A full *in situ* experiment was performed using the copper source in order to ascertain that the structural changes that occurred over time. In order to do this the following protocol was observed. An initial data set was collected on a non-irradiated sample in order to get the base structure (Fig 222a). This was followed by two further data collections at three hours intervals between them, while the sample was kept under UV irradiation. After the first 3 hours of irradiation, there was a partial migration of the cis-keto C-N bond towards the trans-keto conformation. At the time of the second data collection the crystal had been under the UV irradiation for a total of 11.5 hours, showing a complete transformation from the cis-keto structure to the trans-keto, though there is no overall change in the percentage of keto to enol tautomer within the material (Fig 222b) . The dihedral angle of the molecule was found at values

between 64 and 66° depending on temperature and irradiation status, but still in the region expected for a material to be purely photochromic (Table 5).

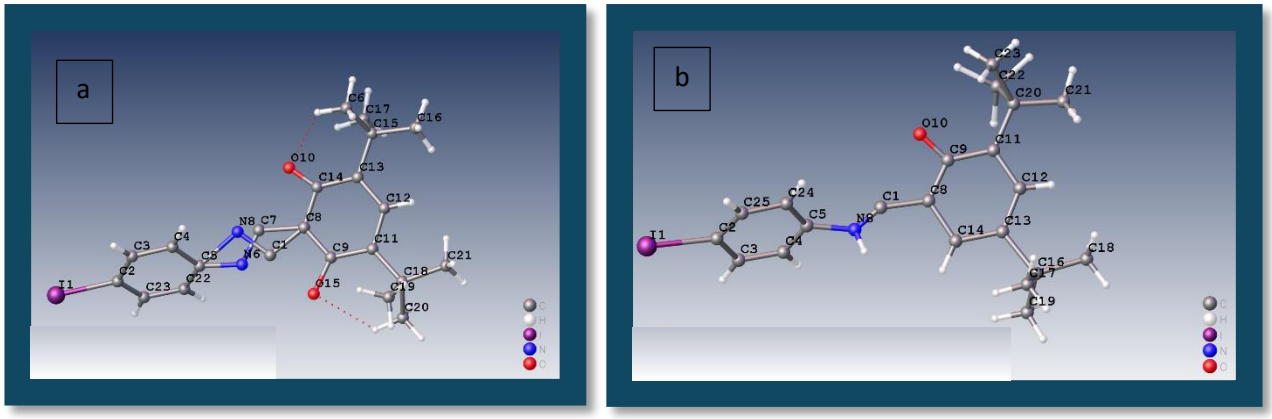


Figure 222: SCXRD structures a) non-irradiated (left) and b) irradiated (right) of compound 11

Table 5: Occupancy of Keto and enol states of compound 11

Temperature (K)	**Irradiated**	**OH Occupancy (%)**	**NH Occupancy (%)**	**Dihedral angle (°) Enol**	**Dihedral angle (°) Keto**
290	NO	62.8(1)	37.2(2)	63.44(2)	64.07(1)
290	YES	64.3(2)	35.7(1)	63.56(5)	64.07(2)
290	NO	69.0(1)	31.0(3)	65.04(2)	65.65(4)
120	NO	67.7(3)	32.3(2)	63.27(3)	64.06(1)

For the 3-iodo analogue SCXRD data were collected whilst irradiating the sample *in situ* as already described for 3,5-di*tert*butylsalicylidene-4-Iodoaniline.

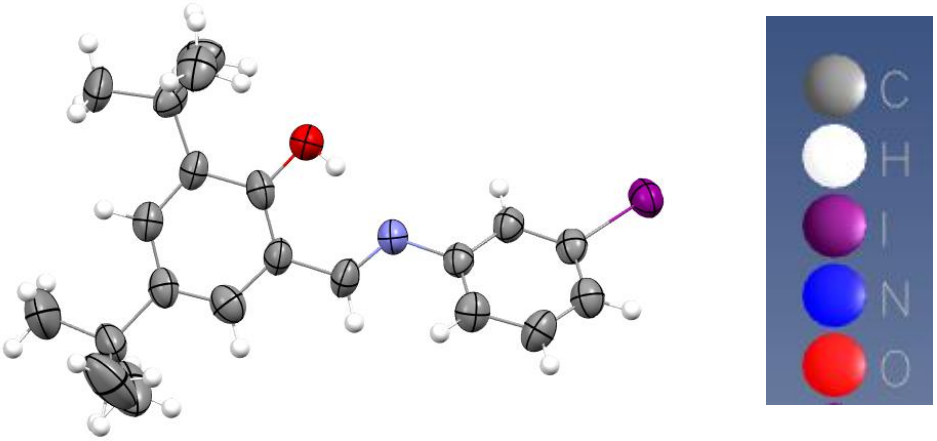


Figure 223: Molecular structure of the non-irradiated 3,5-ditertbutylsalicylidene-3-Iodoaniline at 293 K. (Ellipsoids represented at 50% level)

The structural determination of the non-irradiated sample showed only the enol tautomer (Fig 223), similarly to what seen with the other photochromic materials. Unlike the para-iodo analogue of this compound, which is photochromic, in this case there is no disorder around the imine linking bridge.

A second set of single crystal x-ray data was collected after 36 hours *in situ* irradiation (Fig 224). Unlike with the non-irradiated sample the hydrogen atom position associated with the tautomerisation could not be located in the Fourier difference map (neither on the oxygen nor on the nitrogen atoms), so percentage occupancies of the two enol/keto forms could not be calculated. As seen across all of these materials there were no significant changes to the enol C-O bond length post irradiation.

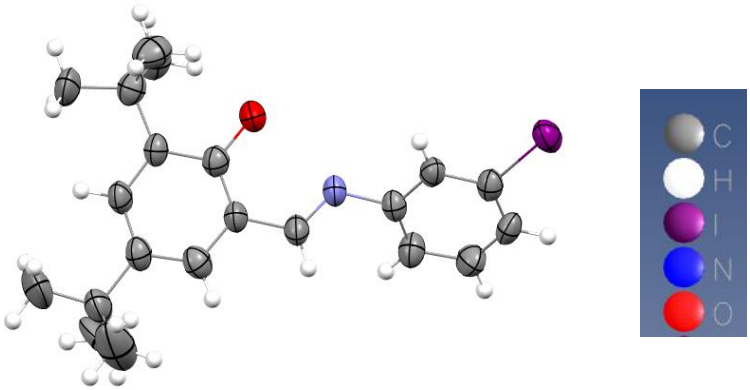


Figure 224: ellipsoidal irradiated structure of 3,5-ditertbutylsalicylidene-3-Iodoaniline at 293 K

A thorough comparison of the two structures in 3 dimensions, allowed to probe the effect of irradiation on the packing and the intermolecular interactions (Fig 225). The packing shows layers of molecules oriented head to head and tail to tail. There are no close contacts for either the irradiated or non-irradiated structure in contrast to what is seen for the para and ortho analogues of 3,5-di*tert*butylsalicylidene-3-Iodoaniline. Measuring the distances between layers of the molecule which are oriented in opposite directions there is an increase in the distance between Iodine atoms in the irradiated structure over the non-irradiated along the b-axis. The opposite change can be seen in the distance between the imine nitrogen of one molecule and the close ring of the next layer. Distances within the layers remain consistent throughout.

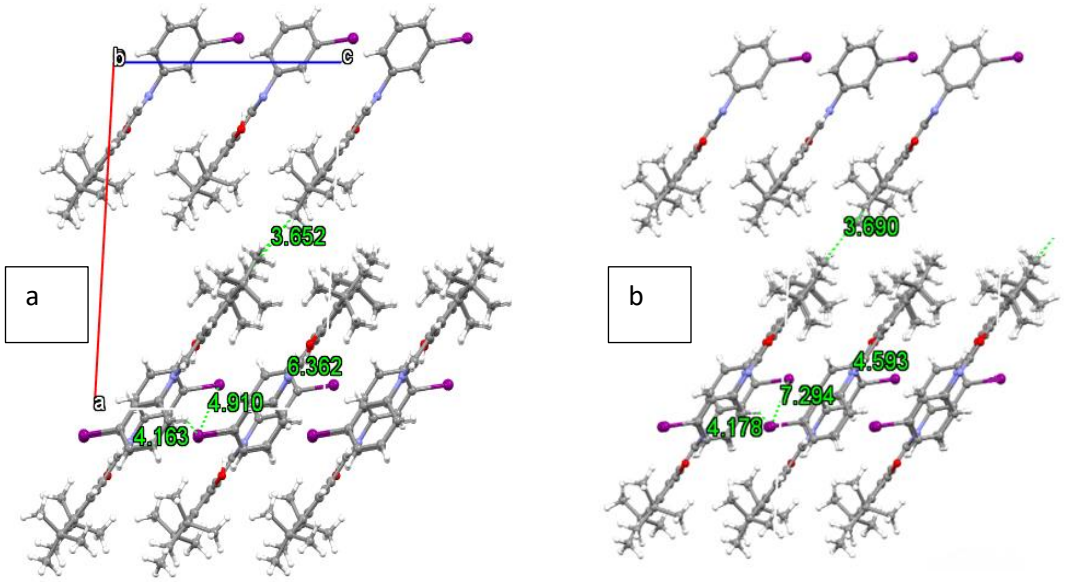


Figure 225: packing of a) Non-irradiated and b) irradiated (right) structures of compound 19 showing variations intermolecular distances.

As stated in chapter 4.1 the dihedral angle between the two rings in the molecule is a good indication of the behaviour of the compound. An angle of over 40° means that a compound is more likely to be photochromic, whilst an angle below 20° is a clear sign of thermochromism. The region between 20° and 40° is more of a 'grey zone' in which both chromic behaviour types can be displayed. There are slight variations in the dihedral angle of 3,5-di*tert*butylsalicylidene-3-Iodoaniline upon irradiation (Fig 226). Pre-irradiation the dihedral angle is observed to be 46.24(2)°, while post irradiation 3,5-di*tert*butylsalicylidene-3-Iodoaniline has a dihedral angle of 45.85(3)° showing that chromotropism observed is not a result of a large change in dihedral angle within the molecule.

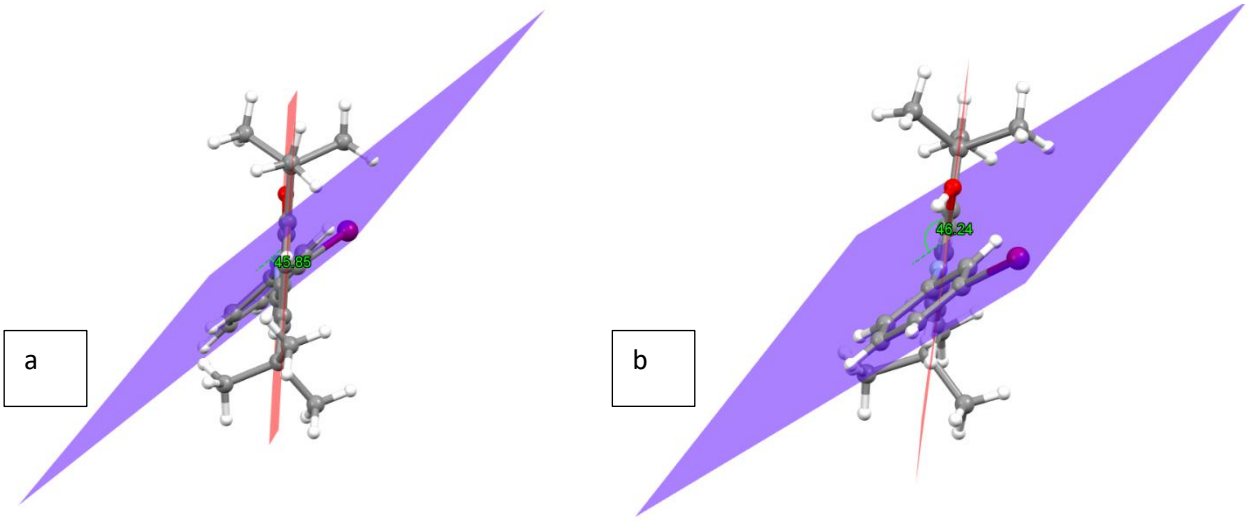


Figure 226: Dihedral angles of the a) irradiated and b) non-irradiated states of compound 19.

Differences can also be observed in the torsion angles between the rings and the linking C-N bridge (Fig 227), with the irradiated structure showing more planarity than the non-irradiated one. With an angle between the aldehyde ring and the linking bridge in the irradiated structure of 0.38° *vs* 4.63° in the non-irradiated structure. Conversely the torsion between the linking C-N bridge and the aniline ring is larger in the irradiated structure (46.60°), than in the non-irradiated one (44.82°).

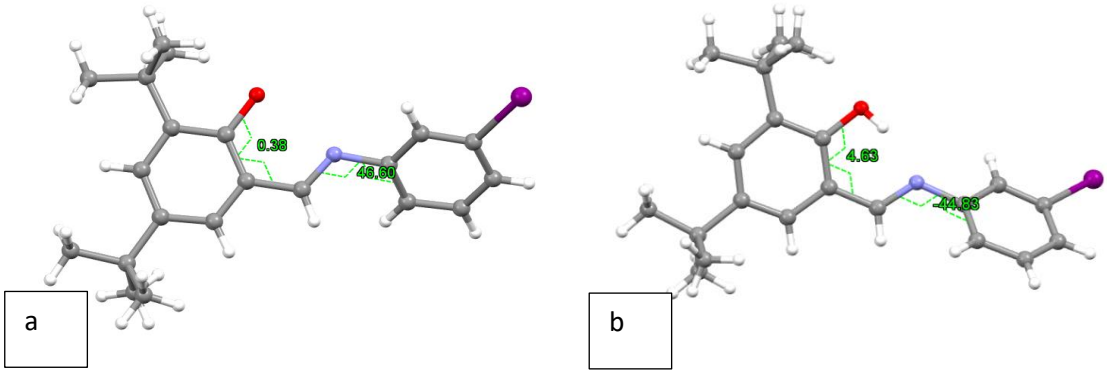


Figure 227: torsion angles across C-N bridge in the a) irradiated and b) non-irradiated structures of compound 19.

Finally for the 2-Iodo analogue SCXRD data was collected at regular intervals between 320 and 100 K (Fig 228), with a further data collection at 50 K. Between 320 and 120 K 3,5-di*tert*butylsalicylidene-2-iodoaniline was found entirely in the enol tautomer, upon reaching 100 K the keto tautomer was found with a hydrogen occupancy of 26.9 (11) %. At 50 K the keto hydrogen occupancy was found to be 21.0 (11) %. The lower keto occupancy at 50 K could be due to a stabilisation of the equilibrium between tautomers at the lower temperature.

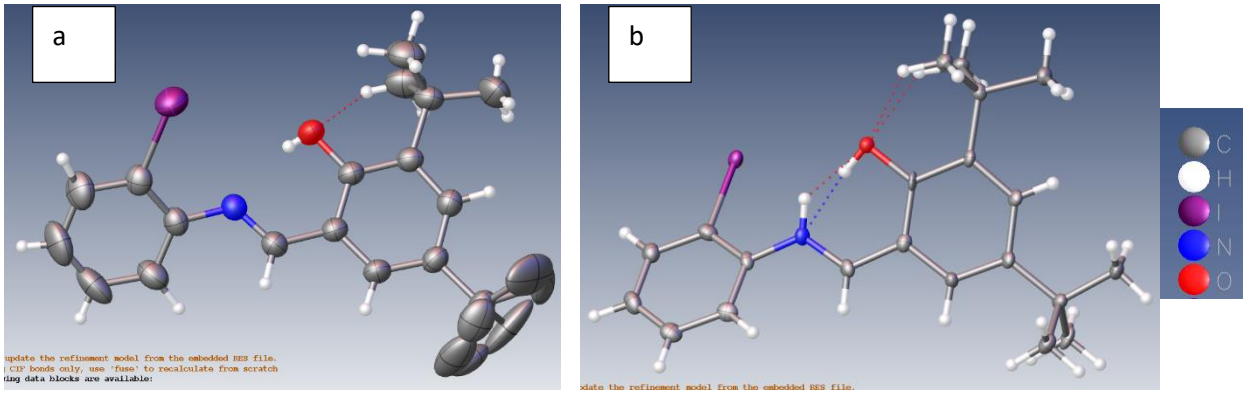


Figure 228: SCXRD structure of compound 18: a) Enol tautomer , b) Keto tautomer

The collection of Raman spectra was the third step in analysing this group of compounds first offline using bench top setups. To collect baseline spectral data for 3,5-di*tert*butyl-(salicylidene)-4-Iodoaniline, the Raman spectrometer used during the combined *in situ* Raman scattering and neutron diffraction experiment, was attached to a focusing microscope and employed the 785 nm near IR laser. At room temperature (298 K) the spectrum presents a distinct fluorescent background with peaks associated with both the keto and enol structures, in agreement with the X-ray diffraction results which demonstrate the presence of both the enol and keto structures at all temperatures (Fig 229).

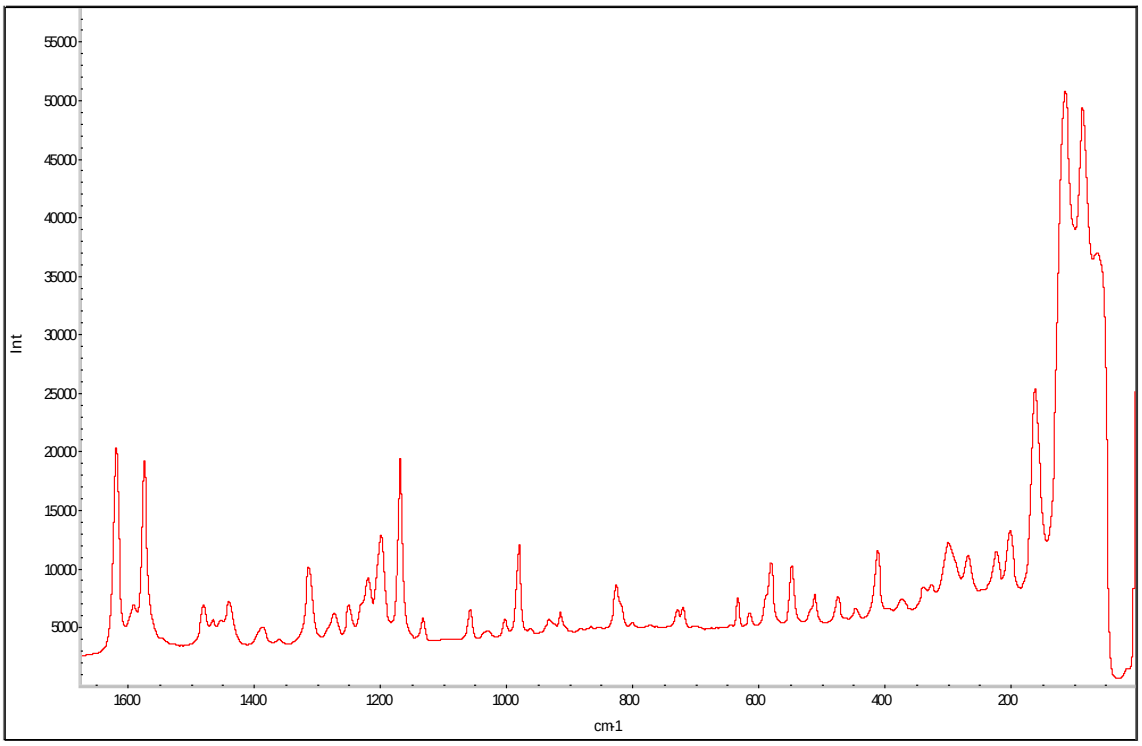


Figure 229: Raman spectra of compound 11 at 298 K

For 3,5-di*tert*butylsalicylidene-2-Iodoaniline a series of variable temperature Raman spectra were collected at ISIS, showed variations in the peak positions that coincide with expected configurational changes within the molecule (Fig 230). The measurements were done with the portable Raman spectrometer used during the *in situ* Raman scattering and neutron diffraction measurements which only allows for a relatively low resolution.

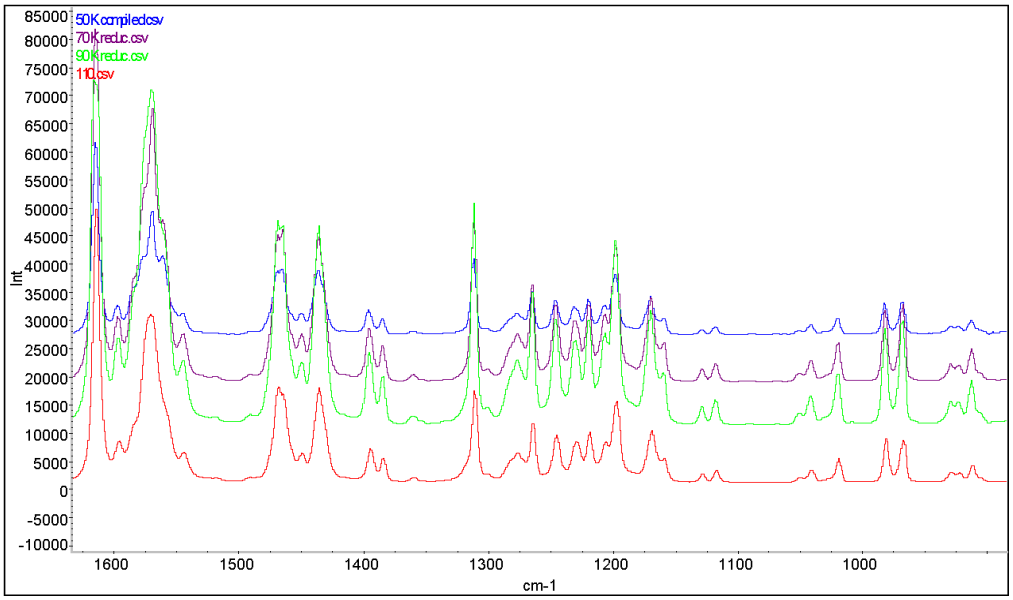


Figure 230: 1640 - 800 cm^{-1} region of offline low temperature collection for compound 18

To get a better understanding of the structural changes observed, high resolution spectra were collected by Dr Leonardo Del Rosso at temperatures ranging from 11 to 290 K at IFAC, CNR, Italy. The spectra were collected in 4 windows to cover a range between 1800 and 30 cm^{-1} with centres at 300, 800, 1300 and 1600 cm^{-1}. A high wavenumber region with the centre 3000 cm^{-1} was also sampled at 3 temperatures (290, 110 and 20 K). The difference in resolution between the two spectrometers can be seen by directly comparing the data collected at 110 K (Fig 231), where peak splitting (blue arrow) can already be seen in the high-resolution data that are not present in the ISIS Raman data. There is also less peak broadening present in the high-resolution data.

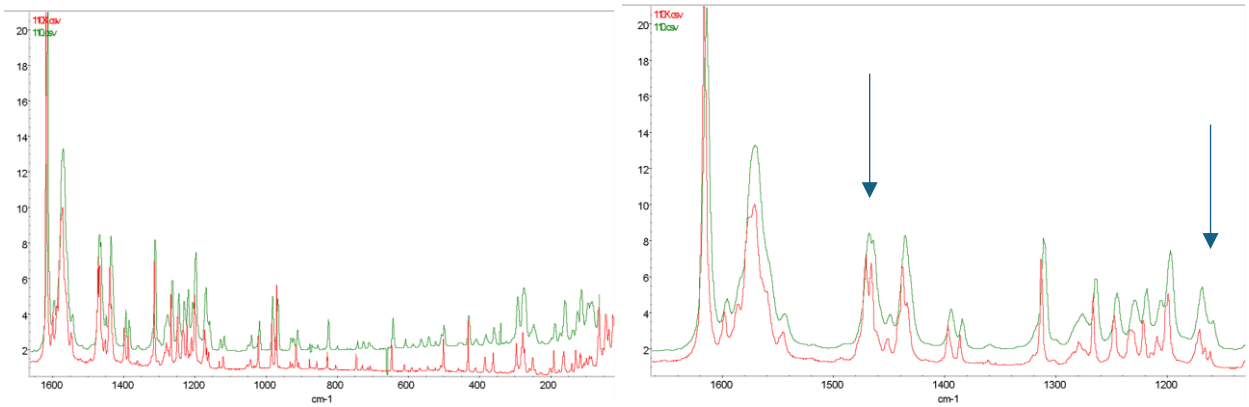


Figure 231: Comparison between insitu (Green) and High resolution (red) Raman spectra at 110 K for compound 18

The peak assignments were finalised with the help of DFT simulations of the Raman spectra utilising the CASTEP software for each of the two tautomers. The overall trend across the

temperature range showed that as the temperature was decreased, more peaks could be assigned to the Keto tautomer than to the enol tautomer. New peaks developed but also peaks already present resolved, split, or moved. To monitor the increase of the keto compound throughout the experiment, specific peaks were identified that only corresponded to the keto tautomer (Fig 232). These were at 1129, 1118, 1041 and 1028 cm^{-1} (Table 6).

Table 6: peak position and assignment for tautomer monitoring region of compound 18 (full table in appendix)

Peak position (cm^{-1})	**Keto - assignment**	**Enol - assignment**
1129.79	NH wag	
1118.95	NH/Ar-H wag	
1089		Aniline ring deformation
1069		*Tert*butyl asymmetric stretch
1051.69		*Tert*butyl CH/ aniline ring deformation
1041.78	CH, NH wag aniline ring deformation	
1032.76		Aniline ring deformation
1028.88	NH wag	
1020.54	NH OOP wag	*Tert*-butyl/ aldehyde ring deformations
1009	*Tert*butyl asymmetric stretch/ aniline ring deformation	

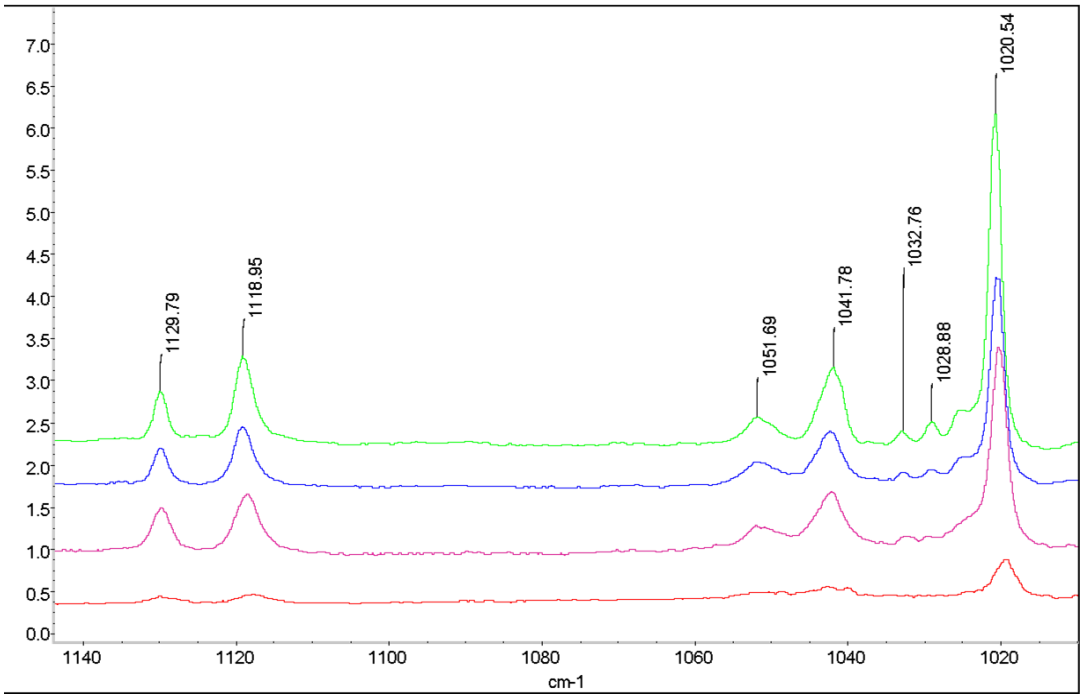


Figure 232: Spectra of tautomer monitoring region. 11 K (Green), 50 K (Blue), 170 K(Purple), 280 K (Red) of compound 18 showing development of new peaks associated with the keto tautomer upon decreasing temperature..

For the peaks assigned to the keto tautomer the overall trend is an increase in intensity with a decrease in temperature, with some peaks only beginning to develop once the temperature reaches around 100 K (Fig 233).

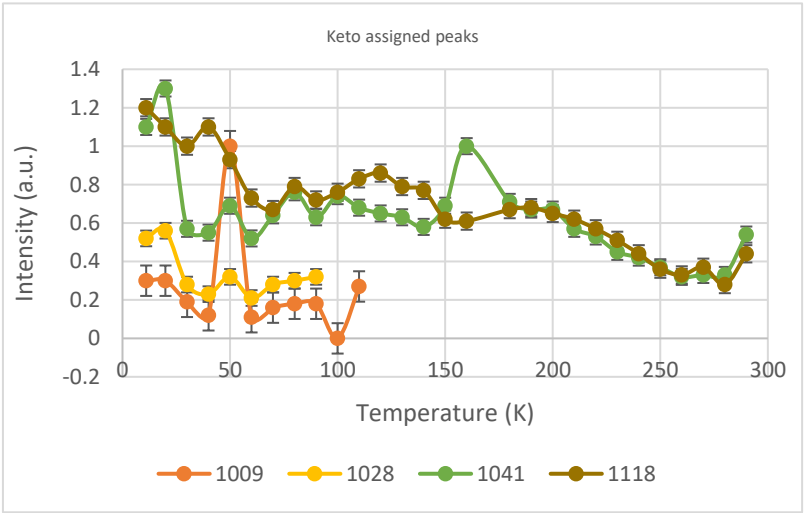


Figure 233: Graph showing the trend of intensities in the peaks assigned to the keto tautomer for compound 18.

Whilst the enol tautomer assigned peaks (1032 and 1051 cm^{-1}) have a relatively consistent intensity across the entire temperature range, some peaks are not present at all temperatures (Fig 234). The only exception were the data points at 11 and 20 K for the peak at 1020 cm^{-1} (Fig 235). This is due to an increase in the keto occupancy and hence an increased contribution to that peak's intensity from the NH OOP wag.

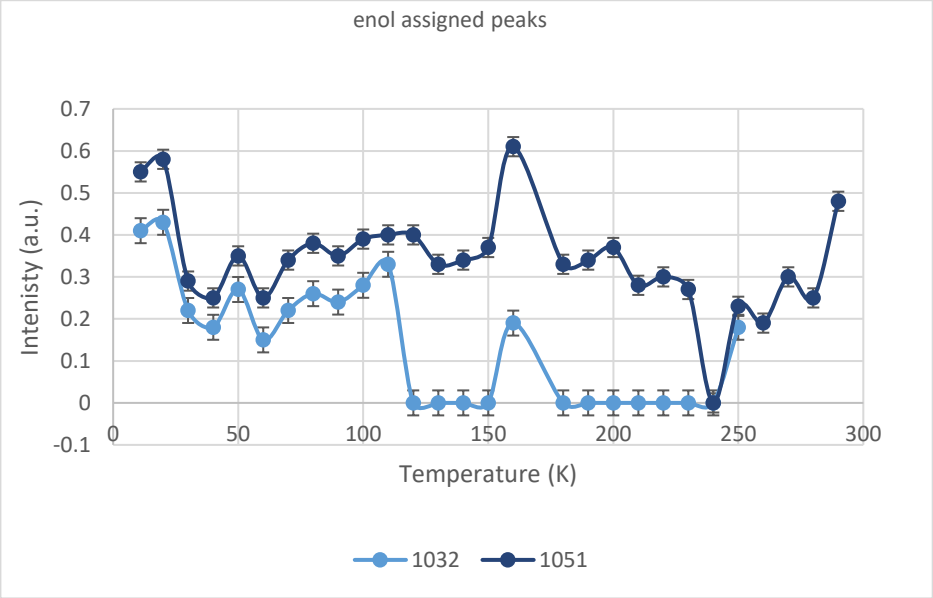


Figure 234: Graph showing the trend of intensities in the peaks assigned to the enol tautomer for compound 18.

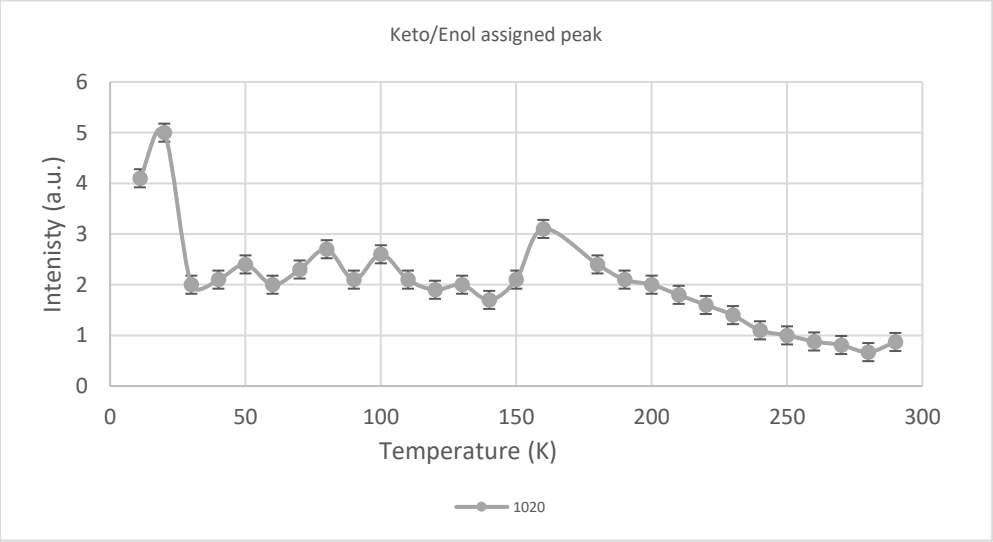


Figure 235: Graph showing the trend of intensities in the peak assigned to both tautomers for compound 18.

The second region of interest is between 1680 and 1140 cm^{-1}. In this region it is again possible to see the development of the keto structure with new peaks developing. Additionally, there was

splitting of peaks merged at high temperatures into the separate vibrations at lower temperatures.

In the first temperature range 290 – 170 K (Fig 236) the peaks are sharpening and increasing in intensity as the temperature is decreased. In the second temperature range between 170 and 100 K there are slight variations in the lattice vibration region (Fig 237) with additional peak splitting.

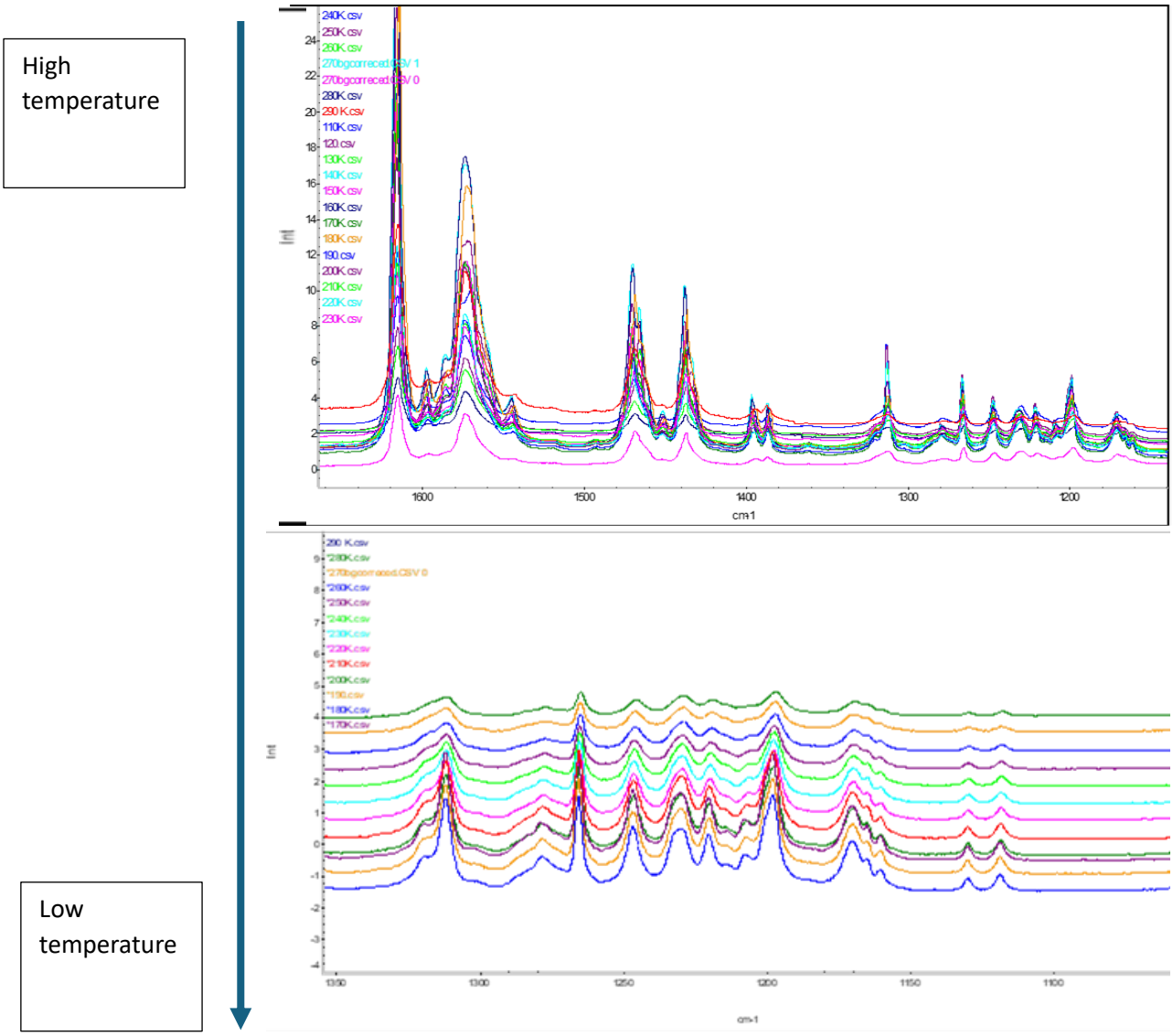


Figure 236: Raman spectra expansions demonstrating peak changes between 290 and 170 K in compound 18.

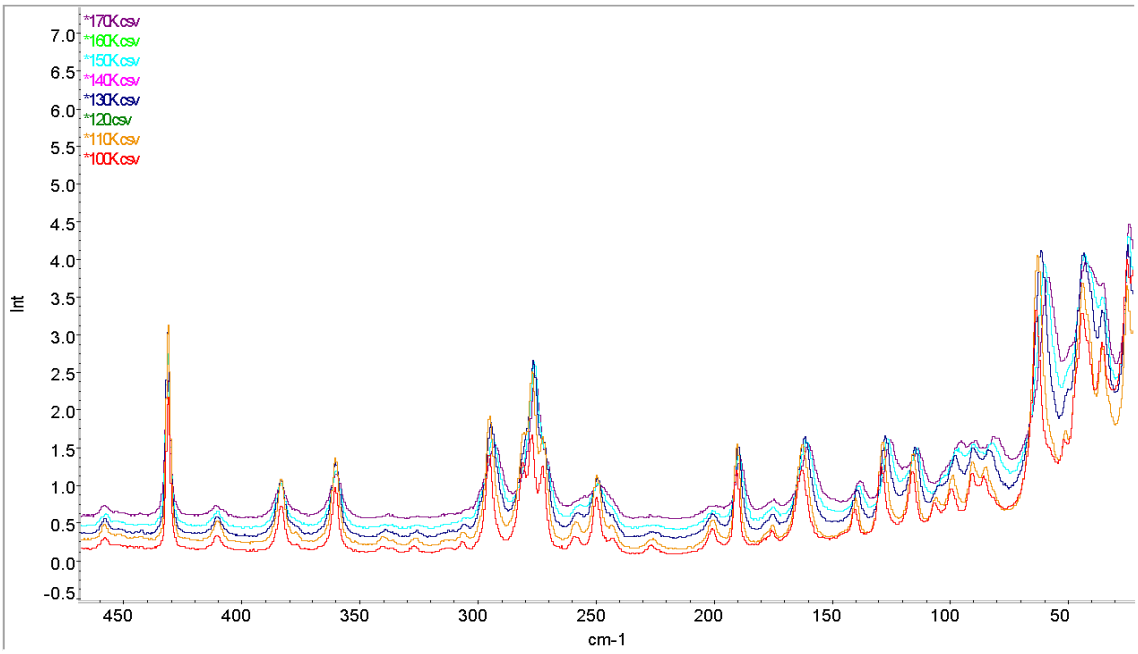


Figure 237: Raman spectra expansion of the lattice vibration region between 170 and 100 K of compound 18

In the third temperature range between 100 K and 50 K (Fig 238) more peak splitting can be seen,

as well as new peaks appearing that can be assigned to the keto tautomer (Table 7).

Table 7: peak assignments at 100 K for compound 18 (full table found in appendix)

Peak position (cm^{-1})	**Keto assignment**	**Enol assignment**
1616.04		OH bend
1598.44	NH bend, CN stretch	
1586.30	NH bend, CH wag	
1578.05	Aniline ring deformations	
1571.11	Aniline ring deformations	
1562.50	Aniline ring deformations, NH bend	Aniline ring deformations, OH bend
1545.35	Aniline ring deformations	
1470.79	*Tert*-butyl CH bends	
1465.56	*Tert*-butyl CH bends	
1450.38	*Tert*-butyl CH bends	
1437.84	*Tert*-butyl CH bends	
1433.53	*Tert*-butyl CH wag	
1397.07		*Tert*-butyl CH wag
1385.76	*Tert*-butyl CH wag	
1360.50	*Tert*-butyl CH wag	
1312.79	Ring CH wag	
1279.32	deformation	
1266.07	Deformation	
1247.18		*Tert*-butyl deformation
1233.26	Ring CH deformations	*Tert*-butyl deformation
1220.77	Ring CH wag	
1208.71	CH bend	
1200.61	Imine CH/ NH wag	
1198.10	CH wag	
1170.26	Imine CH/ NH wag	
1165.01		Aldehyde ring CH wag
1160.03		Aniline ring CH wag

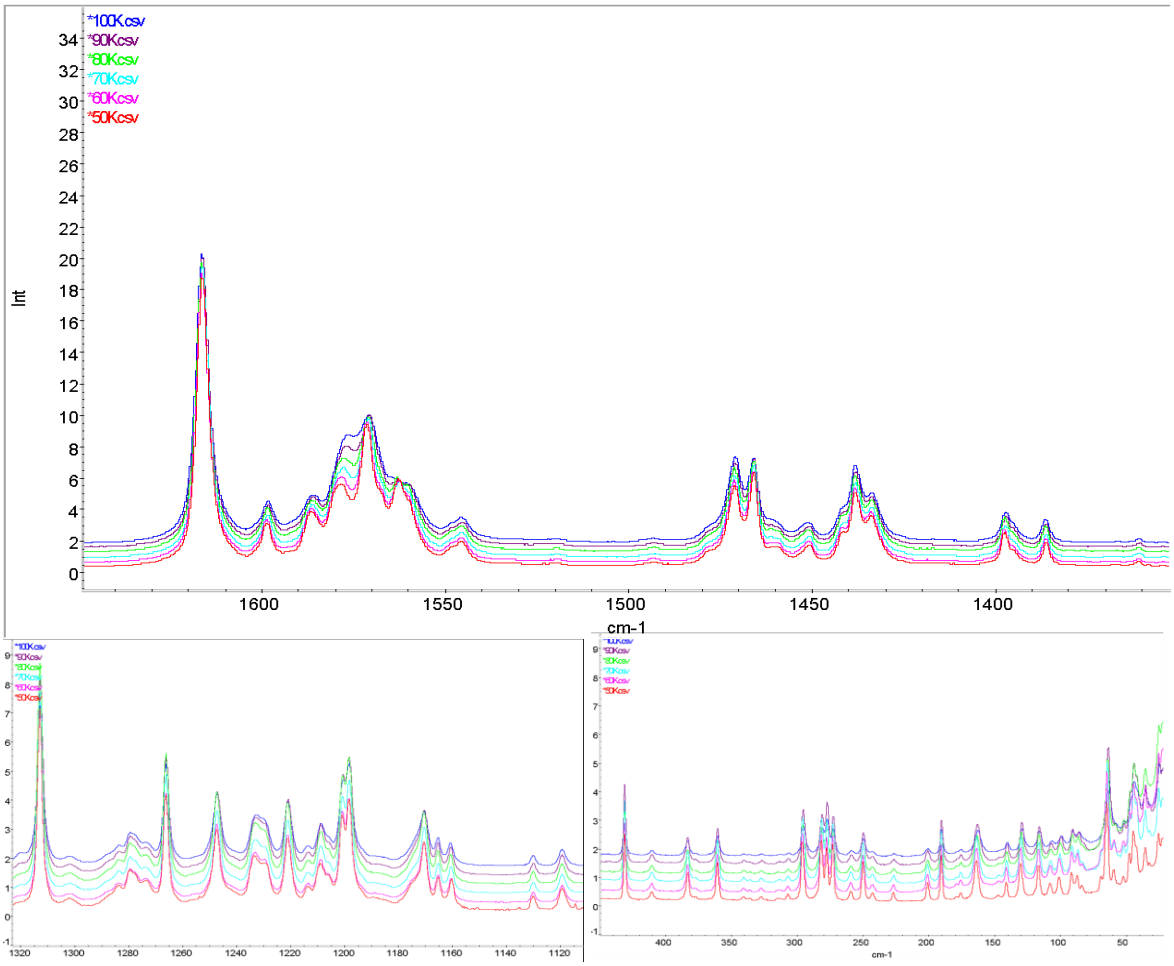


Figure 238: Raman spectra expansions demonstrating peak changes between 100 and 50 K in compound 18

Below 50 K (Fig 239) the overall peak resolution between increases and there are further changes in the lattice vibration region (Table 8), including increases in intensity for peaks already present.

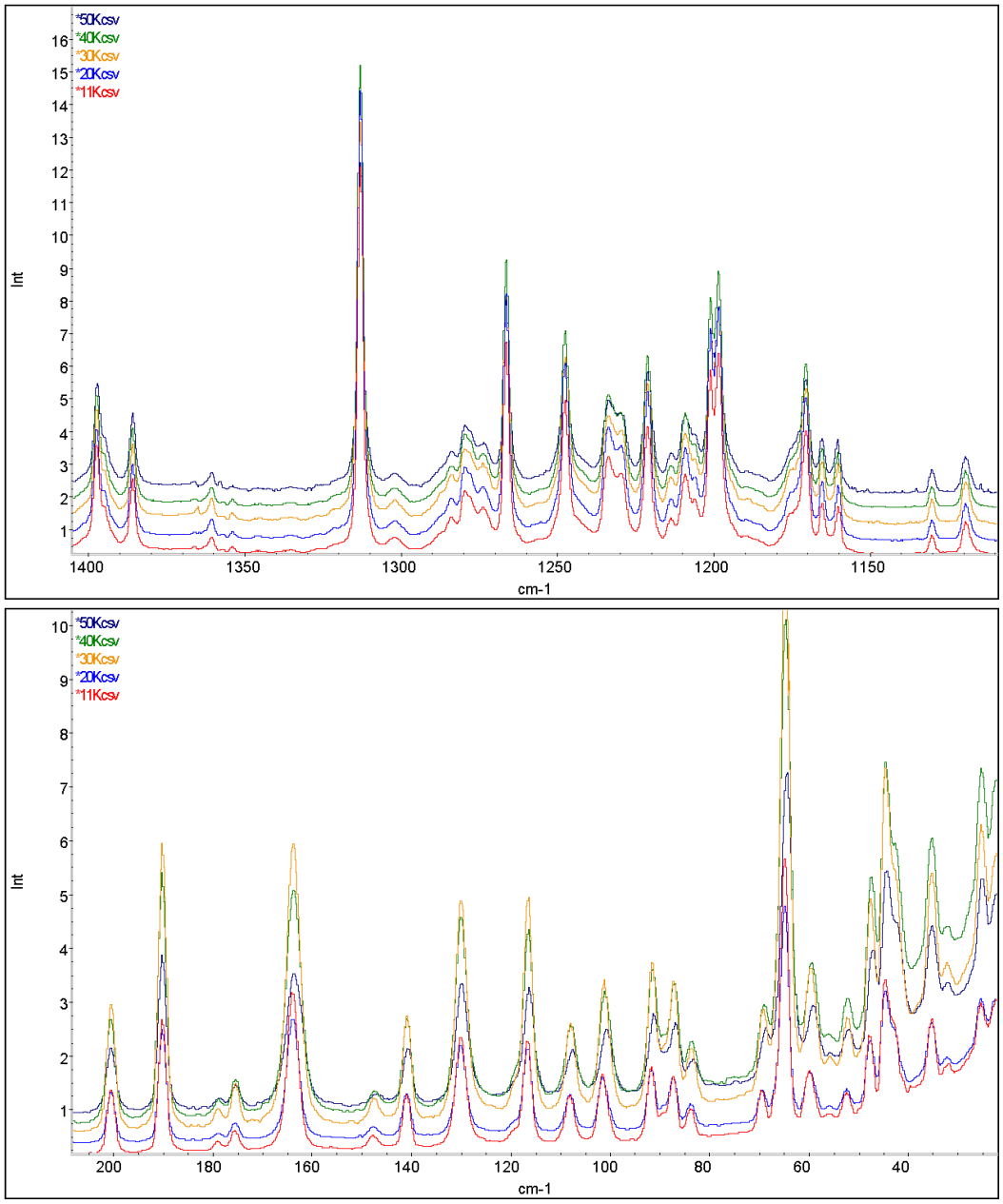


Figure 239: Raman spectra expansions demonstrating peak changes between 50 and 11 K for compound 18.

Table 8: peak assignments at 11 K for compound 18 (full table in appendix)

Peak position (cm^{-1})	**Keto assignment**	**Enol assignment**
1616.10		OH bend
1598.66	NH OOP bend	Aniline ring deformation
1586.58	NH OOP bend	
1578.78	Aniline ring deformation	
1571.47		Aniline ring deformation
1562.80	Aniline ring deformation	
1545.51	Aniline ring deformation	
1518.86		3-Tert-butyl asymmetric CH bend
1493.27		3-Tert-butyl asymmetric CH bend
1470.92		3-Tert-butyl asymmetric CH bend
1465.59	Tert-butyl asymmetric CH bend	
1458.81	CH bends	
1450.48	Tert-butyl asymmetric CH bend	
1441.31	Tert-butyl asymmetric CH bend	
1397.25	N OOP deformation	
1385.78		Tert-butyl symmetric CH bend(umbrella)
1360.56	Tert-butyl symmetric CH bend (umbrella)	
1312.84	Ring OOP CH bends, OOP NH bend	
1301.87		Ring CH bends
1283.72	Ring deformations	Tert-butyl symmetric CH bend (umbrella)
1279.39	Ring OOP CH bends, OOP NH bend	
1273.62		Imine CH OOP bend
1266.13		Imine CH OOP bend
1247.27		Tert-butyl CH wag
1233.40	Ar-H bends	
1229.33	CH deformations	
1220.84	Ar-H bends	
1220.84	Ar-H bends	
1213.37		Aniline Ar-H bend, Tert-butyl CH wag, OH bend
1208.76	Imine CH OOP bend	
1205.77	Imine CH OOP bend	
1200.70	Imine CH OOP bend, NH wag	
1198.16	Tertbutyl CH bend	
1170.21	Imine CH bend, NH wag, Tert-butyl CH bend	
1164.93		Aldehyde Ar-H bend
1159.75		Aniline Ar-H bend

Peak assignments confirmed that there was an increase in the keto occupancy as the temperature decreased. However, it was not until the temperature was below 50 K that any major structural changes were easily observed, despite indications beginning to appear at around 100 K.

The final step was collecting single crystal neutron diffraction data and accompanying *in situ* Raman scattering spectra where possible, for both the 4-Iodo and 2-Iodo analogues. It was not possible to collect this data for the 3-Iodo analogue due to lack of both beam time and a usable sized good quality crystal.

The initial set of data for 3-5-di*tert*butylsalicylidene-4-Iodoaniline (compound 11) was collected at 250 K using the *in situ* Raman scattering centre stick with two sample chambers; a quartz capillary holding the crystal for the neutron diffraction experiment and, an optical chamber which was filled with multiple smaller crystals for collecting the Raman scattering spectra. At this temperature both the cis-keto and cis-enol states were found at a 40.0(2) : 60.0(2) ratio (Fig 240).

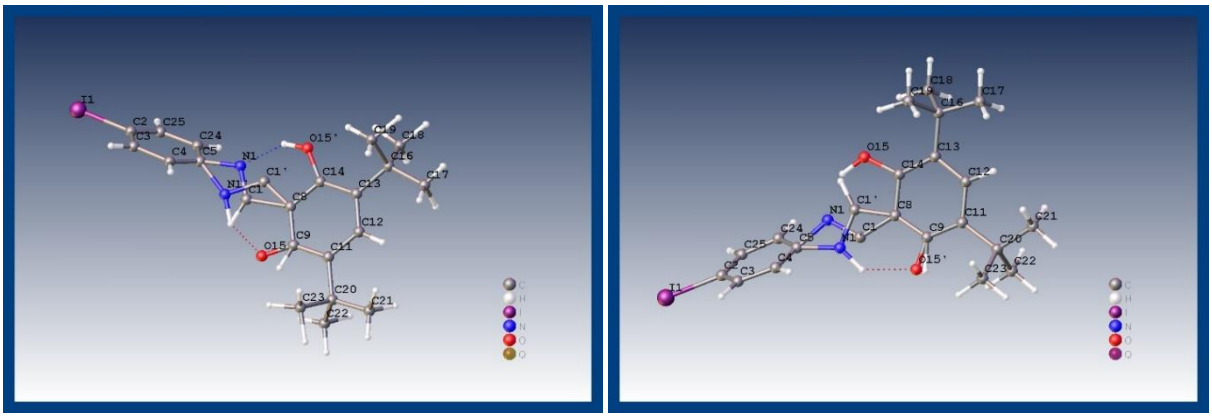


Figure 240: Neutron diffraction structure of compound 11 at 250 K (left) and 110 K (right)

Table 9: Enol and Keto occupancies form neutron diffraction at variable temperatures

Temperature (K)	Irradiated	OH Occupancy (%)	NH Occupancy (%)	Dihedral angle (°) Enol	Dihedral angle (°) Keto
250	NO	60.15(2)	39.85(22)	66.22(14)	65.41(21)
110	NO	56.58(31)	43.42(21)	64.64(11)	63.44(24)
280	Yes	61.12(21)	38.88(23)	65.07(21)	65.59(22)

A second set of data was collected at 110 K using the same experimental setup. Again, both the keto and enol tautomers were present though the ratio shifted to a 44.3(2) : 55.7(1) (Table 9). At 110 K Raman spectra were collected when the beam was both off and on, in order to see whether the neutron beam had any effect on the data (as seen in Fig 241, no effect was observed on the Raman spectra).

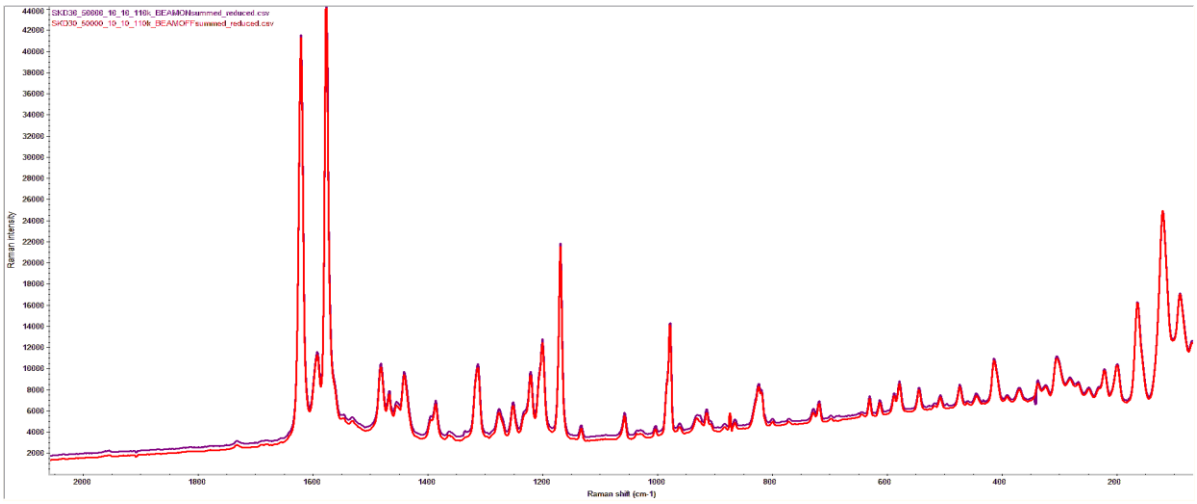


Figure 241: Raman spectra of compound 11 collected in-situ when the neutron beam was on(purple) and off (red)

When comparing the Raman spectra at 250 K and 110 K, there is a slight increase in the fluorescent background with decreasing temperature, while the relative intensities and positions of the peaks show no significant changes. This is further confirmed when comparing the initial spectrum collected at 295 K (RT), though between RT and 250 K there are large increases in relative peak intensities (Fig 242). Major changes in peak position were not expected for this compound due to both structures being present at all temperatures and no extreme shifts in the ratio of occupancies of the two tautomers.

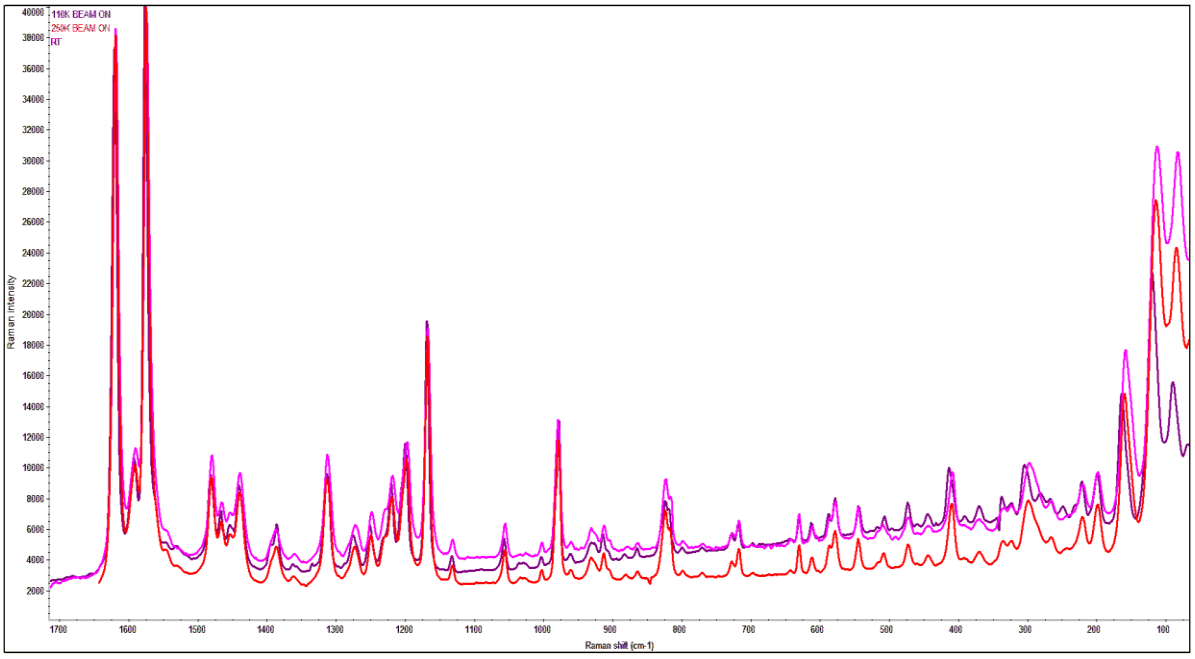


Figure 243: Raman spectra collected in-situ at 110 K (purple), 250 K (red) and RT (pink)

A second experiment was conducted on an irradiated crystal of 3,5-di*tert*butyl-(salicylidene)-4-iodoaniline (Fig 243). The crystal was centred with respect to the Raman laser and neutron beam within the sample holder capillary and irradiated overnight with the 365 nm UV lamp in a dark box. For this experiment the sample chamber allowed for the Raman laser to be focused directly on the sample situated in the neutron beam. In order to minimise the amount of white light seen by the irradiated crystal during mounting on the central stick in the CCD on the SXD instrument, the capillary was wrapped in aluminium.

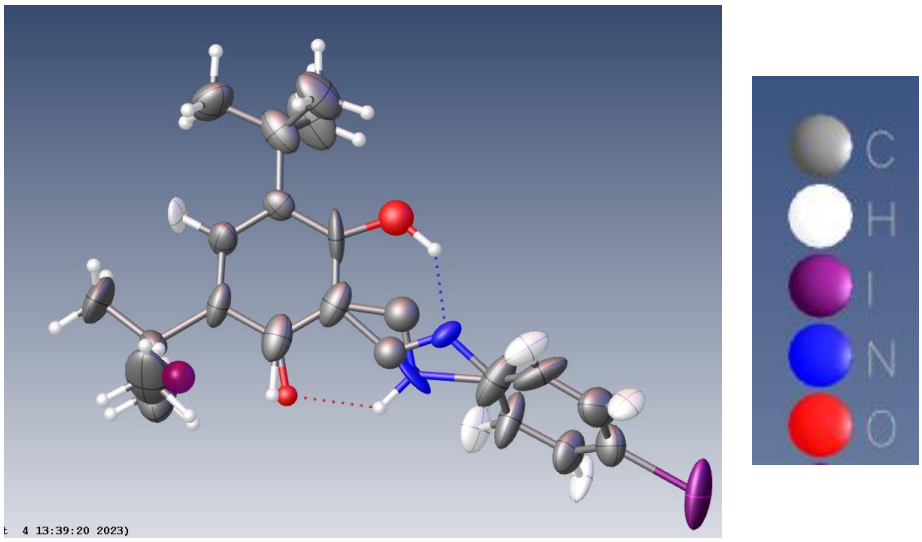


Figure 242: Neutron diffraction structure of irradiated state of compound 11.

Results from this experiment showed that unlike in the case of the X-ray experiment with the *in situ* irradiated sample, the excited trans-keto state was not identified. The only structure identified was that of the cis-keto state as seen in the non-irradiated sample. When removed from SXD the crystal retained the deep colour associated with the irradiated state.

Non-observation of the excited keto state could be a consequence of the samples no longer being under UV irradiation. There is likely to be a brief period of time after the removal of the irradiation when the excited keto state could be observed but it is unknown for how long this lasts. The deep colouration that the crystals maintained, even after over a day in the neutron beam, could be an artifact of the excitation and relaxes back to the non-irradiated state with a hysteresis. It was found that the reversion times for these 3,5-di*tert*butyl- materials at a controlled temperature in the dark exceeds 3 weeks, while the excitation to the point where surface colouration is visible takes as little as one hour. Our previous x-ray experiment in which the samples were irradiated *in situ*, demonstrated that under continuous irradiation it was possible to identify the excited keto state after a period of 11-19 hours depending on the compound.

The Raman spectra collected both online of the irradiated and non-irradiated structures of 3-5-di*tert*butylsalicylidene-4-iodoaniline were compared against the offline Raman spectra collected using same spectrometer from the *in situ* Raman stick with the microscope configuration (Fig 244). There are very few distinct differences between the irradiated and non-irradiated spectra, this was expected as both the keto and enol tautomers are constantly present irrespective of state or temperature. Upon irradiation there is an increased fluorescent background, the offline vs online irradiated samples show a difference in the noise level of the background.

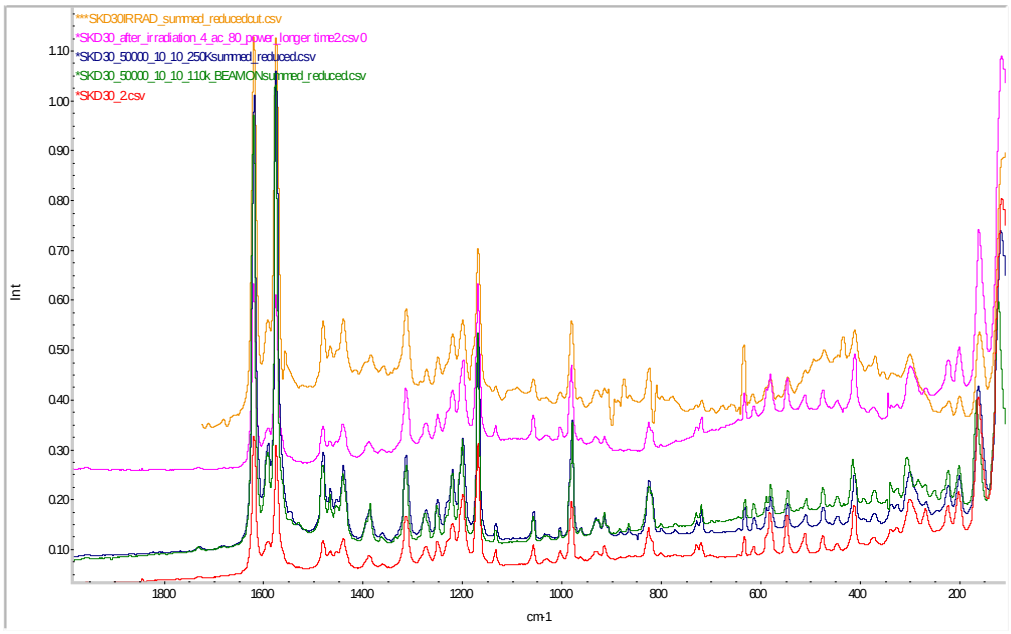


Figure 244: Comparisons of variable temperature non-irradiated and 280 K irradiated Raman spectra of compound 11. Orange- irradiated, purple – irradiated extended collection, blue- 250 K on beam line, green – 110 K on beam line and red - 295 K.

In comparison for the 3-5-di*tert*butylsalicylidene-2-iodoaniline Data was collected initially at 110 K using the *in situ* Raman scattering central stick in its dual chamber configuration (Fig 245). At this temperature the enol tautomer was the only one identified with no rotational disorder around either of the *tert*butyl groups.

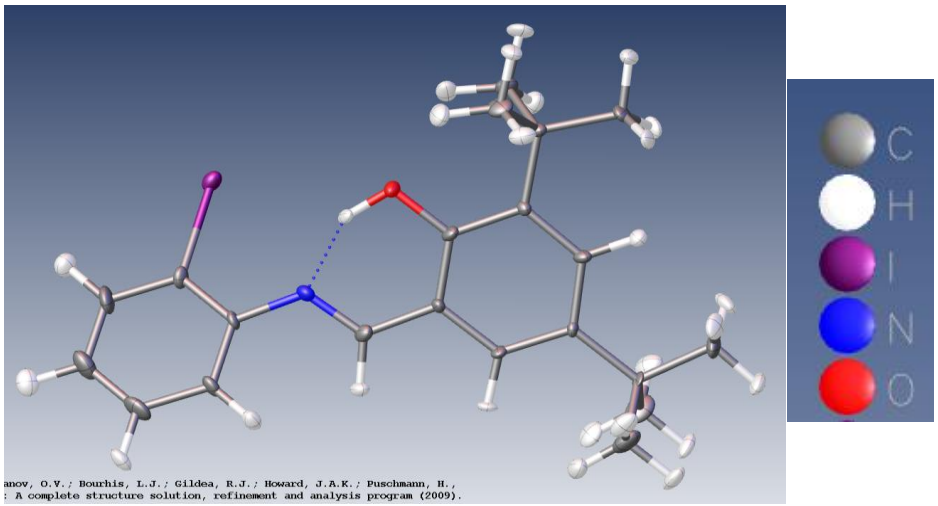


Figure 245: Structure for neutron diffraction experiment at 110 K of compound 18

The second data set was collected again using the *in situ* Raman scattering central stick, this time utilising the single sample chamber configuration. As data had already been collected at 110 K the first data collection attempt was made at 10 K however, as the experiment continued it became apparent that the intensity of the Bragg peaks were decreasing. Reciprocal space reconstructions at both 110 and 10 K, showed a large increase in the background compared to the peak intensity at 10 K over 110 K (Fig 246). There was peak splitting and powder rings, a sharp contrast to the clear periodic Bragg pattern seen at 110 K.

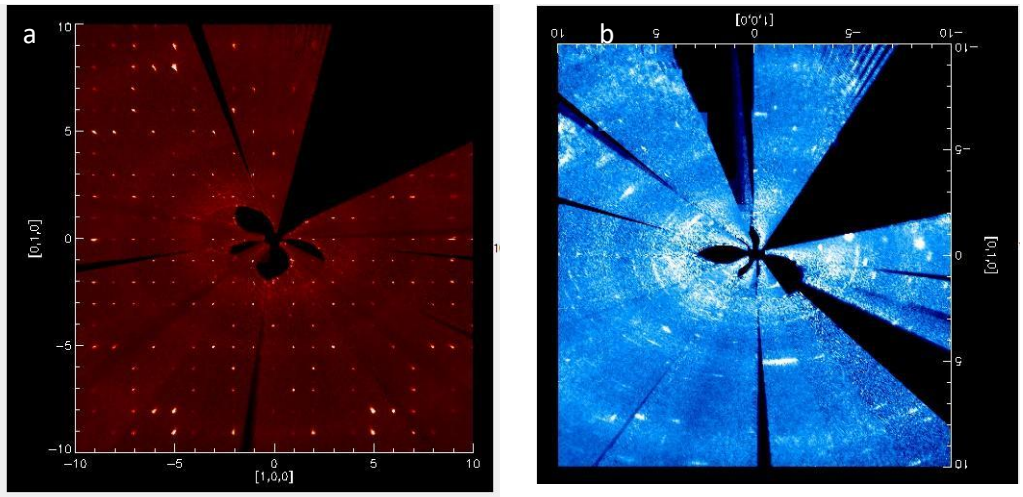


Figure 246: reciprocal space reconstructions at a) 110 K and b) 10 K of compound 18 from neutron diffraction data on SXD

Comparing the 10 K Neutron Data against the 50 K X-ray diffraction data, we could notice already at 50 K that something was happening to the crystal: each Bragg peak was split in two and additional peaks started to appear between the lattice planes (Fig 247). This is similar to what was seen with the other thermochromic materials in this type, 3,5-di*tert*butylsalicylideneaniline.

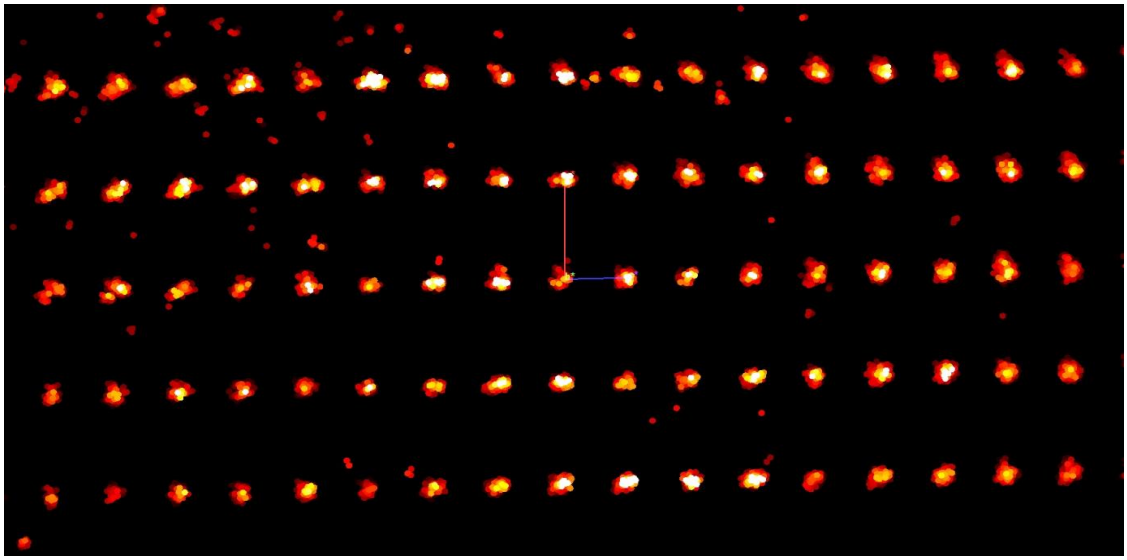


Figure 247: 50 K X-ray diffraction reciprocal space reconstruction of compound 18

The larger neutron crystal showed significant damage after the experiment which was not seen in the X-ray crystal. The sample had changed from a translucent yellow, to a clouded yellow, when examined more closely under the microscope, further alterations could be seen to the crystal with a number of cracks and fractures throughout (Fig 248). This level of damage in a crystal was not observed in other samples of the same series and can be an indication of stress building up in the crystal at very low temperatures.

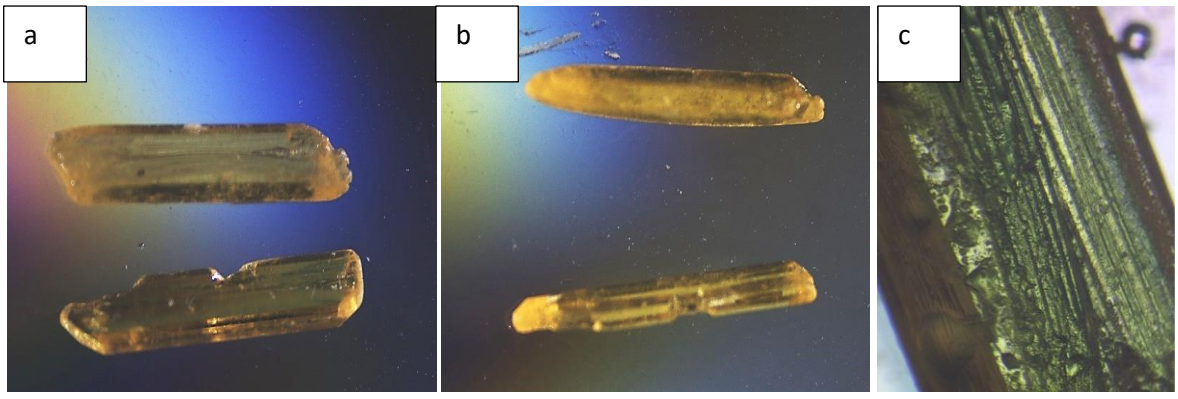


Figure 248: comparisons of a) pre- and b) post- neutron experiment crystals, c) close up image of post neutron experiment crystal damage in 3,5-ditertbutylsalicylidene-2-iodonailine.

Upon examining the Raman spectra collected *in situ* during the neutron diffraction experiments using the specialised Raman Spectrometer central stick, it can be observed that the intensity of the peaks decreased with the decreasing temperature (Fig 249). Between the first spectra taken at 10 K and the second (labelled as possibleLT) there is a clear drop off in the sample. Once

removed from the sample environment it became clear that the sample had moved so that it was no longer in the path of the Raman laser. This is further indication of possible physical damage to the crystal as each end had been stuck in place within the capillary using vacuum grease. In the second collection at 10 K (possibleLT) there are no identifiable data peaks in the spectrum, hence, it is unusable for investigating structural changes.

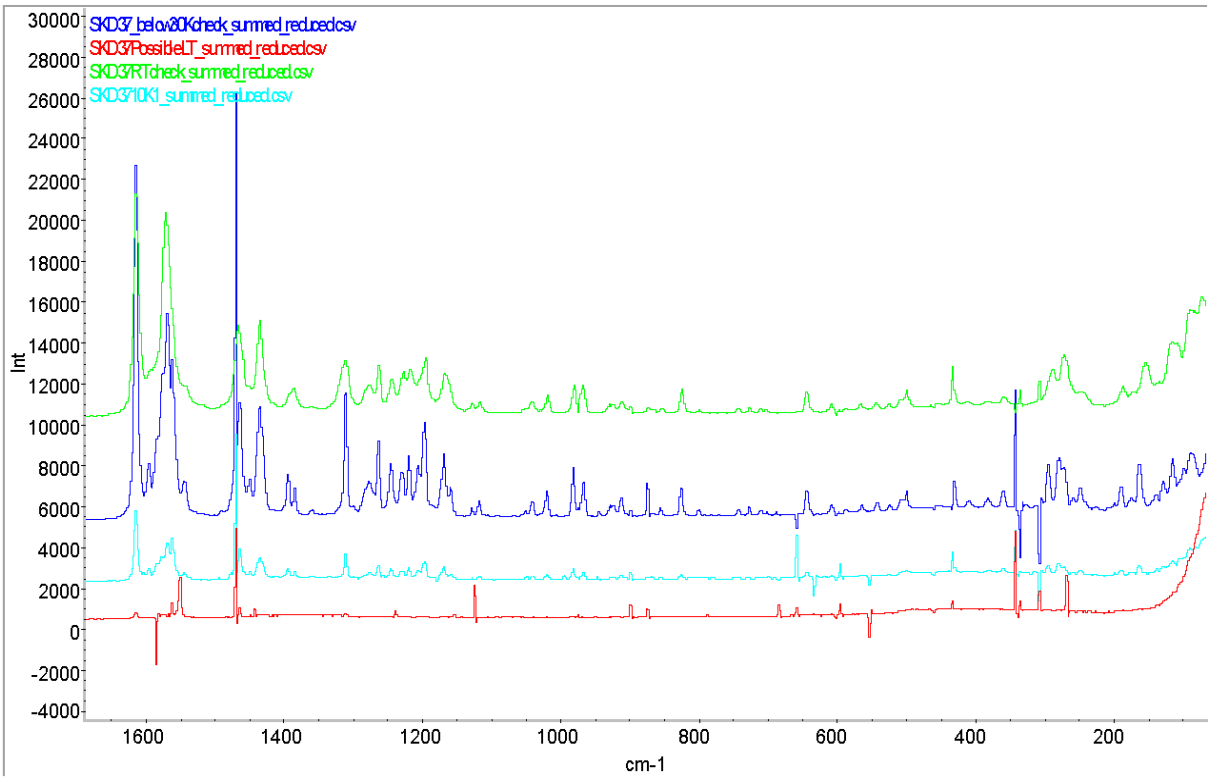


Figure 249: Variable temperature Raman spectra collected insitu of compound 18. Blue - < 30 K, red – second check at 10 K, green, 295 K, turquoise – 10 K.

In the spectra between the RT and below 30 K there are increases in intensity of the peaks at low wavenumbers (Fig 250). In the peaks between 230 and 280 cm^{-1} there is a mixture of peak merging and peak splitting, below this there are increases in the resolution between peaks. This is caused by the shift between the keto and enol tautomers and hence the relative strength or position of those peaks within that structure.

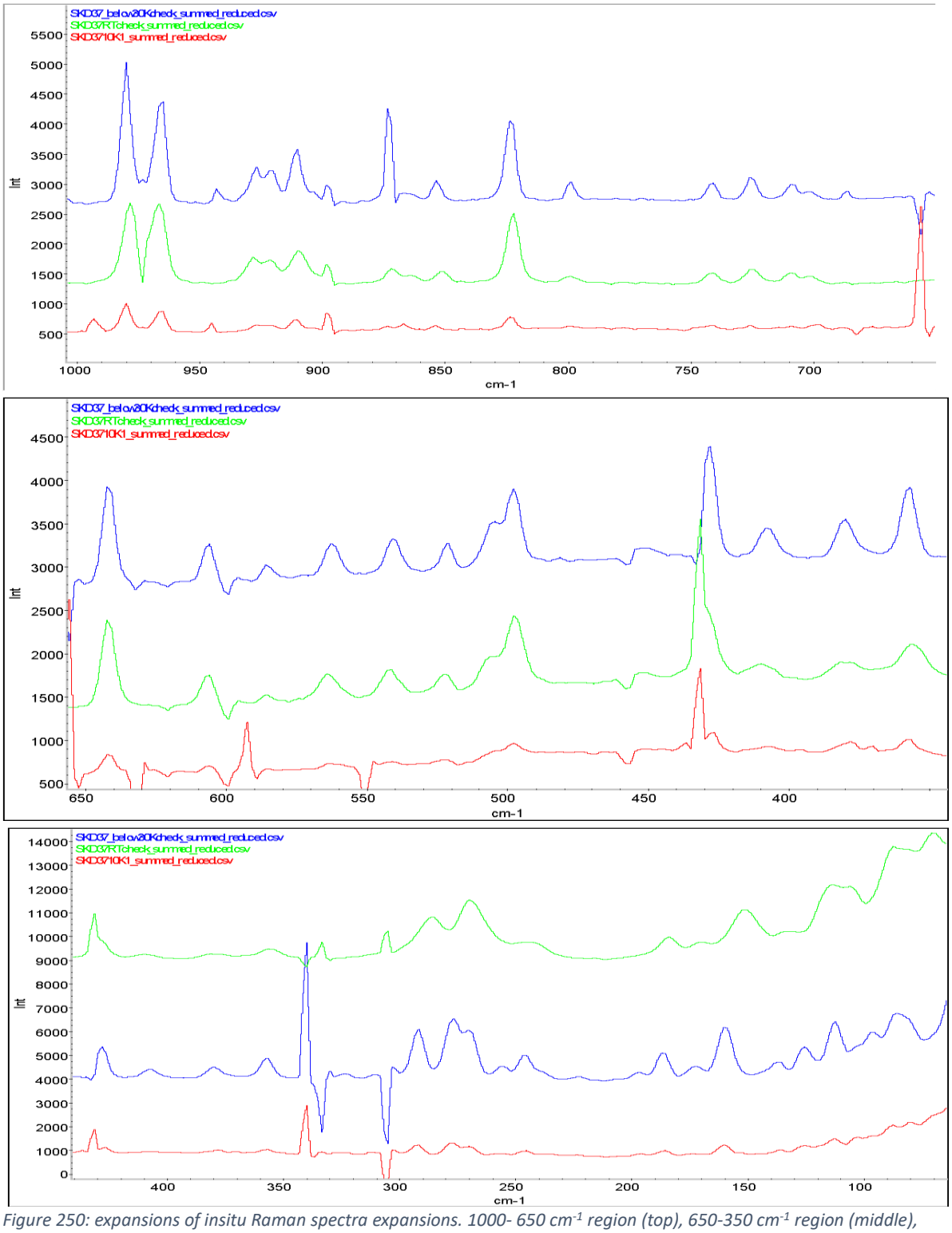


Figure 250: expansions of insitu Raman spectra expansions. 1000- 650 cm^{-1} region (top), 650-350 cm^{-1} region (middle), 450 -40 cm^{-1} region (bottom). Blue- below 30 K, Red- 10 K, Green – 295 K.

In the 1350 to 1000 cm^{-1} region the two peaks at 1240 and 1230 cm^{-1} are clearly resolved, whilst there is peak splitting from the two original peaks seen between 1210 and 1140 cm^{-1}. There are intensity shifts for the peaks seen between 1100 and 1130 cm^{-1} between the room temperature and below 30 K check, but the lack of peak intensity makes any changes difficult to identify (Fig 251).

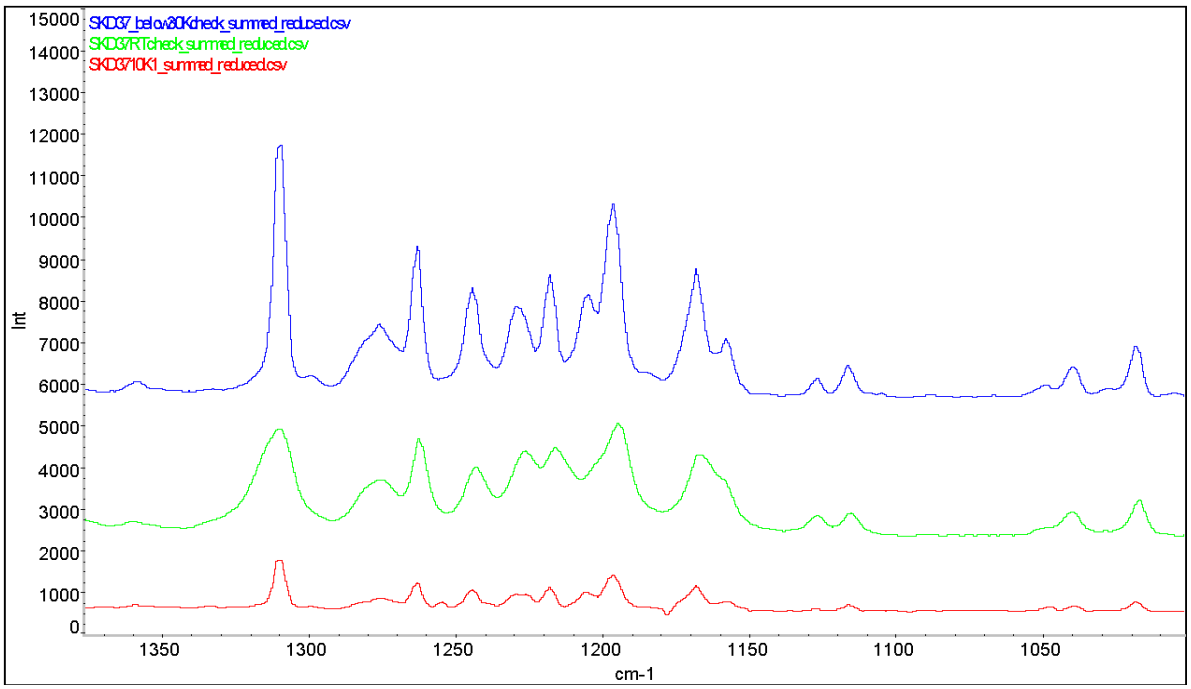


Figure 251: 1350 - 1000 cm^{-1} expansion of the insitu Raman spectra for compound 18: 300 K green, <30 K blue, 10 K red.

The next stage was to compare *in situ* collected data for 3,5-di*tert*butylsalicylidene-2-Iodoaniline to the high resolution data collected at IFAC. Comparing the RT *in situ* data to that collected at 270 K, in the 1620 to 110 cm^{-1} region, the peak matchup is fairly consistent, though the dual peaks clearly seen between 1440 and 1380 cm^{-1} are still merged in the data collected *in situ (Fig 252)*.

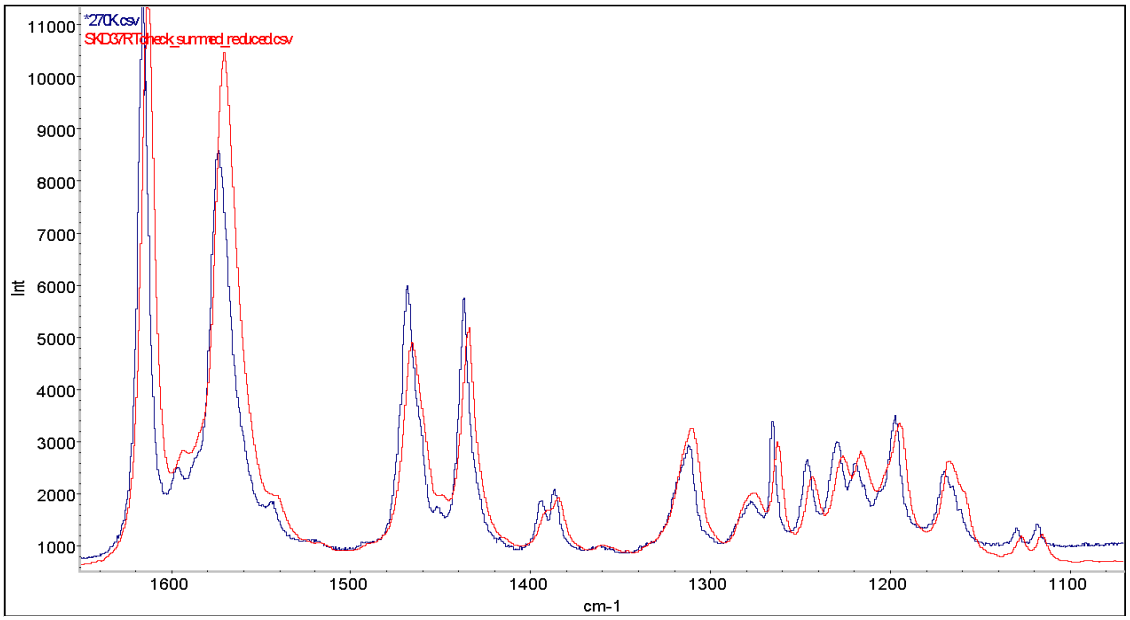


Figure 253: 1650-1090 cm^{-1} expansion of High resolution (blue) and in situ (red) Raman spectra of compound 18

The other comparison region at this temperature is 480 to 60 cm^{-1}, there are slight differences in peak positions between the *in situ* data and high resolution data (Fig 253). Overlapping peaks are not well resolved in the *in situ* data compared to the high resolution data, there are however, two extra peaks in the *in situ* data between 300 and 350 cm^{-1}.

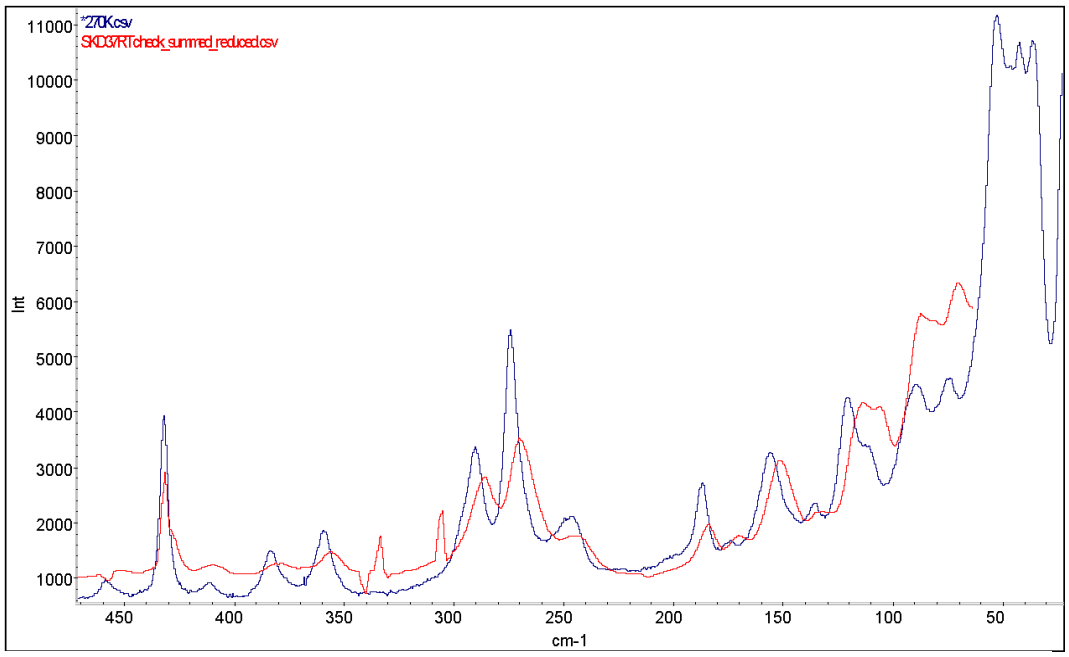


Figure 252: 480-30 cm^{-1} expansion of High resolution (blue) and insitu (red) Raman spectra of compound 18

Another comparison could be made between the spectra taken once the temperature reached below 30 K. The splitting of overlapping peaks is clearer in the high resolution data compared to the *in situ* data as expected, and some of the weaker peaks are more easily identifiable. Below 300 cm^{-1} there is an increased number of peaks in the data from IFAC, the broader peaks from the *in situ* data are separated into the individual components (Fig 254).

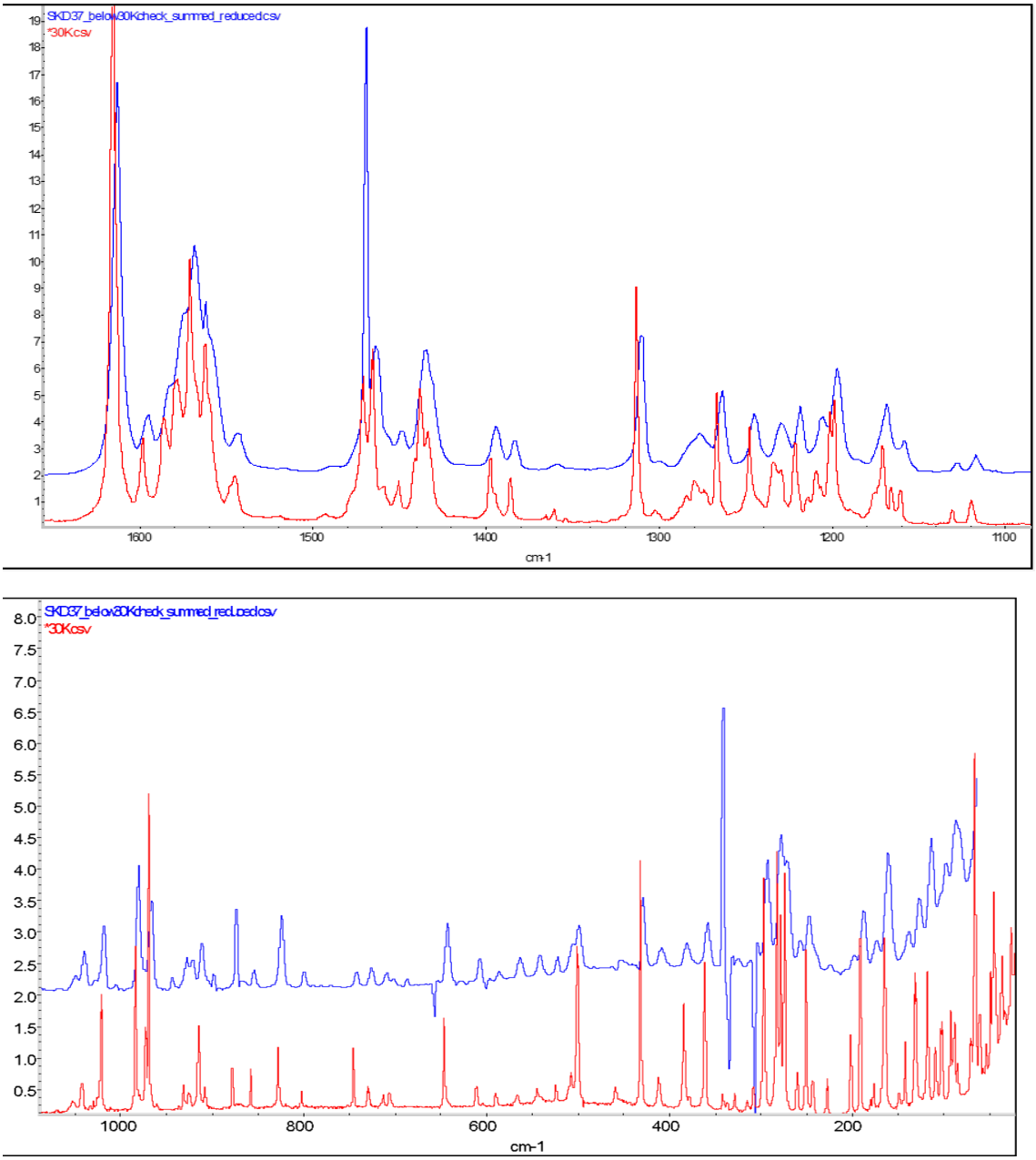


Figure 254: 1640-1090 cm^{-1} expansion of High resolution (red) and insitu (blue) Raman spectra of compound 18 (top), 1090-60 cm^{-1} expansion of High resolution (red) and insitu (blue) Raman spectra of compound 18 (bottom).

The final comparison is the first set of data collected at 10 K before the sample moved out of the Raman laser beam (Fig 255). The weak intensity of the *in situ* collected data in comparison to the high resolution data, means that some peaks easily identifiable in the latter are not well defined in the former. As with the other data set the higher resolution data allows a better clarity between otherwise overlapping peaks, though the peak positions are shifted to slightly higher wavenumbers. This could be due to the different wavelength laser used for the two experiments, 532 nm for the high resolution and 785 nm for the *in situ* data.



Figure 255: 1640-1090 cm^{-1} expansion of High resolution (red) and insitu (purple) Raman spectra of compound 18 (top), 1090 - 60 cm^{-1} expansion of High resolution (red) and insitu (purple) Raman spectra of compound 18 (bottom)

Intuitively, ortho and para substitutions of the iodine atom on the aniline ring should give similar macroscopic properties because of the same type of resonance structures produced on an aniline ring but experimental evidence gives a different picture. The position of the Iodine on the ring directly affects the electronegativity of the Imine-Nitrogen. In the meta/para position, the iodine should have an inductive effect increasing basicity of the Imine-Nitrogen and hence making it a stronger H-bond acceptor. Whilst in the ortho position the iodine decreases the basicity of the Imine-Nitrogen comparatively, making it a weaker H-bond acceptor[1]. As for the steric hindrance, the large iodine atom in the ortho position has a direct effect on the mobility the Imine-bridge, possibly restricting its rotation.

The dihedral angle between the two rings in the molecule has also a secondary effect on the intramolecular interactions in the solid state. The rotation of the aniline ring around the C-N bond, prevents the iodine atom from interacting directly with the delocalised electrons of the next nearest aniline ring in both 4-iodo and 3-iodo analogues. With the 3-iodo analogue there is no close interaction from the iodine to the neighbouring aniline ring as the distance between planes is over 3.7 Å even though the iodine atom is positioned centrally with regards to the nearest aniline ring hence, it is possible that there is a long distance interaction that has some halogen bond character stabilising the structure. Whilst in the 4-iodo analogue the iodine is positioned just off centre from the ring so that it cannot fully interact with the delocalised electrons. In contrast, with the 2-iodo analogue the only thermochromic material of the three, the iodine atom is positioned near-centrally with regards to the next nearest ring, so that it can interact with delocalised electrons of that ring restricting the rotation of the molecule and increasing the intermolecular interactions. The interaction is not end-to-centre but between parallel aniline ring planes (Fig 256).

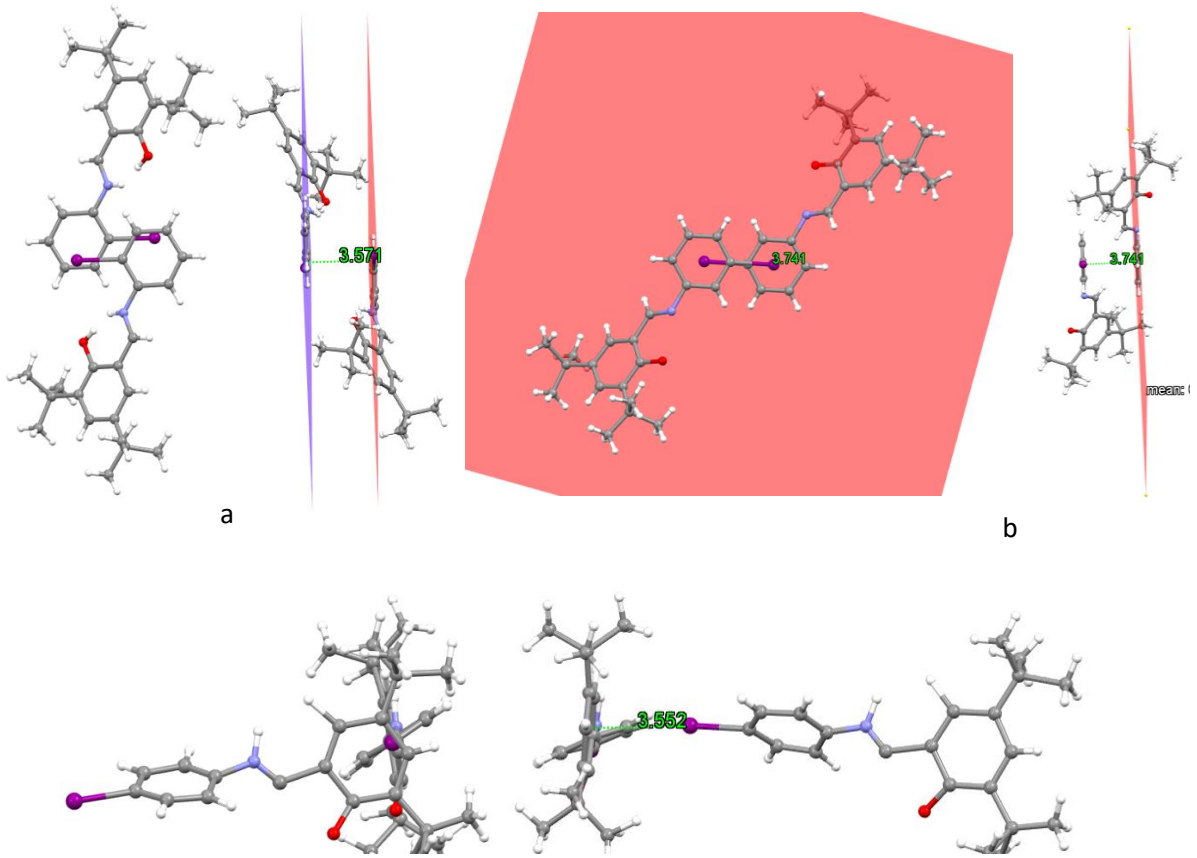


Figure 256: a) intermolecular interactions of Iodine in compound 18. b) intermolecular interactions of Iodine in compound 19. c) intermolecular interactions of Iodine in compound 11

4.3.3.3 Group 2: 4-bromo and 4-iodoaniline analogues

As described under group 1 N-(3,5-di-*tert*-butylsalycilidene)-4-iodoaniline is a photochromic material, with a dihedral angle of 64°. To assess N-(3,5-di-*tert*-butylsalycilidene)-4-bromoaniline for photochromic properties, a sample of the recrystallised material was first irradiated in the dark box (TLC) with a 365 nm UV-lamp, as with the other photochromic materials. In contrast to what had been expected as well as, what had been previously seen with the other two synthesised photochromic materials, there was no colour change of the crystals after being irradiated for 3 hours. To assess if a longer irradiation time was required, the sample was returned to the dark box and left for 18 hours after which it was removed and was found to have retained the colouration associated with the non-irradiated state. A different UV source was obtained specifically for irradiating the photochromic samples, and a new dark box was created from a polystyrene box and black vinyl bag. When irradiated overnight with the new lamp

for at least 18 hours, the crystal underwent the expected colour change (yellow to orange) (Fig 257). The different result with the new irradiation conditions might mean that the initial dark box was not completely enclosed from natural light in the same way as the second box was. The requirement for a tinted viewing window to see the TLC plates as well as the fabric panel through which the plates are placed in the box allowed a small amount of light in[1].

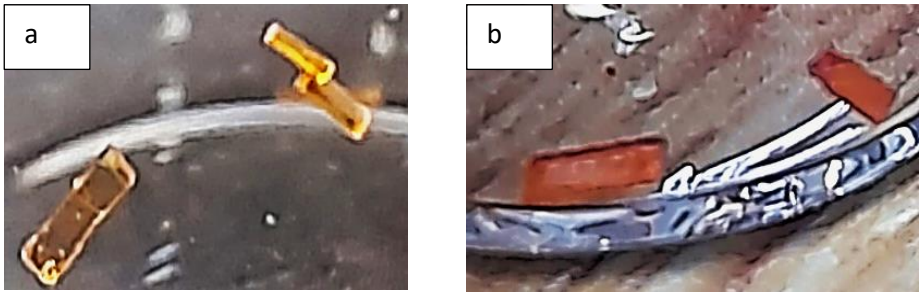


Figure 257: Pre (a) and Post (b) irradiated crystals of N-(3,5-ditertbutylsalicylidene)-4-Bromoaniline

The determination of any thermochromic properties N-(3,5-di*tert*butylsalicylidene)-4-Bromoaniline may have had was completed using a series of SCXRD measurements at various temperatures between 290 and 50 K. this identified the same $P2_1/c$ space group as with the 4-iodo and an internal dihedral angle of 27° between the rings. N-(3,5-di*tert*butylsalicylidene)-4-Bromoaniline demonstrates reverse thermochromism, this can be identified as a gain of colouration (usually from yellow to orange) rather than a loss of colouration as seen with the specifically thermochromic materials (Fig 258). In the case of compound 12, an increase in the keto occupancy as the temperature was decreased was observed, from 0 % at 295 K up to 20.0(1) % at 120 K before reaching a 23.0(2) % occupancy at 50 K. in contrast to the photochromic transition seen for the 4-iodo analogue the enol to trans-keto transition for the

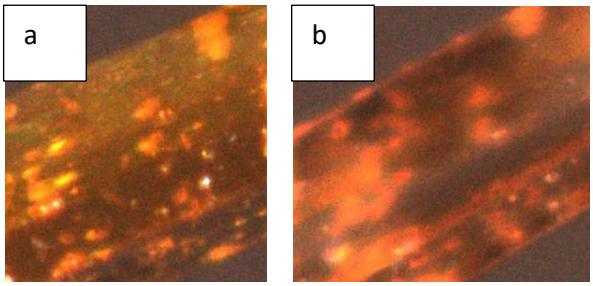


Figure 258: Crystal of compound 12 at a) 200 K and b) 120 K

[1] The TLC dark box requires a tinted viewing window and a fabric panel to view and accommodate the TLC plates and this might mean that the sealing-off of the natural light is not complete.

reverse thermochromism was an enol to cis-keto transition as seen with solely thermochromic materials.

An *in situ* UV-Irradiation X-ray diffraction experiment was also conducted in accordance with the experimental set up reported for N-(3,5-di*tert*butylsalicylidene)-4-iodoaniline. After the initial collection of the diffraction pattern for the non-irradiated sample, a collection strategy was set up so that each collection was started after a period of waiting, these periods were set as 3, 6, 3, 6, 9, and 2.5 hours sequentially (Fig 259). Unlike for the 4-Iodo analogue, after 11.5 hours of irradiation there were no visible structural changes in 4-Bromo-(3-5-di*tert*butylsalicylidene)-aniline. It took around 16.5 hours UV irradiation for structural changes to be observable. The keto structure formed was however the cis-keto structure, with an occupancy of 13.9(1) % reaching an eventual maximum occupancy of 20.2(3) % (after over 30 hours), not the expected trans-keto structure.

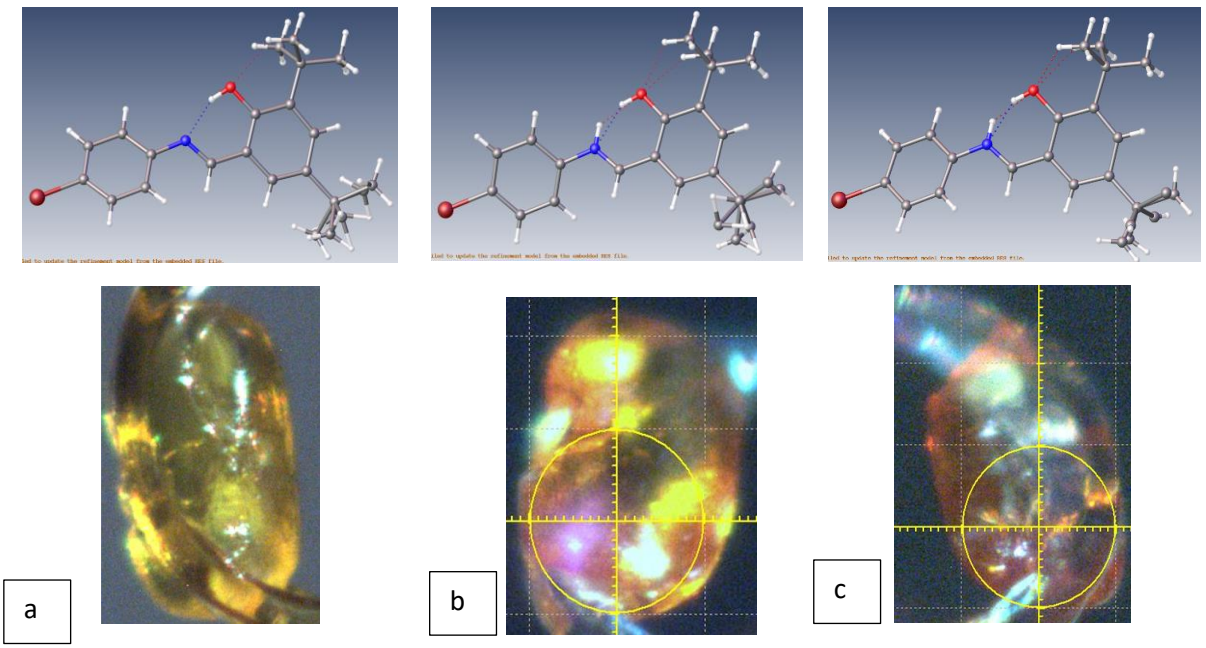


Figure 259: images of compound 5 in three states under in situ UV-irradiation during SCXRD a) non irradiated, b) 11.5 hours irradiation, c) 16.5 hours irradiation

To further investigate the tautomerisation between the enol and keto states, Raman Spectra were collected in multiple set ups : i) at different temperatures (Fig 260); ii) at different temperatures with fixed UV irradiation time; iii) at constant irradiation times with temperature ramping.

In the first set of measurements, as the temperature decreased there were changes associated both with the configurational changes within the molecule, and the changes in the resolution of the peaks (peaks sharpening) due to the reduced thermal motion.

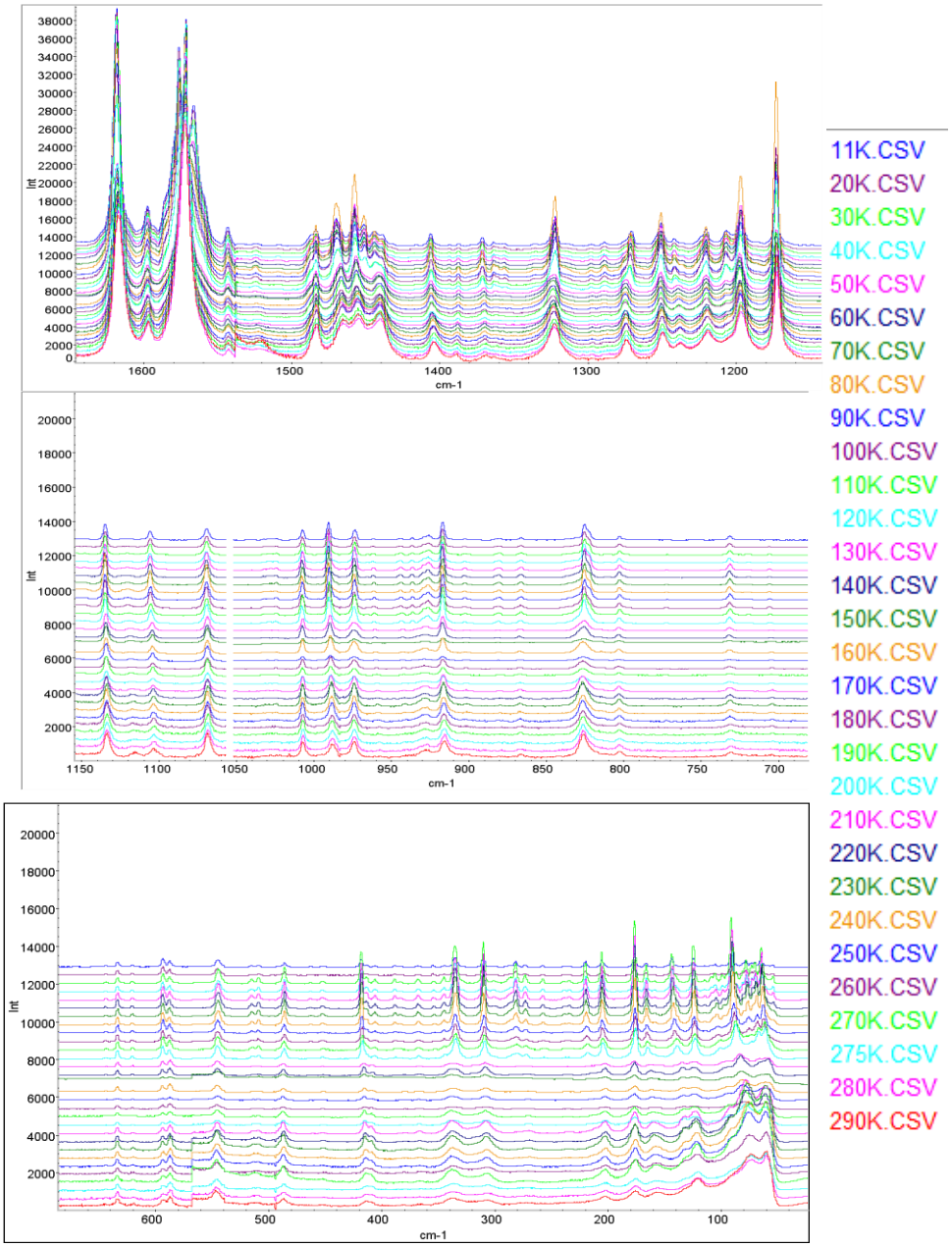


Figure 260: Raman spectra expansions of compound 12 showing the development of new peaks accompanying the enol to keto tautomerisation. Front-to back decreasing in temperature.

In the mid-wavenumber region, there are a number of peak changes that can be used to identify the transformation of the enol structure into the keto. The appearance of a peak at 1205 cm^{-1} is associated with the out-of-plane NH wag and is directly linked to the amount of keto tautomer that is formed (Fig 261) .

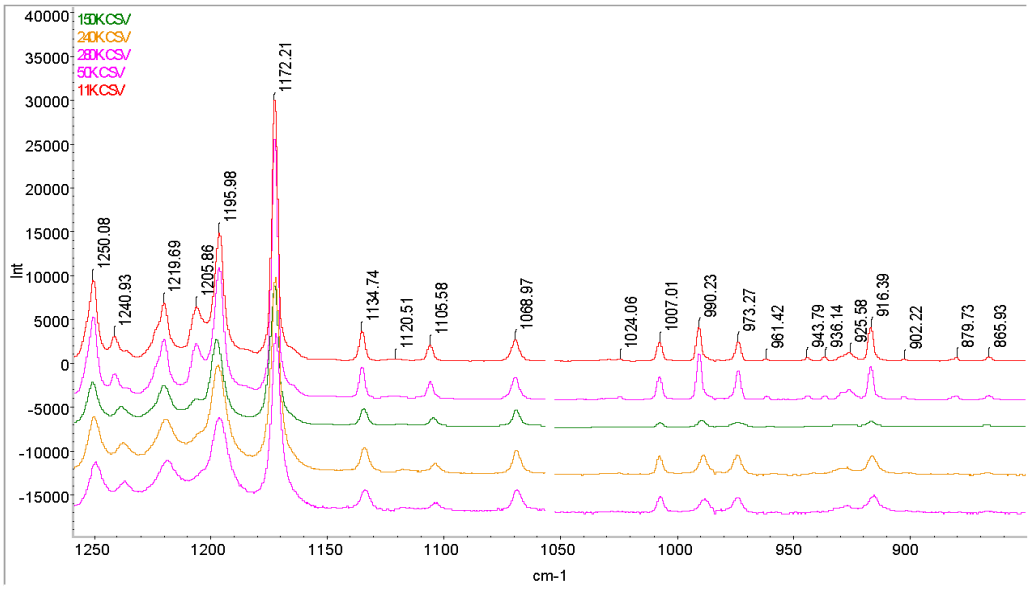


Figure 262: Key area Raman spectra expansion of compound 12

Within the higher wavenumber region there is a sharpening and broadening of peaks as the ratio between the keto and enol tautomer changes. With decreasing temperature, the peak at 1597 cm^{-1} for the enol tautomer broadens, whilst the peak at 1618 cm^{-1} associated with the keto tautomer sharpens (Fig 262).

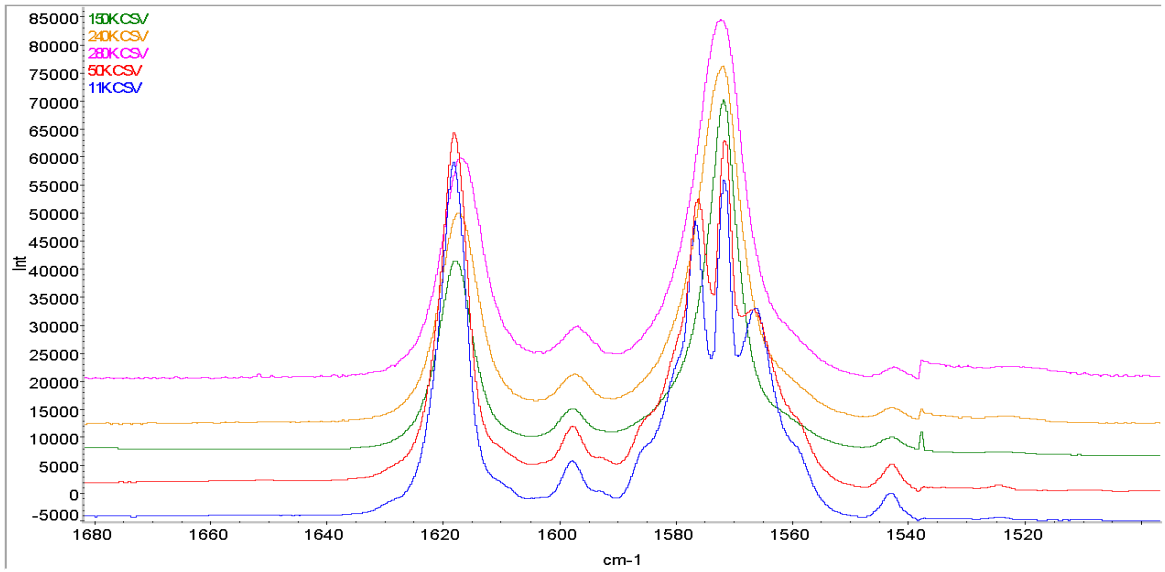


Figure 261: 1680 to 1500 cm^{-1} wavenumber region of irradiated Raman spectra of compound 12

In the second set up, the data was collected only below 1000 cm^{-1}. The largest changes can be seen between 700 and 400 cm^{-1}(Fig 263). Though there are resolution differences between the different collections, there are transitions between multiple and single peaks over the length of irradiation. Whilst the C-Br vibration is consistently present as expected, variation in other

vibrations (mainly molecular deformations) are assigned to the keto structure with greater frequency for the lower temperature spectra (Table 10).

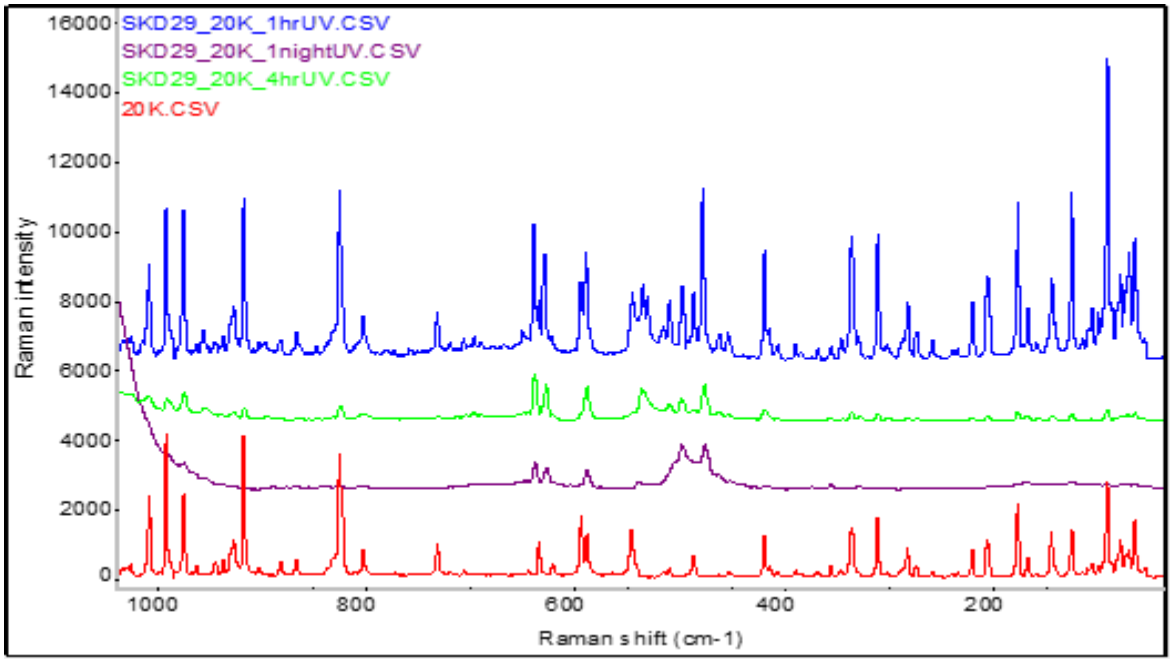


Figure 263: 1000 to 100 cm^{-1} wavenumber region irradiated Raman spectra of compound 12

Table 10: Key peak assignments in 680 to 400 cm^{-1} wavenumber region of irradiated and non-irradiated spectra of compound 12 at 20 K

	Non-irradiated	**1 hour**	**4 hours**	**1 night**	**Assignment**
Wavenumbers cm^{-1}		638	638	637	Enol
	633	633			Keto
		628	625	625	Keto
	621	621			Enol
	593	593	598		Keto
	588	588		588	Keto
	544	544	544	544	Keto/Enol
		534	534		Keto
		529			Keto
	514	514			Enol
	509	509	509	504	Keto
		496	496	496	Keto
	485	485	485	485	Keto
		476	476	475	Keto
		461	461	460	Keto
	452	451	452		Enol

In the final set up, there are changes as the temperature increases some peaks lose intensity or disappear completely. However, it cannot be stated whether that is due to the increase in temperature or the lag between collection and irradiation time (Fig 264). There is also a lack of consistent exposure, as after four hours the UV lamp source used began to function only intermittently with no recognisable pattern.

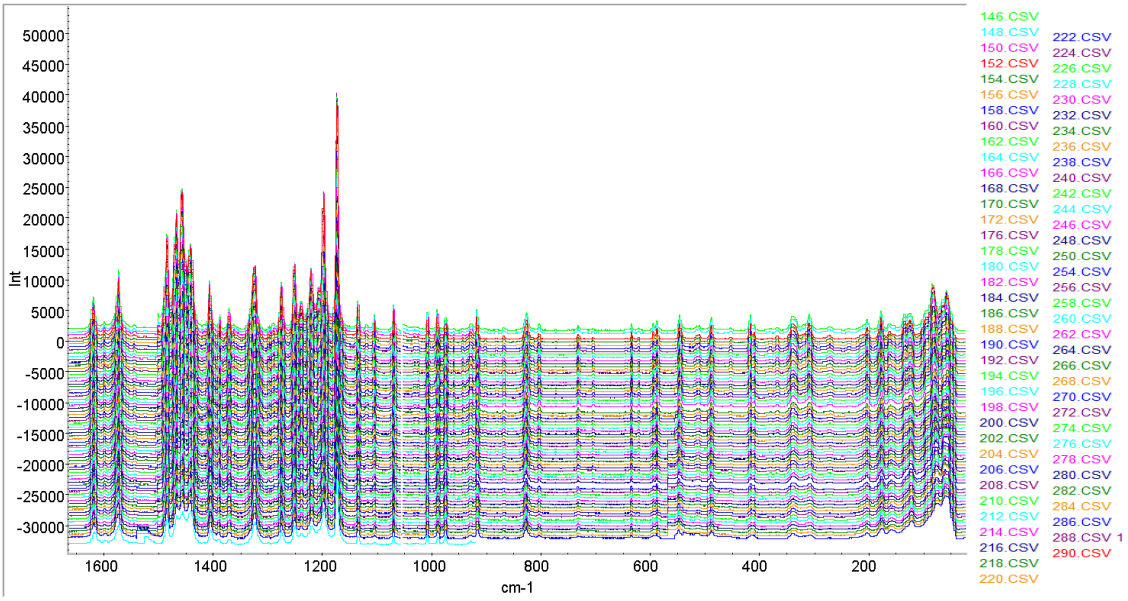


Figure 264: Raman Spectra of third set-up for compound 12. Increasing in temperature back to front.

From organic chemistry it is known that the substituent groups for compounds of this type are all withdrawing electrons from the benzene ring, in the following order of electron withdrawing ability: NO_2 > Br > I. Having both the 4-Iodo- and 4-Bromo- analogues allows the comparison of the effect of different halogens on the same ring position, in particular the effect of orbital overlap between the substituent and the benzyl ring and hence the resulting effect on the imine-Nitrogen. The smaller Bromine atom allows for a greater orbital overlap than that of the iodine atom, this results in an easier transfer of the electron density to and from the ring, affecting the dihedral angle making the molecule more planar than the iodo-analogue. The larger iodo group also adds to the steric hindrance within the molecule, though due to the para positioning of the substituent in these compounds that is not a significant effect on the intramolecular interactions but could however have a small effect in the crystal packing of the unit cell.

Bromine also has a higher electronegativity than iodine to pull electron density from the ring and hence, helps the imine-nitrogen become more basic and a better hydrogen bond acceptor. This can also be noted by the difference in the Hammett parameters[44] for the two atoms in the para position, 0.23 for bromine and 0.18 for iodide, showing the bromine has a stronger combined effect (electronegativity and substituent position) than the iodine of the rest of the molecule.

Of the two analogues the 4-iodo is both the more stable and easier to convert of the two taking only 11.5 hours compared to 18 hours of the 4-bromo before structural changes are noticeable in the diffraction results under UV irradiation. The reversion time in the dark is also a week longer at 3 weeks rather than the 2 weeks for the 4-bromo. The larger dihedral angle between the rings 64° over 27° is a significant part of the ease of conversion as discussed for type 1 (4.3.3.2). Another consideration is the presence of both tautomers in all states for N-(3,5-di*tert*butylsalicylidene)-4-iodoaniline making the transition a cis to trans conversion rather than enol to keto changing the energy required.

4.3.3.4 Group 3: Meta position substitution on the aniline ring

As explained in group 1 N-(3,5-di*tert*butylsalicylidene)-3-iodoaniline is a photochromic material with a dihedral angle of 46°. Similarly, N-(3,5-di*tert*butylsalicylidene)-3-nitrooaniline is also a photochromic material. To ascertain the photochromic nature of the material a small amount of the sample was placed in a dark box and irradiated with a UV 365 nm lamp (as used for TLC plates) for 3 hours, resulting in a visible colour change from yellow (non-irradiated) to orange (irradiated). Once removed from the dark box the sample would revert to the non-irradiated colouration after 10 minutes, if left in the dark with no white light exposure the irradiated colouration lasted 4 weeks.

SCXRD was utilised to investigate the structural changes associated with the transition between the non-irradiated and irradiated structures. The investigation was completed in two parts, the first a variable temperature experiment to determine any thermochromic properties, the second an *in situ* UV irradiation experiment to observe the photochromic related structural changes.

SCXRD data on N-(-3,5-di*tert*butylsalicylidene)-3-nitroaniline was initially collected at two temperatures (295.6 and 100 K) for the thermochromic property investigation, using a molybdenum x-ray source. The structural determination at 295.6 K evidenced a dihedral angle of 49.6(2)° between the two rings, this decreased to 48.2(1)° at 100 K, with the enol occupancy remaining at 100 % throughout (Fig 265) and a symmetry of $P\bar{1}$. There was no observable paling of the crystal colour, hence demonstrating no major thermochromic properties. The dihedral angle is calculated from the planes of the two rings. The oxydril hydrogen forms a hydrogen bond with the imine nitrogen (1.6(2) Å) which gives rise to a third pseudo six-membered ring almost planar to the salicylidene ring.

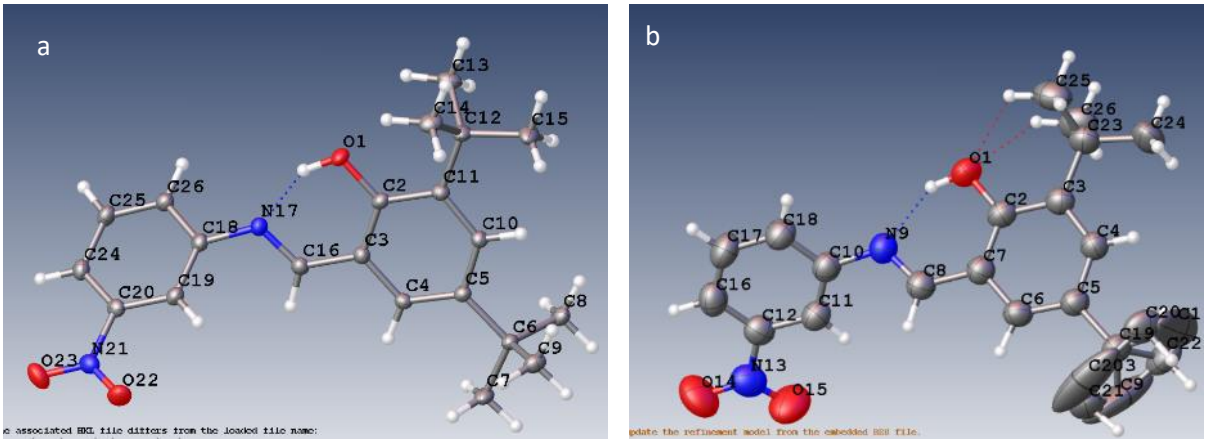


Figure 265: Structure of N-(-3,5-ditertbutylsalicylidene)-3-nitroaniline at a) 100 K and b) 295.6 K .

For the first investigation into the photochromic properties of the compound, a crystal was irradiated *in situ* for 14 hours at 280 K with two datasets collected, with a molybdenum source respectively 3 and 11.5 hours after starting irradiation. The diffraction data revealed no change in the enol/keto occupancy nor any cis – trans isomerisation of the linking C-N bridge. The dihedral angle also remained at 49.6(1)°. Though a colour change from yellow to orange was visibly observed upon irradiation (Fig 266), none of the expected structural changes within the molecule were observed. These results suggest that a longer exposure might be required for the cis-trans isomerisation to have occurred or that a conversion threshold must be met for the tautomerisation to be observed by diffraction. Another possible explanation of these results is that the mechanism of the photo-colourisation might be different from the expected proton transfer and therefore involve an electronic change rather than simply a structural one.

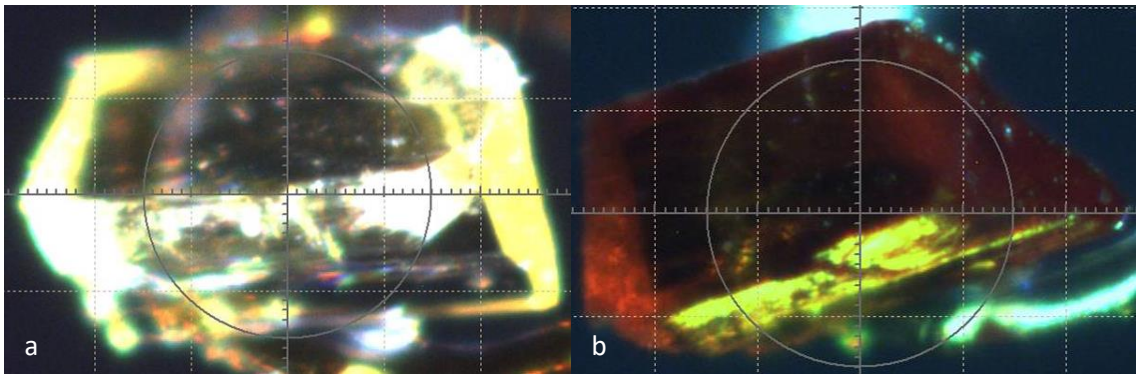


Figure 266: photo of the a) Non-Irradiated crystal and b) Irradiated crystal of compound 4

In view of the changes observed in the diffraction data of N-(3,5-ditertbutylsalicylidene)-4-iodoaniline when using different sources (Mo *vs* Cu), additional data for N-(-3,5-di*tert*butylsalicylidene)-3-nitroaniline was also collected using Cu-K_α radiation. This data collection showed the progressive formation of the cis-keto isomer, reaching a maximum keto structure occupancy of 19.4(2) % under *in situ* irradiation at 290 K using Cu-K_α radiation.

Once a structural and strategy determination run was completed, a set of data were collected on the non-irradiated crystal. A series of collections were then set, and the UV-lamp was switched on and the crystal left for 6 hours under irradiation in the dark. Diffraction data was collected over four hours, using the same initial strategy, another data set was measured after a further 6 hours under irradiation. A third collection was started after a half an hour lag from the end of the second collection. The fourth collection was started after a total of 33.5 hours under irradiation. The fifth collection required the crystal to be recentred, so a new strategy had to be determined, this was also used for the final collection which was started after a 5-hour lag (52.5 hours under irradiation at start of collection).

The first collection demonstrated the expected initial enol configuration of the molecule as previously seen. After irradiation, the first data set showed the presence of the cis-keto form (Fig 267), identified by the hydrogen attached to the imino-nitrogen at 18.9(6)% occupancy. This was unexpected as due to the dihedral angle of the molecule being close to 50°,that would suggest the keto state would be the trans-form as observed for N-(-3,5-ditertbutylsalicylidene)-4-Iodoaniline, as described in 4.3.3.1. The second irradiated data set showed an increase in the

keto occupancy up to 19.4(5) %, but there was then a decrease in the occupancy to 13.5(1) % in the third data set. The fourth data set was unusable due to the movement of the crystal displacing it from the centre of the beam.

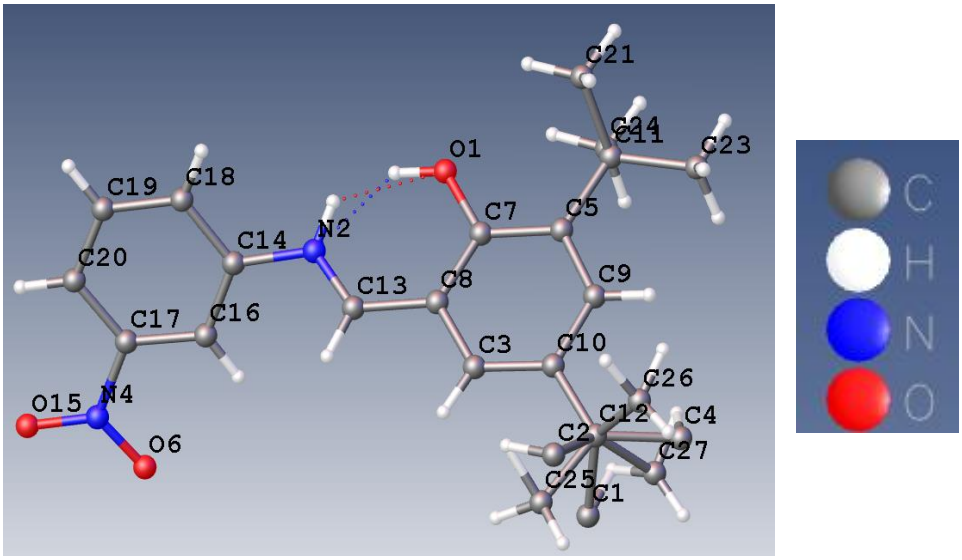


Figure 267: Irradiated structure of compound 4

After recentring, the fifth data set showed a different unit cell to that which had been previously identified. Where the standard unit cell observed for this compound has axes of, approximately 6.0 Å, 10 Å, 16 Å (a, b, c) with angles 101°, 92°, 101° (α, β, γ) and a volume of between around 987- 1004 Å^3 and has a single molecule in the asymmetric unit. This data set found axes of approximately 10 Å, 18 Å, 18 Å (a, b, c) with angles 111°, 101°, 96° (α, β, γ) and volume of 3009.33(1) Å^3 for the unit cell containing three molecules in the asymmetric unit (Fig 268). However, the space group remained $P\bar{1}$. Only one of the three molecules showed tautomerisation to the keto state at an occupancy of 29 (1) %.

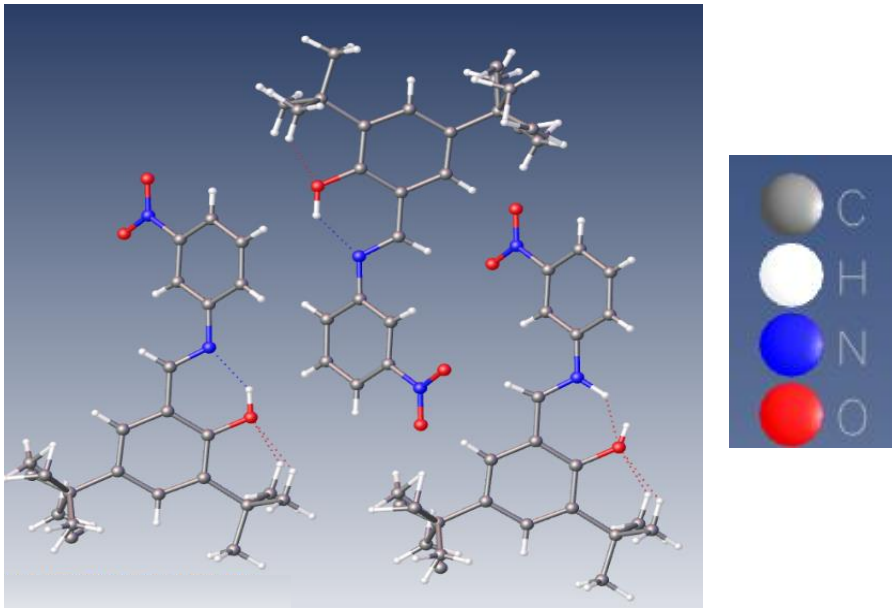


Figure 268: pseudo 3 molecule asymmetric unit of 3,5-ditertbutylsalicylidene-3-nitroaniline

The sixth data set, which was measured 11 hours post recentring, showed a reversion back to the standard unit cell, as well as a majority conversion back to the enol form, with a keto occupancy of only 7.6(2) %.

As the new unit cell from the fifth data was unexpected the data was examined closely and a reciprocal space plot revealed additional peaks between the main Bragg planes from the original cell, commonly found with twinned or transient structures. It was reported in the literature that the needle like polymorph of the compound bends up to 70°, using a 365 nm pulse laser at 5 to 40 mW cm^{-2} for 30 s, though typically this is around 30° depending on crystal thickness (chapter 4.1). The structure for which this was observed, conversely to what we have found, reports that the keto structure present is the trans-keto. To what extent the phenomena would be present with the cis-keto has yet to be determined. It is possible that the unit cell change is a demonstrable result of the mechanical change in the crystals, or the reverse where the mechanical change is the cause of the unit cell change. It can hence be proposed that the formation of a pseudo three-molecule asymmetric unit in the crystal structure after 4 days of irradiation, is due to the slow movement of the sample during the data collection as it bent away from the UV lamp, and it no longer sits at the centre of the x-ray beam.

Because the irradiation of the crystal took place over 5 days, coupled with the movement of the crystal the sample had to be reoriented twice, the resulting exposure of the sample to natural light reduced the relative keto occupancy in the crystal.

An initial Raman spectrum was collected using the 780 nm laser with a table top Raman spectrometer in the 100 – 3400 cm^{-1} range at 293 K on 3,5-di*tert*butylsalicylidene-3-nitroaniline. The experiment showed that there was a high fluorescent background, although the majority of the key peaks were identifiable (Fig 269) for the enol structure.

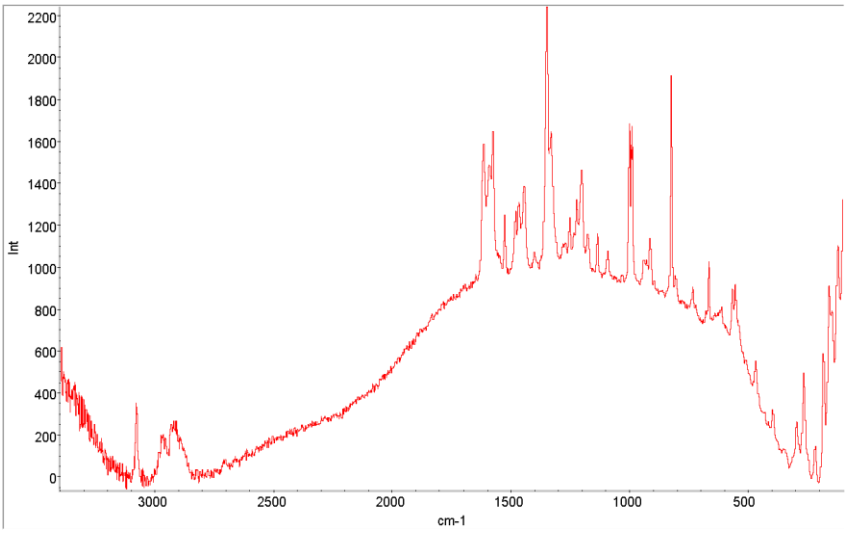


Figure 269: Raman spectra of compound 4 at 293 K

Additional spectra were then collected on the irradiated sample using the 785 nm laser and offline set up as described for N-(-3,5-ditertbutylsalicylidene)-4-Iodoaniline (Fig 270). A comparison to the non-irradiated crystal shows that there are changes in peak intensities (red arrows) as well as the development of new peaks (Green Arrows) and the loss of others (purple arrows). There are shifts in the intensities of peaks at 1344, 1323, 1204, 1197, 938, 928, 213 and 143 cm^{-1}. Whilst new peaks develop at 291, 537, 606 cm^{-1}, and there is the loss of peaks at 837, 741 cm^{-1}.

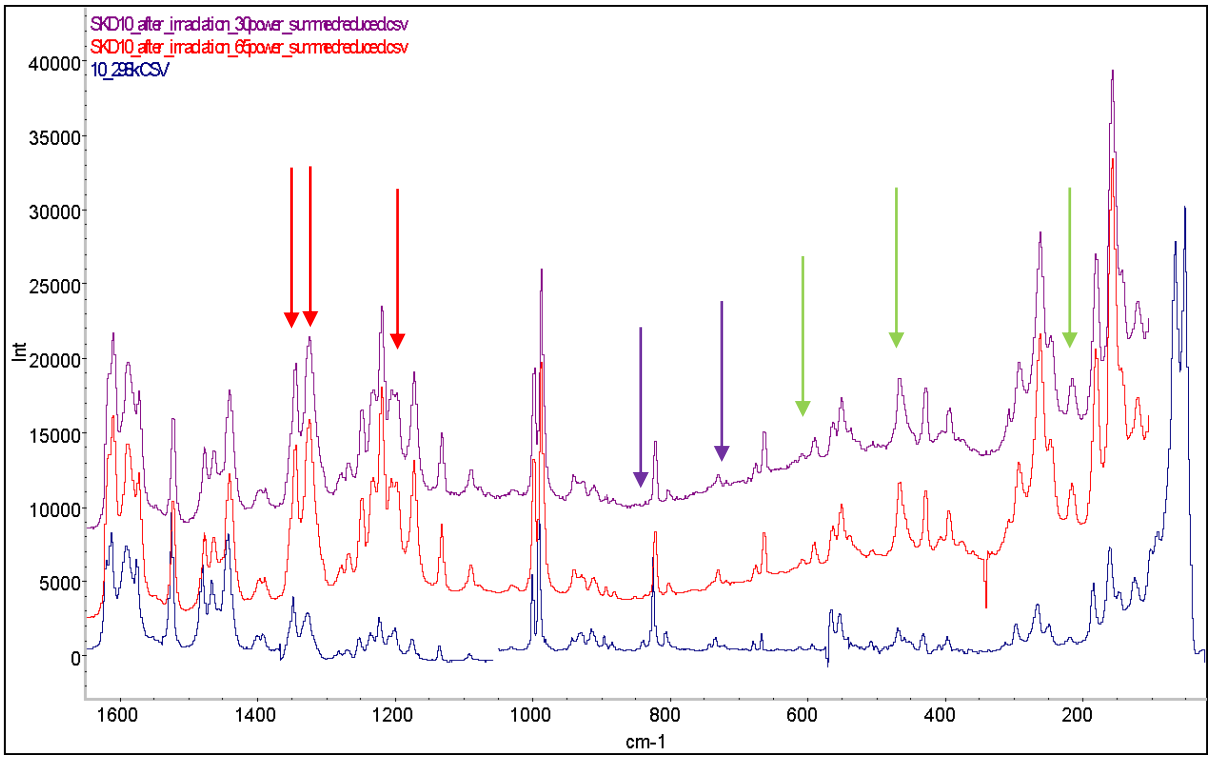


Figure 270: Irradiated and non-irradiated Raman Spectra of compound 4. Purple -post irradiation at 30 % power, Red- post irradiation at 65 % power and blue – non irradiated.

To better investigate the structural changes spectroscopically with respect to both temperature and irradiation, crystals of N-(-3,5-ditertbutylsalicylidene)-3-nitroaniline were taken to IFAC, an institute of the Italian National Research council (CNR) in Florence, where spectra were collected with a high resolution 532 nm laser with the help of Dr Leonardo Del Rosso and Professor Lorenzo Ulivi. Unlike the spectrometers available at ISIS and Keele University, the set-up of the Raman equipment as well as having a higher resolution spectrometer (resulting in smaller collection windows) also included a series of four notch filters in the secondary flight path of the quasi backscattering layout, ostensibly to remove the incident laser light, and has the knock on effect of reducing the fluorescence reaching the detector.

The sample for these experiments sits in a high-vacuum cryostat, covered with a copper shielding tube, with an indium-sealed quartz window in a steel flange (Fig 271).

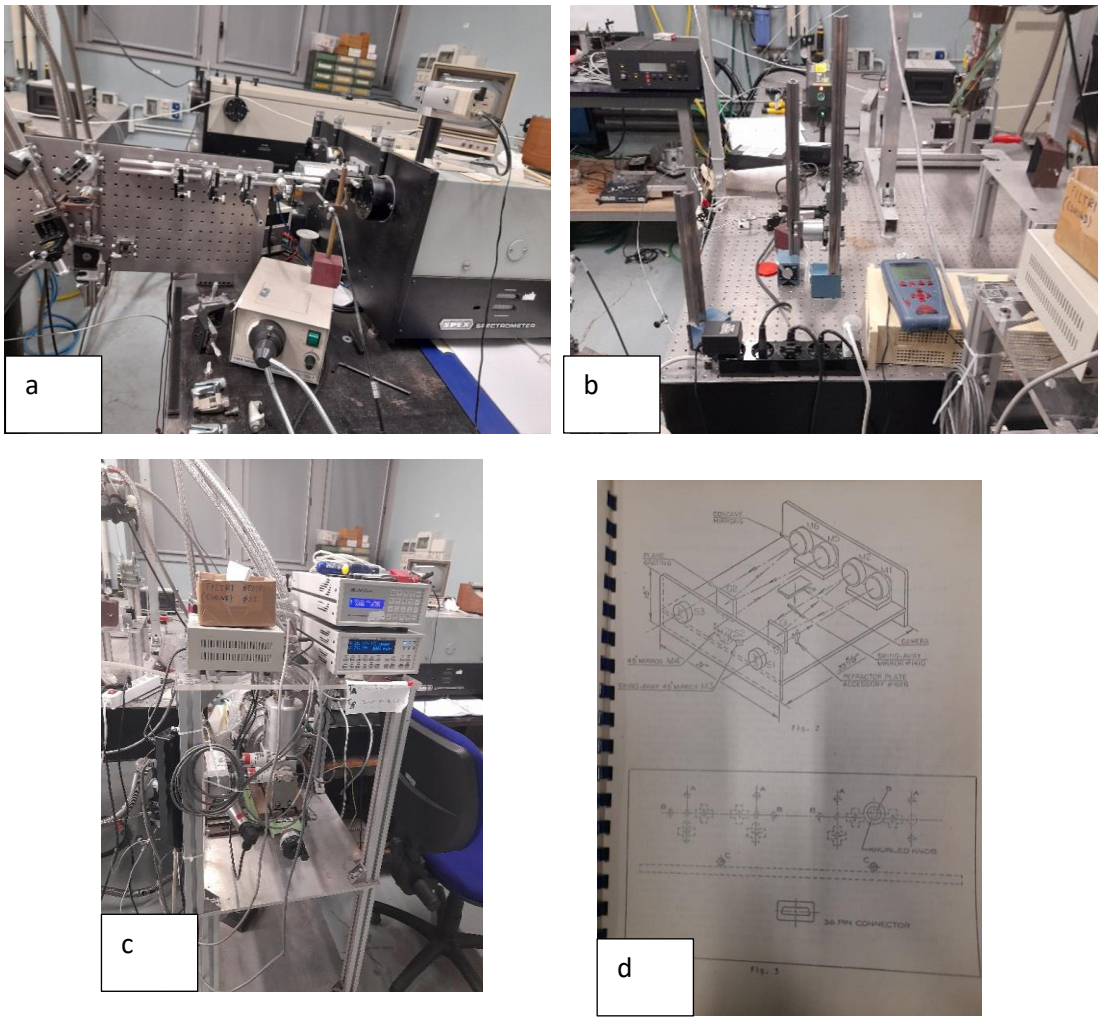


Figure 271: a) Notch filters and entrance to monochromator, b) initial flight path of laser with mirror and pinholes to move the laser to the correct height, c) sample position, d) schematic of monochromator

To cover the entire spectral range necessary to observe the structural changes for N-(-3,5-ditertbutylsalicylidene)-3-nitroaniline, the data was collected in 4 windows with centres at 300, 800, 1300 and 1600 cm^{-1}. These were then "stitched" together to form the complete spectrum for each experimental run. Data were collected both on the irradiated and non-irradiated samples at the following temperatures 20, 70, 110, 270 and 298 K. The sample was irradiated with a UV 365 nm lamp in the dark for at least 3 hours at each temperature below 298 K, before being continuously irradiated during the data collection (Fig 272/3). To revert the sample to the

non-irradiated state the main light of the lab was switched on for at least 30 mins, though the sample would fully revert visually (orange to yellow colouration) within 10 minutes.

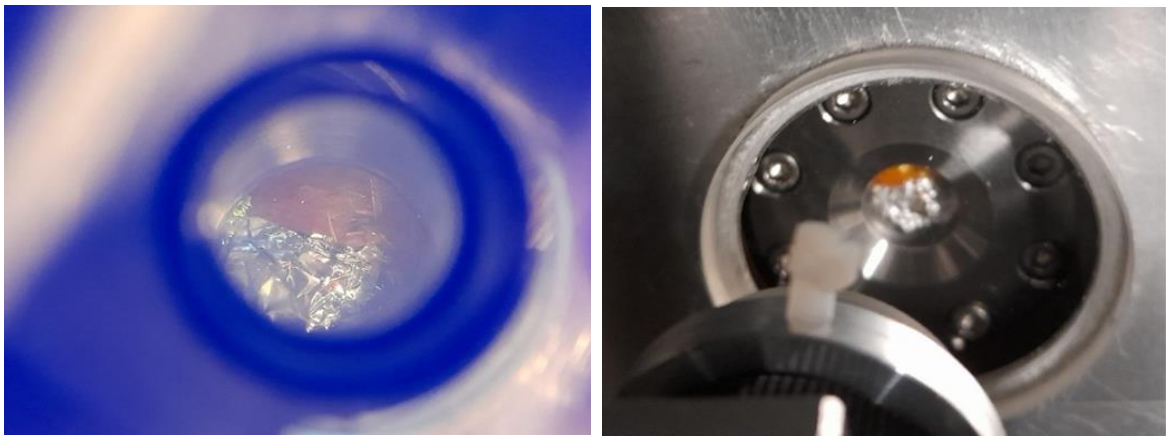


Figure 272: view of irradiated sample in the sample position in the high resolution Raman scattering set up.

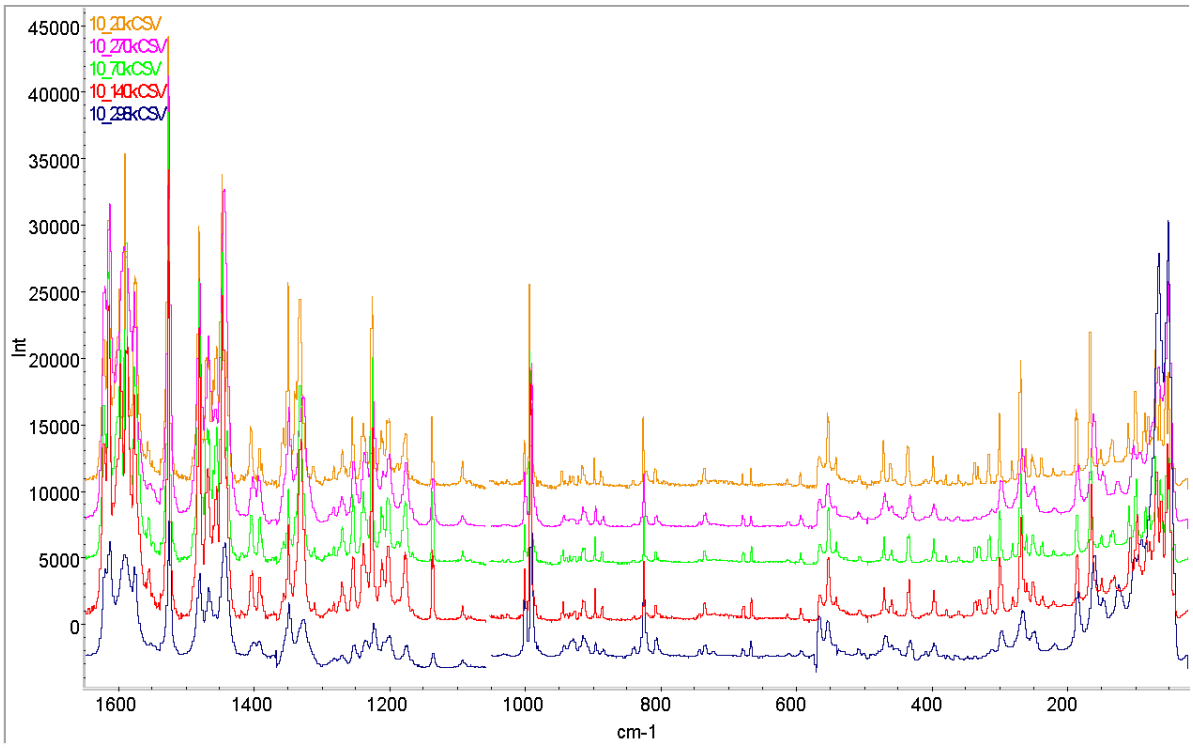


Figure 273 : Variable temperature Raman spectra of compound 4 in the non-irradiated state. Orange – 20 K, pink – 270 K, green – 70 K, red – 140 K, blue – 298 K.

As the temperature is decreased towards 20 K, there are some overlapping peaks at around 1600 cm^{-1} that are resolved, as well as the development of new peaks and shifts in peak intensities as a consequence of them being associated with one structure over the other (Fig 274).

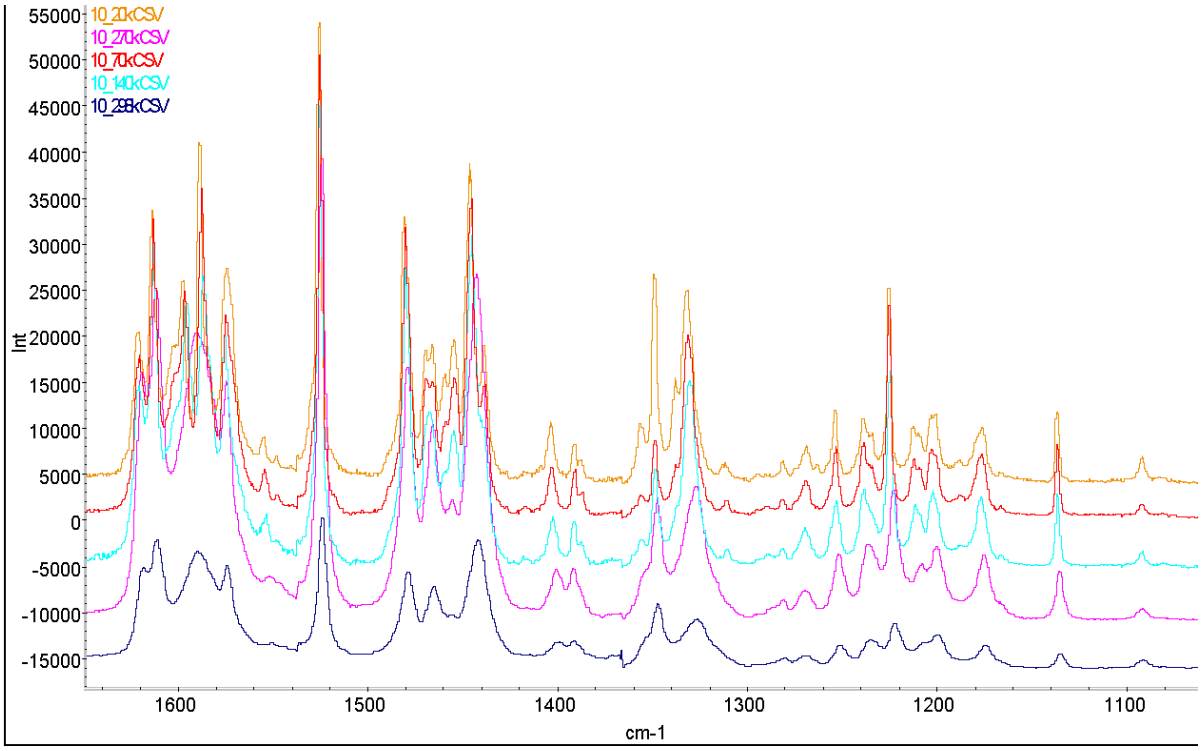


Figure 275: 1650 to 1090 cm^{-1} window of Raman spectra for compound 4. Orange – 20 K, pink – 270 K, red – 70 K, turquoise – 140 K, blue – 298 K.

In the 1700 – 1000 cm^{-1} wavenumber region there are peaks associated with the NH and OH bends, and there is an increase in the intensity of the peak at 1268 cm^{-1} which is associated with an NH bond In Phase (IP) wag (full tables of peak assignments at 20 and 270 K can be found in the appendix). There is a loss in intensity of the peak at 845 cm^{-1} which is associated with the *tert*butyl asymmetric bends of the enol structure (Fig 275).

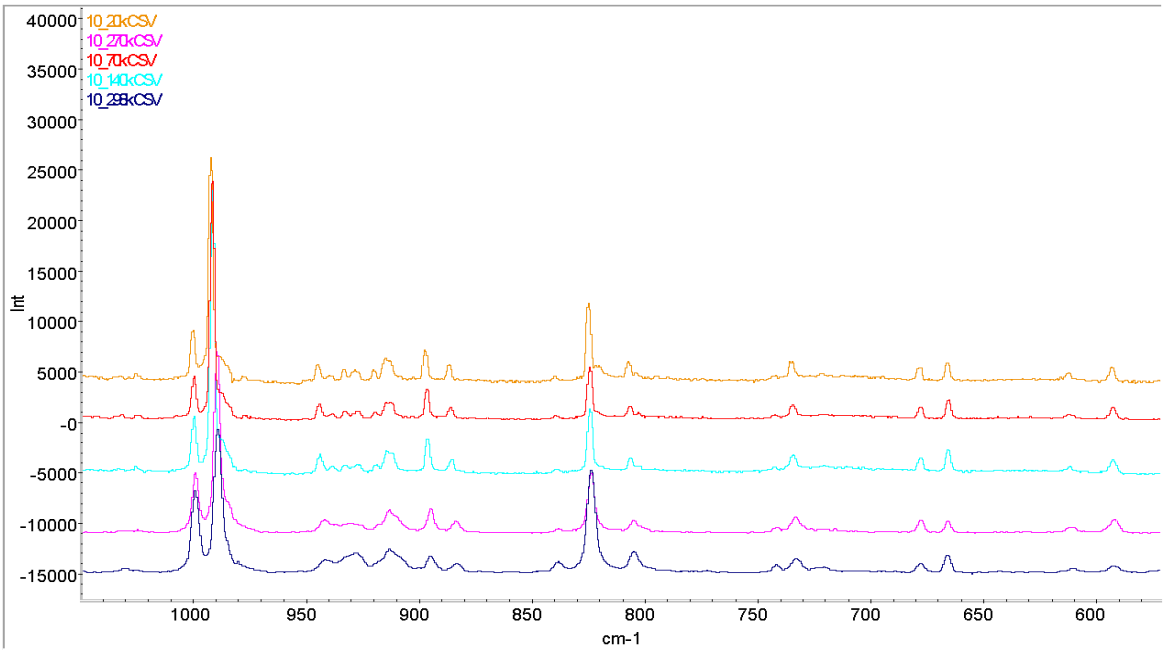


Figure 274: 1100 to 550 cm^{-1} window of Raman spectra for compound 4. Orange – 20 K, pink – 270 K, red – 70 K, turquoise – 140 K, blue – 298 K.

In the low wavenumber region, there are new peaks developing at 335 cm^{-1} and 359 cm^{-1} associated with the keto structure (Fig 276) at temperatures below 140 K.

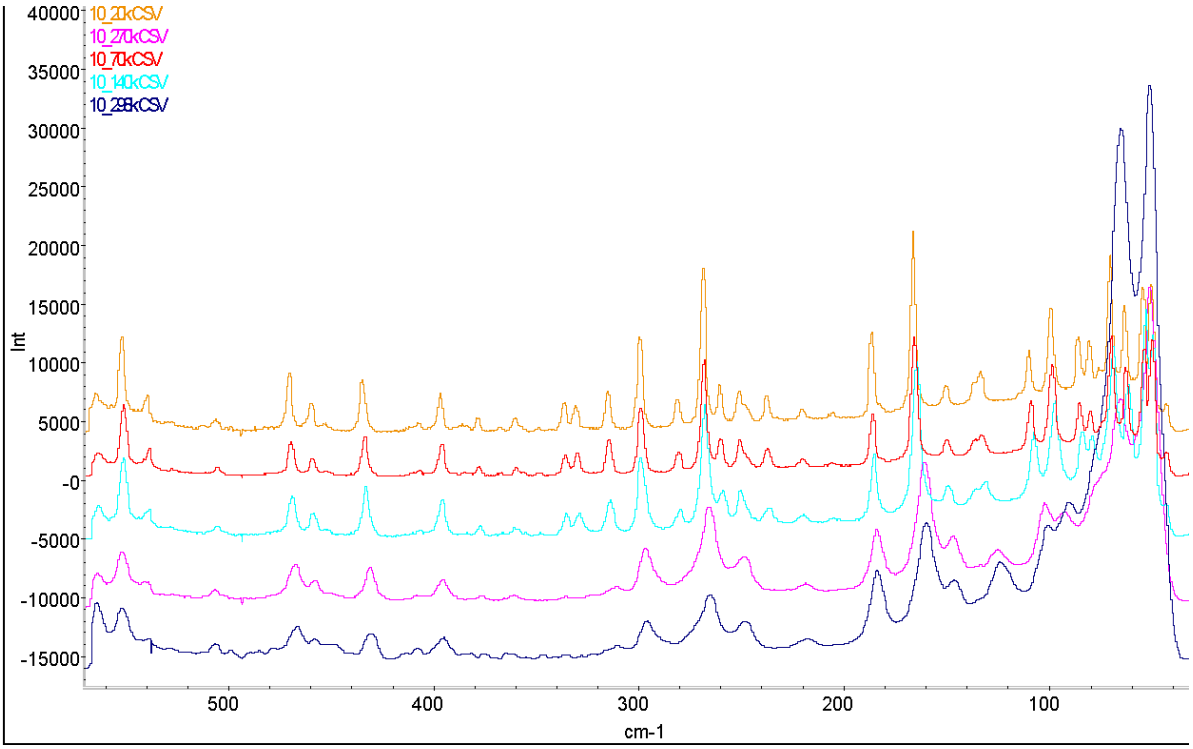


Figure 276: : 650 to 60 cm^{-1} window of Raman spectra for compound 4. Orange – 20 K, pink – 270 K, red – 70 K, turquoise – 140 K, blue – 298 K.

A similar pattern of spectral changes with respect to temperature is seen with the UV irradiated structures as with the non-irradiated structure (Fig 277/8).

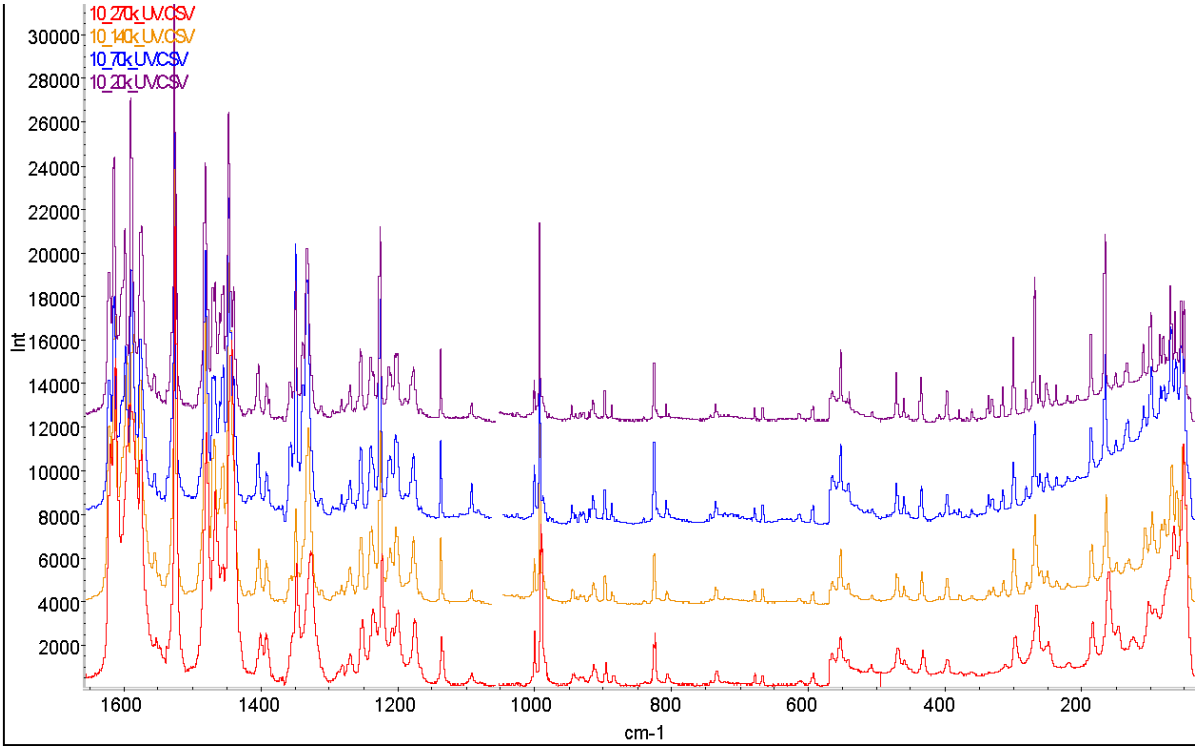


Figure 277: Raman spectra of the irradiated state of compound 4. Purple – 20 K irradiated, blue – 70 K irradiated, orange – 140 K irradiated, red 270 K irradiated.

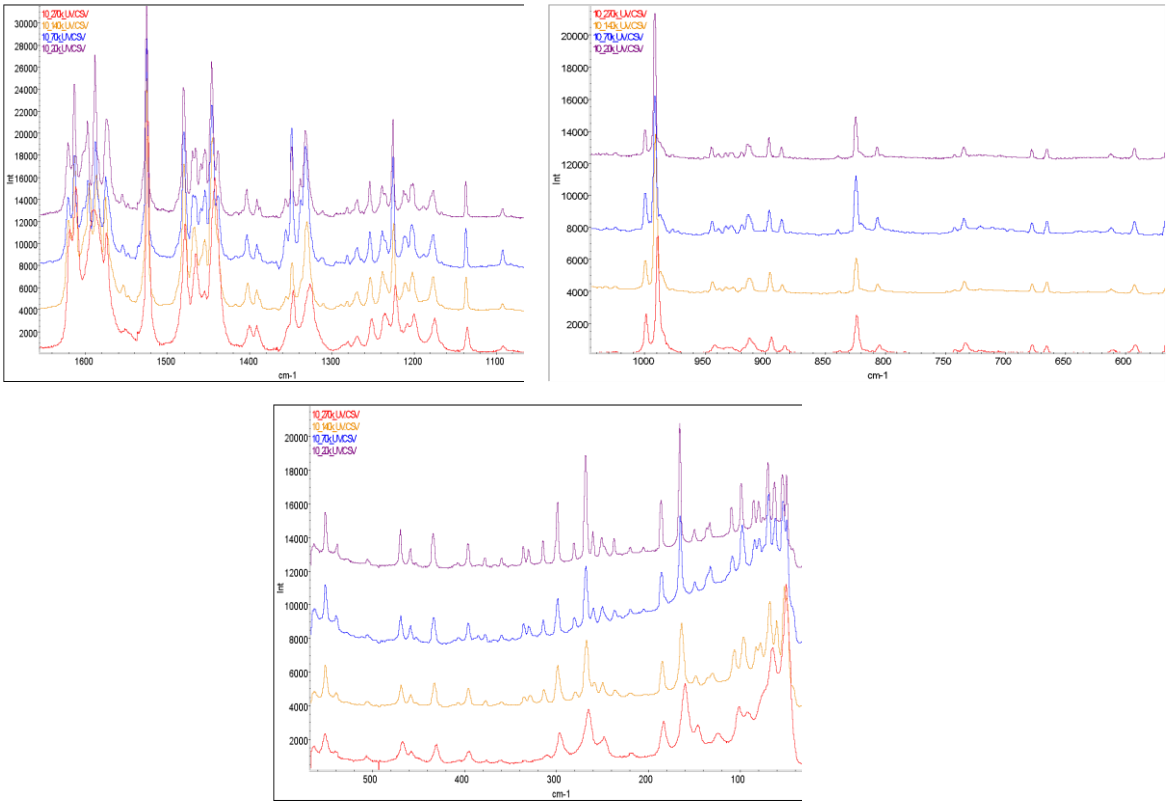


Figure 278: expansions of Raman spectra for compound 4 irradiated state. Purple – 20 K irradiated, blue – 70 K irradiated, orange – 140 K irradiated, red 270 K irradiated.

Comparison of the irradiated and non-irradiated spectra at 140 K showed no major differences. In contrast, the spectra at room temperature displayed shifts both in intensities as well as the developments of new peaks (Fig 279). For example, after irradiation a second peak develops at around 1400 cm^{-1}, whilst the relative intensities of the peaks around 1200 cm^{-1} shift.

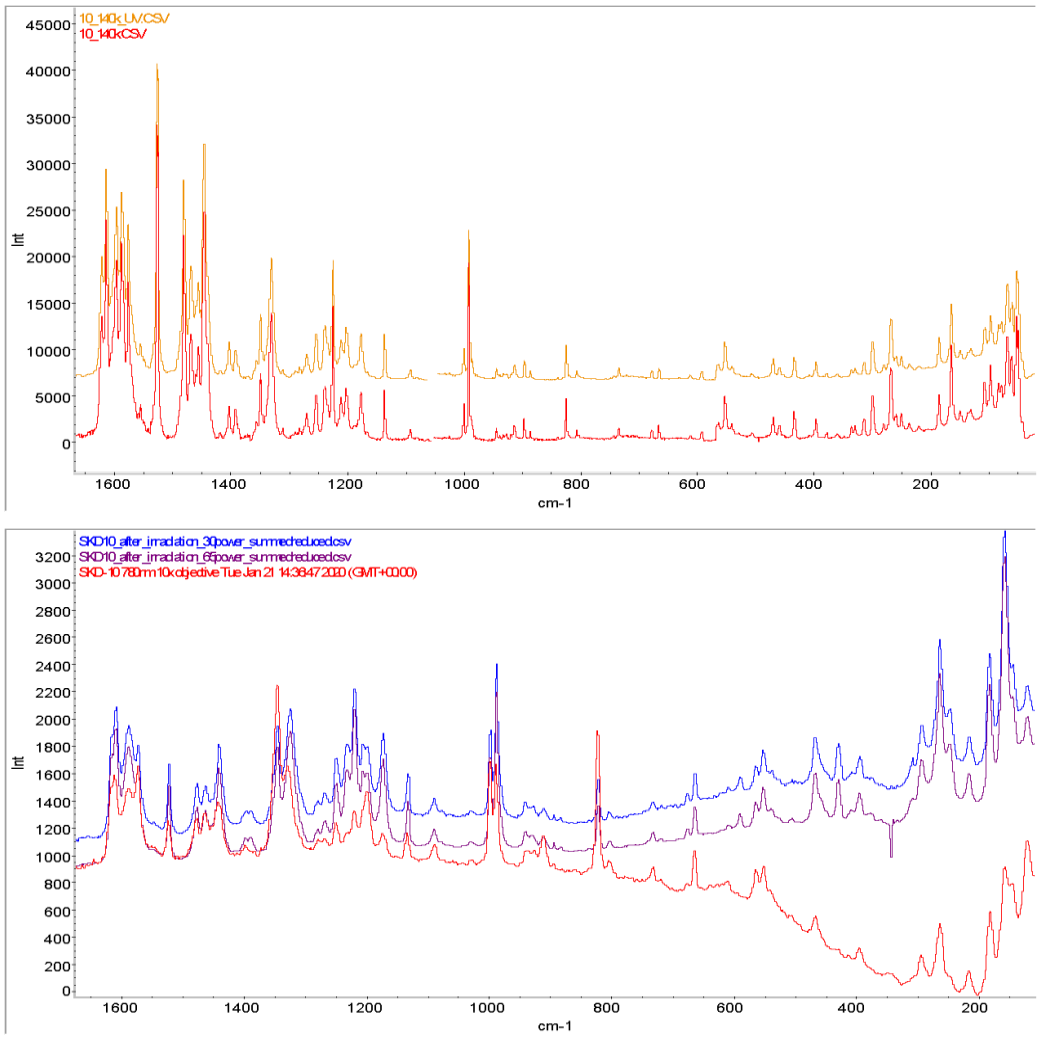


Figure 279: comparison of irradiated and non-irradiated Raman spectra at 140 K (top; orange-140 K irradiated, red-140 K non-irradiated) and 295 K (bottom; blue – irradiated 30 % power, purple – irradiated 65 % power, red- non-irradiated) of compound 4

The *in situ* Raman scattering and neutron diffraction experiment was performed using the improved sample environment which had been used for the second Neutron diffraction experiment on N-(3,5-ditertbutylsalicylidene)-4-Iodoaniline. In this case the crystal sitting in the neutron beam was illuminated by the laser used in the Raman scattering experiment at the same time. Data was also collected in an offline irradiated crystal of N-(-3,5-ditertbutylsalicylidene)-3-nitroaniline. Comparing the on and offline irradiated Raman data against each other as well as with the non-irradiated collection, there are differences in the level of background noise for the on and offline spectra as well as slight differences in relative peak intensities (Fig 280). It is possible that some of these differences could be due to alterations in irradiation time length. Longer irradiation times were used for the online spectra as well as a longer time between removal of sample from irradiation and collection of the spectra.

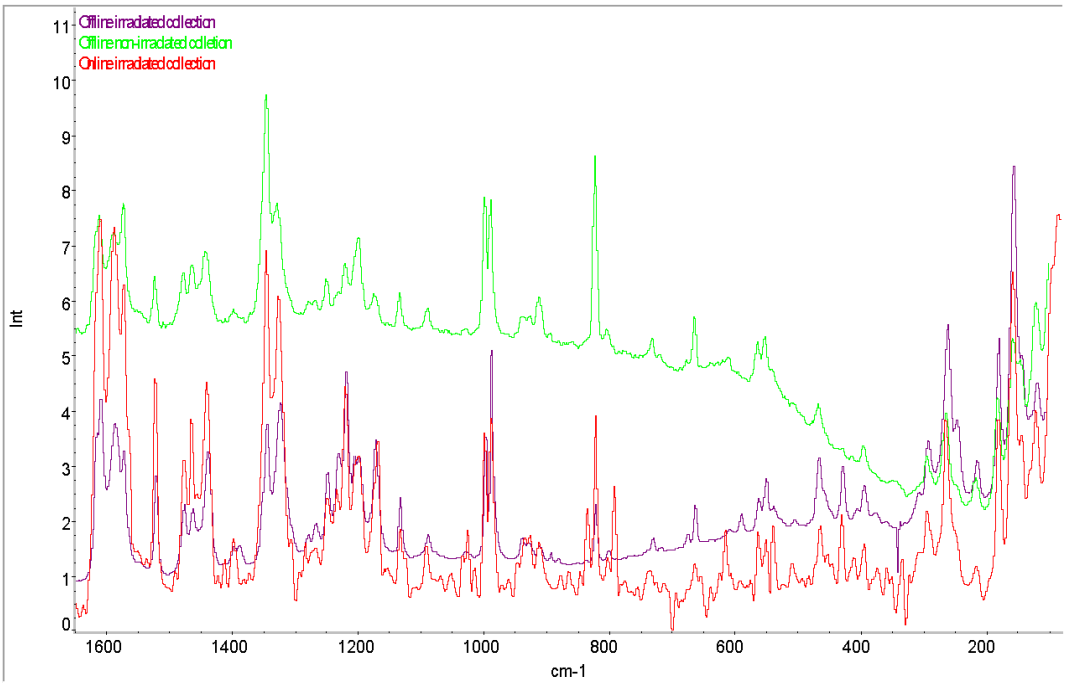


Figure 280: comparisons of the insitu irradiated (red) Raman spectra of compound 4 against the offline irradiated (purple) and offline non-irradiated (green) spectra.

Key peak intensity differences can be seen in the higher wavenumber region where there is an increased intensity for the Keto structure assigned peaks relative to that assigned for the enol structure (Table 11).

Table 11: Key Raman Peak assignments for compound 4

Position (cm^{-1})	**Keto Assignment**	**Enol Assignment**
1590	NH OOP bend	
1574	-	OH IP bend, ring deformations, CH wag
1344	–	aniline ring deformations
1325	bridge CH IP wag	bridge CH IP wag

We again observed contrasting results between the Neutron diffraction experiment and the *in situ* irradiated X-ray diffraction experiment. Only the enol form (associated with the non-irradiated state) was identified in the neutron diffraction data, though the irradiated state (orange colour) was maintained throughout (Fig 281). As discussed earlier, the online irradiated spectra had similarities to both the offline irradiated and non-irradiated spectra at different points. Due to the length of time required for the neutron diffraction experiment (2 days) it is likely that as the irradiated state is only metastable the keto structure cannot be identified outside of direct irradiation *via* Neutron diffraction. Additional experiments would be required to validate this hypothesis.

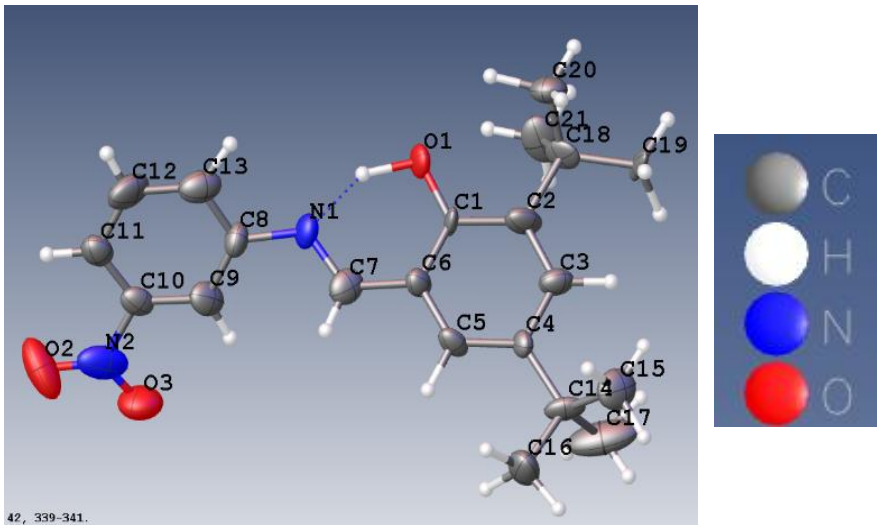


Figure 281: Neutron diffraction structure of compound 4

Looking overall at all photochromic materials 3-nitro, 4-Iodo, 4-Bromo and 3-Iodo, we observed a link between the ease of conversion to the irradiated keto state and the dihedral angle (see Table 12). The larger the angle the less irradiation time is required for the conversion to proceed. Based on the experimental times these were at about 14, 16, 18 and 17 hours respectively for 4-Iodo, 3-nitro, 4-Bromo and 3-Iodo before structural changes were observable (i.e. observable keto hydrogen occupancy) in a diffraction experiment. However, visible colour changes were observed after only 3 hours for the 4-iodo, 3-nitro and 3-iodo analogues, and 5 hours for 4-bromo. When looking at the reversion rate for samples left in the dark to thermally fade, it was found that 3-nitro had the longest relaxation time, taking around 4 weeks to completely revert to the ground enol state. 4-Iodo had the next longest relaxation time, at around 2 weeks, while 3-iodo took around 1.5 weeks and 4-bromo took 1 week. All four compounds took less than 10 minutes to fully revert when left in natural light, this time could therefore be reduced if the intensity of the light was increased. It can hence be concluded that the dihedral angle is a rate determining factor in the conversion under dark conditions but not under natural white light.

Table 12: Table of chromicity, dihedral angles, irradiation time, reversion time and fluorescence level in SA derivatives

Compound	Photo/ Thermochromic	Dihedral angle (°)	Irradiation time (Hrs)	Reversion Time (weeks)	Fluorescence (low-medium-High)	Temperature fluorescence is present (K)
1	Thermochromic	10/15	N/A	N/A	High	120-10
2	Thermochromic	30	N/A	N/A	Medium	298
3 (I)	Thermochromic	6	N/A	N/A	High	120-10
3 (II)	Thermochromic	1	N/A	N/A	High	120-10
4	Photochromic	49	3	2	Medium	298-10
5	Thermochromic	28	N/A	N/A	Medium	298
6	Thermochromic	30	N/A	N/A	High	298
8	Thermochromic	11	N/A	N/A	High	298
9(I)	Thermochromic	20/7	N/A	N/A	High	298
9(II)	Thermochromic	12	N/A	N/A	High	298
10	Thermochromic	21	N/A	N/A	Medium-high	298-250
11	Photochromic	64	3	4	Low	298-120
12	Photochromic	26	5	1	Low	298-10
18	Thermochromic	36	N/A	N/A	Low	298-10
19	Photochromic	46	4	1.5	Medium-high	298

In table 12 the differences in the occurrence of fluorescence between the thermochromic and photochromic compounds are also shown. The Raman spectra of the photochromic materials at the temperatures (see table 12) where data was collected, all show a medium to low level of fluorescence, meaning that the fluorescence signal contributed slightly to increase the background or, in the worst case, masked only few of the weaker peaks present in the spectrum. The thermochromic materials showed medium-high to high fluorescence resulting in a more important masking of most, if not all, of the peaks present in the spectrum. This was particularly prevalent at lower temperatures for the majority of thermochromic compounds, even where low fluorescence had been demonstrated at 295 K.

The larger crystals grown for the neutron experiments of compounds 4, 10, 11 and 18 along with those grown for 1 and 3 showed growth faults. As the temperature was decreased on the thermochromic materials (compounds 10 and 18) the quality of the crystals further degrade, reducing the intensity of the Bragg peaks as well as, in some cases giving rise to powder rings where permanent damage to the crystal occurred.

As seen in the neutron diffraction experiments for both photochromic compounds 11 and 4, when removed from the exciting UV source the excited Keto state is non-observable in diffraction with a bulk probe. A surface probe such as Raman Scattering can still observe the keto state. The way in which the keto state is excited by an outside UV light source means, that the process of tautomerisation cascades from the outside towards the centre of the crystal, as such the keto state is observed earlier in surface probes than in the bulk.

4.4 Conclusions

In this chapter the relationship between thermochromism and photochromism in Salicylaldehyde aniline derivatives was investigated. An ease of conversion between the irradiated photochromic state and the size of the internal dihedral angle between the two rings was identified. As such the larger the dihedral angle the easier the conversion to the irradiated state was seen in a shorter irradiation time. The stability of the irradiated state under ambient conditions was consistent across all photochromic materials, however, the more resonance structures the compound had the more stable the irradiated states was when left in the dark. With the thermochromic compounds the investigation lead to questions about the influence of fluorescence on the visible colour change as the expected enol to keto tautomerisation was not distinguishable in all of the compounds. Typically the level of fluorescence displayed increased with a decrease in temperature, the only contradiction to that observed was with 3,5-di*tert*butylsaliscylideneaniline where the fluorescence decreased with response to a decrease in the temperature.

4.5 References

1 H. Sugiyama and H. Uekusa, *CrystEngComm*, 2018, **20**, 2144–2151.

2 M. D. Cohen and G. M. J. Schmidt, in *Journal of Physical Chemistry*, American Chemical Society, 1962, vol. 66, pp. 2442–2446.

3 E. Hadjoudis and I. M. Mavridis, *Chem Soc Rev*, 2004, **33**, 579–588.

4 J. Harada, H. Uekusa and Y. Ohashi, *J Am Chem Soc*, 1999, **121**, 5809–5810.

5 T. Fujiwara, J. Harada and K. Ogawa, *Journal of Physical Chemistry A*, 2009, **113**, 1822–1826.

6 K. Ogawa, J. Harada, T. Fujiwara and S. Yoshida, *Journal of Physical Chemistry A*, 2001, **105**, 3425–3427.

7 C. C. Ersanli, Ç. Albayrak, M. Odabaşoğlu and A. Erdönmez, *Acta Crystallogr Sect E Struct Rep Online*, 2004, **60**, o389–o391.

8 Y. Y. Wang, Z. Yu, Y. Sun, Y. Y. Wang and L. Lu, *Spectrochim Acta A Mol Biomol Spectrosc*, 2011, **79**, 1475–1482.

9 I. Casades, M. Álvaro, H. García and M. N. Pillai, *European J Org Chem*, 2002, **13**, 2074–2079.

10 K. Ogawa, T. Fujiwara and J. Harada, *Molecular Crystals and Liquid Crystals Science and Technology. Section A. Molecular Crystals and Liquid Crystals*, 2000, **344**, 169–178.

11 W. Theilacker, G. Kortüm and G. Friedheim, *Chem Ber*, 1950, **83**, 508–519.

12 H. Koshima, K. Takechi, H. Uchimoto, M. Shiro and D. Hashizume, *Chemical Communications*, 2011, **47**, 11423–11425.

13 J. Harada, H. Uekusa and Y. Ohashi, *J Am Chem Soc*, 1999, **121**, 5809–5810.

14 A. Carletta, J. Dubois, A. Tilborg and J. Wouters, *CrystEngComm*, 2015, **17**, 3509–3518.

15 K. M. Hijas, S. Madan Kumar, B. C. Manjunath, R. Nagalakshmi, H. K.M., K. S. Madan, M. B.C. and N. R., *Spectrochim Acta A Mol Biomol Spectrosc*, 2019, **222**, 117227.

16 Y.-Y. Yu, *Acta Crystallogr Sect E Struct Rep Online*, 2011, **67**, o889–o889.

17 S. Pikoli, E. Hosten and A. Abrahams, *J Coord Chem*, 2020, **73**, 1055–1076.

18 G. Y. Yeap, S. T. Ha, N. Ishizawa, K. Suda, P. L. Boey and W. A. K. Mahmood, *J Mol Struct*, 2003, **658**, 87–99.

19 M. Köse, G. Ceyhan, E. Atci, V. McKee and M. Tümer, *J Mol Struct*, 2015, **1088**, 129–137.

20 S. Cai, G. Zhu, X. Cen, J. Bi, J. Zhang, X. Tang, K. Chen and K. Cheng, *Bioorg Med Chem*, 2018, **26**, 2041–2050.

21 A. Carletta, F. Spinelli, S. D'Agostino, B. Ventura, M. R. Chierotti, R. Gobetto, J. Wouters and F. Grepioni, *Chemistry - A European Journal*, 2017, **23**, 5317–5329.

22 K. M. Hutchins, S. Dutta, B. P. Loren and L. R. Macgillivray, *Chemistry of Materials*, 2014, **26**, 3042–3044.

23 François Robert, A. D. Naik, B. Tinant, Raphaël Robiette and Y. Garcia, *Chemistry - A European Journal*, 2009, **15**, 4327–4342.

24 H. Houjou, T. Kato, H. Huang, Y. Suzuki, I. Yoshikawa and T. Mutai, *Cryst Growth Des*, 2019, **19**, 1384–1390.

25 K. Johmoto, T. Ishida, A. Sekine, H. Uekusa and Y. Ohashi, *Acta Crystallogr B*, 2012, **68**, 297–304.

26 V. T. Kasumov, A. A. Medjidov, N. Yayli and Y. Zeren, *Spectrochim Acta A Mol Biomol Spectrosc*, 2004, **60**, 3037–3047.

27 A. Spangenberg, M. Sliwa, R. Métivier, R. Dagnélie, A. Brosseau, K. Nakatani, R. Pansu and I. Malfant, *J Phys Org Chem*, 2007, **20**, 992–997.

28 H. E. Mason, J. A. K. Howard and H. A. Sparkes, *Acta Crystallogr C Struct Chem*, 2021, **77**, 659–667.

29 Z. Zhang, M. Suzuki, Y. Yang, I. Yoshikawa, Q. Yin and H. Houjou, *CrystEngComm*, 2020, **22**, 4903–4913.

30 J. L. Bernstein, *Acta Crystallogr*, 1967, **22**, 747–748.

31 J. Csaszar, Acta Chimica Hungarica, 1990, **127**, 165–169.

32 M. D. Cohen, G. M. J. Schmidt and S. Flavian, The Journal of Physical Chemistry, 1964, 2041-2051.

33 N. Jaiswal, A. K. Kushwaha, A. P. Singh and R. K. Dubey, *Main Group Metal Chemistry*, 2019, **42**, 28–36.

34 I. Sidir, Y. G. Sidir, H. Berber and F. Demiray, *J Mol Liq*, 2015, **206**, 56–67.

35 G. Kaur, S. Singh, A. Sreekumar and A. R. Choudhury, *J Mol Struct*, 2016, **1106**, 154–169.

36 R. Wang and J. Xu, *Arkivoc*, 2010, **2010**, 293–299.

37 C. T. Cao, W. Zhou and C. Cao, *J Phys Org Chem*, 2017, **30**, e3672.

38 C. M. da Silva, D. L. da Silva, C. V. B. Martins, M. A. de Resende, E. S. Dias, T. F. F. Magalhães, L. P. Rodrigues, A. A. Sabino, R. B. Alves and Â. de Fátima, *Chem Biol Drug Des*, 2011, **78**, 810–815.

39 C. C. T. Cao, W. Zhou and C. C. T. Cao, *J Phys Org Chem*, 2020, **33**, e4028.

40 C. Bäumler and R. Kempe, *Chemistry - A European Journal*, 2018, **24**, 8989–8993.

41 N. Zwettler, M. E. Judmaier, L. Strohmeier, F. Belaj and N. C. Mösch-Zanetti, *Dalton Transactions*, 2016, **45**, 14549–14560.

42 J. S. Bennett, K. L. Charles, M. R. Miner, C. F. Heuberger, E. J. Spina, M. F. Bartels and T. Foreman, *Green Chemistry*, 2009, **11**, 166–16.

43 B. A. I Biggs and R. A. Robinson, 1954, **51**, 343.

44 C. Hansch, A. Leo and R. W. Taft, *Chem. Rev*, 1991, **91**, 165–195.

45 Ö. Özdemir, *J Photochem Photobiol A Chem*, 2019, **380**, 111868.

5 Spin Crossover Phenomena

5.1 Introduction and Literature review

Spin crossover (SCO) is a phenomenon that occurs in some metallo-organic complexes in which the spin state of the central metal atom switches between a high-spin and a low-spin state when an external stimulus is applied. The change in state can be induced in multiple different ways e.g., thermally, photoinduced and pressure induced[1] and is often accompanied by a colour change in the material. The origin of this effect is a competition between enthalpy, favours the low spin state (LS) and entropy where the higher configurational and vibrational entropy of the high spin state (HS) which surmounts the enthalpy contribution of strong metal-ligand bonds found low spin state (LS).[2] Spin crossover can also be accompanied by other changes to the physical properties found of these complexes such as; changes in the magnetic moment, dielectric constant, and electric resistance of the material. [2] SCO materials are very sensitive to small changes in energetic stimuli therefore, they have been used as part of switchable liquid crystals, sensory and memory devices and in nanoparticles and thin films.

The first evidence for spin crossover compounds appeared in the 1930's when researchers noticed unusual responses in iron(III) complexes. Though not attributed to spin crossover at the time, the subsequent developments which were the result of the introduction of ligand field theory, and enabled the properties of these materials to be explained when allowance was made for the effect of external stimuli in the ground states of these molecules. Ligand field theory allows the prediction of properties for transition metal complexes that can aid in the identification of those complexes most likely to demonstrate the spin crossover phenomenon.[1]

1) First row transition metals with 4-7d electrons in an octahedral geometry are the most likely to exhibit SCO properties. SCO is less likely to occur when transversing over the second and third row transition metals, due to the increase in ligand field strength crowded compared to the insignificant changes in spin pairing energy, hence the metals will exist in a low spin state.

2) If other features are retained (ligand type) and the oxidation state of the metal in a complex is increased, it is not expected that the higher oxidation state complex would retain the same SCO properties but instead adopt more LS character. This is again due to changes being larger with the ligand field strength than the spin pairing energy.

3) Transition metals with 5-7 d electrons are more likely to undergo thermally induced SCO, this is because of the competition between the mean spin-pairing energy and the ligand field stabilisation energy.

4) Hund's rule exchange energy says that when P (pairing energy) is comparable in magnitude to the cubic crystal-field splitting $\Delta = 10\ Dq$[3]

Close to the point at which the complex switches between HS and LS states the ligand field stabilisation is close in magnitude to the pairing energy, i.e. the difference between the two values is of the order of magnitude of the thermal energy (k_BT).[4]

There are essentially three synthetic strategies developed to create cooperativity and strengthen it due to the essential nature of cooperative interactions for SCO in the solid state. Using Iron-Nitrogen based complexes as an example cooperativity can be described as the 'transfer of volume-work due to the spin-state related elongation of the Fe–N bond by a rigid ligand' [5,6]. These are:[7]

1) Incorporation of a hydrogen-bonded network

2) Coordination of bridging ligands

3) Incorporation of π-stacking moieties

Some spin-cross over compounds, display both photo and thermal induced change for example, with the Iron(II) complexes $[Fe(ptz)_6](BF_4)_2$ and $[Fe(2\text{-}pic)_3]Cl_2 \cdot EtOH$ (discussed in more detail later).

Spin-crossover can be categorised into 5 types:[7]

A) Gradual – appears in solution where there is near no cooperativity

B) Abrupt

C) With hysteresis

D) Step-wise

E) Incomplete

The route by which SCO materials are prepared has an influence on their behaviour. Mechanical processes such as ball milling or crushing crystals, tends to increase the HS fraction at lower temperatures making the curve for the transition more gradual. Haddad *et al* as well as Muller *et al* proposed that the method introduces defects into the crystals which can also be achieved by rapid precipitation[8,9]. Another effect is particle size. In a recent study on an Iron (II) complex, Lada *et al* suggested that the smaller the particle size the higher the temperature at which spin crossover occurs[10,11].

5.1.2 Thermally induced SCO

The largest proportion of thermal SCO materials that have been synthesised and characterised belong to three classes of complexes, in which the transition metal are Iron(II), Iron(III) and Cobalt(II) Six-coordinate SCO complexes of iron(III) generally exhibit S = 1/2 ↔ S = 5/2 spin transitions, whereas for five coordinate systems an intermediate S = 3/2 ↔ S = 5/2 spin transition is observed in iron(II) compounds involving the change of electron configuration $t_{2g}^6e_g^0$ ($^1A_{1g}$, LS) ↔ $t_{2g}^4e_g^2$ ($^5T_{2g}$, HS), this mainly occurs for six - coordinate compounds (Fig 159). While with Cobalt(II) the transition is $t_{2g}^6e_g^1$ (^2E_g, LS) ↔ $t_{2g}^5e_g^2$ ($^4T_{1g}$, HS). Other classes which are less well represented include $3d^4$ complexes of chromium(II), manganese(III), $3d^5$ complexes of manganese(III) and, $3d^6$ complexes of cobalt(III); demonstrating $t_{2g}^4 e_g^0$ ($^3T_{1g}$, LS) ↔ $t_{2g}^3 e_g^1$ (^5E_g, HS), $t_{2g}^5e_g^0$ ($^2T_{2g}$, LS) ↔ $t_{2g}^3 e_g^2$ ($^6A_{1g}$, HS) and $t_{2g}^6e_g^0$ ($^1A_{1g}$, LS) ↔ $t_{2g}^4e_g^2$ ($^5T_{2g}$, HS) transitions respectively. [1] Cooperative transitions are accompanied by a hysteresis demonstrating a kind of memory effect.[4] Due to the e_g antibonding character, any changes in population density give rise to a corresponding change in the metal-ligand bond length (an increase in population leads to an increase in bond length). The reverse change is true of the t_{2g} orbital population changes, which affect the back bonding between the metal and the π* antibonding orbital of the ligand. [1] The thermal energy is transformed into vibrational energy by the SCO centre,

this leads to the population of the excited vibrational levels moving up to the adiabatic potential crossing point, this is where the transformation between the HS and LS state takes place in accordance with the Franck-Condon principle (Fig 282).

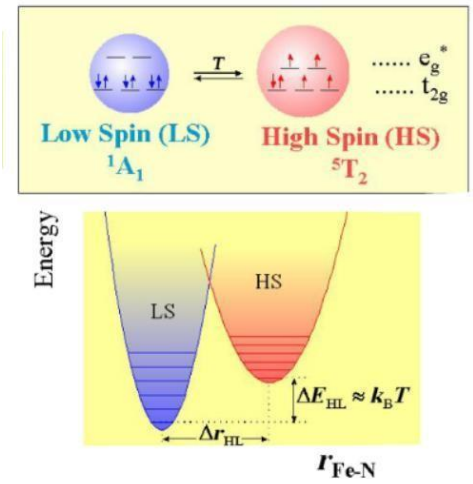


Figure 282: Electronic configuration for the effect of temperature on spin transition[7]

According to Renz[12], the essential condition required for thermal SCO, is that the difference between the zero- point vibrational energy gap for the HS and LS configurations is of the order of the thermal energy of the system kT. [13,14]

In a 2011 review by Halcrow[2] it was suggested that the temperature at which spin would be reduced, and crossover occurs could be tuned by changes to the structure of the complex. By increasing steric crowding in a spin crossover complex, the $T_{1/2}$ (the point at which half of the molecules are in each spin state) is raised as the larger high spin state is favoured. A similar change can be brought about by placing a weaker-ligand field donor into the complex providing all other parameters remain equal. Higher levels of rigidity for the ligands and the effects that this then has on conformational considerations are important to the thermodynamics of spin crossover materials. Along that vein, an increase in the ligand chelate ring size corresponds to a consistent reduction in $T_{1/2}$ which can be attributed to the ligand strain also increasing, larger six-longer bond lengths membered rings favour a less compact HS.[2]

For salt materials in which there can be hydrogen bonding between the cation and anion due to the presence of hydrogen bond donors in the ligand donor groups, the strength of the anion-cation

interaction has been proposed to play a role in lowering the $T_{1/2}$. As such, the stronger the hydrogen bonding the lower the basicity of the surrounding ligand donor groups and hence the lower $T_{1/2}$. Where there is no possibility of hydrogen bonding it is then proposed that $T_{1/2}$ is affected by the charge: size ratio of the anion or its electronegativity, with stronger electrostatic interactions favouring a LS complex, and hence there is an increase in $T_{1/2}$ for smaller anions.[2] The hydration level of a complex also has the possibility to alter $T_{1/2}$ by stabilising the LS complexes.

Pressure can also alter the point at which spin transition in thermal SCO occurs, when applying pressure, the metal ligand bond is shortened and hence the ligand field strength is increased so the LS state is expected to be favoured as the HS state is destabilised due to its, typically, larger volume (Fig 283). This is due to the increase in the relative displacement of well potential which is a result of the increase in pressure causing both a decrease in ΔR and an increase in ΔE_{HL} hence decreasing the ΔE^{a}_{HL} (activation energy).

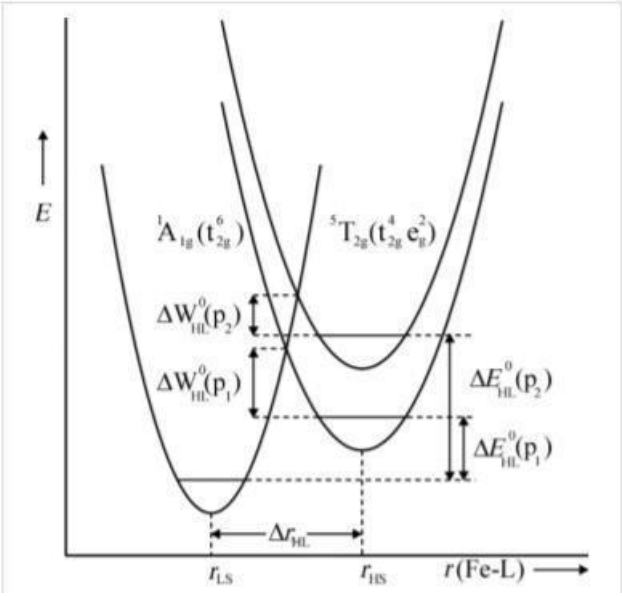


Figure 283: Electronic system for the effects of pressure on spin state transitions[7]

5.1.3 LIESST (Light Induced Excited Spin State Trapping)

LIESST is the light induced low spin to high spin conversion at low temperatures observed in a spin crossover compound. It was first observed with $[Fe(ptz)_6](BF_4)_2$ (ptz=1-polytetrazole) where a thermal spin transition between high spin and low spin states can be produced from a low spin state to a long lived metastable high spin state below the normal temperature of transition using green light. This can then be reconverted to LS using red light. An energy barrier is built up between the potential wells of the two states caused by the larger Metal-Ligand bond distance in the HS compared to the LS. Because radiative decay between the $^5T_1$ and $^1A_1$ is both spin and parity forbidden, the thermal relaxation of the LIESST metastable HS occurs through non-adiabatic tunnelling through the barrier, rather than with the classical passing over the barrier, the temperature dependence of the decay is the result of the thermal population of the vibronic levels of the $^5T_2$ manifold[15]. The lifetime of the LIESST metastable state is dependent on the ligand field strength at any given temperature, the smaller the difference between the lowest vibronic levels of the HS and the LS, ΔE_{HL}^0, the weaker the ligand field strength and the longer the lifetime. Another factor that leads to a longer lifetime for the metastable HS is the length of the metal-ligand bond distance. As a consequence of the smaller changes in the metal-ligand distance in conjunction with the smaller changes in the configurational energy that occur for Fe(III) and Co(II), compared to Fe(II), will result in the HS state having a shorter lifetime.[4]

5.1.4 Iron (II) complexes

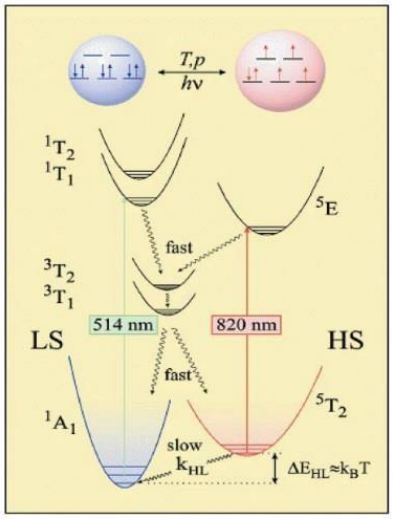


Figure 284: Electronic system for iron(II) complexes[16]

Iron (II) complexes can be tuned to be high spin or low spin based on the ligands. Using ligand theory a high spin ground state can be found within a weak ligand field with regular octahedral symmetry, a strong ligand field creates a low spin ground state (Fig 284). The majority of Fe(II) complexes of interest in the field have the general formulas $[FeL_6]^{n+}$ or $[Fe(NCX)_2L_4]$ where the 'L' ligand is a nitrogen donor and X is either S or Se or a related pseudohalide[17]. The greatest change in ligand metal bond length between HS and LS is found in in the complexes involving Fe(II) and nitrogen containing ligands. This induces larger cooperativity between spin centres during SCO which causes abrupt thermal transitions which may have hysteresis. The rate of relaxation for Fe(II) LIESST complexes is 10^7 slower than that of comparable Fe(III) complexes. The crystal field strength 10 Dq can be determined from the parity-forbidden, but for spin allowed d-d transitions, this is near 12 000 cm^{-1} for HS and 18 000 cm^{-1} for LS.

The transition from HS to LS can lead to a reduction in the metal ligand bond length of up to 10%. The cause of this reduction is because that in this type of octahedral complex it is the antibonding e_g orbitals that are empty in the LS state and occupied in the HS in compared to the t_{2g}-orbitals which are nonbonding or only slightly bonding in nature. In the high spin state, the Fe-Ligand bond is longer than that in the low spin state by around 0.2 $\dot{A}$, this is due to the antibonding e_g orbitals being doubly occupied. The difference in the electron population affects the strength of the metal-ligand bond and the changes in which can be monitored using vibrational spectroscopy, the typical frequency for a

metal-ligand bond vibration in IR is expected to be around 350-450 cm^{-1} in the HS, while it shifts to 200-300 cm^{-1} in the LS. It has also been found that non-coordinating anions or solvent molecules can "feel" the changes in the spin state at the metal centre which are linked by hydrogen bonding or van der Waals or other similar interactions.[4] This can be observed in changes in the vibrational modes of the linking species. Finally, the increase in the metal to ligand bond lengths consequently leads to an increase in the overall molecule size shifting from LS to HS.

Another technique used to track the shift between states is UV – Vis spectroscopy due to the colour change that accompanies the transition. The shift tends to be from near colourless in HS state to more intensely coloured in the LS state so there is a shift in the absorption intensities. The electric dipole ligand field transitions (d-d transition) involved in the shift are parity forbidden but spin allowed causing the intense colouration that is seen particularly in the LS UV-Visible region which distinguishes the two spin states involved. If the ligand field transitions are not hidden by more intense parity- and spin allowed charge transfer bands, they are well resolved.[7]

The different structures can also be monitored using crystal-structure determination. This is done by monitoring changes in the metal-ligand bond lengths and angles for continuous transition where space group changes are not observed. For discontinuous transitions a space group change is observed. These changes occur due to the rearrangement of the valence electrons in the slightly bonding t_{2g} orbitals and the antibonding e_g orbitals.[7] The charge reorganisation leads to a longer metal-ligand bond length in the HS compared to the LS, this is accompanied by a 3-4% change in the unit cell volume. The application of single crystal diffraction can allow for the identification of specific ordering and intermolecular interactions such as π-stacking and the existence of hydrogen bonding which aid in cooperative interactions.

5.1.4.1 $[Fe(2\text{-}pic)_3]X_2 \cdot Solv$ series

$[Fe(2\text{-}pic)_3]X_2 \cdot Solv$ is one of the most comprehensively studied Fe(II) spin crossover complex series (X=I, Br, Cl). The SCO occurs by both thermal and light induced means, and has been studied using x-ray crystal structure determination, Mössbauer spectroscopy, magnetic susceptibility, absorption spectroscopy, Raman spectroscopy, specific heat capacity, NMR and ESR.[18–23,10,24,25]

The $[Fe(2\text{-pic})_3]^{2+}$ salt has been used to study solvent and hydration effects. The hydrogen bonded network between the ligand and the solvent stabilises the LS state hence raising $T_{1/2}$ by increasing the level of cooperativity.[26] The ethanol solvate has a steep transition curve around 115 K , the methanol has a slightly more gradual transition around 150 K, whereas the mono-hydrate shows broad hysteresis between 200 K and 290K, the dihydrate does not demonstrate any spin transition at all but remains consistently in the LS.[7] Both the propan-1-ol and the tert-butyl solvates have been studied and remain high-spin in all studied conditions, due to inhibiting the molecular rearrangement that occurs in the pyridyl rings that are trans to each other in the meridional arrangement of the ligands. In this rearrangement the ligands should migrate around the iron centre so that the trans-N{pyridyl}-Fe-N{pyridyl} angle increases by around 7°, compared to what is seen in the LS state. There is also often disorder associated with the alcohol solvent molecules that sit in the space between the two pyridyl groups with the presence of C-H···π contacts, as a result of the expansion the expansion of the angle during spin-crossover moves the one of the rings closer to the solvent.[2]

The $[Fe(2\text{-pic})_3]^{2+}$ salts have also been used to study the effect of modifying the non-coordinating anion (not directly coordinated to the metal centre). The degree of completion and steepness of the ST curve increases in the order iodide < bromide < chloride. There are differences in the trends of halides based on whether or not the salt is solvated, as 2-pic contains hydrogen bond donors the strength of the cation – anion interaction affects the spin crossover process. The stronger the hydrogen bonding the weaker the ligand-metal interaction hence the favouring of HS and the lowering of $T_{1/2}$, in contrast, the isostructural solvates $[Fe(2\text{-pic})_3]X_2 \cdot EtOH$ (X = Cl and Br) have essentially the same $T_{1/2}$.[2]

There have been deuteration studies on the ethanol and methanol solvates of the Chloride salt, where both the NH_2 of the ligand and the OH group of the alcohol were deuterated.[17,19] These studies demonstrate a change in the transition temperature that moves to about 15 K higher, yet the degree of cooperativity seems to remain the same. This change could be a reflection of effect on the Metal-Ligand bond vibrations in cooperativity or changes to the intermolecular hydrogen bonding. In line

with this the deuteration of other points in the ligand (pyridine ring) or the methylene group show a smaller change to $T_{1/2}$.[17,19]

5.1.4.1.1 $[Fe(2\text{-}pic)_3]Cl_2 \cdot EtOH$

5.1.4.1.1.1 Thermal

The thermal transition of $[Fe(2\text{-}pic)_3]Cl_2 \cdot EtOH$ occurs via a two-step transition without an ordered intermediate phase (IP) upon cooling shifting from HS at room temperature through an IP into LS at lower temperatures. There is a small plateau between 122 K and 114 K and most crystallographic studies have reported that there are no changes in the space group upon transition with a single iron site in the asymmetric unit and the iron sites remain crystallographically equivalent.[27] The IP is built up of ordered clusters of HS-LS pairs, these lack long range ordering due to the next-nearest neighbour distance estimations of the correlation lengths. This was determined by reproducing the experimental transition curve with a Monte Carlo computational analysis with cluster variation methods[27]. During the intermediate phase the unit cell seems to double in size with one iron site being mainly in the HS the other being predominately in the LS this is classed as 're-entrant' phase transition. The switch through the IP between HS and LS shows a discontinuous change in the lattice parameters and atomic coordinates, if there was no IP the change would classify as an apparent iso-structural first order phase transition.[27] Slight differences in the spin-ordering on two separate high-spin sites with an order parameter of 0.72, show that the ordering is not perfect. [27]

5.1.4.1.1.2 LIESST

Continuous interest in $[Fe(2\text{-}pic)_3]Cl_2 \cdot EtOH$ was due to its nature as a photoinduced spin crossover complex. $[Fe(2pic)_3]Cl_2 \cdot EtOH$ demonstrates LIESST at least below 25 K. However, there are issues with using single crystals because they disintegrate into a micro crystalline powder at these temperatures. It is thought that this is due to the introduction of gradients caused by the HS moving through the crystal as the transformation is induced. Tuning of the radiation conditions has shown that using a radiation wavelength that sits on the edge of the MLCT transition (Metal Ligand Charge Transfer), ensures that no concentration gradients are created.

The efficiency of conversion to HS from LS in this system is roughly 0.82, because of the higher intensity of the $^1A_1 \rightarrow {}^3T_1$ and $^3T_2$ bands compared to the $^5T_2 \rightarrow {}^5E$ band.[28] Below 10 K the life-time of the metastable HS is over 5 and a half hours, when the temperature is taken above 50 K that lifetime decreases to only several hundreds of seconds. In 2002 a study by C. Enachescu *et al*[29] determined that the quantum efficiency of this system is not dependent on the intensity of the irradiation.

A Raman study of the photoinduced phase by Tayagaki and Tanaka[30], suggests that the LIESST HS and the thermal induced HS phase are in fact different. They observed extra Raman bands in the LIESST Raman compared to that of the thermal prepared state, and proposed that a reason for this is that a symmetry lowering is taking place in the process, due to cooperative Jahn-Teller distortion. An additional X-ray diffraction study by Guerin *et al,* reported that there were indeed structural differences between the two high spin phases.[31]

5.1.4.2 $[Fe(ptz)_6]X_2$

$[Fe(ptz)_6](BF_4)_2$ is another Iron(II) complex that has been studied, like $[Fe(2\text{-pic})_3]Cl_2 \cdot EtOH$ it also displays both thermal spin crossover and LIESST behaviour. The complex crystallise in colourless hexagonal plates which turn a deep violet when dropped in liquid nitrogen. Five different phases can be formed under different temperatures using LIESST and reverse-LIESST[32], under varying conditions.

1) An ordered structure with R3 symmetry which consists of HS molecules above temperatures of 110 K

2) After rapid cooling (30 K min^{-1}) to below 110 K a super-cooled high temperature phase consisting of LS molecules that retains the R3 symmetry.

3) Below 50 K after rapid cooling and irradiation with a green laser the structure consists of metastable HS molecules.

4) After annealing (3) below 110 K then slowly cooling (1 K min^{-1}) a disordered structure of LS molecules is formed.

5) A disordered HS LIESST phase formed from the disordered LS phase[33].

The LIESST ordered structure of $[Fe(ptz)_6](BF_4)_2$ has been studied with neutron powder diffraction and INS by K. Ridier *et al*[34] but, they found it difficult to identify the HS/LS fractions from the whole diffraction pattern. Instead they used two peaks that would 'feel' the spin shift of the iron(II) centre the most, (113) (Q1 ≈ 1.31 $A^{\circ -1}$) and (202) (Q2 ≈ 1.41 $A^{\circ -1}$). The material is also found to have a hysteresis during thermal conversion between high and low spin states. The thermal conversion between HS and LS is due to the $^5T_{2g} \rightleftharpoons {}^1A_{1g}$ spin transition. The point at which both spin states are in equal fraction is known as the transition temperature. For the ptz complex this is at around 130 K with hysteresis. At low temperatures (50 K) the complex can be found in the triclinic space group P $\bar{1}$. A powder diffraction study showed that there is a 50 $Å^3$ volume difference in the unit cells between the thermal high and low spin states. Using magnetic susceptibility measurements, it has been shown that the transition is complete at 123.5 K when cooling whilst the transition completes at 131 K when warming.

There is only one spin-allowed absorption band in the HS state corresponding to the $^5T_{2g} \rightarrow {}^5E_g$ transition. For the LS state there are 2 spin-allowed absorption bands each corresponding to $^1A_{1g} \rightarrow {}^1T_{1g}$ and $^1A_{1g} \rightarrow {}^1T_{2g}$ transitions.

Further to this $[Fe(ptz)_6](PF_6)_2$ has also been studied using single crystal neutron diffraction, showing a transition temperature between the high and low spin states of 74 K at ambient pressure, this does increase to 102 K when the external pressure is increased to 1 kbar. Between the HS and LS states there is a volume difference per molecule of 24 $Å^3$. This complex in contrast to the BF_4 does not display a hysteresis during transition upon cooling and rewarming. Down to 130 K the complex has the crystallographic space group P$\bar{1}$ with no crystallographic data having been collected below this point.

Another way used to tune the transition in spin-crossover compounds is *via* metal dilution, i.e. introducing another metal into the complex, an example of this is by introducing manganese into the $[Fe(phen)_2(NCS)_2]$ system or zinc into $[Fe(2\text{-}pic)_3]Cl_2 \cdot EtOH$ or$[Fe(ptz)_6](BF_4)_2$. The introduction of the competing metals gradually weakens the field strength and causes quenching of the spin transition.

5.1.4.3 $[Fe(isoxazole)_6]^{2+}$

For the compounds in this series, there are differing patterns of spin crossover which are seemingly anion dependent. For the complex containing the BF_4^- anion spin crossover occurs as part of a two-step transition process, whereas, for the complex containing the ClO_4^- anion spin crossover occurs during a continuous one step transition process.

$[Fe(isoxazole)_6](BF_4)_2$ structural investigations show that there are two different iron sites in the complex labelled as Fe1 and Fe2, which explains the two-step transition. Upon cooling the first step of the transition occurs at 192 K and is associated with the Fe2 site; this has no centre of inversion and an average Fe-N bond length of 2.169 Å, the average distance between the oxygen atoms of the neighbouring ligands in each ligand pair is 3.315 Å. The second step in the transition occurs at 91 K and is associated with the centrosymmetric Fe1 site. In this case the O-O distance is 4.09 Å, but the Fe-N distance is 2.179 Å. Fe1 sits on the $\bar{3}$ symmetry element whereas the Fe2 sits in the 3-fold symmetry axis, the ratio between the two sites is 1:2 for Fe1:Fe2. At the point where the first step of the transition occurs (192 K), 1/3 of the iron sites (Fe2) had transitioned from HS to LS.

The transitions have also been examined with respect to the effect they have on the magnetic moment of the molecule. At 270 K, i.e. well above the initial transition temperature (192 K) the magnetic moment is 5.0[1] or 5.25 μ_B[22]. At 130 K, below the first transition the moment drops to 3.30 or 3.20 μ_B, in sequence with 2/3 of the Fe sites being in a LS configuration. When tested below the second transition point (91 K) at < 70 K, the moment reaches 2.0 or 1.90 μ_B and at this point only about 13 % of the sites remain in HS configuration. Upon rewarming back to near room temperature there is a near imperceptible hysteresis of 1 K. Between 150 K and 110 K there was a plateau in the magnetic moment, this was originally thought to be because of impurities in the compound, however the reproducibility of the phenomena means that this hypothesis is unlikely.

There is a crystallographic change that accompanies the spin crossover[2] from $P\bar{3}$ above and through the first step of the transition, to $P\bar{1}$ after the second step of the transition. This is also accompanied by a contraction of the Fe-N bonds which also leads to an overall reduction in the size of the unit cell

of around 6 %. [Fe(isoxazole)$_6$](BF_4)$_2$'s change in spin state is also seen as a colour change from pale pink/ purple in the HS state, to a darker purple/ blue in the LS state.

When investigating the effect of the complex on absorption bands the shifts from the bands of the free ligand[1], the extent of which is in sequence with stability of the metal ions as described in the Irving Williams series[1], the presence of absorption bands at 1050 and 520 cm^{-1} along with the absence of bands at 750 and 350 cm^{-1}, [1] allow for the assumption that the BF_4^- anion is not bonded to the metal centre; this also leads to the conclusion that the complexes are true solvates.[1]

During the procedure to grow the crystals it was found that if the complex was recrystalised from a mixture of the ligand (20 %) and nitromethane. The resulting product had less labile ligands, therefore it more stable, however, the compound is still very moisture sensitive.

[Fe(isoxazole)$_6$](ClO_4)$_2$ structural[3] and magnetic investigations show a single step transition between the HS and LS states, but as with the (BF_4) complex there are two independent Fe sites. The Fe1 site sits on a centre of inversion and lies along the C_3 axis, meanwhile, Fe2 sits on a three-fold symmetry site with no inversion centre. The unit cell contains three Fe(II) atoms at a ratio of 1:2 for the Fe1: Fe2 sites, there is symmetry found between the two Fe2 sites which is caused by the Fe1 inversion centre. There is little difference between the Fe-N average bond lengths of the two sites, for Fe1 this is 2.171 Å and 2.175 Å for Fe2; the separation average between the oxygens of the trans isoxazole ligands is 5.04 Å.

Structural studies using single-crystal x-ray crystallography were performed only at 250 K, this is because below this temperature the crystals suffered cracks and damages which prevented further data collection. At 295 K , these studies have identified a trigonal crystal system with $P\bar{3}$ space group.

When studying the IR bands of the complex just as with the (BF_4) anion, the presence of bands at 1090 and 620 cm^{-1}, as well as the absence of bands at 930 and 455 cm^{-1}, suggest that the anions are not bonded to the complex and it is hence a true solvate. When taken above the melting point of 393.15 K it was found that the complex decomposes.

The magnetic studies showed a phase transition at 210 $\pm$ 5 K with a crossover temperature of 213 K (DSC). The magnetic moment show as a function of temperature showed steady drop from 5.1 μ_B at 270 K, to 1.9 μ_B between 240 K and 180 K, then down to 0.8 μ_B when taken below 10 K. The colour transition that accompanies this change is from a pale purple to a dark purple. The change in moment between 240 and 180 K suggests that around 18 % of the iron sites remain in a HS state, this percentage however is contestable. It is reported in the 1985[3] study that there was an error in reporting that placed the percentage of HS iron at 40 % in an earlier paper due to a calculation error upon applying the equation $X_{HS} = \frac{\mu^2}{\mu_{HS}^2}$, this apparent error is however a closer match to that of the Mössbauer data. Upon rewarming there is a 9 K hysteresis and so the phase transition now appears at 220 $\pm$ 5 K. For the Mössbauer study, it was reported that the magnetic moment of 1.85 μ_B corresponds to 37 % of the iron sites being in a HS state. The study suggests that of the three iron sites only two undergo spin transition, from HS at room temperature to LS below liquid nitrogen temperatures.

5.1.5 Iron (III)

Iron (III) complexes that demonstrate thermal spin transition often have a FeN_4O_2 chromophore. The HS shows a metal-ligand charge transfer (500-550 nm) band, the intensity of this band decreases in the LS which shows an increased intensity in lower energy bands occurring at (600-700 nm).

In these complexes, the HS Iron ions have unpaired electrons in their e_g antibonding orbitals, that become vacant when the complex shifts to the LS state. As is the case with Iron (II) this results in longer metal-ligand bond lengths in the HS compared to the LS, the change is ~ 0.10- 0.13 A[7].

The LS ground state $^2T_{2g}$ converts to the HS ground state $^6A_{1g}$ as there are more degrees of freedom in the HS state, hence the entropy term of Gibbs free energy is the driving force of the process[7]. Fe (III), which generally undergoes a gradual transition, has a relatively small domain size of 5 nm compared to the estimated domain size of 77-95 nm for some Fe (II) abrupt transitions. The smaller domain size means that the influence of intermolecular interactions is reduced and hence there is less cooperativity, as such each molecule converts independently and consequently the transition occurs gradually over a larger temperature range.

There are some Iron (III) complexes that convert more rapidly, according to Nihei *et al.* the factors that could cause the rapid change include: the shorter bond lengths such complexes have in comparison to those that convert gradually, the effectiveness of the nuclear tunnelling which could also be affected by some of the vibrational modes being anharmonic, the occurrence of a strong interaction through the excited $^4T_{1g}$ state between $^2T_{2g}$ and $^6A_{1g}$.[35]

This rapid conversion also occurs with LIESST iron(III) complexes and as such the life-time of these are shorter than that of iron(II), the structural changes are larger than that expected for thermal SCO. It is possible to produce a different type of light induced SCO by the introduction of potential photo-isomerisable ligands[12,35].

5.1.6 Cobalt (II) and (III)

Cobalt (II) and (III) spin crossover complexes have not been studied as extensively as those of Iron (II) and (III). This could either be due to the lack of an abrupt spin crossover transition compared to the energy barrier differences between the two metal complexes. or alternatively, the lack of a suitable precise analysis technique for monitoring the spin transition curve in such a way that is afforded by Mössbauer spectroscopy for iron complexes.[36] In contrast with iron systems LIESST phenomena has not yet been demonstrated in cobalt systems. Cobalt has been used as a SCO centre with isoxazole as a ligand, the colour change noted was between orange and red and isostructural to the Fe(II) isoxazole complex, based on the X-ray powder pattern. [37]

5.1.7 Nickel (II)

Nickel (II) SCO have been studied to various degrees. The Ni(II) isoxazole complex[37] was studied in conjunction with other isoxazole complexes showed a violet to blue transition. The tabulated information in the paper showed that the complex is isostructural to both the cobalt and iron complexes. [37]

Another Nickel SCO complex studied was $Ni(cyclam)_2I_2$, this showed a gradual transition from HS at 390 K to LS at 2 K[38,39,40,41,42]. The SCO phenomena was identified using multiple techniques such as SCXRD at 390, 200 and 10 K, SQUID measurements at 395 and 2 K and quantum chemical calculations. An application for this material is as a catalyst for reduction of CO_2[43]. The SCO HS to LS transition is a $^3B_{1g}$ to $^1A_{1g}$ transition.[38]

Over the course of this chapter I will delve into the synthesis and characterisation of 4 different SCO complexes with Co and Ni centres, these are $Co(tetrazole)_6(BF_4)_2$, $Ni(tetrazole)_6(BF_4)_2$, $Co(tetrazole)_6(PF_6)_2$ and $Ni(Cyclam)I_2$. The characterisation of the SCO properties of these complexes and their precursors was completed using SCXRD, SQUID magnetic measurements and DSC (Differential Scanning Calorimetry).

5.2 Experimental

Three different types of SCO materials were produced based on their ligands with one of three metal ion centres (Fe(II), Co(II) and Ni(II)), these ligands were isoxazole[1], tetrazole and cyclam (1,4,8,11-tetraazacyclotetradecane). The production of these materials was met with different levels of success due to the air sensitivity of some of the SCO materials as well as the form (i.e. powder or single crystal) or phase (i.e. crystalline or amorphous) of the final product.

5.2.1 Isoxazole

There are three suggested spin crossover materials using isoxazole as a ligand, the metal centres for these are Fe(II), Co(II) and Ni(II)[2,3]. The synthesis of these complexes followed the methodology suggested by Driessen [1]. The Metal (II) tetrafluoroborate was added to a solution of 5 mL Nitromethane and 4 mL Acetic Anhydride. Then, 7 equivalents of isoxazole were added. During the initial attempts the solutions were placed to crystallise in freezers at different temperatures, the first set at -18°C and the second at -40°C, but the resulting products were white powders not consistent with the expected coloured complexes. In the third attempt instead of placing the solutions into the freezer, Diethyl ether was added to the solution before they were sealed to induce liquid-liquid diffusion.

For both the Ni(II) and the Co(II) this methodology caused the growth of purple and orange crystals respectively. In contrast however, the Fe(II) reaction did not show any crystallisation only a precipitation of a white solid, similarly to what had been seen using the initial methodology.

The methodology for the Fe(II) complex was again updated, so that a piece of clean iron metal sheet was first placed into the solution before the iron tetrafluoroborate was added, in order to try and prevent the Fe(II) salt from oxidising to Fe(III). Once the iron complex was dissolved the iron sheet was removed and then the isoxazole was added. The resulting solution was significantly lighter than what was observed with previous attempts. Diethyl ether was then added before the solution was sealed and left to react. After 24 hours needle like crystals were observed in the solution.

Using the Ni(II) and Co(II) crystals an attempt was made at collecting single crystal x-ray data moving the crystals straight from the solution into fluorinated oil. While the crystals lasted long enough in the beam to collect an initial unit cell, they dissolved in about 15 minutes leaving a small bubble of oil. This was not purely a result of the energy transported by the x-ray beam, as the sample left in the oil on a microscope slide also dissolved leaving a coloured spot in the oil matching that of the crystals. An attempt to transfer the crystals from the solution into a capillary was then attempted both in air and under nitrogen in a glove box, but the solution evaporated too quickly. To make it possible to transfer the sample into a capillary the diethyl ether was switched with toluene, this meant that the reaction solution no longer evaporated instantaneously as soon as the lid was removed from the reaction vessel. Due to the size of the capillaries relative to the needles or pipettes used, the transfer of the crystals from the reaction vessel was not successful but the change in reaction solvents did allow for multiple attempts over an extended period.

5.2.2 Tetrazole

Production of the $M(tetrazole)_6(BF_4)_2$ complex (M=Co, Ni) was carried out from the metal BF_4 salt. (0.4g) of the salt was dissolved in water, to which the tetrazole in acetonitrile was added (6 mL). The solution went through a gel phase before solidifying into coloured blocks. These blocks where thought to be single crystals as they had faces and cleaved cleanly. However, when placed on the single crystal X-ray diffractometer, the diffraction pattern showed broad features, resembling scattering associated with amorphous materials with only very few Bragg peaks that did not produce a unit cell upon indexing. The blocks were then thought to be amorphous glasses or solidified gels, which would require further identification by XAFs.

To produce the $M(tetrazole)_6(PF_6)_2$ complex (M=Co), the starting point was the metal powder (1.5 g), that was dissolved in water with HPF_6 (100 ml total, 33 % weight) and left to completely react. Once the reaction was completed any excess metal was filtered off and the solution left for the water to evaporate. The $Co(PF_6)$ salt formed plate-like deep-pink crystals. The $Co(PF_6)$ salt was then redissolved in water before the tetrazole was added and the solution left for the water to evaporate. This resulted in the formation of pale pink crystals and orange pink powder.

5.2.3 Ni(cyclam)I_2

Nickel(II) iodide (300 mg, 0.991 mmol) was dissolved in hot 1-butanol (200 mL) then added to a solution of cyclam (254.1 mg, 1.268 mmol) in ethanol (10 mL). The solution was stirred for 4 min at 100 °C and filtered to remove the solid residue. This was allowed to slowly cool before being set up for crystallisation *via* liquid vapour diffusion of diethyl ether. The crystals produced were dark red to near black in colour and around 0.5 mm^3 or less in volume. There were two visible morphologies in the crystals formed one block like, the other needle like.

5.3 Results and Discussion

5.3.1 M(tetrazole)$_6$BF$_4$

The blocks of M(tetrazole)$_6$BF$_4$ (M=Co, Ni) were studied using SQUID measurements to assess their magnetic susceptibility (see fig 285 and 286). Such measurements allow testing of how the temperature affects the magnetic moment and also if there are any hysteresis in the magnetic effects with the application of an external magnetic field.

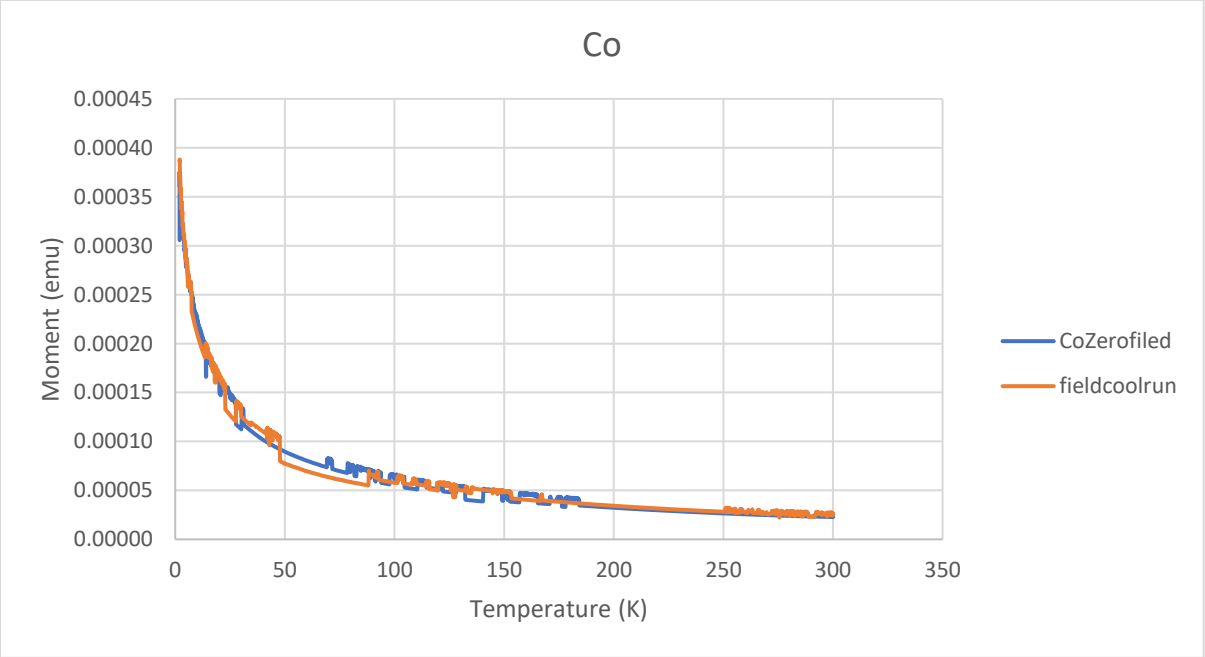


Figure 285:Magnetic Susceptibility of Co(tetrazole)$_6$(BF$_4$)$_2$ between 300 and 2 K

Tested over a wide temperature range these materials showed no notable hysteresis. The complexes were softer than expected which made the loading difficult, the samples were loaded into a straw sample holder. After the experiment when the samples were removed from the instrument, the Co complex was found to have fractured into smaller pieces. This had been caused by the motion of the sample stick through the super-magnet coil at rapid speeds, accounting for some of the noise in the resulting data (fig 285).

The relationship between the magnetic susceptibility and temperature for both materials is indicative of a paramagnetic material. In a paramagnetic material the spin states are randomly oriented.

To calculate the μ_{eff} of the materials the Curie-Weiss law is applied.

$$\frac{1}{susceptibility} = \frac{Temp}{C} - \frac{\phi}{C} \qquad \textit{Eq. 26}$$

Where C is the Curie constant and ϕ is the Weiss constant. As the gradient of the plot mol/emu (Fig 285, grey curve) is $\frac{1}{C}$ the C is calculated to be 0.5434 for the Ni complex, hence the μ_{eff} can be calculated to be 2.09 B.M. This is lower than the spin-only magnetic contribution for an Ni(II) ion (2.82 B.M).

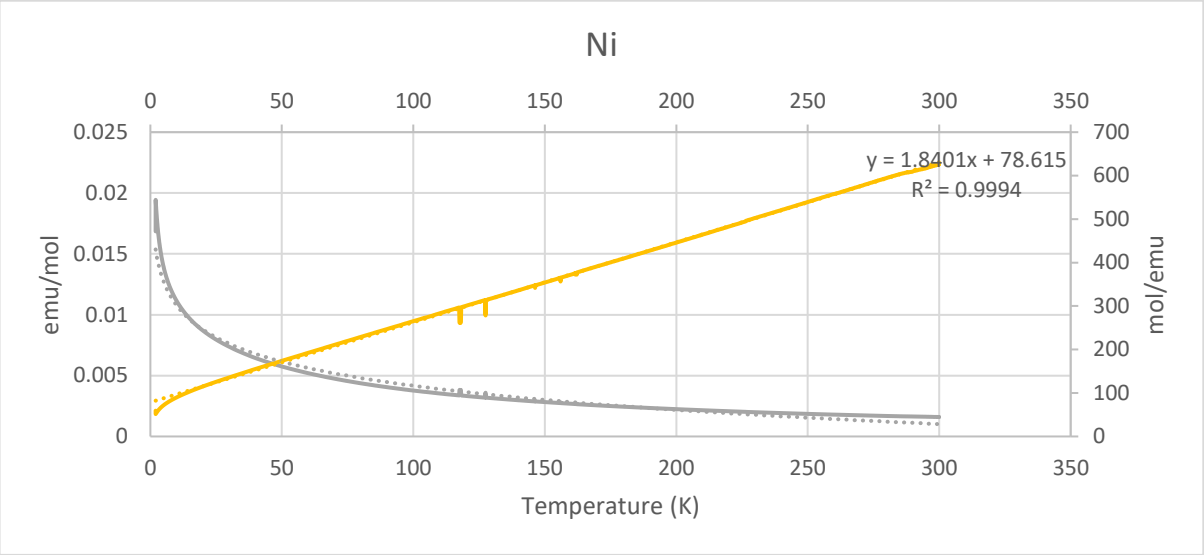


Figure 286: Magnetic Susceptibility of Ni(tetrazole)$_6$(BF$_4$)$_2$ between 300 and 2 K with Curie-Weiss Law

Applying the same equations to the Co(II) complex data (Fig 287, orange curve), C is calculated to be 0.5546 hence, μ_{eff} is 2.11 B.M. For the HS state the spin only contribution to μ_{eff} is equal to 3.873 B.M. whilst the LS contribution is 1.732 B.M. As the experimental μ_{eff} is higher than what would be expected for a phase pure LS material but lower than that of a phase pure HS material, therefore indicating that there is a mixture of spin states present in the material if the correct octahedral complex has been produced. The value of 2.11 BM μ_{eff} could indicate that the complex produced was square planar in nature.

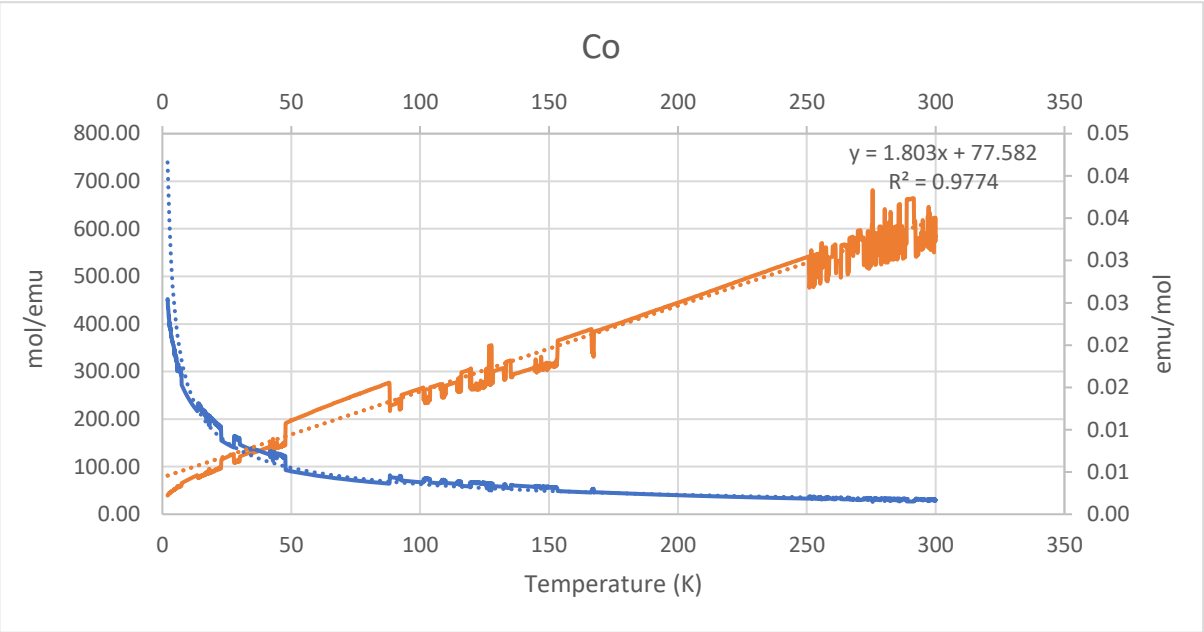


Figure 287: Magnetic Susceptibility of Co(tetrazole)$_6$(BF$_4$)$_2$ between 300 and 2 K with Curie-Weiss Law

5.3.2 Co(tetrazole)$_6$(PF$_6$)$_2$

Upon using SCXRD on the crystals thought to be Co(tetrazole)$_6$(PF$_6$)$_2$ they were revealed instead to be the starting Co(PF$_6$) salt, but the amount of the powder recovered from solution was not enough to complete a proper PXRD identification. Additional attempts to produce the Co(tetrazole)$_6$(PF$_6$)$_2$ complex led to the formation of orange clear crystals. When examined using SCXRD these crystals showed no Bragg peaks, but only a cloud out intense scattering hitting the detector suggesting an amorphous/glass-like nature of the samples, (Fig 288). The confirmation of the synthesis of the correct complex would require XAFS analysis as with the BF$_4$ counterparts.

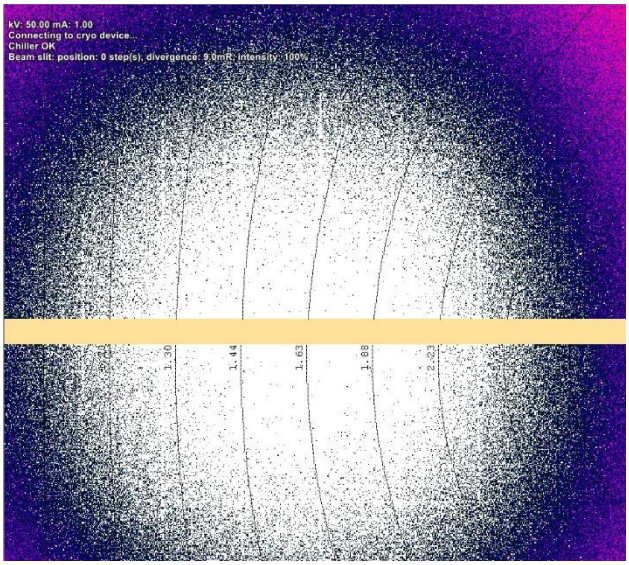


Figure 288: Scatter on X-ray detector from glass phase Co(tetrazole)(PF$_6$)

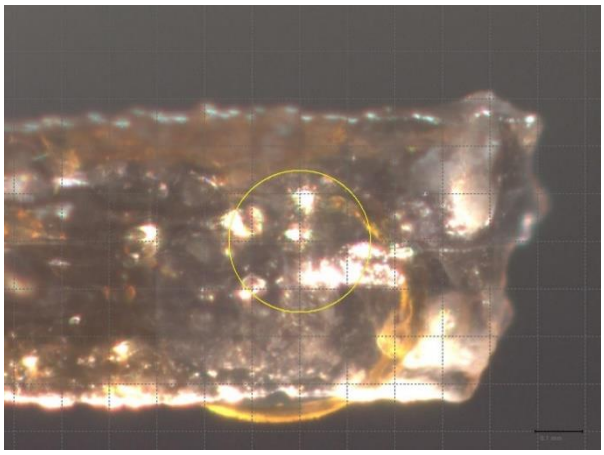


Figure 289: Crystal of $Co(PF)_6$ 6 H_2O

Data was collected at both 295 K and 150 K on the $Co(PF_6)$ salt (Fig 289) confirming the sample to be a hexa-hydrate. Between these two temperatures a phase change occurs with the sample transforming from a Rhombohedral $R\,\bar{3}\,m$ structure at room temperature (Fig 290a), to a Monoclinic P 2_1/c structure at 150 K (Figure 291b).

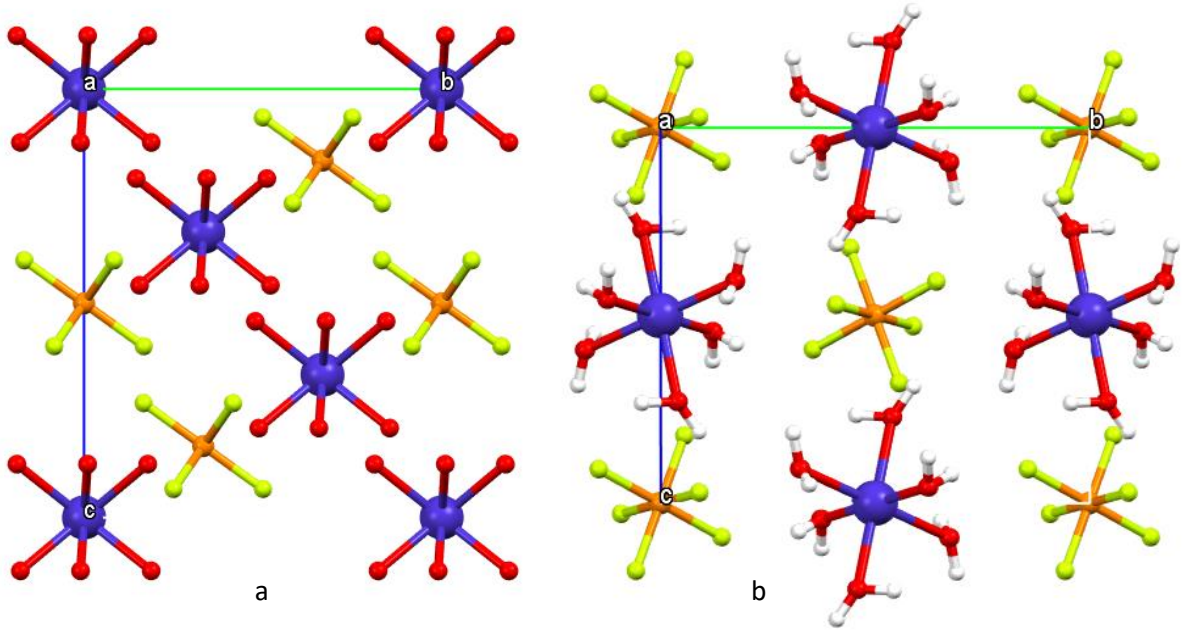


Figure 290: a) 295 K Rhombohedral structure of $Co(PF_6) \cdot 6\ H_2O$, b) 150 K Monoclinic structure of $Co(PF_6) \cdot 6\ H_2O$

At 295 K two oxygen positions can be identified in the hydrate surrounding the Co centre at a distance of 2.088 Å, the P-F bond of the anion has a bond length of 1.650 Å. Both the Co and P atoms sit on special positions (inversion centres), the water molecules are disordered around the Co atom (Fig 291).

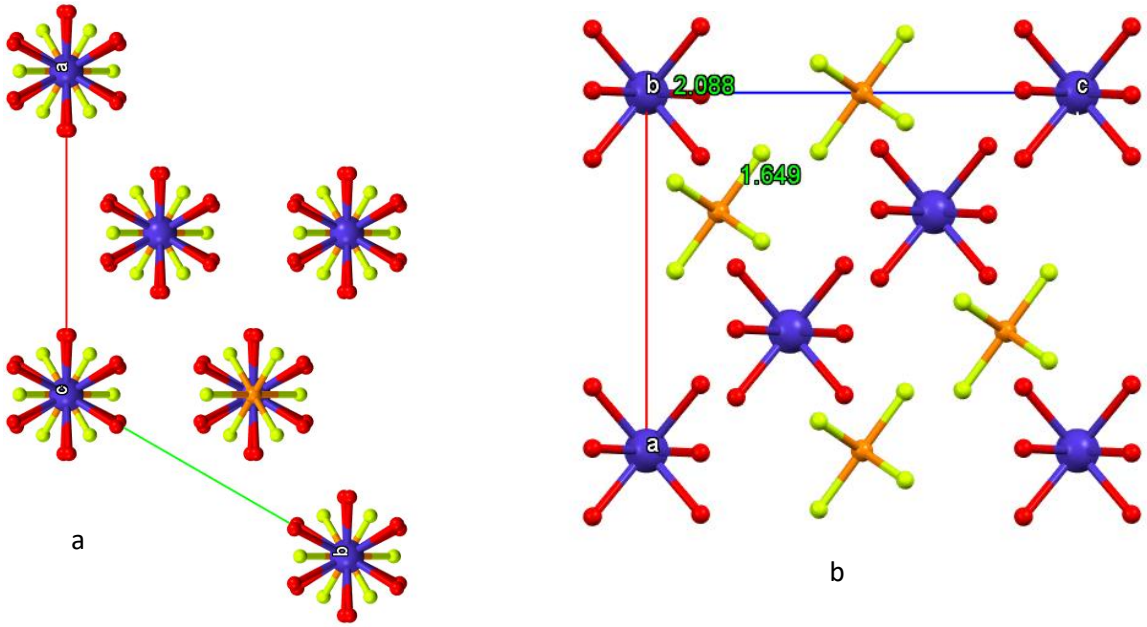


Figure 291: views along the a) c-axis and b) b-axis of the 295 K Rhombohedral structure of $Co(PF_6) \cdot 6\ H_2O$

At 150 K only a single independent oxygen position can be identified in the hydrate per position, however both hydrogen positions can be identified (Fig 292). Two pairs of the bond lengths between the O and Co centre remain close to the rhombohedral phase at 2.09 Å with a slightly shorter pair of Co-O bonds at 2.065 Å. There is a slight extension of the P-F bond to around 1.69 Å (Table 13). Along both the c-axis and a-axis the PF_6 and $Co(H_2O)_6$ are arranged in chains.

Table 13: Key bond lengths for 150 K Monoclinic phase of $Co(PF_6) \cdot 6\ H_2O$

Atom1	**Atom2**	**Length (Å)**
Co1	O2	2.083(1)
Co1	O4	2.092(3)
Co1	O5	2.065(2)
P6	F7	1.693(2)
P6	F8	1.687(3)
P6	F9	1.689(2)

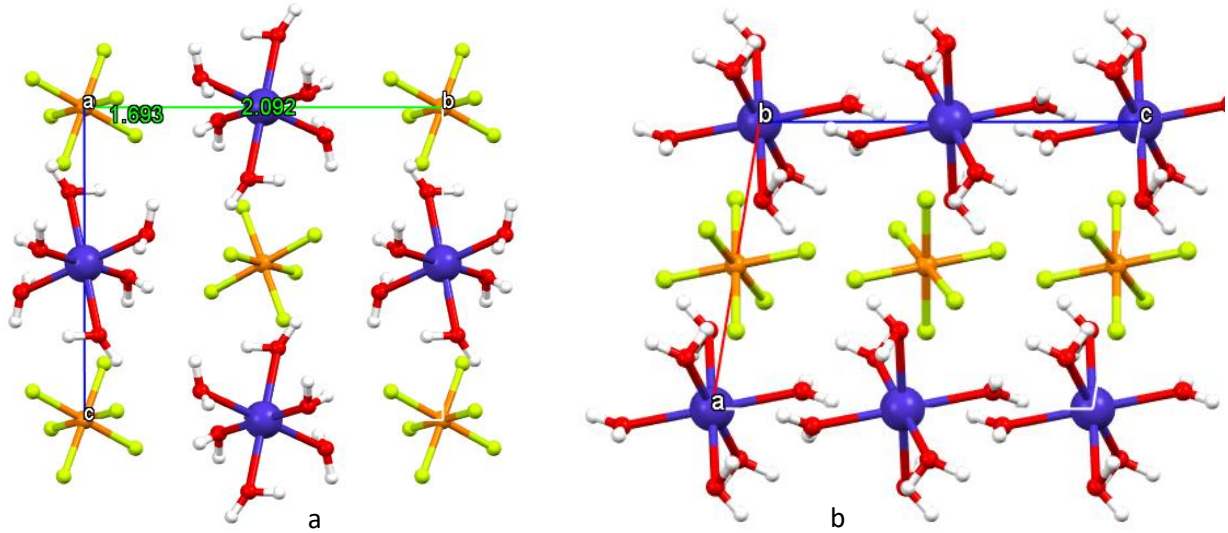


Figure 292: views along the a) a-axis and b) b-axis of the 150 K Monoclinic structure of $Co(PF_6) \cdot 6\ H_2O$

To better locate the transition temperature between the low and high temperature structures a DSC experiment was performed (Fig 293). A sample of $Co(PF_6) \cdot 6\ H_2O$ was run through 2 cycles of cooling and warming allowing the identification of the phase change upon cooling at 249 K, while upon warming a hysteresis places the transition temperature at 263 K. The reversible nature of the transition qualifies it as a first order phase transition.

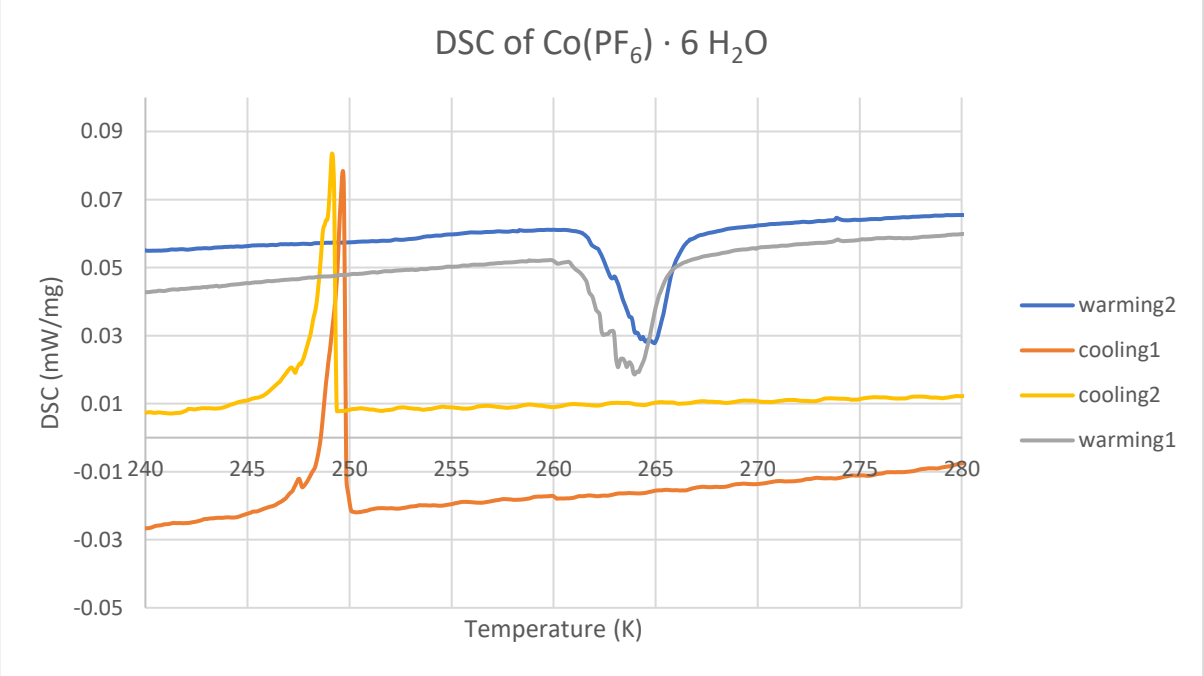


Figure 293: DSC graph of $Co(H_2O)_6(PF_6)$ showing the hysteresis in the phase change between the rhombohedral high temp phase and the monoclinic low temp phase.

There are two different types of hydrogen bonds in the low temperature monoclinic phase of $Co(PF_6) \cdot 6\ H_2O$ (Fig 294). The first is between the water molecules in the shell surrounding the Co^{2+} ion at a distance of 2.632(2) Å (O-H distance), the second is between a water molecule and the PF_6 molecule at a distance of 2.461(3) Å (H-F distance).

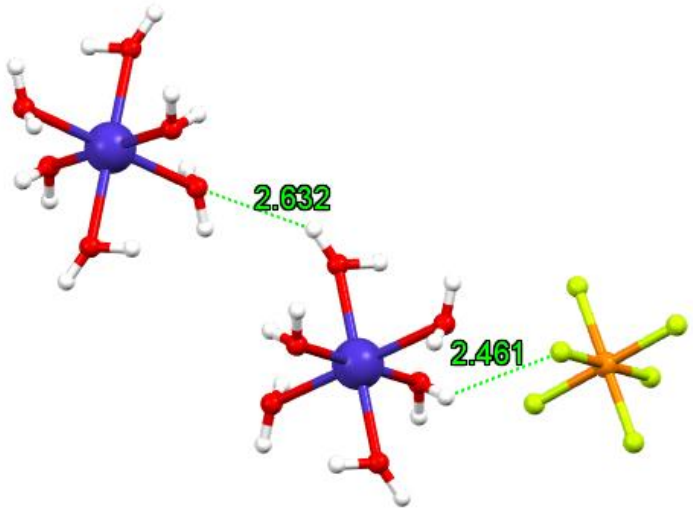


Figure 294: Hydrogen bonding in monoclinic phase of $Co(H_2O)_6(PF_6)$

The hydrogen bonding scheme in the room temperature Rhombohedral phase is relatively similar to that of the Monoclinic phase at low temperature (Fig 295). The water molecules in the solvation sphere around the Co^{2+} ion form hydrogen bonding between each other at a distance of 2.645(2) Å (O-O distance). The fluorine atom in the PF_6 molecule forms short contacts with two water molecules in different solvation shells around the Co, making a bifurcated hydrogen bond, at distances of 2.758(3) Å and 2.823(1) Å. Further structural information can be found in the appendix.

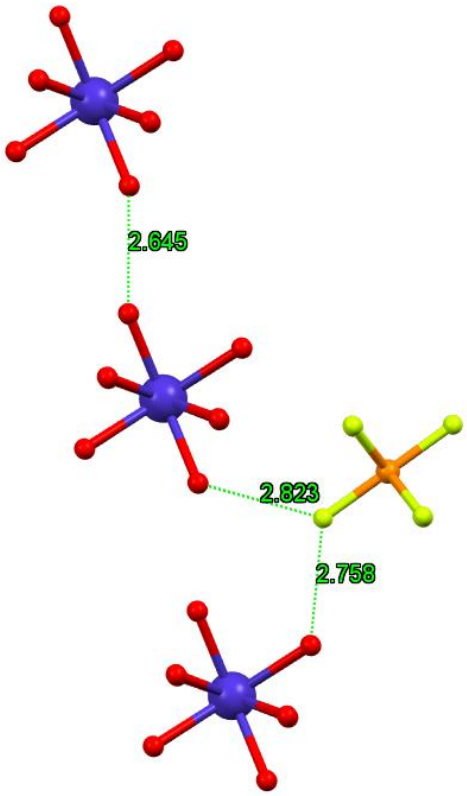


Figure 295: Hydrogen bonding in the Rhombohedral phase of $Co(H_2O)_6(PF_6)$

5.3.3 Ni(Cyclam)

Ni(Cyclam)I_2 has been previously structurally studied to investigate its magnetic properties [40,41]as well as, as a catalyst in the reduction of CO_2 to CO[4]. The compound is known to demonstrate a gradual spin crossover from high spin at 390 K to low spin at 10 K , *via* a $^3B_{1g}$ to $^1A_{1g}$ transition. Single crystal structural data has been published[41] at 390, 200 and 120 K. At 390 K the complex is found in the High Spin state, at both 200 and 120 K the structure is found in the Low Spin state. The change in state is characterised by the shortening of the Ni-N bonds and the consequent elongating of the Ni-I bonds, distorting the octahedra.

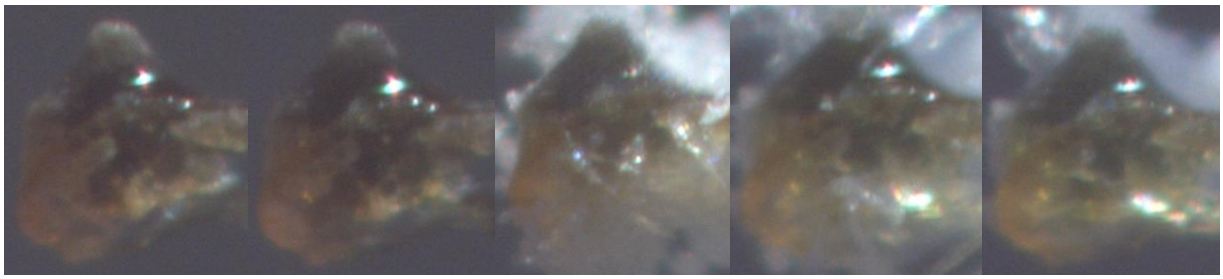


Figure 296: Left to Right – 295, 250, 180, 120 and 90 K

Single crystal x-ray diffraction data was collected at ISIS, Harwell initially between 295 K and 90 K (Fig 296), showing bond lengths at all temperatures in agreement with the reported LS structure (Fig 297).

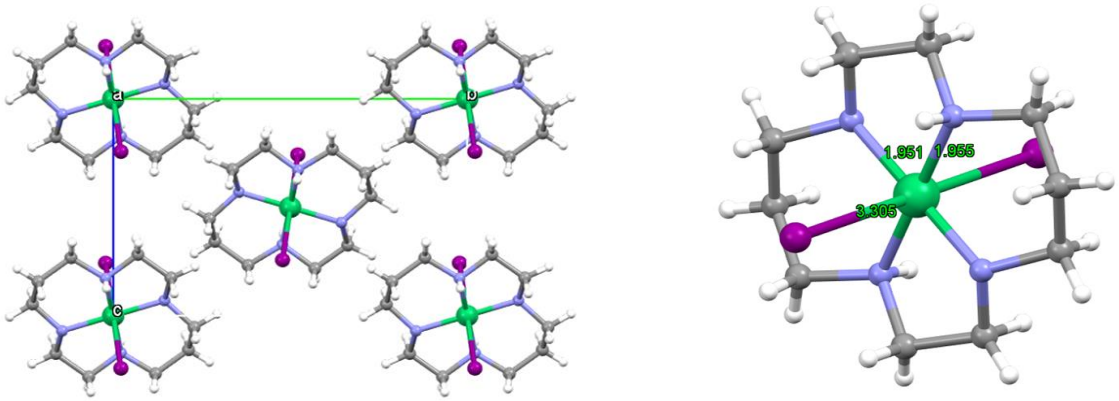


Figure 297: Expected bond lengths and structure of the LS structure

Between 295 K and 90 K, the distortions in the angles between the Iodine and Nitrogen atoms through the metal centre show a decrease with temperature. The structure is getting closer to a more octahedral structure, i.e. the deviations from perfect octahedral geometry decrease with decreasing temperature (Fig 298).

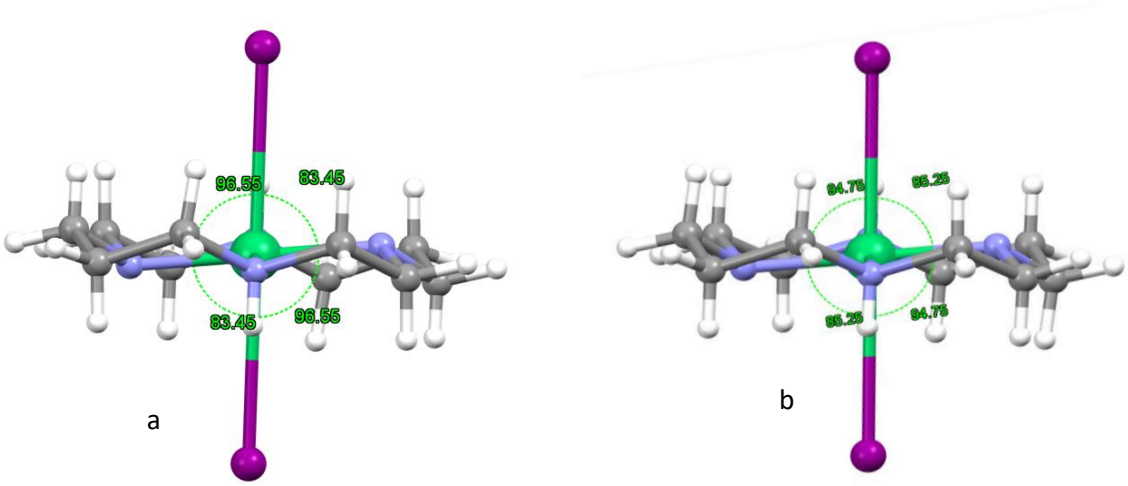


Figure 298: Angles between I-Ni-N at a) 295 K and b) 90 K for Ni(cyclam)I_2

At 90 K close contacts between the complex can be seen between iodine atoms to the hydrogen atoms of a cyclam ligand in the next molecular plane, along the b-axis with a distance of 3.157(2) Å. At 295 K the closest contact from the Iodine is now smaller (2.989(4) Å) but with a larger angle between the macrocycle planes, with the close contacts along the a-axis (Fig 299). At 180 K there are close contacts along both the a-axis and b-axis at distances of 2.985(1) Å and 3.180(3) Å respectively (Fig 300). Whilst at 120 K there are no suggested close contacts in any direction shorter than the sum of the Van Der Waals radii.

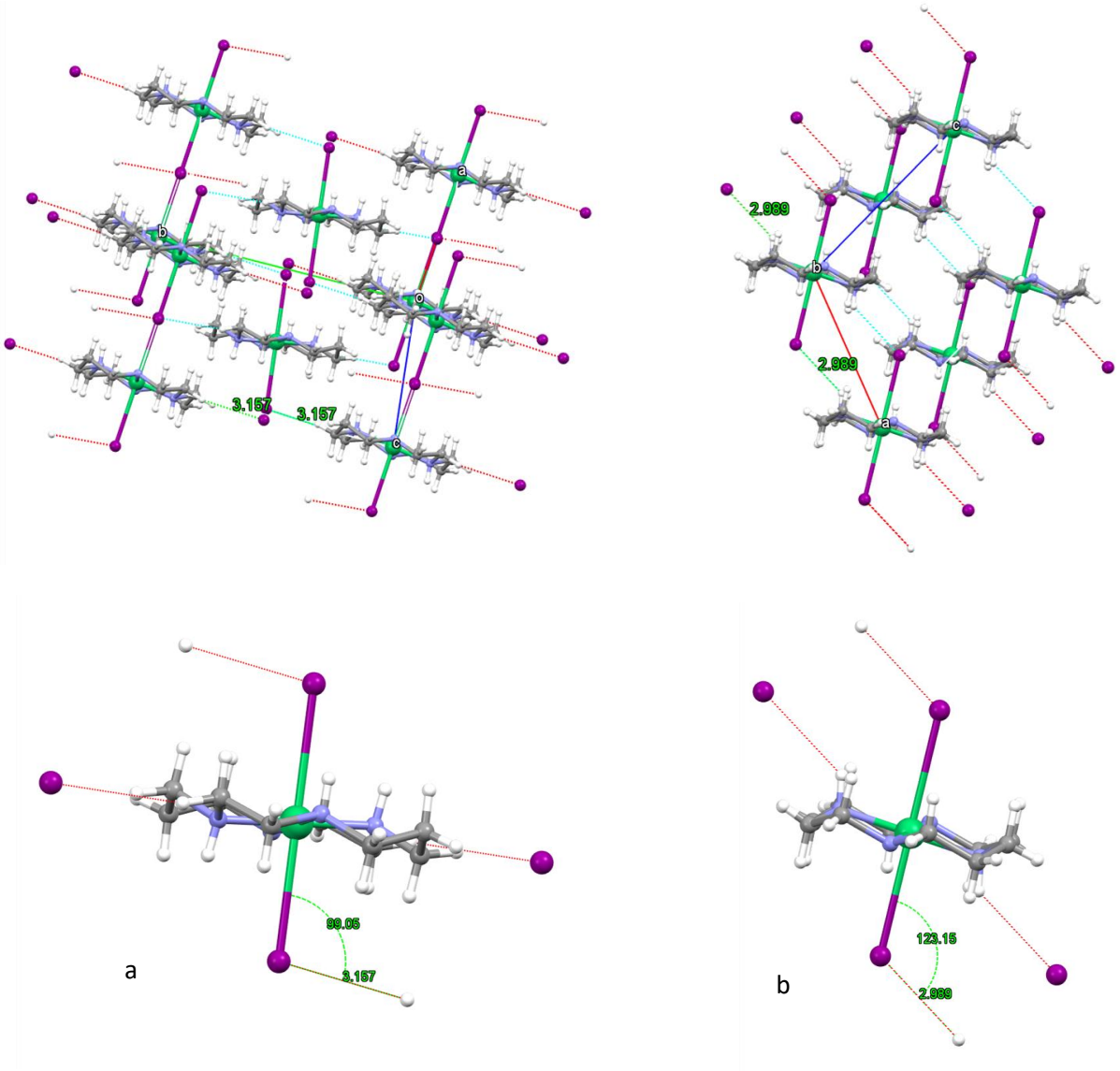


Figure 299: Intermolecular distances and angles at a) 90 K and b) 295 K of Ni(cyclam)I_2

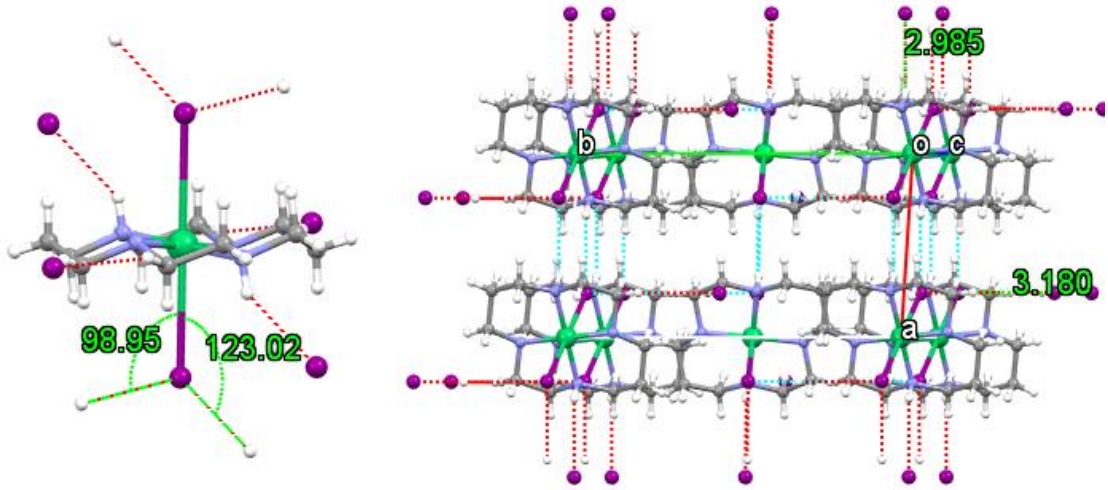


Figure 300: Close contacts for Ni(cyclam)I_2 at 180 K

After the crystal had been remounted using a glue that could survive the higher temperatures data was then collect over the temperature range 300 to 410 K (Fig 301) showing a slight colour darkening as the crystal was heated.

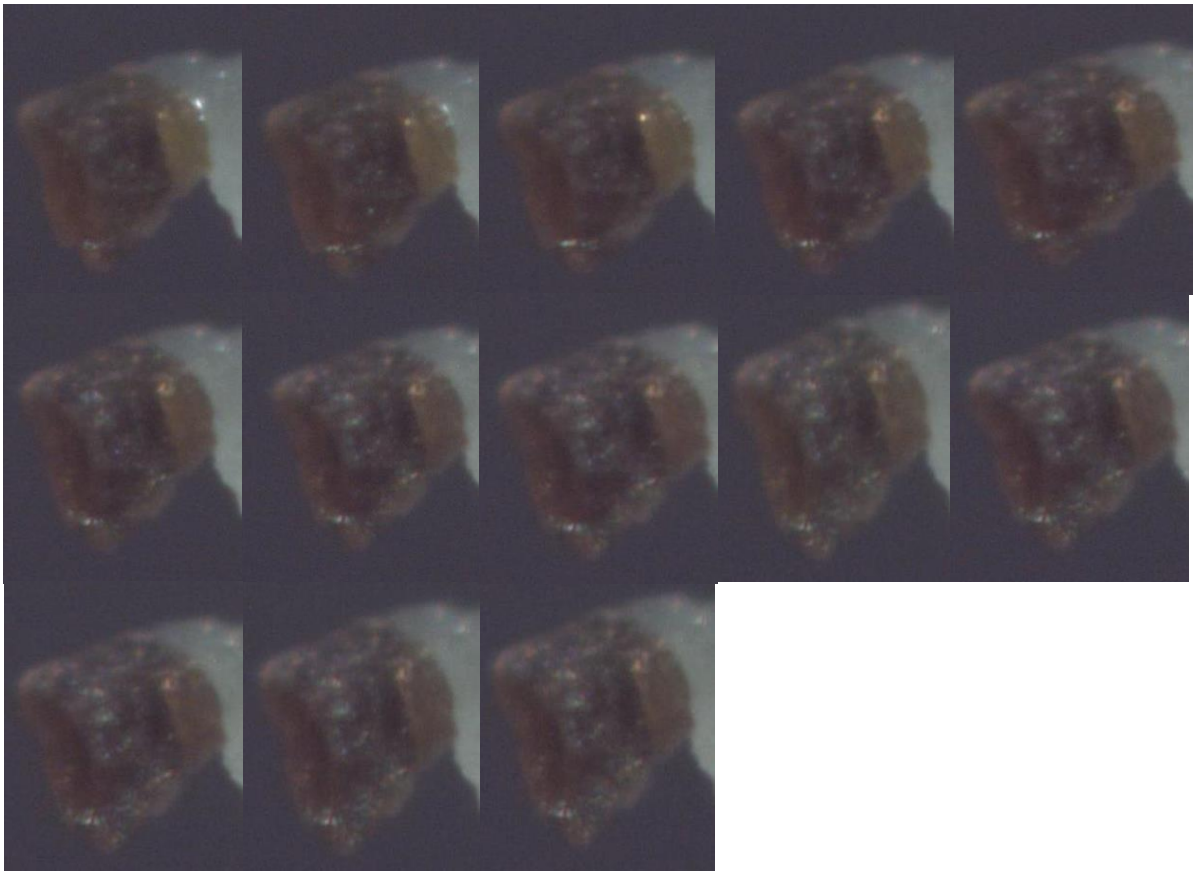


Figure 301: Mounted crystal of Ni(cyclam)I_2 at 300 K, 320 K, 340 K, 360 K, 370 K, 380 K, 390 K, 400 K, 410 K, 390 K, 380 K,360 K, 340 K from left to right.

At these temperatures there were three short contacts two between iodine and hydrogen atoms (3.033(2) Å and 2.996(4) Å) and one involving only hydrogen atoms (2.292(2) Å) (Fig 302). This feature is seen consistently as the temperature increases with only slight variation in bond length.

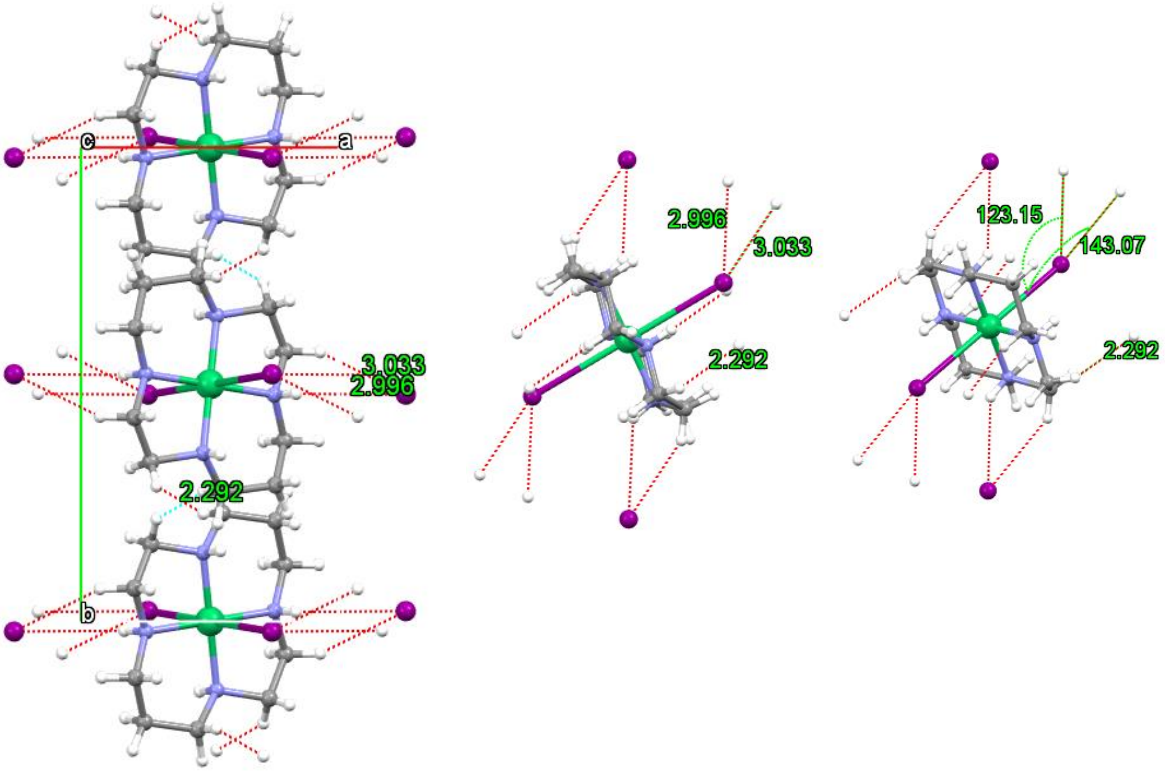


Figure 302: Close contacts for Ni(cyclam)I_2 between 300 k and 410 K

In addition with increasing temperature there are small changes in the I-Ni-I angle such as to make the coordination around the nickel atom become more symmetrical (Fig 303).

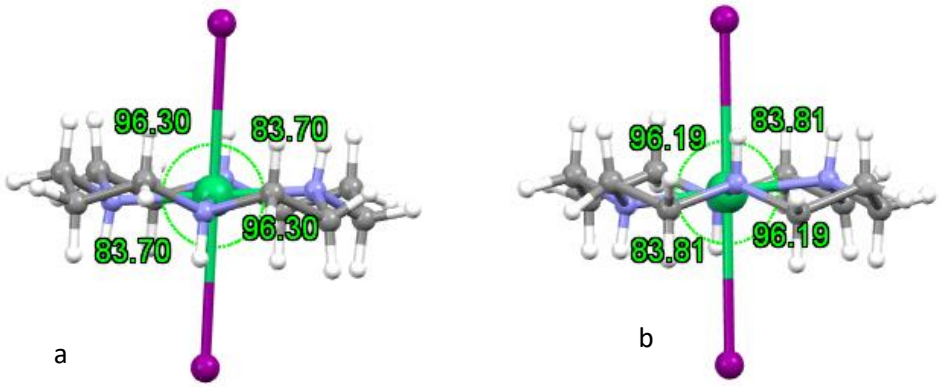


Figure 303: Angles between I-Ni-N a) 400 K and b) 410 K of Ni(cyclam)I_2

Considering the entire temperature range between 90 K and 295 K there is an overall increase in the difference between the two angles, this drops sharply at 300 K before levelling out (Fig 304).

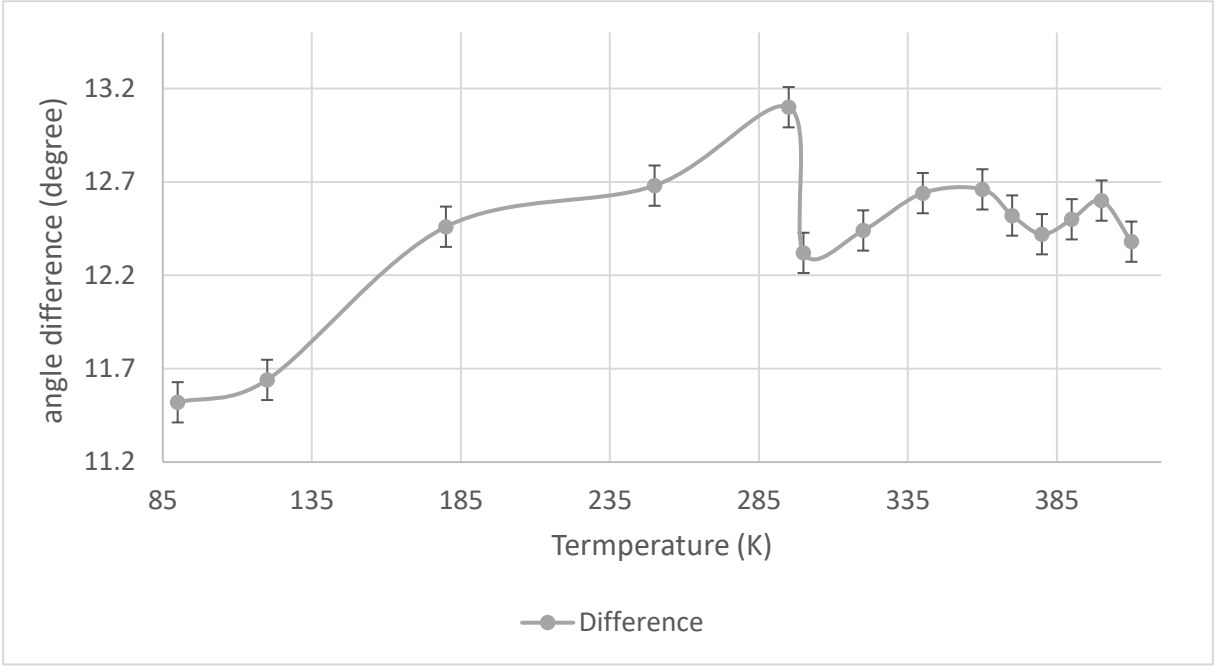


Figure 304: I-Ni-N angle difference with respect to temperature for Ni(cyclam)I_2.

The structural determinations gave the opportunity to investigate changes in bond lengths, there are three main bonds to consider. The first is the central Ni-I bond with the data collected in two sets; first on cooling from 295 K to 90 K, and then, in a second experiment on heating from 300 K to 410 K with a subsequent cooling run to 340 K (red curve) (Fig 305).

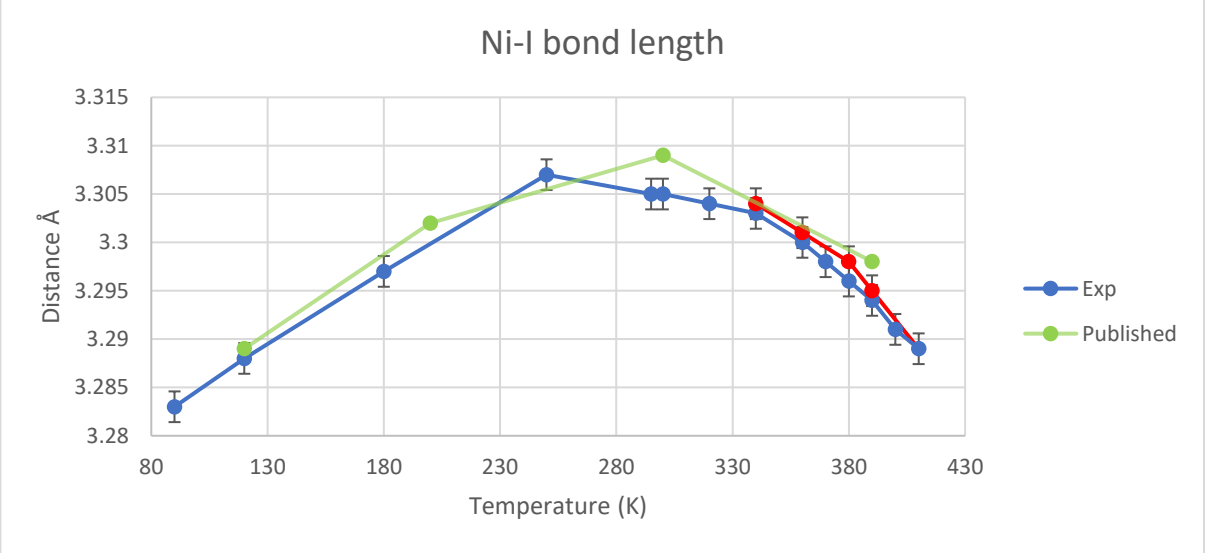


Figure 305: Graph of Ni-I bond length variations with respect to temperature experimental vs published for Ni(cyclam)I_2. Exp line is red upon cooling

Looking at the blue experimental curve in Fig 183 there is a possible slight increase in the Ni-I bond length with temperature between 295 K and 250 K although the values are within errors. From 250 K to 90 K there is a steady decrease in the bond length from 3.307(2) Å to 3.283(3) Å. Above 300 K there is also a decrease in the Ni-I bond length initially gradually but with an increased rate as the temperature increases. The overall shape of the curve agrees with the data previously published[41,] although the max peak of the curve is significantly lower (50 K) this could be due to variation between samples, or an increased number of data points collected compared to that already published[41]. As described in Horii *et al*[41]. the HS state has shorter Ni-I bond lengths accounting for the decrease in both length as the temperature is increased. To explain the decreased bond length at low temperatures there are two possibilities, the first is that the bond length are contracting with the decrease in temperature as expected for thermal contraction. The second possibility is that as Yamauchi *et al*[5] state at low temperatures the shortened Ni-I bond approaches octahedral symmetry as the iodine exerts a great ligand field interaction in the axial direction enforcing a HS state.

The second (Fig 306) and third (Fig 307) bond lengths investigated are the two equatorial Ni-N bond lengths. Opposite pairs of Ni-N bonds show matching contractions and expansions with respect to temperature, though these changes are not consistent across all four nitrogen atoms, hence the need to be treated separately. Between the highest and lowest temperatures of the two bond lengths, there is a corresponding overall arc of an increase in the bond length as the temperature is increased, this compares to the previously published data[37]. However, between the two points for both Ni-N bond pairs, the changes seen were not a consistent increase or decrease, instead there were multiple changes demonstrating both expansion and contraction with no discernible pattern.

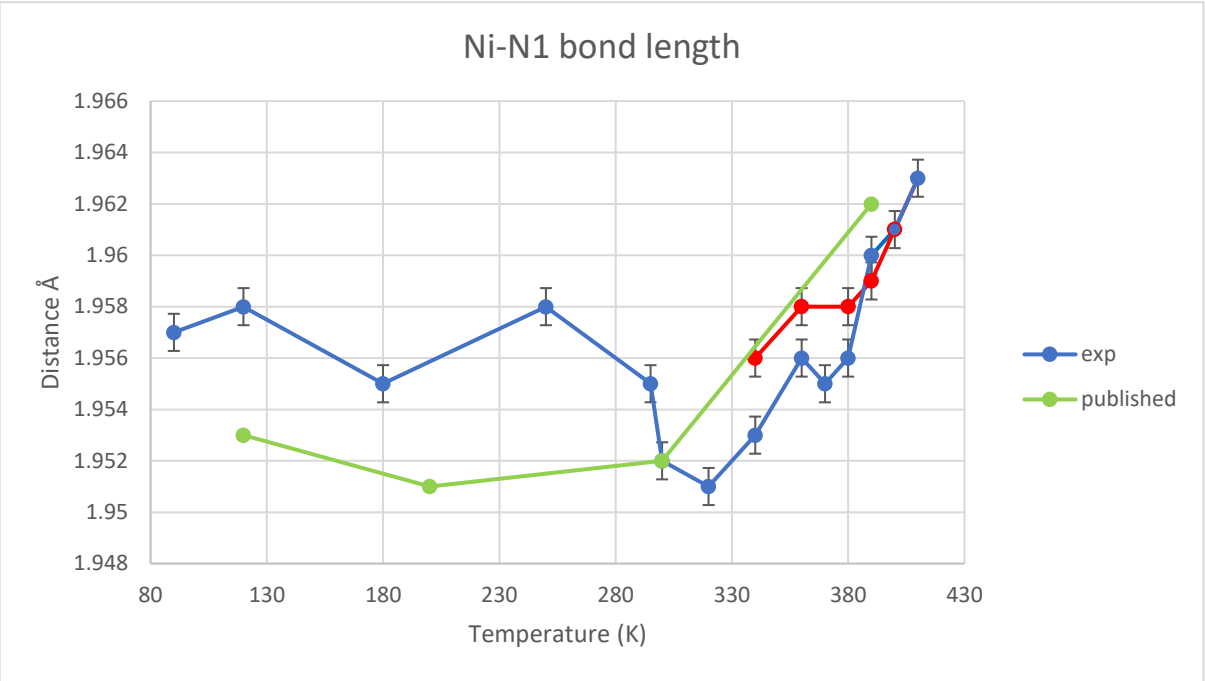


Figure 306: Graph of Ni-N1 bond length variations with respect to temperature experimental vs published for Ni(cyclam)I_2. Exp line is red upon cooling

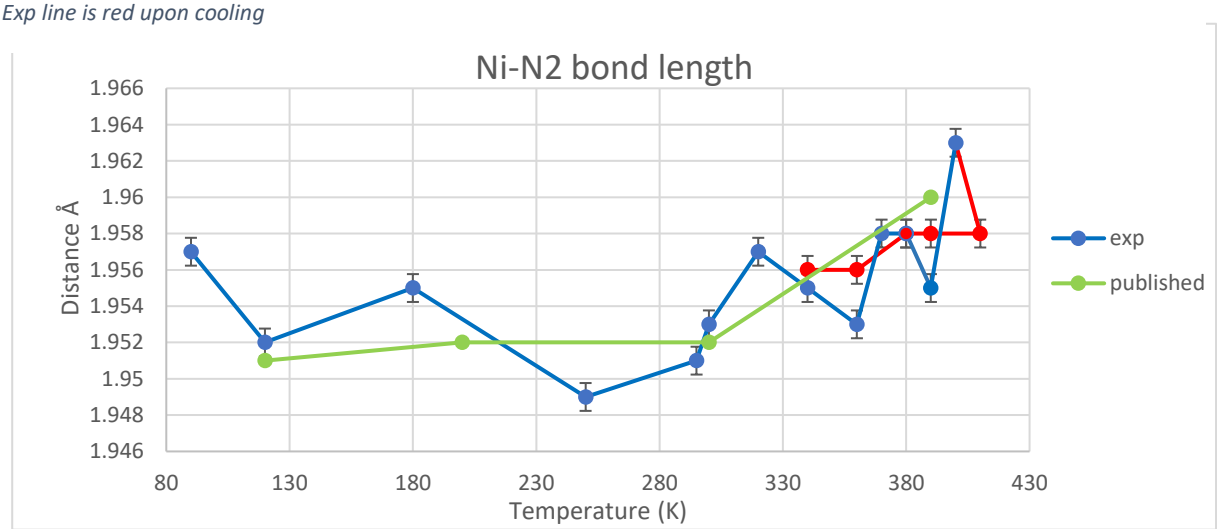


Figure 307: Graph of Ni-N2 bond length variations with respect to temperature experimental vs published for Ni(cyclam)I_2. Exp line is red upon cooling

Grown in the same recrystallisation batch, a second polymorph of Ni(cyclam)I_2 was identified (Fig 308), with needle-like morphology compared to the block morphology of the first polymorph. The structure determination of this polymorph shows an orthorhombic system with P $2_12_12_1$ symmetry, in which only one iodine atom is covalently bonded to the Ni atom, while the second is a free Iodide ion intercalated between the macro cycles. The Ni complexes form zig-zag chains along the b-axis with the angle between iodine atoms through the nickel centres estimated at ~169°. Further

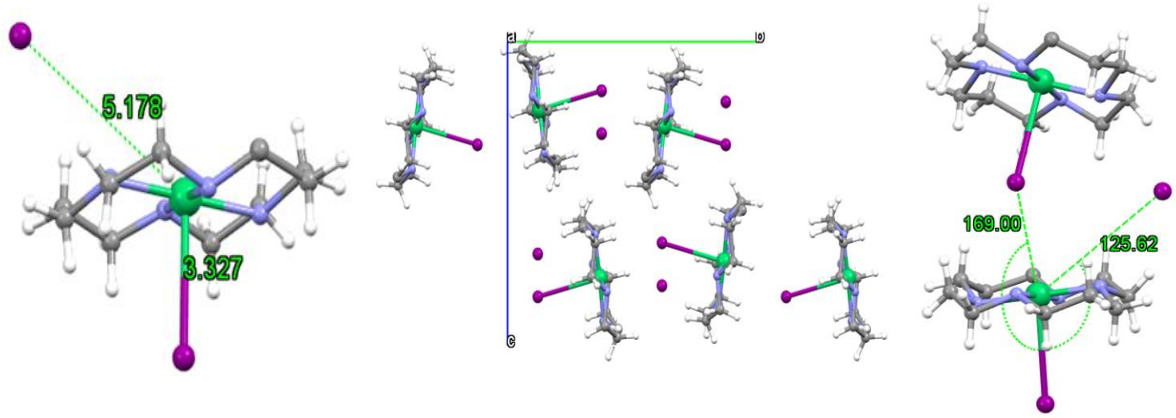


Figure 308: Structure of the second polymorph of Ni(cyclam)I_2

5.4 Conclusion

We successfully made one spin crossover complex, Ni(Cyclam)I_2 finding that the structural changes associated with SCO LS-HS transition though small matched those previously reported in literature. The Co(PF_6) hexahydrate salt was also produced, for which a phase transition at 249 K upon cooling and 263 K upon warming was identified for the first time. Attempts were made to synthesis M(tetrazole)$_6$ (BF_4)$_2$ (M= Co, Ni) complexes which formed gels and could not be assessed for structural changes using diffraction methods, though magnetic susceptibility measurement allowed us to identify the materials as paramagnetic. Co(tetrazole)$_6$ (PF_6)$_2$ complex synthesis was also attempted producing an amorphous glass material that was not characterised further.

5.5 References

1 P. Gütlich, *Eur J Inorg Chem*, 2013, **2013**, 581–591.

2 M. A. Halcrow, *Chem Soc Rev*, 2011, 40, 4119–4142.

3 E. Konig, G. Ritter and S. K. Kulshreshtha, *The Nature of Spin-State Transitions in Solid Complexes of Iron(II) and the Interpretation of Some Associated Phenomena*, Chem Rev., 1985, **85**, 219-234.

4 J. A. Real, A. B. Gaspar and M. Carmen Muñoz, *Dalton Transactions*, 2005, 2062–2079.

5 C. Knoll, D. Müller, M. Seifried, G. Giester, J. M. Welch, W. Artner, K. Hradil, M. Reissner and P. Weinberger, *Dalton Transactions*, 2018, **47**, 5553–5557.

6 J. A. Real, A. B. Gaspar, V. Niel and M. C. Muñoz, *Coord Chem Rev*, 2003, 236, 121–141.

7 P. Gütlich, A. B. Gaspar and Y. Garcia, *Beilstein Journal of Organic Chemistry*, 2013, **9**, 342–391.

8 M. S. Haddad, W. D. Federer, M. W. Lynch and D. N. Hendrickson, *J Am Chem Soc*, 1980, **102**, 1468–1470.

9 E. W. Müller, H. Spiering and P. Gütlich, *Inorg Chem*, 1984, **23**, 119–120.

10 Z. G. Lada, K. S. Andrikopoulos, A. Chrissanthopoulos, S. P. Perlepes and G. A. Voyiatzis, *Inorg Chem*, 2019, **58**, 5183–5195.

11 H. H. Wei and Y. C. Jean, *Chem Phys Lett*, 1984, **106**, 523–526.

12 P. Gütlich, Y. Garcia, A. D. Naik, T.-A. D. Nguyen and F. Renz, *J. Phys.: Conf. Ser*, 2010, **217**, 12022.

13 P. Gutlich, A. Hauser and H. Spiering, *Angew Chem Int Ed Engl*, 1994, **33**, 2024–2054.

14 P. Gütlich and H. A. Goodwin, in *Top Curr Chem*, 2012, vol. 233, pp. 1–47.

15 A. Hauser, *Coord Chem Rev*, 1991, **111**, 275–290.

16 P. Gütlich, A. Hauser and H. Spiering, *Angewandte Chemie International Edition in English*, 1994, **33**, 2024–2054.

17 M. A. Halcrow, *Polyhedron*, 2007, **26**, 3523–3576.

18 M. Sorai, J. Ensling, K. M. Hasselbach and P. Gütlich, *Chem Phys*, 1977, **20**, 197–208.

19 P. Gütlich, *Journal de Physique Colloques*, **40**, C2, 378, DOI:10.1051/jphyscol:19792133.

20 H. Paulsen, V. Schünemann, A. X. Trautwein and H. Winkler, *Coord Chem Rev*, 2005, 249, 255–272.

21 F. Vereda, *Iron Oxides: From Nature to Applications*, 2016, 295–323.

22 M. Sorai, J. Ensling and P. Gütlich, *Chem Phys*, 1976, **18**, 199–209.

23 L. Wiehl, G. Kiel, C. P. Köhler, H. Spiering and P. Gütlich, *Inorg Chem*, 1986, **25**, 1565–1571.

24 K. Kaji and M. Sorai, *Thermochim Acta*, 1985, **88**, 185–190.

25 P. Gutlich, S. Decurtins, K. M. Hasselbach, H. Spiering and A. Hauser, *Inorg Chem*, 1985, **24**, 2174–2178.

26 M. Mikami, M. Konno and Y. Saito, *Acta Crystallogr B*, 1980, **36**, 275–287.

27 D. Chernyshov, M. Hostettler, K. W. Törnroos and H. B. Bürgi, *Angewandte Chemie - International Edition*, 2003, **42**, 3825–3830.

28 H. Romstedt, A. Hauser and H. Spiering, *Journal of Physics and Chemistry of Solids*, 1998, **59**, 265–275.

29 C. Enachescu, U. Oetliker and A. Hauser, *Journal of Physical Chemistry B*, 2002, **106**, 9540–9545.

30 T. Tayagaki and K. Tanaka, *Phys Rev Lett*, 2001, **86**, 2886–2889.

31 X. Qiang, Z. Sheng-Jiang and C. Xing-Lai, *Journal of Physics: Conference Series OPEN ACCESS*, , DOI:10.1088/1742-6596/21/1/022.

32 L. H. Böttger, A. I. Chumakov, C. Matthias Grunert, P. Gütlich, J. Kusz, H. Paulsen, U. Ponkratz, V. Rusanov, A. X. Trautwein and J. A. Wolny, *Chem Phys Lett*, 2006, **429**, 189–193.

33 J. Kusz, M. Zubko, R. B. Neder and P. Gütlich, *Acta Crystallogr B*, 2012, **68**, 40–56.

34 K. Ridier, G. A. Craig, F. Damay, T. Fennell, M. Murrie and G. Chaboussant, *Phys Rev B*, 2017, **95**, 94403.

35 M. Nihei, T. Shiga, Y. Maeda and H. Oshio, *Coord Chem Rev*, 2007, **251**, 2606–2621.

36 J. Letard, P. Guionneau and L. Goux-Capes, in *Spin Crossover in Transition Metal Coumpounds III*, eds. P. Gutlich and H. A. Goodwin, Springer-Verlag, 1st edn., 2004, vol. 235, pp. 23–62, 182–229.

37 W. L. Driessen and P. H. van der Voort, *Inorganica Chim Acta*, 1977, **21**, 217–222.

38 W. Hibbs, A. M. Arif, P. J. van Koningsbruggen and J. S. Miller, *CrystEngComm*, 1999, **1**, 12–14.

39 W. Hibbs, P. J. Van Koningsbruggen, A. M. Arif, W. W. Shum and J. S. Miller, *Inorg Chem*, 2003, **42**, 5645–5653.

40 J. Yamauchi, H. Tsuji, N. Sakai and Y. Kawamura, Chem Lett , 2003, **32**, 368–369, *https://doi.org/10.1246/cl.2003.368*.

41 Y. Horii, Y. Kanegae, K. Takahashi, A. Fuyuhiro, M. Noguchi, H. Suzuki and M. Nakano, *Inorg Chem*, 2020, **59**, 5418–5423.

42 L. Prasad and A. Mcauley, *Acta Cryst. C,* 1983, **39**, 9 ,1175-1177.

43 J. D. Froehlich and C. P. Kubiak, *Inorg Chem*, 2012, **51**, 3932–3934.

6 Conclusions

During this thesis we have covered the development and testing of an *in situ* Raman scattering and neutron diffraction central stick, moving from a dual chamber sample holder to a single chamber sample holder. Improvements were made to the stability of the laser probe by making modifications to the focusing lens holder and, further improvements were made to the sample chamber to facilitate quicker sample change overs. Further developments to the central stick to allow for a wider range of experiments such as attachments for different irradiation sources, or cameras to visualise the sample position have been suggested.

Also covered was an investigation into the thermochromic and photochromic properties of salicylaldehyde aniline derivatives. Finding further confirmation that the substitution on the aniline ring has a significant effect on the property presentation by effecting the electronegativity of the imine nitrogen, as well as the steric encumbrance and, the internal dihedral angle between the two rings. All the materials showed an element of thermochromism but only a few showed photochromism. For the thermochromic materials, the majority showed identifiable tautomerisation between the enol and keto state, the few that did not however, still demonstrated an increase in the level of fluoresence with a decrease in temperature, making Raman scattering data collection difficult, if not impossible. Only one of the photochromic materials demonstrated the expected cis-enol to trans-keto tautomerisation upon photo irradiation, for the remaining three, two demonstrated the cis-enol to cis-keto tautomerisation as seen with the thermochromic materials, whilst in the irradiated state of the third structure the critical hydrogen position was not identifiable. The crystal structures for 3,5-ditertbutylsalicylidene-3-Iodoaniline and 3,5-ditertbutylsalicylidene-2-Iodoaniline were determined for the first time, as well as a new polymorph of 4-Chloro-(salicylidene)-aniline.

We successfully synthesised Ni(Cyclam)I_2 confirming that there are structural changes associated with the SCO LS-HS transition, though small, that matches those that had been previously published. The Co(PF_6) hexahydrate salt was also crystallised, for which a phase change at 249 K upon cooling and 263 K upon warming, (Rhombohedral high temperature phase to a Monoclinic low temperature

phase) was identified for the first time. Attempts were made to synthesis M(tetrazole)$_6$(BF_4)$_2$ (M= Co, Ni) complexes which formed gels and could not be assessed for structural changes using diffraction methods. Nevertheless, magnetic susceptibility measurements allowed the materials to be identified as paramagnetic. Co(tetrazole)$_6$ (PF_6)$_2$ complex synthesis was also attempted producing an amorphous glass material that was not further characterised.

7 Future Work

The research work done in this thesis dealt with two classes of compounds:

1) Salicylaldehyde aniline derivatives

2) Spin Cross over complexes

For the salicylaldehyde aniline derivatives, we showed that the chromotropism of these materials is more complex than what originally reported in the literature. It is not simply the motion of one hydrogen atom in the structure, but also the electronegativity, position, and the steric encumbrance of the substituents on the benzene rings, that do affect the structure and the behaviour of these material (whether they show photochromism or thermochromism at the macroscopic scale).

In order to gain a greater understanding of the root cause of the properties of these materials, other effects that we observed during our investigations would require further attention. For example: the role of fluorescence, and its resulting effect on the colour change of thermochromic materials; and the role of irradiation on the stability of photochromic materials.

Fluorescence is the emission of light in materials that can absorb energy. In this work, it was counterintuitive to see that most of the materials exhibiting fluorescence were the thermochromic ones and that fluorescence increased with lowering the temperature. A more systematic study of the fluorescence in these materials, possibly with the help of some type of fluorescence spectroscopy or additional Raman and INS measurements, could offer some insights on such behaviour.

As for the role of irradiation in photochromic compounds: in this thesis we noticed that, according to the substituent on the aniline ring and the internal dihedral angle between the two rings, there are variations in the exposure time needed to induce the conversion between the non-irradiated and irradiated states. During our investigation, the irradiated state of some materials could not be identified upon offline UV-irradiation, therefore further neutron diffraction studies could be performed using *in situ* UV-irradiation. Further studies of other photochromic materials with either different substituents or different substituent positions, could allow for better understanding of the conversion controls for more practical applications.

As a continuation of this work, the investigation of additional halides substituents in ortho/meta/para position could help in completing the picture of photo/thermochromic property presentation.

Further investigations into the unexpected single crystal to 'powder' like transformation seen for compounds 10 (reversibly) and 18 (irreversibly) is necessary to determine the route cause and nature of the transitions and how this affects the final properties of the material.

For the spin crossover complexes future work should include the synthesis of more air stable materials. The instability of the majority of the spin crossover complexes that where synthesised in this thesis work, made their structural investigation quite difficult (impossible in some cases), but would also make practical applications difficult. Further investigations into Ni(cyclam)I_2 would require the identification of a synthetic method that allows for the control or identification of polymorphs formation. This would allow for the growth of larger crystals, which would be necessary to perform the variable temperature *in situ* neutron diffraction and Raman scattering experiments.

To complete the work discussed in this thesis, the analysis of the glass/amorphous state of the probable Ni(tetrazole)$_6$(BF_4), Co(tetrazole)$_6$(BF_4), and Co(tetrazole)$_6$(PF_6) compounds would be required, using XAFS to confirm material composition and structure. Furthermore, inducing the crystallisation of Co(tetrazole)$_6$(PF_6) either from the glass directly or from the melt, using lasers, or using different synthesis pathways would allow for proper structural studies to investigate the SCO properties. Furthermore, the SCO properties of complexes containing magnetic metals could be facilitated by the use of magnetic susceptibility studies to get insight on the type of spin transition occurring in these materials, as well as the extent of it.

8 Appendix

8.1 Salicylaldehyde aniline derivatives

Compound 1

Table 14: ^{1}H NMR assignments for compound 1

δ (ppm)	Multiplicity	Integration	J coupling (Hz)	Assignment
13.41	s	1H		H_i
9.66	s	1H		H_a
8.89	s	1H		H_d
7.58	dd	1H	7.7, 1.6	H_h
7.39-7.28	m	3H		H_{e-g}
6.94	dd	2H	13.5, 7.5	H_b
6.86-6.80	m	2H		H_c

^{1}H NMR Expansions

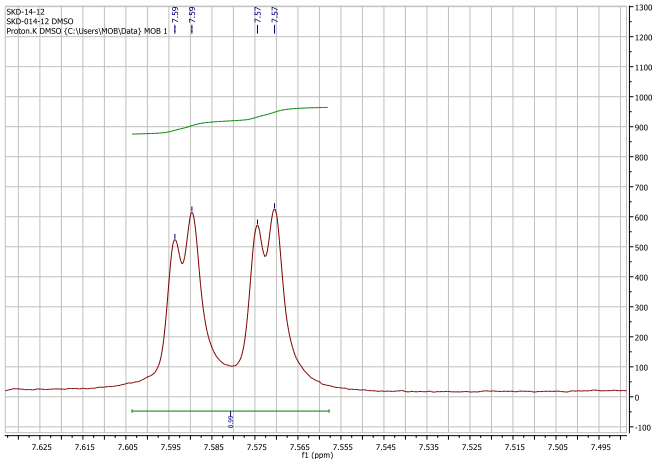


Figure 309: Expansion 1 of ^{1}H NMR for compound 1

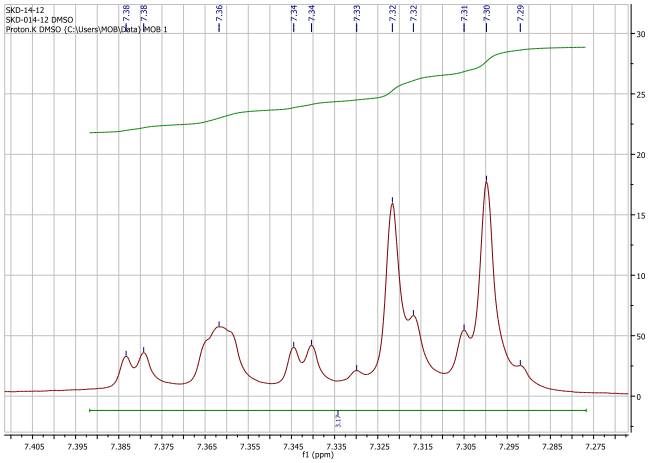


Figure 310: Expansion 2 of ^{1}H NMR for compound 1

Table 15: 13C NMR assignments for compound 1

δ (ppm)	**Integration**	**Assignment**
160.63	1	7
160.54	1	10
157.31	1	1
139.61	1	6
133.09	1	9
132.64	1	13
123.11	2	4/5
119.82	1	11
119.53	1	8
116.92	1	12
116.46	2	2/3

^{13}C NMR Expansions

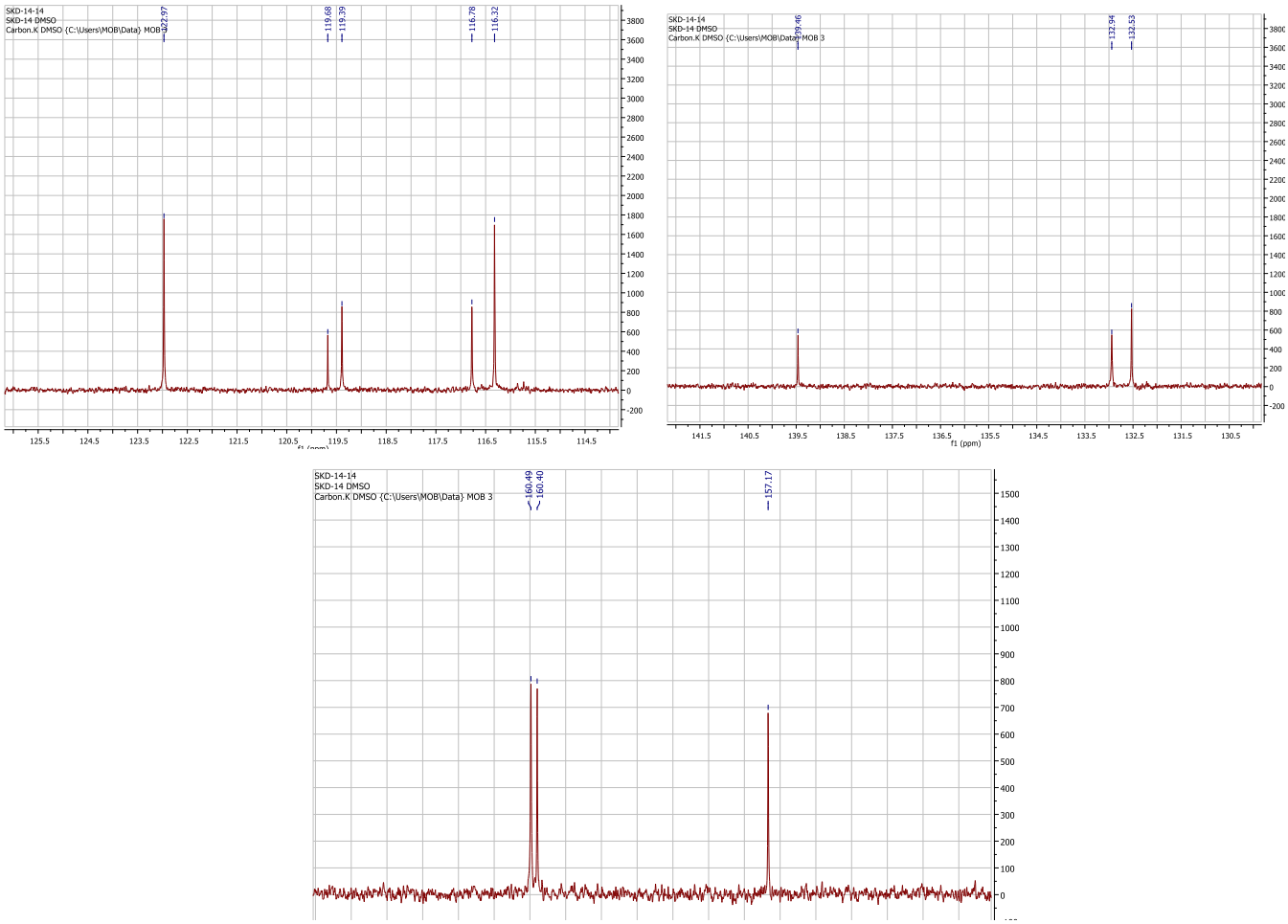


Figure 311: Expansions of ^{13}C NMR spectrum for compound 1

Table 16: Tabulated absorbtion λ_{max} for compound 1

abs	**Wavelength (nm)**	**abs**	**Wavelength (nm)**
1.03	349	0.56	268

Table 17: Raman Peak assignments for compound 1

Position (cm^{-1})	**Keto Assignment**	**Enol Assignment**
3069		aniline OH stretch
1597		OH bend, OOP bridge CH bend
1569		Bridge CH wag
1518	NH wag OH bend	
1457		Ar-H wag, OH bend
1360	aniline Ar-H wag	Aldehyde OH bend
1317	NH wag	
1259	aldehyde Ar-H wag	
1231		Aniline Ar-H wag
1186	aldehyde Ar-H wag/ NH wag,	Ar-H wag
1168		Ar-H wag
1149	aniline Ar-H wag/ NH wag	
1029	Aniline Ar-H wag,	aldehyde Ar-H OOP bend/OH bend
968		aldehyde Ar-H OOP bend
908	NH, CH bridge OOP bend	
802		aniline Ar-CH OOP bend
769	aniline OH/NH bend	Aniline OH bend
712		aldehyde OH bend
641	molecular deformation	ring deformations
563		aniline Ar-H OOP bend, aldehyde ring deformation
488	Ar-ring deformations	
390	aniline ring rotation	
272	Ar-ring rotation	Ar-ring rotation
234		molecular deformations
214	Ar-ring rotations	
138		molecular deformations
111		aniline ring rotations

Table 18: Peak assignments of INS spectrum of compound 1 at 10 K

Position (cm^{-1})	Keto Assignment	Enol Assignment
43.77	Molecular deformations	
60.86	Single molecule Molecular deformations	
80.46	Single molecule Molecular deformations	
105.37		Molecular deformation
115.24	Aniline ring rotations	
147.05		Molecular deformations
166.26	Molecular deformations	
196.84	Single molecule Molecular deformations	
220.08	Single molecule (2) NH IP wag, aniline CH IP wag	
236.74		OOP deformations
273.74	Single molecule (2) OOP CH/NH bends	
344.92	NH OOP wag, Bridge CH IP wag	
393.64		Single molecule molecular deformations
411.80		Single molecule aniline ring OOP deformations
432.47		Single molecule aniline ring OOP deformations
459.88		Single molecule (2) aniline ring IP deformations
492.99	Single molecule (2) aniline ring and bridge deformations	
523.58	Single molecule OOP molecular deformations/	Single molecule OOP molecular deformations/
543.27	Single molecule (2) molecular deformations	
561.58	Single molecule (2) IP deformations, single molecule aniline ring deformation	
619.74	Single molecule (2) IP deformations, single molecule aniline ring deformation	Single molecule (2) IP deformations, single molecule aniline ring deformation
642.27	Single molecule IP molecular deformations, single molecule aniline ring deformation	
712.45		Aniline OH OOP bend, aniline ring deformation
738.96	Single molecule (2) aldehyde ring CH OOP wag	
761.97	Single molecule aldehyde ring CH OOP wag	

802.63	Single molecule (2) CH aniline OOP bend/ Single molecule CH aldehyde OOP bend	Single molecule (2) CH aniline OOP bend/ Single molecule CH aldehyde OOP bend
832.55		Single molecule (2) CH aniline OOP bend
855.81	Single molecule aldehyde ring CH OOP wag	
926.60	Single molecule aldehyde ring CH OOP wag	
953.17	Single molecule (2) aniline ring CH OOP wag	
979.41	Single molecule (2) CH aniline OOP bend, aniline OH OOP bend/ Single molecule (2) CH aniline OOP bend	Single molecule (2) CH aniline OOP bend, aniline OH OOP bend/ Single molecule (2) CH aniline OOP bend
1014.91	Single molecule aniline ring deformations/ NH & bridge CH IP wag	
1110.19		aniline OH OOP bend
1170.71	Single molecule aniline CH IP wag	
1229.38	Aniline CH IP wags/ single molecule molecular deformations	aniline CH IP wags/ single molecule molecular deformations
1279.02	Single molecule aldehyde CH IP wag	
1304.22	single molecule aniline CH IP wags, OH IP wag	single molecule aniline CH IP wags, OH IP wag
1348.41		Single molecule CH IP wags
1402.90		single molecule aniline CH IP wags
1474.52	Single molecule Aniline ring CH/OH OOP wag	
1609.41	Single molecule Aniline ring CH/OH OOP wag	Single molecule Bridge CH IP wag
1666.57		Aldehyde OH IP wag
2143.37		Aldehyde OH IP wag
2317.82	Aniline OH IP stretch	
2865.16	Aniline OH IP stretch	
2950.94	NH IP stretch	
3064.68		Aldehyde OH IP wag

SCXRD

The SCXRD data was collected using a Molybdenum source on a Bruker SCXRD, the data was then integrated using the Bruker Apex 2 software. The outputted .ins and .hkl files were then inputted into the CRYSTALS SCXRD analysis software where the structure was determined using the SIR92 programme.

Table 19: Crystallographic X-ray data for compound 1

Crystal system	Monoclinic			
Space group	P 2_1/c			
Z	4			
Crystal size (mm)	0.12x0.38x0.72			
Radiation type	X-ray Molybdenum			
Wavelength (nm)	0.71073			
Temperature (K)	**50**	**130**	**160**	**293**
Cell parameters (Å)	= 22.0310(5) b=10.7002(3) c= 8.7315(3) α =90 β=91.724(3) γ=90	a= 22.03420(5) b=10.74390(3) c= 8.7671(3) α =90 β=91.728(3) γ=90	a= 22.04141(5) b=10.75400(3) c= 8.791403) α =90 β=91.655(3) γ=90	a= 22.08070(3) b=10.83110(2) c= 8.92230(2) α =90 β=91.525(3) γ=90
Cell volume (Å^3)	2057.41(9)	2074.521(11)	2082.985(12)	2133.086(8)
Total no. of reflections	22968	8512	28558	31783
No of reflection with I/σ(I) > 2	5034	3356	3728	3614
R(sigma)	0.03	0.0485	0.042	0.0482
Parameters/Restraints	36/0	374/0	2/0	245/0
R1, wR2, Goof	0.048, 0.103, 0.963	0.109, 0.173, 0.908	0.063, 0.148, 0.995	0.0497, 0.1123,0.952
R1 after Fourier merging / No of unique reflections	0.0003/5048	0.0004/ 3357	0.003, 6333	0.0370/ 3615
Scan type	2THETA/OMEG	PHIOMEGA	PHIOMEGA	PHIOMEGA
Theta max	29.47	26.63	30.53	24.76
hkl limits	H min = -28 H max = 30 K min = -14 K max = 14 L min = -10 L max = 11	H min = -25 H max = 25 K min = -12 K max = 12 L min = -10 L max = 10	H min = -31 H max = 31 K min = -15 K max = 15 L min = -12 L max = 12	H min = -25 H max = 25 K min = -12 K max = 12 L min = -10 L max = 10

Low/temperature neutron single-crystal diffraction

A suitable crystal of 4-(2-Hydroxyphenyliminomethylene)Phenol for neutron diffraction, measuring approximately 4 x 3 x 2 mm, was grown via slow evaporation of ethanol from a concentrated solution. Diffraction data were collected using the single-crystal diffractometer SXD at the ISIS spallation neutron source (Oxfordshire, UK; Keen *et al*., 2006) at 300, 210, 120, 70 and 10 K. Time-of-flight Laue diffraction data were collected in a series of six orientations at each temperature, with a counting time per orientation of ~2 h 45 m at 10, 70 and 120 K, ~3 h 20 mins at 210 and 300 K. The diffraction spots were initially indexed with the unit cells available from the x-ray measurements at the corresponding temperatures where possible and then from the closest Neutron cell. Bragg intensities were extracted using the 3D-profile fitting method implemented in the SXD2001 software (Gutmann, 2017) and corrected for Lorenz effect. No absorption correction for the shape of the crystal was applied.

Refinement details

Final cell parameters at each temperature were refined against the fitted positions of the Bragg peaks after 3D profile integration. The starting models for structural refinement were based on the atomic coordinates of the non-hydrogen atoms from the X-ray structure at room temperature, while all hydrogen atoms were located from neutron Fourier difference maps. As there were two individual molecules within the unit cell each molecule to be refined.

All structures were refined by full matrix least squares on F^2 using SHELXL (Sheldrick, 2008).

Table 20: Crystallographic Data for Neutron Diffraction experiment of compound 1

Crystal system	Monoclinic				
Space group	$P\ 2_1/c$				
Z	4				
Crystal size (mm)	4 x 3 x 2 mm				
Radiation type	Neutron				
Wavelength (nm)	0.35 – 6.5 Å				
Temperature (K)	**10**	**70**	**120**	**210**	**300**
Cell parameters (Å)	a: 22.034(3) b:10.744(3) c: 8.767(3) α / γ a:90 β: 91.73(5)	a: 22.1296(3) b:10.7264(3) c: 8.7894(3) α / γ a:90 β: 91.69(5)	a: 22.1297(3) b:10.75193) c: 8.81873) α / γ a:90 β: 91.72(5)	a: 22.1333(3) b:10.7994(3) c: 8.88513) α / γ a:90 β: 91.68(5)	a: 22.1400(3) b:10.82903) c: 8.9344(3) α / γ a:90 β: 91.58(5)
Cell volume ($Å^3$)	2074.52(1)	2085.44(2)	2097.34(2)	2122.85(1)	2141.24(3)
Total no. of reflections	4262	3984	3799	3520	3102
No of reflection with $I/\sigma(I) > 4$	4221	3977	3797	3517	3099
R(sigma)	0.0481	0.0474	0.0481	0.0454	0.0439
Parameters/Restraints	335	397	384	384	384
R1, wR2, Goof	0.0594, 0.1571, 1.224	0.0634, 0.1787, 0.884	0.0659, 0.1865, 0.919	0.0684, 0.1957, 0.969	0.0730, 0.2017, 1.009
R1 after Fourier merging / No of unique reflections	0.056/2415	0.0577/2124	0.0607/1964	0.0621/1693	0.0665/1485
Max resolution (Å)	0.41	0.52	0.54	0.57	0.67
Nuclear density Fourier difference residuals: $\Delta\rho_{max}$, $\Delta\rho_{min}$	1.71, -1.50	1.14, -1.13	1.04, -0.96	0.88, -0.96	0.74, -0.93

Compound 2

Preliminary characterisation

δ (ppm)	Multiplicity	Integration	J coupling (Hz)	Assignment
13.40	s	1H		H_h
9.73	s	1H		H_a
8.88	s	1H		H_d
7.67	d	1H	2.7	H_g
7.38	dd	1H	8.8, 2.7	H_f
7.34-7.28	m	2H		H_b
6.69	d	1H	8.8	H_e
6.87-6.81	m	2H		H_c

NMR

Table 21: 1H NMR Assignments for compound 2

^{1}H NMR Expansions

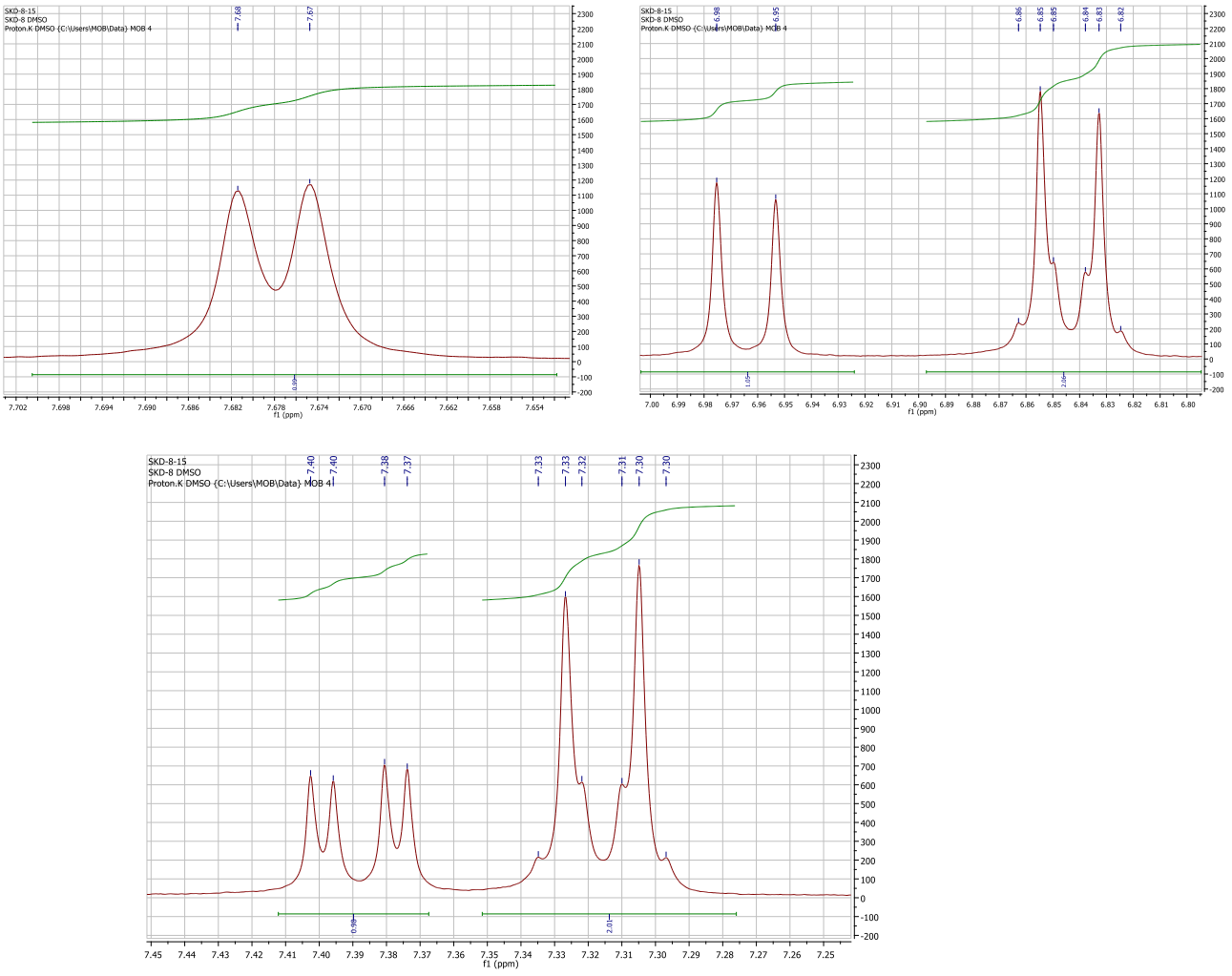


Figure 312: Expansions of ^{1}H NMR spectrum for compound 2

Table 22: ^{13}C NMR assignments for compound 2

δ (ppm)	Integration	Assignment
158.82	1	7
158.70	1	10
157.28		1
138.87	1	6
131.97	1	11
130.79	1	9
122.81	2	4/5
122.34	1	13
120.69	1	12
118.46	1	8
116.00	2	3/2

^{13}C NMR Expansions

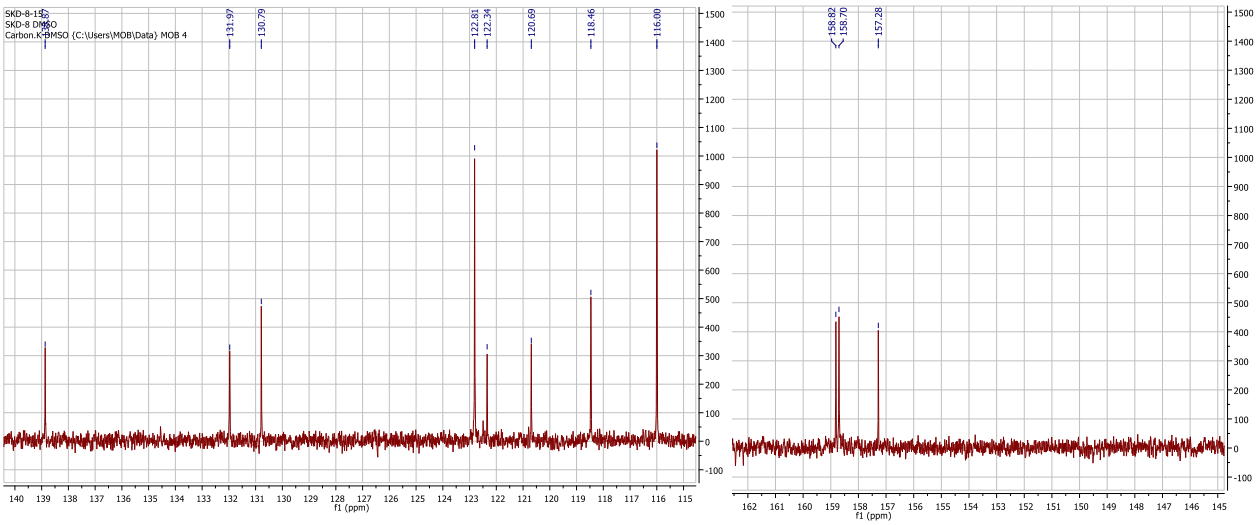


Figure 313: Expansions of ^{13}C NMR spectrum for compound 2

Table 23:Tabulated UV-VIs absorption λ_{max} of compound 2

abs	Wavelength (nm)	abs	Wavelength (nm)
1.01	359	0.48	271

SCXRD

Collected at Keele at 230, 200, 170, 140 and 110 K using a molybdenum source on a Bruker model SCXRD. The resulting data was integrated using the Bruker Apex 2 software. The outputted .ins and .hkl files were then inputted into the CRYSTALS SCXRD analysis software where the structure was determined using the SIR92 programme.

Compound 2 is a thermochromic material with a monoclinic P $2_1/c$ space group, the colour change from orange to yellow, as the temperature is decreased from 260 K through 200 K to 110 K. The internal dihedral angle of the molecule shifts from 30.48° at 230 K to 30.57° at 110K. This is unusually large for a thermochromic material where the dihedral angle is expected to be below 20°.

At 230 K the keto/enol hydrogen can be found at a ratio of 63.6: 36.4 whereas at 110 K the hydrogen can be found in the keto position on the nitrogen with an 100% occupancy.

Table 24: X-ray Crystallographic data for compound 2 using Mo source

Crystal system	Monoclinic				
Space group	P $2_1/c$				
Z	4				
Crystal size (mm)	1x 1x 2 mm				
Radiation type	X-ray Molybdenum				
Wavelength (nm)	0.71073				
Temperature (K)	**110**	**140**	**170**	**200**	**230**
Cell parameters (Å)	a =7.074(1) b =12.499(2) c = 12.471(3) α /γ=90 β=92.351(2)	a =7.046(2) b =12.467(4) c=12.484(5) α /γ=90 β=92.421(1)	a= 7.068(1) b = 12.476(5) c = 12.488(4) α /γ=90 β=92.58(1)	a=7.0903(1) b=12.474(2) c=12.513(1) α /γ=90 β=92.657(3)	a=7.1155(2) b=12.4662(3) c=12.5475(1) α /γ=90 β=92.760(2)
Cell volume ($Å^3$)	1101.7(2)	1095.7(2)	1100.1(1)	1105.6(1)	1111.7(3)
Total no. of reflections	2623	2616	2635	2557	2565
No of reflection with I/σ(I) > 2	1142	1935	1903	1841	1298
R(sigma)	0.0932	0.0343	0.0480	0.0447	0.141
Parameters/Restraints	191	154	155	181	198
R1, wR2, Goof	0.1378, 0.2963, 0.9612	0.1469, 0.2558, 0.9413	0.0774, 0.1450, 0.9768	0.0876, 0.1595, 0.9610	0.0706, 0.1343, 0.9528
R1 after Fourier merging / No of unique reflections	1080	897	1325	1067	2546
Max resolution (Å)					
Scan type	2THETA/OMEGA	2THETA/OMEGA	2THETA/OMEGA	2THETA/OMEGA	2THETA/OMEGA
Theta max	28.989	28.058	27.650	27.685	27.676
hkl limits	Hmin, Hmax -9 9 Kmin, Kmax -17 16 Lmin, Lmax -16 16	Hmin, Hmax -9 9 Kmin, Kmax -16 16 Lmin, Lmax -16 16	Hmin, Hmax -16 16 Kmin, Kmax -16 16 Lmin, Lmax -9 9	Hmin, Hmax -16 16 Kmin, Kmax -16 16 Lmin, Lmax -9 9	Hmin, Hmax -16 16 Kmin, Kmax -16 16 Lmin, Lmax -9 9

Compound 3

Preliminary characterisation

Table 25: ^{1}H NMR assignments for compound 3

δ (ppm)	Multiplicity	Integration	J coupling (Hz)	Assignment
13.02	s	1H		H_h
8.93	s	1H		H_d
7.75	d	1H	2.7	H_g
7.50-7.37	m	5H		H_{a-c}
7.35-30	m	1H		H_f
7.00	d	1H	8.8	H_e

^{1}H NMR Expansions

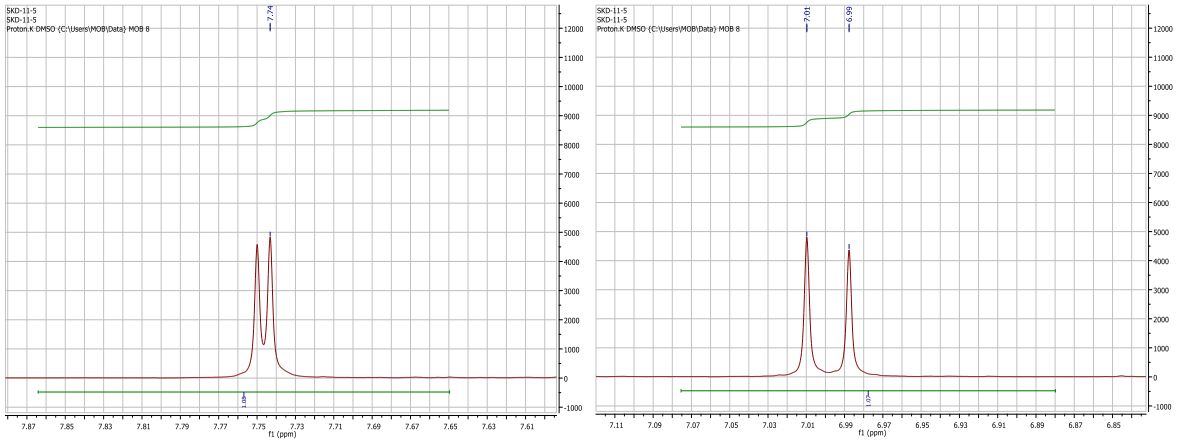


Figure 314: ^{1}H NMR expansions for compound 3

Table 26: ^{13}C NMR assignments of compound 3

δ (ppm)	Integration	Assignment
162.02	1	7
158.92	1	10
147.90	1	6
132.74	1	11
131.03	1	13
129.51	2	2/3
127.26	1	9
122.55	1	1
121.41	2	4/5
120.59	1	8
118.64	1	12

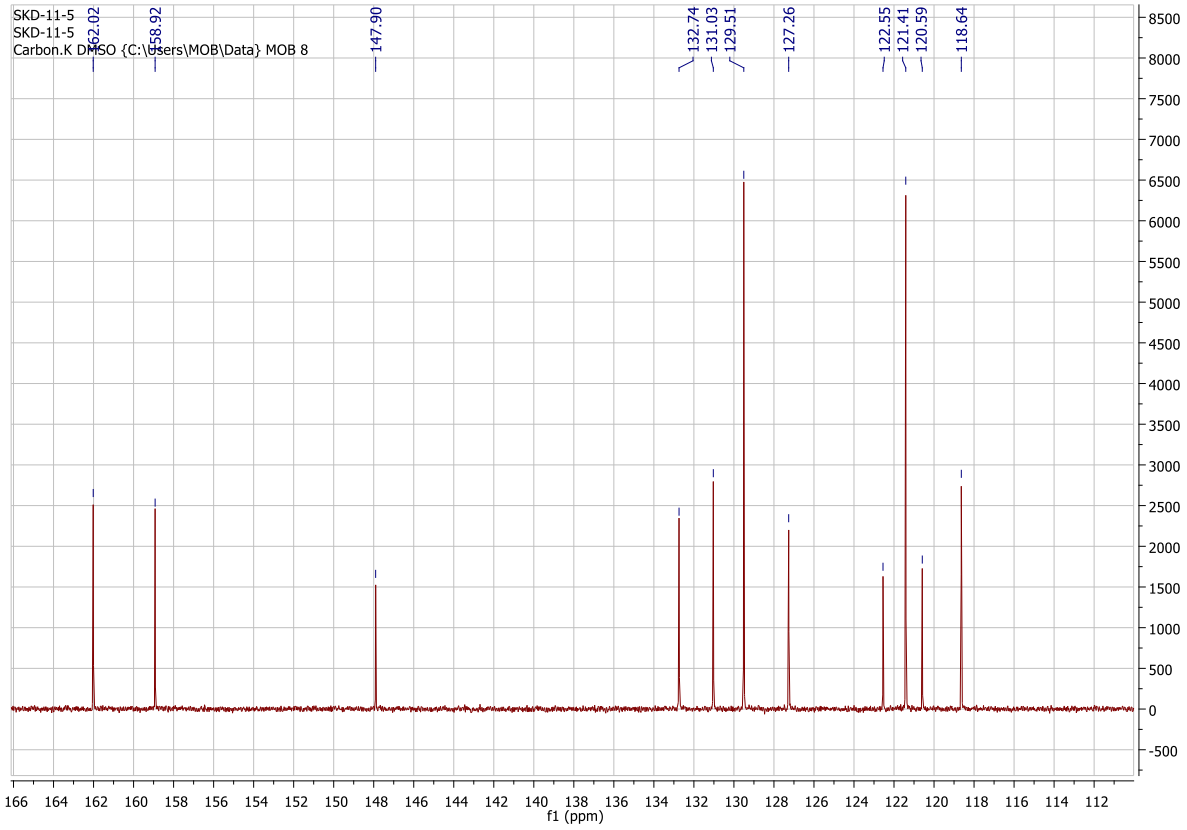


Figure 315: Expansion of ^{13}C NMR spectrum of compound 3

Table 27: Tabulated UV-VIs absorption λ_{max} of compound 3

abs	Wavelength (nm)	abs	Wavelength (nm)	abs	Wavelength (nm)	abs	Wavelength (nm)
0.99	346	0.86	320	0.88	304	1.08	270

SCXRD

Data was collected on the SCXRD at Keele at 120, 140 and 298 K using a molybdenum source on a Bruker SCXRD. The resulting data was integrated using the Bruker Apex 2 software. The outputted .ins and .hkl files were then inputted into the CRYSTALS SCXRD analysis software where the structure was determined using the SIR92 programme.

Compound 3 is a thermochromic material with a Monoclinic P $2_1/n$ space group, the colour change from orange to yellow, as the temperature is decreased from 298 K through 140 K to 120 K. The internal dihedral angle of the molecule shifts from 5.70° at 298 K to 6.01° at 120 K.

At 120 K the keto/enol hydrogen can be found 100 % in the enol position on the oxygen whereas at 293 and 250 K the hydrogen can be found in the keto position on the nitrogen.

A second polymorph was also collected having an orthorhombic P c a 21 space group. The internal dihedral angle of the molecule shifts from 0.78° at 298 K to 1.22° at 120 K.

Table 28: Crystallographic Data for compound 3 (I)

Crystal system	Monoclinic		
Space group	P 2_1/n		
Z	4		
Crystal size (mm)	0.289x0.130x0.047		
Radiation type	X-ray Molybdenum		
Wavelength (nm)	0.71073		
Temperature (K)	**120**	**140**	**298**
Cell parameters (Å)	a= 4.55020(1) b=19.40630(2) c= 12.04980(3) α /γ=90 β=94.995(1)	a= 4.54240(4) b=19.37180(3) c= 12.03120(1) α /γ=90 β=94.013(2)	a= 4.60130(2) b=19.57790(1) c= 12.15790(1) α /γ=90 β=95.344(2)
Cell volume(Å^3)	1059.986(3)	1054.629(3)	1090.47(3)
Total no. of reflections	13475	13109	12579
No of reflection with I/σ(I) > 2	1806	1764	1227
R(sigma)	0.0768	0.0729	0.1441
Parameters/Restraints	61	154/6	185
R1, wR2, Goof	0.0351, 0.757, 1.0057	0.0357, 0.0711, 1.0119	0.0468, 0.0979,1.000
R1 after Fourier merging / No of unique reflections	0.046,2195	0.049, 2179	0.065, 1950
Scan type	2THETA/OMEGA	2THETA/OMEGA	2THETA/OMEGA
Theta max	26.539	26.521	25.179
hkl limits	H min = -5 H max = 5 K min = -24 K max = 24 L min = -15 L max = 14	H min = -5 H max = 5 K min = -24 K max = 23 L min = -15 L max = 14	H min = -5 H max = 4 K min = -23 K max = 23 L min = -14 L max = 14

Table 29: Crystallographic data for compound 3(II)

Crystal system	Orthorhombic	
Space group	$Pca2_1$	
Z	4	
Crystal size (mm)	0.007x0.265x0.540	
Radiation type	X-ray Molybdenum	
Wavelength (nm)	0.71073	
Temperature (K)	**120**	**290**
Cell parameters (Å)	a= 12.19563(2) b=4.4869(1) c= 19.31140(4) α/β/γ=90	a= 12.21956(1) b=4.52720(2) c= 19.52970(3) α/β/γ=90
Cell volume (Å^3)	1053.731(2)	1090.116(2)
Total no. of reflections	14215	14870
No of reflection with I/σ(I) > 2	1845	1640
R(sigma)	0.050	0.056
Parameters/Restraints	185/1	145/1
R1, wR2, Goof	0.0302, 0.0774, 0.9917	0.0367, 0.0586, 1.0271
No of unique reflections	1936	1942
Max resolution (Å)		
Scan type	2THETA/OMEGA	2THETA/OMEGA
Theta max	25.383	25.112
hkl limits	H min = -14 H max = 14 K min = -5 K max = 5 L min = -23 L max = 23	H min = -14 H max = 14 K min = -5 K max = 5 L min = -23 L max = 23

Neutron

A suitable crystal of N-(4-chlorosalicylidene)-aniline for neutron diffraction, measuring approximately 1 x 2 x 5 mm, was grown via evaporation concentrated ethanol solution at 20 °C. Diffraction data were collected using the single-crystal diffractometer SXD at the ISIS spallation neutron source (Oxfordshire, UK; Keen *et al.*, 2006) at 120 K and 10 K. Time-of-flight Laue diffraction data were collected in a series of four orientations, with a counting time per orientation of ~3 h. The diffraction spots were initially indexed with the unit cells available from the x-ray measurements at the corresponding temperature. Bragg intensities were extracted using the 3D-profile fitting method implemented in the SXD2001 software (Gutmann, 2017) and corrected for Lorenz effect. No absorption correction for the shape of the crystal was applied. All structures were refined by full matrix least squares on F^2 using SHELXL (Sheldrick, 2008).

Refinement details

The molecule was refine anisotropically and showed no disorder across the molecule. However, to avoid some atoms going non-positive definite in the anisotropic refinement of the diagonal components were restrained to reasonable values.

Table 30: Crystallographic Data for Neutron diffraction of compound 3

Crystal system	Monoclinic	
Space group	P 2_1/c	
Z	4	
Crystal size (mm)	4 x 3 x 2	
Radiation type	Neutron	
Wavelength (nm)	0.35 – 6.5 Å	
Temperature (K)	**120**	**10**
Cell parameters (Å)	a: 4.565(3) b:19.4456(3) c: 12.060(3) alpha/gamma:90 beta: 94.867(4)	a: 4.5532(3) b:19.3008 (7) c: 12.0522(6) alpha/gamma:90 beta: 94.9245(6)
Cell volume (Å^3)	1066.70	1055.24
Total no. of reflections	12895	12794
No of reflection with I/σ(I) > 4	1032	1024
R(sigma)	0.0805	0.0803
Parameters/Restraints	111/0	111/0
R1, wR2, Goof	0.1270, 0.3151, 1.547	0.1231,0.3018, 1.477
R1 after Fourier merging / No of unique reflections	0.0695/467	0.1045/467
Max resolution (Å)	0.57	0.57
Nuclear density Fourier difference residuals: $\Delta\rho_{max}$, $\Delta\rho_{min}$	1.05, -1.32	1.05, -1.32

Compound 4

Preliminary characterisation

NMR

Table 31:1H NMR assignments of compound 4

δ (ppm)	Multiplicity	Integration	J coupling (Hz)	Assignment
13.18	s	1H		H_j
8.73	s	1H		H_e
8.15	t	1H	1.8	H_f
8.14-8.09	m	1H		H_d
7.66-7.52	m	3H		H_{a-c}
7.30	d	1H	2.4	H_f
1.50	s	9H		H_i
1.36	s	9H		H_g

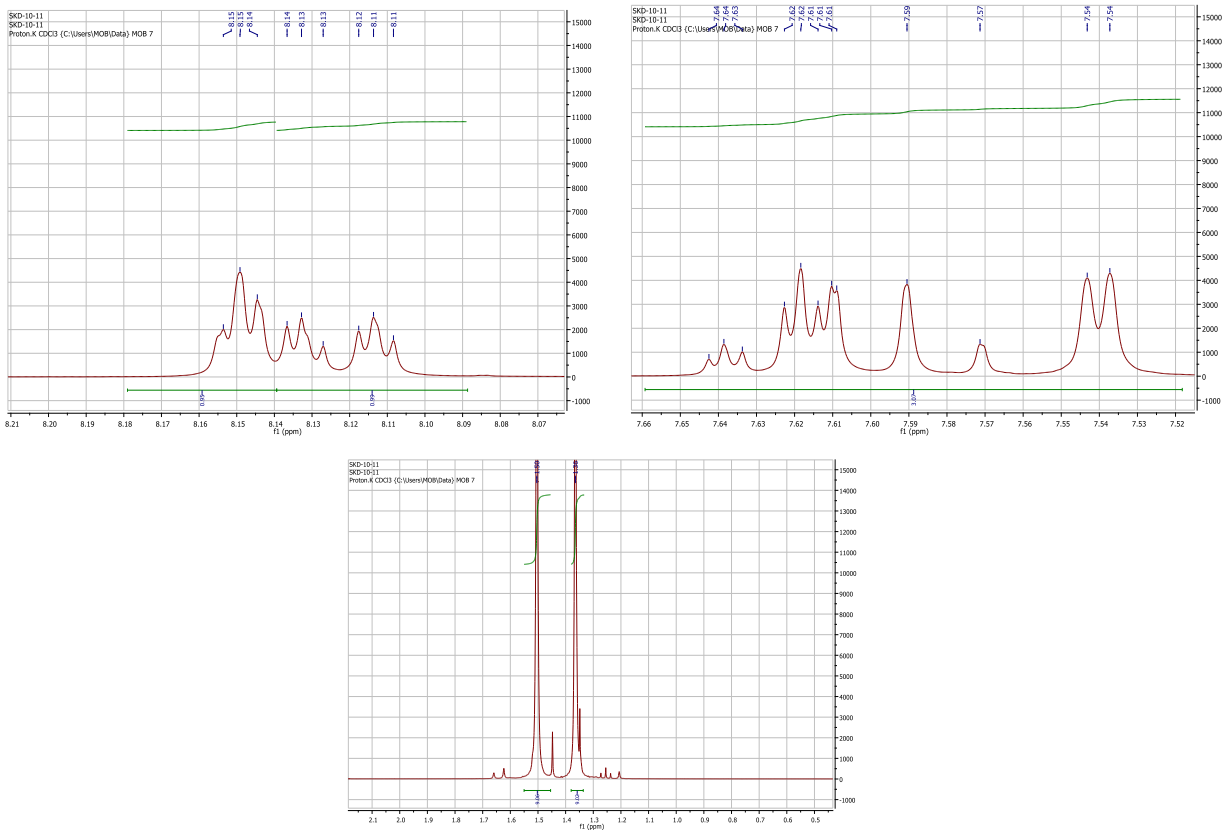


Figure 316: ^{1}H NMR spectrum expansions for compound 4

Table 32: ^{13}C NMR assignments for compound 4

δ (ppm)	Integration	Assignment
181.66	1	7
166.02	1	10
158.42	1	11
149.95	1	6
141.08	1	2
137.23	1	12
130.17	1	3
129.17	1	9
127.89	1	13
127.36	1	5
120.98	1	8
117.90	1	1
115.63	1	4
35.12	1	18
34.21	1	14
31.41	3	19-21
29.39	3	15-17

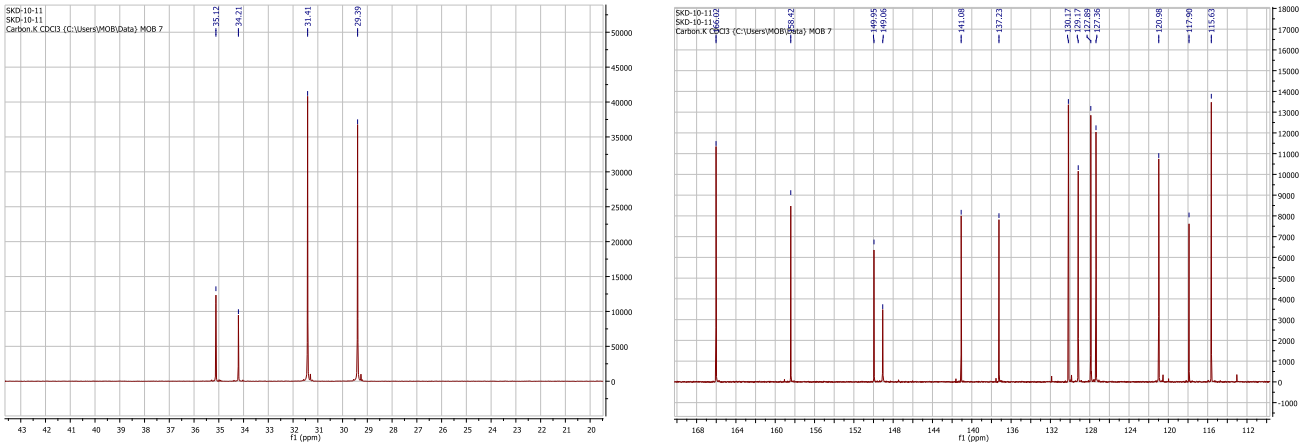


Figure 317: 13C NMR spectrum expansions for compound 4

Table 33: Tabulated UV-VIs absorption λ_{max} of compound 4

abs	Wavelength (nm)	abs	Wavelength (nm)
0.40	374	1.04	280

Raman Spectroscopy assignments

Table 34: Raman Peak assignments at 20 K for compound 4

Position (cm^{-1})	**Keto Assignment**	**Enol Assignment**
1620	NH OOP bend, Bridge CH OOP bend	–
1613	–	CH IP wag, ring deformations
1597	NH OOP bend	–
1588	CH IP wag	–
1574	–	OH IP bend, ring deformations, CH wag
1554	CH wag	–
1547	CH wag	–
1536	Aniline CH IP wag	–
1525	*tert*butyl asymmetric bend	*tert*butyl umbrella bend
1480	*tert*butyl CH asymmetric bend	–
1469	*tert*butyl CH asymmetric bend	–
1465	–	*tert*butyl CH asymmetric wag
1458	–	*tert*butyl CH scissor bend, deformations
1454	–	*tert*butyl CH scissor bend, deformations
1445	–	IP OH and CH bends
1438	–	*tert*butyl CH umbrella bend
1402	*tert*butyl CH umbrella bend	–
1390	–	*tert*butyl CH umbrella bend
1386	–	*tert*butyl CH umbrella bend
1355	Aniline CH OOP bend	–
1348	–	aniline ring deformations
1337	aniline CH wag	aniline CH OOP bend
1331	bridge CH IP wag	bridge CH IP wag
1310	–	aldehyde CH bend
1280	–	ring deformations, CH asymmetric stretch
1268	NH IP wag, Ar- CH wag	–
1252	*tert*butyl CH asymmetric bend	–

1237	aniline CH bend	–
1233	*tert*butyl rotation	–
1224	–	molecular deformations
1211	–	Ring CH bends
1210	–	Aldehyde CH wag
1201	–	Aldehyde CH wag
1199	aniline CH wag	*tert*butyl asymmetric bend
1187	aniline CH wag	*tert*butyl asymmetric bend
1175	aniline CH wag	*tert*butyl asymmetric bend
1135	Aniline OOP CH bend	–
1091	-	CH OOP bend
999	*tert*butyl asymmetric bend	–
991	*tert*butyl asymmetric bend	–
944	Aldehyde CH OOP bend	–
932	Aldehyde CH OOP bend	–
927	Aldehyde CH OOP bend	–
919	–	Ar-H OOP bend
914	–	OH IP bend
896	NH IP wag	–
886	–	aldehyde CH IP wag
839	–	molecular deformations
824	*tert*butyl CH umbrella bend	–
806	*tert*butyl CH umbrella bend	–
734	–	molecular deformations
677	ring deformations, NH IP wag	–
665	Ring CH bend, NH IP wag	–
611	–	molecular deformations
592	molecular deformations	molecular deformations
564	–	Molecular deformations
551	–	molecular deformations
539	molecular deformations	–

470	molecular deformations	–
459	Molecular deformations	–
434	molecular deformations, Aniline CH IP wag	–
396	–	*tert*butyl CH umbrella bend
377	–	*tert*butyl CH umbrella bend
359	*tert*butyl symmetric CH wag	–
335	*tert*butyl rotation	–
330	*tert*butyl rotation	–
314	–	CH OOP bends
298	*tert*butyl rotation	–
280	*tert*butyl rotation	–
268	*tert*butyl asymmetric bends	–
260	*tert*butyl rotation	–
250	–	*tert*butyl CH wag
236	–	*tert*butyl CH wag
219	molecular deformations	–
204	*tert*butyl rotation/ molecular deformation	–
185	aniline ring rotation	–
165	molecular deformation	*tert*butyl CH symmetric bend
149	Molecular deformation	deformation
132	–	aldehyde ring deformation
108	–	molecular deformations
98	molecular deformations	–
84	-	molecular deformations
79	molecular deformations	–
69	-	molecular deformations
62	molecular deformations	–
53	–	molecular deformations
49	–	molecular deformations
42	–	molecular deformations

Table 35: Raman peak assignments at 270 K for compound 4

Position (cm^{-1})	**Keto Assignment**	**Enol**
1619	NH OOP bend, Bridge CH OOP bend	–
1611	–	CH IP wag, ring deformations
1590	NH OOP bend	
1574	-	OH IP bend, ring deformations, CH wag
1551	CH wag	–
1524	*tert*butyl asymmetric bend,	*tert*butyl umbrella bend
1478	*tert*butyl CH asymmetric bend	–
1465	–	*tert*butyl CH asymmetric wag
1455	–	*tert*butyl CH scissor bend, deformations
1444		IP OH and CH bends
1400	*tert*butyl CH umbrella bend	–
1391	–	*tert*butyl CH umbrella bend
1346	–	aniline ring deformations
1326	bridge CH IP wag	bridge CH IP wag
1280	–	ring deformations, CH asymmetric stretch
1269	NH IP wag, Ar- CH wag	–
1251	*tert*butyl CH asymmetric bend	–
1235	aniline CH bend	–
1222	–	molecular deformations
1207	–	Aldehyde CH wag
1199	aniline CH wag	*tert*butyl asymmetric bend
1174	aniline CH wag	*tert*butyl asymmetric bend
1134	Aniline OOP CH bend	–
1090	–	CH OOP bend
998	*tert*butyl asymmetric bend	–
969	*tert*butyl asymmetric bend	–
941	Aldehyde CH OOP bend	–

912	–	OH IP bend
894	NH IP wag	–
804	*tert*butyl CH umbrella bend	–
732	–	molecular deformations
677	ring deformations, NH IP wag	–
665	Ring CH bend, NH IP wag	–
591	molecular deformations	molecular deformations
563	–	Molecular deformations
552	–	molecular deformations
467	molecular deformations	–
457	Molecular deformations	–
430	molecular deformations,	Aniline CH IP wag
395	*tert*butyl CH umbrella bend	–
296	*tert*butyl rotation	*tert*butyl rotation
265	*tert*butyl asymmetric bends	–
247	–	*tert*butyl CH wag
217	molecular deformations	–
183	aniline ring rotation	–
159	molecular deformation	–
145	molecular deformation	molecular deformation
124	–	aldehyde ring deformation
101	–	molecular deformations
91	molecular deformations	–
64	molecular deformations	–
49	–	molecular deformations

Table 36: Raman Peak assignments of irradiated compound 4

Position (cm^{-1})	**Keto Assignment**	**Enol Assignment**
1609.15	–	CH IP wag, ring deformations
1587.23	NH OOP bend	–
1572.72	–	OH IP bend, ring deformations, CH wag
1521.51	*tert*butyl asymmetric bend,	*tert*butyl umbrella bend
1476.35	*tert*butyl CH asymmetric bend	–
1463.42	–	*tert*butyl CH asymmetric wag
1439.21	–	IP OH and CH bends
1411.16	*tert*butyl CH umbrella bend	–
1397.48	*tert*butyl CH umbrella bend	–
1344.27	–	aniline ring deformations
1325.35	bridge CH IP wag	bridge CH IP wag
1282.94	–	ring deformations, CH asymmetric stretch
1265.75	NH IP wag, Ar- CH wag	–
1247.23	*tert*butyl CH asymmetric bend	–
1232.45	aniline CH bend	–
1219.08	–	molecular deformations
1198.52	aniline CH wag	*tert*butyl asymmetric bend
1166.94	aniline CH wag	*tert*butyl asymmetric bend
1131.70	Aniline OOP CH bend	–
1089.01	–	CH OOP bend
1013.83	–	molecular deformations
996.48	*tert*butyl asymmetric bend	–
986.08	*tert*butyl asymmetric bend	–
958.94	*tert*butyl asymmetric bend	–
925.48	–	*tert*butyl asymmetric bends
910.51	–	OH IP bend
876.31	NH OOP wag, aldehyde CH IP wag	–
863.16	*tert*butyl symmetric bends	–

845.11	–	*tert*butyl asymmetric bends
834.10	NH IP wag, aniline CH IP wag	–
820.38	–	Nitro deformations, *tert*butyl deformations
800.54	NH IP wag, aniline CH IP wag	–
790.11	–	Aniline CH OOP wag
773.77	Aniline CH IP wag	–
733.96	–	molecular deformations
692.16	Aniline CH IP wag, NH IP wag, Nitro group deformation	–
662.76	ring deformations, NH IP wag	–
637.97	Aldehyde CH IP wag	–
613.14	–	Molecular deformations
562.08	–	Molecular deformations
549.71	molecular deformations	–
536.98	–	Molecular deformations
506.98	–	*tert*butyl deformations
463.07	molecular deformations	–
427.90	molecular deformations,	Aniline CH IP wag
409.24	*tert*butyl umbrella bend	–
392.71	–	*tert*butyl CH umbrella bend
372.59	–	molecular deformations
356.77	*tert*butyl rotation, Aldehyde deformations	–
332.06	*tert*butyl rotation	–
292.59	*tert*butyl rotation	*tert*butyl rotation
262.46	–	*tert*butyl wag
214.49	molecular deformations	–
179.27	–	aniline ring rotation
155.28	molecular deformation	–
119.62	–	aldehyde ring deformation

SCXRD

Compound 4 data was collected on the SCXRD at ISIS, Harwell at 120 and 290 K using a molybdenum source. The resulting data was integrated automatically in the CrysAlisPro software embedded with the Olex programme. The outputted .ins and .hkl files were then inputted into the CRYSTALS SCXRD analysis software where the structure was determined using the SIR92 programme.

The crystals are pale yellow in colour and have a preference for a needle like morphology though plate could be obtained through warm recrystallisation and slow cooling before being left to evaporate from ethanol.

Table 37: Crystallographic X-ray data for variable temperature experiement

Crystal system	Triclinic			
Space group	P $\bar{1}$			
Z	2			
Crystal size (mm)_	1 x 2 x 4			
Radiation type	X-ray Molybdenum			
Wavelength (nm)	0.71073			
Temperature (K)	**100**	**160**	**250**	**293**
Cell parameters (Å)	a= 6.09038(1) b=10.2900(2) c= 16.2442(2) α =102.183(3) β=92.257(1) γ=103.083(2)	a= 6.09802(2) b=10.3076(3) c= 16.3236(2) α =102.131(1) β=92.127(2) γ=102.951(6)	a= 6.06899(4) b=10.3211(2) c= 16.5595(2) α =101.692(2) β=92.0901(1) γ=102.1957(2)	a= 6.037230(2) b=10.31616(1) c= 16.76083(3) α =101.205(5) β=92.214(2) γ=101.527(2)
Cell volume (Å^3)	965.19(5)	973.78(2)	989.41(2)	1000.068(1)
Total no. of reflections	22349	22598	23114	23114
No of reflection with I/σ(I) > 2	3704	4248	3483	3334
R(sigma)	0.0241	0.0234	0.0246	0.0246
Parameters/Restraints	236/0	235/0	235/0	263/0
R1, wR2, Goof	0.0474, 0.01398, 0.9987	0.0511, 0.1535, 1.0000	0.0556, 0.1817, 0.9806	0.0562,0.1819, 0.9520
R1 after Fourier merging / No of unique reflections	0.0310/4890	0.03/4938	0.0310/5030	0.0333/5099
Max resolution (Å)				
Scan type				
Theta max	29.608	29.591	29.596	29.595
hkl limits	H min = -8 H max = 8 K min = -13 K max = 14 L min = -22 L max = 21	H min = -8 H max = 8 K min = -13 K max = 14 L min = -22 L max = 22	H min = -8 H max = 8 K min = -13 K max = 14 L min = -22 L max = 22	H min = -8 H max = 8 K min = -13 K max = 14 L min = -23 L max = 23

Due to the finding of radiation damage using molybdenum for the photoproduct the *in situ* irradiation was collected using a copper source. An *in situ* irradiation experiment was completed over 5 days including 2 recentring of the sample.

Table 38: Crystallographic X-ray data for compound 4 using Copper source

Crystal system	Triclinic
Space group	P $\bar{1}$
Z	2
Crystal size (mm)	1 x 1 x 6 mm
Radiation type	X-ray Copper
Wavelength (nm)	1.54184
Irradiation	Non-irradiated
Temperature (K)	**293**
Cell parameters (Å)	a = 6.04164(16) b = 10.3261(3) c = 16.7687(4) α = 101.212(2) β = 92.223(2) γ = 101.548(2)
Cell volume (Å^3)	1002.11(5)
Total no. of reflections	17519
No of reflection with I/σ(I) > 2	3024
R(sigma)	0.0323
Parameters/Restraints	263/0
R1, wR2, Goof	0.0620, 0.1702, 1.0477
R1 after Fourier merging / No of unique reflections	0.0580/3648
Scan type	2thetaomega
Theta max	68.659
hkl limits	H min = -6 H max = 7 K min = -12 K max = 11 L min = -20 L max = 20

Table 39: Crystallographic X-ray data for compound 4 using Copper source in situ irradiation

Crystal system	Triclinic				
Space group	P $\bar{1}$				
Z	2				
Crystal size (mm)	1 x 2 x 3				
Radiation type	X-ray Copper				
Wavelength (nm)	1.54184				
Irradiation		*In situ* UV irradiation			
Temperature (K)	**Collection1**	**Collection2**	**Collection 3**	**Collection 5**	**Collection6**
Cell parameters (Å)	a = 6.04781(2) b = 10.34524(3) c = 16.74923(3) α = 101.178(4) β = 92.332(5) γ = 101.607(5)	a = 6.05131(16) b =10.3425(2) c = 6.76496(19) α = 101.235(3) β =92.226(3) γ =101.634(4)	a=6.04194(14) b=10.3332(17) c=6.7722(19) α = 101.201(3) β =92.192(3) γ =101.518(3)	a=10.33026(19) b=18.04236(2) c=18.13436(2) α = 111.752(3) β =101.549(3) γ =96.536(3)	a=6.045470(12) b=10.331010(16) c=6.769751(18) α =101.195(2) β =92.199(2) γ =101.536(3)
Cell volume (Å^3)	1003.56	1004.65	1003.258	3009.34	1003.429
Total no. of reflections	7972	9142	9396	25033	8589
No of reflection with I/σ(I) > 2	4002	4175	4172	11188	3780
R(sigma)	0.034	0.031	0.029	0.045	0.034
Parameters/Restraints	264/0	264/0	264/0	788/0	264/0
R1, wR2, Goof	0.138, 0.34, 0.998	0.095, 0.278, 1.017	0.072, 0.201 0.955	0.121, 0.394, 1.131	0.058, 0.176, 1.008
R1 after Fourier merging / No of unique reflections	0.04/4004	0.03/4176	0.03/4173	0.03/11183	0.02/3781
Scan type	2thetaomega	2thetaomega	2thetaomega	2thetaomega	2thetaomega
Theta max	87.62	84.99	80.32	72.02	71.38
hkl limits	H min = -7 H max = 6 K min = -13 K max = 13 L min = -21 L max = 21	H min = -7 H max = 7 K min = -13 K max = 13 L min = -21 L max = 21	H min = -7 H max = 6 K min = -13 K max = 13 L min = -21 L max = 21	H min = -12 H max = 12 K min = -18 K max = 22 L min = -22 L max = 14	H min = -6 H max = 7 K min = -12 K max = 11 L min = -20 L max = 20

Neutron

A suitable crystal of N-(3,5-di-tert-butylsalicylidene)-3-nitroaniline for neutron diffraction, measuring approximately 4 x 3 x 2 mm, was grown via slow evaporation of ethanol from a concentrated solution then irradiated for over 24 hours using 365 nm UV irradiation. Diffraction data were collected using the single-crystal diffractometer SXD at the ISIS spallation neutron source (Oxfordshire, UK; Keen *et al*., 2006) at 270 K. Time-of-flight Laue diffraction data were collected in a series of six orientations at each temperature, with a counting time per orientation of ~ 6 hrs. The diffraction spots were initially indexed with the unit cells available from the x-ray measurements corresponding to the *in situ* irradiated data, and then from the closest Neutron cell. Bragg intensities were extracted using the 3D-profile fitting method implemented in the SXD2001 software (Gutmann, 2017) and corrected for Lorenz effect. No absorption correction for the shape of the crystal was applied. All structures were refined by full matrix least squares on F^2 using SHELXL (Sheldrick, 2008).

Refinement details

The system was refined anisotropically for the two 6-membered rings and attached hydrogens and nitro group. The data showed large rotation movement of the tert-butyl groups which translated into elongated ellipsoids for the terminal carbon atoms from the anisotropic refinement, but no multiple positions were included in the refinement. The hydrogens of the tert-butyl groups were refined isotropically in the riding mode.

Table 40: Crystallographic neutron data for compound 4

Crystal system	Monoclinic
Space group	P $\bar{1}$
Z	2
Crystal size (mm)	4 x 3 x 2 mm
Radiation type	Neutron
Wavelength (nm)	0.35 – 6.5 Å
Temperature (K)	**280**
Cell parameters (Å)	a: 6.057(3) b:10.381(3) c: 16.816(3) alpha: 101.0(1) beta: 92.23(5) gamma: 102.0(2)
Cell volume (Å^3)	1011.74
Total no. of reflections	2029
No of reflection with I/σ(I) > 4	1960
R(sigma)	0.0341
Parameters/Restraints	340
R1, wR2, Goof	0.0987, 0.2570, 2.323
R1 after Fourier merging / No of unique reflections	0.0987, 993
Max resolution (Å)	0.89
Nuclear density Fourier difference residuals: $\Delta\rho_{max}$, $\Delta\rho_{min}$	1.24, -1.16
Extinction coeff.	

Compound 5

Preliminary Characterisation

Table 41: 1H NMR assignments for compound 5

δ (ppm)	Multiplicity	Integration	J coupling (Hz)	Assignment
12.51	s	1H		H_j
9.07	s	1H		H_e
8.27	t	1H	2.1	H_d
8.15	ddd	1H	8.2, 2.2, 1.0	H_a
7.86	ddd	1H	8.0, 2.0, 1.0	H_b
7.74	t	1H	8.1	H_c
7.31	dd	1H	7.9, 1.4	H_f
7.17	dd	1H	8.0,1.4	H_g
6.94	t	1H	7.9	H_h
3.83	s	3H		H_i

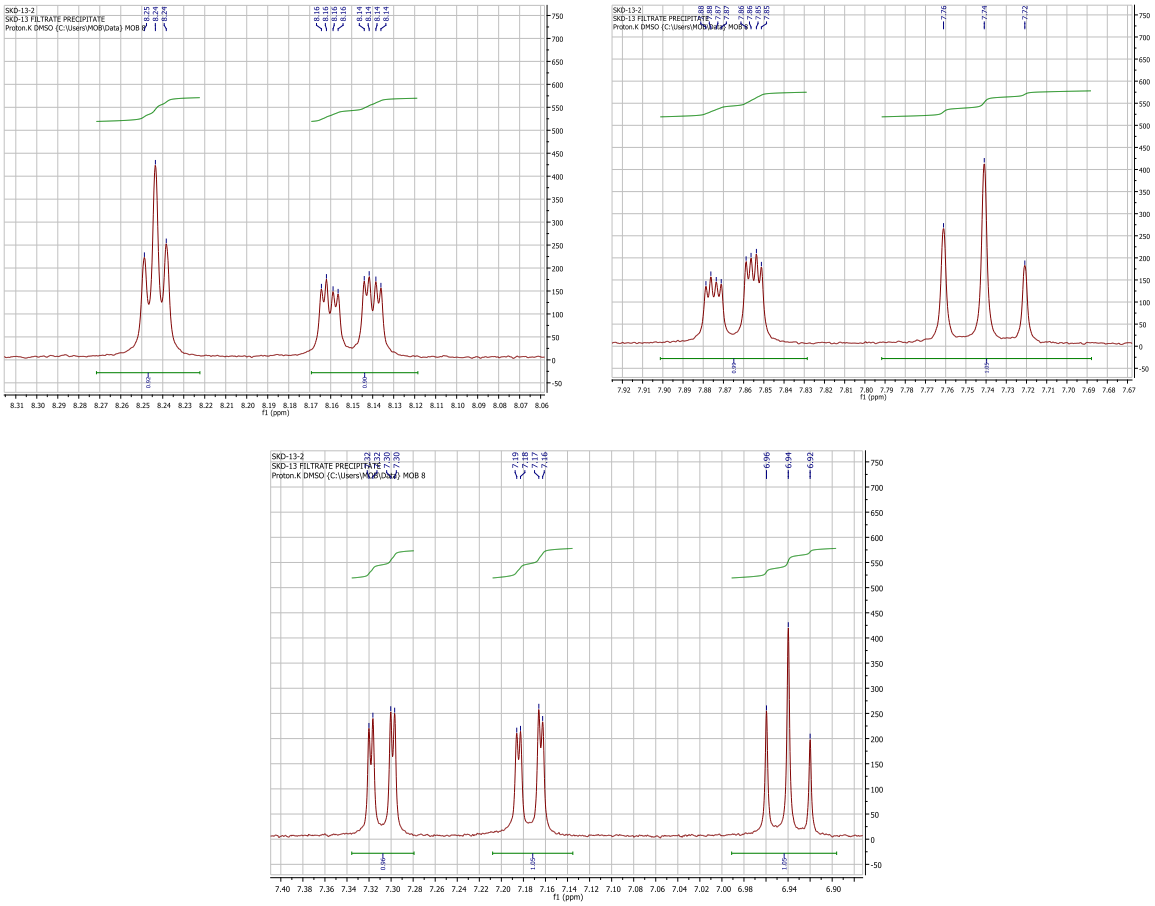


Figure 318: [1]H NMR spectrum expansions of compound 5

Table 42: ^{13}C NMR peak assignments for compound 5

δ (ppm)	Integration	Assignment
166.02	1	7
150.72	1	12
149.84	1	10
148.91	1	6
148.23	1	2
131.01	1	9
128.74	1	3
124.16	1	11
121.40	1	5
119.50	1	8
119.10	1	1
116.29	1	13
116.02	1	4
56.13	1	14

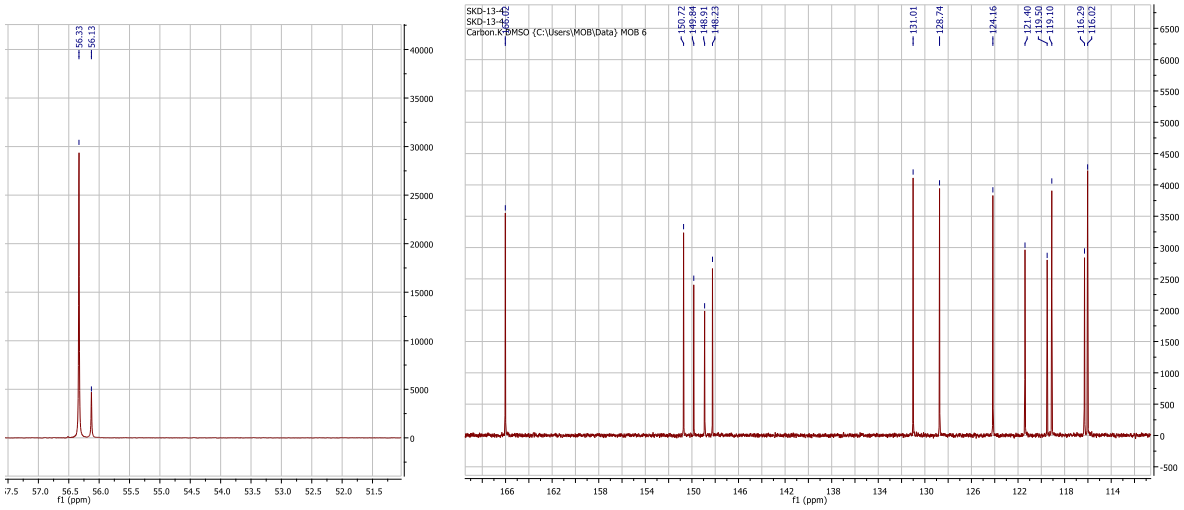


Figure 319: 13C NMR spectrum expansion of compound 5

Table 43: Tabulated UV-VIs absorption λ_{max} of compound 5

abs	Wavelength (nm)	abs	Wavelength (nm)
0.47	336	1.43	260

SCXRD

SCXRD data was collected on the Bruker APEX2 SCXRD instrument at Keele at 130 and 293 K. The orange needle became paler in colour upon the decrease in temperature. A triclinic system with a $P\bar{1}$ space group was observed.

Table 44: Tabulated SCXRD data for compound 5 at 130 and 293 K

Crystal system	Triclinic	
Space group	$P\bar{1}$	
Z	2	
Crystal size (mm)	1 x 1.5 x 3	
Radiation type	X-ray Molybdenum	
Wavelength (nm)	0.71073	
Temperature (K)	**130**	**293**
Cell parameters (Å)	**a** 4.75280(3) **b** 11.17680(5) **c** 11.87664(5) α 92.456(7) β 101.493(6) γ 93.546(6)	**a** = 4.80000(6) **b** = 11.34770(9) **c** = 12.07090(9) α = 93.481(8) β =100.334(8) γ =94.227(8)
Cell volume (Å^3)	616.084	643.23
Total no. of reflections	8258	3240
No of reflection with I/σ(I) > 2	1604	770
R(sigma)	0.1283	0.1172
Parameters/Restraints	181/0	182/4
R1, wR2, Goof	0.0737, 0.1624, 0.9551	0.0864, 0.2259, 1.0061
R1 after Fourier merging / No of unique reflections	0.1283/2735	0.1172/1220
Scan type	2THETA/OMEGA	2THETA/OMEGA
Theta max	27.347	22.203
hkl limits	Hmin, Hmax -6 6 Kmin, Kmax -13 14 Lmin, Lmax -15 15	Hmin, Hmax -4 5 Kmin, Kmax -10 12 Lmin, Lmax -12 12

Compound 6

Table 45: Tabulated masses and moles for compound 6 synthesis

Compound	**Mr (g/mol^{-1})**	**Mass (g)**	**Volume (mL)**	**mol**	**mmol**	**equiv**
aniline	93.13	1.0217	1	0.01051	10.51	1
2-hydroxy-3-methoxybenzaldehyde	152.15	1.6789	-	0.011035	11.03	1
ethanol	-	-	40	-	-	-
Product	227.28	2.2594	-	0.009941	9.94	-
-	-	-	-	yield	94.59	-

Preliminary characterisation

Table 46: 1H NMR assignments for compound 6

δ (ppm)	**Multiplicity**	**Integration**	**J coupling (Hz)**	**Assignment**
13.23	s	1H		H_j
8.95	s	1H		H_d
7.49-7.44	m	2H		H_c
7.41	d	2H	7.1	H_b
7.31	t	1H	7.2, 1	H_a
7.24	dd	1H	7.9, 1.4, 1	H_e
7.13	dd	1H	8.0, 1.3	H_f
6.91	t	1H	7.9, 1	H_g
3.82	s	3H		H_i

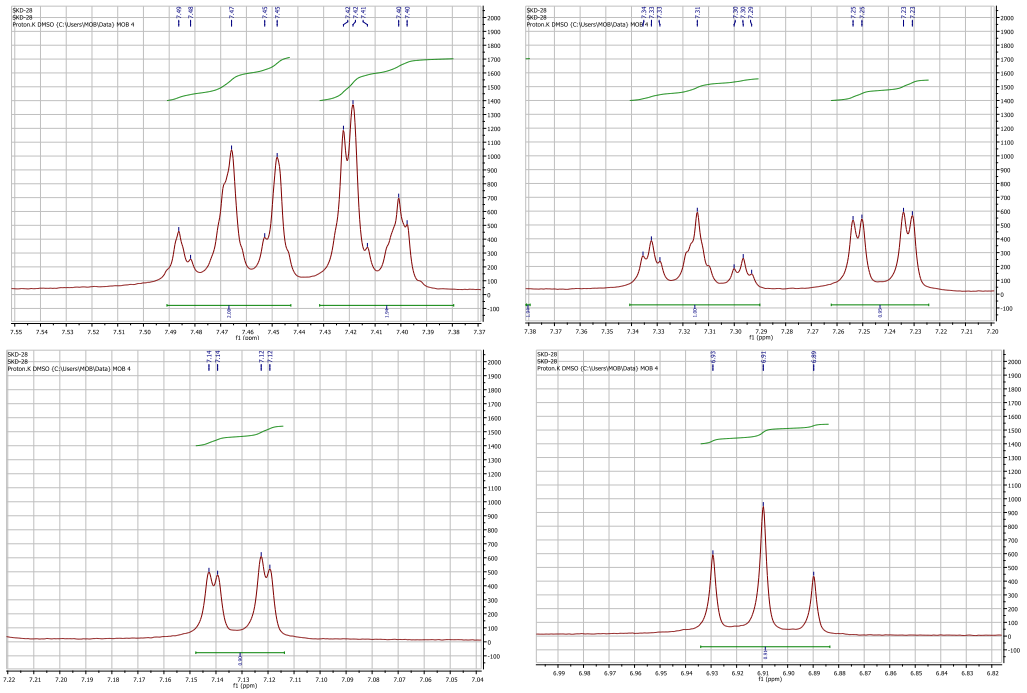


Figure 320: 1H NMR spectrum expansions of compound 6

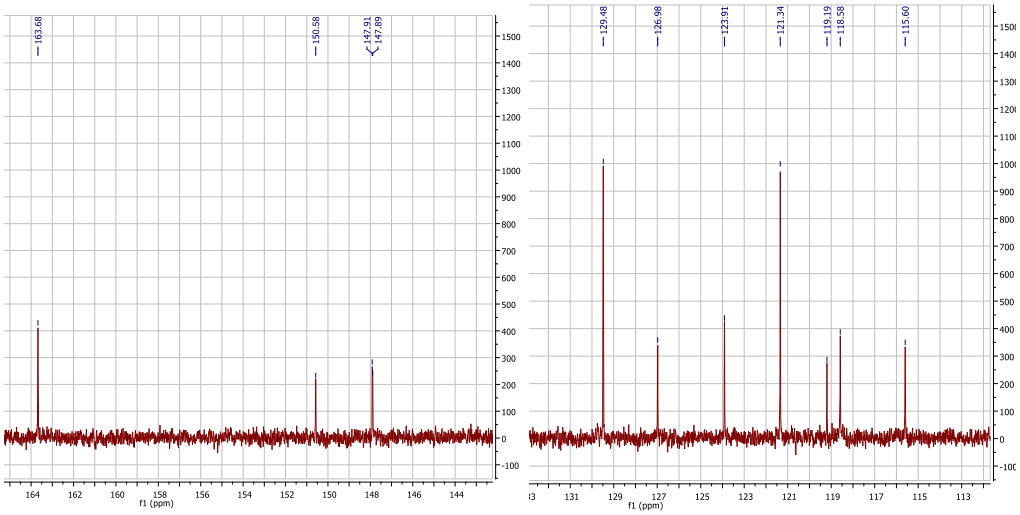


Figure 321: 13C NMR expansions for compound 6

Table 47:13C NMR assignments for compound 6

δ (ppm)	Integration	Assignment
163.68	1	7
150.58	1	6
147.91	1	12
147.89	1	10
129.48	2	2/3
126.98	1	9
123.91	1	11
121.34	2	4/5
119.19	1	1
118.58	1	8
115.60	1	13
55.89	1	14

Table 48: Tabulated UV-VIs absorption λmax of compound 6

abs	Wavelength (nm)
0.41	312

SCXRD

Data was collected on the SCXRD at ISIS, Harwell at 50, 100, 200 and 293 K using a molybdenum source. The resulting data was integrated automatically in the CrysAlisPro software embedded with the Olex programme. The outputted .ins and .hkl files were then inputted into the CRYSTALS SCXRD analysis software where the structure was determined using the SIR92 programme.

For collecting data at 50 K the helix system including a beryllium shield to reach the needed temperature. The beryllium shield left some peaks on the detector that had to be accounted for in the background removal so that the sample peaks were clean and hence the results unaffected. Upon returning to collect the data it was found that the pin to which the crystal was attached was no longer in place on the goniometer. Due to this, half of the data that should have been collected was missing and the resulting refinements were not of a decent a quality as would have otherwise been expected. For the other temperatures an oxford nitrogen stream cryostat was used as temperature control, with the data collected as a single data collection multi-temperature strategy.

SKD28 is a thermochromic material with an orthorhombic P $2_12_12_1$ space group, the colour change from red through orange to yellow, as the temperature is decreased from 293 K through 200 K to 100 K. The internal dihedral angle of the molecule shifts from 30.03° at 293 K to 30.38° at 100 K. There was no change in the enol and keto hydrogen occupancy across the temperatures, leaving a consistent enol structure at all times.

The molecules are stacked head to tail along the c- axis in zig-zag chains of alternating directions. There is no significant changes across the temperatures to the packing structure or within the bond changes of the molecule that could not be attributed to thermal contraction.

Table 49: : Crystallographic X-ray data of compound 6

Crystal system	Orthorhombic			
Space group	$P\ 2_1 2_1 2_1$			
Z	4			
Crystal size (mm)	1 x 1 x 1.2			
Radiation type	X-ray Molybdenum			
Wavelength (nm)	0.71073			
Temperature (K)	**50**	**100**	**200**	**293**
Cell parameters (Å)	a =6.0344(1) b =8.9987(1) c = 20.8937(2) α/β/γ=90	a =6. 038790(2) b =9. 040190(3) c=20. 90376(1) α/β/γ=90	a= 6.0568(1) b = 9.0968(4) c = 20.9498(2) α/β/γ=90	a=6.079467(3) b=9.174354 (2) c=21.048369(2) α/β/γ=90
Cell volume ($Å^3$)	1134.6(2)	1141.174(3)	1154.28(1)	1173.978(7)
Total no. of reflections	4071	6713	7215	10847
No of reflection with I/σ(I) > 2	1142	1935	1903	1584
R(sigma)	0.0932	0.0343	0.0480	0.0447
Parameters/Restraints	69	206	206	206
R1, wR2, Goof	0.1109, 0.2784, 0.9924	0.0367, 0.0861, 0.9820	0.0549, 0.0830, 1.0885	0.064, 0.129, 0.935
R1 after Fourier merging / No of unique reflections	1424	2083	2213	2222
Max resolution (Å)				
Scan type	2THETA/OMEGA	2THETA/OMEGA	2THETA/OMEGA	2THETA/OMEGA
Theta max	28.989	32.207	32.531	32.24
hkl limits	Hmin, Hmax -7 5 Kmin, Kmax -11 11 Lmin, Lmax -23 26	Hmin, Hmax -8 8 Kmin, Kmax -12 11 Lmin, Lmax -20 30	Hmin, Hmax -8 8 Kmin, Kmax -13 13 Lmin, Lmax -7 30	Hmin, Hmax -8 8 Kmin, Kmax -13 13 Lmin, Lmax -30 29

Compound 7

Table 50: Tabulated masses and moles for systhesis of compound 7 attempt 2

Compound	Mr (g/mol^{-1})	Mass (g)	Volume (mL)	mol	mmol	equiv
4-Hydroxyaniline	109.13	0.5871	_	0.00538	5.38	1
2-hydroxy-3-methoxybenzaldehyde	152.15	0.8274	_	0.005438	5.44	1
methanol	_	_	70		_	_
Product	243.28	0.9741	_	0.004004	4.00	
				yield	74.43	

Preliminary Characterisation

NMR

Table 51: 1H NMR assignments for compound 7

δ (ppm)	Multiplicity	Integration	J coupling (Hz)	Assignment
13.59	s	1H		H_j
9.64	s	1H		H_a
8.88	s	1H		H_d
7.31	d	2H	8.8	H_c
7.17	dd	1H	7.8, 1.3	H_e
7.07	dd	1H	8.0, 1.3	H_f
6.87	t	1H	7.9	H_g
6.84	d	2H	8.7	H_b
3.80	s	3H		H_i

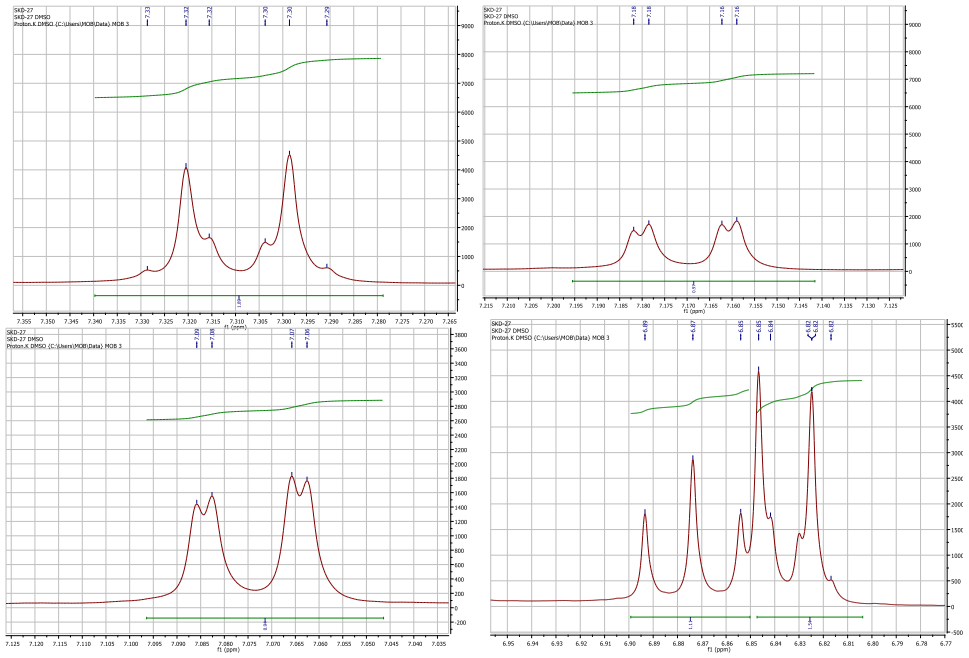


Figure 322:1H NMR spectrum expansions for compound 7

Table 52: 13C NMR assignments for compound 7

δ (ppm)	Integration	Assignment
160.35	1	7
156.99	1	1
150.40	1	12
147.85	1	10
139.00	1	6
123.71	1	9
122.63	2	4/5
119.33	1	11
118.41	1	8
115.97	2	2/3
115.03	1	13
55.84	1	14
44.61	methanol	

Table 53: Tabulated UV-VIs absorption λmax of compound 7

abs	Wavelength (nm)
0.69	339

Compound 8

Table 54: tabulated masses and moles for synthesis of compound 8

Compound	Mr (g/mol^{-1})	Mass (g)	Volume (mL)	mol	mmol	equiv
4-Bromoaniline	172.02	1.1655	-	0.006775	6.78	1
2-hydroxy-3-methoxybenzaldehyde	152.15	1.0881	-	0.007151	7.15	1
ethanol	-	_	60	-	-	-
Product	306.17	2.025	-	0.006614	6.61	-
-	-	-	-	yield	97.62	-

Preliminary characterisation

NMR

Table 55: 1H NMR assignments for compound 8

δ (ppm)	Multiplicity	Integration	J coupling (Hz)	Assignment
13.36	s	1H		H_h
8.61	s	1H		H_c
7.57-7.50	m	2H		H_a
7.20-7.13	m	2H		H_b
7.05-6.98	m	2H		H_d/H_f
6.90	t	1H	7.9	H_e
3.94	s	3H		H_g

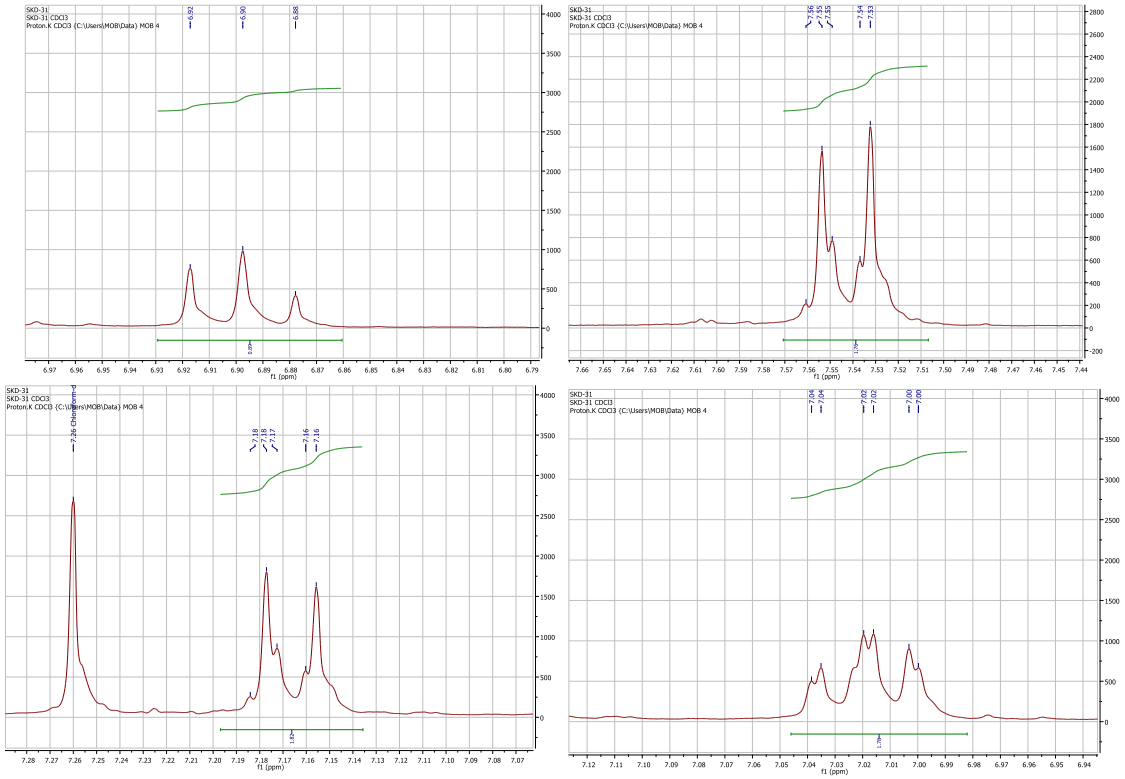


Figure 323: 1H NMR spectrum expansions for compound 8

Table 56: 13C NMR assignments for compound 8

δ (ppm)	Integration	Assignment
163.19	1	7
151.50	1	6
148.66	1	12
147.42	1	10
132.67	2	3/2
124.02	1	11
122.98	1	8
120.63	2	4/5
119.11	1	1
118.89	1	13
115.21	1	9
56.38	3	14

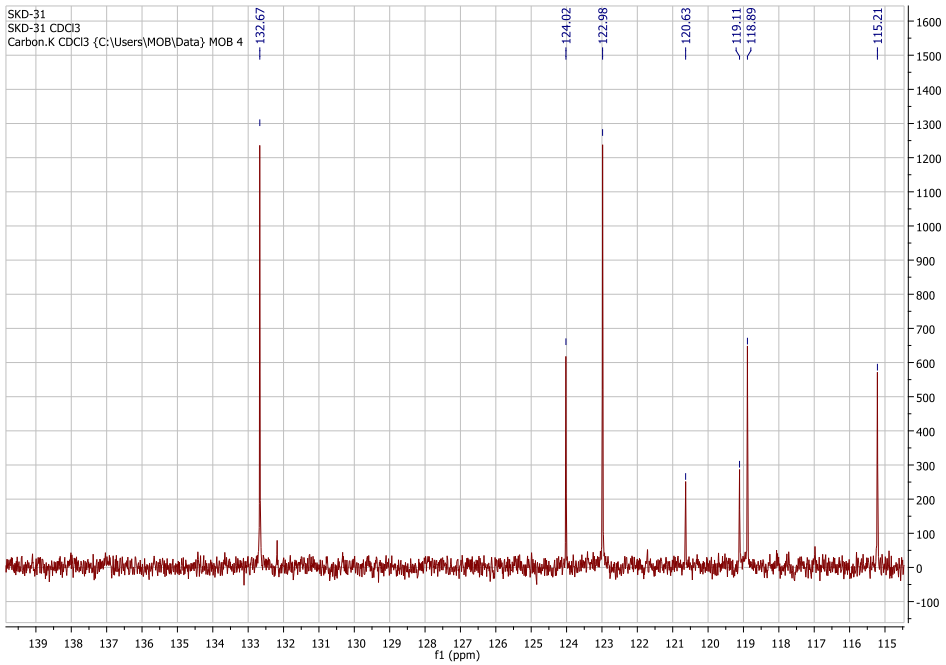


Figure 324: 13C NMR spectrum expansion for compound 8

Table 57: Tabulated UV-VIs absorption λmax of compound 8

abs	**Wavelength (nm)**
0.72	318.00

SCXRD

Data was collected on the SCXRD at ISIS, Harwell at 120, 250 and 293 K using a molybdenum source. The resulting data was integrated automatically in the CrysAlisPro software embedded with the Olex programme. The outputted .ins and .hkl files were then inputted into the CRYSTALS SCXRD analysis software where the structure was determined using the SIR92 programme.

SKD31 is a thermochromic material with an orthorhombic P $2_12_12_1$ space group, the colour change from red through orange to yellow, as the temperature is decreased from 293 K through 250 K to 120 K. The internal dihedral angle of the molecule shifts from 12.99° at 293 K to 10.84° at 120 K.

At 120 K the keto/enol hydrogen can be found 100 % in the enol position on the oxygen whereas at 293 and 250 K the hydrogen can be found in the keto position on the nitrogen.

Table 58: Tabulated X-ray crystallographic data for compound 8

Crystal system	Orthorhombic		
Space group	P $2_12_12_1$		
Z	4		
Crystal size (mm)			
Radiation type	X-ray Molybdenum		
Wavelength (nm)	0.71073		
Temperature (K)	100	200	293
Cell parameters (Å)	a= 4.82710(2) b=12.5385(1) c= 20.3602(3) α/β/γ=90	a= 4.89378(2) b=12.5347(3) c= 20.5255(2) α/β/γ=90	a= 4.923130(2) b=12.53403(2) c= 20.58242(3) α/β/γ=90
Cell volume (Å^3)	1232.29(2)	1259.08(5)	1270.072(1)
Total no. of reflections	42549	43684	44051
No of reflection with I/σ(I) > 2	1863	1692	2758
R(sigma)	0.1020	0.1586	0.1441
Parameters/Restraints	212/80	1	212/80
R1, wR2, Goof	0.0686, 0.1357, 1.1342	0.1636, 0.2845, 1.0762	0.1682, 0.07021.1857
R1 after Fourier merging / No of unique reflections	0.0686,1863	0.1636, 1746	0.1658 , 3212
Max resolution (Å)			
Scan type			
Theta max	29.455	29.327	29.364
hkl limits	H min = -6 H max = 6 K min = -16 K max = 16 L min = -26 L max = 26	H min = -6 H max = 6 K min = -16 K max = 16 L min = -26 L max = 26	H min = -6 H max = 6 K min = -16 K max = 16 L min = -26 L max = 27

Compound 9

Table 59: Tabulated masses and moles for compound 9 synthesis

Compound	Mr (g/mol^{-1})	Mass (g)	Volume (mL)	mol	mmol	equiv
4-Iodoaniline	219.02	1.4383	-	0.006567	6.57	1
2-hydroxy-3-methoxybenzaldehyde	152.15	1.0408	-	0.006841	6.84	1
ethanol	-	-	40	-	-	-
Product	353.17	2.1768	-	0.006164	6.16	-
-	-	-	-	yield	93.86	-

Preliminary Characterisation

NMR

Table 60: 1H NMR assignments for compound 9

δ (ppm)	Multiplicity	Integration	J coupling (Hz)	Assignment
13.36	s	1H		H_h
8.61	s	1H		H_c
7.74	d	2H	8.0	H_d/H_f
7.07-6.98	m	4H		H_a/H_b
6.90	t	1H	7.6	H_e
3.94	s	3H		Hg

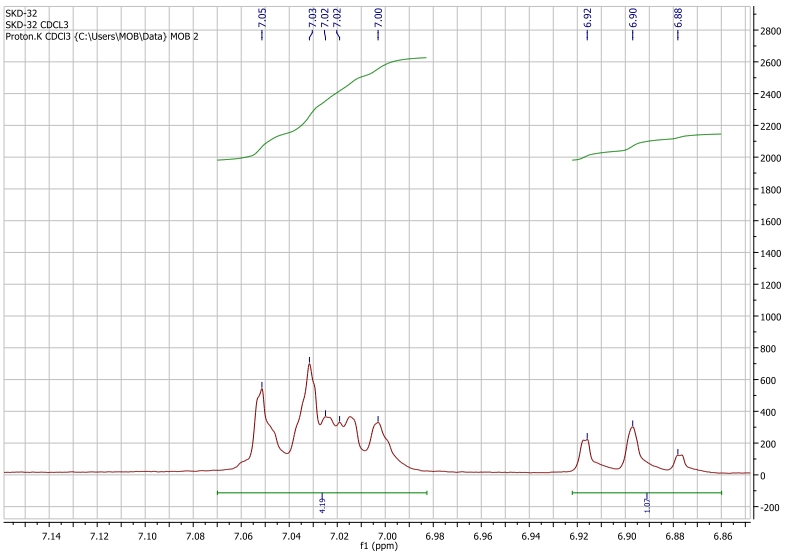


Figure 325: 1H NMR spectrum expansion for compound 9

Table 61:13C NMR assignments for compound 9

δ (ppm)	Integration	Assignment
163.02	1	7
151.34	1	10
148.46	2	6/12
138.46	3	2/3/11
123.83	1	1
123.11	3	5/4/9
118.65	1	8
115.04	1	13
77.28	Solvent	
77.16		
76.96		
76.64		
56.18	1	14

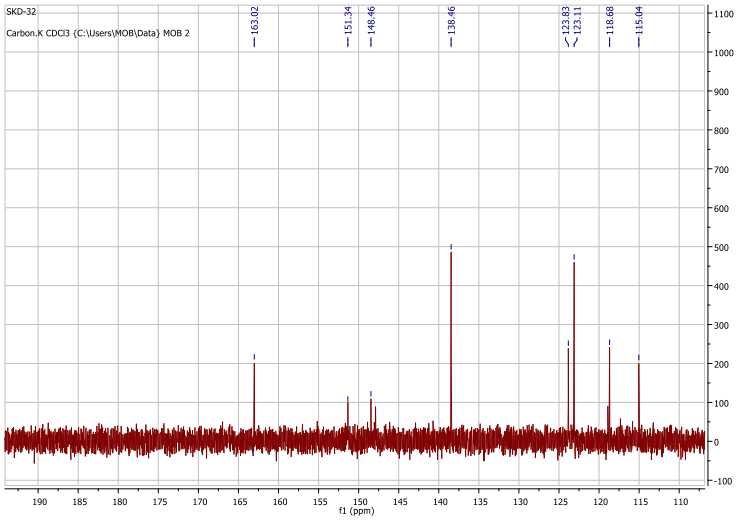


Figure 326: 13C NMR expansion for compound 9

Table 62: Tabulated UV-VIs absorption λmax of compound 9

abs	Wavelength (nm)
1.45	321.00

SCXRD

Data was collected on the SCXRD at ISIS, Harwell at 100, 200 and 295 K using a molybdenum source. The resulting data was integrated automatically in the CrysAlisPro software embedded with the Olex programme. The outputted .ins and .hkl files were then inputted into the CRYSTALS SCXRD analysis software where the structure was determined using the SIR92 programme.

SKD32 is a thermochromic material with a triclinic P $\bar{1}$ space group when grown form ethyl acetate, the colour change from red through orange to yellow, as the temperature is decreased from 295 K through 200 K to 100 K. There are two individual molecules in the unit cell with internal dihedral angles of the molecules shifting from 19.34° and 6.68° at 295 K to 19.59° and 7.63° at 100 K.

At all temperatures the keto/enol hydrogen was found in the enol position on the oxygen atom on each molecule.

Table 63: Crystallographic X-ray data for triclinic polymorph of compound 9

Crystal system	Triclinic		
Space group	P $\bar{1}$		
Z	5		
Crystal size (mm)	2 x3 x 4		
Radiation type	X-ray Molybdenum		
Wavelength (nm)	0.71073		
Temperature (K)	**100**	**200**	**295**
Cell parameters (Å)	a= 11.0764(1) b=12.2192(2) c= 12.4552(2) α =110.272(3) β=106.399(1) γ=102.950(2)	a= 11.14217(6) b=12.31688(5) c= 12.58817(4) α =110.0950(4) β=107.2902(2) γ=103.2670(1)	a= 11.215130(1) b=12.433929(1) c= 12.747280(21) α =109.966(2) β=108.180(1) γ=103.6255(2)
Cell volume (Å^3)	1416.62(1)	1439.26(2)	1466.23(2)
Total no. of reflections	45610	47297	48471
No of reflection with I/σ(I) > 2	7621	7422	6255
R(sigma)	0.067	0.0572	0.042
Parameters/Restraints	325/0	325/0	333/4
R1, wR2, Goof	0.0663, 0.1675, 0.995	0.0659, 0.1672, 0.9801	0.0938, 0.2295, 0.9964
No of unique reflections	8829	8959	9210
Max resolution (Å)			
Scan type			
Theta max	32.787	32.762	32.898
hkl limits	H min = -16 H max = 16 K min = -18 K max = 17 L min = -18 L max = 18	H min = -16 H max = 16 K min = -18 K max = 17 L min = -19 L max =18	H min = -17 H max = 16 K min = -18 K max = 18 L min = -19 L max = 19

Table 64: Crystallographic X-ray data for orthorhombic polymorph of compound 9

Crystal system	Orthorhombic	
Space group	$P\ 2_1 2_1 2_1$	
Z	4	
Crystal size (mm)	0.5 x 1.2 x 2 mm	
Radiation type	X-ray Molybdenum	
Wavelength (nm)	0.71073	
Temperature (K)	**120**	**220**
Cell parameters (Å)	a= 4.9211(9) b=12.325(2) c= 21.343(4) α /β/γ = 90	a= 4.9511(9) b=12.525(2) c= 21.413(4) α /β/γ = 90
Cell volume ($Å^3$)	1324.(4)	1327.8(4)
Total no. of reflections	20693	20693
No of reflection with I/σ(I) > 2	2860	2860
R(sigma)	0.067	0.0572
Parameters/Restraints	163/0	163/0
R1, wR2, Goof	0.037, 0.084, 0.974	0.047, 0.094, 1.004
No of unique reflections	2864	2866
Scan type	PHI/OMEGA	PHI/OMEGA
Theta max	27.19	27.19
hkl limits	H min = -6 H max = 6 K min = -15 K max = 15 L min = -25 L max =26	H min = -6 H max = 6 K min = -15 K max = 15 L min = -25 L max =26

Compound 10

Table 65: Tabulated masses and moles for compound 10 synthesis

Compound	**Mr (g/mol^{-1})**	**Mass (g)**	**Volume (mL)**	**mol**	**mmol**	**equiv**
3,5-di-*tert*-butylsalicaldehyde	234.33	2.46	-	0.010498	10.50	1
aniline	93.13	1.0217	1	0.01051	10.51	1
ethanol	-	-	50	-	-	-
product	309.46	2.4171	-	0.007811	7.81	1
-	-	-	-	yield	74.40	-

Preliminary Characterisation

NMR

Table 66: 1H NMR assignments for compound 10

δ (ppm)	**Multiplicity**	**Integration**	**J coupling (Hz)**	**Assignment**
13.70	s	1H		H_J
8.64	s	1H		H_d
7.46	d	1H	2.3	H_e
7.41	t	2H	7.7	H_c
7.30-7.24	m	3H		H_a/H_b
7.22	d	1H	2.3	H_g
1.48	s	9H		H_i
1.33	s	9H		H_f

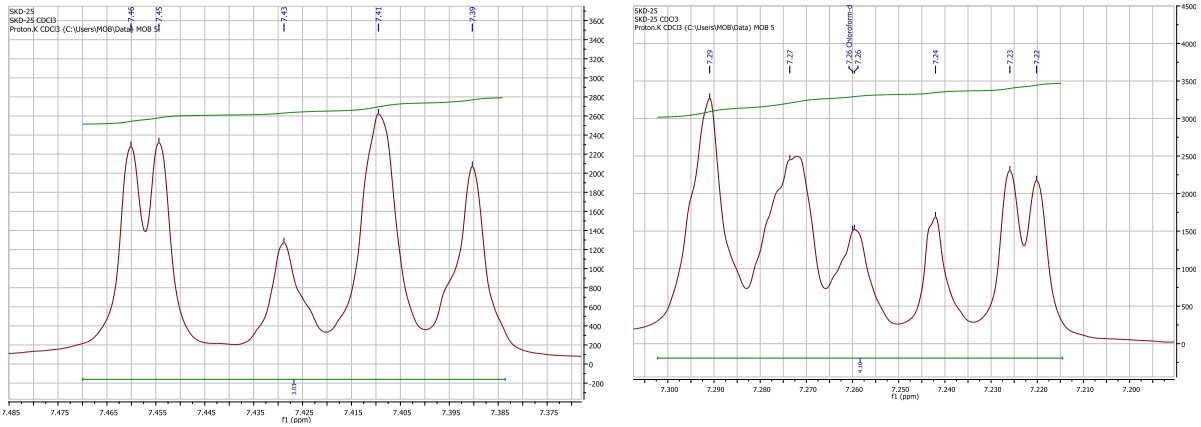


Figure 327:1H NMR expansions for compound 10

Table 67: 13C NMR assignments for compound 10

δ (ppm)	Integration	Assignment
163.65	1	7
158.09	1	10
148.57	1	6
140.39	1	11
136.82	1	12
129.16	2	2/3
127.84	1	9
126.64	1	13
126.35	1	1
121.01	2	4/5
118.13	1	8
34.94	1	14
34.02	1	18
31.31	3	15-17
29.27	3	19-21

Table 68: Tabulated UV-VIs absorption λmax of compound 10

abs	Wavelength (nm)
0.87	353

Raman Peak Assignments

Table 69: Raman peak assignments for compound 10 collected upon warming between 250 K - 300 K

Position (cm^{-1})	**Keto Assignment**	**Enol Assignment**
82.55	Molecular deformation	Molecular deformation
116.57	Molecular deformation	
135.48	Molecular deformation	
156.09	Molecular deformation	
175.49	Molecular deformation	
265.98		*Tert*butyl rotations
280.38	*Tert*butyl rotations	
405.06	Aniline ring OOP deformations CH OOP bends	
451.79	Molecular deformations	Molecular deformation
485.71		*Tert*butyl asymmetric deformation
535.37	*Tert*butyl asymmetric deformation	
558.02	Bridge OOP deformation	
592.58	*Tert*butyl asymmetric deformation/ Bridge OOP deformation	
615.37	Bridge IP deformation/ ring IP rotation	
699.24	Molecular deformation	
726.10	Molecular deformation	Molecular deformation
757.44		Aniline ring CH OOP bend
821.32	Aniline ring asymmetric OOP CH wag	
863.80		Aniline and aldehyde ring IP stretch and OOP bends
872.89	Aldehyde CH OOP wag	
906.44		*Tert*butyl asymmetric bend
911.40		*Tert*butyl asymmetric deformation
927.88		*Tert*butyl asymmetric deformation
996.98	Aniline ring asymmetric OOP CH wag	

1024.51		Aniline ring IP wag
1102.26	Aniline ring asymmetric IP CH wag/ *Tert*butyl asymmetric deformation	
1122.52	Aldehyde CH OOP wag	
1128.39	Aldehyde CH OOP wag	
1152.53	Aldehyde CH OOP wag	
1168.44		Aniline ring IP wag
1193.50		Aniline ring IP wag
1215.20	Aniline ring asymmetric IP CH wag	
1228.21	*Tert*butyl asymmetric deformation	
1246.08	*Tert*butyl asymmetric deformation	
1272.16	NH IP wag/ Bridge CH IP wag	
1287.60	Molecular deformation	
1317.77	*Tert*butyl asymmetric deformation/ *Tert*butyl umbrella bend	
1399.19	*Tert*butyl umbrella bend	
1434.51		*Tert*butyl asymmetric deformation
1441.72		*Tert*butyl symmetric stretch/ *Tert*butyl asymmetric bend
1457.66		*Tert*butyl asymmetric deformation
1485.68	*Tert*butyl asymmetric deformation	
1561.97		OH bend/ bridge CN deformation/ bridge CH OOP wag
1569.28		Aniline/Aldehyde CH IP wag
1574.22	NH OOP wag	
1612.72	NH IP wag/ Ring CH OOP wag	

Table 70: Raman peak assignments for compound 10 at 250 K

Position (cm^{-1})	Keto Assignment	Enol Assignment
77.20	*Tert*butyl asymmetric bend	
118.37	Molecular deformation	
157.43	Molecular deformation	
176.03	Molecular deformation	
203.29	*Tert*butyl rotations	
266.04		*Tert*butyl rotations
282.12	*Tert*butyl rotations	
305.40		
346.39		
405.31		
450.73		
486.16		
502.09	Aniline CH OOP wag/ bridge OOP deformation	
535.71	*Tert*butyl asymmetric deformation	
558.08	Bridge OOP deformation	
592.56	*Tert*butyl asymmetric deformation/ Bridge OOP deformation	
615.41	Bridge IP deformation/ ring IP rotation	
652.45		
682.06		
698.82	Molecular deformation	
726.93	Molecular deformation	Molecular deformation
757.45		Aniline ring CH OOP bend
811.33		
821.77	Aniline ring asymmetric OOP CH wag	
872.91	Aldehyde CH OOP wag	
897.83	Aniline ring asymmetric OOP CH wag	
912.11		*Tert*butyl asymmetric deformation
928.15		*Tert*butyl asymmetric deformation
997.25	Aniline ring asymmetric OOP CH wag	
1024.24		Aniline ring IP wag
1122.53	Aldehyde CH OOP wag	
1128.95	Aldehyde CH OOP wag	
1152.66	Aldehyde CH OOP wag	
1168.98		Aniline ring IP wag
1194.59		Aniline ring IP wag
1215.98	Aniline ring asymmetric IP CH wag	
1228.98	*Tert*butyl asymmetric deformation	

1247.26	*Tert*butyl asymmetric deformation	
1271.76	NH IP wag/ Bridge CH IP wag	
1288.39	Molecular deformation	
1318.60	*Tert*butyl asymmetric deformation/ *Tert*butyl umbrella bend	
1386.06	*Tert*butyl umbrella bend	
1400.72	*Tert*butyl umbrella bend	
1434.51		*Tert*butyl asymmetric deformation
1444.98		*Tert*butyl symmetric stretch/ *Tert*butyl asymmetric bend
1458.27	*Tert*butyl asymmetric deformation	
1486.26		OH bend/ bridge CN deformation/ bridge CH OOP wag
1562.16		Aniline/Aldehyde CH IP wag
1574.72	NH OOP wag	
1613.30	NH IP wag/ Ring CH OOP wag	

Table 71: Raman Peak assignments for compound 10 at 120 K

Position (cm^{-1})	Keto Assignment	Enol Assignment
70.54	*Tert*butyl asymmetric bend	
81.01	Molecular deformation	
123.10	Molecular deformation	
159.35	Molecular deformation	
177.06	Molecular deformation	
204.05	*Tert*butyl rotations	
248.13		
261.29	*Tert*butyl asymmetric bend	
266.05		*Tert*butyl rotations
284.22	*Tert*butyl rotations	
305.45	*Tert*butyl rotations	*Tert*butyl rotations
347.63	*Tert*butyl rotations	*Tert*butyl rotations
405.72	*Tert*butyl rotations	*Tert*butyl rotations
431.56	*Tert*butyl rotations	*Tert*butyl rotations
451.03	*Tert*butyl rotations	*Tert*butyl rotations
486.39	*Tert*butyl rotations	*Tert*butyl rotations
501.41	Aniline CH OOP wag/ bridge OOP deformation	
535.39	*Tert*butyl asymmetric deformation	
557.50	Bridge OOP deformation	
592.56	*Tert*butyl asymmetric deformation/ Bridge OOP deformation	
615.29	Bridge IP deformation/ ring IP rotation	
698.84	Molecular deformation	
727.57	Molecular deformation	Molecular deformation
757.90		Aniline ring CH OOP bend
765.45	Aniline Ring CH OOP bend	
822.18	Aniline ring asymmetric OOP CH wag	
828.71	Aldehyde CH OOP wag	
883.36	Aniline ring asymmetric OOP CH wag	
897.86		*Tert*butyl asymmetric deformation
913.10		*Tert*butyl asymmetric deformation
928.35	Aniline ring asymmetric OOP CH wag	
997.43		Aniline ring IP wag
1024.50		
1110.34	Molecular deformation	
1122.48	Aldehyde CH OOP wag	
1129.04	Aldehyde CH OOP wag	
1152.55	Aldehyde CH OOP wag	
1169.52		Aniline ring IP wag
1195.77		Aniline ring IP wag

1217.40	Aniline ring asymmetric IP CH wag	
1230.06	*Tert*butyl asymmetric deformation	
1248.47	*Tert*butyl asymmetric deformation	
1271.79	NH IP wag/ Bridge CH IP wag	
1289.32	Molecular deformation	
1319.51	*Tert*butyl asymmetric deformation/ *Tert*butyl umbrella bend	
1385.52	*Tert*butyl umbrella bend	
1402.37	*Tert*butyl umbrella bend	
1434.31		*Tert*butyl asymmetric deformation
1442.21	Aldehyde CH OOP wag	
1445.44		*Tert*butyl symmetric stretch/ *Tert*butyl asymmetric bend
1458.86	*Tert*butyl asymmetric deformation	
1487.09		OH bend/ bridge CN deformation/ bridge CH OOP wag
1500.03	Aniline ring CH IP wag. *Tert*butyl deformation	
1561.91		Aniline/Aldehyde CH IP wag
1575.23	NH OOP wag	
1613.84	NH IP wag/ Ring CH OOP wag	

Table 72: Raman Peak assignments for compound 10 at 90 K

Position (cm^{-1})	Keto Assignment	Enol Assignment
71.90	*Tert*butyl asymmetric bend	
82.55	Molecular deformation	
124.59	Molecular deformation	
159.77	Molecular deformation	
177.50	Molecular deformation	
204.16	*Tert*butyl rotations	
248.35		*Tert*butyl rotations
261.41	*Tert*butyl asymmetric bend	
266.06		*Tert*butyl rotations
284.48	*Tert*butyl rotations	
329.74		Molecular deformation
340.11		*Tert*butyl Rock
348.37		*Tert*butyl rotations
393.02		*Tert*butyl rotations
405.83		*Tert*butyl umbrella bend
431.50		Aniline ring CH OOP asymmetric bend
450.43		Ring OOP deformations
486.51		*Tert*butyl asymmetric rock
500.94	Aniline CH OOP wag/ bridge OOP deformation	
535.56	*Tert*butyl asymmetric deformation	
557.51	Bridge OOP deformation	
592.60	*Tert*butyl asymmetric deformation/ Bridge OOP deformation	
615.28	Bridge IP deformation/ ring IP rotation	
639.80	Aniline ring deformation	
655.85		Aldehyde CH OOP wag
682.06		Aldehyde CH OOP wag
698.84	Molecular deformation	
758.19		Aniline ring CH OOP bend
822.35	Aniline ring asymmetric OOP CH wag	
828.93	Aldehyde CH OOP wag	
872.75		Aldehyde CH OOP wag
884.57	Aniline ring asymmetric OOP CH wag	
913.39		*Tert*butyl asymmetric deformation
971.06		Molecular deformation
981.85		Aniline ring OOP Asymmetric wag
997.55		Aniline ring IP wag
1023.98		Aniline ring IP wag
1086.59	Molecular deformation	
1110.35	Aldehyde CH OOP wag	
1122.48	Aldehyde CH OOP wag	

1129.68	Aldehyde CH OOP wag	
1152.67		Aniline ring IP wag
1169.71		Aniline ring IP wag
1196.00		Aniline ring IP wag
1217.67	Aniline ring asymmetric IP CH wag	
1230.98	*Tert*butyl asymmetric deformation	
1248.85	*Tert*butyl asymmetric deformation	
1272.03	NH IP wag/ Bridge CH IP wag	
1290.18	Molecular deformation	
1319.73	*Tert*butyl asymmetric deformation/ *Tert*butyl umbrella bend	
1385.39	*Tert*butyl umbrella bend	
1402.76	*Tert*butyl umbrella bend	
1434.31		*Tert*butyl asymmetric deformation
1445.52		*Tert*butyl symmetric stretch/ *Tert*butyl asymmetric bend
1458.98	*Tert*butyl asymmetric deformation	
1487.27		OH bend/ bridge CN deformation/ bridge CH OOP wag
1500.35	Aniline ring CH IP wag. *Tert*butyl deformation	
1561.91		Aniline/Aldehyde CH IP wag
1569.04		Aniline ring IP wag
1575.33	NH OOP wag	
1585.32	Aniline ring IP CH wag/ NH IP wag	
1589.49	Aniline ring IP CH wag/ NH IP wag	
1613.97	NH IP wag/ Ring CH OOP wag	

Table 73: Raman Peak assignments for compound 10 at 60 K

Position (cm^{-1})	Keto Assignment	Enol Assignment
72.08	*Tert*butyl asymmetric bend	
124.70	Molecular deformation	
159.91	Molecular deformation	
177.45	Molecular deformation	
204.27	*Tert*butyl rotations	
248.38		*Tert*butyl rotations
261.44	*Tert*butyl asymmetric bend	
284.52	*Tert*butyl rotations	
305.50		*Tert*butyl rotations
336.77		*Tert*butyl Rock
348.11		*Tert*butyl rotations
405.94		*Tert*butyl rotations
450.52		*Tert*butyl umbrella bend
486.49		*Tert*butyl asymmetric rock
535.60	*Tert*butyl asymmetric deformation	
547.05		Molecular deformation
557.46	Bridge OOP deformation	
592.65	*Tert*butyl asymmetric deformation/ Bridge OOP deformation	
615.27	Bridge IP deformation/ ring IP rotation	
698.86	Molecular deformation	
758.13		Aniline ring CH OOP bend
822.37	Aniline ring asymmetric OOP CH wag	
872.89		Aldehyde CH OOP wag
884.86	Aldehyde ring CH OOP wag	
913.37		*Tert*butyl asymmetric deformation
928.42	Aniline ring asymmetric OOP CH wag	
971.62		Molecular deformation
981.92		Aniline ring OOP Asymmetric wag
997.57		Aniline ring IP wag
1023.76	Aldehyde CH OOP wag	
1090.13		Aniline ring IP wag
1110.32	Molecular deformation	
1122.48	Aldehyde CH OOP wag	
1129.72	Aldehyde CH OOP wag	
1152.71	Aldehyde CH OOP wag	
1169.75		Aniline ring IP wag
1196.05		Aniline ring IP wag
1217.71	Aniline ring asymmetric IP CH wag	
1231.23	*Tert*butyl asymmetric deformation	

1248.95	*Tert*butyl asymmetric deformation	
1271.92	NH IP wag/ Bridge CH IP wag	
1289.81	Molecular deformation	
1319.78	*Tert*butyl asymmetric deformation/ *Tert*butyl umbrella bend	
1385.33	*Tert*butyl umbrella bend	
1402.75	*Tert*butyl umbrella bend	
1434.32		*Tert*butyl asymmetric deformation
1445.56		*Tert*butyl symmetric stretch/ *Tert*butyl asymmetric bend
1459.00	*Tert*butyl asymmetric deformation	
1487.29		OH bend/ bridge CN deformation/ bridge CH OOP wag
1500.44	Aniline ring CH IP wag. *Tert*butyl deformation	
1561.91		Aniline/Aldehyde CH IP wag
1575.37	NH OOP wag	
1589.59	Aniline ring CH IP wag. NH OOP wag	
1614.01	NH IP wag/ Ring CH OOP wag	

INS peak assignments

Table 74: INS peak assignments for compound 10 at 10 K

Position (cm^{-1})	**Keto Assignment**	**Enol Assignment**
54.87		Molecular deformations
64.66	Molecular deformations	
80.48	Molecular deformations	
98.33	Molecular deformations	
118.41		Molecular deformations
128.40	Molecular deformations	
141.66		Molecular deformations
166.40		Molecular deformations
179.46		Molecular deformations
214.55		Molecular deformations
235.22	Molecular deformations	
248.49		*Tert*butyl rotations
268.97		*Tert*butyl rotations
290.16		*Tert*butyl rotations
311.04	*Tert*butyl rotations	
335.75		*Tert*butyl Rock
348.16		*Tert*butyl rotations
362.04		*Tert*butyl asymmetric Rock
380.00		*Tert*butyl asymmetric Rock
409.64		*Tert*butyl rotations
454.87		*Tert*butyl umbrella bend
504.60		Molecular deformations
536.80		Molecular deformations
560.31	Molecular deformations	
587.06		Molecular deformations
606.24		Molecular deformations
617.06	Molecular deformations	
643.77		Aniline CH OOP wag, Bridge CH OOP wag

688.33	Aniline CH OOP wag, Bridge CH OOP wag	
729.27		Aniline ring CH OOP bend
761.56		Aniline ring CH OOP bend
801.26		*Tert*butyl umbrella bend
830.14		Aldehyde CH OOP wag
886.48		Aldehyde CH OOP wag
926.79	Aldehyde CH OOP wag	
945.45	*Tert*butyl asymmetric bend	
974.34		Molecular deformation
1030.19	Aldehyde CH OOP wag	
1075.61		Aniline ring IP wag
1134.05	Aldehyde CH OOP wag	Aniline ring IP wag
1169.29		Aniline ring IP wag
1204.69		Aniline ring IP wag
1238.21	*Tert*butyl asymmetric bend	
1282.93	Molecular deformation	
1362.26	Aldehyde CH OOP bend/ Bridge CH OOP bend/ Aniline CH IP wag	
1393.31	*Tert*butyl symmetric umbrella bend	
1455.68		*Tert*butyl symmetric stretch/ *Tert*butyl asymmetric bend
1586.16	NH IP wag/ Aniline CH IP wag	
2491.74		OH stretch
2969.70	*Tert*butyl CH stretch	
3069.62		*Tert*butyl CH stretch

SCXRD

Data was collected on the SCXRD at ISIS, Harwell at 120 and 290 K using a molybdenum source. The resulting data was integrated automatically in the CrysAlisPro software embedded with the Olex programme. The outputted .ins and .hkl files were then inputted into the CRYSTALS SCXRD analysis software where the structure was determined using the SIR92 programme.

SKD25 is a thermochromic material with an orthorhombic $Pna2_1$ space group. A pale yellow crystal to start goes near colourless as the temperature is decreased for room temperature to 120 K

Table 75: Tabulated X-ray crystallographic data for compound 10

Crystal system	Orthorhombic	
Space group	$Pna2_1$	
Z	4	
Crystal size (mm)	2 x 2.5 x 4 mm	
Radiation type	X-ray Molybdenum	
Wavelength (nm)	0.71073	
Temperature (K)	**120**	**290**
Cell parameters (Å)	a= 12.31830(1) b=8.88190(2) c= 16.52460(2) α/β/γ=90	a= 12.3861(2) b=8.9797(1) c= 16.6457(2) α/β/γ=90
Cell volume (Å^3)	1807.955(3)	1851.0(2)
Total no. of reflections	10698	13994
No of reflection with I/σ(I) > 2	2312	2044
R(sigma)	0.678	0.0653
Parameters/Restraints	316/1	2/0
R1, wR2, Goof	0.0413, 0.0966, 0.9469	0.0552, 0.1268, 0.9217
No of unique reflections	4239	5642
Max resolution (Å)		
Scan type		
Theta max	30.757	32.715
hkl limits	H min = -17 H max = 12 K min = -12 K max = 10 L min = -20 L max = 23	H min = -17 H max = 18 K min = -12 K max = 12 L min = -23 L max = 24

Neutron diffraction

A suitable crystal of N-(3,5-di-tert-butylsalicylidene)-aniline for neutron diffraction, measuring approximately 4 x 3 x 2 mm, was grown via slow evaporation of ethanol from a concentrated solution. Diffraction data were collected using the single-crystal diffractometer SXD at the ISIS spallation neutron source (Oxfordshire, UK; Keen *et al.*, 2006) at 280 K. Time-of-flight Laue diffraction data were collected in a series of five orientations, with a counting time per orientation of ~5 h. The diffraction spots were initially indexed with the unit cells available from the x-ray measurements at the corresponding temperature and then from the closest Neutron cell. Bragg intensities were extracted using the 3D-profile fitting method implemented in the SXD2001 software (Gutmann, 2017) and corrected for Lorenz effect. No absorption correction for the shape of the crystal was applied.

Refinement details

Final cell parameters at each temperature were refined against the fitted positions of the Bragg peaks after 3D profile integration. The starting models for structural refinement were based on the atomic coordinates of the non-hydrogen atoms from the X-ray structure at room temperature, while all hydrogen atoms were located from neutron Fourier difference maps.

All structures were refined by full matrix least squares on F^2 using SHELXL (Sheldrick, 2008).

Table 76: Tabulated Neutron crystallographic data for compound 10

Crystal system	Orthorhombic	
Space group	$Pna2_1$	
Z	4	
Crystal size (mm)	4 x 3 x 2 mm	
Radiation type	Neutron	
Wavelength (nm)	0.35 – 6.5 Å	
Temperature (K)	**250**	**50**
Cell parameters (Å)	a: 12.318(3) b:8.8852(3) c: 16.525(3) alpha/gamma/beta: 90	-
Cell volume ($Å^3$)	1807.95(1)	-
Total no. of reflections	4053	-
No of reflection with I/σ(I) > 4	3688	-
R(sigma)	0.0462	-
Parameters/Restraints	323/1	-
R1, wR2, Goof	0.1135,0.2912,1.480	-
R1 after Fourier merging / No of unique reflections	0.0621/1693	-
Max resolution (Å)	0.89	-
Nuclear density Fourier difference residuals: $\Delta\rho_{max}$, $\Delta\rho_{min}$	0.88, -0.96	-

Compound 11

Table 77: Tabulated masses and moles for synthesis of compound 11

Compound	Mr (g/mol^{-1})	Mass (g)	Volume (mL)	mol	mmol	equiv
4-Iodoaniline	219.02	0.9495	-	0.004335	4.34	1
3,5-di-tert-butylsalicaldehyde	234.33	1.0701	-	0.004567	4.57	1
ethanol	-	-	40	-	-	-
Product	435.35	1.4619	-	0.003357	3.36	-
-	-	-	-	yield	77.46	-

Preliminary Characterisation

NMR

Table 78: 1H NMR assignments for compound 11

δ (ppm)	Multiplicity	Integration	J coupling (Hz)	Assignment
13.46	s	1H		H_h
8.61	s	1H		H_c
7.73	d	2H	8.6	H_a
7.47	d	1H	2.3	H_d
7.22	d	1H	2.3	H_f
7.04	d	2H	8.6	H_b
1.48	s	9H		H_e
1.33	s	9H		H_g

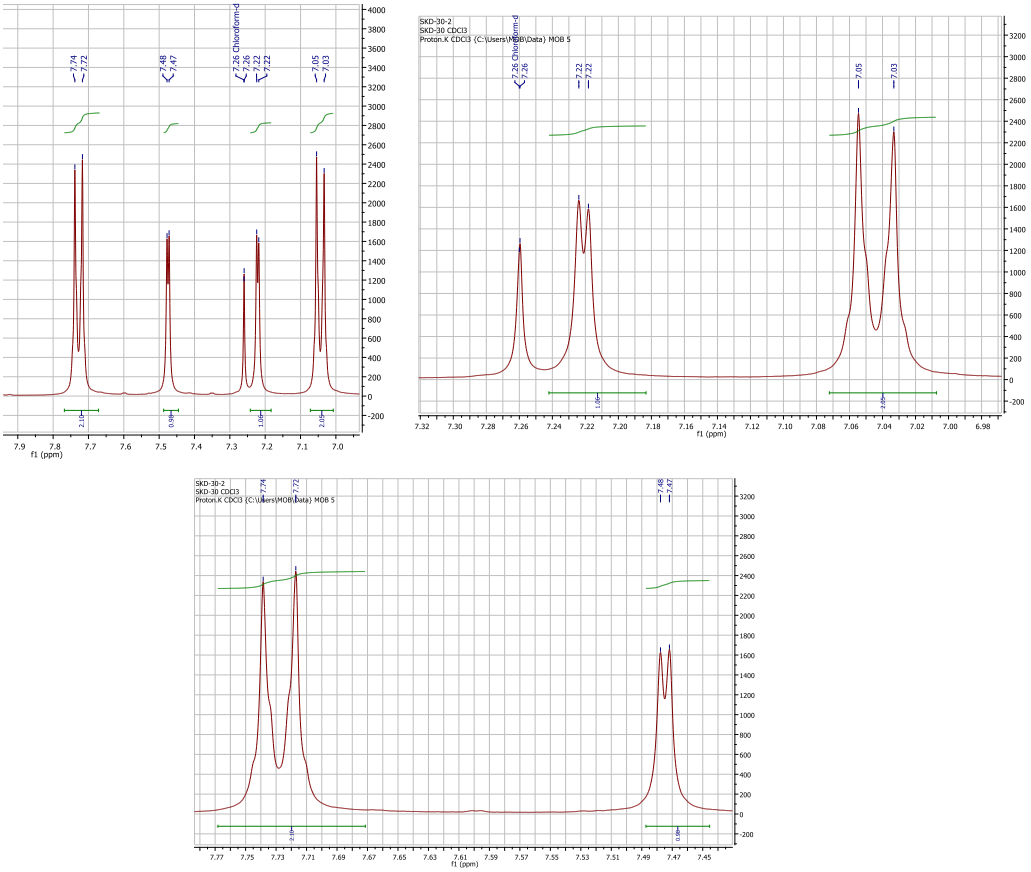


Figure 328: 1H NMR spectrum expansions for compound 11

Table 79: 13C NMR assignments for compound 11

δ (ppm)	Integration	Assignment
164.32	1	7
158.43	1	10
148.55	1	6
140.91	1	11
138.55	1	12
137.24	2	2/3
128.57	1	9
127.09	1	13
123.32	2	4/5
118.29	1	8
91.17	1	1
35.25	1	14
34.34	1	18
31.60	3	15/16/17
29.56	3	19/20/21

Table 80: Tabulated UV-VIs absorption λmax of compound 11

abs	Wavelength (nm)	abs	Wavelength (nm)
1.17	315	0.88	359

Raman Spectroscopy

Table 81: Raman spectroscopy peak assignments for compound 11 at 11 K

Position (cm^{-1})	**Keto Assignment**	**Enol Assignment**
88.64	molecular deformation	
118.69	aldehyde deformation	
162.66		*tert*butyl rotation
198.18	*tert*butyl rotation	
220.32		molecular deformation
247.86		*tert*butyl rotation
266.26	*tert*butyl rotation	
280.50	*tert*butyl rotation	
303.28		*tert*butyl rotation
322.44	aldehyde deformation	*tert*butyl asym bend
336.39	*tert*butyl rotation	
343.68		*tert*butyl asym bend
368.90		*tert*butyl rotation
389.93	*tert*butyl wag	
412.52		*tert*butyl asym wag
443.46		*tert*butyl asym wag/OH bend
472.34	*tert*butyl /aldehyde deformation	
506.13		*tert*butyl asym wag/OH OOP wag
543.46	bridge/aldehyde deformation, C-I	– C-I
577.46	Molecular Deformation	Molecular Deformation
586.63		
611.72	Molecular Deformation	Molecular Deformation
629.36	Molecular Deformation	Molecular Deformation
696.83	aldehyde OOP wag	
717.56	NH OOP wag	
727.43		aniline CH OOP wag/deformation
770.18	NH OOP wag	
798.70	NH OOP wag/ aniline CH OOP wag	

822.85	*tert*butyl umbrella bend/ aniline CH OOP wag	
863.97	Aldehyde C-1-H OOP wag	
881.96	Aldehyde C-1-H OOP wag	Aldehyde C-1-H OOP wag
913.43	Aldehyde C-4-H OOP wag	
929.81	aldehyde deformation/ aniline CH OOP wag	
960.45		bridge CH OOP wag
977.33		aniline CH OOP wag/deformation
1002.56	Aldehyde/*tert*butyl deformation	Aldehyde/*tert*butyl deformation
1028.46		aniline CH OOP wag/deformation
1056.27	*tert*butyl rotation	
1132.03	aniline/aldehyde CH IP wag	
1168.02	aniline/aldehyde CH IP wag	
1199.51	aldehyde deformation/ *tert*butyl rotation	
1219.92	aldehyde IP CH wag/ *tert*butyl asym bend	
1250.64		*tert*butyl asym bend
1275.05	aldehyde IP CH wag/ *tert*butyl asym bend/ NH IP wag	
1312.10		aniline CH IP wag/deformation
1361.99	aniline IP CH wag/ NH IP wag	
1385.43	aniline IP CH wag/ NH IP wag	
1440.14	aldehyde C-1-H IP wag/ *tert*butyl asym bend	
1453.45		*tert*butyl asym bend
1466.29	aldehyde C-1-H IP wag, *tert*butyl asym bend, NH IP wag	*tert*butyl asym wag
1480.97	*tert*butyl asym bend, NH IP wag	*tert*butyl asym wag
1530.80	*tert*butyl asym bend, NH IP wag	
1575.95		aniline CH IP wag/deformation
1591.74	aldehyde C-1-H IP wag	aniline CH IP wag/deformation
1620.13	aldehyde C-1-H IP wag	bridge CH IP wag

Table 82: Raman Spectroscopy peak assignments for compound 11 at 250 K

Position (cm^{-1})	**Keto Assignment**	**Enol Assignment**
83.51	molecular deformation	
113.07	aldehyde deformation	
158.53		*tert*butyl rotation
197.52	*tert*butyl rotation	
219.45		molecular deformation
264.61	*tert*butyl rotation	
297.90	*tert*butyl rotation	
322.40	aldehyde deformation	*tert*butyl asym bend
334.42	*tert*butyl rotation	
368.76		*tert*butyl rotation
408.74		*tert*butyl asym wag
442.73		*tert*butyl asym wag/OH bend
471.68	*tert*butyl /aldehyde deformation	
507.22		*tert*butyl asym wag/OH OOP wag
543.91	bridge/aldehyde deformation, C-I	C-I
577.62	Molecular Deformation	Molecular Deformation
585.66		Molecular Deformation
611.11	Molecular Deformation	Molecular Deformation
629.52	Molecular Deformation	Molecular Deformation
716.76	NH OOP wag	
726.93		aniline CH OOP wag/deformation
769.90	NH OOP wag	
797.96	NH OOP wag/ aniline CH OOP wag	
822.90	*tert*butyl umbrella bend/ aniline CH OOP wag	
863.44	Aldehyde C-1-H OOP wag	
880.25	Aldehyde C-1-H OOP wag	Aldehyde C-1-H OOP wag
912.18	Aldehyde C-4-H OOP wag	
930.25	aldehyde deformation/ aniline CH OOP wag	

960.04		bridge CH OOP wag
977.97		aniline CH OOP wag/deformation
1001.93	Aldehyde/*tert*butyl deformation	Aldehyde/*tert*butyl deformation
1032.73		aniline CH OOP wag/deformation
1055.35	*tert*butyl rotation	
1131.35	aniline/aldehyde CH IP wag	
1167.20	aniline/aldehyde CH IP wag	
1197.81	aldehyde deformation/ *tert*butyl rotation	
1218.71	aldehyde IP CH wag/ *tert*butyl asym bend	
1249.09		*tert*butyl asym bend
1272.70	aldehyde IP CH wag/ *tert*butyl asym bend/ NH IP wag	
1312.68		aniline CH IP wag/deformation
1361.20	aniline IP CH wag/ NH IP wag	
1386.11	aniline IP CH wag/ NH IP wag	
1439.19	aldehyde C-1-H IP wag/ *tert*butyl asym bend	
1452.98		*tert*butyl asym bend
1465.38	aldehyde C-1-H IP wag/ *tert*butyl asym bend/NH IP wag	*tert*butyl asym wag
1479.92	*tert*butyl asym bend/NH IP wag	*tert*butyl asym wag
1574.62		aniline CH IP wag/deformation
1590.48	aldehyde C-1-H IP wag	aniline CH IP wag/ deformation
1618.88	aldehyde C-1-H IP wag	bridge CH IP wag,

Table 83: Raman Spectroscopy peak assignments for compound 11 at 298 K

Position (cm^{-1})	**Keto Assignment**	**Enol Assignment**
81.48	molecular deformation	
111.36	aldehyde deformation	
157.15		*tert*butyl rotation
197.28	*tert*butyl rotation	
219.08		molecular deformation
264.62	*tert*butyl rotation	
296.41	*tert*butyl rotation	
322.70	aldehyde deformation	*tert*butyl asym bend
333.93	*tert*butyl rotation	
368.67		*tert*butyl rotation
407.65		*tert*butyl asym wag
442.91		*tert*butyl asym wag/OH bend
471.45	*tert*butyl /aldehyde deformation	
508.12		*tert*butyl asym wag/OH OOP wag
544.09	bridge/aldehyde deformation, C-I	C-I
577.49	Molecular Deformation	
585.50		Molecular Deformation
610.53	Molecular Deformation	Molecular Deformation
629.59	Molecular Deformation	Molecular Deformation
716.57	NH OOP wag	
726.30		aniline CH OOP wag/deformation
769.10	NH OOP wag	
798.15	NH OOP wag/ aniline CH OOP wag	
815.44	NH OOP wag/ aniline CH OOP wag	
822.58	*tert*butyl umbrella bend/ aniline CH OOP wag	
863.35	Aldehyde C-1-H OOP wag	
911.69	Aldehyde C-4-H OOP wag	
930.12	aldehyde deformation/ aniline CH OOP wag	

959.49		bridge CH OOP wag
978.11		aniline CH OOP wag/deformation
1001.64	Aldehyde/*tert*butyl deformation	Aldehyde/*tert*butyl deformation
1024.90		aniline CH OOP wag/deformation
1055.02	*tert*butyl rotation	
1130.98	aniline/aldehyde CH IP wag	
1166.76	aniline/aldehyde CH IP wag	
1196.83	aldehyde deformation/ *tert*butyl rotation	
1217.95	aldehyde IP CH wag/ *tert*butyl asym bend	
1248.35		*tert*butyl asym bend
1271.80	aldehyde IP CH wag/ *tert*butyl asym bend/ NH IP wag	
1312.04		aniline CH IP wag/deformation
1359.99	aniline IP CH wag/ NH IP wag	
1386.68	aniline IP CH wag/ NH IP wag	
1438.80	aldehyde C-1-H IP wag/ *tert*butyl asym bend	
1464.99	aldehyde C-1-H IP wag/ *tert*butyl asym bend/NH IP wag	*tert*butyl asym wag
1479.35	*tert*butyl asym bend/NH IP wag	*tert*butyl asym wag
1573.75		aniline CH IP wag/deformation
1589.68	aldehyde C-1-H IP wag	aniline CH IP wag/deformation,
1618.28	aldehyde C-1-H IP wag	bridge CH IP wag

SCXRD

Table 84: Crystallographic X-ray data of compound 11 with copper under in situ irradiation

Crystal system	Monoclinic		
Space group	P 2_1/c		
Z	4		
Crystal size (mm)	1 x 2 x 3 mm		
Radiation type	X-ray Copper		
Wavelength (nm)	1.54184		
Irradiation time (h/m)	**Pre-irradiation**	**3**	**11/30**
Cell parameters (Å)	a= 9.16748(2) b=12.50849(6) c= 18.10531(1) α =90 β=103.199(2) γ=90	a= 9.1720(2) b=12.5486(4) c= 18.1262(2) α =90 β=103.248(2) γ=90	a= 9.1734(1) b=12.5511(1) c= 18.1314(1) α =90 β=103.222(1) γ=90
Cell volume (Å^3)	2021.32(3)	2030.73(2)	2032.25(3)
Total no. of reflections	20512	20575	20595
No of reflection with I/σ(I) > 2	3767	3618	3643
R(sigma)	0.0783	0.0816	0.0853
Parameters/Restraints	245/0	245/0	227/0
R1, wR2, Goof	0.0938, 0.2234, 1.0577	0.1000, 0.2481, 1.2292	0.0949, 0.2391, 1.0649
R1 after Fourier merging / No of unique reflections	0.19/ 4407	0.2010/ 4423	0.2100/ 4426
Max resolution (Å)			
Scan type			
Theta max	81.219	81.720	82.391
hkl limits	H min = -11 H max = 11 K min = -14 K max = 15 L min = -22 L max = 23	H min = -10 H max = 11 K min = -14 K max = 16 L min = -23 L max = 23	H min = -11 H max = 11 K min = -14 K max = 16 L min = -22 L max = 23

Table 85: Crystallographic X-ray data for compound 11 with molybdenum

Crystal system	Monoclinic	
Space group	P 2_1/c	
Z	4	
Crystal size (mm)	1 x 2 x 3 mm	
Radiation type	X-ray Molybdenum	
Wavelength (nm)	0.71073	
Temperature (K)	**120**	**290**
Cell parameters (Å)	a= 9.1797(2) b=12.2727(2) c= 18.0841(3) α =90 β=103.000(1) γ=90	a= 9.17630(1) b=12.54680(1) c= 18.13920 (2) α =90 β=103.318(2) γ=90
Cell volume (Å^3)	1985.13	2032.26(1)
Total no. of reflections	25382	25882
No of reflection with I/σ(I) > 2	4720	3434
R(sigma)	0.0485	0.0431
Parameters/Restraints	245/0	245/0
R1, wR2, Goof	0.0823, 0.1592, 1.0136	0.0871, 0.1893, 0.9856
R1 after Fourier merging / No of unique reflections	0.0520/ 6651	0.0370/ 6789
Max resolution (Å)		
Scan type		
Theta max	32.765	32.570
hkl limits	H min = -13 H max = 13 K min = -17 K max = 18 L min = -25 L max = 27	H min = -13 H max = 13 K min = -18 K max = 18 L min = -26 L max = 27

There is distinct disorder across the C-N linker between the rings including the enol/keto oxygen. The dominant structure is that of the enol isomer, at a ratio of 69:31 at 290 K, then at 66: 34 at 120 K. As the material is photochromic in nature no large change in the enol/keto ratio were expected with regards to the decrease in temperature.

Neutron diffraction

Variable Temperature

A suitable crystal of N-(3,5-di-tert-butylsalicylidene)-4-iodoaniline for neutron diffraction, measuring approximately 4 x 3 x 2 mm, was grown via slow evaporation of ethanol from a concentrated solution. Diffraction data were collected using the single-crystal diffractometer SXD at the ISIS spallation neutron source (Oxfordshire, UK; Keen *et al.*, 2006) at 250 and 110 K. Time-of-flight Laue diffraction data were collected in a series of five orientations at each temperature, with a counting time per orientation of ~3 h 45 for 2 higher angles and 4 h 45 m for 3 lower angles at 110 K. The counting time per orientation at 250 K was 6 h 30 m. The diffraction spots were initially indexed with the unit cells available from the x-ray measurements at the corresponding temperatures where possible, and then from the closest Neutron cell. Bragg intensities were extracted using the 3D-profile fitting method implemented in the SXD2001 software (Gutmann, 2017) and corrected for Lorenz effect. No absorption correction for the shape of the crystal was applied. All structures were refined by full matrix least squares on F^2 using SHELXL (Sheldrick, 2008).

Refinement details

The system was refined anisotropically for the two 6-membered rings and attached hydrogens and iodine atom. The obvious disorder across the bridging carbon nitrogen linker as well as the resulting disorder of the oxygen atom positions were refined isotropically as two sets of possible positions at a ratio of 42.8 to 57.2 % keto to enol respectively. The data showed large rotation movement of the tert-butyl groups which translated into elongated ellipsoids for the terminal carbon atoms from the anisotropic refinement, but no multiple positions were included in the refinement. The hydrogens of the tert-butyl groups were refined isotropically in the riding mode.

Table 86: Crystallographic Neutron data for variable temperature experiment of compound 11

Crystal system	Monoclinic	
Space group	P $2_1/c$	
Z	4	
Crystal size (mm)	4 x 3 x 2 mm	
Radiation type	Neutron	
Wavelength (nm)	0.35 – 6.5 Å	
Temperature (K)	**110**	**250**
Cell parameters (Å)	a: 9.2312(3) b:12.5505(3) c: 18.2716(3) α/γ:90 β: 103.072(5)	a: 9.2312(3) b:12.5505(3) c: 18.2716(3) α/γ:90 β: 103.072(5)
Cell volume (Å^3)	2062.0(1)	2062.0(6)
Total no. of reflections	3637	2568
No of reflection with I/σ(I) > 4	3636	2565
R(sigma)	0.0433	0.0429
Parameters/Restraints	281/9	281/9
R1, wR2, Goof	0.1466, 0.3696, 1.903	0.1588, 0.3809, 2.007
R1 after Fourier merging / No of unique reflections	0.1338/1385	0.1388/958
Max resolution (Å)	0.57	0.42
Nuclear density Fourier difference residuals: $\Delta\rho_{max}$, $\Delta\rho_{min}$	1.47, -2.14	1.24, -1.16
Extinction coeff.		

Irradiated sample

A suitable crystal of, N-(3,5-di-tert-butylsalicylidene)-4-iodoaniline for neutron diffraction, measuring approximately 4 x 3 x 2 mm, was grown via slow evaporation of ethanol from a concentrated solution then irradiated for over 24 hours using 365 nm UV irradiation. Diffraction data were collected using the single-crystal diffractometer SXD at the ISIS spallation neutron source (Oxfordshire, UK; Keen *et al*., 2006) at 270 K. Time-of-flight Laue diffraction data were collected in a series of six orientations at each temperature, with a counting time per orientation of ~ 6 hrs. The diffraction spots were initially indexed with the unit cells available from the x-ray measurements corresponding to the *in situ* irradiated data, and then from the closest Neutron cell. Bragg intensities were extracted using the 3D-profile fitting method implemented in the SXD2001 software (Gutmann, 2017) and corrected for Lorenz effect. No absorption correction for the shape of the crystal was applied. All structures were refined by full matrix least squares on F^2 using SHELXL (Sheldrick, 2008).

Refinement details

The system was refined anisotropically for the two 6-membered rings and attached hydrogens and iodine atom. The obvious disorder across the bridging carbon nitrogen linker as well as the resulting disorder of the oxygen atom positions were refined isotropically as two sets of possible positions at a ratio of 44.8 to 56.2 % keto to enol respectively. The data showed large rotation movement of the tert-butyl groups which translated into elongated ellipsoids for the terminal carbon atoms from the anisotropic refinement, but no multiple positions were included in the refinement. The hydrogens of the tert-butyl groups were refined isotropically in the riding mode.

Table 87: Crystallographic Neutron data for irradiated sample of compound 11

Crystal system	Monoclinic
Space group	P 2_1/c
Z	4
Crystal size (mm)	4 x 3 x 2 mm
Radiation type	Neutron
Wavelength (nm)	0.35 – 6.5 Å
Temperature (K)	**270**
Cell parameters (Å)	a: 9.192(3) b:12.5981(3) c: 18.1966(3) α/γ:90 β: 103.5303(5)
Cell volume (Å^3)	2048.72(3)
Total no. of reflections	2599
No of reflection with I/σ(I) > 4	2564
R(sigma)	0.0200
Parameters/Restraints	257/4
R1, wR2, Goof	0.1446, 0.3647, 3.527
R1 after Fourier merging / No of unique reflections	0.1388/1002
Max resolution (Å)	0.89
Nuclear density Fourier difference residuals: $\Delta\rho_{max}$, $\Delta\rho_{min}$	1.24, -1.16

Compound 12

Table 88: Tabulated masses and moles for synthesis of compound 12

Compound	Mr (g/mol^{-1})	Mass (g)	Volume (mL)	mol	mmol	equiv
4-Bromoaniline	172.02	0.7330	_	0.004261	4.26	1
3,5-di-tert-butylsalicaldehyde	234.33	1.0142	_	0.004328	4.33	1
ethanol	_	_	40	_	_	_
Product	388.35	1.3488	_	0.003473	3.47	
				yield	81.51	

Preliminary Characterisation

Table 89: 1H NMR assignments for compound 12

δ (ppm)	Multiplicity	Integration	J coupling (Hz)	Assignment
13.72	s	1H		H_h
8.99	s	1H		H_c
7.65	m	2H		H_a
7.50	d	1H	2.4	H_g
7.45-7.42	m	1H		H_d
7.41	m	2H		H_b
1.42	s	9H		H_e
1.30	s	9H		H_g

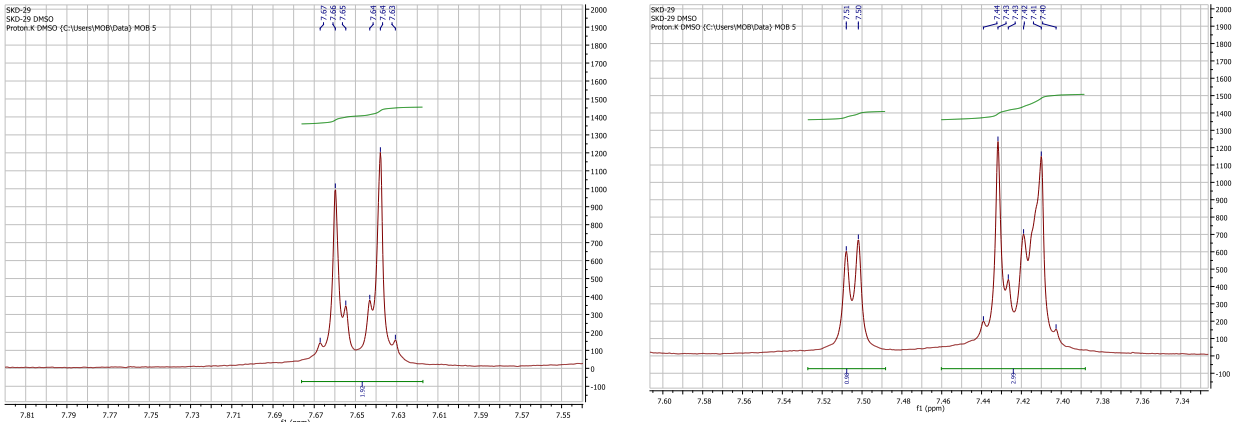


Figure 329: 1H NMR expansions for compound 12

Table 90:13C NMR assignments for compound 12

δ (ppm)	Integration	Assignment
166.27	1	7
157.99	1	10
147.48	1	6
140.75	1	11
136.34	1	12
132.79	2	2/3
128.28	1	9
128.11	1	13
124.06	2	4/5
119.91	1	8
118.67	1	1
35.10	1	14
34.41	1	18
31.72	3	15/16/17
29.72	3	19/20/21

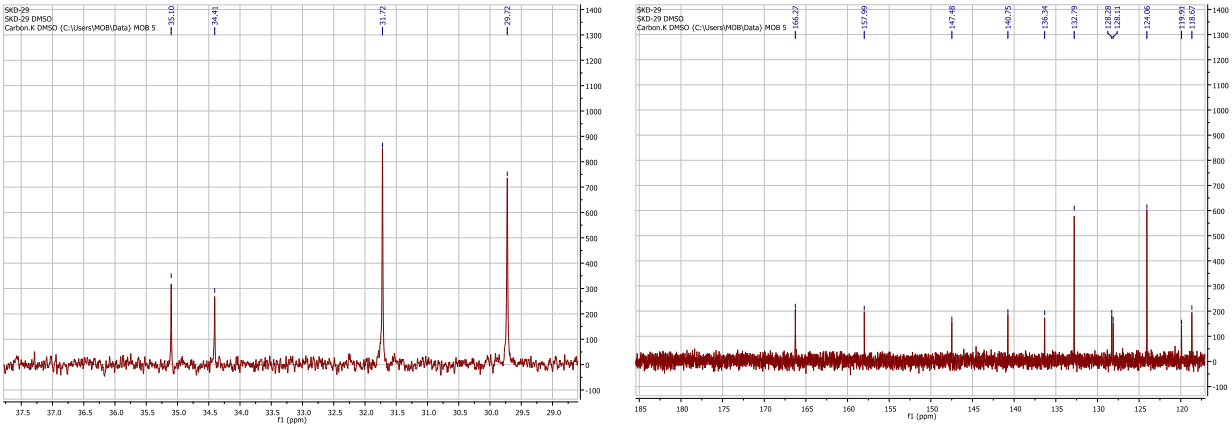


Figure 330: 13C NMR expansions for compound 12

Table 91: Tabulated UV-VIs absorption λmax of compound 12

abs	Wavelength (nm)	abs	Wavelength (nm)
1.21	312	0.90	358

Raman Spectroscopy Peak assignments

Table 92: Raman spectroscopy peak assignments of compound 12 at 11 K

Position (cm^{-1})	**Keto Assignment**	**Enol Assignment**
1618	NH IP wag/ aniline ring deformation	
1597		OH bend, bridge CH IP wag
1576	aniline CH IP wag	aniline CH IP wag
1566	aldehyde ring deformation	
1542	*tert*butyl CH bend	
1524	*tert*butyl asymmetric CH bend	
1483		*tert*butyl asymmetric umbrella bend
1469	*tert*butyl asymmetric CH bend	
1457	*tert*butyl asymmetric CH bend/ Ring OOP CH bend	
1451	CH IP wag	
1443	CH IP wag	
1438	CH IP wag	
1405		aniline CH wag / *tert*butyl umbrella bend
1393	*tert*butyl symmetric umbrella bend	
1386	*tert*butyl symmetric umbrella bend	
1371		aniline CH IP wag
1363		CH OOP wag
1356		CH OOP wag
1321	bridge CH IP wag	aniline ring deformation
1297	CH wag OOP	*tert*butyl CH bend
1288	CH OOP wag	
1270	NH wag/ CH wag	
1250		CH wag
1240		aniline CH IP wag
1219		aniline CH IP wag

1205	NH wag OOP	aniline CH wag
1195	NH wag OOP	aniline CH wag
1172	NH wag IP	
1134	aniline CH OOP bend	aniline CH OOP bend
1105	*tert*butyl asymmetric CH bend	
1068	*tert*butyl asymmetric CH bend	
1031	Aniline CH OOP bend	
1028	Aniline CH OOP bend	
1024		Aldehyde/ *tert*butyl CH wag, OH bend
1007	*tert*butyl rotations	
996	*tert*butyl rotations	
990	*tert*butyl rotations	
973	*tert*butyl asymmetric bend	
965	aniline CH OOP bend	
961		aniline ring CH wag
943		molecular deformations
936	*tert*butyl asymmetric bends	
925		aldehyde OH stretch
916		aldehyde OH stretch
902	aldehyde IP CH wag	
879		Aldehyde IP CH wag
865	aldehyde OOP CH wag	Aldehyde IP CH wag
824	aldehyde OOP CH wag	
801	Aniline CH OOP wag	
771	aldehyde ring deformation	
730		molecular deformation
718		molecular deformation, CH OOP bends
705		aniline ring deformation
643	aniline ring deformation	aniline ring deformation
633	CH IP bends	molecular deformation

620	molecular deformations	
593	molecular deformations	
587	molecular deformations	
544	CH OOP wag, C-Br	molecular deformations, C-Br
514		CH OOP wag
508	aniline CH OOP bend	
485	aniline CH OOP bend	
463	molecular deformation	
451	*tert*butyl symmetric bend	
417		aniline ring deformation
413	*tert*butyl deformation	
405	*tert*butyl asymmetric CH bends	
388	aldehyde deformation	
382	aldehyde deformation	
367		*tert*butyl asymmetric bends
353	*tert*butyl asymmetric wag	
344	*tert*butyl CH asymmetric bends	
334	*tert*butyl asymmetric bends	aniline ring/ *tert*butyl deformations
309	*tert*butyl asymmetric bends	aldehyde ring deformations
300	*tert*butyl asymmetric bends	
280	*tert*butyl asymmetric bends	
272	*tert*butyl asymmetric bends	
256	*tert*butyl asymmetric bends	
238		*tert*butyl rotations
233	*tert*butyl rotations	
219	*tert*butyl rotations	
204	Aldehyde/*tert*butyl deformations	
175	molecular deformations	
165	molecular deformations	
157		molecular deformations

142	molecular deformations	
123	molecular deformations	
113	molecular deformations	
107	molecular deformations	
104	molecular deformations	
92	molecular deformations	
90	Aldehyde/*tert*butyl deformations	
85	aniline ring rotation	
79	*tert*butyl rotations	
77	aniline ring rotation	
72	molecular deformation	
69	molecular deformation	
63	molecular deformation	
53		molecular deformation

Table 93: Raman spectroscopy peak assignments for compound 12 at 50 K

Position (cm^{-1})	**Keto Assignment**	**Enol Assignment**
1617	NH IP wag	
1597	aniline CH wag	OH wag, Aldehyde CH IP wag
1576	aniline CH wag,	Aniline CH OOP wag and deformations
1571	aniline CH IP wag	aniline CH IP wag
1566		OH wag, aniline CH IP wag and deformations
1542	aldehyde CH IP wag	
1524	*tert*butyl asymmetric bend	*tert*butyl asymmetric bend
1483		*tert*butyl asymmetric bend
1469		*tert*butyl asymmetric bend
1457		Aldehyde IP CH wag
1451	*tert*butyl asymmetric wag	
1443		Aldehyde IP CH wag
1405		*tert*butyl umbrella bend
1393	5- *tert*butyl asymmetric wag	
1386	*tert*butyl symmetric bend	
1371	aniline ring deformations	
1362		CH IP wag
1356		CH IP wag
1321	CH IP wag	CH IP wag
1297	CH IP wag	
1288	CH IP wag	
1270		Aldehyde CH IP wag, *tert*butyl asymmetric bend
1250		*tert*butyl asymmetric bend
1240		aniline CH IP wag
1219		CH IP wag
1205	NH wag OOP	CH IP wag
1196	CH IP wag, NH wag OOP	CH IP wag

1172	Aldehyde CH IP wag, NH wag IP	Aldehyde CH IP wag
1134	Aniline CH IP was	Aldehyde CH IP wag
1105	aniline CH IP wag	aniline CH IP wag
1069		*tert*butyl asymmetric bend
1007		Aldehyde CH, *tert*butyl, OH IP wag
990	*tert*butyl asymmetric bend	*tert*butyl asymmetric bend
973		Bridge CH IP wag
943	*tert*butyl asymmetric bend	*tert*butyl asymmetric bend
935	aniline CH symmetric OOP wag	
925		OH OOP wag
916		OH OOP wag
824	aniline CH Symmetric OOP wag	
801	aniline CH Symmetric OOP wag	
730		molecular deformations
633	molecular deformations	
593	CH IP wag	
587		Molecular deformations
544	Aldehyde deformations, C-Br	C-Br
514		Molecular deformations
508	Aniline CH OOP wag	
485	Molecular deformations	
417		Molecular deformations
405	*tert*butyl symmetric wag	
387	*tert*butyl symmetric wag	
367		*tert*butyl symmetric bend
353	*tert*butyl rotation and deformation	*tert*butyl rotation and deformation
344	*tert*butyl rotation and deformation	

334	*tert*butyl rotation	*tert*butyl rotation
309	*tert*butyl rotation	
280		*tert*butyl asymmetric bend
272	*tert*butyl rotation	
256	*tert*butyl rotation	*tert*butyl rotation
233		*tert*butyl rotation
218	*tert*butyl rotation	
204		*tert*butyl rotation
175	molecular deformations	
165		molecular deformation
142	*tert*butyl OOP wag	Molecular deformations
123		molecular rotations
103	*tert*butyl wag	
97		molecular deformations
89	*tert*butyl rotation	
76		molecular deformation
68	molecular deformation	molecular deformation
62	molecular deformation	
52	molecular deformation	molecular deformation

Table 94: Raman spectroscopy peak assignments for compound 12 at 150 K

Position (cm^{-1})	**Keto Assignment**	**Enol Assignment**
1617	NH IP wag OH wag	Aldehyde CH IP wag
1597	aniline CH wag	OH wag, Aldehyde CH IP wag
1571	aniline CH IP wag	aniline CH IP wag
1542	aldehyde CH IP wag	
1483		*tert*butyl asymmetric bend
1466		*tert*butyl asymmetric bend
1456		Aldehyde IP CH wag
1440		Aldehyde IP CH wag
1405		*tert*butyl umbrella bend
1386	*tert*butyl symmetric bend	
1369	aniline ring deformations	
1322	CH IP wag	CH IP wag
1274		Aldehyde CH IP wag, *tert*butyl asymmetric bend
1250		*tert*butyl asymmetric bend
1238		aniline CH IP wag
1219		CH IP wag
1197	CH IP wag, NH OOP wag	CH IP wag
1172	Aldehyde CH IP wag	Aldehyde CH IP wag
1134	Aniline CH IP wag	Aldehyde CH IP wag
1104	aniline CH IP wag	aniline CH IP wag
1086	aniline CH IP wag	
1006		Aldehyde CH, *tert*butyl, OH IP wag
988		*tert*butyl asymmetric bend
973		Bridge CH IP wag
916		OH OOP wag
825	aniline CH Symmetric OOP wag	
586		Molecular deformations
544	Aldehyde deformations, C-Br	C-Br

486	Molecular deformations	
415		Molecular deformations
338	*tert*butyl rotation	
308	*tert*butyl rotation	
201		*tert*butyl rotation
175	molecular deformations	
123		molecular rotations
103	*tert*butyl wag	
80		molecular deformation
57		molecular deformation

Table 95: Raman spectroscopy peaks assignments for compound 12 at 240 K

Position (cm^{-1})	**Keto Assignment**	**Enol Assignment**
1617	NH IP wag,	
1597	aniline CH wag	OH wag, Aldehyde CH IP wag
1571	aniline CH IP wag	aniline CH IP wag
1542	aldehyde CH IP wag	
1522		*tert*butyl asymmetric bend
1483	*tert*butyl asymmetric bend	tertbutyl asymmetric bend
1465		*tert*butyl asymmetric bend
1455		Aldehyde IP CH wag
1440		Aldehyde IP CH wag
1404		*tert*butyl umbrella bend
1387	*tert*butyl symmetric bend	
1369	aniline ring deformations	
1322	CH IP wag	CH IP wag
1297	CH IP wag	
1274		Aldehyde CH IP wag, *tert*butyl asymmetric bend
1250		*tert*butyl asymmetric bend
1237		aniline CH IP wag
1219		CH IP wag
1196	CH IP wag	CH IP wag
1171	Aldehyde CH IP wag	Aldehyde CH IP wag
1133	Aniline CH IP wag	Aldehyde CH IP wag
1117		aniline CH IP wag
1103	aniline CH IP wag	aniline CH IP wag
1068		*tert*butyl asymmetric bend
1007		Aldehyde CH, *tert*butyl, OH IP wag
988	*tert*butyl asymmetric bend	*tert*butyl asymmetric bend
973		Bridge CH IP wag
926		OH OOP wag
915		OH OOP wag

866	aniline CH Symmetric OOP wag	OH OOP wag
826	aniline CH Symmetric OOP wag	
802	aniline CH Symmetric OOP wag	
730		molecular deformations
633	molecular deformations	
592	CH IP wag	
586		Molecular deformations
545	Aldehyde deformations, C-Br	C-Br
509	Aniline CH OOP wag	
486	Molecular deformations	
413		Molecular deformations
336	*tert*butyl rotation	*tert*butyl rotation
306		*tert*butyl asymmetric bend
200		*tert*butyl rotation
174	molecular deformations	
156	*tert*butyl OOP wag	Molecular deformations
120		molecular rotations
75		molecular deformation
59		molecular deformation

Table 96: Raman Spectroscopy peak assignments for compound 12 at 280 K

Position (cm^{-1})	**Keto Assignment**	**Enol Assignment**
1616	NH IP wag	OH wag, Aldehyde CH IP wag
1597	aniline CH wag	aniline CH wag
1572		aniline CH IP wag
1482		*tert*butyl asymmetric bend
1454		Aldehyde IP CH wag
1439		Aldehyde IP CH wag
1404		*tert*butyl umbrella bend
1387		*tert*butyl symmetric bend
1368	aniline ring deformations	
1322		CH IP wag
1274		Aldehyde CH IP wag, *tert*butyl asymmetric bend
1249		*tert*butyl asymmetric bend
1236		aniline CH IP wag
1218		CH IP wag
1196	CH IP wag	CH IP wag
1171	Aldehyde CH IP wag	Aldehyde CH IP wag
1133	Aniline CH IP wag	Aldehyde CH IP wag
1116		aniline CH IP wag
1102	aniline CH IP wag	aniline CH IP wag
1068		*tert*butyl asymmetric bend
1006		Aldehyde CH, *tert*butyl, OH IP wag
987	*tert*butyl asymmetric bend	
973		Bridge CH IP wag
926		OH OOP wag
914		OH OOP wag
825	aniline CH Symmetric OOP wag	
802	aniline CH Symmetric OOP wag	

729		molecular deformations
633	molecular deformations	
593	CH IP wag	
586		Molecular deformations
546	Aldehyde deformations, C-Br	C-Br
485	Molecular deformations	
412		Molecular deformations
334	*tert*butyl rotation	*tert*butyl rotation
305		*tert*butyl asymmetric bend
200		*tert*butyl rotation
175	molecular deformations	
155	*tert*butyl OOP wag	Molecular deformations
119		molecular rotations
71		molecular deformation
59		molecular deformation

Table 97: Raman Spectroscopy peak assignments for compound 12 at 100 K after 1 night UV

Position (cm^{-1})	**Keto Assignment**	**Enol Assignment**
1006		Aldehyde CH, *tert*butyl, OH IP wag
989	*tert*butyl asymmetric bend	*tert*butyl asymmetric bend
960		*tert*butyl asymmetric bend
942	*tert*butyl asymmetric bend	*tert*butyl asymmetric bend
935	aniline CH symmetric OOP wag	
925		OH OOP wag
915		OH OOP wag
899	NH OOP wag	
879		Aldehyde CH OOP wag
865	Aldehyde CH OOP wag	
824	aniline CH Symmetric OOP wag	
801	aniline CH Symmetric OOP wag	
730		molecular deformations
704		Aniline CH OOP bends, Aniline ring deformations
643	molecular deformations	
637		Aldehyde CH OOP wag
633	Aldehyde CH OOP wag	
627		OH IP wag, Molecular deformations
620		OH IP wag, Molecular deformations
593	CH IP wag	
587		Molecular deformations
545	Aldehyde deformations, C-Br	C-Br
514		Molecular deformations
509	Aniline CH OOP wag	
496		Aniline CH OOP wag, *tert*butyl asymmetric bend
485	Molecular deformations	
476	Aniline CH OOP wag	
462	*tert*butyl asymmetric bend	Molecular deformations

451	*tert*butyl asymmetric bend	
416		Molecular deformations
405	*tert*butyl symmetric wag	
386	*tert*butyl symmetric wag	
366		*tert*butyl symmetric bend
351	*tert*butyl rotation and deformation	*tert*butyl rotation and deformation
343	*tert*butyl rotation and deformation	
334	*tert*butyl rotation	*tert*butyl rotation
308	*tert*butyl rotation	
280		*tert*butyl asymmetric bend
271	*tert*butyl rotation	
255	*tert*butyl rotation	*tert*butyl rotation
237		*tert*butyl rotation
217	*tert*butyl rotation	
203		*tert*butyl rotation
174	molecular deformations	
164		molecular deformation
157		Molecular deformations
139	*tert*butyl OOP wag	Molecular deformations
122		molecular rotations
100	*tert*butyl wag	
86	*tert*butyl rotation	
78		molecular deformation
65	molecular deformation	molecular deformation
61	molecular deformation	
49	molecular deformation	

Table 98: Raman Spectroscopy peak assignments for compound 12 at 20 K after 1 Hr UV

Position (cm^{-1})	**Keto Assignment**	**Enol Assignment**
1007		Aldehyde CH, *tert*butyl, OH IP wag
973	*tert*butyl asymmetric bend	*tert*butyl asymmetric bend
961		*tert*butyl asymmetric bend
955	Aniline CH asymmetric bends	
942	*tert*butyl asymmetric bend	*tert*butyl asymmetric bend
936	aniline CH symmetric OOP wag	
925		OH OOP wag
916		OH OOP wag
879		Aldehyde CH OOP wag
865	Aniline CH OOP wag	
825	aniline CH Symmetric OOP wag	
802	aniline CH Symmetric OOP wag	
731		molecular deformations
718		Molecular deformations
705		Aniline Ring CH OOP wag, ring deformations
695	Aniline CH OOP wag	
689	Aniline CH OOP wag	
649	molecular deformations	
638		Aldehyde CH OOP wag
633	Aldehyde CH OOP wag	
628		Molecular deformations
621		Molecular deformations
593	CH IP wag	
588		Molecular deformations
544	Aldehyde deformations, C-Br	C-Br
534	*tert*butyl asymmetric bend	
529	*tert*butyl asymmetric bend	

514		Molecular deformations
509	Aniline CH OOP wag	
496	*tert*butyl asymmetric bend	
485	Molecular deformations	
476	Aniline CH OOP wag	
461	*tert*butyl asymmetric wag	
452		*tert*butyl asymmetric wag
418		Molecular deformations
405	*tert*butyl symmetric wag	
388	*tert*butyl symmetric wag	
367		*tert*butyl symmetric bend
353	*tert*butyl rotation and deformation	*tert*butyl rotation and deformation
344	*tert*butyl rotation and deformation	
334	*tert*butyl rotation	*tert*butyl rotation
327		*tert*butyl asymmetric wag, Bridge CH OOP wag
309	*tert*butyl rotation	
301	*tert*butyl wag	
285	*tert*butyl rotation	
280		*tert*butyl asymmetric bend
272	*tert*butyl rotation	
256	*tert*butyl rotation	*tert*butyl rotation
238		*tert*butyl rotation
233	*tert*butyl rotation	
219	*tert*butyl rotation	
204		*tert*butyl rotation
175	molecular deformations	
165		molecular deformation
157		molecular deformations
142	3 - *tert*butyl OOP wag	

139	*tert*butyl OOP wag	Molecular deformations
123		molecular rotations
113	*tert*butyl wag	
107	*tert*butyl wag	
98		*tert*butyl asymmetric wag
90	*tert*butyl rotation	
86	*tert*butyl rotation	
77		molecular deformation
69	molecular deformation	molecular deformation
63	molecular deformation	
54	molecular deformation	molecular deformation

SCXRD

Table 99: Crystallographic X-ray data for compound 12 under in situ irradiation 1-3

Crystal system	Monoclinic		
Space group	P 2_1/c		
Z	4		
Crystal size (mm)	1 x 1 x 2 mm		
Radiation type	X-ray Copper		
Wavelength (nm)	1.54184		
Irradiation time (h/m)	**Pre-irradiation**	**3**	**11/10**
Cell parameters (Å)	a= 18.0421(2) b=10.5877(5) c= 10.3641(3) α =90 β=92.868(2) γ=90	a= 18.0357(2) b=10.58994(3) c= 10.35753(4) α =90 β=92.8555(4) γ=90	a= 18.0351(1) b=10.59102(3) c= 10.35705(4) α =90 β=92.8567(1) γ=90
Cell volume (Å^3)	1977.31(2)	1975.81(2)	1975.84(5)
Total no. of reflections	11034	11173	11185
No of reflection with I/σ(I) > 2	3204	3198	3484
R(sigma)	0.0271	0.0196	0.0177
Parameters/Restraints	245/0	245/0	245/0
R1, wR2, Goof	0.0483, 0.1496, 1.0099	0.0410, 0.1148, 0.9904	0.0423, 0.1201, 1.0006
R1 after Fourier merging / No of unique reflections	0.0506/3498	0.0220/3807	0.02/3802
Theta max	72.199	72.163	72.143
hkl limits	H min = -22 H max =22 K min = -13 K max = 6 L min = -12 L max = 12	H min = -22 H max = 10 K min = -12 K max = 12 L min = -22 L max = 22	H min = -20 H max = 22 K min = -12 K max = 12 L min = -22 L max = 22

Table 100: Crystallographic X-ray data for compound 12 under in situ irradiation collection 4-7

Crystal system	Monoclinic			
Space group	P 2_1/c			
Z	4			
Crystal size (mm)	1 x 1 x 2 mm			
Radiation type	X-ray Copper			
Wavelength (nm)	1.54184			
Irradiation time (h/m)	**16/20**	**24/30**	**35/40**	**40/20**
Cell parameters (Å)	a= 18.0361(1) b=10.59067(3) c= 10.35664(3) α =90 β=92.8612(2) γ=90	a= 18.0357(5) b=10.59203(2) c= 10.35682(3) α =90 β=92.8566(3) γ=90	a= 18.0370(1) b=10.59305(3) c= 10.35574(3) α =90 β=92.8610(2) γ=90	a= 18.0368(5) b=10.59344(5) c= 10.35596(4) α =90 β=92.8665(2) γ=90
Cell volume (Å^3)	1975.81(3)	1976.05(1)	1976.18(3)	1976.26(3)
Total no. of reflections	11201	11132	11220	11211
No of reflection with I/σ(I) > 2	3474	3467	3475	3197
R(sigma)	0.0186	0.0192	0.0186	0.0180
Parameters/Restraints	246/4	246/0	246/0	246/0
R1, wR2, Goof	0.0416, 0.1160, 1.0035	0.0415, 0.0998, 0.9970	0.0430, 0.1204, 1.0165	0.0394, 0.1099, 1.0082
R1 after Fourier merging / No of unique reflections	0.02/3800	0.0210/ 3802	0.0210/3803	0.0190/3801
Theta max	72.149	72.125	72.113	72.106
hkl limits	H min = -22 H max = 20 K min = -12 K max = 12 L min = -22 L max = 22	H min = -22 H max = 20 K min = -12 K max = 6 L min = -12 L max = 12	H min = -22 H max = 22 K min = -12 K max = 6 L min = -12 L max = 12	H min = -22 H max = 20 K min = -12 K max = 6 L min = -12 L max = 12

Due to the finding that using a molybdenum source causes radiation damage with the photoproduct the *in situ* irradiation of the sample was collected using a copper source. The SCXRD at ISIS, Harwell was set up in line with previous irradiation experiments such that no natural light could enter into the sample cabinet. A non-irradiated crystal of the compound was mounted on a loop pin using grease a placed on the goniometer head before being centred. A pre-experiment was collected, and a strategy determined before a full collection was started on the non-irradiated sample. A collection strategy was then set up so that each collection was started after a period of waiting these were staggered as 3, 6, 3, 6, 9 and 2.5 hours. The UV-lamp was switched on just as the first 3 hour waiting time began.

Table 101: Variable temperature crystallographic X-ray data for compound 12

Crystal system	Monoclinic	Monoclinic	
Space group	P 2_1/c	P 2_1/c	
Z	4	4	
Crystal size (mm)	1 x 1 x 2 mm	1 x 1 x 2 mm	
Radiation type	X-ray Copper	X-ray Molybdenum	
Wavelength (nm)	1.54184	0.71073	
Temperature (K)	**50**	**120**	**290**
Cell parameters (Å)	a =17.38692(2) b=10.717640(16) c = 10.114590(16) α/ γ=90 β= 90.195(3)	a= 17.73130(3) b=10.57230(3) c= 10.19180(3) α/ γ=90 β= 91.341(4)	a= 18.02710(4) b=10.57870(3) c= 10.34650(3) α/ γ=90 β= 92.813
Cell volume (Å^3)	1884.810(3)	1910.038(9)	1970.734(12)
Total no. of reflections	3045	23965	26362
No of reflection with I/σ(I) > 2	2877	2623	3000
R(sigma)	0.030	0.03	0.063
Parameters/Restraints	218/100	246/4	245/0
R1, wR2, Goof	0.0408, 0.1091, 1.0044	0.067, 0.150, 1.019	0.1554, 0.1613, 1.0034
No of unique reflections	3020	5387	5778
Scan type	2thetaomega	2thetaomega	2thetaomega
Theta max	71.964	30.82	32.805
hkl limits	H min = -21 H max = 21 K min = -13 K max = 12 L min = -12 L max = 11	H min = -24 H max = 22 K min = -14 K max = 12 L min = -13 L max = 14	H min = -27 H max = 24 K min = -15 K max = 15 L min = -15 L max = 14

Compound 13

Table 102: tabulated masses and moles for synthesis of compound 13

Compound	Mr (g/mol^{-1})	Mass (g)	Volume (mL)	mol	mmol	equiv
4-Bromoaniline	172.02	1.1248	-	0.006539	6.54	1
5-Chlorosalicylaldehyde	156.56	1.0061	-	0.006426	6.43	1
ethanol	-	-	40	-	-	-
Product	310.8	1.9521	-	0.006285	6.29	-
-	-	-	-	yield	96.12	-

Preliminary characterisation

NMR

Table 103: 1H NMR assignments for compound 13

δ (ppm)	Multiplicity	Integration	J coupling (Hz)	Assignment
12.97	s	1H		H_g
8.53	s	1H		H_c
7.56	d	2H	8.2	H_a
7.37	d	1H	2.5	H_d
7.33	dd	1H	9.1, 2.9	H_e
7.16	d	2H	8.1	H_b
6.98	d	1H	8.8	H_f

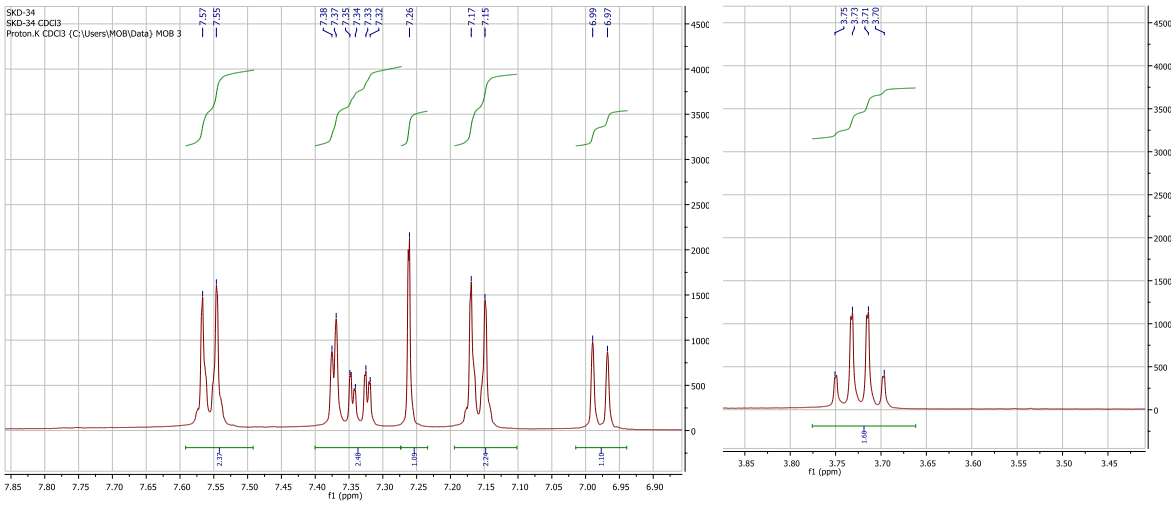


Figure 331: 1H NMR expansions for compound 13

Table 104: 13C NMR assignments for compound 13

δ (ppm)	Integration	Assignment
162.15	1	7
162.04	1	10
147.44	1	6
133.73	2	2/3
133.07	1	11
131.78	1	13
132.78	1	9
123.29	2	4/5
119.40	1	8

Table 105: Tabulated UV-VIs absorption λmax of compound 13

abs	Wavelength(nm)	abs	Wavelength(nm)
0.17	352	0.15	324

Compound 14

Table 106: Tabulated masses and moles for synthesis of compound 14

Compound	Mr (g/mol^{-1})	Mass (g)	Volume (mL)	mol	mmol	equiv
4-Iodoaniline	219.02	1.4981	-	0.00684	6.84	1
5-Chlorosalicylaldehyde	156.56	1.0718	-	0.006846	6.85	1
ethanol	-	-	40	-	-	-
Product	357.58	2.0875	-	0.005838	5.84	-
-	-	-	-	yield	85.35	-

Preliminary characterisation

Table 107: 1H NMR assignments for compound 14

δ (ppm)	Multiplicity	Integration	J coupling (Hz)	Assignment
12.73	s	1H		H_g
8.93	s	1H		H_c
7.85-7.79	m	2H		H_a
7.75	d	1H	2.7	H_f
7.45	dd	1H	8.8, 2.7	H_e
7.25-7.19	m	2H		H_b
7.00	d	1H	8.8	H_d

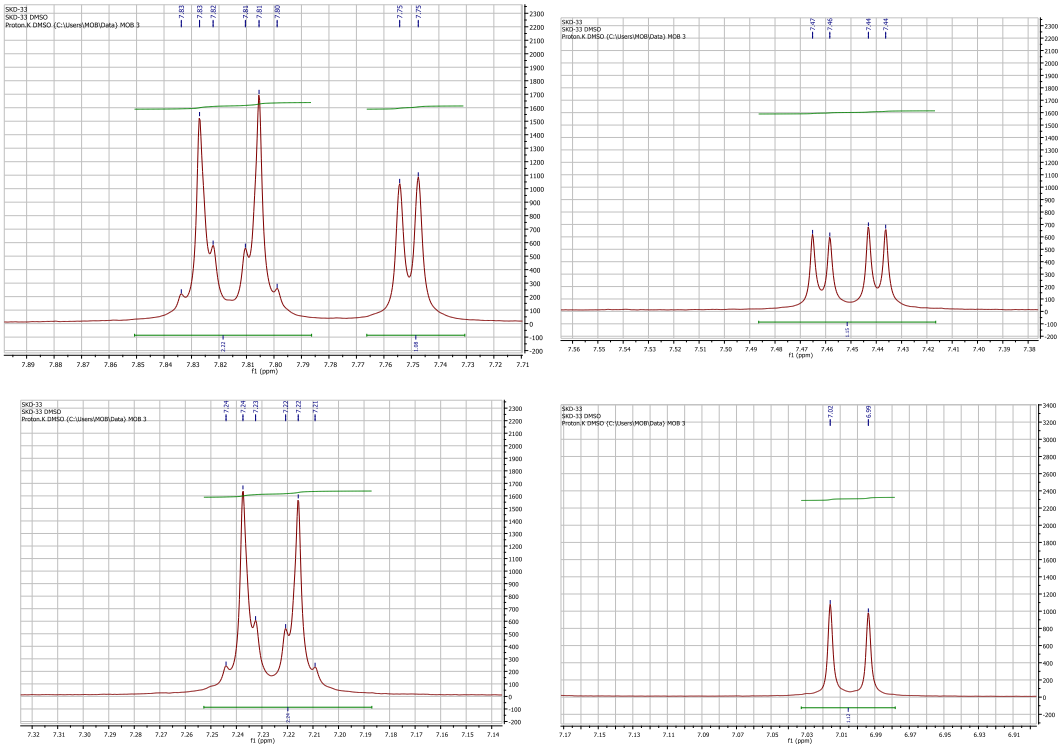


Figure 332: 1H NMR expansions for compound 14

Table 108:13C NMR assignments for compound 14

δ (ppm)	Integration	Assignment
162.81	1	7
159.47	1	10
148.42	1	6
138.85	2	2/3
133.59	1	11
131.49	1	13
124.38	1	9
123.38	2	4/5
121.29	1	8
119.31	1	12
93.21	1	1
56.75	Solvent	
19.18		

Table 109: Tabulated UV-Vis absorption λmax of compound 14

abs	Wavelength (nm)	abs	Wavelength (nm)
0.14	352	0.13	327

Compound 15

Table 110: tabulated masses and moles for synthesis of compound 15

Compound	Mr (g/mol^{-1})	Mass (g)	Volume (mL)	mol	mmol	equiv
4-Iodoaniline	219.02	2.0847	-	0.009518	9.52	1
Salicylaldehyde	122.12	1.1674	1.3	0.009119	9.12	1
ethanol	-	-	40	-	-	-
Product	323.14	2.9109	-	0.009008	9.01	-
-	-	-	-	yield	98.79	-

Preliminary characterisation

NMR

Table 111:1H NMR assignments for compound 15

δ (ppm)	Multiplicity	Integration	J coupling (Hz)	Assignment
12.89	s	1H		H_h
8.50	d	1H	11.4	H_c
7.65	T	2H	9.9	Ha
7.34-7.23	M	2H		Hb
7.00-6.81	M	4H		H_{d-g}

Table 112:13C NMR assignments for compound 15

δ (ppm)	Integration	Assignment
163.54	1	7
161.60	1	10
148.66,	1	6
138.95	2	2/3
133.98	1	9
132.89	1	13
123.61	2	4/5
119.68	1	8/11
117.82	1	13
91.96	1	1

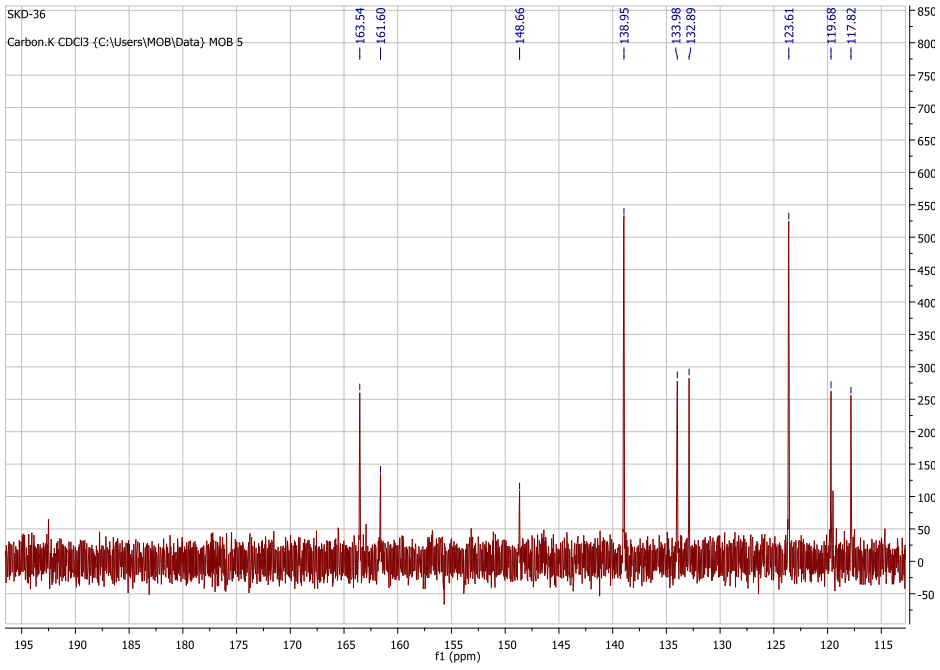


Figure 333: ^{13}C NMR spectrum expansion of compound 15

Table 113: Tabulated UV-Vis absorption λmax of compound 15

abs	Wavelength (nm)	Abs	Wavelength (nm)
0.68	346	0.65	323

Compound 16

Table 114: Tabulated masses and moles for synthesis of compound 16

Compound	Mr (g/mol^{-1})	Mass (g)	Volume (mL)	mol	mmol	equiv
4-Bromoaniline	172.02	1.6483	-	0.009582	9.58	1
Salicylaldehyde	122.12	1.1674	1.3	0.009119	9.12	1
ethanol	-	-	40	-	-	-
Product	276.14	2.4826	-	0.00899	8.99	-
-	-	-	-	yield	93.83	-

Preliminary characterisation

NMR

Table 115: 1H NMR assignments for compound 16

δ (ppm)	Multiplicity	Integration	J coupling (Hz)	Assignment
12.97	s	1H		H_h
8.60	s	1H		H_c
7.55	D	2H	8.1	H_a
7.42-7.37	M	2H		H_e/H_f
7.16	D	2H	8.1	H_b
7.03	D	1H	8.6	H_d
6.96	T	1H	7.5	H_g

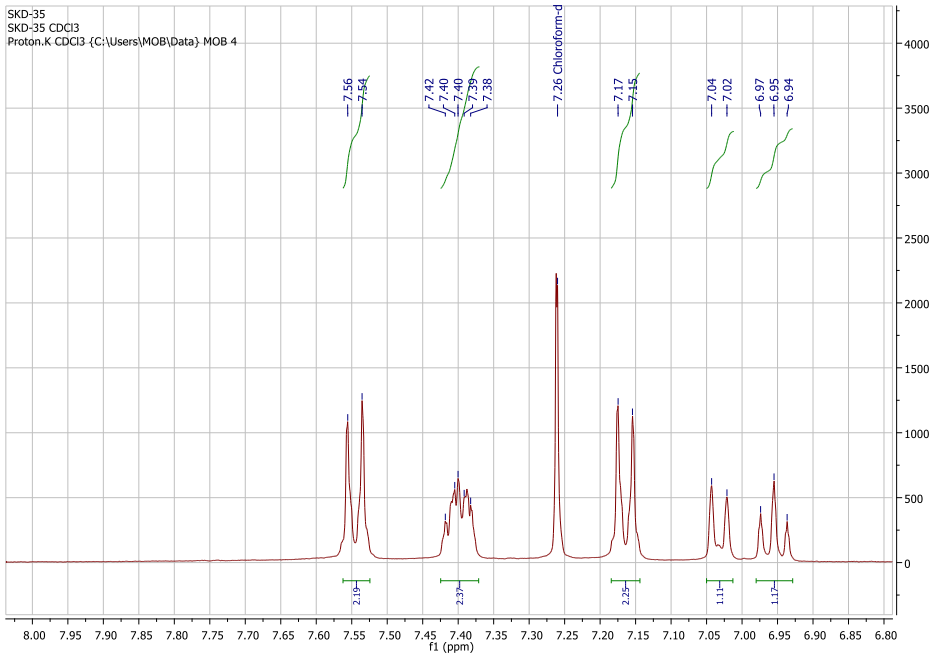


Figure 334:1H NMR spectrum expansion of compound 16

Table 116:13C NMR assignments for compound 16

δ (ppm)	Integration	Assignment
163.20	1	7
161.28	1	10
147.68	1	6
133.66	1	9
132.66	2	2/3
132.57	2	13
122.97	2	4/5
120.54	1	11
119.38	1	8
119.18	1	1
117.49	1	12

Table 117: Tabulated UV-Vis absorption λmax of compound 16

Abs	Wavelength (nm)	Abs	Wavelength (nm)	Abs	Wavelength (nm)
0.29	344	0.28	320	0.27	304

Compound 17

Table 118: Tabulated masses and moles for synthesis of compound 17

Compound	Mr (g/mol^{-1})	Mass (g)	Volume (mL)	mol	mmol	equiv
4-hydroxyaniline	109.13	1.1807	-	0.010819	10.82	1
benzaldehyde	106.12	1.04	1.1	0.009967	9.97	1
ethanol	-	-	30	-	-	-
Product	197.25	1.7463	-	0.008853232	8.85	-
-	-	-	-	yield	81.83	-

Preliminary characterisation

NMR

Table 119:1H NMR assignments for compound 17

δ (ppm)	Multiplicity	Integration	J coupling (Hz)	Assignment
9.52	s	1H		Ha
8.60	s	1H		H_d
8.01-7.80	m	2H		H_e
7.48	m	3H		H_f, H_g
7.20	d	2H	11.8	H_c
6.80	d	2H	11.8	H_b

Table 120: 13C NMR assignments for compound 17

δ (ppm)	Integration	Assignment
156.93	1	7
156.11	1	10
142.36	1	6
136.25	1	9
130.63	1	13
128.53	2	2/3
128.04	2	4/5
122.28	2	8/11
115.49	2	12/1

Table 121: Tabulated UV-Vis absorption λmax of compound 17

abs	Wavelength (nm)
1.88	337

SCXRD

Data was collected on the SCXRD at Keele at 120 and 220 K using a molybdenum source. The resulting data was integrated using the Bruker Apex 2 software. The outputted .ins and .hkl files were then inputted into the CRYSTALS SCXRD analysis software where the structure was determined using the SIR92 programme.

At 120 K there is a dihedral angle between the rings of 18.83°, this decreases to 18.40 at 220 K.

Table 122: Crystallographic X-ray data of compound 17

Crystal system	Monoclinic	
Space group	P 2_1/n	
Z	4	
Crystal size (mm)	0.094x0.198x0.642	
Radiation type	X-ray Molybdenum	
Wavelength (nm)	0.71073	
Temperature (K)	**120**	**220**
Cell parameters (Å)	a= 6.45410(2) b=14.45860(3) c= 10.91770(1) α/γ=90 β=90.978(2)	a= 6.474(2) b=14.722(2) c= 10.913(4) α/γ=90 β=90.99(4)
Cell volume (Å^3)	1018.661(2)	1040.0(2)
Total no. of reflections	10917	10112
No of reflection with I/σ(I) > 2	1193	885
R(sigma)	0.075	0.136
Parameters/Restraints	181	180/82
R1, wR2, Goof	0.1004, 0.2282, 1.0256	0.1423, 0.3018, 1.1899
No of unique reflections	1763	1130
Max resolution (Å)		
Scan type	2THETA/OMEGA	2THETA/OMEGA
Theta max	28.341	29.548
hkl limits	H min = -8 H max = 8 K min = -18 K max = 17 L min = -13 L max = 14	H min = -8 H max = 8 K min = -18 K max = 18 L min = -14 L max = 15

Compound 18

Preliminary Characterisation

NMR

Table 123:1H NMR assignments of compound 18

δ (ppm)	Multiplicity	Integration	J coupling (Hz)	Assignment
13.21	s	1H		H_j
8.51	s	1H		H_e
7.92	dd	1H	1.30, 7.89	H_b
7.49	d	1H	2.34	H_f
7.398	td	1H	1.36, 15.47	H_c
7.23	d	1H	2.45	H_h
7.14	dd	1H	1.47, 7.92	H_d
6.966	td	1H	1.50, 15.47	H_a
1.49	s	9H		H_i
1.33	s	9H		H_g

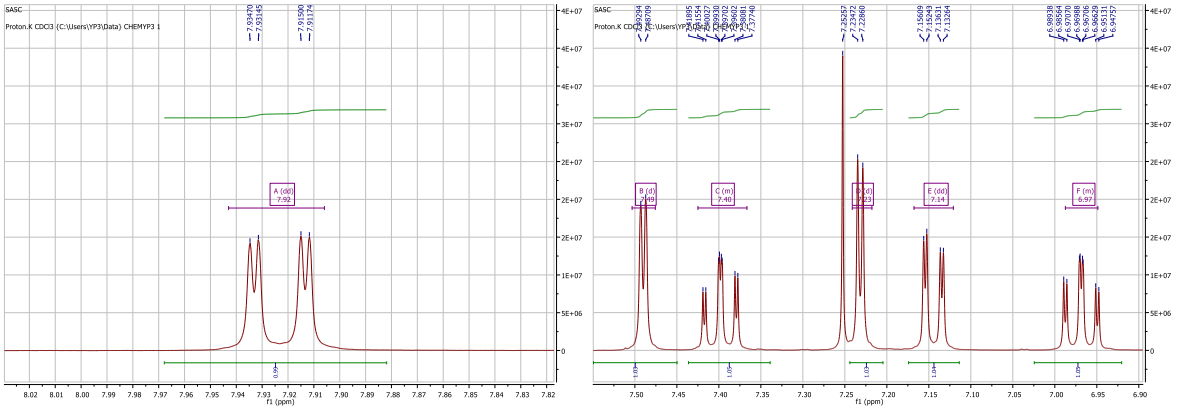


Figure 335:1H NMR spectrum expansions of compound 18

Table 124: 13C NMR assignments for compound 18

δ (ppm)	Integration	Assignment
29.41	3	14
31.45	3	16
34.19	1	13
35.18	1	15
96.00	1	5
118.07	1	4
118.62	1	8
127.12	1	11
127.75	1	9
128.64	1	3
129.42	1	1
137.24	1	12
139.34	1	2
140.68	1	10
150.42	1	6
158.39	1	17
164.52	1	7

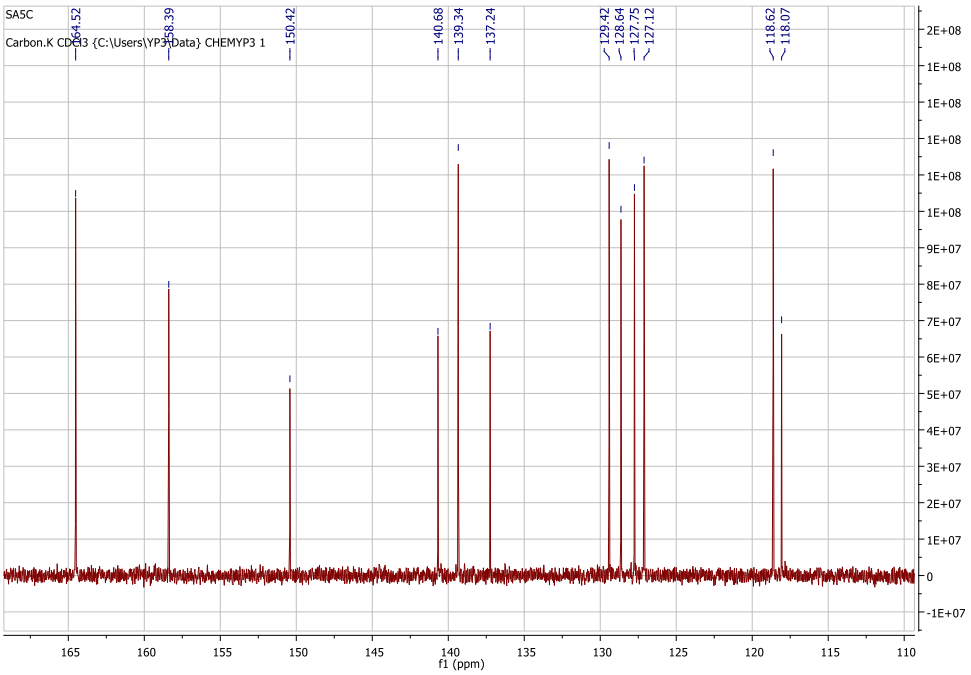


Figure 336: 13C NMR spectrum expansion of compound 18

Table 125: Raman Spectrum peak assignments for compound 18 at 11 K

Position (cm^{-1})	**Keto Assignment**	**Enol**
1616		OH bend
1598	NH OOP bend	aniline ring deformation
1586	NH OOP bend	
1578	aniline ring deformations	
1571		aniline ring deformations
1562	aniline ring deformations	
1545	aniline ring deformations	
1518		3-*tert*butyl asymmetric CH bends
1493		3-*tert*butyl asymmetric CH bends
1470		3-*tert*butyl asymmetric CH bends
1465	*tert*butyl asymmetric CH bends	
1458	Ar-H bends	
1450	*tert*butyl asymmetric CH bends	
1441	*tert*butyl asymmetric CH bends	
1397	N OOP deformations	
1385		*tert*butyl umbrella CH bends
1360	*tert*butyl umbrella CH bends	
1312	OOP Ar-H/NH bends	
1301		Ar-H bends
1283	ring deformations	*tert*butyl asymmetric CH bends
1279	Ar-H/ NH OOP bends	
1273		Ar-H OOP bends
1266		Ar-H OOP bends
1247		*tert*butyl CH wag
1233		Ar-H IP bends
1229		Ar-H IP bends
1220		Ar-H IP bends
1213		Aniline CH bends, *tert*butyl CH wag, OH IP bend
1208	Bridge CH, NH OOP bends	
1205	Bridge CH, NH OOP bends	
1200	Bridge CH, NH IP bends	
1198	*tert*butyl umbrella CH bends	
1170	*tert*butyl umbrella CH bends, NH bend. Bridge CH bend	
1164		Aldehyde CH bend
1159		Aniline CH Bend
1129	NH IP wag	
1118	NH/Ar-H Ip wag	
1051		*tert*butyl umbrella CH bends, Aniline ring deformation
1041	CH/NH wag, aniline ring deformation	
1032		aniline ring deformation
1028	NH IP wag	
983	*tert*butyl rotation	
972	Bridge CH OOP wag	

968	Bridge CH OOP wag	
930	aniline CH asymmetric OOP bend	
924		Aldehyde Ar-H OOP bend
914		Aldehyde Ar-H OOP wag
907	NH bend	
876	aldehyde CH OOP wag	
857		aldehyde CH OOP bend
826	Ar-H was	
801	*tert*butyl symmetric CH bends	
744	aniline CH OOP bend	
728		Enol -aniline CH OOP bend
711	aniline CH OOP bend	
705	aniline CH OOP bend	
645	C–I	C–I
609	ring deformations	
588	aldehyde ring deformations	
565	aldehyde ring deformations	
544		*tert*butyl asymmetric CH bends
523		molecular deformations
499		molecular deformations
457	aldehyde ring deformation	
430		aniline CH OOP bend
410	aniline CH OOP bend	
383	*tert*butyl deformations	
360	*tert*butyl symmetric CH bends	
340		*tert*butyl asymmetric CH bends
327	*tert*butyl symmetric CH bends	
313	*tert*butyl rotations	
306	*tert*butyl asymmetric CH bends	
295	*tert*butyl rotations	
281	*tert*butyl rotations	
277		*tert*butyl asymmetric CH bends
272		*tert*butyl asymmetric CH bends
259	*tert*butyl asymmetric CH bends	
249	*tert*butyl rotations	
242	*tert*butyl rotations	
226	*tert*butyl rotations	
200	*tert*butyl rotations	
190		Molecular deformations
178	aniline CH OOP bend	
175	aniline ring rotation	
163	molecular deformations/aniline ring rotations	
147	Molecular deformations	
140		*tert*butyl CH wag
129	Aldehyde ring deformation	
116		Aniline CH OOP bend
108		Aniline ring deformations
101	molecular rotations	
91		*tert*butyl rotations
87		*tert*butyl rotations

83	molecular rotations	
69		molecular rotations
64	molecular deformations	
59		*tert*butyl rotations
57		molecular deformations
44		molecular deformations
35	molecular deformations	
31	molecular deformations	
25	molecular deformations	

Table 126: Raman spectrum peak assignments for compound 18 at 170 K

Position (cm^{-1})	**Keto Assignment**	**Enol Assignment**
1616		OH bend
1597	NH OOP bend,	aniline ring deformation
1573		aniline ring deformations
1544	aniline ring deformations	
1518		3-*tert*butyl asymmetric CH bends
1492		3-*tert*butyl asymmetric CH bends
1465	*tert*butyl asymmetric CH bends	
1451	*tert*butyl asymmetric CH bends	
1437	*tert*butyl asymmetric CH bends	
1395	N OOP deformations	
1386		*tert*butyl umbrella CH bends
1312	OOP Ar-H/NH bends	
1278	Ar-H/ NH OOP bends	
1265		Ar-H OOP bends
1246		*tert*butyl CH wag
1229		Ar-H IP bends
1220		Ar-H IP bends
1213		Aniline CH bends, *tert*butyl CH wag, OH IP bend
1207	Bridge CH, NH OOP bends	
1197	*tert*butyl umbrella CH bends	
1169	*tert*butyl umbrella CH bends, NH bend. Bridge CH bend	
1164		Aldehyde CH bend
1160		Aniline CH Bend
1129	NH IP wag	
1118	NH/Ar-H IP wag	
1051		Enol -*tert*butyl umbrella CH bends, Aniline ring deformation
1041	CH/NH wag, aniline ring deformation	
1032		aniline ring deformation
1020	NH IP wag	
982	*tert*butyl rotation	
971	Bridge CH OOP wag	
968	Bridge CH OOP wag	
930	aniline CH asymmetric OOP bend	
923		Aldehyde Ar-H OOP bend
913		Aldehyde Ar-H OOP wag
905	NH bend	
875	aldehyde CH OOP wag	
855		aldehyde CH OOP bend
826	Ar-H was	
801	Keto -*tert*butyl symmetric CH bends	
744	aniline CH OOP bend	
728		Enol -aniline CH OOP bend
712	aniline CH OOP bend	
705	aniline CH OOP bend	
645	C–I	C–I

609	ring deformations	
588	aldehyde ring deformations	
565	aldehyde ring deformations	
544		*tert*butyl asymmetric CH bends
507		molecular deformations
499		molecular deformations
457	aldehyde ring deformation	
431		aniline CH OOP bend
410	aniline CH OOP bend	
383	*tert*butyl deformations	
359	*tert*butyl symmetric CH bends	
292	*tert*butyl rotations	
275		*tert*butyl asymmetric CH bends
248	*tert*butyl rotations	
188		Molecular deformations
174	aniline ring rotation	
159	molecular deformations/aniline ring rotations	
137		*tert*butyl CH wag
124	Aldehyde ring deformation	
112		Aniline CH OOP bend/ Aniline ring deformations
94		*tert*butyl rotations
88		*tert*butyl rotations
57		molecular deformations
41		molecular deformations
23	molecular deformations	

Table 127: Raman Spectrum peak assignments of compound 18 at 50 K

Position (cm^{-1})	Keto Assignment	Enol Assignment
1616.04		OH bend
1598.44	NH OOP bend	aniline ring deformation
1586.30	NH OOP bend	
1578.05	aniline ring deformations	
1571.11		aniline ring deformations
1562.50	aniline ring deformations	
1545.35	aniline ring deformations	
1492.73		3-*tert*butyl asymmetric CH bends
1470.79		3-*tert*butyl asymmetric CH bends
1465.56	*tert*butyl asymmetric CH bends	
1450.38	*tert*butyl asymmetric CH bends	
1437.84	*tert*butyl asymmetric CH bends	
1433.52	*tert*butyl asymmetric CH bends	
1397.07	N OOP deformations	
1385.76		*tert*butyl umbrella CH bends
1360.50	*tert*butyl umbrella CH bends	
1312.79	OOP Ar-H/NH bends	
1302.02		Ar-H bends
1283.56	ring deformations	*tert*butyl asymmetric CH bends
1279.32	Ar-H/ NH OOP bends	
1266.07		Ar-H OOP bends
1247.18		*tert*butyl CH wag
1233.26		Ar-H IP bends
1220.77		Ar-H IP bends
1213.28		Aniline CH bends, *tert*butyl CH wag, OH IP bend
1208.71	Bridge CH, NH OOP bends	
1200.61	*tert*butyl umbrella CH bends	
1198.10	*tert*butyl umbrella CH bends	
1170.26	*tert*butyl umbrella CH bends, NH bend. Bridge CH bend	
1165.01		Aldehyde CH bend
1160.02		Aniline CH Bend
1129.82	NH IP wag	
1119.00	NH/Ar-H IP wag	
1114.13	NH/Ar-H IP wag	
1052.05		*tert*butyl umbrella CH bends, Aniline ring deformation
1041.78	CH/NH wag, aniline ring deformation	
1020.46	NH IP wag	
983.19	*tert*butyl rotation	
972.05	Bridge CH OOP wag	
968.57	Bridge CH OOP wag	
930.43	aniline CH asymmetric OOP bend	
924.86		Aldehyde Ar-H OOP bend

913.92		Aldehyde Ar-H OOP wag
907.03	NH bend	
876.84	aldehyde CH OOP wag	
856.83		aldehyde CH OOP bend
826.53	Ar-H wag	
801.43	*tert*butyl symmetric CH bends	
744.74	aniline CH OOP bend	
728.41		aniline CH OOP bend
712.06	aniline CH OOP bend	
705.56		aniline CH OOP bend
647.72	aniline CH OOP bend	
645.42	C–I	C–I
609.96	ring deformations	
588.71	aldehyde ring deformations	
565.53	aldehyde ring deformations	
543.90		*tert*butyl asymmetric CH bends
522.94		*tert*butyl asymmetric CH bends
507.00		molecular deformations
499.70		molecular deformations
458.14	aldehyde ring deformation	
430.83		aniline CH OOP bend
410.13	aniline CH OOP bend	
382.89	*tert*butyl deformations	
360.24	*tert*butyl symmetric CH bends	
340.39		*tert*butyl asymmetric CH bends
327.12	*tert*butyl symmetric CH bends	
306.82	*tert*butyl asymmetric CH bends	
295.60	*tert*butyl rotations	
281.32	*tert*butyl rotations	
277.23		*tert*butyl asymmetric CH bends
272.68		*tert*butyl asymmetric CH bends
258.87	*tert*butyl asymmetric CH bends	
249.55	*tert*butyl rotations	
242.28	*tert*butyl rotations	
226.56	*tert*butyl rotations	
200.46	*tert*butyl rotations	
190.11		Molecular deformations
175.28	aniline ring rotation	
163.54	molecular deformations/aniline ring rotations	
140.63		*tert*butyl CH wag
129.75	Aldehyde ring deformation	
116.18		Aniline CH OOP bend
107.43		Aniline ring deformations
100.54	molecular rotations	
91.05		*tert*butyl rotations
86.71		*tert*butyl rotations
83.18	molecular rotations	
68.47		molecular rotations
64.24	molecular deformations	
58.93		*tert*butyl rotations

51.75		molecular deformations
46.94		molecular deformations
44.09	molecular deformations	
35.02	molecular deformations	
24.85	molecular deformations	

Table 128: Raman Spectrum peak assignments for compound 18 at 250 K

Position (cm^{-1})	**Keto Assignment**	**Enol Assignment**
1615.82		OH bend
1596.27	NH OOP bend	aniline ring deformation
1573.78		aniline ring deformations
1544.56	aniline ring deformations	
1468.76	*tert*butyl asymmetric CH bends	
1451.70	*tert*butyl asymmetric CH bends	
1436.96	*tert*butyl asymmetric CH bends	
1394.30	N OOP deformations	
1386.25		*tert*butyl umbrella CH bends
1362.88		*tert*butyl umbrella CH bends
1311.65	OOP Ar-H/NH bends	
1277.65	Ar-H/ NH OOP bends	
1265.15		Ar-H OOP bends
1245.91		*tert*butyl CH wag
1229.25		Ar-H IP bends
1219.42		Ar-H IP bends
1197.15	*tert*butyl umbrella CH bends	
1169.78	*tert*butyl umbrella CH bends, NH bend. Bridge CH bend	
1129.54	NH IP wag	
1117.84	NH/Ar-H IP wag	
1042.25	CH/NH wag, aniline ring deformation	
1019.47	NH IP wag	
981.65	*tert*butyl rotation	
971.13	Bridge CH OOP wag	
968.32	Bridge CH OOP wag	
930.91	aniline CH asymmetric OOP bend	
923.78		Aldehyde Ar-H OOP bend
913.04		Aldehyde Ar-H OOP wag
905.31	NH bend	
874.93	aldehyde CH OOP wag	
854.71		aldehyde CH OOP bend
825.51	Ar-H was	
801.77	*tert*butyl symmetric CH bends	
744.50	aniline CH OOP bend	
727.59		aniline CH OOP bend
712.51	aniline CH OOP bend	
704.85	aniline CH OOP bend	
645.18	C–I	C–I
609.98	ring deformations	
589.05	aldehyde ring deformations	
565.99	aldehyde ring deformations	
543.15		*tert*butyl asymmetric CH bends
523.82		molecular deformations
498.99		molecular deformations
492.69		molecular deformations
457.40	aldehyde ring deformation	

431.64		aniline CH OOP bend
410.43	aniline CH OOP bend	
383.51	*tert*butyl deformations	
359.27	*tert*butyl symmetric CH bends	
335.03		*tert*butyl symmetric CH bends
290.28	*tert*butyl rotations	
273.98		*tert*butyl asymmetric CH bends
246.32	*tert*butyl rotations	
186.87		Molecular deformations
156.02	molecular deformations/aniline ring rotations	
135.57		*tert*butyl CH wag
120.71	Aldehyde ring deformation	
88.28		*tert*butyl rotations
75.69		*tert*butyl rotations
52.95		molecular deformations
41.73		molecular deformations
35.92	molecular deformations	

Table 129: Raman Spectrum peak assignments for compound 18 at 100 K

Position (cm^{-1})	Keto Assignment	Enol Assignment
1616.14		OH bend
1598.11	NH OOP bend	aniline ring deformation
1585.69	NH OOP bend	
1576.21	aniline ring deformations	
1570.55		aniline ring deformations
1545.34	aniline ring deformations	
1470.60		3-*tert*butyl asymmetric CH bends
1465.63	*tert*butyl asymmetric CH bends	
1450.72	*tert*butyl asymmetric CH bends	
1437.85	*tert*butyl asymmetric CH bends	
1433.42		
1396.81	N OOP deformations	
1386.03		*tert*butyl umbrella CH bends
1360.43		*tert*butyl umbrella CH bends
1312.64	OOP Ar-H/NH bends	
1279.17	Ar-H/ NH OOP bends	
1265.98		Ar-H OOP bends
1247.01		*tert*butyl CH wag
1232.51		Ar-H IP bends
1220.74		Ar-H IP bends
1213.26		Aniline CH bends, *tert*butyl CH wag, OH IP bend
1208.50	Bridge CH, NH OOP bends	
1198.08	*tert*butyl umbrella CH bends	
1170.23	*tert*butyl umbrella CH bends, NH bend. Bridge CH bend	
1165.10		Aldehyde CH bend
1160.44		Aniline CH Bend
1129.76	NH IP wag	
1119.04	NH/Ar-H Ip wag	
1042.13	CH/NH wag, aniline ring deformation	
1020.26	NH IP wag	
982.99	*tert*butyl rotation	
971.81	Bridge CH OOP wag	
968.48	Bridge CH OOP wag	
930.45	aniline CH asymmetric OOP bend	
923.72		Aldehyde Ar-H OOP bend
913.69		Aldehyde Ar-H OOP wag
906.65	NH bend	
876.69	aldehyde CH OOP wag	
856.44		aldehyde CH OOP bend
826.44	Ar-H was	
801.58	*tert*butyl symmetric CH bends	
744.60	aniline CH OOP bend	
728.32		aniline CH OOP bend
711.96	aniline CH OOP bend	

705.54	aniline CH OOP bend	
645.29	C–I	C–I
609.88	ring deformations	
588.68	aldehyde ring deformations	
565.46	aldehyde ring deformations	
544.03		*tert*butyl asymmetric CH bends
499.61		molecular deformations
457.72	aldehyde ring deformation	
430.96		aniline CH OOP bend
410.07	aniline CH OOP bend	
382.97	*tert*butyl deformations	
360.01	*tert*butyl symmetric CH bends	
294.76	*tert*butyl rotations	
280.41	*tert*butyl rotations	
276.78		*tert*butyl asymmetric CH bends
272.09		*tert*butyl asymmetric CH bends
249.33	*tert*butyl rotations	
200.12	*tert*butyl rotations	
189.81		Molecular deformations
162.18	molecular deformations/aniline ring rotations	
139.58		*tert*butyl CH wag
128.55	Aldehyde ring deformation	
115.30		Aniline CH OOP bend
98.70	molecular rotations	
89.99		*tert*butyl rotations
85.18	molecular rotations	
62.77	molecular deformations	molecular deformations
43.34	molecular deformations	molecular deformations
34.87	molecular deformations	molecular deformations
24.27	molecular deformations	

SCXRD

Table 130: Crystallographic X-ray data for compound 18

Crystal system	Monoclinic		
Space group	P 2_1/c		
Z	4		
Crystal size (mm)	1 x 2 x 2 mm		
Radiation type	X-ray Copper	X-ray Molybdenum	
Wavelength (nm)	1.54184	0.71073	
Temperature (K)	**50 K**	**120**	**320**
Cell parameters (Å)	a= 17.24562(3) b=10.79770(2) c= 10.58243(2) α =90 β=99.939(4) γ=90	a= 17.22380(3) b=10.79000(3) c= 10.63670(3) α =90 β=99.681(3) γ=90	a= 17.25750(3) b=10.87340(3) c= 10.87750(3) α =90 β=97.270 γ=90
Cell volume (Å^3)	1941.02(2)	1948.625(3)	2024.728(15)
Total no. of reflections	7625	30765	32274
No of reflection with I/σ(I) > 2	3174	5631	4115
R(sigma)	0.065	0.074	0.065
Parameters/Restraints	218/0	217/0	245/0
R1, wR2, Goof	0.0657, 0.1837, 0.9921	0.040, 0.113, 0.992	0.0813, 0.1691, 0.9947
R1 after Fourier merging / No of unique reflections	0.07/ 3353	0.02/ 5637	0.045/ 5748
Scan type	2theataomeaga	2theataomeaga	2theataomeaga
Theta max	71.940	29.803	29.203
hkl limits	H min = -20 H max = 20 K min = -12 K max = 13 L min = -10 L max = 11	H min = -23 H max = 24 K min = -15 K max = 14 L min = -15 L max = 15	H min = -23 H max = 24 K min = -15 K max = 14 L min = -15 L max = 15

Table 131: Crystallographic data for compound 18 160 K to 280 K

Crystal system	Monoclinic			
Space group	$P\ 2_1/c$			
Z	4			
Crystal size (mm)	1 x 2 x 2 mm			
Radiation type	X-ray Molybdenum			
Wavelength (nm)	0.71073			
Temperature (K)	**280**	**240**	**200**	**160**
Cell parameters (Å)	a= 17.23390(3) b=10.85640(2) c= 10.84020(2) α =90 β=97.746(4) γ=90	a= 17.21760(3) b=10.83790(3) c= 10.79640(3) α =90 β=98.215(3) γ=90	a= 17.20680(4) b=10.82110(3) c= 10.75010(3) α =90 β=98.690 γ=90	a= 17.20504 (3) b=10.806350(3) c= 10.69730(3) α =90 β=99.188 γ=90
Cell volume ($Å^3$)	2009.673(13)	1993.964(18)	1978.65(2)	1962.885(18)
Total no. of reflections	32000	32000	31604	31301
No of reflection with I/σ(I) > 2	4469	4825	4883	5040
R(sigma)	0.060	0.074	0.035	0.048
Parameters/Restraints	245/0	236/0	245/0	245/0
R1, wR2, Goof	0.0727, 0.1761, 1.0524	0.0661, 0.1478, 1.0664	0.0569, 0.1538, 1.0769	0.0490, 0.1304, 0.9255
R1 after Fourier merging / No of unique reflections	0.041/ 5768	0.0237/ 5716	0.045/ 5669	0.033/ 5673
Scan type	2theataomeaga	2theataomeaga	2theataomeaga	2theataomeaga
Theta max	29.820	29.263	29.203	29.203
hkl limits	H min = -20 H max = 20 K min = -12 K max = 13 L min = -10 L max = 11	H min = -23 H max = 24 K min = -15 K max = 14 L min = -15 L max = 15	H min = -23 H max = 24 K min = -15 K max = 14 L min = -15 L max = 15	H min = -23 H max = 24 K min = -15 K max = 14 L min = -15 L max = 15

Neutron diffraction

Experiment 1

A suitable crystal of , N-(3,5-di-tert-butylsalicylidene)-2-iodoaniline for neutron diffraction, measuring approximately 4 x 3 x 2 mm, was grown via cooling of a concentrated ethanol solution at -20 °C. Diffraction data were collected using the single-crystal diffractometer SXD at the ISIS spallation neutron source (Oxfordshire, UK; Keen *et al.*, 2006) at 110 K. Time-of-flight Laue diffraction data were collected in a series of four orientations, with a counting time per orientation of ~3 h. The diffraction spots were initially indexed with the unit cells available from the x-ray measurements at the corresponding temperature. Bragg intensities were extracted using the 3D-profile fitting method implemented in the SXD2001 software (Gutmann, 2017) and corrected for Lorenz effect. No absorption correction for the shape of the crystal was applied. All structures were refined by full matrix least squares on F^2 using SHELXL (Sheldrick, 2008).

Refinement details

The molecule was refine anisotropically and showed no disorder across the molecule. However, to avoid some atoms going non-positive definite in the anisotropic refinement of the diagonal components were restrained to reasonable values.

Table 132: Crystallographic Neutron data for compound 18 experiment 1

Crystal system	Monoclinic
Space group	P 2_1/c
Z	4
Crystal size (mm)	4 x 3 x 2 mm
Radiation type	Neutron
Wavelength (nm)	0.35 – 6.5 Å
Temperature (K)	**110**
Cell parameters (Å)	a: 17.3247(3) b:10.8862(3) c: 10.7206(3) α/γ:90 β: 99.7141(5)
Cell volume (Å^3)	1992.92(3)
Total no. of reflections	3186
No of reflection with I/σ(I) > 4	3170
R(sigma)	0.0447
Parameters/Restraints	429/36
R1, wR2, Goof	0.082, 0.2135, 1.189
R1 after Fourier merging / No of unique reflections	0.0695/1808
Max resolution (Å)	0.57
Nuclear density Fourier difference residuals: $\Delta\rho_{max}$, $\Delta\rho_{min}$	1.05, -1.32

Experiment 2

A suitable crystal of , N-(3,5-di-tert-butylsalicylidene)-2-iodoaniline for neutron diffraction, measuring approximately 4 x 3 x 2 mm, was grown via cooling of a concentrated ethanol solution at -20 °C. Diffraction data were collected using the single-crystal diffractometer SXD at the ISIS spallation neutron source (Oxfordshire, UK; Keen *et al.*, 2006) at 110 K. Time-of-flight Laue diffraction data were collected in a series of four orientations, with a counting time per orientation of ~3 h. The diffraction spots were initially indexed with the unit cells available from the x-ray measurements at the corresponding temperature. Bragg intensities were extracted using the 3D-profile fitting method implemented in the SXD2001 software (Gutmann, 2017) and corrected for Lorenz effect. No absorption correction for the shape of the crystal was applied. All structures were refined by full matrix least squares on F^2 using SHELXL (Sheldrick, 2008)..

Table 133: Crystallographic Neutron data for compound 18 experiment 2

Crystal system	Monoclinic
Space group	P $2_1/c$
Z	4
Crystal size (mm)	4 x 3 x 2 mm
Radiation type	Neutron
Wavelength (nm)	0.35 – 6.5 Å
Temperature (K)	**10**
Cell parameters (Å)	a: 17.3199(3) b:10.8307(3) c: 10.6327(3) α/γ:90 β: 100.4781(5)
Cell volume (Å^3)	1992.92(2)
Total no. of reflections	3186
No of reflection with I/σ(I) > 4	3170
R(sigma)	0.0447
Parameters/Restraints	429/36
R1, wR2, Goof	0.0811,0.2111, 1.179
R1 after Fourier merging / No of unique reflections	0.0683/1808
Max resolution (Å)	0.57
Nuclear density Fourier difference residuals: $\Delta\rho_{max}$, $\Delta\rho_{min}$	1.05, -1.32

Compound 19

SCXRD

Table 134: Crystallographic X-ray data for compound 19

Crystal system	Monoclinic		
Space group	P 2_1/c		
Z	4		
Crystal size (mm)	0.289x0.130x0.047		
Radiation type	X-ray Copper		
Wavelength (nm)	1.54180		
Temperature (K)	**295**	**295**	**295**
Irradiated	**Yes**	**No**	**Yes - *in situ***
Cell parameters (Å)	a= 16.38472(3) b=10.94024(2) c= 11.55338(2) α /γ=90 β=93.462(1)	a= 16.39539(5) b=10.942100(4) c= 11.557460(2) α /γ=90 β=93.425(3)	a= 16.395258(1) b=10.942209(5) c= 11.448420(2) α /γ=90 β=93.413(2)
Cell volume (Å^3)	2067.196(3)	2069.704(2)	2070.105(3)
Total no. of reflections	10210	11558	11580
No of reflection with I/σ(I) > 2	2747	3154	3076
R(sigma)	0.139	0.084	0.078
Parameters/Restraints	217/0	221/2	217/0
R1, wR2, Goof	0.0707, 0.1708, 0.9199	0.1432, 0.3941, 1.6809	0.1455, 0.3968,1.6995
R1 after Fourier merging / No of unique reflections	0. 139, 3973	0.1513, 3999	0.065, 3980
Scan type	2THETA/OMEGA	2THETA/OMEGA	2THETA/OMEGA
Theta max	26.539	26.521	25.179
hkl limits	H min = -20 H max = 20 K min = 0 K max = 13 L min = 0 L max = 14	H min = -20 H max = 20 K min = 0 K max = 13 L min = 0 L max = 14	H min = -14 H max = 13 K min = 0 K max = 13 L min = 0 L max = 20

8.2 Spin Crossover complexes

Ni(Cyclam)I_2

Table 135: Crystallographic data of Ni(Cyclam)I_2 between 90 K and 295 K

Crystal system	Monoclinic				
Space group	P 2_1/c				
Z	4				
Crystal size (mm)	0.289x0.130x0.047				
Radiation type	X-ray Molybdenum				
Wavelength (nm)	0.71073				
Temperature (K)	**90**	**120**	**180**	**250**	**295**
Cell parameters (Å)	a= 7.50698(1) b=12.8422(5) c= 8.7959(4) α /γ=90 β=112.040(1)	a= 7.5130(4) b=12.8400(2) c= 8.80786(3) α /γ=90 β=112.037(2)	a= 7.52275(2) b=12.85109(2) c= 8.83270(3) α /γ=90 β=111.992(2)	a= 7.54918(3) b=12.8900(5) c= 8.85855(1) α /γ=90 β=111.919(2)	a= 7.53758(3) b=12.8800(5) c= 8.87787(2) α /γ=90 β=111.808(3)
Cell volume (Å^3)	786.0(2)	787.60(2)	791.77(2)	799.71(3)	800.22(3)
Total no. of reflections	5582	5614	5649	5722	11580
No of reflection with I/σ(I) > 2	1740	1741	1737	1716	1691
R(sigma)	0.0193	0.017	0.0188	0.0203	0.024
Parameters/Restraints	123/5	123/5	123/5	123/5	123/5
R1, wR2, Goof	0.0202, 0.0497, 0.9659	0.0188, 0.0465, 1.0226	0.0199, 0.0470, 0.9872	0.0222, 0.0502, 0.9766	0.0274, 0.0610, 0.9811
R1 after Fourier merging / No of unique reflections	0. 139, 1810	0. 017, 1813	0. 015, 1826	0. 015, 1843	0.065, 1853
Scan type	2theta/omega	2theta/omega	2theta/omega	2theta/omega	2theta/omega
Theta max	25.159	25.140	25.275	25.241	25.179
hkl limits	H min = -9 H max = 9 K min = 0 K max = 17 L min = 0 L max = 10	H min = -9 H max = 9 K min = 0 K max = 17 L min = 0 L max = 10	H min = -9 H max = 9 K min = 0 K max = 17 L min = 0 L max = 11	H min = -9 H max = 9 K min = 0 K max = 17 L min = 0 L max = 11	H min = -9 H max = 9 K min = 0 K max = 17 L min = 0 L max = 11

Table 136: Crystallographic data of Ni(Cyclam)I_2 between 300 K and 370 K

Crystal system	Monoclinic				
Space group	P 2_1/c				
Z	4				
Crystal size (mm)	0.289x0.130x0.047				
Radiation type	X-ray Molybdenum				
Wavelength (nm)	0.71073				
Temperature (K)	**300**	**320**	**340**	**360**	**370**
Cell parameters (Å^3)	a= 7.55513(1) b=12.89263(2) c= 8.86866(4) α /γ=90 β=111.802(3)	a= 7.55660(1) b=12.9008(1) c= 8.87350(3) α /γ=90 β=111.744(2)	a= 7.56203(1) b=12.91317(2) c= 8.88061(2) α /γ=90 β=111.709(6)	a= 7.56642(3) b=12.9275(1) c= 8.88684(3) α /γ=90 β=111.654(2)	a= 7.56760(3) b=12.9333(2) c= 8.89060(2) α /γ=90 β=111.619(4)
Cell volume (Å^3)	802.06(2)	803.49(2)	805.68(2)	807.92(3)	808.95(2)
Total no. of reflections	5251	5614	5275	5302	5299
No of reflection with I/σ(I) > 2	1644	1633	1623	1589	1588
R(sigma)	0.0267	0.0278	0.0297	0.0314	0.0308
Parameters/ Restraints	79/0	79/0	79/0	79/0	79/0
R1, wR2, Goof	0.0307, 0.0631, 0.9779	0.0327, 0.0645, 0.9839	0.0347, 0.666, 0.9805	0.0376, 0.0722, 0.9878	0.0373, 0.0675, 0.9806
R1 after Fourier merging / No of unique reflections	0. 021, 1855	0. 017, 1864	0. 021, 1867	0. 034, 1868	0.021, 1873
Scan type	2theta/omega	2theta/omega	2theta/omega	2theta/omega	2theta/omega
Theta max	25.031	25.014	25.281	25.258	25.157
hkl limits	H min = -9 H max = 9 K min = 0 K max = 17 L min = 0 L max = 11	H min = -9 H max = 9 K min = 0 K max = 17 L min = 0 L max = 11	H min = -9 H max = 8 K min = 0 K max = 17 L min = 0 L max = 11	H min = -9 H max = 8 K min = 0 K max = 17 L min = 0 L max = 11	H min = -9 H max = 8 K min = 0 K max = 17 L min = 0 L max = 11

Table 137: Crystallographic data of Ni(Cyclam)I_2 between 380 K and 410 K and 390 cooling

Crystal system	Monoclinic				
Space group	P 2_1/c				
Z	4				
Crystal size (mm)	0.289x0.130x0.047				
Radiation type	X-ray Molybdenum				
Wavelength (nm)	0.71073				
Temperature (K)	**380**	**390**	**400**	**410**	**390-Cooling**
Cell parameters (Å)	a= 7.56922(2) b=12.94119(3) c= 8.89392(4) α /γ=90 β=111.584(4)	a= 7.57150(2) b=12.95060(1) c= 8.89637(3) α /γ=90 β=111.554(2)	a= 7.57158(4) b=12.95387(3) c= 8.89982(2) α /γ=90 β=111.524(2)	a= 7.57593(2) b=12.9665(2) c= 8.90587(2) α /γ=90 β=111.480(3)	a= 7.57400(1) b=12.95345(3) c= 8.90041(2) α /γ=90 β=111.544(3)
Cell volume (Å^3)	810.11(2)	811.33(2)	821.03(2)	814.09(3)	812.21(2)
Total no. of reflections	5316	5328	5349	5359	5336
No of reflection with I/σ(I) > 2	1558	1557	1525	1503	1548
R(sigma)	0.0333	0.0330	0.0342	0.0352	0.0342
Parameters/Restraints	79/0	79/0	79/0	79/0	79/0
R1, wR2, Goof	0.0408, 0.0761, 0.9763	0.0414, 0.0716, 0.9799	0.0431, 0.0775, 0.9752	0.0458, 0.0791, 0.9731	0.0426, 0.0776, 0.9748
R1 after Fourier merging / No of unique reflections	0.032, 1874	0. 021, 1881	0. 022, 1880	0. 023, 1891	0.021, 1882
Scan type	2theta/omega	2theta/omega	2theta/omega	2theta/omega	2theta/omega
Theta max	25.143	25.128	25.121	25.096	25.118
hkl limits	H min = -9 H max = 8 K min = 0 K max = 17 L min = 0 L max = 11	H min = -9 H max = 8 K min = 0 K max = 17 L min = 0 L max = 11	H min = -9 H max = 8 K min = 0 K max = 17 L min = 0 L max = 11	H min = -9 H max = 8 K min = 0 K max = 17 L min = 0 L max = 11	H min = -9 H max = 8 K min = 0 K max = 17 L min = 0 L max = 11

Table 138: Crystallographic data of Ni(Cyclam)I_2 between 380 K and 340 K upon cooling

Crystal system	Monoclinic		
Space group	P 2_1/c		
Z	4		
Crystal size (mm)	0.289x0.130x0.047		
Radiation type	X-ray Molybdenum		
Wavelength (nm)	0.71073		
Temperature (K)	**380- Cooling**	**360- Cooling**	**340-Cooling**
Cell parameters (Å)	a= 7.57248(3) b=12.94523(4) c= 8.89687(3) α /γ=90 β=111.582(2)	a= 7.56887(5) b=12.92987(3) c= 8.88869(4) α /γ=90 β=111.639(5)	a= 7.56316(2) b=12.90416(3) c= 8.87003(2) α /γ=90 β=111.788(2)
Cell volume (Å^3)	810.99(7)	808.58(2)	803.84(3)
Total no. of reflections	5335	5326	5255
No of reflection with I/σ(I) > 2	1554	1582	1596
R(sigma)	0.0328	0.0317	0.0317
Parameters/Restraints	79/0	79/0	79/0
R1, wR2, Goof	0.0406, 0.0736, 0.9715	0.0383, 0.0691, 0.9786	0.0372, 0.0855, 0.9735
R1 after Fourier merging / No of unique reflections	0.021, 1878	0. 022, 1875	0. 027, 1857
Scan type	2THETA/OMEGA	2THETA/OMEGA	2THETA/OMEGA
Theta max	25.132	25.159	25.275
hkl limits	H min = -9 H max = 8 K min = 0 K max = 17 L min = 0 L max = 11	H min = -9 H max = 8 K min = 0 K max = 17 L min = 0 L max = 11	H min = -9 H max = 8 K min = 0 K max = 17 L min = 0 L max = 11

Table 139: Crystallographic data of Ni(Cyclam)I_2 polymorph 2 at 298 K

Crystal system	Orthorhombic	
Space group	P 2_1 2_1 2_1	
Z	4	
Crystal size (mm)	0.289x0.050x0.047	
Radiation type	X-ray Molybdenum	
Wavelength (nm)	0.71073	
Temperature (K)	**298**	**298**
Cell parameters (Å)	a= 9.83437(3) b=12.94616(2) c= 13.06151(2) α /γ/β= 90	a= 9.81216(3) b=12.93073(4) c= 13.04597(2) α /γ/β= 90
Cell volume (Å^3)	1662.956(3)	1655.252(2)
Total no. of reflections	6766	6023
No of reflection with I/σ(I) > 2	2603	2338
R(sigma)	0.0824	0.0934
Parameters/Restraints	154/0	154/0
R1, wR2, Goof	0.1011, 0.2194, 0.9064	0.1119, 0.2452, 0.8481
R1 after Fourier merging / No of unique reflections	0. 048, 3616	0. 081, 3552
Scan type	2THETA/OMEGA	2THETA/OMEGA
Theta max	25.288	25.238
hkl limits	H min = -13 H max = 12 K min = 0 K max = 16 L min = 0 L max = 17	H min = -12 H max = 12 K min = 0 K max = 16 L min = 0 L max = 17

$Co(PF)_6 \cdot 6H_2O$

Table 140: $Co(PF)_6 \cdot 6H_2O$ phase change upon cooling

Crystal system	Rhombohedral	Monoclinic
Space group	R $\bar{3}$ m	P 2_1/c
Z	36	4
Crystal size (mm)	0.5x0.2x0.1	
Radiation type	X-ray Molybdenum	
Wavelength (nm)	0.71073	
Temperature (K)	**295**	**150**
Cell parameters (Å)	a= 9.3529(1) b=9.3529(1) c= 9.7437(3) α /γ= 90 β = 120.0(1)	a= 6.4447(2) b=9.4785(5) c= 8.4061(8) α /γ= 90 β = 99.342(2)
Cell volume (Å^3)	738.159(3)	506.694(2)
Total no. of reflections	1847	3216
No of reflection with I/σ(I) > 2	243	1000
R(sigma)	0.1402	0.0822
Parameters/Restraints	20/0	91/12
R1, wR2, Goof	0.0896, 0.2383, 0.9626	0.0770, 0.2075, 0.9898
R1 after Fourier merging / No of unique reflections	0. 015, 244	0. 024, 1122
Scan type	2THETA/OMEGA	2THETA/OMEGA
Theta max	25.056	25.238
hkl limits	H min = -10 H max = 0 K min = 0 K max = 11 L min = 0 L max = 12	H min = -18 H max = 8 K min = 0 K max = 12 L min = 0 L max = 11